



T.C.
ÇANAKKALE ONSEKİZ MART ÜNİVERSİTESİ
LİSANSÜSTÜ EĞİTİM ENSTİTÜSÜ

***CANAKKALE ONSEKİZ MART UNIVERSITY
JOURNAL OF ADVANCED
RESEARCH IN NATURAL AND
APPLIED SCIENCES***



ISSN 2757-5195

Journal of Advanced Research in Natural and Applied Sciences (abbreviated as J. Adv. Res. Nat. Appl. Sci. or JARNAS) is an international, peer-reviewed, and open-access journal.

J. Adv. Res. Nat. Appl. Sci. is a science journal focusing on new science theories or their applications.

JARNAS was founded in 2015, and its first issue was published on 29 Dec 2015.

Language: As of 2024, JARNAS accepts contributions in American English only.

Frequency: 4 Issues Per Year

Publication Dates: March, June, September, and December

ISSN: 2757-5195

Editor-in-Chief: [Hüseyin Çavuş](#)

Email: jarnas.journal@gmail.com

Publisher: Çanakkale Onsekiz Mart University

APC: JARNAS incurs no article processing charges.

Review Process: Double-Blind Peer Review

DOI Numbers: The published papers are assigned DOI numbers.

Journal Boards

Editor-in-Chief

[Hüseyin Çavuş](#)

h_cavus@comu.edu.tr

Çanakkale Onsekiz Mart University, Türkiye

Editors

[Ali Bilici](#)

alibilici@comu.edu.tr

Çanakkale Onsekiz Mart University, Türkiye

[Fahri Aliçavuş](#)

fahrialicavus@comu.edu.tr

Çanakkale Onsekiz Mart University, Türkiye

[Nurcihan Hacıoğlu Doğru](#)

nhacioglu@comu.edu.tr

Çanakkale Onsekiz Mart University, Türkiye

[Serdar Enginođlu](#)

serdarenginoglu@gmail.com

Çanakkale Onsekiz Mart University, Türkiye

[Aykut Or](#)

aykutor@comu.edu.tr

Çanakkale Onsekiz Mart University, Türkiye

[Burcu Mestav](#)

burcumestav@comu.edu.tr

Çanakkale Onsekiz Mart University, Türkiye

[Alper Sađlık](#)

alpersaglik@gmail.com

Çanakkale Onsekiz Mart University, Türkiye

[Samet Memiş](#)

samettmemis@gmail.com

Bandırma Onyedi Eylül University, Türkiye

[Volkan Eskizeybek](#)

veskizeybek@comu.edu.tr

Çanakkale Onsekiz Mart University, Türkiye

[Ayça Aydođdu](#)

ayca.aydogdu@comu.edu.tr

Çanakkale Onsekiz Mart University, Türkiye

[Özgür Turay Kaymakçı](#)

okaymakci@comu.edu.tr

Çanakkale Onsekiz Mart University, Türkiye

[Mehmet Ali Yücel](#)

aliyucel@comu.edu.tr

Çanakkale Onsekiz Mart University, Türkiye

[Murat Efgan Kibar](#)

efgankibar@kocaeli.edu.tr
Kocaeli University University, Türkiye

[Mehmet Özgür](#)

mehmetozgur@comu.edu.tr
Çanakkale Onsekiz Mart University, Türkiye

[Deniz Şanlıyüksel Yücel](#)

denizsyuksel@comu.edu.tr
Çanakkale Onsekiz Mart University, Türkiye

[Bulut Ozan Ceylan](#)

bceylan@bandirma.edu.tr
Bandırma Onyedli Eylül University, Türkiye

[Abdulkadir Atalan](#)

abdulkadiratalan@gmail.com
Çanakkale Onsekiz Mart University, Türkiye

Section Editors

Mathematics

[Mehmet Gümüş](#), Çanakkale Onsekiz Mart University, Türkiye

[Tuğçe Aydın](#), Çanakkale Onsekiz Mart University, Türkiye

[Ebu Talib Çelik](#), Çanakkale Onsekiz Mart University, Türkiye

[Gönül Selin Savaşkan](#), Çanakkale Onsekiz Mart University, Türkiye

[Hakan Şahin](#), Bursa Teknik University, Türkiye

[Erdal Ulualan](#), Kütahya Dumlupınar University, Türkiye

[Muhammad Riaz](#), Punjab University, Pakistan

Physics

[Doğukan Taşer](#), Çanakkale Onsekiz Mart University, Türkiye

[Emrah Sarıca](#), Başkent University, Türkiye

[Hyo-Seob Kim](#), Korea Institute of Industrial Technology, Korea

[Neslihan Alan](#), İstanbul University, Türkiye

Biology

[Çiğdem Gül](#), Çanakkale Onsekiz Mart University, Türkiye

[Nurşen Çördük](#), Çanakkale Onsekiz Mart University, Türkiye

[Ersin Karabacak](#), Çanakkale Onsekiz Mart University, Türkiye

[Sefer Demirbaş](#), Namık Kemal University, Türkiye

[Tuğba Ergül Kalaycı](#), Recep Tayyip Erdoğan University, Türkiye

[Abdelkarim Laatamna](#), University of Djelfa, Algeria

Chemistry

Serkan Karakaya, Çanakkale Onsekiz Mart University, Türkiye

[Gülbin Kurtay](#), Hacettepe University, Türkiye

[Arianit A. Reka](#), University of Tetova, Republic of North Macedonia

Information and Computing Sciences

[Engin Şahin](#), Çanakkale Onsekiz Mart University, Türkiye

[Sait Can Yücebaş](#), Çanakkale Onsekiz Mart University, Türkiye

[Uğur Erkan](#), Karamanoğlu Mehmetbey University, Türkiye

[Serhat Kılıçarslan](#), Bandırma Onyediy Eylül University, Türkiye

[Mehmet Akif Bülbül](#), Kayseri University, Türkiye

[Bharat Garg](#), Thapar Institute of Engineering and Technology, India

Chemical Engineering

[Filiz Uğur Nigiz](#), Çanakkale Onsekiz Mart University, Türkiye

[Hasan Arslanoğlu](#), Çanakkale Onsekiz Mart University, Türkiye

[Derya Ünlü](#), Bursa Teknik University, Türkiye

Meltem Yıldız, Kocaeli Üniversitesi, Türkiye

Özge Kerkez Kuyumcu, Marmara Üniversitesi, Türkiye

Environmental Engineering

[Simgе Taner Çankaya](#), Kocaeli University, Türkiye

Elif Durna Pişkin, Kocaeli University, Türkiye

Food Engineering

Neşe Yılmaz Tuncel, Çanakkale Onsekiz Mart University
Dilvin İpek, Çanakkale Onsekiz Mart University

Maritime Engineering

[Oğuzhan Der](#), Bandırma Onyedi Eylül University, Türkiye
[Cağlar Karatug̃](#), İstanbul Technical University, Türkiye
[Tayfun Uyanık](#), İstanbul Technical University, Türkiye
[Onur Akdaş](#), Dokuz Eylül University, Türkiye
[Pelin Erdem](#), Tyne Coast College, United Kingdom
[Mina Tadros](#), Newcastle University, United Kingdom

Fluid Mechanics and Thermal Engineering

[Hatice Sinem Şaş Çaycı](#), Sabancı University, Türkiye

Material Engineering, Mechanical Engineering

[Bircan Haspulat Taymaz](#), Konya Technical University, Türkiye
[Okan Demir](#), Konya Technical University, Türkiye

Manufacturing and Industrial Engineering

[Murat Koyunbakan](#), Kütahya Dumlupınar University, Türkiye

Control Engineering, Mechatronics and Robotics

[Yusuf Şahin](#), Niğde Ömer Halisdemir University, Türkiye

Mechanical Engineering

[Emine Feyza Şükür](#), Samsun University, Türkiye
Adem Yar, Bingöl Üniversitesi, Türkiye

Automotive Engineering

[Ferhat Yıldırım](#), Çanakkale Onsekiz Mart University, Türkiye

Nanotechnology

[Adem Yar](#), Bingöl University, Türkiye

Geomatics Engineering

[Ali Melih Bařaraner](#), Yıldız Teknik Üniversitesi, Türkiye

[Atınç Pırtı](#), Yıldız Teknik Üniversitesi, Türkiye

[İsmail Rakip Karas](#), Karabük University, Türkiye

[Şükran Yalpir](#), Konya Technical University, Türkiye

[Osman Sami Kırtılođlu](#), İzmir Katip Çelebi Üniversitesi, Türkiye

Civil Engineering

[İlknur Dalyan](#), Çanakkale Onsekiz Mart University, Türkiye

[Fevziye Ayça Saraçođlu](#), Çanakkale Onsekiz Mart University, Türkiye

Fatih Yonar, Çanakkale Onsekiz Mart University, Türkiye

[Selen Aktan](#), Çanakkale Onsekiz Mart University, Türkiye

[Muhammet Gökhan Altun](#), Çanakkale Onsekiz Mart University, Türkiye

[Erdiñ Keskin](#), Kırklareli University, Türkiye

[Rasoul Daneshfaraz](#), University of Maragheh, İran

Geological and Mining Engineering

[İsmail Onur Tunc](#), Çanakkale Onsekiz Mart University, Türkiye

[Şebnem Önder](#), Çanakkale Onsekiz Mart University, Türkiye

[Mustafa Çınar](#), Çanakkale Onsekiz Mart University, Türkiye

[Alper Baba](#), İzmir Institute of Technology, Türkiye

Built Environment and Design

[Pelin Fırat ÖRS](#), Çanakkale Onsekiz Mart University, Türkiye

Tutku AK, Çanakkale Onsekiz Mart University, Türkiye

[Elif SAĞLIK](#), Çanakkale Onsekiz Mart University, Türkiye

[Ali Tolga ÖZDEN](#), Çanakkale Onsekiz Mart University, Türkiye

Electrical and Electronics Engineering

[Muzaffer Yücel](#), Çanakkale Onsekiz Mart University, Türkiye

[Muharrem Mercimek](#), Yıldız Technical University, Türkiye

[Muhammed Ali Nur Öz](#), Sakarya University of Applied Sciences, Türkiye

Statistics

[Berrin GÜLTAY](#), Çanakkale Onsekiz Mart University, Türkiye

[Canan Güneş](#), Çanakkale Onsekiz Mart University, Türkiye

[Hande Konşuk Ünlü](#), Hacettepe University, Türkiye

[Kadir Karakaya](#), Selçuk University, Türkiye

[Aynur Yonar](#), Selçuk University, Türkiye

Occupational Health and Safety

[Gülçin Özcan Ateş](#), Çanakkale Onsekiz Mart University, Türkiye

Statistics Editor

[Burcu Mestav](#)

burcumestav@comu.edu.tr

Çanakkale Onsekiz Mart University, Türkiye

Language Editor

Öznur Cengiz Çeliker

oznurcengiz@comu.edu.tr

Çanakkale Onsekiz Mart University, Türkiye

[Mehmet Yıldız](#)

mehmetyildiz@comu.edu.tr

Çanakkale Onsekiz Mart University, Türkiye

Layout Editors

[Burak Arslan](#)

tburakarslan@gmail.com

Çanakkale Onsekiz Mart University, Türkiye

Kenan Sapan

kenannsapan@gmail.com

Çanakkale Onsekiz Mart University, Türkiye

Production Editors

[Deniz Fidan](#)

fidanddeniz@gmail.com

Çanakkale Onsekiz Mart University, Türkiye

[Rabia Özpınar](#)

rabiaozpınar@gmail.com

Bandırma Onyedi Eylül University, Türkiye

CONTENTS

Research Article **Page : 493–505**

1. A Comprehensive Monte Carlo Simulation Study on Multiple Comparison Methods after ANOVA

Hanife Avcı , Osman Dağ

Research Article **Page : 506–519**

2. Modifiye DMPD Yöntemi ile Süperoksit Radikali Süpürme Aktivitesi ve Toplam Antioksidan Kapasite Tayini

Ferda Dondurmacioğlu

Research Article **Page: 520–529**

3. A Criticism of the Kyoto Protocol with an Objective Approach

Sertaç Atabey , Z. Fuat Toprak

Research Article **Page : 530–541**

4. Lipschitz Operators Associated with Weaklypp-Compact and Unconditionallypp-Compact Sets

Ayşegül Keten Çopur , Ramazan İnal

Research Article **Page : 542–559**

5. Optimization of Low-Calorific Coal Application at Different Loads in 600 MW Supercritical Thermal Power Plant with the PROMETHEE-GAIA Method

Aykut Emir , Ali Riza Motorcu , Hülya Demirören

Research Article **Page : 560–570**

6. Blood Vessel Segmentation and Classification of Diabetic Retinopathy with Machine Learning-Based Ensemble Model

Cihan Akyel , Bünyamin Ciyilan

Research Article **Page : 571–586**

7. Evaluation of Recombinant Antibody Production Efficiency in CHO Cells with Sleeping Beauty Transposon Vector System

Pelin Kolçak Yaşlı , Seda Kulabaş , Evren Doruk Engin

Research Article **Page : 587–600**

8. Particle Shape-Based Evaluation of the Leaching of Sphalerite Ore in Dilute Acid Solutions

Tuğba Deniz Tombal , İlgin Kurşun Ünver , Mert Terzi

Research Article **Page : 601–613**

9. Seismic Risk Evaluation of Existing Reinforced Concrete Buildings: A Case Study for Çanakkale-Türkiye

Muhammed Benek , Selen Aktan

Research Article **Page : 614–626**

10. Cost and Benefit Analysis of Different Buildings Through Reuse of Treated Greywater

Elif Ayyüce Kılınç , Asude Hanedar , Aysegül Tanık , Erdem Görgün

Research Article **Page : 627–639**

11. Effects of Pervari Honey from Türkiye on Proliferation, Oxidative Stress, and Apoptosis of Human Breast Cancer Cells

Muazzez Derya Andeden , Pınar Altın Çelik , Mustafa Çakır , Ramazan Üzen , Hamiyet Altuntaş

Research Article **Page : 640–658**

12. Composite Sand–Clay Infrastructural Soil Fills: Characteristic Consolidation and Hydraulic Properties

Tanay Karademir , Burcu Dışkaya

Research Article **Page : 659–668**

13. Effects of Pleurotus Eryngii (DC.) Qué. Mushroom Extracts on Cell Proliferation in Breast and Colon Cancer Cell Lines

Ferah Cömert Önder , Gülce Davutlar , Alper Önder , Hakan Allı , Mehmet Ay

Research Article **Page : 669–683**

14. Multi-Focus Image Fusion Using Energy Valley Optimization Algorithm

Harun Akbulut

Research Article **Page : 684–701**

15. Multi-Band Optical Variability of Blazar 1ES 2344+514 on Diverse Time-Scales

Aykut Özdönmez

Research Article **Page : 702–725**

16. Unlocking Cognitive Horizons by Exploring the Influence of Maps on Primary School Pupils: An Examination Conducted in North Macedonia

Edmond Jonuzi , Hüseyin Zahit Selvi

Research Article **Page : 726–734**

17. Effect of Sound Absorption on Noise Reduction in the Automotive Industry

Muammer Yaman , Cüneyt Kartay

Research Article **Page : 735-746**

18. AeroRunway: Diverse Weather and Time of Day Aerial Dataset for Autonomous Landing Training

Nesil Bor , Nergis Pervan Akman , Ali Berkol

Research Article **Page : 747-760**

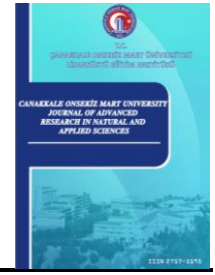
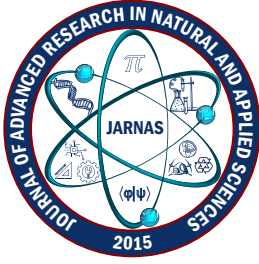
19. An Overview of Traditional and Next-Generation Earthquake Early Warning Systems

Süleyman Tunç , Berna Tunç , Deniz Çaka , Emrah Budakoğlu

Research Article **Page : 761-770**

20. Ergonomic Risk Analysis of Working Postures for a Textile Factory Worker

Güler İmamoğlu , Bestem Esi



A Comprehensive Monte Carlo Simulation Study on Multiple Comparison Methods after ANOVA

Hanife Avcı¹ , Osman Dağ^{2,*} 

^{1,2}Department of Biostatistics, Faculty of Medicine, Hacettepe University, Ankara, Türkiye

Article Info

Received: 31 Jan 2024

Accepted: 05 May 2024

Published: 30 Sep 2024

Research Article

Abstract – Multiple comparison methods are applied to control the type I error rate at the nominal level. In this study, we investigate the performance of multiple comparison methods after analysis of variance (ANOVA) is implemented under different conditions. We include Bonferroni, Holm, Hochberg, Hommel, Benjamini-Hochberg (BH), and Benjamini-Yekutieli (BY) correction methods. Monte-Carlo simulation study is applied to assess their performances under different patterns, including sample size and group number combinations. Wide inferences are drawn on considered methods, and suggestions are provided for selecting appropriate methods. Moreover, the methods are implemented on three different types of real-life data sets to emphasize the importance of these correction methods in the research.

Keywords – ANOVA, Monte Carlo simulation, pairwise comparison, type I error rate, variance homogeneity

1. Introduction

Testing equality of means is a general process in many data applications. In this study, we compare multiple comparison methods after ANOVA concerning controlling the type I error rate (α) at its nominal level. There exist many multiple comparison tests in the literature [1]. We include Bonferroni [2], Holm [3], Hommel [4], Hochberg [5], Benjamini-Hochberg (BH) [6], and Benjamini-Yekutieli (BY) [7] comparison methods in this study. These methods adjust the estimated type I error rate using the number of hypotheses tested. The number of hypotheses is specified by the number of groups compared in ANOVA. For instance, the total number of hypotheses becomes $k(k - 1)/2$ when the number of groups compared within ANOVA is k . Each pair in the comparison for testing the hypotheses is called a family. The type I error rate is called the family-wise error rate (FWER) since each family is compared separately [8].

Multiple comparison methods are used in various fields. Bender and Lange [9] discussed adjustment methods for multiple comparisons in medical and epidemiological studies. Westphal and Troendle [10] proposed multiple comparison methods based on resampling that control FWER. They noted that the methods could be applied specifically to gene expression data but more generally to multivariate and multigroup data. Blakesley et al. [11] proposed the Hommel and Hochberg methods for mildly correlated measures to increase power while controlling type I errors in neuropsychological data sets. Felix and Menezes [12] showed that BH correction provided the best type I error rate and the second strongest correction by varying the sample size, sample distribution, and degree of variability. Staffa and Zurakowski [13] suggested that surgeons use multiple comparison methods, including Bonferroni, Tukey, Scheffe, Holm, and Dunnett while planning clinical or

¹hanife.avci@hacettepe.edu.tr; ²osman.dag@hacettepe.edu.tr (Corresponding Author)

research studies. Their study discussed the results of each approach for controlling FWER on pediatric surgical research data.

In a study conducted by Dimitriev et al. [14], the Bonferroni method was used to investigate the effects of stress on heart rate and heart rate variability (HRV) measurements. Participants were divided into three groups according to baseline HRV (<25th percentile, 25th -75th percentile, and >75th percentile). Stress-related changes were compared in HRV groups. Kharola et al. [15] criticized the work done by Dimitriev et al. [14] concerning using multiple comparison methods. They stated that the Holm method was more powerful than the Bonferroni method. In our simulation study, this design fits the one extreme pattern with three groups and a sample size between 50 and 100. The findings state that the Holm method has a type I error rate larger than its nominal level, while Bonferroni holds the nominal level. That is, the Holm method may find a difference when the difference is not real.

Musicus et al. [16] assessed the effects of text-based alerts, health picture alerts, sugar picture alerts, and control on parents' beverage choices for their children in a virtual convenience store. They used the Holm method for multiple comparisons after ANOVA. In our simulation study, this study design approximately fits the equal N pattern with four groups and a large sample size. Our findings reveal that the Holm method has a type I error rate larger than its nominal level, while Bonferroni holds the nominal level. In other words, the Holm technique might detect a difference when no one exists.

Generally, the researchers are unaware of choosing an appropriate method when performing multiple comparisons. However, this situation leads to misleading serious consequences. Therefore, the researchers should consider the number of groups, the sample size, and the pattern of sample sizes to reduce the risk of misleading consequences while conducting multiple comparison methods. No study compares multiple comparison tests' type I error rates in different scenarios, such as sample size, number of groups, and other sample size designs. Therefore, this study is essential to give recommendations for the applied researchers on selecting appropriate multiple comparison methods under various scenarios.

This study compares multiple comparison methods' type I error rates at different sample sizes, sample size patterns (under equal N, progressive N, and one extreme scenario), and the number of groups after ANOVA. Therefore, a comprehensive Monte-Carlo simulation study is conducted to compare multiple comparison tests' type I error rates.

This study has some limitations since ANOVA is conducted under certain assumptions. These assumptions of ANOVA are independence of observations within and between groups, normality (i.e., k samples are drawn randomly from a normal distribution), and variance homogeneity (i.e., k populations have identical variances).

The sections of the paper are organized as follows: Section 2 introduces the multiple comparison methods in chronological order. Section 3 provides the Monte-Carlo simulation study and its results. Section 4 presented the implementation of the pairwise comparison methods following ANOVA in R. Finally, the paper concludes with a summary of the main findings and a discussion of the results of similar studies.

2. Materials and Methods

This section includes six multiple comparison methods commonly used in the literature.

2.1. Bonferroni Correction

Bonferroni correction is one of the most widely used approaches for multiple comparisons [2]. The Bonferroni multiple comparison test is conservative when the large sample size and the number of pairwise comparisons increases [3]. With a pre-specified significance level (α) and the number of hypotheses tested (m), the adjusted significance level is calculated as follows:

$$\alpha'_{(i)} = \frac{\alpha}{m} \quad (2.1)$$

2.2. Holm Correction

The less conservative Holm method is proposed after the Bonferroni correction [3]. Holm correction is more powerful than Bonferroni correction [17]. Holm method controls the false discovery rate (FDR). In the Holm method, the p-value for each hypothesis is arranged from least to greatest. For the i^{th} ordered hypotheses $H_{(i)}$, the formula is given in (2.2) for the type I error rate:

$$\alpha'_{(i)} = \frac{\alpha}{m - i + 1} \quad (2.2)$$

In this part, we include an example to clarify Holm's correction. For instance, we have three groups to compare with ANOVA and obtain statistically significant results. After that, we apply multiple comparison methods to adjust estimated type I error rates. We obtain p-values of 0.002, 0.010, and 0.035 (given in order from smallest to largest) for hypotheses I-III, respectively. For the smallest p-value (0.002), we obtain the nominal type I error rate for the comparison as follows: $\alpha'_{(i)} = \frac{\alpha}{m-i+1} = \frac{0.05}{3-1+1} \cong 0.0167$. We compare the smallest p-value (0.002) with its nominal rate (0.0167). The hypotheses are rejected since the p-value of 0.002 is smaller than 0.0167. The following steps are similar to the other hypotheses and α' 's are estimated as 0.0167, 0.025, and 0.05, respectively.

2.3. Hochberg Correction

Like the Holm method, Hochberg correction uses the same formula to calculate the associated significance levels [5]. Hochberg's multiple comparison method, controlling FDR, is more powerful than the Holm method [18]. Both multiple comparison methods compare ordinal p-values with the same set of critical values. The algorithm of the method is the same as within the Holm method, except that the p-values are ordered from largest to smallest [18]. Thus, the Hochberg method rejects a hypothesis that results in all hypotheses being rejected (2.2).

2.4. Hommel Correction

Simes revised the Bonferroni method and proposed a new multiple comparison method by combining all m hypotheses [19]. However, Hommel extended this new method to test each hypothesis (Hommel 1988) since Simes method cannot be used to evaluate each hypothesis alone. The decisions for the individual hypotheses can be performed in the following simpler way: $j = \max\{i \in \{1, 2, \dots, m\} : p_{(m-i+k)} > \frac{ka}{i} \text{ for } k \in \{1, 2, \dots, i\}\}$. If the maximum value does not exist, reject all H_i ($i \in \{1, 2, \dots, m\}$), otherwise, reject all H_i with $p_i \leq \alpha/j$. It is not easy to calculate adjusted p-values with the Hommel method. It can be easily calculated with the pair comp function in the oneway tests R package.

2.5. Benjamini-Hochberg (BH) Correction

Benjamini and Hochberg [6] developed a method called BH (known as false discovery rate, FDR) to control FDR. It is often preferred when the number of hypotheses is large. BH multiple comparison method is preferred since it is simpler than other methods. First, m hypotheses are arranged in order from largest to smallest according to their p-values ($i \in \{1, 2, \dots, m\}$). The q value is the upper bound of FDR (e.g., $q = 0.05$). BH critical value of each p-value is calculated using the $\frac{i}{m} q$ formula. p_i is the p-value related to the H_i hypotheses, and k is the largest I:

$$k = \max\left\{p_i \leq \frac{i}{m} q\right\} \quad (2.4)$$

The p values are compared with the critical BH value. The largest p-value that is less than the critical BH value is found. All p-values under this largest value are considered statistically significant.

2.6. Benjamini and Yekutieli (BY) Correction

Benjamini and Yekutieli proposed a more conservative multiple comparison method than BH to control FDR [7]. BY method is similar to the BH method. However, the way of finding k is different from the BH method.

$$k = \max \left\{ i: p_{(i)} \leq \frac{i}{m} \tilde{q}, \tilde{q} = \frac{q}{\sum_{i=1}^m \frac{1}{i}} \right\} \quad (2.5)$$

where the q value is an upper bound of FDR. Unlike other multiple comparison methods, the BY correction method considers the dependency of hypotheses. The difference between BH and BY is the dependency structure. Benjamini and Yekutieli proved that the estimator is valid under some forms of the dependency structure.

3. Results

This study compares the type-I error rates of six correction methods with the Monte Carlo simulation study. Moreover, add the results obtained without correction to emphasize the importance of multiple comparison methods.

3.1. Simulation Design

Monte Carlo simulation is applied to show the performances of these tests for scenarios where normality and homogeneity of variance assumptions are met. The algorithm of the simulation study is planned as follows.

- i.* Random samples are generated from a normal distribution with a mean of 0 and a standard deviation of 1 as much as the number of groups.
- ii.* The number of groups is set to 3 - 4 (small), 5 - 6 (medium), and 7 - 10 (large).
- iii.* The sample sizes for each group are 10, 20, 30, 40, 50, and 100.
- iv.* The sample size patterns are specified as equal N, progressive N, and one extreme scenario is given in Table 1.

All steps are repeated 10,000 runs, and type I errors are calculated. After calculating the type I error for each pairwise comparison, we combine the type I error rates as given in Equation 6.

$$\hat{\alpha}_n = 1 - \prod_{i=1}^h (1 - \hat{\alpha}_{i,n}) \quad (3.1)$$

where $h = \binom{k}{2}$ and k is the number of groups.

3.2. Simulation Results

This study compares the performances of multiple comparison tests concerning sample size designs of equal, progressive, and one-extreme cases. The results are presented in Tables 2-4. We outline the results according to the number of groups for selecting the appropriate methods for practical use.

When k is small: The type I error of the Holm method is closest to the nominal level when the sample size is equal and smaller than 40 under the equal N scenario. For instance, the type I error rates of the Holm method vary between 0.049-0.051 when $k = 3$. In the same scenario, the type I error rates of the Bonferroni method range from 0.045 to 0.048, while those of the Hommel method range from 0.051 to 0.054. On the other hand, the Bonferroni method holds the nominal level of type I error when the number of observations exceeds 40. For example, the type I error rates of the Bonferroni method vary between 0.049-0.050 when $k = 3$. Under

progressive N and one extreme scenario, the Bonferroni method holds the nominal level of type I error rate in all observation numbers.

When k is medium: Results obtained under equal N, progressive N, and one extreme scenario show similar patterns. Type I error of the Hommel method holds the nominal level when the number of observations is equal and lower than 30. The type I error rate of the Bonferroni method is very close to the nominal level when the number of observations exceeds 30.

When k is large: Under equal N, progressive N, and one extreme scenario, Bonferroni, Holm, Hommel, and Hochberg methods hold the nominal level of type I error rate regardless of the number of observations.

When the multiple comparison methods are not applied, the type I error rates increase excessively as the number of groups and comparisons increase. For example, when the number of groups is 9, and the number of observations in each group is 10 under the equal N scenario, multiple comparison methods give results ranging from 0.018 to 0.078. In the same scenario, the type I error reaches 0.834 without any corrections.

Table 1. Simulation study the sample size patterns

	Progressive N	Equal N	One extreme
k=3	8	10	8
	10	10	8
	12	10	14
Average N	10	10	10
k=4	7	10	8
	9	10	8
	11	10	8
	13	10	16
Average N	10	10	10
k=5	6	10	8
	8	10	8
	10	10	8
	12	10	8
	14	10	18
Average N	10	10	10
k=6	5	10	8
	7	10	8
	9	10	8
	11	10	8
	13	10	8
	15	10	20
Average N	10	10	10
k=7	7	10	8
	8	10	8
	9	10	8
	10	10	8
	11	10	8
	12	10	8
	13	10	22
Average N	10	10	10
k=8	6	10	8
	7	10	8
	8	10	8
	9	10	8
	11	10	8
	12	10	8
	13	10	8
	14	10	24
Average N	10	10	10
k=9	6	10	8
	7	10	8
	8	10	8
	9	10	8
	10	10	8
	11	10	8
	12	10	8
	13	10	8
	14	10	26
Average N	10	10	10

Table 1. (Continued) Simulation study sample size patterns

	Progressive N	Equal N	One extreme
k=10	5	10	8
	6	10	8
	7	10	8
	8	10	8
	9	10	8
	11	10	8
	12	10	8
	13	10	8
	14	10	8
	15	10	28
Average N	10	10	10

Table 2. Type I error for equal

Group	Method	$\hat{\alpha}_{10}$	$\hat{\alpha}_{20}$	$\hat{\alpha}_{30}$	$\hat{\alpha}_{40}$	$\hat{\alpha}_{50}$	$\hat{\alpha}_{100}$
3	Bonferroni	0.048	0.045	0.047	0.047	0.049	0.050
	Holm	0.051	0.049	0.051	0.050	0.053	0.055
	Hommel	0.054	0.051	0.054	0.052	0.057	0.057
	Hochberg	0.053	0.050	0.052	0.051	0.055	0.055
	BH	0.060	0.058	0.059	0.057	0.062	0.065
	BY	0.031	0.030	0.031	0.031	0.030	0.035
	None	0.141	0.140	0.140	0.135	0.142	0.143
4	Bonferroni	0.046	0.047	0.048	0.050	0.051	0.054
	Holm	0.048	0.049	0.051	0.053	0.054	0.057
	Hommel	0.051	0.051	0.053	0.054	0.056	0.059
	Hochberg	0.048	0.050	0.051	0.053	0.055	0.057
	BH	0.064	0.065	0.068	0.069	0.070	0.075
	BY	0.024	0.025	0.024	0.026	0.028	0.030
	None	0.261	0.263	0.266	0.256	0.267	0.274
5	Bonferroni	0.047	0.042	0.047	0.051	0.051	0.054
	Holm	0.049	0.043	0.048	0.052	0.053	0.056
	Hommel	0.050	0.045	0.050	0.054	0.055	0.057
	Hochberg	0.049	0.044	0.049	0.053	0.054	0.056
	BH	0.069	0.066	0.074	0.076	0.076	0.080
	BY	0.020	0.017	0.020	0.024	0.024	0.027
	None	0.388	0.393	0.401	0.392	0.397	0.408
6	Bonferroni	0.045	0.044	0.047	0.051	0.053	0.052
	Holm	0.046	0.045	0.048	0.053	0.054	0.054
	Hommel	0.047	0.046	0.049	0.055	0.055	0.055
	Hochberg	0.046	0.045	0.048	0.053	0.054	0.054
	BH	0.071	0.071	0.077	0.089	0.086	0.088
	BY	0.019	0.017	0.018	0.024	0.025	0.024
	None	0.529	0.531	0.541	0.532	0.536	0.548
7	Bonferroni	0.045	0.044	0.046	0.051	0.051	0.050
	Holm	0.046	0.046	0.047	0.053	0.052	0.051
	Hommel	0.047	0.047	0.047	0.053	0.054	0.052
	Hochberg	0.046	0.046	0.047	0.053	0.052	0.051
	BH	0.073	0.079	0.079	0.087	0.089	0.086
	BY	0.016	0.017	0.018	0.023	0.023	0.020
	None	0.646	0.651	0.663	0.656	0.652	0.664
8	Bonferroni	0.043	0.044	0.049	0.053	0.048	0.051
	Holm	0.044	0.044	0.049	0.054	0.050	0.051
	Hommel	0.045	0.045	0.050	0.054	0.050	0.052
	Hochberg	0.044	0.044	0.049	0.054	0.050	0.051
	BH	0.077	0.079	0.086	0.090	0.087	0.087
	BY	0.016	0.016	0.017	0.019	0.019	0.019
	None	0.756	0.758	0.768	0.760	0.760	0.770
9	Bonferroni	0.043	0.048	0.049	0.054	0.050	0.052
	Holm	0.044	0.048	0.050	0.056	0.051	0.053
	Hommel	0.044	0.049	0.050	0.056	0.051	0.053
	Hochberg	0.044	0.048	0.050	0.056	0.051	0.053
	BH	0.078	0.085	0.091	0.096	0.090	0.096
	BY	0.018	0.016	0.016	0.020	0.018	0.019
	None	0.834	0.839	0.844	0.841	0.841	0.847
10	Bonferroni	0.042	0.045	0.046	0.050	0.052	0.052
	Holm	0.042	0.046	0.046	0.051	0.053	0.052
	Hommel	0.042	0.046	0.047	0.052	0.053	0.053
	Hochberg	0.042	0.046	0.046	0.051	0.053	0.052
	BH	0.077	0.084	0.092	0.097	0.102	0.096
	BY	0.013	0.016	0.016	0.016	0.017	0.017
	None	0.893	0.899	0.904	0.900	0.899	0.904

Boldfaced values indicate the closest type I error rates to the nominal ones.

Table 3. Type I error for progressive

Group	Method	$\hat{\alpha}_{10}$	$\hat{\alpha}_{20}$	$\hat{\alpha}_{30}$	$\hat{\alpha}_{40}$	$\hat{\alpha}_{50}$	$\hat{\alpha}_{100}$
3	Bonferroni	0.049	0.047	0.049	0.048	0.052	0.049
	Holm	0.053	0.051	0.053	0.052	0.056	0.054
	Hommel	0.056	0.053	0.056	0.056	0.057	0.057
	Hochberg	0.055	0.052	0.055	0.054	0.056	0.055
	BH	0.061	0.059	0.062	0.061	0.063	0.063
	BY	0.030	0.030	0.035	0.030	0.036	0.034
	None	0.140	0.140	0.143	0.144	0.146	0.150
4	Bonferroni	0.046	0.052	0.049	0.048	0.049	0.050
	Holm	0.050	0.055	0.052	0.051	0.051	0.052
	Hommel	0.052	0.057	0.054	0.052	0.054	0.053
	Hochberg	0.051	0.056	0.052	0.051	0.052	0.052
	BH	0.066	0.069	0.068	0.068	0.068	0.069
	BY	0.024	0.026	0.026	0.027	0.028	0.027
	None	0.267	0.266	0.269	0.266	0.260	0.263
5	Bonferroni	0.045	0.043	0.046	0.049	0.048	0.050
	Holm	0.046	0.045	0.048	0.051	0.049	0.052
	Hommel	0.048	0.046	0.050	0.052	0.050	0.054
	Hochberg	0.047	0.045	0.049	0.051	0.049	0.052
	BH	0.069	0.070	0.071	0.075	0.069	0.079
	BY	0.020	0.018	0.022	0.023	0.022	0.024
	None	0.394	0.389	0.396	0.409	0.391	0.405
6	Bonferroni	0.050	0.047	0.047	0.052	0.052	0.047
	Holm	0.051	0.049	0.049	0.054	0.053	0.048
	Hommel	0.052	0.050	0.050	0.056	0.054	0.050
	Hochberg	0.051	0.049	0.049	0.054	0.053	0.048
	BH	0.083	0.077	0.080	0.090	0.081	0.081
	BY	0.020	0.021	0.020	0.023	0.024	0.019
	None	0.536	0.533	0.544	0.544	0.536	0.547
7	Bonferroni	0.050	0.050	0.053	0.051	0.052	0.052
	Holm	0.051	0.050	0.054	0.052	0.053	0.054
	Hommel	0.052	0.051	0.055	0.053	0.054	0.055
	Hochberg	0.051	0.050	0.054	0.052	0.053	0.054
	BH	0.081	0.087	0.095	0.083	0.087	0.088
	BY	0.020	0.017	0.023	0.018	0.018	0.022
	None	0.656	0.662	0.666	0.668	0.672	0.658
8	Bonferroni	0.042	0.046	0.049	0.053	0.050	0.047
	Holm	0.043	0.047	0.050	0.054	0.051	0.048
	Hommel	0.043	0.048	0.050	0.055	0.052	0.049
	Hochberg	0.043	0.047	0.050	0.054	0.051	0.048
	BH	0.074	0.082	0.088	0.093	0.089	0.086
	BY	0.014	0.020	0.019	0.021	0.017	0.019
	None	0.755	0.757	0.765	0.769	0.769	0.771
9	Bonferroni	0.049	0.048	0.052	0.054	0.052	0.052
	Holm	0.050	0.049	0.053	0.055	0.052	0.053
	Hommel	0.051	0.050	0.053	0.056	0.053	0.053
	Hochberg	0.050	0.049	0.053	0.055	0.053	0.053
	BH	0.089	0.094	0.094	0.097	0.098	0.100
	BY	0.016	0.016	0.020	0.022	0.020	0.020
	None	0.838	0.848	0.846	0.844	0.840	0.845
10	Bonferroni	0.045	0.046	0.053	0.052	0.054	0.054
	Holm	0.045	0.046	0.054	0.052	0.055	0.055
	Hommel	0.046	0.047	0.054	0.053	0.055	0.055
	Hochberg	0.046	0.046	0.054	0.052	0.055	0.055
	BH	0.080	0.091	0.103	0.102	0.104	0.104
	BY	0.013	0.015	0.019	0.017	0.022	0.020
	None	0.898	0.904	0.901	0.902	0.904	0.902

Boldfaced values indicate the closest type I error rates to the nominal ones.

Table 4. Type I error for one extreme

Group	Method	$\hat{\alpha}_{10}$	$\hat{\alpha}_{20}$	$\hat{\alpha}_{30}$	$\hat{\alpha}_{40}$	$\hat{\alpha}_{50}$	$\hat{\alpha}_{100}$
3	Bonferroni	0.050	0.046	0.049	0.053	0.050	0.050
	Holm	0.053	0.050	0.053	0.056	0.053	0.054
	Hommel	0.056	0.052	0.056	0.059	0.056	0.057
	Hochberg	0.055	0.051	0.055	0.057	0.054	0.056
	BH	0.062	0.057	0.061	0.065	0.061	0.063
	BY	0.033	0.029	0.033	0.032	0.032	0.032
	None	0.137	0.137	0.142	0.142	0.144	0.147
	Bonferroni	0.047	0.049	0.050	0.050	0.051	0.049
4	Holm	0.050	0.053	0.052	0.054	0.053	0.052
	Hommel	0.053	0.054	0.054	0.057	0.055	0.054
	Hochberg	0.051	0.053	0.053	0.054	0.053	0.052
	BH	0.066	0.069	0.069	0.071	0.069	0.068
	BY	0.026	0.028	0.026	0.027	0.028	0.027
	None	0.261	0.266	0.262	0.271	0.263	0.262
	Bonferroni	0.044	0.046	0.049	0.052	0.052	0.050
	Holm	0.046	0.048	0.051	0.053	0.055	0.052
5	Hommel	0.047	0.049	0.052	0.055	0.056	0.053
	Hochberg	0.046	0.048	0.051	0.053	0.055	0.052
	BH	0.068	0.071	0.074	0.080	0.075	0.077
	BY	0.021	0.020	0.024	0.023	0.025	0.024
	None	0.396	0.397	0.393	0.413	0.404	0.406
	Bonferroni	0.046	0.045	0.051	0.051	0.053	0.052
	Holm	0.047	0.047	0.053	0.053	0.054	0.054
	Hommel	0.048	0.048	0.055	0.054	0.056	0.055
6	Hochberg	0.047	0.047	0.053	0.053	0.054	0.054
	BH	0.073	0.076	0.082	0.086	0.088	0.085
	BY	0.021	0.022	0.024	0.020	0.025	0.022
	None	0.531	0.531	0.539	0.539	0.539	0.542
	Bonferroni	0.054	0.049	0.048	0.053	0.050	0.051
	Holm	0.055	0.050	0.049	0.054	0.052	0.052
	Hommel	0.056	0.051	0.051	0.055	0.053	0.053
	Hochberg	0.055	0.050	0.050	0.054	0.052	0.052
7	BH	0.088	0.083	0.087	0.091	0.091	0.091
	BY	0.024	0.019	0.020	0.019	0.021	0.021
	None	0.657	0.654	0.662	0.667	0.665	0.659
	Bonferroni	0.049	0.049	0.051	0.049	0.053	0.051
	Holm	0.051	0.050	0.052	0.050	0.054	0.051
	Hommel	0.052	0.051	0.052	0.051	0.055	0.052
	Hochberg	0.051	0.050	0.052	0.050	0.054	0.051
	BH	0.088	0.095	0.095	0.095	0.093	0.091
8	BY	0.017	0.019	0.022	0.019	0.021	0.018
	None	0.763	0.763	0.767	0.771	0.766	0.767
	Bonferroni	0.045	0.047	0.051	0.049	0.056	0.053
	Holm	0.045	0.048	0.052	0.049	0.057	0.054
	Hommel	0.046	0.048	0.053	0.050	0.058	0.055
	Hochberg	0.045	0.048	0.052	0.049	0.057	0.054
	BH	0.080	0.091	0.093	0.097	0.106	0.105
	BY	0.017	0.015	0.019	0.018	0.024	0.020
9	None	0.845	0.848	0.836	0.852	0.847	0.847
	Bonferroni	0.044	0.047	0.052	0.049	0.053	0.047
	Holm	0.044	0.048	0.053	0.050	0.054	0.048
	Hommel	0.045	0.049	0.053	0.051	0.054	0.049
	Hochberg	0.044	0.048	0.053	0.050	0.054	0.048
	BH	0.082	0.090	0.097	0.098	0.102	0.098
	BY	0.013	0.015	0.018	0.017	0.020	0.017
	None	0.897	0.904	0.902	0.905	0.903	0.901

Boldfaced values indicate the closest type I error rates to the nominal ones.

3.3. Demonstration of the Pairwise Comparison Methods

This section demonstrates how to apply multiple comparison methods to three real data applications. ANOVA and multiple comparison methods are conducted on cholesterol data using aov test and pair comp functions, respectively, available in the oneway tests R package [20]. The associated p-values of all multiple comparison methods are placed in Table 5.

3.3.1. Cholesterol Data

In this part, we work with the cholesterol data set collected by Westfall, available in a multcomp R package [21]. A clinical study assesses the effect of three formulations of the same drug on reducing cholesterol. The formulations are 20 mg at once (1 time), 10 mg twice a day (2 times), and 5 mg four times a day (4 times). In addition, two competing drugs are used as control groups (drug D and drug E). The study aims to find which formulations, if any, are efficacious and how these formulations compare with the existing drugs. This data set has 50 observations (10 observations for each treatment). The descriptive statistics (mean ± standard deviation) are 5.78±2.88, 9.22±3.48, 12.37±2.92, 15.36±3.45, and 20.95±3.35 for the groups, 1time, 2time, 4times, drugD, and drugE, respectively.

In this part, we apply ANOVA for the comparison of the groups. Before ANOVA, we assess the normality of the reduced amount in cholesterol values for five treatment groups. All groups satisfy the assumption of normality (e.g., Shapiro-Wilk normality test: all p-values=0.4541 – 0.9696). Moreover, Levene’s homogeneity test suggests that the variances of the five treatment methods are homogeneous (p-value = 0.9875).

```
library(oneway tests)
model <- aov.test(response ~ trt, data = cholesterol)
One-Way Analysis of Variance (alpha = 0.05)
-----
data: response and trt
statistic: 32.43283
num df: 4
denom df: 45
p-value: 9.818516e-13
Result: The difference is statistically significant.
-----
```

Since the p-value obtained as a result of ANOVA is smaller than 0.05, there is a statistically significant difference between the treatment groups ($F = 32.43283$, $df_{num} = 4$, $df_{denom} = 45$, $p - value = 9.818516 \times 10^{-13}$). After obtaining statistically significant results in ANOVA, we need to investigate the groups which create the difference. In this part, we make pairwise comparisons with the Hommel method since our simulation results suggest that the Hommel method holds a nominal level of type I error rate when the number of groups is 5. The number of observations in each group is 10.

```
paircomp(model, adjust.method = "hommel")
Hommel Correction (alpha = 0.05)
-----
```

	Level (a)	Level (b)	p.value	No difference
1	1time	2times	5.139629e-02	Not reject
2	1time	4times	4.664132e-04	Reject
3	1time	drugD	2.066193e-05	Reject
4	1time	drugE	2.444640e-08	Reject
5	2times	4times	5.139629e-02	Not reject
6	2times	drugD	4.343976e-03	Reject
7	2times	drugE	3.951905e-06	Reject
8	4times	drugD	5.139629e-02	Not reject
9	4times	drugE	6.398084e-05	Reject
10	drugD	drugE	6.950361e-03	Reject

```
-----
```

According to the result obtained adjusting with the Hommel method, statistical differences in cholesterol reduction between all other pairs are significant, except for three pairs: 1time-2times, 2times-4 times, and 4times-drugD.

3.3.2. Diet and Weight Loss Data

In this part, we work with the diet data set in the WRS2 R package [22]. Weight loss is studied for three different types of diets. There are 24 observations in diet group A, 25 in diet group B, and 27 in diet group C, with a total of 76 observations. The descriptive statistics (mean \pm standard deviation) are 3.30 ± 2.24 , 3.27 ± 2.46 , and 5.15 ± 2.40 for the diet types A, B, and C, respectively.

In this section, we perform ANOVA for the comparison of diet groups. Before ANOVA, we check the normality of the weight loss in diet values for three different diet groups. The normality assumption is met for all groups (e.g., Shapiro-Wilk normality test: all p-values = 0.0774 – 0.8721). Further, Levene's homogeneity test states that the variances of the three temperature methods are homogeneous (p-value = 0.6122).

Since the p-value obtained as a result of ANOVA is smaller than 0.05, there is a statistically significant difference between the diet groups ($F = 5.383104$, $df_{num} = 2$, $df_{denom} = 73$, and p-value = 0.006595853). After obtaining statistically significant results in ANOVA, we need to investigate the groups which create the difference. In this part, we make pairwise comparisons with the Bonferroni method since our simulation results suggest that the Bonferroni method holds a nominal level of type I error rate when the number of groups is three. The sample size pattern is progressive N. The result obtained adjusting with Bonferroni method points out that, diet type C leads to statistically greater weight loss than the others

3.3.3. Pottery Data

In this part, we work with the pottery data set in the carData R package [23]. The data give the chemical composition of ancient pottery found at three sites in Great Britain: AshleyRails, IsleThorns, and Llanedyrn. There are 5 observations in the AshleyRails group, 5 in the IsleThorns group, and 14 in the Llanedyrn group, totaling 24 observations. The descriptive statistics (mean \pm standard deviation) are 17.32 ± 1.66 , 18.18 ± 1.77 , and 12.56 ± 1.38 for AshleyRails, IsleThorns, and Llanedyrn sites, respectively. The Caldicot site was not included in this part since there were two ancient potteries.

In this section, we perform ANOVA for the comparison of site groups. Before ANOVA, we check the normality of the Aluminum values for three different groups. The normality assumption is met for all groups (e.g., Shapiro-Wilk normality test: all p-values = 0.780 – 0.967). Furthermore, Levene's homogeneity test states that the variances of three sites are homogeneous (p-value = 0.950).

Since the p-value obtained as a result of ANOVA is less than 0.05, there is a statistically significant difference between the three sites ($F = 34.52644$, $df_{num} = 2$, $df_{denom} = 21$, p-value = 2.296561×10^{-7}). After obtaining a statistically significant result in ANOVA, we need to investigate the sites making the difference. In this section, we make pairwise comparisons with the Bonferroni method since our simulation results illustrate that the Bonferroni method holds a nominal type I error rate in extreme cases where the number of groups is three. The sample size design is one extreme.

The results obtained by correcting with the Bonferroni method show that the Llanedyrn group leads to statistically smaller aluminum than the AshleyRails and IsleThorns sites.

In comparisons of two or more groups, multiple comparison tests are employed to investigate the difference if there is a statistically significant difference among the groups. At this point, multiple comparison tests are performed to control Type I error rates. Although studies are published in the literature to control type I error rates, it is important to choose an appropriate multiple comparison test under different conditions. Therefore, it will be important to provide researchers with an overview of multiple comparison tests under various scenarios.

Table 5. The p-values of all multiple comparison methods on cholesterol, diet, and pottery data sets

Data sets	Level (a)	Level (b)	Bonferroni	Holm	Hommel	Hochberg	BH	BY	None
Cholesterol	1time	2times	0.269	0.081	0.051	0.051	0.034	0.098	0.027
	1time	4times	0.001	0.000	0.000	0.000	0.000	0.000	0.000
	1time	drugD	0.000	0.000	0.000	0.000	0.000	0.000	0.000
	1time	drugE	0.000	0.000	0.000	0.000	0.000	0.000	0.000
	2times	4times	0.419	0.084	0.051	0.051	0.047	0.136	0.042
	2times	drugD	0.009	0.005	0.004	0.005	0.002	0.005	0.001
	2times	drugE	0.000	0.000	0.000	0.000	0.000	0.000	0.000
	4times	drugD	0.514	0.084	0.051	0.051	0.051	0.151	0.051
	4times	drugE	0.000	0.000	0.000	0.000	0.000	0.000	0.000
	drugD	drugE	0.017	0.007	0.007	0.007	0.002	0.007	0.002
Diet	A	B	1.000	0.962	0.962	0.962	0.962	1.000	0.962
	A	C	0.020	0.020	0.013	0.015	0.011	0.021	0.007
	B	C	0.022	0.020	0.015	0.015	0.011	0.021	0.007
Pottery	AshleyRails	IsleThorns	1.000	0.451	0.451	0.451	0.451	0.827	0.451
	AshleyRails	Llanedyrn	0.000	0.000	0.000	0.000	0.000	0.000	0.000
	IsleThorns	Llanedyrn	0.000	0.000	0.000	0.000	0.000	0.000	0.000

All p-values are rounded to three decimals. Associated p-values of suggested methods are written in bold.

4. Discussion

In this paper, we compare the type I error rates of Bonferroni, Holm, Hommel, Hochberg, BH (FDR), and BY multiple comparison methods under different conditions with Monte Carlo simulation and three real data applications. Blakesley et al. [11] introduced the Hommel and Hochberg techniques tailored for moderately correlated measures to enhance statistical power while maintaining control over type I errors within neuropsychological datasets. Felix and Menezes [12] showed that BH correction provides a smaller type I error rate by varying the sample size and sample distribution. Staffa and Zurakowski [13] proposed that surgeons use multiple comparison methods, including Bonferroni, Tukey, Scheffe, Holm, and Dunnett. They provide guidance on strategies for how to handle multiplicity and multiple significance testing in surgical research studies. Kharola et al. [15] criticized the work done by Dimitriev et al. [14] concerning using multiple comparison methods. They stated that the Holm method was more powerful than the Bonferroni method.

5. Conclusion

The criteria for selecting multiple comparison tests in the literature are not clearly defined, leaving uncertainty about the appropriateness of their application in various scenarios. Furthermore, selecting these multiple comparison methods without considering factors like group sizes, sample sizes and sample size designs could produce misleading results. For 3-4 groups, we recommend Bonferroni correction when the number of observations is equal and greater than 50 and Holm correction when the number of observations is less than 50 under the equal N scenario. We recommend the Bonferroni method under progressive N and one extreme scenario regardless of the number of observations. For 5-6 groups, we suggest the Bonferroni method when the number of observations is equal and more than 40 and the Hommel correction when the number of observations is less than 40 under all sample size patterns. For 7 or more groups, we propose Bonferroni, Holm, Hommel, and Hochberg methods under all sample size patterns regardless of the number of observations. In future studies, simulation studies are planned on which post-hoc test should be used under non-normality and/or heterogeneity.

Author Contributions

All the authors equally contributed to this work. They all read and approved the final version of the paper.

Conflicts of Interest

All the authors declare no conflict of interest.

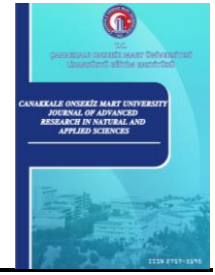
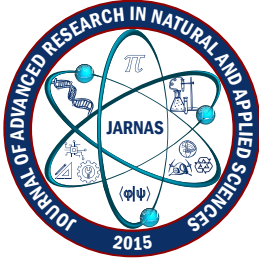
Ethical Review and Approval

No approval from the Board of Ethics is required.

References

- [1] S. K. Sarkar, C. K. Chang, *The Simes method for multiple hypotheses testing with positively dependent test statistics*, Journal of the American Statistical Association 92 (440) (2012) 1601–1608.
- [2] O. J. Dunn, *Multiple comparisons among means*, Journal of the American Statistical Association 56 (293) (1961) 52–64.
- [3] S. Holm, *A simple sequentially rejective multiple test procedure*, Scandinavian Journal of Statistics 6 (2) (1979) 65–70.
- [4] G. Hommel, *A stagewise rejective multiple test procedure based on a modified Bonferroni test*, Biometrika 75 (2) (1988) 383–386.
- [5] Y. Hochberg, *A sharper Bonferroni procedure for multiple tests of significance*, Biometrika 75 (4) (1988) 800–802.
- [6] Y. Benjamini, Y. Hochberg, *Controlling the false discovery rate—a practical and powerful approach to multiple testing*, Journal of the Royal Statistical Society Series B (Methodological) 57 (1) (1995) 289–300.
- [7] Y. Benjamini, D. Yekutieli, *The control of the false discovery rate in multiple testing under dependency*, The Annals of Statistics 29 (4) (2001) 1165–1188.
- [8] S. Lee, D. K. Lee, *What is the proper way to apply the multiple comparison test?*, Korean Journal of Anesthesiology 71 (5) (2018) 353–360.
- [9] R. Bender, S. Lange, *Adjusting for multiple testing—when and how?*, Journal of Clinical Epidemiology 54 (4) (2001) 343–349.
- [10] P. H. Westfall, J. F. Troendle, *Multiple testing with minimal assumptions*, Biometrical Journal 50 (5) (2008) 745–755.
- [11] R. E. Blakesley, S. Mazumdar, M. A. Dew, P. R. Houck, G. Tang, C. F. Reynolds, M. A. Butters, *Comparisons of methods for multiple hypotheses testing in neuropsychological research*, Neuropsychology 23 (2) (2009) 255–264.
- [12] V. B. Felix, A. F. B. Menezes, *Comparisons of ten corrections methods for t-test in multiple comparisons via Monte Carlo study*, Electronic Journal of Applied Statistical Analysis 11 (01) (2018) 74–91.
- [13] S. J. Staffa, D. Zurakowski, *Strategies in adjusting for multiple comparisons: A primer for pediatric surgeons*, Journal of Pediatric Surgery 55 (9) (2020) 1699–1705.
- [14] D. A. Dimitriev, E. V. Saperova, O. S. Indeykina, A. D. Dimitriev, *Heart rate variability in mental stress: The data reveal regression to the mean*, Data in Brief 22 (2019) 245–250.

- [15] S. S. Kharola, D. Gupta, A. Agrawal, *Heart rate variability in mental stress: The data reveal regression to the mean*, Indian Statistical Institute Bangalore Centre (2023) 19 pages.
- [16] A. A. Musicus, L. A. Gibson, S. L. Bellamy, J. A. Orr, D. Hammond, K. Glanz, K. G. Volpp, M. B. Schwartz, A. Bleakley, A. A. Strasser, C. A. Roberto, *Effects of sugary beverage text and pictorial warnings: A randomized trial*, American Journal of Preventive Medicine 64 (5) (2023) 716–727.
- [17] M. Giacalone, Z. Agata, P.C. Cozzucoli, A. Alibrandi, *Bonferroni-Holm and permutation tests to compare health data: Methodological and applicative issues*, BMC Medical Research Methodology 18 (81) (2018) 1–9.
- [18] S. Chen, Z. Feng, X. Yi, *A general introduction to adjustment for multiple comparisons*, Journal of Thoracic Disease 9 (6) (2017) 1725–1729.
- [19] R. J. Simes, *An improved Bonferroni procedure for multiple tests of significance*, Biometrika 73 (1986) 751–754.
- [20] O. Dag, N. A. B. Dolgun, N. M. Konar, *Onewaytests: An R package for one-way tests in independent groups designs*, The R Journal 10 (1) (2018) 175–199.
- [21] T. Hothorn, F. Bretz, P. Westfall, *Simultaneous inference in general parametric models*, Biometrical Journal 50 (3) (2008) 346–363.
- [22] P. Mair, R. Wilcox, *Robust statistical methods in R using the WRS2 package*, Behavior Research Methods 52 (2020) 464–488.
- [23] J. Fox, S. Weisberg, B. Price, *carData: Companion to Applied Regression Data Sets*, 2022.



Modifiye DMPD Yöntemi ile Süperoksit Radikali Süpürme Aktivitesi ve Toplam Antioksidan Kapasite Tayini

Ferda Dondurmacıoğlu¹

¹İstanbul Üniversitesi-Cerrahpaşa, Mühendislik Fakültesi, Kimya Bölümü, İstanbul, Türkiye

Makale Bilgisi
Gönderim: 27 Ekim 2023
Kabul: 17 Mayıs 2024
Yayın: 30 Eylül 2024
Araştırma Makalesi

Öz – Reaktif oksijen türleri içinde yer alan süperoksit radikalleri lipid peroksidasyonuna neden olan tehlikeli türler üretebilir. Bu nedenle süperoksit radikali tayini, süpürülmesi çok önemlidir. Çalışmamız β -Nicotinamid adenin dinükleotid indirgenmiş disodyum tuz hidrati ve fenazin metosulfat (NADH-PMS) sisteminden üretilen süperoksit radikalının *N, N*-dimetil-*p*-fenilendiamin dihidroklorür (DMPD) ile etkileşimi sonucu pembe renkli DMPD-yarıkınon (DMPDQ) radikali oluşturmasına dayanmaktadır. Süperoksit radikali giderme aktivitesine sahip süpürücüler (antioksidan, bitki çayları) varlığında daha az DMPDQ radikali üretimi nedeniyle renk yoğunluğu azalır. Renkli referans çözeltisinin ve radikal süpürücü içeren örnek çözeltisinin absorbansı 552 nm’de ölçülmüştür. Referans çözelti ile örnek çözeltisinin absorbans farkı (ΔA) bulunmuştur. ΔA ile süpürücü derişimi orantılıdır. Çalışmada, trolox (TR) ve farklı antioksidanların (AOX) süperoksit radikal süpürücü etkisi araştırılmıştır. Yöntemle üç farklı bitki çayı infüzyon çözeltisinin süperoksit radikal süpürücü etkisi ölçülmüştür. Bitki çayı derişimleri ile yüzde inhibisyon değerleri arasında çizilen grafikten bitki çaylarının %50 inhibisyon (EC50) değerleri bulunmuştur. Bulunan EC50 değerleri nitroblue tetrazolium (NBT) ve 2,2’-azino-bis(3-etilbenzotiyazolin-6-sülfonik asit (ABTS) yöntemi EC50 değerleriyle karşılaştırılmıştır. Ayrıca bitki çayı infüzyonlarının ABTS, bakır(II) iyonu indirgeme esaslı antioksidan kapasite (CUPRAC) yöntemi ve çalışılan yöntemde toplam antioksidan kapasite değerleri (TAC) hesaplanıp, karşılaştırılmıştır.

Anahtar Kelimeler – Antioksidan kapasite, NADH-PMS, *N, N*-dimetil-*p*-fenilendiamin dihidroklorür, süperoksit radikali, yüzde inhibisyon

Determination of Superoxide Radical Scavenging Activity and Total Antioxidant Capacity by Modified DMPD Method

¹Department of Chemistry, Faculty of Engineering, İstanbul University-Cerrahpaşa, İstanbul, Türkiye

Article Info
Received: 27 Oct 2023
Accepted: 17 May 2024
Published: 30 Sep 2024
Research Article

Abstract – Among the reactive oxygen species, Superoxide radicals can produce dangerous species that cause lipid peroxidation. Therefore, the determination and scavenging of superoxide radicals is critical. Our study is based on the interaction of the superoxide radical produced from the β -Nicotinamide adenine dinucleotide reduced disodium salt hydrate and phenazine methosulfate (NADH-PMS) system with *N, N*-dimethyl-*p*-phenylenediamine dihydrochloride (DMPD) to form the pink colored DMPD-quinone (DMPDQ) radical. In the presence of scavengers with superoxide radical scavenging activity (antioxidants, herbal teas) the color intensity decreases due to reduced DMPDQ radical production. The absorbance of the colored reference solution and the sample

solution containing the radical scavenger was measured at 552 nm. The difference in absorbance (ΔA) between the reference solution and the sample solution was found. ΔA is proportional to the scavenger concentration. In the study, the superoxide radical scavenging effect of trolox (TR) and different AOXs was investigated. The superoxide radical scavenging effect of three different herbal tea infusion solutions was measured with this method. From the graph drawn between herbal tea concentrations and percentage inhibition values, 50% inhibition (EC50) values of herbal teas were found. The EC50 values found were compared with the EC50 values of the nitroblue tetrazolium (NBT) and the 2,2 -azino-bis(3-ethylbenzothiazoline-6-sulfonic acid) (ABTS) method. In addition, ABTS, cupric reducing antioxidant capacity (CUPRAC), and this study total antioxidant capacity (TAC) values of herbal tea infusions were calculated and compared.

Keywords – Antioxidant capacity, NADH-PMS, N,N-dimethyl-p-phenylenediamine dihydrochloride, superoxide radical, percentage inhibition

1. Giriş

Eşleşmemiş elektrona sahip olan radikaller hem çok kısa ömürlü hem de çok reaktiflerdir [1]. Moleküler oksijen biyosferdeki en önemli elektron alıcısıdır [2]. Oksijen yaşam için gerekli bir moleküldür [3]. Çift radikal yapısından dolayı eşleşmemiş elektronları kolaylıkla kabul eder ve serbest radikaller oluşur [2].

Serbest radikaller iç etkenler (normal hücre metabolizması) ve çevre kirliliği, sigara içilmesi, radyasyon, ilaç gibi dış etkenler sonucu üretilir. Hüresel redokstan kaynaklanan serbest radikaller çoğunlukla reaktif oksijen türleri (ROS) ve reaktif nitrojen türlerinden (RNS) oluşur. Kısmen indirgenmiş oksijen formları, yani $O_2^{\cdot-}$, H_2O_2 ve HO^{\cdot} , moleküler oksijenden kimyasal olarak daha aktiftir ve bu nedenle topluca “reaktif oksijen türleri” (ROS) olarak adlandırılırlar [4]. ROS ve RNS hem toksik hem de faydalı türlerdir. Düşük ve orta seviyelerde ROS ve RNS'nin vücudun bağışıklık sistemi üzerinde önemli etkileri vardır. Yüksek seviyelerde olduğunda tüm hücre yapılarına zarar verebilir [3]. ROS arasında süperoksit ($O_2^{\cdot-}$), hidrojen peroksit (H_2O_2), hidroksil (HO^{\cdot}), peroksil (ROO^{\cdot}) ve alkoksil (RO^{\cdot}) radikalleri yer alır. Hücreler için oldukça zararlı olabilen ROS'lar serbest radikal zincir reaksiyonlarının başlatılması ve yayılmasında rol oynarlar [2]. Pro-oksidanlar olarak bilinen reaktif oksijen türlerinin oluşumu, aerobik yaşamın bir özelliğidir. Pro-oksidanların oluşumu, enzimatik ve/veya enzimatik olmayan antioksidanlar tarafından dengelenir. ROS'lar vücuttan kademeli olarak yok edilemediğinde oksidatif strese (OS) yol açar. OS, pro-oksidan/antioksidan dengesinin pro-oksidanlar lehine kaymasından kaynaklanır. OS kanser, otoimmün hastalıklar, yaşlanma, katarakt, romatoid artrit, kardiyovasküler ve nörodejenarativ hastalıklar, Alzheimer ve Parkinson gibi birçok hastalık ile ilişkilidir [3].

Yiyecekler ve takviye olarak dışarıdan alınan (eksojen) veya insan vücudunda üretilen (endojen) antioksidanlar (AOX) ile oksidatif strese karşı korunma mekanizmaları vardır. Endojen ve eksojen AOX'lar serbest radikal süpürücü olarak serbest radikallerin sebep olduğu hasarları önlerler veya onarırlar. Dolayısıyla dejenaratif hastalık ve kanser riski azalır [3, 5].

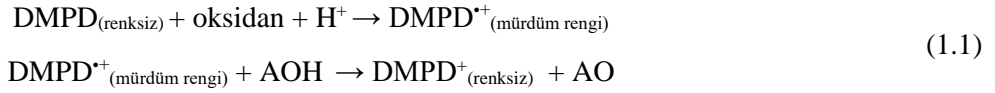
Biyolojik sistemlerde bulunan en reaktif türler Fenton reaksiyonu sonucu oluşan hidroksil ve mitokondride solunum zinciri yan ürünü olarak oluşan süperoksit radikalleridir [6, 7]. Hücrelerdeki mitokondrinin oksijen kullanarak enerji üretiminde ATP (adenozin trifosfat) oluşumu sonucu süperoksit serbest radikalleri meydana gelir [8, 9].

Birçok bilim adamı oksijenin toksik etkisinin fazla miktarda süperoksit radikali oluşmasından ileri geldiğine inanmaktadır [1, 10]. Süperoksit radikali diğer ROS türlerine göre daha az aktif olmasına rağmen lipidlerin peroksidasyonuna neden olan daha tehlikeli türler üretebilir. Süperoksit radikali geçiş metallerini indirgeyebilmesi ve hidrojen peroksit kaynağı olmasından dolayı çok önemlidir. Doku hasarına neden olabilen aktif serbest radikallerin öncül bileşenidir [11]. İki molekül süperoksit proton alarak hidrojen peroksit (H_2O_2) ve moleküler oksijene (O_2) dönüşür. Ayrıca süperoksit anyonu azot monoksit (NO) ile reaksiyona girerek peroksinitrit ($ONOO^{\cdot-}$) ve azot oksitleri (NO_x) dahil olmak üzere çok toksik ROS üretebilir [7, 12].

Reaktif oksijen türlerinin fazla üretilmesi nedeniyle organizmanın doğal savunması baskı altına alınır. Oksidatif stres durumu oluşur. Hüresel ve hücre dışı proteinler, lipidler, nükleik asitler oksidatif hasara uğrar

ve doku hasarı oluşur. AOX aktivitesi taşıyan gıdaların doğal tüketimi sağlık riskleri ve doku yaralanmalarıyla mücadelede önemli rol oynar. Günümüzde ROS'un insan sağlığı üzerine etkileri ve AOX'lar gittikçe artan ilgi alanı haline gelmiştir. Hastalıkların önlenmesinde AOX takviyelerin kullanımı, radikallerin faydalı biyolojik işlevlerini yerine getirmelerine engel olmadan fazla serbest radikal düzeylerinin düşürülmesine yardımcı olurlar. Bu nedenle bitkisel ekstraktların AOX kapasite düzeyinin ölçülmesi önemlidir [5, 13, 14]. Toplam antioksidan kapasite (TAC) ölçümünde en çok kullanılan yöntemler; 2,2'-azino-bis(3-etilbenzotiyazolin-6-sülfonik asit (ABTS) [15], CUPric Reducing Antioxidant Capacity (CUPRAC) (bakır(II) iyonu indirgeme esaslı antioksidan kapasite) [13], demir (III) iyonu indirgeyici antioksidan güç yöntemi (FRAP) [16] ve 2,2-Difenil-1-pikrilhidrazil (DPPH) radikal süpürme kapasitesi yöntemi [17] biçimindedir.

Yapılan çalışmalarda çeşitli gıda maddelerinin AOX kapasiteleri ile birlikte radikal süpürme etkinlikleri de incelenmektedir [18, 19]. Bu yöntemler arasında *N, N*-dimetil-*p*-fenilen diamin hidroklorür (DMPD) yöntemi önemlidir. Hirayama ve Unohara [20] ultra eser miktardaki demirin katalitik tayininde DMPD kullanmışlardır. Daha sonra yapılan bir çalışmada DMPD'den oksitlenmiş renkli ürün oluşumunun engellenmesine dayanan şarapta TAC tayini yapılmıştır [18]. Yöntemde ABTS/TEAC (troloks eşdeğer antioksidan kapasite) [15] yöntemindeki ABTS radikale benzer şekilde katyonik DMPD-yarıkinon (DMPDQ) radikali (mürdüm renkli) oluşturularak TAC tayin edilmiştir, bkz. (1.1) [18]. Oksidan ortamında oluşan renkli DMPDQ radikali (DMPD⁺ [sic] in [18]) çözeltilisine antioksidan (AO) eklenmesiyle çözelti renksizleşir [18]. Yiyecek ve içecek örneklerinde DMPD reaktifi ile TAC tayininde örnek çözeltisi içinde bulunan AOX'ların radikal süpürme etkinliği, radikal başlangıçtaki renk şiddetinin azalmasına bağlı olarak toplam antioksidan kapasite (TAC) olarak hesaplanır [18, 21].



OS durumunun değerlendirilmesinde DMPD testinden faydalanılabilir. DMPD testi kullanılarak, eklenen AOX derişiminin bir fonksiyonu olarak OS azalmaları arasında eğrisel bir ilişki kurularak OS değerlendirilebilir. Oksidatif dönüşüm ve antioksidan kapasite arasında ters bir ilişki vardır [22]. Saha vd. [22] DMPD kolorimetrik testi ile şeker hastalığına sahip hastaların plazmasındaki antioksidan savunma seviyelerini tayin etmişlerdir. Serbest radikal hasarı ile birlikte antioksidanların TAC değerleri de ölçülebilir [23]. Diğer ROS türlerine göre daha az aktif olan süperoksit radikali lipidlerin peroksidasyonuna neden olan daha tehlikeli türler üretebilmesi nedeniyle süperoksit anyon radikali süpürme aktivitesi önemlidir [11].

Daha önceki çalışmamızda [24] süperoksit anyon radikali süpürme aktivitesi ve toplam antioksidan kapasite (TAC) tayini aynı anda yapılmıştır. Çalışmada NADH/PMS sistemi ile üretilen süperoksit anyonu DMPD reaktifini pembe renkli DMPDQ katyonik radikale oksitlemiş ve bir katyon değişim Nafyon® membranı tarafından tutulmuştur. Nafyon® membranın kolorimetrik olarak 514 nm'deki renk değişimine bağlı olarak süperoksit anyon radikali tayin edilmiştir. Süperoksit radikali süpürme aktivitesi sergileyen AOX'lar daha az DMPDQ radikali üretimine neden olarak Nafyon® membranında renk yoğunluğunun azalmasına yol açar. Çözeltinin 514 nm'deki absorbans farkı AOX derişimiyle orantılıdır. Membran renginin koyuluğuna bağlı olarak ortamdaki süperoksit anyon radikali ve AOX varlığı çıplak gözle de tespit edilebilmiştir. Çalışmada troloks (TR) ve farklı AOX'ların süperoksit radikali süpürme etkisine dayanarak toplam antioksidan kapasiteleri (TAC) dolaylı yoldan troloks eşdeğer olarak hesaplanmıştır. AOX'ın süperoksit radikali süpürmesinde AOX derişimi ile ΔA arasında çizilen grafikten kalibrasyon denklemleri, lineer derişim aralıkları çıkarılmıştır. Süperoksit radikali içeren örnek çözeltisinde AOX varlığında ölçüm için seçilen dalga boyunda (514 nm) absorbansdaki düşüşe bağlı olarak Nafyon® membran üzerinde tayin yapılmış ve TAC hesaplanmıştır. TR kalibrasyon eğrisinin eğiminin (molar absorplama katsayısı - ε_{TR}) kullanılan antioksidan kalibrasyon eğrisinin eğimine (molar absorplama katsayısı - ε_{AOX}) bölünmesiyle Troloks Eşdeğer Antioksidan Kapasite Katsayısı (TEAC katsayısı) hesaplanmıştır. TEAC katsayısı yüksek olan AOX'lar yüksek süperoksit anyon radikali süpürme etkisine sahiptir.

Nafyon® membran tayin yöntemini modifiye ettiğimiz bu çalışmamızda membran yerine sulu çözeltide çalışılmıştır. Nafyon® membran ile yapılan çalışmanın hassasiyeti daha fazla olmasına rağmen Nafyon® membran mevcut olmadığı durumlarda sulu çözeltide çalışma gerekli olmaktadır. DMPD reaktifi ile süperoksit radikali süpürme aktivitesi ve TAC tayini için yöntemin sulu çözelti çalışma şartları modifiye edilmiştir. NADH-PMS sistemi ile üretilen süperoksit radikalının DMPD reaktifi ile etkileşimi sonucu renklene çözeltinin renk şiddeti AOX varlığında AOX derişimiyle ters orantılı olarak azalmıştır. Süperoksit radikali içeren sulu çözeltideki renkli katyonik DMPDQ radikali 505 ve 552 nm’de maksimum absorbans vermiştir (bkz. Şekil 2). Çalışma dalga boyu olarak 552 nm seçilmiştir. Kullanılacak reaktif optimizasyonu sonucu yöntem 5 farklı AOX’a uygulanmıştır. AOX kalibrasyon grafikleri, lineer aralıkları ve TEAC katsayıları belirlenmiştir. Yöntem 3 farklı bitki çayı infüzyonuna uygulanarak siyah çay (*Camellia sinensis*), adaçayı (*Salvia officinalis*) ve kuşburnu çayı (*Rosa canina L.*) TAC tayini yapılmıştır. Radikal süpürücünün (bitki çayı) süperoksit radikaline etkisi için süpürücü derişimi ile yüzde inhibisyon (bkz. (1.2)) arasında çizilen grafikten EC50 değerleri hesaplanmıştır. Süperoksit anyon radikalının yüzde ellisinin giderilmesi için gerekli olan süpürücü miktarı (EC50 değerleri) µg/mL cinsinden hesaplanmış ve sonuçlar referans NBT-formazan ve ABTS yöntemindeki EC50 değerleri ile karşılaştırılmıştır. Bitki çaylarının TAC değerleri mmol TR/g bitki çayı cinsinden hem modifiye yöntemle hem de CUPRAC [13] ve ABTS [15] yöntemleri ile hesaplanmıştır.

$$\text{Yüzde inhibisyon} = (A_{Rf} - A_{Ör}) * 100 / A_{Rf} \quad (1.2)$$

Burada, A_{Rf} , süperoksit radikali içeren radikal süpürücü (AOX, bitki çayı) içermeyen referans çözeltisinin 552 nm’deki suya karşı absorbansını ve $A_{Ör}$, Süperoksit radikali ve radikal süpürücü (AOX, bitki çayı) içeren çözeltinin 552 nm’de suya karşı okunan absorbansını temsil etmektedir.

Referans NBT formazan yönteminde, NADH-PMS sistemi tarafından üretilen süperoksit radikali NBT reaktifi ile mavi renkli formazan ürünü oluşturur. Süperoksit radikal süpürücülerin (antioksidanların) eklenmesiyle inhibe edilen mavi renkli formazan ürünün rengi açılır. Süperoksit süpürücü antioksidanlar 560 nm’de azalmış absorbans ile daha az formazan oluşumuna neden olarak süperoksit radikal süpürme aktivitesinin ölçümünü mümkün kılar [25].

2. Materyal ve Yöntem

2.1. Materyal

Analitik saflıktaki kimyasal maddeler ve kaynakları; troloks ((±)-6-hidroksi-2,5,7,8-tetrametilkroman) (TR) (Fluka), (±)-kateşin hidrat (CAT), 2,2’-azinobis(3-etilbenzothiazolin-6-sulfonik asit) diamonyum tuzu (ABTS), *N, N*-dimetil-*p*-fenilendiamin dihidroklorür (DMPD), neokuproin (2,9-dimetil-1,10-fenantrolin hidroklorür), etanol (EtOH) (HPLC saflıkta), β-Nicotinamid adenin dinükleotid indirgenmiş disodyum tuz hidratı (NADH), fenazin metosulfat (PMS), L-glutasyon (indirgenmiş) (GSH), L-askorbik asit (AA), nitrotetrazolium mavi klorür (NBT), asetik asit (CH₃COOH), sodyum asetat trihidrat (CH₃COONa·3H₂O) (Sigma-Aldrich), disodyum hidrojen fosfat dihidrat (Na₂HPO₄·2H₂O) (Merck), sodyum fosfat mono bazik dihidrat (NaH₂PO₄·2H₂O) (Riedel-de Haen), hidroklorik Asit (HCl) (Sigma-Aldrich), amonyum asetat (NH₄COO) (Riedel de Haen).

2.2. Yöntem

2.2.1. Çözeltiler

2,0×10⁻² M DMPD stok çözeltisi 41,8 mg DMPD reaktifi biraz su ve 0,5 M 0,1 mL HCl ile çözülüp distile su eklenerek son hacim 10 mL olacak şekilde hazırlanmıştır [26]. 25 mL 4,0×10⁻³ M DMPD çalışma çözeltisi hazırlanırken 5 mL 2,0×10⁻² M DMPD ve distile su kullanılmıştır. 0,2 M tampon çözeltisi pH=5,7 asetat tamponu asetik asit ve sodyum asetat ile hazırlanmıştır. 936 µM NADH ve 500 µM PMS stok çözeltisi distile

suda çözülmüştür. 500 µM PMS stok çözeltisi distile su ile 120 µM çalışma çözeltisine seyreltilmiştir. Antioksidan stok çözeltileri $5,0 \times 10^{-3}$ M troluks, $1,0 \times 10^{-2}$ M kateşin ve $1,0 \times 10^{-2}$ M rutin etanolde, $2,0 \times 10^{-3}$ M glutasyon ve $2,0 \times 10^{-2}$ M askorbik asit distile suda çözülmüştür.

2.2.2. Modifiye NADH/PMS/DMPD Yöntemi

Modifiye NADH/PMS/DMPD yönteminde enzimatik olmayan süperoksit radikal üretimi NADH-PMS sistemiyle gerçekleştirilmiştir [25]. Yöntemde kullanılacak DMPD, NADH ve PMS reaktiflerinin optimum derişimlerinin belirlenmesi amacıyla aşağıda belirtilen hacim aralıklarında denemeler yapılmıştır.

Yöntem; 936 µM NADH (0,025 – 0,6) mL, $4,0 \times 10^{-3}$ M DMPD (0,050 – 0,6) mL, 0,2 M pH 5,7 asetat tamponu 0,25 mL üzerine 120 µM PMS (0,025-0,8) mL eklenip distile su ile deney çözelti hacmi 2,0 mL olacak şekilde hazırlanmıştır. Reaksiyon karışımı 50°C su banyosunda 30 dakika bekletilmiştir [24]. Çözelti absorbansı suya karşı 552 nm’de okunmuştur (Şekil 1).

2.2.3. Yöntem Üzerine Antioksidan Etkisi

Optimizasyon sonrası yöntem; 936 µM NADH 0,2 mL + $4,0 \times 10^{-3}$ M DMPD 0,5 mL + 0,2 M pH 5,7 asetat tamponu 0,25 mL + x mL AOX + 120 µM PMS 0,4 mL eklenip distile su ile çözelti hacmi 2,0 mL olacak şekilde hazırlanmıştır. Yöntem 5 farklı çeşit AOX’a (TR, GSH, CT, RT ve AA) uygulanmıştır. Süpürücü olarak EtOH’de çözünen AOX’lar kullanıldığında çözelti içindeki toplam EtOH hacmi 0,1 mL olacak şekilde ayarlanmıştır. Toplam 0,1 mL EtOH sonrası çözelti son hacmi distile su ile 2,0 mL’ye tamamlanmıştır. Suda çözünen AOX’lar kullanıldığında EtOH çözeltiye hiç eklenmemiştir. Çözeltideki AOX’ın süperoksit radikali süpürücü etkisi AOX derişimine bağlı olarak incelenmiştir. Deneylede kullanılan her bir AOX derişimi ile ΔA (bkz. (2.1)) arasında çizilen grafiklerden AOX kalibrasyon denklemleri bulunmuştur. Her bir AOX derişimine bağlı olarak radikal süpürme etkinliğinin lineer olduğu aralık belirlenmiştir. Kalibrasyon denklemleri ve lineer aralıklar molarite (M) cinsinden hesaplanmıştır. Antioksidanların troluks eşdeğer antioksidan kapasite (TEAC) katsayıları hesaplanmıştır (bkz. (2.2)).

$$\Delta A = A_{Rf} - A_{ör} \quad (2.1)$$

Burada, A_{Rf} , süperoksit radikali içeren radikal süpürücü (AOX, bitki çayı) içermeyen referans çözeltisinin 552 nm’de suya karşı okunan absorbansını ve $A_{ör}$, süperoksit radikali içeren radikal süpürücü (AOX, bitki çayı) içeren çözeltinin 552 nm’de suya karşı okunan absorbansını temsil etmektedir.

$$TEAC \text{ Katsayısı} = \epsilon_{AOX} / \epsilon_{TR} \quad (2.2)$$

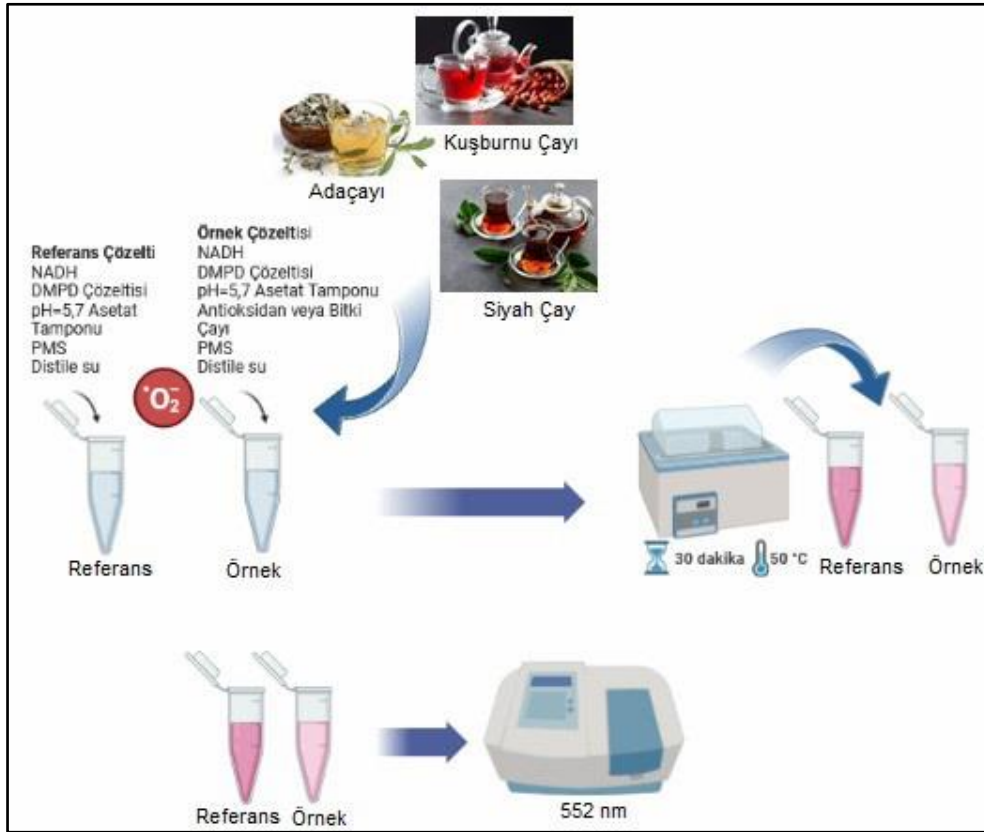
Burada, ϵ_{AOX} , kullanılan antioksidanın molar absorplama katsayısını ve ϵ_{TR} , TR’nin molar absorplama katsayısını temsil etmektedir.

2.2.4. Yöntemin Bitki Çaylarına Uygulanışı

Modifiye yöntem ile marketten satın alınan poşet siyah çay (*Camellia sinensis*), adaçayı (*Salvia officinalis*) ve kuşburnu çayı (*Rosa canina L.*) infüzyon (demleme) çözeltilerinin süperoksit anyon radikali süpürme etkinliği incelenmiş ve mmol TR/g bitki çayı cinsinden TAC tayini yapılmıştır. Ayrıca CUPRAC ve ABTS ile de TAC tayini yapıp, sonuçlar karşılaştırılmıştır. Bitki çaylarının µg/mL cinsinden EC50 değerleri modifiye edilen yöntemle, referans NBT-formazan ve ABTS yöntemindeki EC50 değerleri ile karşılaştırılmıştır.

EC50 değerleri ve TAC tayini için poşet bitki çayları tartılmıştır. Ortalama tartımı 1,48 g olan 3 farklı poşet adaçaya, ortalama tartımı 2,48 g olan 3 farklı poşet kuşburnu çaya ve ortalama tartımı 2,091 g olan siyah çaya infüzyon uygulanmıştır. Tartılan poşet çaylar 250 mL 100°C kaynar suda 2 dakika sallanarak 3 dakika

bekletilerek toplam 5 dakika demlenmiştir [27]. Çay infüzyon çözeltileri süzülüp, gerekli seyreltmelerden sonra denemelerde kullanılmıştır (Şekil 1).



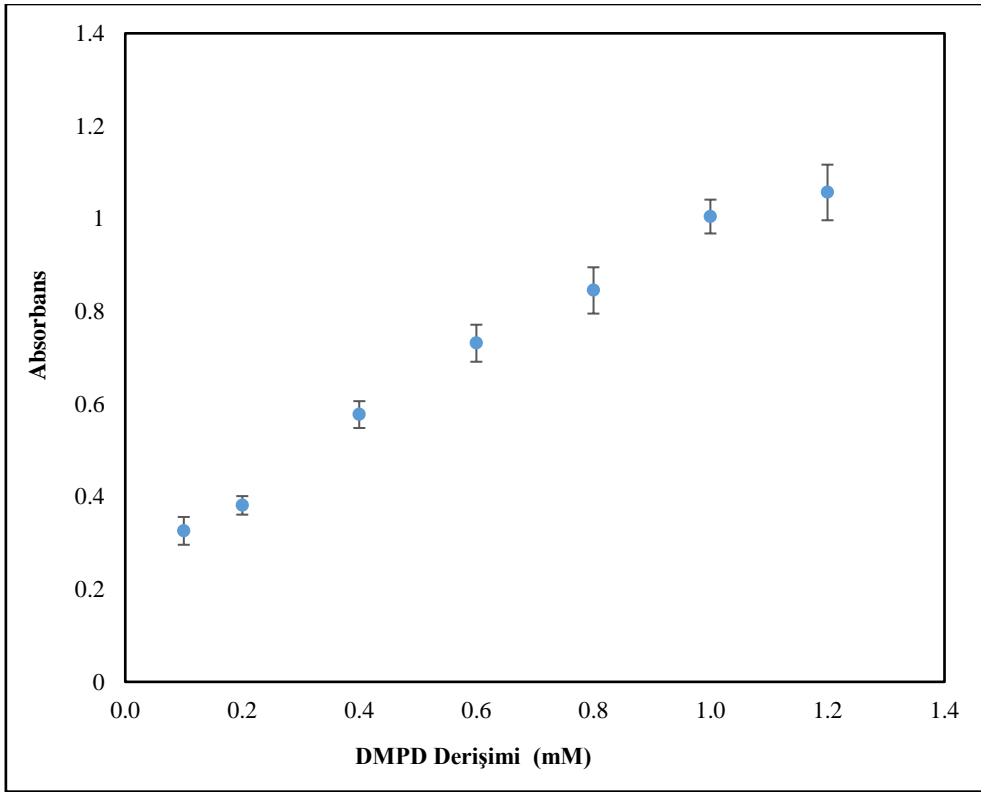
Şekil 1. Modifiye DMPD yöntemi diyagramı

3. Bulgular ve Tartışma

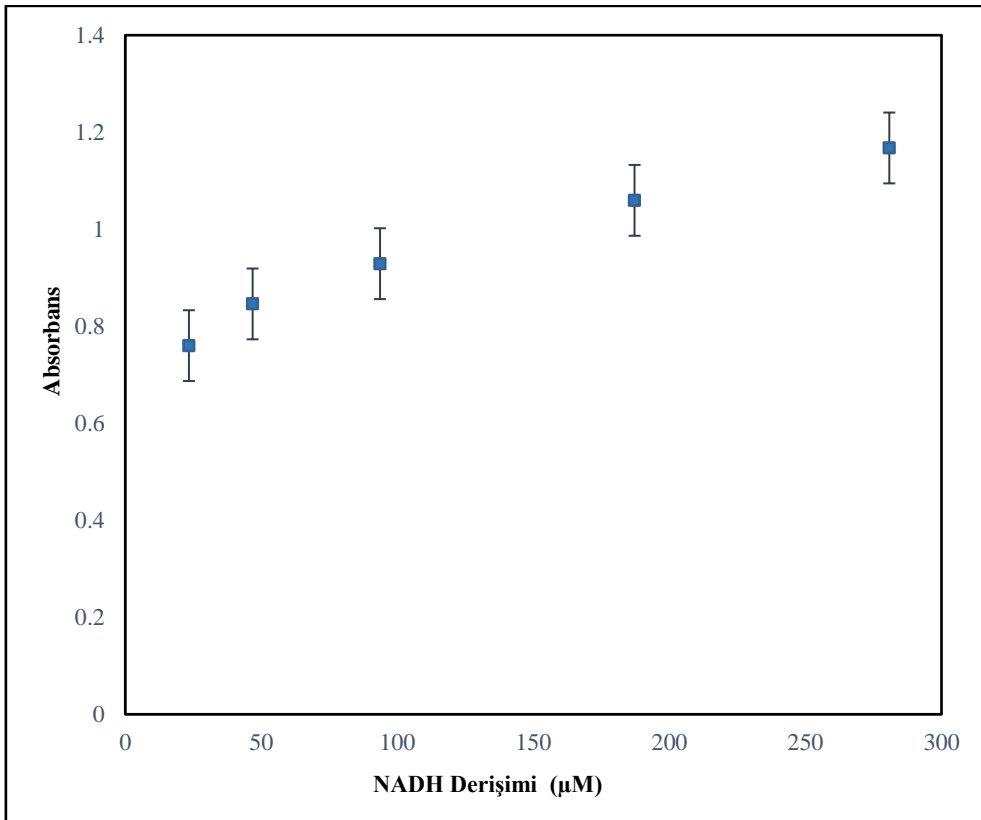
3.1. Modifiye NADH/PMS/DMPD Yöntem Optimizasyon Sonuçları

Yöntemde DMPD reaktifi ve süperoksit radikali içeren ortamda absorbandaki düşüşe göre tayin yapılacağından referans (radikal süpürücü içermeyen) çözelti absorbanı 0,9-1,1 olabilecek reaktif derişimleri seçilmiştir. $4,0 \times 10^{-3}$ M DMPD reaktifinden 0,05; 0,1; 0,2; 0,3; 0,4; 0,5 ve 0,6 mL alınıp 2,0 mL deney çözeltisi toplam hacmine bölünerek deney çözeltisi toplam hacmindeki DMPD derişimleri hesaplanmıştır. (Deney çözeltisindeki DMPD derişimleri: 0,1; 0,2; 0,4; 0,6; 0,8; 1,0 ve 1,2 mM DMPD'dir.) Deney çözeltisindeki DMPD derişimleri ile absorbanda optimizasyon grafiği çizilmiştir (Şekil 2). Aynı şekilde 936 μ M NADH reaktifinden 0,05; 0,1; 0,2; 0,4 ve 0,6 mL alınıp 2,0 mL deney çözeltisi toplam hacmine bölünerek deney çözeltisi toplam hacmindeki NADH derişimleri ve 120 μ M PMS reaktifinden 0,025; 0,05; 0,1; 0,2; 0,4; 0,6 ve 0,8 mL alınıp 2,0 mL deney çözeltisi toplam hacmine bölünerek deney çözeltisi toplam hacmindeki PMS derişimleri hesaplanmıştır (Deney çözeltisindeki NADH derişimleri: 27,4; 46,8; 93,6; 187,2 ve 280,8 μ M NADH'dir. Deney çözeltisindeki PMS derişimleri: 1,5; 3; 6; 12; 24; 36 ve 48 μ M PMS'dir). Deney çözeltisindeki NADH derişimleri ile absorbanda (Şekil 3) ve PMS derişimleri ile absorbanda (Şekil 4) arasında optimizasyon grafikleri çizilmiştir.

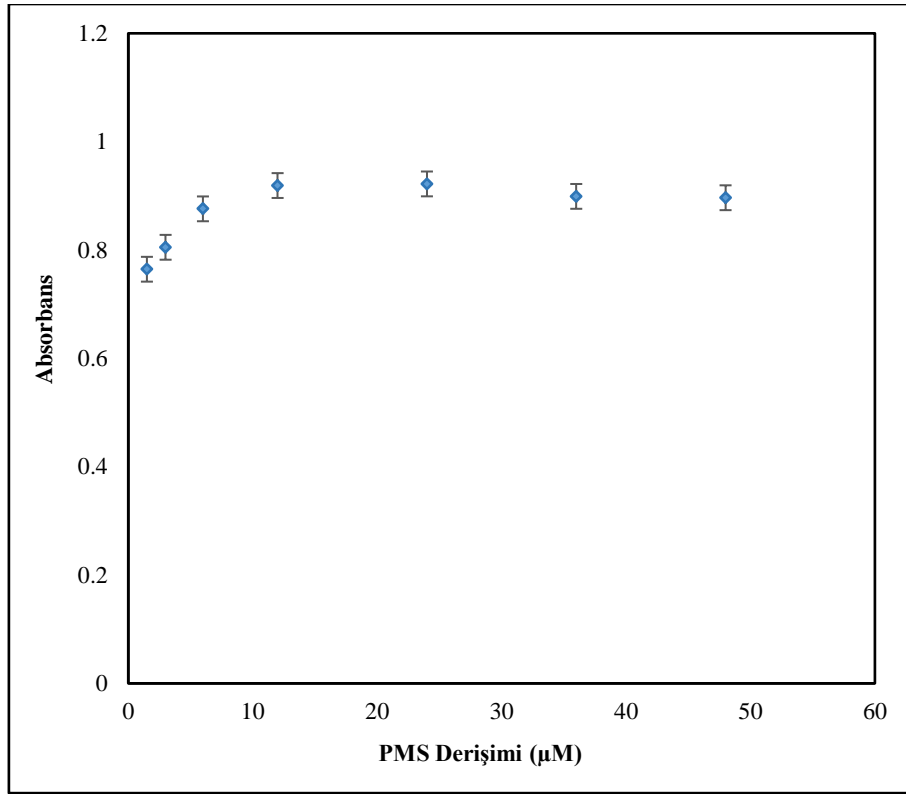
Yöntemde referans absorbandındaki düşüşe göre tayin yapılacağından DMPD, NADH ve PMS optimizasyon grafiklerinden referans (radikal süpürücü içermeyen) çözelti absorbanı 0,9-1,1 arasında olan DMPD, NADH ve PMS derişimleri en uygun derişim olarak seçilmiştir. En uygun derişimler DMPD için, 1,0 mM DMPD; NADH için, 93,6 μ M NADH ve PMS için, 24 μ M PMS'dir. Süperoksit radikali içeren ortamda renklenen deney çözeltisinin süpürücü (AOX veya bitki çayı) ilavesiyle DMPD radikali süpürüldükçe çözelti renginde azalma meydana gelir. Dolayısıyla, absorbanda düşüş oluşur.



Şekil 2. DMPD optimizasyonu (Ölçüm dalga boyu 552 nm)



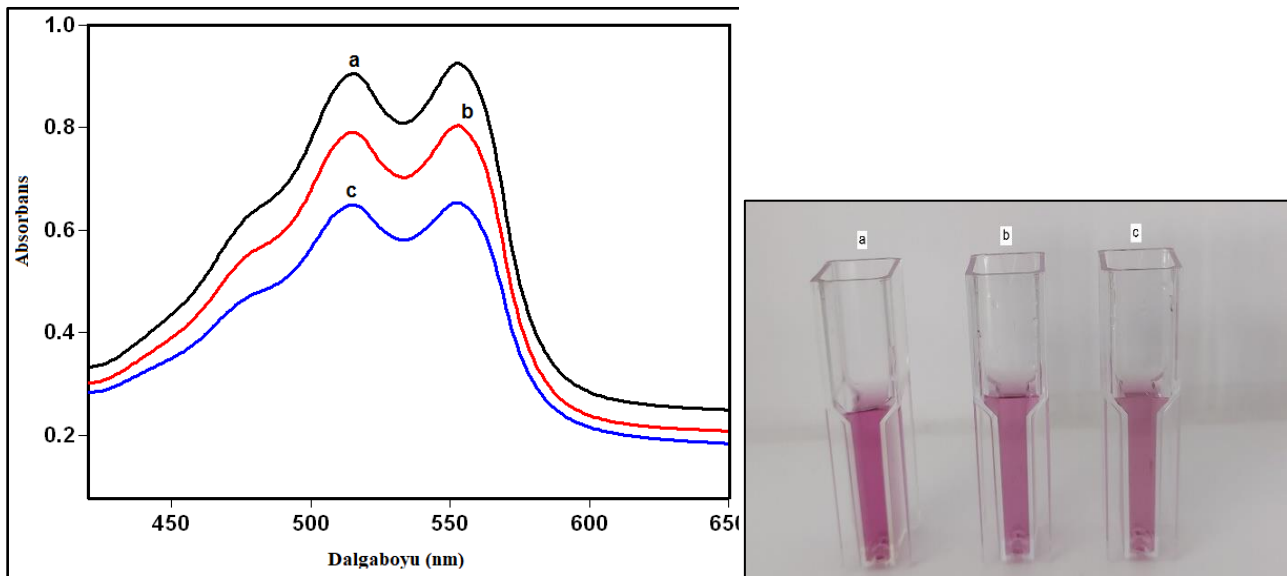
Şekil 3. NADH optimizasyonu (Ölçüm dalga boyu 552 nm)



Şekil 4. PMS optimizasyonu (Ölçüm dalga boyu 552 nm)

3.2. Antioksidan ve Bitki Çaylarının Yöntem Üzerindeki Etkisi

Yöntem optimizasyonu sonrası süperoksit anyon radikali üzerine 5 farklı AOX'ın (troloks, glutatyon, kateşin, rutin ve askorbik asit) ve 3 farklı bitki çayı infüzyonunun etkisi incelenmiştir. AOX kalibrasyon grafikleri, lineer aralıkları ve TEAC katsayıları belirlenmiştir (Tablo 1 ve Şekil 5). Yöntem 3 farklı bitki çayı infüzyonuna uygulanarak siyah çay (*Camellia sinensis*), adaçayı (*Salvia officinalis*) ve kuşburnu çayı (*Rosa canina L.*) TAC değerleri mmol TR/g bitki çayı cinsinden hem modifiye yöntemle hem de CUPRAC ve ABTS yöntemi ile hesaplanmıştır. Bitki çayların süperoksit radikali süpürme aktivitesi modifiye edilen yöntemle EC50 değerleri µg/mL cinsinden hesaplanmıştır. Sonuçlar referans NBT-formazan ve ABTS yöntemindeki EC50 değerleri ile karşılaştırılmıştır (Tablo 2 ve Şekil 6).



Şekil 5. a) DMPD ve süperoksit radikali içeren sulu çözelti b) DMPD, süperoksit radikali ve $1,0 \times 10^{-5}$ M troloks içeren çözelti c) DMPD, süperoksit radikali ve $4,0 \times 10^{-5}$ M troloks içeren çözelti

Tablo 1. Antioksidanların kalibrasyon denklemleri, lineer aralık ve TEAC sayıları

Antioksidan (AOX)	Kalibrasyon Denklemi	Lineer Aralık	TEAC Sayısı
Troloks (TR)	$\Delta A = 3002,4C + 0,053$ $R^2 = 0,9856$	$1,0 \times 10^{-5} - 1,0 \times 10^{-4} M$	1
Glutasyon (GSH)	$\Delta A = 9198,9C + 0,0991$ $R^2 = 0,9913$	$1,0 \times 10^{-5} - 5,0 \times 10^{-5} M$	3,06
Kateşin (CT)	$\Delta A = 10177C + 0,0211$ $R^2 = 0,9958$	$1,0 \times 10^{-5} - 6,0 \times 10^{-5} M$	3,39
Askorbik Asit (AA)	$\Delta A = 1980,5C - 0,159$ $R^2 = 0,9860$	$1,25 \times 10^{-4} - 5,0 \times 10^{-4} M$	0,66
Rutin (RT)	$\Delta A = 361,6C + 0,136$ $R^2 = 0,9669$	$1,0 \times 10^{-4} - 8,0 \times 10^{-4} M$	0,12

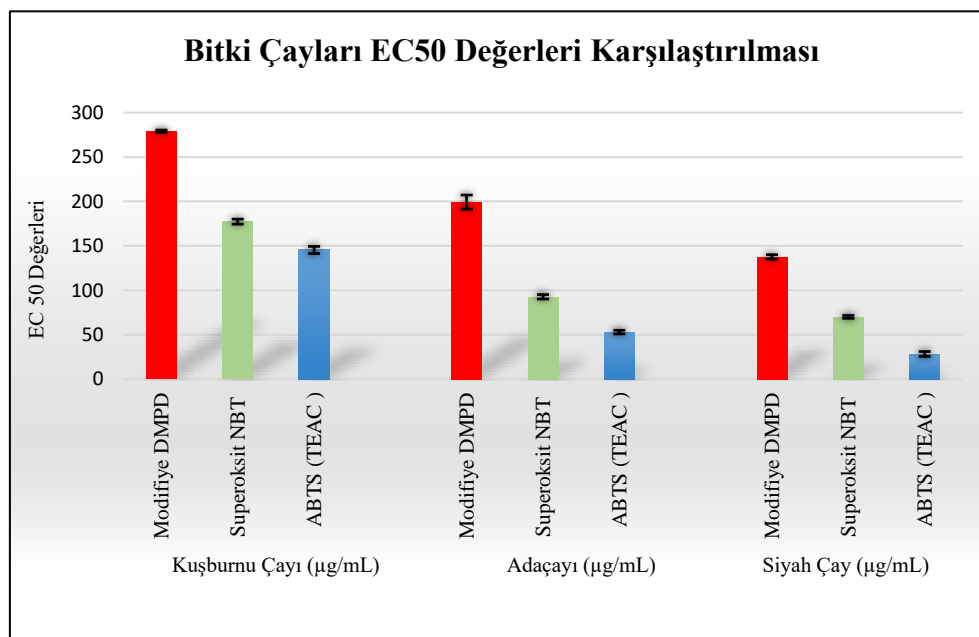
Tablo 1’de görüldüğü üzere AOX’ların NADH/PMS sistemi ile üretilen süperoksit anyon radikali süpürme aktivitesi TEAC katsayılarına göre $CT > GSH > TR > AA > RT$ şeklinde sıralanabilir. Süperoksit radikali süpürmesine bağlı olarak ΔA ile antioksidan derişimi arasında çizilen grafikten AOX’ların kalibrasyon denklemleri çıkarılıp, lineer aralıkları bulunmuştur (bkz. Tablo 1).

Tablo 2. Bitki çayı infüzyonlarının önerilen yöntem, CUPRAC ve ABTS TAC değerleri

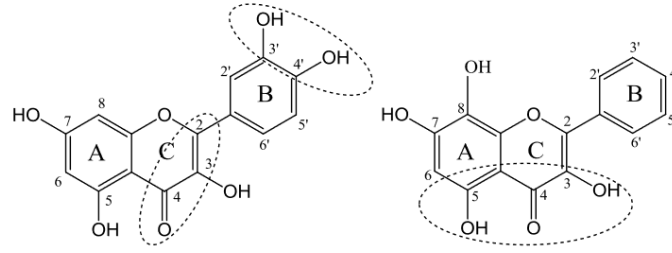
Bitki Çayı	Önerilen DMPD Yöntemi	CUPRAC Yöntemi	ABTS Yöntemi
Kuşburnu Çayı TAC değeri (mmol TR /g Bitki Çayı) ^a	$0,32 \pm 0,015$	$0,29 \pm 0,010$	$0,22 \pm 0,006$
Adaçayı (mmol TR/g Bitki Çayı) ^a	$0,59 \pm 0,064$	$0,47 \pm 0,043$	$0,36 \pm 0,047$
Siyah Çay (mmol TR /g Bitki Çayı) ^a	$1,86 \pm 0,099$	$1,02 \pm 0,049$	$0,73 \pm 0,044$

^a Sonuçlar TR ekivalent olarak hesaplanmıştır. $\bar{x} \pm$ standart sapma; $N = 3$

Bitki çaylarının süperoksit radikali %50 inhibisyon değerleri (EC50) modifiye yöntem, NBT-formazan ve ABTS yöntemine göre $\mu\text{g/mL}$ cinsinden Şekil 6’da gösterilmiştir. Şekil 6 incelendiğinde bitki çaylarının modifiye edilen yöntemde EC50 değerleri; kuşburnu çayı, 279 $\mu\text{g/mL}$, 199,3 $\mu\text{g/mL}$ adaçayı ve siyah çay 137,6 $\mu\text{g/mL}$ ’dir. NBT-formazan yönteminde EC50 değerleri; kuşburnu çayı 177,3 $\mu\text{g/mL}$, adaçayı 92,7 $\mu\text{g/mL}$ ve siyah çay 70,1 $\mu\text{g/mL}$ ’dir. ABTS yöntemindeki EC50 değerleri; kuşburnu çayı 145,4 $\mu\text{g/mL}$, adaçayı 52,9 $\mu\text{g/mL}$ ve siyah çay 28,3 $\mu\text{g/mL}$ ’dir. Tablo 2’de görüldüğü üzere üç farklı antioksidan kapasite tayin yöntemi uygulanan bitki çayı infüzyonlarının üç yöntemde de (önerilen modifiye DMPD, CUPRAC ve ABTS) TAC değerleri yüksekten düşüğe doğru siyah çay, kuşburnu çayı ve adaçayı şeklinde sıralanabilir. Yani süperoksit radikalininin yüzde elli oranında süpürülmesi için en az miktarda kullanılan siyah çay infüzyon çözeltisi en yüksek TAC değerine sahiptir.

**Şekil 6.** Bitki çayları EC50 değerleri karşılaştırılması

Yöntemde uygulanan beş farklı antioksidan çözeltisinin ve siyah çay, adaçayı, kuşburnu çayı bitki çayı infüzyonlarının süperoksit radikali süpürme aktiviteleri içerdikleri fenolik bileşiklerin yapısı ile ilişkilidir. Bitkilerde bol miktarda bulunan flavonoidler fenolik bileşiklerdir.



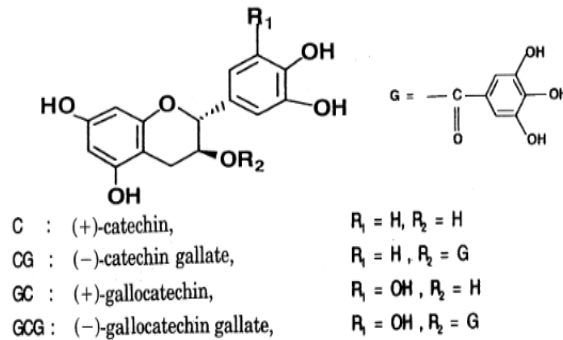
Şekil 7. Flavonoidlerin antioksidan aktivite yapı ilişkisi [28]

Şekil 7’de de gösterildiği gibi flavonoidler (antioksidanlar) aşağıdaki özelliklerin birine veya birkaçına sahip olduklarında daha yüksek antioksidan aktivite gösterirler [28]:

- Elektron delokalizasyonuna katkı sağlayan B halkasındaki o-dihidroksi (kateşol- iki komşu hidroksil grubu taşıyan benzen halkası) yapısına sahip olması,
- C halkasındaki ikinci ve üçüncü karbonlar arası çifte bağ ve C halkasının dördüncü karbonundaki keto grubunun B halkasından elektron delokalizasyonunu artırması (Aromatik bileşiğin elektron delokalizasyonu antioksidan güç ile doğru orantılıdır),
- Antioksidanların maksimum radikal süpürme etkisine sahip olabilmesi için A ve C halkalarının üçüncü ve beşinci pozisyonunda hidroksil gruplarının olması gerekmektedir. Ayrıca 5-hidroksi-4-keto grubu güçlü bir metal kelatlayıcıdır ve antioksidan etkinliğini artırır [29, 30].

Literatürde süperoksit radikali üzerine antioksidan aktivitesi ve bitki çayları (siyah çay, adaçayı ve kuşburnu çayı) üzerine yapılan çalışmalarda Şekil 7’de üzerinde anlatıldığı gibi flavonoidlerin yapısının antioksidan aktivitesi üzerine etkili olduğu gösterilmiştir.

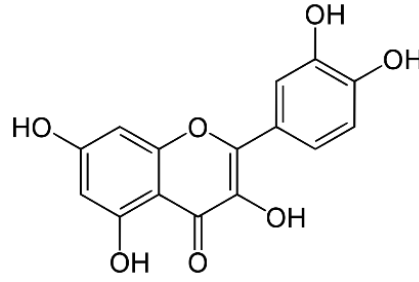
Çayın (*Camellia sinensis*) ana bileşeni kateşinlerdir (Şekil 8). Flavonoidlerin flavan-3-ol alt grubuna [31] ait kateşinlerin süperoksit radikali süpürme etkisi B halkasındaki kateşol ve pirogallol grubuna bağlıdır [32-34].



Şekil 8. Kateşin yapısı [35]

Çay büyük ölçüde kateşinleri içerdiği için çayın antioksidan özellikleri önemli oranda kateşinlerden kaynaklanmaktadır. Yıldırım vd. [36]’nin çalışmasında Türk çayının antioksidan aktivitesinin adaçayı antioksidan aktivitesinden daha yüksek olduğu gözlenmiştir. Farklı bir çalışmada çay kateşinlerinin süperoksit radikali süpürme etkisi incelenmiştir [37].

Yapılan diğer bir çalışmada [38] hem enzimatik (ksantin/ksantin oksidaz) hem de enzimatik olmayan (NADH/PMS) sistemiyle oluşturulan süperoksit radikalının süpürülmesinde kateşinler dışındaki flavonoidlerin etkisi araştırılmıştır. Çalışmada flavonoid alt grubu flavonollere [31] ait kuersetin (Şekil 9), mirisetin ve rutin antioksidanları en fazla süperoksit radikali süpürme aktivitesi göstermiştir.



Şekil 9. Kuersetin

Karakaya vd. [39] tarafından yapılan çalışmada siyah çay, adaçayı, kuşburnu çayının kuersetin, luteolin, apigenin, kaemferol içerikleri ve miktarları karşılaştırılmış en fazla içeriğe siyah çayın daha sonra adaçayının ve son olarak kuşburnu çayının sahip olduğu görülmüştür.

Modifiye DMPD yönteminin uygulandığı siyah çay, adaçayı ve kuşburnu çayının süperoksit radikali süpürme aktivitesi hem literatürler dikkate alındığında hem de sonuçlarımıza göre büyükten küçüğe doğru siyah çay, adaçayı ve kuşburnu çayı şeklinde sıralanmaktadır. Siyah çayın aktivitesinin adaçayı ve kuşburnu aktivitesinden yüksek olması; çayın içerdiği kateşinler, kuersetin, luteolin, apigenin, kaemferol antioksidanlarının miktarı ve etkisinden kaynaklanmaktadır [40].

Modifiye DMPD yöntemi, CUPRAC ve ABTS yöntem sonuçlarına göre bitki çaylarının TAC değerleri (bkz. Tablo 2) ve Şekil 6'daki EC50 değerleri incelendiğinde sonuçların literatürlerdeki antioksidan yapı aktivite ilişkisi ile uyumlu olduğu gözlenmektedir.

4. Sonuçlar

Çalışmada NADH/PMS sistemi ile üretilen süperoksit radikali tarafından DMPD reaktifi pembe renkli DMPDQ radikaline oksitlenir. Süperoksit süpürme aktivitesi sergileyen radikal süpürücü varlığında daha az DMPDQ radikali oluşumu nedeniyle çözeltinin renk yoğunluğu azalır. 552 nm dalga boyundaki absorpsiyon ölçümü sonrası radikal süpürücü içermeyen referans çözeltisi ile süpürücü içeren örnek çözeltisi arasında ΔA hesaplanmıştır. ΔA ile AOX derişimi arasında çizilen grafikten AOX'ların molarite cinsinden kalibrasyon eğrileri, lineer aralıkları ve TEAC katsayıları hesaplanmıştır (Tablo 1). TEAC katsayılarına göre AOX'lar sıralandığında CT'nin en yüksek RT'nin en düşük süperoksit radikali süpürme aktivitesine sahip olduğu görülür. Süpürücü olarak kuşburnu çayı, adaçayı ve siyah çay infüzyon çözeltilerine çalışılan modifiye yöntem, NBT-formazan ve ABTS yöntemi uygulanıp, EC50 değerleri hesaplanmıştır. Tüm yöntemlerdeki EC50 değerleri karşılaştırılıp düşükten yükseğe doğru sıralandığında tüm yöntemlerde en düşük EC50 değerinin siyah çaya ait olduğu görülmüştür. Siyah çaydan sonra adaçayı ve kuşburnu çayı gelmektedir. EC50 değeri en düşük olan siyah çay en yüksek radikal süpürme aktivitesine sahiptir (bkz. Şekil 6). Ayrıca bitki çayları infüzyonlarının süperoksit radikali süpürme etkisine bağlı olarak çalışılan modifiye yöntem, CUPRAC ve ABTS yöntemleri ile TAC değerleri hesaplanmıştır (bkz. Tablo 2). Tablo 2'de görüldüğü üzere önerilen DMPD, CUPRAC ve ABTS yöntemi uygulanan bitki çayı infüzyonlarının üç yöntemde de TAC değerleri yüksekten düşüğe doğru siyah çay, adaçayı ve kuşburnu çayı olarak sıralanmaktadır. Yani süperoksit radikalinin yüzde elli oranında süpürülmesi için kullanılan siyah çay infüzyon çözeltisi en yüksek TAC değerine sahiptir. Tablo 2'deki bitki çayı infüzyonlarının TAC değerleri incelendiğinde EC50 değerleri ile TAC değerlerinin tutarlı olduğu görülmektedir. Modifiye edilen yöntemle 552 nm'de absorpsiyon ölçümü yapılmadan da çıplak gözle çözeltinin rengindeki değişime bakılarak ortamdaki hem süperoksit radikali hem de antioksidan varlığı tespit edilebilir.

Yazar Katkıları

Yazar makalenin son halini okuyup onaylamıştır.

Çıkar Çatışması

Yazar hiçbir çıkar çatışması olmadığını beyan etmektedir.

Etik İnceleme ve Onay

Etik Kurulu'ndan onay alınmasına gerek yoktur.

Teşekkür

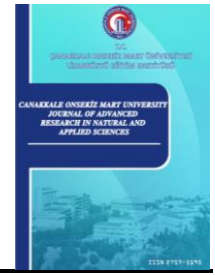
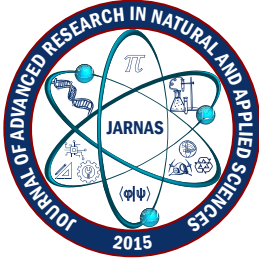
Bu çalışma, 114Z089 proje numarasıyla Türkiye Bilimsel ve Teknolojik Araştırma Kurumu (TÜBİTAK) ve FDP-2017-24832 proje numarasıyla Bilimsel Araştırma Projeleri Koordinasyon Birimi tarafından desteklenmiştir.

Kaynakça

- [1] B. Halliwell, *Reactive species and antioxidants. Redox biology is a fundamental theme of aerobic life*, Plant Physiology 141 (2) (2006) 312-322.
- [2] P. A. Riley, *Free radicals in biology: Oxidative stress and the effects of ionizing radiation*, International Journal of Radiation Biology 65 (1) (1994) 27-33.
- [3] L. A. Pham-Huy, H. He, C. Pham-Huy, *Free radicals, antioxidants in disease and health*, International Journal of Biomedical Science 4 (2) (2008) 89-96.
- [4] V. I. Lushchak, O. Lushchak, *Interplay between reactive oxygen and nitrogen species in living organisms*, Chemico-Biological Interactions 349 (2021) 109680 6 pages.
- [5] B. Halliwell, *Free radicals and antioxidants: Updating a personal view*, Nutrition Reviews 70 (5) (2012) 257-265.
- [6] B. Li, S. B. Vik, Y. Tu, *Theaflavins inhibit the ATP synthase and the respiratory chain without increasing superoxide production*, The Journal of Nutritional Biochemistry 23 (8) (2012) 953-960.
- [7] H. Takahashi, A. Nishina, R. H. Fukumoto, H. Kimura, M. Koketsu, H. Ishihara, *Selenocarbamates are effective superoxide anion scavengers in vitro*, European Journal of Pharmaceutical Sciences 24 (4) (2005) 291-295.
- [8] M. D. Brand, *The sites and topology of mitochondrial superoxide production*, Experimental Gerontology 45 (7-8) (2010) 466-472.
- [9] S. Dimauro, E. A. Schon, *Mitochondrial respiratory-chain diseases*, The New England Journal of Medicine 348 (26) (2003) 2656-2668.
- [10] I. Fridovich, *Oxygen toxicity: A radical explanation*, Annual Review of Biochemistry 201 (8) (1995) 1203-1209.
- [11] B. Halliwell, J. M. C. Gutteridge, *Oxygen toxicity, oxygen radicals, transition metals and disease*, Biochemical Journal 219 (1) (1984) 1-14.
- [12] G. Martemucci, C. Costagliola, M. Mariano, L. D'andrea, P. Napolitano, A. G. D'Alessandro, *Free radical properties, source and targets, antioxidant consumption and health*, Oxygen 2 (2) (2022) 48-78.
- [13] R. Apak, K. Güçlü, M. Özyürek, S. E. Karademir, *Novel total antioxidant capacity index for dietary polyphenols and vitamins C and E, using their cupric ion reducing capability in the presence of neocuproine: CUPRAC method*, Journal of Agricultural and Food Chemistry 52 (26) (2004) 7970-7981.

- [14] F. Shahidi, P. Ambigaipalan, *Phenolics and polyphenolics in foods, beverages and spices: Antioxidant activity and health effects - A review*, Journal of Functional Foods 18 (2015) 820–897.
- [15] R. Re, N. Pellegrini, A. Proteggente, A. Pannala, M. Yang, C. Rice-Evans, *Antioxidant activity applying an improved ABTS radical cation decolorization assay*, Free Radical Biology and Medicine 26 (9–10) (1999) 1231–1237.
- [16] I. F. F. Benzie, J. J. Strain, *Ferric reducing/antioxidant power assay: Direct measure of total antioxidant activity of biological fluids and modified version for simultaneous measurement of total antioxidant power and ascorbic acid concentration*, Analytical Biochemistry 239 (1996) 70–76.
- [17] W. Brand-Williams, M. E. Cuvelier, C. Berset, *Use of a free radical method to evaluate antioxidant activity*, LWT - Food Science and Technology 28 (1) (1995) 25–30.
- [18] V. Fogliano, V. Verde, G. Randazzo, A. Ritieni, *Method for measuring antioxidant activity and its application to monitoring the antioxidant capacity of wines*, Journal of Agricultural and Food Chemistry 47 (3) (1999) 1035–1040.
- [19] M. D. Rivero-Pérez, P. Muñiz, M. L. González-Sanjosé, *Antioxidant profile of red wines evaluated by total antioxidant capacity, scavenger activity, and biomarkers of oxidative stress methodologies*, Journal of Agricultural and Food Chemistry 55 (14) (2007) 5476–5483.
- [20] K. Hirayama, N. Unohara, *Spectrophotometric catalytic determination of an ultratrace amount of iron(III) in water based on the oxidation of N, N-Dimethyl-p-phenylenediamine by hydrogen peroxide*, Analytical Chemistry 60 (23) (1988) 2573–2577.
- [21] M. N. Ashgar, I. U. Khan, M. N. Arshad, L. Sherin, *Evaluation of antioxidant activity using an Improved DMPD radical cation decolorization assay*, Acta Chimica Slovenica 54 (2007) 295–300.
- [22] P. Saha, P. Banerjee, L. Auddya, P. Pal, M. Das, M. Dutta, S. Sen, M. C. Mondal, A. Kumar, U. K. Biswas, *Simple modified colorimetric methods for assay of total oxidative stress and antioxidant defense in plasma: Study in diabetic patients*, Archives of Medicine 7 (5) (2015) 1–7.
- [23] S. D. Çekiç, A. N. Avan, S. Uzunboy, R. Apak, *A colourimetric sensor for the simultaneous determination of oxidative status and antioxidant activity on the same membrane: N, N-Dimethyl-p-phenylene diamine (DMPD) on Nafion*, Analytica Chimica Acta 865 (1) (2015) 60–70.
- [24] F. Dondurmacioğlu, A. N. Avan, R. Apak, *Simultaneous detection of superoxide anion radicals and determination of the superoxide scavenging activity of antioxidants using an N,N- dimethyl-p-phenylene diamine/Nafion colorimetric sensor*, Analytical Methods 9 (43) (2017) 6202–6212.
- [25] M. Nishikimi, N. Appaji Rao, K. Yagi, *The occurrence of superoxide anion in the reaction of reduced phenazine methosulfate and molecular oxygen*, Biochemical and Biophysical Research Communications 46 (2) (1972) 849–854.
- [26] M. P. Chagas, J. C. C. Santos, E. B. G. N. Santos, T. D. Oliveira, M. Korn, *Exploiting iminoquinone free radical production for thiol based drugs determination in pharmaceutical formulations*, Journal of the Brazilian Chemical Society 20 (9) (2009) 1646–1652.
- [27] R. Apak, K. Güçlü, M. Özyürek, S. Esin Karademir, E. Erçağ, *The cupric ion reducing antioxidant capacity and polyphenolic content of some herbal teas*, International Journal of Food Sciences and Nutrition 57 (5–6) (2006) 292–304.
- [28] D. Amic, D. Davidovi-Ami, D. Belo, V. Rastija, B. Lui, N. Trinajsti, *SAR and QSAR of the antioxidant activity of flavonoids*, Current Medicinal Chemistry 14 (2007) 827–845.
- [29] A. T. Diplock, J. L. Charuleux, G. Crozier-Willi, F. J. Kok, C. Rice-Evans, M. Roberfroid, W. Stahl, J. Viña-Ribes, *Functional food science and defence against reactive oxidative species*, British Journal of Nutrition 80 (S1) (1998) 77–112.

- [30] C. A. Rice-Evans, N. J. Miller, G. Paganga, *Structure-antioxidant activity relationships of flavonoids and phenolic acids*, Free Radical Biology & Medicine 20 (7) (1996) 933–956.
- [31] M. Atinç, İ. Kalkan, *Flavonoids in food and their health benefits*, Aydın Gastronomy 2 (1) (2018) 31–38.
- [32] K. Furuno, T. Akasako, N. Sugihara, *The contribution of the pyrogallol moiety to the superoxide radical scavenging activity of flavonoids*, Biological and Pharmaceutical Bulletin 25 (1) (2002) 19–23.
- [33] A. A. Bunaciu, A. F. Danet, Ş. Fleschin, H. Y. Aboul-Enein, *Recent applications for in vitro antioxidant activity assay*, Critical Reviews in Analytical Chemistry 46 (5) (2016) 389–399.
- [34] B. A. Sutherland, R. M. A. Rahman, I. Appleton, *Mechanisms of action of green tea catechins, with a focus on ischemia-induced neurodegeneration*, The Journal of Nutritional Biochemistry 17 (5) (2006) 291–306.
- [35] T. Toyo'oka, T. Kashiwazaki, M. Kato, *On-line screening methods for antioxidants scavenging superoxide anion radical and hydrogen peroxide by liquid chromatography with indirect chemiluminescence detection*, Talanta 60 (2-3) (2003) 467–475.
- [36] A. Yildirim, A. Mavi, M. Oktay, A. A. Kara, O. F. Algur, V. Bilaloglu, *Comparison of antioxidant and antimicrobial activities of Tilia (Tilia argentea Desf ex DC), sage (Salvia triloba L.), and Black tea (Camellia sinensis) extracts*, Journal of Agricultural and Food Chemistry 48 (10) (2000) 5030–5034.
- [37] T. Unno, F. Yayabe, T. Hayakawa, H. Tsuge, *Electron spin resonance spectroscopic evaluation of scavenging activity of tea catechins on superoxide radicals generated by a phenazine methosulfate and NADH system*, Food Chemistry 76 (2) (2002) 259–265.
- [38] J. Robak, R. J. Gryglewski, *Flavonoids are scavengers of superoxide anions*, Biochemical Pharmacology 37 (5) (1988) 837–841.
- [39] S. Karakaya, S. Nehir El, *Quercetin, luteolin, apigenin and kaempferol contents of some foods*, Food Chemistry 66 (3) (1999) 289–292.
- [40] S. Salman, G. Öz, R. Felek, A. Haznedar, T. Turna, F. Özdemir, *Effects of fermentation time on phenolic composition, antioxidant and antimicrobial activities of green, oolong, and black teas*, Food Bioscience 49 (2022) 101884 9 pages.



A Criticism of the Kyoto Protocol with an Objective Approach

Sertaç Atabey¹ , Zeynel Fuat Toprak² 

¹Department of Civil Engineering, Graduate School of Natural and Applied Sciences, Dicle University, Diyarbakır, Türkiye

²Department of Civil Engineering, Dicle University, Diyarbakır, Türkiye

Article Info

Received: 13 Mar 2024

Accepted: 31 May 2024

Published: 30 Sep 2024

Research Article

Abstract – The Kyoto Protocol, established to reduce greenhouse gas emissions, one of the human-induced causes of climate change, imposes obligations on developed countries. In this study: 1) what obligations the articles of the Kyoto Protocol impose on the countries that are party to the protocol, 2) whether the articles of the protocol are impartial, equal, and fair in their obligations to the contracting countries and their binding, 3) how the economic support of developed countries to reduce emissions to developing countries can be evaluated in the context of the principle of equality/justice, 4) it has been discussed whether the non-bindingness of the countries those are not party to the protocol. Considering all protocol items, the discussion was made from a critical but constructive point of view. It can be said that the obligations arising from the Kyoto Protocol bring disadvantages for some countries compared to others.

Keywords – Kyoto Protocol, global climate change, greenhouse gas emission, equality, justice

1. Introduction

Approximately 90% of academic studies show evidence of global climate change. Unfortunately, scientists have not fully agreed on the causes and consequences of global climate change as they have on the problem's existence. Therefore, today, the problem is still discussed. As a matter of fact, the authors state that there is not such a strong consensus among scientists in answering the questions "why", "how", and "how much" [1]. While some scientists argue that climate change is a natural process and that there have been thermal and ice ages in the past [2], some scientists say that the problem is caused by humans and is caused by gases that are known to have a greenhouse effect as a result of fossil energy sources use. IPCC reports are at the forefront of making this claim. Al-Amin et al. [3] state, "The impact of climate change and global warming is a product of human greedy activities and begins with technological mastery, which over time has dangerous consequences on the environment and has repercussions."

Global climate change seriously threatens the naturalness and compatibility of our planet in terms of meteorological events and, accordingly, humans and other living life, particularly in the last few decades. In order to overcome such a serious problem that globally affects life and the quality of life, governments, scientific circles, non-governmental organizations, and all sectors can inevitably contribute to the solution of the problem with global participation. Research on climate change is carried out, and meetings are held by wide circles, especially the scientific community. As a result of these efforts, the Kyoto Protocol was accepted among the parties to the United Nations Framework Convention on Climate Change (UNFCCC) in 1997 at the 3rd Conference of the Parties in Kyoto and entered into force in 2005. Currently, 191 countries, including

¹sertac_atabey@yahoo.com (Corresponding Author); ²toprakzf@dicle.edu.tr

EU countries, are parties to the protocol. The protocol consists of 28 articles. In addition, the Paris Agreement was signed in 2015 within the scope of the UNFCCC to reduce climate change and adapt to the problem and entered into force in 2016.

In UNFCCC, the countries parties to the convention are classified into two groups: industrialized countries and countries transitioning to a market economy. The Kyoto Protocol (KP) constantly refers to this classification, bringing various binding obligations between developing and developed countries, resulting in some sanctions.

Brunnée [4] states that "the success or failure of KP's market-based mechanisms largely depends on the balance in the rules governing these mechanisms." Vanderheiden [5], on the other hand, argues that climate change can be seen as a question of intergenerational justice and is a useful framework for discussing the ideals of equality and responsibility set by the 1992 UNFCCC and international climate policy architecture. However, according to Falkner [6], demands for fairness in sharing the burden of climate change mitigation have been at the center of international climate negotiations since the late 1980s. Similarly, even more assertively, Demirci [7] states, "After the KP, there was a certain burden distribution on the countries that were party to the protocol, but since there was dissatisfaction with almost all parties in the context of justice, climate change was constantly discussed in the negotiations held after the protocol in terms of financial and benefits." Santos [8] also expresses his concerns on the issue, saying that the protocol only sets emission reduction targets for industrialized countries according to the principle of differentiated responsibilities, and this situation leads to a deep division in the views of developed and developing countries on cooperation and equality issues. Güneş [9], on the other hand, criticizes the KP as "it is a contract that imposes significant restrictions on production and trade in the functioning of the private sector, based on market mechanisms, and carries much heavier obligations, which has serious economic consequences compared to other environmental agreements." Böhringer [10] pointed out the flexibility of the Protocol and thought that the flexibility must be emphasized. From an economic point of view, globalization in production is fundamentally reshaping how a "just" solution to the problem of climate change should be created [11]. Based on all these, the study's main purpose is to question whether the obligations imposed by the KP on the countries that are parties to the protocol are equal and fair, and to reveal the necessity of eliminating any situations contrary to the principles of equality and justice. With this approach, the authors emphasize the need for a fair distribution of obligations. This study has tried to understand whether the comments made are reasonable and sufficient by evaluating the few studies that have included criticisms that KP may have created some injustices. In addition, how to approach these evaluations from different angles and whether new interpretations can be brought has been another aim of this study. The Kyoto Protocol articles formed the study's main material, and other studies were also supportive. The necessary analyses were made and the issues that could cause problems were tried to be determined, and then suggestions were made on what can be done to solve these problems.

2. International Emission Amounts and Kyoto Protocol

The countries that bear the highest responsibility for environmental pollution are some G8 countries, which are the USA, Canada, Russia, Germany, Japan, and England, with 10-20 tons of CO₂ emissions per capita [12]. While only a few of the developing countries group announced their digitized emission and limitation targets in the ongoing negotiations around the KP, it remains uncertain how the United States (USA), which is not a party to the KP, can contribute to the ongoing negotiations based on the protocol [13]. Rosen [14] expresses this situation as follows: More questions may arise as to why policymakers chose to focus on an agreement that had little impact on key players for 15 years, even though there are countries not bound by the KP, such as China and the United States, which together are responsible for around 40 percent of global carbon dioxide emissions.

However, we believe that this statement contradicts the rates given above. Because if China and the USA alone cause emissions by 40%, it seems too ambitious to say that middle-income developing countries mostly cause emissions when the emission rate or volume of Japan, EU countries and other developed countries is

considered. It could not be put into effect for a long time because at least 55 countries were responsible for a minimum of 55% of the total emissions in 1990, which is the condition for the protocol to come into force for the KP to reach its goals officially, are party to the protocol. The countries in question have not signed the protocol [16]. Many countries have heavily discussed the protocol as it does not include much detail about the design and execution of flexibility mechanisms [17].

The first conference of the parties was held in Berlin in 1995. At this meeting, the parties decided to protect the climatic system with a harmonious and equal attitude but with differentiated responsibilities [18]. However, the greenhouse gas emissions of people living in developing countries are very small compared to those of people living in developed countries, and there are serious inequalities in greenhouse gas production between countries [19]. It can also be thought that the fact that the UNFCCC was signed with the participation of almost all countries is related to the fact that the reduction targets and duties were not determined very specifically within the scope of the contract [20].

The USA, which is the country with the highest emission level in the studies revealed and did not accept to ratify the protocol despite signing the protocol, opposed a decision that creates an obligation in the international context and demanded that the emission reduction amounts of the countries be at their initiative [21].

A static partial equilibrium model developed at Center for International Climate and Environmental Research – Oslo (CICERO) predicts that without the USA, KP would reduce only 0.9 percent of emissions globally [22].

According to the UNFCCC, global climate change is anthropogenic. In order to minimize the problem, it is claimed that the KP, which was accepted among the contracting countries, imposes heavy obligations on the parties [9]. We do not fully agree with this claim, but it can be said that the protocol imposes an obligation, even if it is not heavy. In our opinion, the main problem is not the heavy obligations brought by the protocol but the insecurity and concern that these obligations are not shared with a fair approach, both in the articles and the implementation of the articles. For this reason, this study has tried to examine what kind of problems may arise in terms of both the protocol articles and the fair approach required by the universal and ethical rules for the parties or non-parties in the case of the implementation of these articles, and whether there are noticeable problems when the protocol articles are evaluated with an egalitarian approach. Scientific studies on KP have been reviewed with great sensitivity and a wide literature review. In the literature review, many studies were found about KP. Still, it was seen that there were not many studies that handled the protocol with an egalitarian approach with the method followed in this study. In this respect, it is thought that supporting the literature with a study that evaluates the issue with this approach is important in creating constructive suggestions for the KP, which has the participation of almost all countries and aims to solve a crucial problem such as global climate change.

3. Discussion of the Literature Related to the Subject

The success of KP is associated with the balanced rules of the protocol mechanism [4]. This assessment is considered quite reasonable and necessary. In terms of the countries subject to the protocol, it is considered extremely important that the obligations brought by the rules of the protocol mechanism have a delicate balance and impose fair sanctions on all parties. Furthermore, it is essential that the sanctions are proportionally distributed and that the sanctioned countries are determined in a way that they cannot exceed their power and can easily apply. In terms of states, it is thought that the possible arguments and objections that may occur with the opinion that the protocol has these features will be minimized. Therefore, the protocol articles will be implemented more easily.

It is thought that it would be beneficial to evaluate the ideals determined within the scope of UNFCCC with an egalitarian approach in terms of climate policy architecture [5]. This approach is important for the applicability of the UNFCCC and KP. When the architectural structure of KP is handled and discussed to contribute, it will enable some improvements in having a fair structure.

It is stated that after the burden distribution between the countries that are party to the protocol, there is dissatisfaction in the countries, and this causes discussions in the negotiations [7]. This situation can be considered a natural consequence of the formation of doubts among the parties to the protocol about whether the obligations brought by the KP are positioned fairly.

It is stated by Böhringer [10] that the architectural structure of the KP causes serious flexibility and therefore needs to be considered. The flexibility mechanism of the protocol can be partially removed and made more effective. The fact that the protocol formation has a clear and specific structure, and its rules are clear and applicable will impact its healthy workability. Explanation of the flexibility, which must be mandatory in terms of implementation, together with the reasons, will increase the acceptability of the protocol.

From a financial point of view, it is stated that the globalization of production over time essentially reshapes the issue of finding just solutions to climate change [11]. Unless a fair solution to the problem is brought with the KP, the KP itself will become the problem. Since it affects all life sectors, from agriculture to energy, both individually and socially, the protocol, which aims to eliminate or reduce the problem of climate change, requires sensitive and fair planning regarding the obligations that the parties must fulfill.

Although the USA is the country that bears the highest responsibility for CO₂ emissions [12], it is stated that it is unclear how the USA's non-participation will affect the climate change negotiations [13]. These concerns and criticisms are thought to be quite justified. The fact that the USA, which has the greatest impact on environmental pollution in terms of emitted CO₂ (please see Table 1 and Figure 1), is not a party to the KP and naturally does not assume any obligations is one of the biggest concerns of the parties. This concern stems from the suspicion that the protocol cannot be implemented, cannot achieve its goals even if it is implemented, and will be far from justice and equality.

Table 1 shows the total greenhouse gas emissions of some countries with the highest and least greenhouse gas emissions for 2016. The data was obtained from the official website of the Turkish Statistical Institute (TUIK) for 2016. The table helps readers to more easily significant the position of the USA in terms of total greenhouse gas emissions compared to other countries. Here, the five countries with the highest and lowest emissions from the countries shared by TUIK are considered [23]. For the same aim, Figure 1 has been generated from the data in the first part of Table 1. The figure makes the position of the USA more visible among the five countries with the highest total greenhouse gas emissions [23].

Table 1. Total greenhouse gas emissions of some countries with the highest and least greenhouse gas emissions, 2016 (Million tons CO₂ equivalent) [23]

Countries with the Highest Total Greenhouse Gas Emissions	Total Greenhouse Gas Emissions (Million tons CO₂ equivalent)
United States of America	6511.3
Russian Federation	2643.8
Japan	1304.6
Germany	909.4
Canada	704.2
Countries with the Least Total Greenhouse Gas Emissions	Total Greenhouse Gas Emissions (Million tons CO₂ equivalent)
Latvia	11.2
Luxembourg	10.0
Iceland	4.7
Malta	1.9
Liechtenstein	0.2

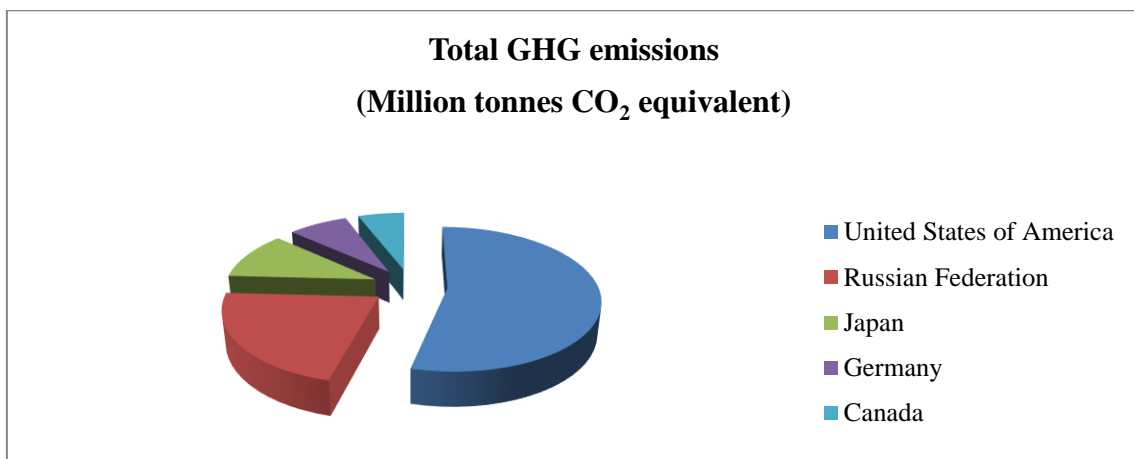


Figure 1. The relative shares of the five countries with the highest greenhouse gas emissions [23]

Akkale [16] states that the condition for the country's participation with a certain emission volume/rate, which is necessary for the KP to enter into force, could not be fulfilled for a long time. It can be said that the prolongation of this process is due to the above-mentioned concerns. On the other hand, Türkeş et al. [17] claim that the protocol's flexibility mechanisms cause serious discussions because it does not have enough details. It can be thought that the protocol has been designed very comprehensively, but it should still have details in a way that does not leave any question marks in terms of states. However, details may complicate the applicability of the protocol. In that case, the articles should be detailed enough not to leave any question marks and simple enough not to hinder their implementation.

Greenhouse gas emissions can show serious differences depending on the technological level that the countries have reached and their level of development. It can be argued that this situation is to be considered by the protocol articles among the countries party to it. However, because all countries in the world cause CO₂ emissions with a low or high level, but not all countries are party to the protocol, there may be questions about whether there is an egalitarian approach to the distribution of obligations. The reason for the incomplete participation in the KP and that almost all countries signed the UNFCCC can be evaluated as the uncertainty in the protocol articles and the insecurity in the implementation.

The fact that the country or countries with the highest amount of emission do not approve the protocol causes the emission reduction obligations to remain on the countries that cause less emission rather than the country that causes it the most. This causes the countries that are party to the protocol to think they are being treated unfairly. It is considered extremely important for the operability of the protocol that the states that are the most responsible for climate change, which threatens human life on a global basis, are more sensitive. As mentioned above, it is stated that some models predict that if the USA is not a party to the protocol, global emissions can only be reduced by 0.9 percent [22]. This rate indicates that even if the parties to the protocol fully fulfill their emission reduction obligations, this will be insufficient on a global scale.

4. Assessments on the Protocol Items

Some articles of the KP are controversial regarding the sanctions it imposes regarding its inclusiveness and applicability. The principle of "common but differentiated responsibilities" is frequently referred to in the protocol text. Paragraph #1 of the third Article of the Protocol obliges Annex I countries to reduce their total greenhouse gas emissions to at least five percent below the 1990 level. Although it seems to be an equal approach, it is impossible for some countries to decrease below the 5% level of 1990, even though they reduce by the same amount in total. To reach the mentioned percent they need to go further reduction. Therefore, even if the obligation to reduce at the same rate seems to be an equal approach, it isn't easy to evaluate it fairly. Instead, it is not proportional; it can be considered as a more equitable approach to create liabilities according to the total emission amounts values. In this way, it will be possible to balance the emissions of all countries at the same level.

On the other hand, the principle of differentiated responsibilities and flexibility also brings the convenience of not meeting this rate due to force majeure. Thus, any country may put forward a force majeure according to its own and may not fulfill its commitment. Therefore, this principle brings the risk that the parties cannot act impartially in a situation requiring a unanimous or majority vote. It may be recommended to remove this principle to prevent countries from abusing it. If this article is removed, fewer countries will take refuge in force majeure, and countries will make more efforts to fulfill their obligations under the article.

In Article #3 of the Protocol at sixth paragraph, it is stated that the Conference of the Parties will provide a certain degree of flexibility to the parties in the transition process to the market economy in Annex-1 in terms of fulfilling the commitments of the protocol. Such flexibility may cause legitimate objections by those not transitioning from party countries to market economies. Therefore, the protocol should be more rigid because such flexibility may mean that the protocol moves away from rigidity. A full, clear and transparent detail has not been made about the extent of the flexibility specified in the article's relevant paragraph. In other words, what its limits will be is not clear.

Article #17 of the Protocol states that the parties included in Annex-B can participate in emissions trading to fulfill their commitments. The issue of climate change, a common problem of all humanity, should be evaluated with great sensitivity by all interlocutors. The transfer of this issue, which is so closely related to the whole earth, humanity, and all living habitats and directly related to the transfer of the natural environment to future generations in a healthy way, to commercial arenas is considered ethically problematic by some circles. It can also be considered that this situation will provide an advantage to economically powerful countries in line with their stake. Therefore, it should not be overlooked that the emissions trading mechanism may cause certain problems in terms of equality and justice for all countries, both parties and non-parties to the protocol. On the other hand, it is considered necessary to develop an alternative to this article in order to help underdeveloped and developing countries make their investments. If an alternative cannot be developed, additional articles or clauses are needed to implement the existing article transparently and fairly.

5. Discussion

5.1. Why was the Kyoto Protocol Needed?

Şen [24] states, "In order for living things to continue their lives, different chemical components must be present in certain proportions, especially in the atmosphere." Carbon emission is one of the main human-induced causes of global climate change. Today's technology releases greenhouse gases, especially CO₂, into the atmosphere. Solar energy reaches the atmosphere as shortwave radiation (in the form of ultraviolet rays and with high energy and light). The ground has less energy, reflecting this energy as longwave radiation in the form of infrared rays. The greenhouse gases prevent reflection; therefore, the earth keeps longwave radiation and warms up.

Van der Geest and Warner [25] present perspectives and data on the loss and damage caused by the adverse effects of climate change. This context shows that climate change has serious economic, social, cultural, and health consequences. However, he is of the opinion that the way to prevent the dangerous consequences of climate change and disaster risks is the investments to be made in this field.

The KP was activated as a result of the need for joint work and organization on issues that could create a dilemma, such as by whom the support and investments to be created at the international level for the solution of the climate change problem, at what level they will be, what kind of way to follow in this regard. Differences such as the different contributions of different countries to the causes of global climate change, the negative effects of the problem being felt at different levels in each country, the fact that each state has different power in the implementation of the sanctions to be brought to the countries required the preparation of the KP in a very inclusive way.

Stories that describe any future event are called scenarios [26]. There are extensive uncertainties in climate

change's future impacts and responses, necessitating scenarios to explore the potential consequences of different response options [27]. Conducting extensive studies on these scenarios, the IPCC was established in 1988 within the United Nations. The IPCC includes various scenarios regarding the possible consequences of climate change in its reports. Among these reports, the Fifth Assessment Report (5th AR) mentions that the earth's temperature may increase to 2°C and possibly rise in sea level [28]. This increase in temperatures and rising sea water levels will seriously threaten the entire ecological environment and living life. Therefore, many articles of the UNFCCC include decisions to reduce greenhouse gas emissions. One of these resolutions aims to reduce human-induced emissions to 1990 levels. In order to control the temperature, increase or to minimize the acceleration of the temperature increase, the need for countries to limit their carbon emissions has arisen. KP is a collection of clauses with sanctions designed to help countries reduce their carbon emissions to a certain level. All countries must take responsibility to prevent or control these expected disasters. In this respect, it is clear that there is a serious need for KP.

5.2. Why Should the Kyoto Protocol be Fair?

The United Nations is an important authority that studies the determination of global problems and their solutions. With this mission, it has concluded that there are obligations that all governments should undertake with global participation in the issue of global climate change, which has become perhaps the most important problem of the world in recent years. It is difficult to make joint decisions on solving problems with global participation, since countries are independent and have decision-making processes and bodies in international relations. States are trying to take steps to protect their national interests regarding the global obligations they have undertaken, and they often try to evaluate the problems, especially from an economic point of view. Due to these situations, agreements and protocols reached with wide participation cannot be implemented or take a long time. To prevent such problems, it may be suggested that countries add a clause specific to climate change to their constitutions. KP also imposes large-scale sanctions on countries to control their greenhouse gas emissions and reduce them, and these sanctions have serious economic dimensions. Therefore, an agreement reached with such broad participation and serious sanctions should be positioned fairly to the parties. Otherwise, developed countries must pay this price by giving up their sustainable development partially or completely. Developing or undeveloped countries, which do not have a serious role in the world's pollution, pay this price by being affected by disasters.

5.3. Where is the Injustice?

It is an inevitable fact that industrial-based carbon emissions are much higher in developed countries than in undeveloped countries. Considering that global climate change is caused by human beings and the reason for this is the gases released into the atmosphere, the countries that cause the most emissions should have more responsibilities and, therefore, more obligations in this regard. For KP's obligations to be fair, there must be a clear, precise, and transparent distinction between developed and undeveloped countries. This transparency is most needed for gas emission reduction or emission and sink inventory. As mentioned above, according to many studies, the USA, which has the highest emission amount globally, has not yet approved the protocol. The lack of participation of the country that causes the most emissions in the scope of emission limitation makes it controversial that the KP has a fair mechanism. Economically, it creates risks for member countries. It may be suggested that the relevant articles of the protocol be revised in this respect. It is discussed by the countries in the relevant meetings that there are still uncertainties about financial sanctions and that the flexibility mechanism created does not impose fair obligations to the parties. It is necessary to seriously consider whether this situation is due to the fairness of the protocol, to the interests of all countries, to the fact that the countries are not sensitive enough to solve a global problem, or to the maneuvering abilities of the countries (which are circumscribed by the protocol articles). In addition, it should be remembered that complying with the Kyoto commitments has important economic consequences. As a result, non-compliance by some parties will raise competitiveness concerns to a large extent [4].

6. Conclusions

In the study, the Kyoto Protocol was evaluated from many aspects and possible improvements were tried to be put forward along with the problems identified in terms of contributing to the solution of the climate change problem. The smooth functioning of the KP is of great importance in making positive progress on the climate change problem. However, as a result of the study, it was concluded that KP has more advantages and disadvantages for some countries than others regarding obligations. In addition, developed countries have a greater impact on global climate change. All countries have a relative impact. However, countries that are not party to the protocol and subsequently left the protocol are not under responsibility. This may cast a shadow over the principles of equality and justice globally. These situations may have unhealthy consequences for the sustainability of the protocol. The flexibility mechanism, one of the protocol's crucial features, can create some situations that can be used in favor and against it. Therefore:

- 1) Even minor changes in the flexibility mechanism formation of the protocol will enable the protocol to turn into a more effective structure.
- 2) However, making the protocol text clearer and more specific and increasing its articles' applicability will benefit its healthy functioning.
- 3) Explaining in detail the flexibility required in terms of implementation, together with their reasons, will facilitate the acceptance of the protocol by the parties to the protocol.
- 4) While all these revisions are being made, the fact that the protocol items are so detailed that they do not create question marks and have a simple structure that will not pose a problem in terms of implementation will have positive results.
- 5) Concerning the issue of climate change, which is one of the most important problems of the whole world, it can be considered ethically problematic to convert the emissions of gases that cause greenhouse gas effects into a commercial field through trading. This situation can create unfair competition and disproportionate power sharing between countries with strong economies and developing countries. Therefore, ensuring that additional changes or alternative articles and clauses are included in the protocol article on this subject will create a more transparent situation regarding equality and justice.
- 6) As well known, the USA, which causes the most greenhouse gas emissions, is not under the Protocol's obligations. This makes the KP controversial concerning having a fair mechanism. In this respect, it is thought that it would be essential to review the relevant articles of the protocol.

Author Contributions

The second author directed the project and supervised this study's findings. The first author devised the main conceptual ideas and developed the theoretical framework. The first author wrote the manuscript with support from the second author. The second author reviewed and edited the paper. All authors read and approved the final version of the paper. This paper is derived from the first author's doctoral dissertation thesis supervised by the second author. The author read and approved the final version of the paper.

Conflicts of Interest

All the authors declare no conflict of interest.

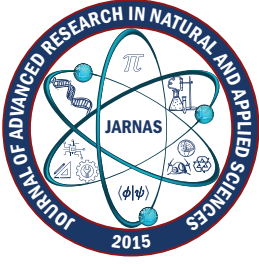
Ethical Review and Approval

No approval from the Board of Ethics is required.

References

- [1] Z. F. Toprak, N. Hamidi, Ş. Toprak, Z. Şen, *Climatic identity assessment of the climate change*, International Journal of Global Warming 1 (5) (2013) 30–45.
- [2] W. M. Budzianowski, *Time delay of global warming*, International Journal of Global Warming 3 (3) (2011) 289–306.
- [3] A. Q. Al-Amin, F. Kari, G. M. Alam, *Global warming and climate change: Prospects and challenges toward long-term policies in Bangladesh*, International Journal of Global Warming 1 (5) (2013) 67–83.
- [4] J. Brunnée, *The Kyoto protocol: A testing ground for compliance theories?*, Heidelberg Journal of International Law 63 (2003) 255–280.
- [5] S. Vanderheiden, *Climate change mitigation, a problem of injustice*, World Science Report (2013) 378–380.
- [6] R. Falkner, *The unavailability of justice—and order—in international climate politics: From Kyoto to Paris and beyond*, The British Journal of Politics and International Relations 2 (21) (2019) 270–278.
- [7] M. Demirci, *Climate change and distributive justice*, Eskişehir Osmangazi University Journal of Economics and Administrative Sciences 2 (8) (2013) 183–203.
- [8] M. Santos, *Global justice and environmental governance: An analysis of the Paris Agreement*, Revista Brasileira de Política Internacional 60 (1) (2017) 18 pages.
- [9] Ş. A. Güneş, *Ensuring compliance with climate change obligations: Kyoto Protocol compliance mechanism*, International Relations Journal 31 (8) (2011) 69–94.
- [10] C. Böhringer, *The Kyoto Protocol: A review and perspectives*, Oxford Review of Economic Policy 3 (19) (2003) 451–466.
- [11] J. Timmons Roberts, B. C. Parks, *Fueling injustice: Globalization, ecologically unequal exchange and climate change*, Globalizations 2 (4) (2007) 193–210.
- [12] S. Çınar, M. Yılmaz, T. A. Fazlılar, *Trade in polluting industries and the environment: A comparison of developed and developing countries*, Journal of Doğuş University 2 (13) (2012) 212–226.
- [13] N. Berberoğlu, *Climate change: Post-Kyoto negotiations and Türkiye*, International Journal of Economic Issues (33) (2009) 18–26.
- [14] A. M. Rosen, *The wrong solution at the right time: The failure of the Kyoto Protocol on climate change*, Politics and Policy 1 (43) (2015) 30–58.
- [15] C. Atici, *Reconciling the flexibility mechanisms of climate policies towards the inclusiveness of developing countries: Commitments and prospects*, Environment, Development and Sustainability 24 (2021) 9048–9067.
- [16] R. G. Akkale, *Kyoto Protocol and Turkey*, Mecmua 1 (2008) 493–515.
- [17] M. Türkeş, U. M. Sümer, G. Çetiner, *Kyoto Protocol flexibility mechanisms*, Journal of Plumbing (52) (2000) 84–100.
- [18] Ö. Dolu, *Flexibility and institutional capacity development of the Kyoto regime*, Master's Thesis Adnan Menderes University (2005) Aydın.
- [19] N. Konak, *Global climate change, Kyoto Protocol flexibility mechanisms, voluntary carbon market and Türkiye: A critical approach*, Alternative Politics 2 (3) (2011) 154–178.
- [20] B. Engin, *Kyoto protocol implementation mechanisms: Flawed or promising concepts?*, Journal of Social Sciences (2) (2010) 30–40.

- [21] V. Ş. Ediger, *The international relations dimension of global climate change and Turkey's policies*, Mülkiye 259 (17) (2008) 133–158.
- [22] C. Hagem, B. Holtsmark, *From small to insignificant. Climate impact of the Kyoto Protocol with and without US*, Oslo University Center for International Climate and Environmental Research 2001 (1) (2001) 10 pages.
- [23] Turkish Statistical Institute, Statistics in Environment, <https://data.tuik.gov.tr/Bulten/Index?p=Istatistiklerle-Cevre-2016-27685>, Accessed 10 Mar 2024.
- [24] Z. Şen, *Climate change and Türkiye*, Journal of Environment City and Climate 1 (1) (2022) 1–19.
- [25] K. Van der Geest, K. Warner, *Loss and damage from climate change: Emerging perspectives*, International Journal of Global Warming 2 (8) (2015) 133–140.
- [26] W. L. Gregory, A. Duran, Scenarios and acceptance of forecasts, In Principles of forecasting, Springer, Boston, 2001, Ch. 16, pp. 519–540.
- [27] R. H. Moss, J. A. Edmonds, K. A. Hibbard, M. R. Manning, S. K. Rose, D. P. Van Vuuren, T. J. Wilbanks, *The next generation of scenarios for climate change research and assessment*, Nature 7282 (463) (2010) 747–756.
- [28] WCRP Report, IPCC AR5: Lessons learned for climate change research and WCRP, International Space Science Institute, Bern, 2015.



Lipschitz Operators Associated with Weakly p -Compact and Unconditionally p -Compact Sets

Ayşegül Keten Çopur¹ , Ramazan İnal² 

¹Department of Mathematics and Computer Science, Faculty of Science, Necmettin Erbakan University, Konya, Türkiye

²Ministry of Education, Konya, Türkiye

Article Info

Received: 12 Mar 2024

Accepted: 04 Jun 2024

Published: 30 Sep 2024

Research Article

Abstract— The study introduces different categories of Lipschitz operators linked with weakly p -compact and unconditionally p -compact sets. It explores some properties of these operator classes derived from linear operators associated with these sets and examines their interconnections. Additionally, it denotes that these classes are extensions of the related linear operators. Moreover, the study evaluates the concept of majorization by scrutinizing both newly obtained and pre-existing results and draws some conclusions based on these findings. The primary method used to obtain the results in the study is the linearization of Lipschitz operators through the Lipschitz-free space constructed over a pointed metric space.

Keywords — Lipschitz compact operator, Lipschitz p -compact operator, Lipschitz weakly p -compact operator, Lipschitz unconditionally p -compact operator, majorization

Subject Classification (2020) 47B10, 26A16

1. Introduction

Various authors have recently engaged in the exploration of Lipschitz versions of diverse bounded linear operators. In 2014, Jiménez-Vargas et al. [1] introduced the concepts of Lipschitz finite-rank, Lipschitz compact, Lipschitz weakly compact and Lipschitz approximable operators. They also obtained some outcomes for these concepts. In 1955, Grothendieck [2] effectively demonstrated that compactness could be examined geometrically by obtaining the necessary and sufficient criteria for a set to be compact in a Banach space. In 2002, motivated by Grothendieck's compactness principle, Sinha and Karn [3] defined the notion of p -compactness (respectively, weakly p -compactness) of a set and also defined the concepts of the p -compact (respectively, weakly p -compact) linear operator and p -approximation property in Banach spaces, which arises naturally from this notion. Later, as modifications of these concepts, Kim [4] introduced the concepts of unconditionally p -compact set and unconditionally p -compact linear operator. Many mathematicians studied the linear operators and approximation properties associated with all these sets [4–8]. Various studies have been conducted in recent years to investigate the properties of p -compact sets and p -compact linear operators. These

¹aketen@erbakan.edu.tr (Corresponding Author); ²rmzninl@gmail.com

studies encompass both nonlinear and linear situations. Inspired by Jiménez-Vargas et al. [1], Achour et al. [9] defined and studied the concept of Lipschitz operators, which are p -compact as a nonlinear extension of p -compact linear operators and considered some features in the linear case for the Lipschitz case. At the same time, they introduced the concepts of Lipschitz free p -compact operator and Lipschitz locally p -compact operator and compared these concepts with each other and showed their different properties. To our knowledge, Lipschitz weakly p -compact and unconditionally p -compact operators have not yet been studied in the literature. In this study, considering the works on weakly p -compact and unconditionally p -compact sets of Kim [4–7] and inspired by the works of Jiménez-Vargas et al. [1] and Achour et al. [9], we consider some classes of Lipschitz operators associated with weakly p -compact and unconditionally p -compact sets. After we provide some notations and basic concepts, we introduce Lipschitz weakly (respectively, unconditionally) p -compact operator and Lipschitz free weakly (respectively, unconditionally) p -compact operator, respectively, and obtain some of their properties. We evaluate the obtained and current results with the concept of majorization and provide some results.

2. Preliminaries

A metric space with a designated base point denoted as 0 is referred to as a pointed metric space. Throughout the study, unless specifically mentioned otherwise, the symbols X and Y represent pointed metric spaces, while E and F represent Banach spaces. B_E represents the closed unit ball of a Banach space E . The symbol \mathbb{K} represents the field space of complex or real numbers. The notation $L(E, F)$ (respectively, $\mathcal{B}(E, F)$) represents the vector space of all the linear operators (respectively, bounded linear operators) from E to F . The dual space of E is $E^* := \mathcal{B}(E, \mathbb{K})$. The notation $\text{Lip}_0(X, Y)$ indicates the set of all the Lipschitz operators $g : X \rightarrow Y$ where $g(0) = 0$. The function

$$\text{Lip}(g) = \sup\{\|g(x) - g(y)\|/d(x, y) : x \neq y, x, y \in X\}$$

defines a norm on $\text{Lip}_0(X, E)$, and $\text{Lip}_0(X, E)$ is a Banach space with the norm [1]. The Banach space $\text{Lip}_0(X, \mathbb{K})$ is Lipschitz dual of X and is denoted by X^\sharp . For a Banach space E , it is clear that $E^* \subset E^\sharp$. For thorough information on Lipschitz operators and their properties, see [10]. For $x \in X$, the function $\delta_x : X^\sharp \rightarrow \mathbb{K}$ is defined as $\delta_x(g) = g(x)$ such that $g \in X^\sharp$ [1]. Lipschitz-free Banach space of X is defined as the closed linear span of the set $\{\delta_x : x \in X\}$ and denoted by $\mathcal{F}(X)$ [1]. The map $\delta_X : X \rightarrow \mathcal{F}(X)$ is described by $\delta_X(x)(g) = g(x)$, for all $x \in X$ and $g \in X^\sharp$ [1].

We recall certain properties of the Lipschitz-free Banach space in the next lemma.

Lemma 2.1. [1, 11, 12] Let E be a Banach space and X and Y be two pointed metric spaces.

- i.* The function $\delta_X : X \rightarrow \mathcal{F}(X)$ described as $\delta_X(x)(g) = g(x)$, for all $x \in X$ and $g \in X^\sharp$, is a nonlinear isometry.
- ii.* The map $Q_X : X^\sharp \rightarrow \mathcal{F}(X)^*$ given by $Q_X(g)(v) = v(g)$, for all $g \in X^\sharp, v \in \mathcal{F}(X)$, is an isometric isomorphism.
- iii.* The set $B_{\mathcal{F}(X)}$ is convex closed and balanced span of the set $\{(\delta_x - \delta_y)/d(x, y) : x \neq y, x, y \in X\}$.
- iv.* The Lipschitz adjoint of $g \in \text{Lip}_0(X, E)$ is $g^\sharp : E^\sharp \rightarrow X^\sharp$ defined by $g^\sharp(h) = h \circ g$, for all $h \in E^\sharp$. Moreover, $g^\sharp \in \mathcal{B}(E^\sharp, X^\sharp)$ and $\|g^\sharp\| = \text{Lip}(g)$.
- v.* For every operator $g \in \text{Lip}_0(X, E)$, a unique operator $T_g \in \mathcal{B}(\mathcal{F}(X), E)$ exists so that $g = T_g \circ \delta_X$,

in other words, the following diagram commutes and $\|T_g\| = \text{Lip}(g)$:

$$\begin{array}{ccc} X & \xrightarrow{\delta_X} & \mathcal{F}(X) \\ & \searrow g & \downarrow T_g \\ & & E \end{array}$$

vi. For every operator $g \in \text{Lip}_0(X, Y)$, a unique operator $\widehat{g} \in \mathcal{B}(\mathcal{F}(X), \mathcal{F}(Y))$ exists so that $\widehat{g} \circ \delta_X = \delta_Y \circ g$, in other words, the following diagram commutes and $\|\widehat{g}\| = \text{Lip}(g)$:

$$\begin{array}{ccc} X & \xrightarrow{g} & Y \\ \downarrow \delta_X & & \downarrow \delta_Y \\ \mathcal{F}(X) & \xrightarrow{\widehat{g}} & \mathcal{F}(Y) \end{array}$$

The restriction E^* of g^\sharp in Lemma 2.1 *iv* is called Lipschitz transpose of g and denoted by g^t . It is clear that $Q_X \circ g^t = T_g^*$ and $\widehat{g}^* \circ Q_Y = Q_X \circ g^\sharp$, where T_g^* and \widehat{g}^* are adjoint operators of T_g and \widehat{g} , respectively [9].

Unless otherwise stated, throughout the study, $p \geq 1$ and $1/p + 1/p^* = 1$. The Banach space denoted as $l_p(E)$ is defined as the space of all the p -summable sequences in the space E . Here, the norm is given by the formula [3]:

$$\|(x_n)_n\|_p = \left(\sum_{n=1}^{\infty} \|x_n\|^p \right)^{1/p}$$

Besides, $l_p^w(E)$ is a Banach space representing all weakly p -summable sequences in E . The norm of an element $(x_n)_n$ in this space is defined as [3]:

$$\|(x_n)_n\|_p^w = \sup\{\|(x^*(x_n))_n\|_p : x^* \in B_{E^*}\}$$

The space

$$l_p^u(E) := \{(x_n)_n \in l_p^w(E) : \|(0, \dots, 0, x_n, x_{n+1}, \dots)\|_p^w \rightarrow 0 \text{ as } n \rightarrow \infty\}$$

is referred to as the space of all the sequences in E that are unconditionally p -summable. The space is a closed subspace of $l_p^w(E)$ [4]. If a sequence $(x_n)_n \in l_p(E)$ satisfying

$$C \subset \text{p-co}(\{x_n\}) = \left\{ \sum_{n=1}^{\infty} \alpha_n x_n : (\alpha_n)_n \in B_{l_{p^*}} \right\}$$

exists, then the subset C of E is relatively p -compact [3]. If there is $(x_n)_n \in l_p^w(X)$ (respectively, $(x_n)_n \in l_p^u(X)$) satisfying $C \subset \text{p-co}(\{x_n\})$, then C is called relatively weakly p -compact (respectively, relatively unconditionally p -compact) [3] (respectively, [4]). We note that the sets that are relatively p -compact are also relatively unconditionally p -compact. Further, the relatively unconditionally p -compact sets are relatively compact and relatively weakly p -compact [4, 13]. An operator $T \in L(E, F)$ is said to be p -compact (respectively, weakly p -compact, unconditionally p -compact) if $T(B_E)$ is relatively p -compact set (respectively, relatively weakly p -compact set, relatively unconditionally p -compact set) in F [3, 4]. The space of all the p -compact linear operators (respectively, weakly p -compact linear operators, unconditionally p -compact linear operators) from E to F is denoted by the symbol $\mathcal{K}_p(E, F)$ (respectively, $\mathcal{W}_p(E, F)$, $\mathcal{K}_{up}(E, F)$). If $S \in \mathcal{K}_p(E, F)$, then

$$\|S\|_{\mathcal{K}_p} := \inf\{\|(x_n)_n\|_p : S(B_E) \subset \text{p-co}(\{x_n\}), (x_n)_n \in l_p(F)\}$$

is a norm function. Moreover, $(\mathcal{K}_p, \|\cdot\|_{\mathcal{K}_p})$ is a Banach operator ideal [14]. If $S \in \mathcal{W}_p(E, F)$, then

$$\|S\|_{\mathcal{W}_p} := \inf\{\|(x_n)_n\|_p^w : S(B_E) \subset \text{p-co}(\{x_n\}), (x_n)_n \in l_p^w(F)\}$$

is a norm function and also $(\mathcal{W}_p, \|\cdot\|_{\mathcal{W}_p})$ is a Banach operator ideal [7]. If $S \in \mathcal{K}_{up}(E, F)$, then

$$\|S\|_{\mathcal{K}_{up}} := \inf\{\|(x_n)_n\|_p^w : S(B_E) \subset p\text{-co}(\{x_n\}), (x_n)_n \in l_p^u(F)\}$$

is a norm function, and $(\mathcal{K}_{up}, \|\cdot\|_{\mathcal{K}_{up}})$ is a Banach operator ideal [4]. The operator $S \in L(E, F)$ is quasi unconditionally p -nuclear (respectively, quasi weakly p -nuclear) if there is $(x_n^*)_n \in l_p^u(E^*)$ (respectively, $(x_n^*)_n \in l_p^w(E^*)$) such that $\|Sx\| \leq \|(x_n^*(x))_n\|_p$, for all $x \in E$ [4, 6]. The space of all the quasi unconditionally p -nuclear operators (respectively, quasi weakly p -nuclear operators) from E to F is represented by $\mathcal{N}_{up}^Q(E, F)$ (respectively, $\mathcal{N}_{up}^Q_w(E, F)$). For $S \in \mathcal{N}_{up}^Q(E, F)$ (respectively, $S \in \mathcal{N}_{up}^Q_w(E, F)$), let $\|S\|_{\mathcal{N}_{up}^Q} := \inf\|(x_n^*)_n\|_p^w$, where infimum is taken over all the sequences satisfying the condition quasi unconditionally p -nuclear (respectively, quasi weakly p -nuclear). Then, $(\mathcal{N}_{up}^Q, \|\cdot\|_{\mathcal{N}_{up}^Q})$ (respectively, $(\mathcal{N}_{up}^Q_w, \|\cdot\|_{\mathcal{N}_{up}^Q_w})$) is a Banach operator ideal [4, 6]. Let G be a Banach space, $S \in \mathcal{B}(E, F)$, and $T \in \mathcal{B}(E, G)$. If there is a $K > 0$ satisfying $\|Tx\| \leq K\|Sx\|$, for all $x \in E$, then it is said that S majorizes T [15]. Assume that $f \in \text{Lip}_0(X, E)$ and $g \in \text{Lip}(X, F)$. If there is an $M > 0$ satisfying $\|g(x_1) - g(x_2)\| \leq M\|f(x_1) - f(x_2)\|$, for all $x_1, x_2 \in X$, then it is said that f majorizes g [16].

Jiménez-Vargas et al. [1] defined the compactness (respectively, weakly compactness) of a Lipschitz operator as follows:

Definition 2.2. [1] Let $g \in \text{Lip}_0(X, E)$. The operator g is called Lipschitz compact (respectively, Lipschitz weakly compact) if

$$\text{Im}_{\text{Lip}}(g) := \left\{ \frac{g(x) - g(y)}{d(x, y)} : x \neq y, x, y \in X \right\} \subset E$$

is a relatively compact set (respectively, relatively weakly compact set).

Inspired by this definition, Achour et al. [9] defined the p -compactness of a Lipschitz operator as follows.

Definition 2.3. [9] Let $g \in \text{Lip}_0(X, E)$. The operator g is called Lipschitz p -compact if the set $\text{Im}_{\text{Lip}}(g)$ is a relatively p -compact in E .

3. The Main Results

In this section, we introduce the various classes of Lipschitz operators associated with weakly p -compact sets and unconditionally p -compact sets and investigate some of their properties, respectively.

3.1. Lipschitz Weakly p -Compact Operators and Some of Their Properties

Taking inspiration from the concepts of the Lipschitz compact operator defined by [1] and the Lipschitz p -compact operator defined by [9], we define the concept of Lipschitz weakly p -compact operator.

Definition 3.1. Let $g \in \text{Lip}_0(X, E)$. Then, g is called a Lipschitz weakly p -compact operator if the set $\text{Im}_{\text{Lip}}(g)$ is a relatively weakly p -compact subset of E .

The set of all the Lipschitz weakly p -compact operators defined from X to E is represented by the symbol $\text{Lip}_0^{\mathcal{W}_p}(X, E)$.

Remark 3.2. We note that $\text{Im}_{\text{Lip}}(g) \subset g(B_X)$ when X is a Banach space and $g \in L(X, E)$. Thus, $g \in \text{Lip}_0^{\mathcal{W}_p}(X, E)$ as $g \in \mathcal{W}_p(X, E)$. Therefore, Lipschitz operators, which are weakly p -compact, can be thought of as a generalization of linear operators that are weakly p -compact.

Remark 3.3. By [14], it is well known that the set $p\text{-co}(\{x_n\})$ is absolutely convex and norm closed if $p > 1$ and $(x_n)_n \in l_p^w(E)$.

Since the smallest absolutely convex set containing set A is $\text{abco}(A)$, the following lemma is obtained by Remark 3.3.

Lemma 3.4. Let E be a Banach space and $p > 1$. The set $\overline{\text{abco}}(A)$ is a weakly p -compact subset of E if A is a relatively weakly p -compact subset of E .

The following result has been obtained as a modification of Proposition 2.1 in [1] (see also Theorem 3.4 in [9]) for weakly p -compact sets.

Theorem 3.5. Let $g \in \text{Lip}_0(X, E)$ and $p > 1$. Then, $g \in \text{Lip}_0^{\mathcal{W}_p}(X, E)$ if and only if $T_g \in \mathcal{W}_p(\mathcal{F}(X), E)$.

The proof of the theorem is omitted as it can be obtained similarly to steps in Proposition 2.1 [1] using Lemma 3.4.

Kim [6] proved Theorem 3.7 (c) that the adjoint of a linear operator that is weakly p -compact is quasi-weakly p -nuclear. The following proposition is an extension of this result to the Lipschitz case.

Proposition 3.6. Let $p > 1$. If $g \in \text{Lip}_0^{\mathcal{W}_p}(X, E)$, then $g^t \in \mathcal{N}_{\mathcal{W}_p}^Q(E^*, X^\sharp)$ and $\|g^t\|_{\mathcal{N}_{\mathcal{W}_p}^Q} \leq \|T_g\|_{\mathcal{W}_p}$.

PROOF. Let $g \in \text{Lip}_0^{\mathcal{W}_p}(X, E)$. By Theorem 3.5, T_g is a linear operator that is weakly p -compact. Thus, by the result Theorem 3.7 (c) in [6], $T_g^* \in \mathcal{N}_{\mathcal{W}_p}^Q(E^*, \mathcal{F}(X)^*)$ and $\|T_g^*\|_{\mathcal{N}_{\mathcal{W}_p}^Q} \leq \|T_g\|_{\mathcal{W}_p}$. Since $Q_X^{-1} \circ T_g^* = g^t$, by the ideal property of quasi weakly p -nuclear operators, $g^t \in \mathcal{N}_{\mathcal{W}_p}^Q(E^*, X^\sharp)$, and also $\|T_g^*\|_{\mathcal{N}_{\mathcal{W}_p}^Q} \leq \|Q_X\| \|g^t\|_{\mathcal{N}_{\mathcal{W}_p}^Q}$ and $\|g^t\|_{\mathcal{N}_{\mathcal{W}_p}^Q} \leq \|Q_X^{-1}\| \|T_g^*\|_{\mathcal{N}_{\mathcal{W}_p}^Q}$. By Lemma 2.1 *ii*, since Q_X is an isometric isomorphism, it is obtained $\|g^t\|_{\mathcal{N}_{\mathcal{W}_p}^Q} = \|T_g^*\|_{\mathcal{N}_{\mathcal{W}_p}^Q}$. Using $\|T_g^*\|_{\mathcal{N}_{\mathcal{W}_p}^Q} \leq \|T_g\|_{\mathcal{W}_p}$, it is obtained $\|g^t\|_{\mathcal{N}_{\mathcal{W}_p}^Q} \leq \|T_g\|_{\mathcal{W}_p}$. \square

By [3], any sets that are relatively weakly p -compact are also relatively weakly q -compact as $1 \leq p \leq q < \infty$, and by [14], any sets that are relatively weakly p -compact (with $p > 1$) are also relatively weakly compact. Therefore, we directly obtain the following proposition.

Proposition 3.7. Let $g \in \text{Lip}_0(X, E)$ and $1 \leq p \leq q < \infty$. Then, g is Lipschitz weakly q -compact whenever g is Lipschitz weakly p -compact. In particular, if $p > 1$ and g is Lipschitz weakly p -compact, then g is Lipschitz weakly compact.

The following proposition demonstrates that if the hypotheses of Proposition 3.13 in [9] are replaced p -summability of the operator T_f with p -summability of the operator T_f^* , and the Lipschitz compactness of Lipschitz operator g with the Lipschitz weakly p -compactness, then the same result can be obtained.

Proposition 3.8. Let $p > 1$, $f \in \text{Lip}_0(X, E)$, and $g \in \text{Lip}_0(Z, E^*)$, where Z is a pointed metric space. If $g \in \text{Lip}_0^{\mathcal{W}_p}(Z, E^*)$ and the operator T_f^* is p -summing, then $f^t \circ g : Z \rightarrow X^\sharp$ is Lipschitz p -compact.

PROOF. Assume that g is Lipschitz weakly p -compact. By Theorem 3.5, T_g is weakly p -compact. Since T_f^* is p -summing and T_g is weakly p -compact, by Proposition 5.4 [3], the operator $T_f^* \circ T_g$ is p -compact. Moreover, $f^t \circ T_g = Q_X^{-1} \circ T_f^* \circ T_g$ and thus, by the ideal property of \mathcal{K}_p , $f^t \circ T_g$ is a p -compact operator. By Lemma 2.1 *v*, since $T_g \circ \delta_Z = g$, the linerization of $f^t \circ g$ is $f^t \circ T_g$. Thus, by Theorem 3.4 [9], $f^t \circ g$ is Lipschitz p -compact. \square

Kim [7] has obtained a result in Proposition 2.4, which characterizes the factorization of linear operators that are weakly p -compact. Through Kim's result, we get the following result, which characterizes the factorization of a Lipschitz operator that is weakly p -compact.

Theorem 3.9. Let $p > 1$ and $f \in \text{Lip}_0(X, E)$. Then, $f \in \text{Lip}_0^{\mathcal{W}_p}(X, E)$ if and only if there are a quotient space G of l_{p^*} , $g \in \text{Lip}_0^{\mathcal{W}_p}(X, G)$, and $S \in \mathcal{W}_p(G, E)$ such that $f = S \circ g$. Further, $\text{Lip}(f) \leq \|S\|_{\mathcal{W}_p} \text{Lip}(g)$.

PROOF. (\Leftarrow): Assume that $f \in \text{Lip}_0(X, E)$ has the factorization in theorem. Then, $\text{Im}_{\text{Lip}}(f) = S(\text{Im}_{\text{Lip}}(g))$. Since $g \in \text{Lip}_0^{\mathcal{W}_p}(X, G)$, $S(\text{Im}_{\text{Lip}}(g))$ is relatively weakly p -compact. Thus, $f \in \text{Lip}_0^{\mathcal{W}_p}(X, E)$.

(\Rightarrow): Let $f \in \text{Lip}_0^{\mathcal{W}_p}(X, E)$. Thus, by Theorem 3.5, $T_f \in \mathcal{W}_p(\mathcal{F}(X), E)$. By Kim's result Proposition 2.4 [7], there are a quotient space G of l_{p^*} , $S \in \mathcal{W}_p(G, E)$ and $R \in \mathcal{W}_p(\mathcal{F}(X), G)$ such that $T_f = S \circ R$. By Lemma 2.1 v , we obtain $f = S \circ R \circ \delta_X$. Let $g := R \circ \delta_X$. It is clear that $g \in \text{Lip}_0(X, G)$. Hence, by unique of the linearization of g in Lemma 2.1 v is $T_g = R$. Thus, the desired factorization is obtained. Further, by [3], since $\|S\| \leq \|S\|_{\mathcal{W}_p}$, using the norm property in Lemma 2.1 v ,

$$\text{Lip}(f) = \|T_f\| \leq \|S\| \|R\| = \|S\| \|T_g\| \leq \|S\|_{\mathcal{W}_p} \text{Lip}(g).$$

□

It is well known that Davis-Figiel-Johnson-Pelczynski [17] obtained a significant theorem that states that any linear operator that is weakly compact can be factored via a reflexive Banach space. Since every set that is weakly p -compact is also weakly compact while $p > 1$ [14], combining Davis-Figiel-Johnson-Pelczynski theorem [17] and Theorem 3.9, we get the following proposition.

Proposition 3.10. Let $p > 1$ and $f \in \text{Lip}_0(X, E)$. Then, $f \in \text{Lip}_0^{\mathcal{W}_p}(X, E)$ if and only if there are a quotient space G of l_{p^*} , a reflexive Banach space W , $T \in \mathcal{B}(G, W)$, $Q \in \mathcal{B}(W, E)$, and $g \in \text{Lip}_0^{\mathcal{W}_p}(X, G)$ such that $f = Q \circ T \circ g$. Further, $\text{Lip}(f) \leq \|Q\| \|T\| \text{Lip}(g)$.

The following proposition is a modification of the ideal property of Jiménez-Vargas et al., Proposition 2.3 [1], for Lipschitz operators that are weakly p -compact. The proof has been omitted as it can be easily done following their methods and using Theorem 3.5.

Proposition 3.11. Let $p > 1$, $S \in \mathcal{B}(E, F)$, and $f \in \text{Lip}_0(Y, X)$. If $g \in \text{Lip}_0^{\mathcal{W}_p}(X, E)$, then $S \circ g \circ f \in \text{Lip}_0^{\mathcal{W}_p}(Y, F)$.

3.2. Lipschitz Unconditionally p -Compact Operators and Some of Their Properties

In this section, taking inspiration from the concepts of the Lipschitz compact operator defined by [1], and the Lipschitz p -compact operator defined by [9], we define the concept of Lipschitz unconditionally p -compact operator.

Definition 3.12. Let $g \in \text{Lip}_0(X, E)$. Then, g is called Lipschitz unconditionally p -compact operator if the set $\text{Im}_{\text{Lip}}(g)$ is a relatively unconditionally p -compact subset of E .

The set of all the Lipschitz unconditionally p -compact operators defined from X to E is represented by the notation $\text{Lip}_0^{\mathcal{K}_{up}}(X, E)$.

Similar to Remark 3.2, Lipschitz unconditionally p -compact operators can be thought of as a generalization of linear operators that are unconditionally p -compact.

Considering relationships among relatively p -compact, weakly p -compact, and unconditionally p -compact sets and compact sets, we get the following proposition.

Proposition 3.13. Let $g \in \text{Lip}_0(X, E)$. Then, $g \in \text{Lip}_0^{\mathcal{K}_{up}}(X, E)$ if g is Lipschitz p -compact. Moreover, if $g \in \text{Lip}_0^{\mathcal{K}_{up}}(X, E)$, then $g \in \text{Lip}_0^{\mathcal{W}_p}(X, E)$ and also g is Lipschitz compact.

Since $(x_n)_n \in l_p^w(E)$ while $(x_n)_n \in l_p^u(E)$, a result similar to Lemma 3.4 is provided as follows.

Lemma 3.14. Let $p > 1$. The set $\overline{\text{abco}}(A)$ is an unconditionally p -compact set in E if A is a relatively unconditionally p -compact subset of a Banach space E .

The following result has been obtained as a modification of Proposition 2.1 in [1] (see also Theorem 3.4 [9]) for unconditionally p -compact sets.

Theorem 3.15. Let $g \in \text{Lip}_0(X, E)$ and $p > 1$. Then, $g \in \text{Lip}_0^{\mathcal{K}_{up}}(X, E)$ if and only if $T_g \in \mathcal{K}_{up}(\mathcal{F}(X), E)$.

The proof of the theorem has been omitted since it can be done using Lemma 3.14 and following the steps in Proposition 2.1 [1].

Kim [4, 5] demonstrated Theorem 2.4 and Theorem 5.6, respectively, that the unconditionally p -compactness of a linear operator and the quasi unconditionally p -nuclearity of the adjoint of this operator are equivalent. The following proposition is an extension of this result to the Lipschitz case. This proposition also extends Proposition 3.12 [9] to unconditionally p -compact sets.

Proposition 3.16. Let $f \in \text{Lip}_0(X, E)$ and $p > 1$. Then, $f \in \text{Lip}_0^{\mathcal{K}_{up}}(X, E)$ if and only if $f^t \in \mathcal{N}_{up}^Q(E^*, X^\sharp)$. Moreover, $\|f^t\|_{\mathcal{N}_{up}^Q} = \|T_f\|_{\mathcal{K}_{up}}$.

PROOF. Let $f \in \text{Lip}_0(X, E)$ and $p > 1$. By Theorem 3.15, $f \in \text{Lip}_0^{\mathcal{K}_{up}}(X, E)$ if and only if T_f is an unconditionally p -compact operator. By Kim's Theorem 2.4 [4], $T_f^* \in \mathcal{N}_{up}^Q(E^*, \mathcal{F}(X)^*)$ if and only if $T_f \in \mathcal{K}_{up}(\mathcal{F}(X), E)$. Thus, using $Q_X^{-1} \circ T_f^* = f^t$, the desired equivalence is achieved. Further, by Theorem 5.6 [5], since $\|T_f^*\|_{\mathcal{N}_{up}^Q} = \|T_f\|_{\mathcal{K}_{up}}$, $\|f^t\|_{\mathcal{N}_{up}^Q} = \|T_f\|_{\mathcal{K}_{up}}$ is obtained. \square

We obtain the following proposition by combining Kim's Theorem 2.4 [4] and Theorem 3.5 herein.

Proposition 3.17. Let $f \in \text{Lip}_0(X, E)$ and $p > 1$. Assume that the operator T_f maps weakly p -summable sequences into unconditionally p -summable sequences and $S \in \text{Lip}_0^{\mathcal{W}_p}(Z, \mathcal{F}(X))$. Then, $S^t \circ T_f^* \in \mathcal{N}_{up}^Q(E^*, Z^\sharp)$.

PROOF. Since $S \in \text{Lip}_0^{\mathcal{W}_p}(Z, \mathcal{F}(X))$, by Theorem 3.5, $T_S \in \mathcal{W}_p(\mathcal{F}(Z), \mathcal{F}(X))$. Since the operator T_f maps weakly p -summable sequences into unconditionally p -summable sequences, it is obtained $T_f \circ T_S \in \mathcal{K}_{up}(\mathcal{F}(Z), E)$. Thus, by Theorem 2.4 [4], $(T_f \circ T_S)^* \in \mathcal{N}_{up}^Q(E^*, \mathcal{F}(Z)^*)$. Since $T_S^* = Q_Z \circ S^t$, it is obtained $Q_Z \circ S^t \circ T_f^* \in \mathcal{N}_{up}^Q(E^*, \mathcal{F}(Z)^*)$. If it is used that Q_Z is an isometric isomorphism and \mathcal{N}_{up}^Q has the ideal property, then it is obtained $S^t \circ T_f^* \in \mathcal{N}_{up}^Q(E^*, Z^\sharp)$. \square

Combining Theorem 3.15 and some results in [4], we obtained the following theorem.

Theorem 3.18. Let X be a pointed metric space such that $\mathcal{F}(X)^*$ is an injective Banach space, E is an injective Banach space, and $p > 1$. If $f \in \text{Lip}_0^{\mathcal{K}_{up^*}}(X, E)$, then T_f is unconditionally p -nuclear operator.

PROOF. If Theorem 3.15 and Theorem 2.4 [4] are used in order, then $T_f^* \in \mathcal{N}_{up^*}^Q(E^*, \mathcal{F}(X)^*)$ is obtained. By injectivity of $\mathcal{F}(X)^*$ and the result Lemma 2.6 [4], $T_f^* \in \mathcal{N}_{up^*}(E^*, \mathcal{F}(X)^*)$. From the proof of Proposition 2.2 [4], $\mathcal{N}_{up^*} \subset \mathcal{K}_{up}$. Thus, $T_f^* \in \mathcal{K}_{up}(E^*, \mathcal{F}(X)^*)$. By Theorem 2.3 [4], $T_f \in \mathcal{N}_{up}^Q(\mathcal{F}(X), E)$. Since E is an injective Banach space, by Lemma 2.6 [4], T_f is an unconditionally p -nuclear operator. \square

The following remark shows a pointed metric space X such that $\mathcal{F}(X)^*$ is an injective Banach space.

Remark 3.19. By [18], it is well known that if $X = \mathbb{R}$, then $\mathcal{F}(X) = \mathcal{F}(\mathbb{R}) = L_1$. Moreover, $L_1^* = L_\infty$ and L_∞ is an injective Banach space (see Proposition 4.3.8 (ii) [19]). Thus, $\mathcal{F}(X)^*$ is an injective Banach space.

Using Theorem 3.15 and the factorization result of linear operators that are unconditionally p -compact in Theorem 2.2 [5], we obtain the following result concerning the factorization of Lipschitz unconditionally p -compact operators.

Proposition 3.20. Let $f \in \text{Lip}_0(X, E)$ and $p > 1$. Then, $f \in \text{Lip}_0^{\mathcal{K}_{up}}(X, E)$ if and only if a quotient space G of l_p^* , an operator $S \in \mathcal{K}_{up}(G, E)$ and an operator $g \in \text{Lip}_0^{\mathcal{K}_{up}}(X, G)$ satisfying $f = S \circ g$ exist. Further, $\text{Lip}(f) \leq \|S\|_{\mathcal{K}_{up}} \text{Lip}(g)$.

PROOF. Since steps in Theorem obtain the proof 3.9 using Theorem 2.2 [5] and Theorem 3.15, it is omitted. For the norm inequality, if steps in Theorem 3.9 are used with the definitions of $\|\cdot\|_{\mathcal{W}_p}$ and $\|\cdot\|_{\mathcal{K}_{up}}$, then the following inequality is obtained:

$$\text{Lip}(f) = \|T_f\| \leq \|S\| \|R\| \leq \|S\|_{\mathcal{W}_p} \text{Lip}(g) \leq \|S\|_{\mathcal{K}_{up}} \text{Lip}(g).$$

□

Using Theorem 3.4 [9] and the factorization of linear operators that are p -compact in Theorem 2.3 [5], we obtain the following factorization result for Lipschitz p -compact operators.

Theorem 3.21. Let $f \in \text{Lip}_0(X, E)$ and $p > 1$. Then, $f \in \text{Lip}_0^{\mathcal{K}_p}(X, E)$ if and only if a quotient space G of l_{p^*} , an operator $S \in \mathcal{K}_p(G, E)$ and an operator $g \in \text{Lip}_0^{\mathcal{K}_{up}}(X, G)$ satisfying $f = S \circ g$ exist. Further, $\text{Lip}(f) \leq \|S\|_{\mathcal{K}_p} \text{Lip}(g)$.

The proof of the theorem has been omitted since it can be done using Theorem 3.4 [9] and Theorem 2.3 [5] and following the steps in Theorem 3.9.

We modify the ideal property of Jiménez-Vargas et al. [1] for Lipschitz operators that are unconditionally p -compact. The proof has been omitted as it can be done following their methods and using Theorem 3.15.

Proposition 3.22. Let $p > 1$, $S \in \mathcal{B}(E, F)$, and $f \in \text{Lip}_0(Y, X)$. If $g \in \text{Lip}_0^{\mathcal{K}_{up}}(X, E)$, then $S \circ g \circ f \in \text{Lip}_0^{\mathcal{K}_{up}}(Y, F)$.

3.3. Lipschitz Free Weakly and Unconditionally p -Compact Operators

In this section, inspired by the concepts of Lipschitz free (weakly) compact operators defined by [12] and Lipschitz free p -compact operators defined by [9], we define Lipschitz free weakly and unconditionally p -compact operators, investigate some of their properties, and provide relationships among them.

Definition 3.23. Let $p \geq 1$ and $g \in \text{Lip}_0(X, Y)$. If the mapping $\delta_Y \circ g : X \rightarrow \mathcal{F}(Y)$ is Lipschitz weakly p -compact (respectively, Lipschitz unconditionally p -compact), then g is said to be Lipschitz free weakly p -compact (respectively, Lipschitz free unconditionally p -compact).

We denote the set of all the Lipschitz free weakly p -compact (Lipschitz free unconditionally p -compact) operators defined from X to Y with the notation $\text{FLip}_0^{\mathcal{W}_p}(X, Y)$ (respectively, $\text{FLip}_0^{\mathcal{K}_{up}}(X, Y)$).

Some characterizations have been obtained for Lipschitz-free (weakly) compact operators in Theorem 2.3 and Theorem 2.4 [12]. Similar characterizations have been obtained for the p -compactness case by Theorem 4.2 [9]. In the following theorems, we get identical characterizations for unconditionally p -compactness and weakly p -compactness cases. The proofs of these theorems will be made by following their proof steps.

Theorem 3.24. Let $g \in \text{Lip}_0(X, Y)$ and $p > 1$. Then, the following are equivalent.

- i. $g \in \text{FLip}_0^{\mathcal{K}_{up}}(X, Y)$
- ii. $\hat{g} \in \mathcal{K}_{up}(\mathcal{F}(X), \mathcal{F}(Y))$
- iii. $g^\# \in \mathcal{N}_{up}^Q(Y^\#, X^\#)$

PROOF. Let $g \in \text{Lip}_0(X, Y)$. Then, $\delta_Y \circ g \in \text{Lip}_0(X, \mathcal{F}(Y))$. By the uniqueness of linearizations in Lemma 2.1, it is obtained $\hat{g} = T_{\delta_Y \circ g}$. Using Theorem 3.15, we obtain that $g \in \text{FLip}_0^{\mathcal{K}_{up}}(X, Y)$ if and only if $T_{\delta_Y \circ g} \in \mathcal{K}_{up}(X, Y)$. Thus, the equivalence of *i* and *ii* is obtained. The equivalence of *ii* and *iii* follows from the equality $(Q_X)^{-1} \circ \hat{g}^* \circ Q_Y = g^\#$ and the result Theorem 2.4 [4]. □

Remark 3.25. Let $p \geq 1$ and E and F be Banach spaces. By Theorem 3.7 [6], we know that $T^* \in \mathcal{N}_{wp}^Q(F^*, E^*)$ while $T \in \mathcal{W}_p(E, F)$. Since we do not know whether the converse is true, we obtain the following theorem for the weakly p -compactness case of Theorem 3.24. Since the proof of theorem can be analogous to Theorem 3.24 using Theorem 3.5, we provide the following theorem.

Theorem 3.26. Let $g \in \text{Lip}_0(X, Y)$ and $p > 1$. Then, the following are equivalent.

i. $g \in \text{FLip}_0^{\mathcal{W}_p}(X, Y)$

ii. $\widehat{g} \in \mathcal{W}_p(\mathcal{F}(X), \mathcal{F}(Y))$

The notations $\text{FLip}_0^{\mathcal{W}}$, $\text{FLip}_0^{\mathcal{K}}$, and $\text{FLip}_0^{\mathcal{K}_p}$ denote the sets of all the Lipschitz free operators that are weakly compact, compact, and p -compact, respectively.

If the relations among relatively p -compact, unconditionally p -compact, weakly p -compact, compact, and weakly compact sets are considered, the following proposition can be obtained.

Proposition 3.27. Let $1 < p \leq q$. Then, we have the following inclusions.:

i. $\text{FLip}_0^{\mathcal{K}_p} \subset \text{FLip}_0^{\mathcal{K}_{up}} \subset \text{FLip}_0^{\mathcal{W}_p} \subset \text{FLip}_0^{\mathcal{W}}$

ii. $\text{FLip}_0^{\mathcal{K}_p} \subset \text{FLip}_0^{\mathcal{K}_{up}} \subset \text{FLip}_0^{\mathcal{K}} \subset \text{FLip}_0^{\mathcal{W}}$

iii. $\text{FLip}_0^{\mathcal{K}_p} \subset \text{FLip}_0^{\mathcal{K}_{up}} \subset \text{FLip}_0^{\mathcal{W}_p} \subset \text{FLip}_0^{\mathcal{W}_q} \subset \text{FLip}_0^{\mathcal{W}}$

The following proposition demonstrates the relationships among the classes of Lipschitz operators defined about weakly p -compact and unconditionally p -compact sets. The proof of the proposition is done by following the steps in Proposition 4.6 [9].

Proposition 3.28. Let $p > 1$. Then, $\text{FLip}_0^{\mathcal{W}_p} \subset \text{Lip}_0^{\mathcal{W}_p}$ and $\text{FLip}_0^{\mathcal{K}_{up}} \subset \text{Lip}_0^{\mathcal{K}_{up}}$.

PROOF. Let $f \in \text{FLip}_0^{\mathcal{W}_p}(X, E)$. Thus, the set $\text{Im}_{\text{Lip}}(\delta_E \circ f)$ is relatively weakly p -compact. Moreover, by the proof of Proposition 2.2 in [12], $\beta_E(\text{Im}_{\text{Lip}}(\delta_E \circ f) = \text{Im}_{\text{Lip}}(f))$, where $\beta_E : \mathcal{F}(E) \rightarrow E$ is a bounded linear operator, the barycentric map. Then, since the set $\text{Im}_{\text{Lip}}(f)$ is relatively weakly p -compact, $f \in \text{Lip}_0^{\mathcal{W}_p}(X, E)$ is obtained. \square

The following results with ideal properties provide modifications of Proposition 2.6 [12] and Theorem 4.8 [9] for unconditionally p -compact and weakly p -compact sets, respectively. The proof will be done similarly to the proof of Proposition 2.6 [12].

Proposition 3.29. Let W and Z be pointed metric spaces and $p > 1$. Then, $S \circ f \circ T \in \text{FLip}_0^{\mathcal{K}_{up}}(X, W)$ (respectively, $S \circ f \circ T \in \text{FLip}_0^{\mathcal{W}_p}(X, W)$) if $T \in \text{Lip}_0(X, Y)$, $f \in \text{FLip}_0^{\mathcal{K}_{up}}(Y, Z)$ (respectively, $f \in \text{FLip}_0^{\mathcal{W}_p}(Y, Z)$), and $S \in \text{Lip}_0(Z, W)$.

PROOF. If we show $S \circ \widehat{f \circ T} \in \mathcal{K}_{up}(\mathcal{F}(X), \mathcal{F}(W))$, then, by Theorem 3.24, we obtain that $S \circ f \circ T \in \text{FLip}_0^{\mathcal{K}_{up}}(X, W)$. Since $f \in \text{FLip}_0^{\mathcal{K}_{up}}(Y, Z)$, by Theorem 3.24, we get $\widehat{f} \in \mathcal{K}_{up}(\mathcal{F}(Y), \mathcal{F}(Z))$. By the ideal property of \mathcal{K}_{up} , $\widehat{S \circ \widehat{f \circ T}} \in \mathcal{K}_{up}(\mathcal{F}(X), \mathcal{F}(W))$. By Lemma 2.1 *vi*, it is obtained that $S \circ \widehat{f \circ T} = \widehat{S \circ f \circ T}$. Thus, $S \circ \widehat{f \circ T} \in \mathcal{K}_{up}(\mathcal{F}(X), \mathcal{F}(W))$, and by Theorem 3.24, $S \circ f \circ T \in \text{FLip}_0^{\mathcal{K}_{up}}(X, W)$. For weakly p -compact sets, the proof is similar. \square

3.4. Some Results Obtained for Lipschitz Operators Using Majorizations

Inspired by the result Proposition 3.1.3 of Sahraoui [16], using the result Proposition 3 of Barnes [15], the results obtained from this study, and current findings, we obtain the following proposition.

Proposition 3.30. Let $f \in \text{Lip}_0(X, E)$ and $g \in \text{Lip}_0(X, F)$ so that T_f majorizes T_g and $p > 1$. Then, we have the following:

i. g is Lipschitz p -compact operator if f is Lipschitz p -compact operator.

ii. $g \in \text{Lip}_0^{\mathcal{W}^p}(X, F)$ if $f \in \text{Lip}_0^{\mathcal{W}^p}(X, E)$

iii. $g \in \text{Lip}_0^{\mathcal{K}^{up}}(X, F)$ if $f \in \text{Lip}_0^{\mathcal{K}^{up}}(X, E)$

PROOF. If T_f majorizes T_g , then, by Proposition 3 [15], we know that there is an operator $V \in \mathcal{B}(\overline{T_f(\mathcal{F}(X))}, F)$ such that $T_g = V \circ T_f$.

i. If f is a Lipschitz p -compact operator, then, by Theorem 3.4 [9], T_f is a p -compact operator. By the ideal property of \mathcal{K}_p , T_g is a p -compact operator. By Theorem 3.4 [9], g is a Lipschitz operator which is p -compact.

The proofs of *ii* and *iii* can be compared to *i*, using Theorem 3.5 and Theorem 3.15, respectively. \square

Proposition 3.31. Let $f \in \text{Lip}_0(X, E)$ and $g \in \text{Lip}_0(Y, E)$ so that f^t majorizes g^t and $p > 1$. Then, we have the following:

i. g is a Lipschitz p -compact operator if f is a Lipschitz p -compact operator.

ii. $g \in \text{Lip}_0^{\mathcal{K}^{up}}(Y, E)$ if $f \in \text{Lip}_0^{\mathcal{K}^{up}}(X, E)$

PROOF. *i.* If f is Lipschitz p -compact, then, by Proposition 3.12 [9], $f^t : E^* \rightarrow X^\sharp$ is a linear operator that is quasi p -nuclear. Since f^t majorizes g^t , by Proposition 3 [15], there is an operator $V \in \mathcal{B}(\overline{f^t(E^*)}, X^\sharp)$ such that $g^t = V \circ f^t$. Thus, by the ideal property of quasi p -nuclear operators [9], $g^t : E^* \rightarrow X^\sharp$ is a linear operator that is quasi p -nuclear. By Proposition 3.12 [9], g is Lipschitz p -compact operator.

ii. The proof can be compared to *i* using Proposition 3.16. \square

Proposition 3.32. Let $f \in \text{Lip}_0(X, E)$ and $g \in \text{Lip}_0(Y, E)$ such that $\text{Im}_{\text{Lip}}(g) \subset \text{Im}_{\text{Lip}}(f)$ and $p > 1$. If f^t is quasi weakly p -nuclear, then g^t is quasi weakly p -nuclear.

PROOF. If $\text{Im}_{\text{Lip}}(g) \subset \text{Im}_{\text{Lip}}(f)$, then, by Theorem 3.1.1 [16], f^t majorizes g^t . Thus, the proof can be easily obtained by Proposition 3 [15] and the ideal property of quasi-weakly p -nuclear operators. \square

By Proposition 3.1.2 [16], we know that if $f \in \text{Lip}_0(X, E)$, $g \in \text{Lip}_0(X, F)$, and T_f majorizes T_g , then f majorizes g . Moreover, for $f \in \text{Lip}_0(X, E)$, $g \in \text{Lip}_0(X, F)$ which T_f majorizes T_g , by Proposition 3.1.3 [16], we know that f is Lipschitz (weakly) compact, then g is Lipschitz (weakly) compact. The following proposition demonstrates that the same result is obtained if the condition T_f majorizes T_g (see Proposition 3.1.3 [16]) replaced by f majorizes g .

Proposition 3.33. Let $f \in \text{Lip}_0(X, E)$ and $g \in \text{Lip}_0(X, F)$ so that f majorizes g . If f is Lipschitz compact (respectively, Lipschitz weakly compact), then g is Lipschitz compact (respectively, Lipschitz weakly compact).

PROOF. If f majorizes g , then, by Theorem 3.1.1 [16], $R(g^t) \subset R(f^t)$. Moreover, by Proposition 3.5 [1] (respectively, Proposition 3.4 [1]), f is Lipschitz compact (respectively, Lipschitz weakly compact) if and only if f^t is compact (respectively, weakly compact). Since $R(g^t) \subset R(f^t)$, by Proposition 8 [15], g^t is compact (respectively, weakly compact). Then, by Proposition 3.5 [1] (respectively, Proposition 3.4 [1]), g is Lipschitz compact (respectively, Lipschitz weakly compact). \square

4. Conclusion

This study has extensively explored the various classes of Lipschitz operators linked to weakly p -compact and unconditionally p -compact sets. By introducing these operator classes and scrutinizing the properties of associated linear operators, various results have been obtained regarding the properties of these operators. Notably, the study has highlighted that some of these classes are generalizations of related linear operators. Additionally, through evaluating majorization and comparing newly acquired and existing results, the study has drawn meaningful conclusions. Overall, this study contributes to understanding Lipschitz operators related to various sets.

Author Contributions

All the authors equally contributed to this work. This paper is derived from the second author's master's thesis supervised by the first author. They all read and approved the final version of the paper.

Conflicts of Interest

All the authors declare no conflict of interest.

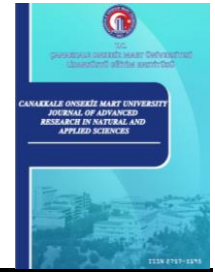
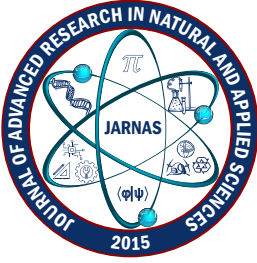
Ethical Review and Approval

No approval from the Board of Ethics is required.

References

- [1] A. Jiménez-Vargas, J. M. Sepulcre, M. Villegas-Vallecillos, *Lipschitz compact operators*, Journal of Mathematical Analysis and Applications 415 (2) (2014) 889–901.
- [2] A. Grothendieck, *Produits tensoriels topologiques et espaces nucléaires*, Memoirs of the American Mathematical Society 16 (1955).
- [3] D. P. Sinha, A. K. Karn, *Compact operators whose adjoints factor through subspaces of l_p* , Studia Mathematica 150 (1) (2002) 17–33.
- [4] J. M. Kim, *Unconditionally p -null sequences and unconditionally p -compact operators*, Studia Mathematica 224 (2) (2014) 133–142.
- [5] J. M. Kim, *The ideal of unconditionally p -compact operators*, The Rocky Mountain Journal of Mathematics 47 (7) (2017) 2277–2293.
- [6] J. M. Kim, *The ideal of weakly p -nuclear operators and its injective and surjective hulls*, Journal of the Korean Mathematical Society 56 (1) (2019) 225–237.
- [7] J. M. Kim, *The ideal of weakly p -compact operators and its approximation property for Banach spaces*, Annales Academiæ Scientiarum Fennicæ Mathematica 45 (2) (2020) 863–876.
- [8] A. Keten Çopur, A. Satar, *Some results on the p -weak approximation property in Banach spaces*, Fundamental Journal of Mathematics and Applications 5 (4) (2022) 234–239.
- [9] D. Achour, E. Dahia, P. Turco, *Lipschitz p -compact mappings*, Monatshefte für Mathematik 189 (2019) 595–609.
- [10] N. Weaver, Lipschitz algebras, World Scientific, Singapore, 1999.

- [11] N. J. Kalton, *Spaces of Lipschitz and Hölder functions and their applications*, *Collectanea Mathematica* 55 (2) (2004) 171–217.
- [12] M. G. Cabrera-Padilla, A. Jiménez-Vargas, *A new approach on Lipschitz compact operators*, *Topology and its Applications* 203 (2016) 22–31.
- [13] J. Diestel, J. H. Fourie, J. Swart, *The metric theory of tensor products: Grothendieck’s resume revisited*. American Mathematical Society, 2008.
- [14] J. M. Delgado, C. Pineiro, E. Serrano, *Operators whose adjoints are quasi p -nuclear*, *Studia Mathematica* 197 (3) (2010) 291–304.
- [15] B. A. Barnes, *Majorization, range inclusion, and factorization for bounded linear operators*, *Proceedings of the American Mathematical Society* 133 (1) (2005) 155–162.
- [16] A. Sahraoui, *Majorizing Lipschitz operators*, Master’s Thesis Université Mohamed Boudiaf (2021) M’sila.
- [17] W. J. Davis, T. Figiel, W. B. Johnson, A. Pełczyński, *Factoring weakly compact operators*, *Journal of Functional Analysis* 17 (3) (1974) 311–327.
- [18] G. Godefroy, *A survey on Lipschitz-free Banach spaces*, *Commentationes Mathematicae* 55 (2) (2015) 89–118.
- [19] F. Albiac, N. J. Kalton, *Topics in Banach space theory*, Springer, New York, 2006.



Optimization of Low-Calorific Coal Application at Different Loads in 600 MW Supercritical Thermal Power Plant with the PROMETHEE-GAIA Method

Aykut Emir¹ , Ali Riza Motorcu² , Hulya Demiroren³ 

¹School of Graduate Studies, Çanakkale Onsekiz Mart University, Çanakkale, Türkiye

²Industrial Engineering, Faculty of Engineering, Çanakkale Onsekiz Mart University, Çanakkale, Türkiye

³Materials Science and Engineering, Faculty of Engineering, Çanakkale Onsekiz Mart University, Çanakkale, Türkiye

Article Info

Received: 19 May 2024

Accepted: 09 Jun 2024

Published: 30 Sep 2024

Research Article

Abstract – This study examined the 600 MW supercritical unit of a 1200 MW imported coal-fired thermal power plant in Çanakkale, Türkiye. Coal blends consisting of low-calorific domestic coal (4087 kcal/kg) and high-calorific imported coal (5954 kcal/kg) were combusted at the single mill and burner level to analyze unit parameters at different loads. Initially, input parameters, levels affecting unit parameters, and output parameters influenced by different coal types were identified and prioritized. Using criteria weights determined by the entropy method, the optimal load and domestic-imported coal blend ratio were determined using the Preference Ranking Organization Method for Enrichment Evaluation-Geometrical Analysis for Interactive Aid (PROMETHEE-GAIA) multicriteria decision-making method. The optimization study concluded that a 450 MW load with a 14.6% domestic coal feed rate is the most suitable alternative.

Keywords – Domestic coal, entropy weighting method, PROMETHEE-GAIA, supercritical, thermal power plant

1. Introduction

In today's constantly evolving energy landscape, the pursuit of eco-friendly and economical energy solutions has gained significance. Importing fuel-based (high-calorific) thermal power plants built with environmental responsibility has long played an important role in meeting the increasing energy demand caused by the rising population in our country and even worldwide. However, with the growing concerns over carbon emissions, resource depletion, and especially economic stability, exploring and utilizing low-cost domestic coal alternatives in such plants has become important.

Using low-calorific domestic coal provides advantages in reducing dependence on foreign markets and mitigating risks associated with supply interruptions. Promoting domestic coal mining in our country can revitalize local economies by creating employment opportunities in coal-rich regions and encouraging economic growth. Additionally, revenues from domestic coal production can be invested in infrastructure development and social welfare programs, thus contributing to national economic prosperity. Domestic coal can reduce carbon emissions and environmental impacts when mined and burned more responsibly than imported coal alternatives. By adhering to strict environmental regulations and investing in clean coal technologies, our country can reduce the ecological footprint of energy production and establish a reliable

¹aykutemir@hotmail.com (Corresponding Author); ²armotorcu@comu.edu.tr; ³hulya.demiroren@comu.edu.tr

energy supply. Thus, countries utilizing local resources can strengthen their energy security and insulate themselves from foreign political tensions [1].

Transitioning from imported coal to lower-calorific domestic coal in our country's imported coal-fired thermal power plants requires a multi-faceted approach addressing technological, economic, and environmental issues. Investing in research and development to overcome technological barriers associated with domestic coal use is essential. Innovations in clean coal technologies, such as carbon capture and storage, coal enrichment, and efficient combustion processes, are key to enhancing the environmental performance of domestic coal use. Additionally, using domestic coal provides an opportunity to balance energy security, economic development, and environmental sustainability. Countries like ours can diversify energy sources, reduce dependence on imported fuels, and revitalize regional economies by utilizing local resources. However, realizing the full potential of domestic coal use requires addressing technological challenges through comprehensive regulatory approaches and committed efforts to encourage its use.

According to the 2022 data from the General Directorate of Mining and Petroleum Affairs (MAPEG) and Enerdata, global total coal production was 817 billion tons, while consumption was 786 billion tons. Our country's total coal production was 10537 million tons, and consumption was 11980 million tons in the same period. Of this consumption, 60.2% was hard coal, and 83.5% was lignite and asphaltite used in thermal power plants. The remaining amounts were used in heating, iron-steel, and other industrial branches [2].

When examining electricity generation sources in Türkiye as of February 2024, it is observed that 11.5% of total production was by natural gas and Liquefied natural gas (LNG) power plants. Dams provided 22.0% of the total production, while run-of-river hydroelectric plants contributed 6.1%. Imported coal power plants accounted for 23.7% of the total production in February, while domestic coal power plants contributed 14.2%. Renewable, wind, geothermal, and solar energy plants contributed 10.4% and 9.1% of the total production, respectively. Other thermal power plants had a 3.1% share in production [3]. These data indicate that Türkiye has a diverse range of sources in electricity production and an energy portfolio that includes a variety of sources. However, this diversity also presents significant challenges and opportunities regarding energy security and sustainability. Intensely using externally dependent sources such as imported coal and natural gas may increase energy imports and exposure to foreign policy risks. Therefore, prioritizing production methods based on local sources such as domestic coal and renewable energy can enhance energy security by reducing dependency. However, these sources can also bring environmental and social impacts, requiring a balanced approach. The further adoption of renewable energy sources and the development of efficient technologies can play a critical role in overcoming these challenges. Additionally, the effective implementation of energy policies and management is crucial. This can help the energy sector achieve its goals of sustainability, security, and economic development.

In order to support these considerations, Hendri and Lubis aimed to determine the optimum blending ratio of medium-grade and low-grade coal for use in energy plants. They evaluated the blending ratios of medium- and low-calorific coal in various combinations (0%, 20%, 40%, and 50%) across different analysis types [4]. Unlike Hendri and Lubis's study, this study investigates the use of mixtures of low-calorific domestic coal and high-calorific imported coal at different percentages (0%, 2%, 14.2%, 15.4%, and 14.6%) and under various load conditions (450MW, 560MW, and 605MW). In a system designed to burn high-calorific imported coal, a controlled and gradual feed of a mixture of high-calorific imported coal and low-calorific domestic coal was introduced and burned using a single mill and burner. Based on the results, criteria such as total unit coal consumption, coal cost, efficiency, SO₂, NO_x, Dust, CO, and the real-time total energy consumption of fans and mills were selected to determine the optimal coal blending ratio and corresponding unit load. To determine the optimal feeding ratio and corresponding unit load from nine different decision alternatives formed according to load and coal feeding ratio, the Preference Ranking Organization Method for Enrichment Evaluation- Geometrical Analysis for Interactive Aid (PROMETHEE-GAIA) method was used as the multicriteria decision-making method, and the Entropy method was used to calculate the importance (weight) of the criteria. A literature review reveals that no studies utilize multicriteria optimization methods to determine

the appropriate coal blend for burning different coal mixtures in such thermal plants. Therefore, this study will be a pioneering effort in this direction.

This study examines the potential of using domestic coal instead of imported coal in thermal plants. It seeks to explain the transformative potential of adopting domestic resources by comprehensively analyzing the advantages and disadvantages of adopting local resources and their impact on energy security, economic development, and environmental sustainability. This study represents an example of the application of PROMETHEE-GAIA, one of the multicriteria decision-making methods, using real-time data from an actual plant in the academic field. It will also serve as an example in the industrial field for using low-calorific coal as a mixture in such plants.

2. Materials and Methods

2.1. System Description and Design Parameters

The plant, located in Çanakkale, has an installed capacity of 2x610 MWe, operating with supercritical steam pressure and temperature. Supercritical thermal power plants operate above the critical point of water (Critical water – $T_c=374.14\text{ }^\circ\text{C}$ – $P_c=22.09\text{ MPa}$) at $610\text{ }^\circ\text{C}$ – 250/285 bar [5]. Table 1 presents some system parameters at maximum load (600 MW). These parameters are design parameters. The plant’s turbine consists of one High-Pressure (HP), one Intermediate-Pressure (IP), and two Low-Pressure (LP) turbines. The steam turbine driving the generator, capable of producing 600 MWe (607.91 MW), operates at supercritical pressure. It consists of a single-stage reheater, one HP, one IP, and two LPA LPB turbines. The fresh steam pressure of the turbine is 24.2 MPa (242 bar), and the fresh steam temperature is $566\text{ }^\circ\text{C}$. The heat consumption of the turbine operating at 3,000 rpm is 7,600 kJ/kWh. HP, IP, and LP steam turbine outlets have intermediate steam extraction lines for use in HP and LP heaters and IP steam outlets in the deaerator. The steam turbine directly connects to a 50 Hz, 22 kV, three-phase alternating current generator. Emergency shutdown valves, turbine control valves, and intermediate extraction lines are located on the steam turbine.

Table 1. Design specifications of the system

Definition	Value	Unit
Power plant	600	MWe
Boiler steam production capacity	1827	ton/h
Generator rated voltage	22	kV
Main steam pressure	24.2	Mpa
Main steam temperature	566	$^\circ\text{C}$
Boiler feed water inlet pressure	29.3	Mpa
Boiler feed water inlet temperature	275	$^\circ\text{C}$
Condenser vacuum pressure	-96	kPa
Turbine speed	3000	rpm
Designed coal consumption (At full load)	200 – 220	Ton/h
Condenser water outlet flow rate	1537	Ton/h
Mill coal conveying air temperature	80	$^\circ\text{C}$

The imported (high-calorific) coal used in the units arrives at the facility’s port through the sea. Coal is unloaded and loaded at the plant’s port using the unloading and loading system and stored in the stockyard via belt conveyors. Again, using belt conveyors, coal taken from the stockyard is passed through crushers and screens to reach appropriate particle sizes and then transferred to coal bunkers. Pulverized coal is sent to

burners in the boiler with mill transport air after being ground in mills. The analysis values of high-calorific Colombian and low-calorific domestic coal types used in the study are presented in Table 2. All analyses in the study were conducted in the plant laboratory.

Table 2. Analysis values of coal types used in the study

Coal Origin	Humidity (%)	Carbon (%)	Volatile (%)	Dust (%)	Sulfur (%)	Upper Cal. Value (kcal/kg)	Lower Cal. Value (kcal/kg)
Colombia	12.4	45.71	34.65	7.24	0.7	6241	5954
Local Coal	20.57	32.22	31.83	15.38	1.05	4368	4087

Pulverized coal combustion in thermal power plants is a critical process where finely ground coal is burned to generate energy [6]. In pulverized coal combustion systems, pulverized coal is sprayed into the combustion chamber using combustion air and suitable burners, similar to gas and liquid fuels. The coal particle remains suspended in the combustion air for a moment in the combustion chamber, dries quickly due to the created turbulence, vaporizes, ignites rapidly, and completes its combustion. The particle size of the coal is of great importance at this point. If the pulverized coal particle size is too small, ignition is risky during transport.

Conversely, if the particle size is large, combustion does not occur at the desired section within the boiler but towards the boiler outlet, resulting in suboptimal fuel efficiency. The sample analysis values for coal particle size per 100 grams taken from the plant after the mills are as follows: for large particles, i.e., above 200 microns, 6.97%; between 200-150 microns, 10.97%; for medium-sized and desired proportions, between 150-106 microns, 11.05%; and between 106-90 microns, 20.91%. For small particles, between 90-63 microns, 21.23%; between 63-40 microns, 17.95%; and for the smallest particles, below 40 microns, 10.92%. These values have been calculated by averaging ten different measurements.

By creating a suitable burner arrangement and operating conditions, the flame fills the combustion chamber as turbulently as possible, avoiding licking the walls and aiming for stable combustion conditions. The heat generated from coal combustion in the combustion chamber is transferred to the water pipes located on the sides of the combustion chamber through convection and radiation heat distribution [7]. The combustion gases ascending within the boiler pass through the superheater at the upper part of the boiler and subsequently through the economizer, where the incoming water is heated, transferring its heat to the steam in the packages and being released to the atmosphere at around 115 °C. The superheated steam, heated by the heat transferred from the combustion gases, is delivered to the turbine.

As seen in Figure 1, the boiler burners in the system total 24. They are positioned in three tiers, with eight burners on each tier facing each other. Pulverized coal entering with air from the burners forms a vortex in the center of the boiler. It burns, transferring its heat to the superheater packages located at the upper part and separating as flue gas. Figure 1 shows the positioning of the boiler superheater packages and burner tiers.

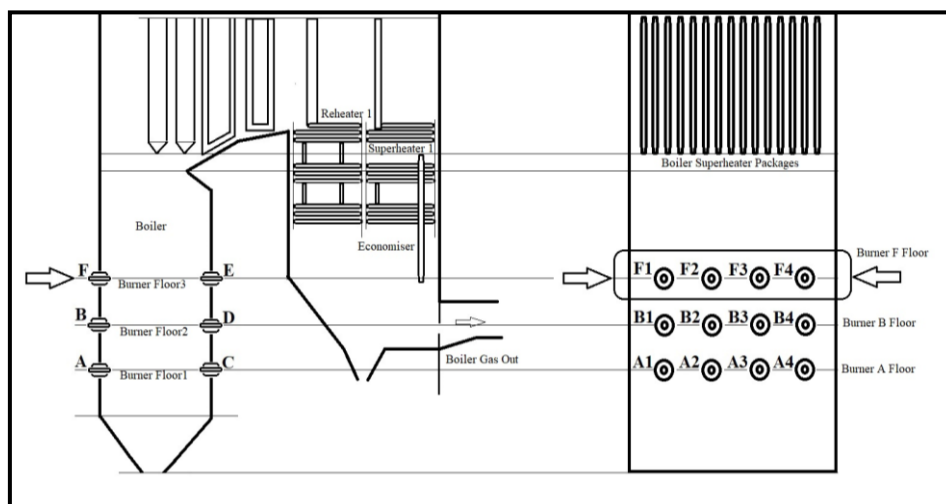


Figure 1. Boiler design and burner layout

The plant's DCS system is controlled by Nexus OnCore Control System software on computers with a Windows operating system. Nexus OnCore control systems are modern systems with a compact structure designed specifically for smaller industrial plants. These systems have been developed to replace programmable logic controllers (PLC) by bringing large plants' advanced diagnostic and operational capabilities to a small form factor. Nexus OnCore Compact Control System can be applied across a wide range of industries, facilitating both the integration of new machinery and the renewal of existing systems. The system consolidates operator information from various equipment and adapts to constantly changing operational needs, enabling more effective plant management [8]. Figure 2 presents the control system view of the turbine section of the thermal power plant where the study was conducted. As seen in the figure, all equipment in the system and real-time system tracking are controlled through the Nexus OnCore program.

All system tracking and data of determined parameters during the study were recorded with this program. Data were taken from the system at five-minute intervals and arranged as hourly averages. The reason for selecting short time intervals was to achieve more accurate data and filter out deviation data.



Figure 2. Distributed Control System (DCS)

During the study, feeding two different types of coal blends to the boiler was closely monitored and recorded. These data were first calculated as hourly averages and then as daily averages. The prepared coal blend was transferred to the coal bunkers, ground in the mill, and directed to the F-tier burners in the boiler, which are the highest. Burning at this tier was to minimize slag deposition on the boiler walls and reduce temperature differences in different regions (especially lower tiers) of the boiler, thus maintaining a homogeneous temperature distribution within the boiler.

This study determined the optimal blend ratio of coal mixtures fed at different loads in a 600 MW supercritical plant by following the steps shown in Figure 3. First, two different calorific coal types were mixed in the specified ratio and sent to the bunker of the mill (Mill F) to be ground. In the second stage, the prepared blend was ground in the mill to reach the appropriate particle size and then sent to the boiler for combustion. In the third stage, the criteria most affected by the combustion of different coal types were determined and monitored before the study, and data were recorded. In the final stage, the data obtained from the combustion and the importance weights of the criteria were calculated using the entropy method, and the optimal coal blend ratio and corresponding unit load were determined using the multicriteria decision-making method PROMETHEE-GAIA (Academic Version).

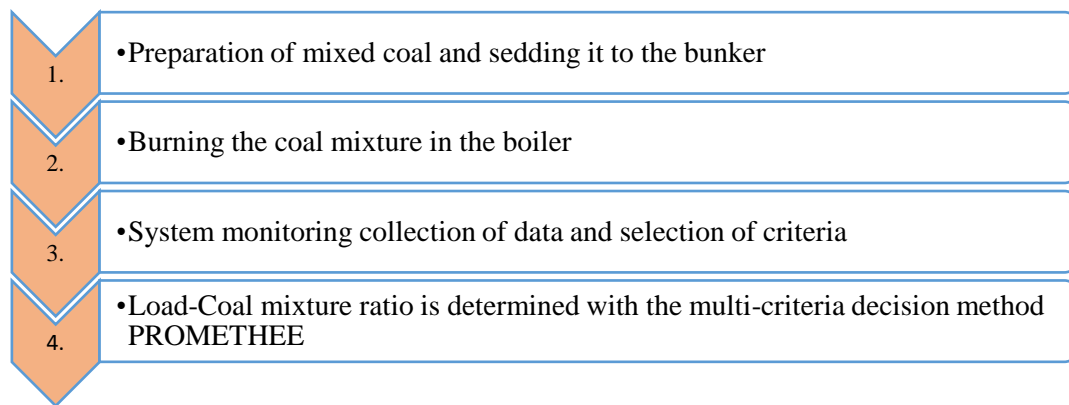


Figure 3. Stage of the study

2.2. System Outputs (Criteria)

The primary criteria identified after the combustion of the blended coal were unit load, total coal consumption, coal cost, overall system efficiency, instantaneous total energy consumption of fans and mills, and flue gas emissions of SO₂, NO_x, dust, and CO, totaling nine.

Unit load: The unit load is the mode of operation of the unit according to the day-ahead schedule, with a maximum load of 600 MW and a minimum load of 350 MW. This value may change according to the load demand from the energy grid at that moment. During this study, since the plant was in commercial operation, it adhered to the instructions of the energy grid managers. During the time covered in the study, the unit load changed according to instructions, and stable operation at the desired load and time was not possible. Nevertheless, data were collected when the unit was stable.

Total coal consumption: Total coal consumption is the hourly total coal consumption fed to the unit. Total coal consumption varies depending on the unit's load at that moment. At the maximum operating load of the unit, total coal consumption is 200-220 tons/hour. It may vary depending on the quality of the coal and the unit's operating load. The domestic coal ratio fed to the unit is included in this value.

Coal cost: Coal cost is calculated based on imported and domestic prices during the study period. As is known, coal prices are determined by international standards and may vary seasonally. The coal prices for the period were determined according to the 2022 hard coal sector report. Imported coal was calculated at \$341/ton, and domestic coal at \$235/ton [9]. Coal cost is an important parameter in thermal power plants. Generally, imported coal is more expensive than domestic coal, but when considered a calorific ally, high-calorific imported coal can be more advantageous for companies. However, imported coal impacts the current account deficit of the country where the plant is located, making the use and promotion of domestic coal more advantageous overall [10].

Unit efficiency: The unit's efficiency is calculated as the ratio of gross energy produced to total energy supplied to the system. Efficiency is important for the unit. The most critical factors affecting efficiency are coal quality and combustion quality. The most significant outputs of combustion quality are flue gas emissions and the unburned carbon ratio in the flue gas ash [11]. The lower the percentage of unburned carbon, the better the combustion. The low proportion of unburned carbon within the boiler signifies efficient combustion. This indicates that the quality of the coal and the quantity and quality of air during combustion are optimal. The power plant manufacturer specifies that this ratio should be less than 4%. This ratio may vary depending on the types of power plants. This ratio can be higher in plants with low coal quality and suboptimal combustion efficiency.

Total energy consumption of fans and mills: The total energy consumption of fans and mills is the equipment most affected by changes in coal quality. Fans must load more than usual to ensure optimal combustion within the boiler with changes in coal quality, drawing more current and consequently more energy. Similarly, with

low-quality coal feeding, the unit requires more coal to maintain its existing load, increasing the mill load and drawing more current and energy. These values change simultaneously, so they are calculated as total current. These are calculated based on the total current drawn by two Inducer Draft Fan (IDF), two Forced Draft Fan (FDF), two Primer Air Fan (PAF), one Booster Fan, and six mill motors (6 kV).

SO₂, NO_x, dust, and CO emissions: SO₂, NO_x, dust, and CO emissions result from flue gas combustion in the boiler. These are parameters directly affected by coal changes. The company is meticulous about the filtration of flue gas emissions from both units. Each unit has one Electrostatic Precipitator (ESP) for dust emission, one Selective Catalytic Reduction (SCR) for NO_x reduction emission, and one Flue Gas Desulphurization (FGD) system for flue gas sulfur emission filtration. Legal limits were observed when applying low-calorific and different types of coal to the system. The limit values set by the Ministry of Environment and Forestry are presented in Table 3 [12].

Table 3. Flue gas emission limit values (2010) [12]

Description	Value	Unit
SO ₂	200	Mg/Nm ³
NO – NO ₂	200	Mg/Nm ³
CO	200	Mg/Nm ³
Dust	30	Mg/Nm ³

2.3. Decision Alternatives

Nine decision alternatives were created by changing the unit load and feed rates against the nine criteria identified in the study during the combustion of the blended coal (Table 4). Table 4 lists the unit’s working load against the ratio of domestic coal fed to the unit. This table shows domestic coal was fed to the unit at different rates under different load conditions. Compared with decision alternatives, the unit’s operation with only imported coal, without any domestic coal feed, is 0%. In the 0% scenario, only imported coal is fed into the unit. When selecting the coal feeding rates in Table 4, the health of the unit’s equipment and operational performance were considered. It was closely monitored to avoid situations that could endanger the system, and the proportions of domestic coal fed were continuously changed. In such large power plants, it is necessary to proceed in a controlled and balanced manner regarding workload and operating methods. Therefore, a single domestic coal feeding rate was not maintained for a long period (more than eight hours). In addition, when selecting the unit’s operating load, the instructions of the energy grid managers were adhered to.

Table 4. Decision alternatives

No	Load MW	Domestic Coal Rate (%)
1	605	2
2	605	14.2
3	605	15.4
4	450	15.4
5	560	15.4
6	560	14.6
7	450	14.6
8	450	0
9	605	0

The study aims to determine the optimal working mode according to the criteria of these nine decision alternatives. In such multicriteria decision-making situations, the most commonly used methods include Analytic Hierarchy Process (AHP), Technique for Order Preference by Similarity to Ideal Solution (TOPSIS), Elimination and Choice Translating Reality (ELECTRE), PROMETHEE-GAIA (Preference Ranking Organization Method), and VlseKriterijumska Optimizacija I Kompromisno Resenje (VIKOR). These methods are preferred according to different levels of complexity and problem types [13].

The PROMETHEE-GAIA, a multicriteria decision-making method, was used to identify the best choice in this study's multicriteria decision-making (optimization) problem. The optimization application was carried out in the Visual PROMETHEE (Academic Version) program. Developed by J.P. Brans, the PROMETHEE method determines the ranking among criteria in multicriteria decision-making [14]. This method is known for its simplicity but performs well in such multicriteria problems. It evaluates and ranks alternatives based on different criteria. This ranking helps decision-makers determine the most appropriate alternative. The preference method of PROMETHEE is based on pairwise comparisons. Each alternative is compared with another within itself and presents the most suitable alternative to the decision-maker [15]. PROMETHEE I and PROMETHEE II provide a complete ranking of decision alternatives. PROMETHEE I is used to obtain partial ranking, while PROMETHEE II is used for complete ranking [14, 16]. Different versions of PROMETHEE (III, IV, V, VI, etc.) have been developed today [17].

The Entropy method was used to determine the importance (weights) of the criteria within the method. The entropy method is a weighting method used to determine the importance of criteria in a ranking problem. Major methods used to assess the importance of criteria in multicriteria decision-making problems include a heuristic method, principal component analysis, Taguchi Method-Signal/Noise Ratio, and entropy method. Compared to these subjective weighting models, the biggest advantage of the entropy method is that it prevents human factors from interfering in weighting indicators, thereby increasing the objectivity of comprehensive evaluation results [17]. For this reason, the entropy weighting method (EWM) has been widely used in decision-making mechanisms in recent years.

3. Results and Discussion

Optimizing coal feed ratios in thermal power plants is crucial for balancing operational efficiency with environmental impact [17]. Table 5 presents a comprehensive dataset evaluating system performance under different loads according to domestic coal feed ratios. Based on these data, meaningful conclusions can be drawn regarding operational scenarios' efficiency and environmental impacts.

As seen in Table 5, total coal consumption (t/h) varies at different loads. For instance, the highest coal consumption was recorded at 605 MW load with a 15.4% domestic coal feed ratio at 214.390 t/h. The efficiency of the power plant generally increases at higher loads. For example, at a 605 MW load with a 15.4% domestic coal feed ratio, the efficiency is 0.413627, while at the same feed ratio, the efficiency drops to 0.409574 at a 450 MW load. This indicates that higher loads can be more efficient but demand more coal.

Environmental emissions are a critical factor in evaluating the performance of thermal power plants. SO₂ emissions, in particular, are associated with high coal consumption and low efficiency [18]. For example, at 605 MW and a 2% domestic coal feed ratio, SO₂ emissions are 335.348 mg/m³, while at the same load with a 0% domestic coal feed ratio, this value drops to 275.898 mg/m³. This suggests that lower domestic coal ratios can reduce SO₂ emissions. NO_x emissions show a similar trend. At a 605 MW load with a 0% domestic coal feed ratio, NO_x emissions are 89.547 mg/m³, while at a 15.4% domestic coal feed ratio, this value is 77.281 mg/m³. This indicates that higher domestic coal ratios can reduce NO_x emissions. Dust and CO emissions vary according to coal feed ratios and load levels. For example, at a 605 MW load with a 0% domestic coal feed ratio, dust emissions are 3.4002 mg/m³, while at a 15.4% ratio, this value drops to 2.9037 mg/m³. Similarly, CO emissions decrease with increasing domestic coal ratios. For instance, at a 605 MW load with a 15.4% domestic coal feed ratio, CO emissions are 41.049 mg/m³; at a 0% ratio, this value is 20.563 mg/m³.

Energy consumption varies at different loads and domestic coal feed ratios. The highest energy consumption is recorded at a 605 MW load with a 14.2% domestic coal feed ratio of 1.627.8 amperes. This value is recorded as 1.624.8 amperes at the same load with a 0% domestic coal feed ratio. These differences in energy consumption indicate the impact of coal feed ratios on energy efficiency.

These data reveal the critical role of domestic coal feed ratios at different loads on operational efficiency and environmental impact in thermal power plants. While higher loads achieve higher efficiency, they can result in higher coal consumption and emissions. Optimizing domestic coal ratios can contribute to more sustainable energy production by reducing environmental emissions [18, 19].

Table 5. Result values of domestic coal feed rates of the system at different loads (Decision matrix for entropy method)

Coal Ratio According to Unit Load	Unit Load (MW/h)	Total Coal Consumption (t/h)	Coal Cost (\$)	Efficiency	SO ₂ Emission mg/m ³	NOx Emission mg/m ³	Dust Emission mg/m ³	CO Emission mg/m ³	Energy Consumption Ampere
605 MW 2% Domestic Coal	604.913	212.532	72.364,112	0.411690	335.348	78.590	2.2046	22.817	1.594.4
605 MW 14.2% Domestic Coal	604.997	213.007	71.808,043	0.414991	327.418	77.378	2.6985	32.022	1.627.8
605 MW 15.4% Domestic Coal	604.870	214.390	72.034,209	0.413627	344.804	77.281	2.9037	41.049	1.604.3
450 MW 15.4% Domestic Coal	451.453	159.181	54.280,721	0.409574	211.187	79.707	2.6067	21.089	1.159.3
560 MW 15.4% Dom. Coal	559.995	197.161	66.322,322	0.415911	283.386	73.737	2.8406	27.014	1.511.9
560 MW 14.6% Dom. Coal	564.812	190.672	64.228,181	0.433155	241.796	71.601	2.8863	22.831	1.500.9
450 MW 14.6% Dom. Coal	449.893	156.008	52.121,928	0.425227	152.921	78.015	2.5577	20.450	1.324.2
450 MW 0% Domestic Coal	455.038	156.923	53.510,822	0.418767	143.742	83.374	3.5648	18.671	1.345.6
605 MW 0% Domestic Coal	604.924	207.269	70.678,624	0.421482	275.898	89.547	3.4002	20.563	1.624.8

Figure 4 presents the interface visual of the Visual PROMETHEE program used as the multicriteria decision-making method in this study. The measurement values of the criteria in Table 5. were entered using the interface shown in Figure 4. As seen in Figure 4, a decision matrix consisting of nine different criteria and nine different alternatives was obtained.

Scenario	Unit Load (MW)	Total Coal Consumption (t/h)	Coal Cost (\$)	Unit Efficiency	SO2 Emission (mg/m3)	NOX Emission (mg/m3)	Dust Emission (mg/m3)	CO Emission (mg/m3)	Total Energy Consumption (Ampere)
605 MW 2% Do...	604,913	212,532	72364,1120	0,411690	335,348	78,590	2,2046	22,817	1594,40
605 MW 14,2% ...	604,997	213,007	71808,0430	0,414991	327,418	77,378	2,6985	32,023	1627,80
605 MW 15,4% ...	604,870	214,390	72034,2090	0,413627	344,804	77,281	2,9037	41,049	1604,30
450 MW 15,4% ...	451,453	159,181	54280,7210	0,409574	211,187	79,707	3,6067	21,090	1159,30
560 MW 15,4% ...	559,995	197,161	66322,3220	0,415911	283,386	73,737	2,8406	27,014	1511,90
560 MW 14,6% ...	564,812	190,672	64228,1810	0,433155	241,796	71,601	2,8863	22,831	1500,90
450 MW 14,6% ...	444,893	156,008	52121,9280	0,425227	152,921	78,015	2,5577	20,450	1324,20
450 MW 0% Do...	455,038	156,923	53510,8220	0,418767	143,742	83,374	3,5648	18,671	1345,60
605 MW 0% Do...	604,924	207,269	70678,6240	0,421482	275,898	89,547	3,4002	20,563	1624,80

Figure 4. Visual PROMETHEE

3.1. Determining Weights Using the Entropy Method

The entropy method is a powerful tool to ensure objectivity, especially in scientific and technical evaluations. Determining the importance of the criteria weights with this method is performed in five steps. These are, respectively [20]:

- Creating the decision matrix
- Normalization
- Calculation of the entropy value
- Determination of the degree of divergence
- Calculation of weights

The criteria weights were determined following these five steps in the entropy method. In the first step, a 9x9 decision matrix was created with the study's results (Table 5) and expressed in (3.1) and Figure 4.

$$X = \begin{bmatrix} x_{11} & x_{12} & \dots & x_{1n} \\ x_{21} & x_{22} & \dots & x_{2n} \\ \vdots & \vdots & \dots & \vdots \\ x_{m1} & x_{m2} & \dots & x_{mn} \end{bmatrix}, \quad i \in \{1,2,\dots,m\} \text{ and } j \in \{1,2,\dots,n\} \quad (3.1)$$

In the second step, normalization was performed by calculating the ratio of each criterion value corresponding to a decision alternative to the total value of that criterion using (3.2). The results of the normalization process (Table 6) and the obtained normalization matrix are presented in Table 7.

$$P_{ij} = \frac{x_{ij}}{\sum_{i=1}^m x_{ij}} \quad (3.2)$$

Table 6. The sum of the criteria for each decision alternative

Unit Load (MW)	Total Coal Consumption (t/h)	Coal Cost (\$)	Efficiency	SO ₂ Emission (mg/m ³)	NOx Emission (mg/m ³)	Dust Emission (mg/m ³)	CO Emission (mg/m ³)	Energy Consumption (Ampere)
4900.895058	1707.141974	577348.962	3.764422848	2316.50	709.23	26.66	226.51	13293.19

Table 7. Normalization matrix

Unit Load (MW)	Total Coal Consumption (t/h)	Coal Cost (\$)	Efficiency	SO ₂ Emission mg/m ³	NOx Emission mg/m ³	Dust Emission mg/m ³	CO Emission mg/m ³	Energy Consumption Ampere
0.123429024	0.12449575	0.12533860	0.109363423	0.14476446	0.110810195	0.082684402	0.100734638	0.119941203
0.123446226	0.12477385	0.12437546	0.110240205	0.141341265	0.109100866	0.10120617	0.141373738	0.122450209
0.123420266	0.12558389	0.12476719	0.109877817	0.148846605	0.108964965	0.108903378	0.181226987	0.120684817
0.092116405	0.09324414	0.09401718	0.108801331	0.091166233	0.112384781	0.135268528	0.093105701	0.087210458
0.114263838	0.11549199	0.11487389	0.110484662	0.122333516	0.103967455	0.10653767	0.119263949	0.113733425
0.115246687	0.11169057	0.11124672	0.115065327	0.10437964	0.100956425	0.108249202	0.100796447	0.112907924
0.09179813	0.09138548	0.09027803	0.112959414	0.066016273	0.109999565	0.095926889	0.090284584	0.099614942
0.092848016	0.09192160	0.09268367	0.111243296	0.062051048	0.117555646	0.133700044	0.082430487	0.101226722
0.123431409	0.12141268	0.12241924	0.111964524	0.11910096	0.126260102	0.127523717	0.090783467	0.122230299

The entropy value was calculated using (3.3) in the third step. For this, first, the product of the logarithm of each criterion value in the normalization matrix (Table 7) was taken (Table 8). Then, the k value was calculated by dividing one by the logarithm of the number of decision alternatives (see (3.4)). In (3.4), m represents the total number of decision alternatives. As previously mentioned, the total number of decision alternatives in this study is nine. The entropy value for each criterion was calculated by multiplying the total of each criterion’s logarithm values by the k value (Table 9).

$$e_j = -k \sum_{i=1}^m P_{ij} \cdot \ln(P_{ij}) \tag{3.3}$$

and

$$k = 1/\ln(m) \tag{3.4}$$

Table 8. $P_{ij} \cdot \ln(P_{ij})$ matrix

Unit Load (MW)	Total Coal Consumption (t/h)	Coal Cost (\$)	Efficiency	SO ₂ Emission mg/m ³	NOx Emission mg/m ³	Dust Emission mg/m ³	CO Emission mg/m ³	Energy Consumption Ampere
-0.2582245	-0.2593848	-0.2602952	-0.2420298	-0.2797786	-0.2437753	-0.2061094	-0.2312127	-0.2543657
-0.2582432	-0.2596858	-0.2592544	-0.2430899	-0.2765452	-0.2417110	-0.2318224	-0.2765762	-0.2571516
-0.2582149	-0.2605591	-0.2596786	-0.2426526	-0.2835288	-0.2415457	-0.2414708	-0.3095365	-0.2551968
-0.2196701	-0.221224	-0.2222827	-0.2413465	-0.2183495	-0.2456536	-0.2706037	-0.2210347	-0.2127438
-0.2478662	-0.2492957	-0.2485779	-0.2433842	-0.2570232	-0.2353487	-0.2385651	-0.2536047	-0.2472448
-0.2490112	-0.2448283	-0.2442983	-0.2488006	-0.2358688	-0.2314997	-0.2406725	-0.2312927	-0.2462728
-0.2192289	-0.2186551	-0.2171061	-0.2463336	-0.1794225	-0.2427997	-0.2248688	-0.2171153	-0.2297561
-0.2206803	-0.2194002	-0.2204539	-0.2442942	-0.1724893	-0.2516682	-0.2690254	-0.2057300	-0.2318489
-0.2582271	-0.2560059	-0.2571175	-0.2451545	-0.2534210	-0.2612840	-0.2626290	-0.2178147	-0.2569095

Table 9. Entropy values of the criteria

Unit Load (MW)	Total Coal Consumption (t/h)	Coal Cost (\$)	Efficiency	SO ₂ Emission (mg/m ³)	NOx Emission (mg/m ³)	Dust Emission (mg/m ³)	CO Emission (mg/m ³)	Energy Consumption (Ampere)
0.996423793	0.996275104	0.99628645	0.999937088	0.981432382	0.999117926	0.994785662	0.984841565	0.984841565

In the fourth step, the degree of divergence for each criterion was calculated using (3.5) (Table 10). The degree of divergence is calculated by subtracting the entropy value from one.

$$d_j = 1 - e_j \tag{3.5}$$

Table 10. Difference degrees of the criteria

Unit Load (MW)	Total Coal Consumption (t/h)	Coal Cost (\$)	Efficiency	SO ₂ Emission (mg/m ³)	NOx Emission (mg/m ³)	Dust Emission (mg/m ³)	CO Emission (mg/m ³)	Energy Consumption (Ampere)
0.003576206	0.003724895	0.003713549	0.000062912	0.018567618	0.000882074	0.005214337	0.015158435	0.002609700

In the final step, the importance weight for each criterion was determined by dividing a criterion's d_j value by the total d_j values of all criteria (see (3.6)). The importance weights (weights) calculated for each criterion using (3.6) are presented in Table 11, and the percentage weights in Table 12.

$$w_j = d_j / \sum_{j=1}^n d_j \tag{3.6}$$

Table 11. Importance degrees (weights) of the criteria w_j

Unit Load (MW/h)	Total Coal Consumption (t/h)	Coal Cost (\$)	Efficiency	SO ₂ Emission (mg/m ³)	NOx Emission (mg/m ³)	Dust Emission (mg/m ³)	CO Emission (mg/m ³)	Energy Consumption (Ampere)
0.06683283	0.069611556	0.069399518	0.001175714	0.346995169	0.016484375	0.097446536	0.283283715	0.048770586

Table 12. Percentage ratios of the importance degrees of the criteria

Unit Load (MW/h)	Total Coal Consumption (t/h)	Coal Cost (\$)	Efficiency	SO ₂ Emission (mg/m ³)	NOx Emission (mg/m ³)	Dust Emission (mg/m ³)	CO Emission (mg/m ³)	Energy Consumption (Ampere)
6.68%	6.96%	6.94%	0.12%	34.70%	1.65%	9.74%	28.33%	4.88%

As seen in Table 12, the highest weights among the criteria were 34.70% for SO₂ from flue gas emissions and 28.33% for CO. Flue gas emission values are the most important parameters in the operating values of solid-fuel thermal power plants. SO₂ and CO are among the parameters most affected by coal changes. The high importance of these criteria relative to others was an expected result. Thus, the weight values of the criteria were calculated in five steps, and the computed weight values for each criterion were entered into the Visual PROMETHEE program (Figure 5).

When applying the PROMETHEE method, it is necessary to determine the preference functions. The PROMETHEE preference function is used to identify deviation among alternatives for each criterion [21]. For this study, the types of preference functions were determined by the preference function selection assistant as a feature provided by the application. Since one of the criteria, unit efficiency, is calculated as a percentage, the threshold value was selected as a percentage.

Scenario1	Unit Load	Total Coal C...	Coal Cost	Unit Efficiency	SO2 Emission	NOX Emission	Dust Emission	CO Emission	Total Energy...
Unit	MW	t/h	\$	--	mg/m3	mg/m3	mg/m3	mg/m3	Ampere
Preferences									
Min/Max	max	min	min	max	min	min	min	min	min
Weight	0,07	0,07	0,07	0,00	0,35	0,02	0,10	0,28	0,05
Preference Fn.	Linear	Linear	Linear	Linear	Linear	Linear	Linear	Linear	Linear
Thresholds	absolute	absolute	absolute	percentage	absolute	absolute	absolute	absolute	absolute
- Q: Indifference	1,000	1,000	1,0000	1	1,000	1,000	1,0000	1,000	1,00
- P: Preference	2,000	2,000	2,0000	2	2,000	2,000	2,0000	2,000	2,00
- S: Gaussian	n/a	n/a	n/a	n/a	n/a	n/a	n/a	n/a	n/a
Statistics									
Minimum	444,893	156,008	52121,9280	0,409574	143,742	71,601	2,2046	18,671	1159,30
Maximum	604,997	214,390	72364,1120	0,433155	344,804	89,547	3,6067	41,049	1627,80
Average	543,988	189,683	64149,8847	0,418269	257,389	78,803	2,9626	25,168	1477,02
Standard Dev.	68,181	23,991	8102,7796	0,006971	71,374	4,941	0,4474	6,798	155,60
Evaluations									
605 MW 2% Do...	604,913	212,532	72364,1120	0,411690	335,348	78,590	2,2046	22,817	1594,40
605 MW 14,2% ...	604,997	213,007	71808,0430	0,414991	327,418	77,378	2,6985	32,023	1627,80
605 MW 15,4% ...	604,870	214,390	72034,2090	0,413627	344,804	77,281	2,9037	41,049	1604,30
450 MW 15,4% ...	451,453	159,181	54280,7210	0,409574	211,187	79,707	3,6067	21,090	1159,30
560 MW 15,4% ...	559,995	197,161	66322,3220	0,415911	283,386	73,737	2,8406	27,014	1511,90
560 MW 14,6% ...	564,812	190,672	64228,1810	0,433155	241,796	71,601	2,8863	22,831	1500,90
450 MW 14,6% ...	444,893	156,008	52121,9280	0,425227	152,921	78,015	2,5577	20,450	1324,20
450 MW 0% Do...	455,038	156,923	53510,8220	0,418767	143,742	83,374	3,5648	18,671	1345,60
605 MW 0% Do...	604,924	207,269	70678,6240	0,421482	275,898	89,547	3,4002	20,563	1624,80

Figure 5. Input matrix using nine criteria and nine alternatives for the PROMETHEE method of multicriteria optimization

Figure 6 presents the PROMETHEE flow chart created based on the Visual PROMETHEE full-ranking result of the decision alternatives in the study. As seen in Figure 6, according to the program’s calculations, the best choice was feeding 0% of domestic coal at a 450 MW load (first row in the PROMETHEE flow table). However, since the study aimed to find the domestic coal feed ratio, the best working mode among the decision alternatives in the table selected was feeding 14.6% of domestic coal at a 450 MW load (second row in PROMETHEE flow table). The figure shows that the domestic coal feed ratio should be reduced as the load increases—the system’s adverse reaction to domestic coal increases in high-load operating conditions. The worst working mode is feeding 15.4% of domestic coal at a 605 MW load.

The PROMETHEE flow chart in Figure 6 shows the Phi, Phi+, and Phi- scores. Positive flow (Phi+) indicates the positive superiority of an alternative over others, while negative flow (Phi-) indicates its negative superiority over others [22, 23]. The working mode with a net superiority value of 0.7004 at a 450 MW load with 0% domestic coal feed was the first choice while feeding 15.4% of domestic coal at a 605 MW load with -0.3672 was the last choice. According to this multicriteria optimization result, the preferred working modes in order are 450 MW load with 14.6% domestic coal feed, 450 MW load with 15.4% domestic coal feed, 560

MW load with 14.6% domestic coal feed, and 605 MW load with 0% domestic coal feed, as their net superiority values are positive.

	action	Phi	Phi+	Phi-
1	450 MW 0% Dom. Coal	0,7004	0,7931	0,0927
2	450 MW 14,6% Dom.	0,5104	0,6587	0,1484
3	450 MW 15,4% Dom.	0,3507	0,5828	0,2321
4	560 MW 14,6% Dom.	0,1272	0,4922	0,3651
5	605 MW 0% Dom. Coal	0,0929	0,4488	0,3559
6	560 MW 15,4% Dom.	-0,2291	0,3363	0,5654
7	605 MW 2% Dom. Coal	-0,3587	0,2332	0,5919
8	605 MW 14,2% Dom.	-0,4717	0,1920	0,6637
9	605 MW 15,4% Dom.	-0,7220	0,0707	0,7927

Figure 6. Visual PROMETHEE flow table

The PROMETHEE GAIA plane in Figure 7 is a representation used in Multicriteria Decision Making (MCDM) processes. It helps decision-makers determine the criteria weights and make choices among alternatives objectively and systematically. This plane is designed to minimize subjective influences from decision-makers [23, 24]. It is designed as a two- and three-dimensional plane showing the alignment of alternatives and criteria. This plane allows decision-makers to see which criteria move in the same or opposite direction with which alternatives. This information helps make healthier and more informed decisions. The GAIA plane also guides decision-makers in selecting among preferences and helps determine the most appropriate alternative. The thick line close to the horizontal axis in the plane indicates the most suitable alternative for decision-makers [25].

The 2D GAIA plane analysis in Figure 7 shows that the “NOx” criterion has the greatest length. Criteria representing conflicting preferences are represented by axes directed in opposite directions, as seen in the case of “Load” and “Energy Consumption.” The position of the criteria indicates their similarity or conflict. The smaller the angle, the more similar the two criteria are. The small angle between “Cost” and “Total Coal Consumption” indicates their similarity. Because the more total coal consumption there is, the higher the cost. Alternatives close to each other show similar performances, such as “450 MW at 14.6% domestic coal” and “450 MW at 15.4% domestic coal.” In the 2D GAIA analysis presented in Figure 7, a multicriteria decision-making process is considered reliable when the quality level is above 70%, which, with a result of 93.6%, indicates that the multicriteria optimization process in this study was successful [26].

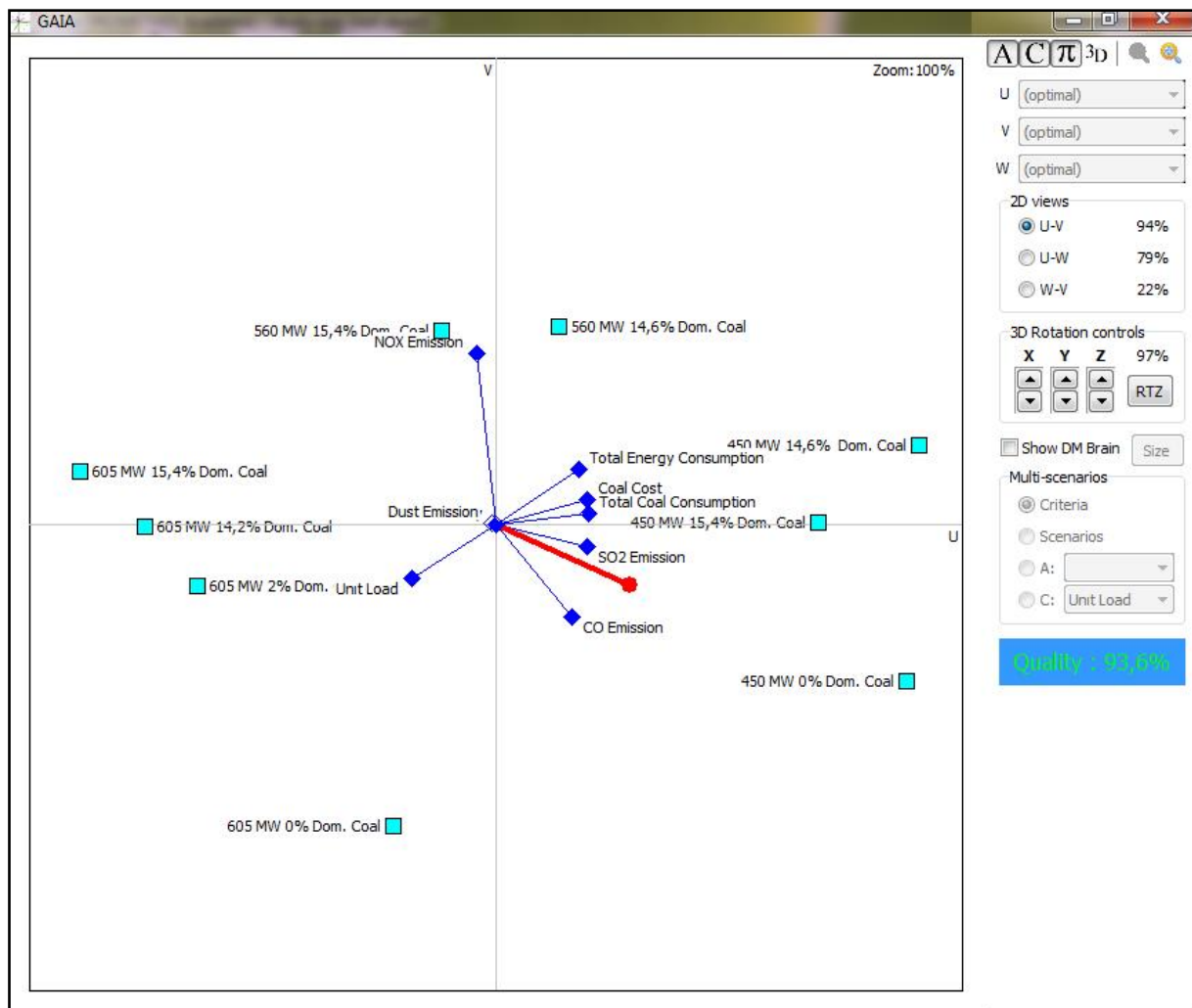


Figure 7. The arrangement of alternatives and criteria on the GAIA plane

4. Conclusion

This study examines domestic and imported coal blends in a 600 MW unit of a supercritical thermal power plant and its various output parameters. The study evaluated the effects of different load and coal blend ratios on plant performance. A controlled and gradual blend of high-calorific imported and low-calorific domestic coal was fed and burned with a single mill and burner in a system designed for high-calorific imported coal combustion. Various criteria were used to determine the optimal coal blend ratio and corresponding unit load based on the system and measurement data obtained. These criteria included total coal consumption, coal cost, efficiency, SO₂, NO_x, dust, CO, and instantaneous total energy consumption of fans and mills. The unit was tested at different domestic coal feed ratios at 605 MW, 560 MW, and 450 MW loads. The analysis and multicriteria decision-making studies concluded:

- According to the calculated criteria weights, the optimal coal blend ratio and corresponding unit load were determined to be 14.6% domestic coal feed at a 450 MW load.
- Physical observations indicated that exceeding the calculated domestic coal tonnage resulted in system instability, equipment malfunctions, and increased slag deposition within the boiler.
- Since a significant portion of the study criteria consisted of flue gas emission values, the most important factor affecting these items is the coal analysis values. Therefore, attention should be paid to the analysis values of coal used in similar future studies. Using domestic coal with worse analysis values may result in significantly different outcomes.

- Based on system observations, analyses, and the experience of this study, burning in the opposite burners on the upper tiers of the boiler may yield better results in similar future studies.
- This study is a short-term study. The long-term consequences of operating such power plants with out-of-design coal types in an uncontrolled manner may be much more severe. It may cause permanent damage to the boiler superheater packages or slag accumulation on the boiler walls, leading to issues requiring long and costly remediation. Therefore, the system should be closely monitored, and the boiler should be inspected at short intervals in similar future studies.

As a result, this study is a pioneering work evaluating the effects of low-calorific domestic and high-calorific imported coal blends on the performance of a 600 MW supercritical thermal power plant under different load conditions and determining the optimal load-blend ratio. This study will be an example of using different coal blends in similar plants. As a continuation of this study, the optimal operating mode under various load conditions can be determined when using the design coal of the system in similar plants. Similarly, the system's optimal operating temperature can be determined by observing changes in air temperature at the outlet parameters of such a plant.

Author Contributions

The first author directed the project and supervised this study's findings. The second author devised the main conceptual ideas and developed the theoretical framework. The first and second authors performed the experiment and statistical analyses. The first author wrote the manuscript with support from the second author. The third author reviewed the paper. All authors read and approved the final version of the paper. This paper is derived from the first author's master's thesis, supervised by the third author.

Conflicts of Interest

All the authors declare no conflict of interest.

Ethical Review and Approval

No approval from the Board of Ethics is required.

Acknowledgment

We thank ICDAS Bekirli Electricity Generation and Investment Inc. for supporting this work.

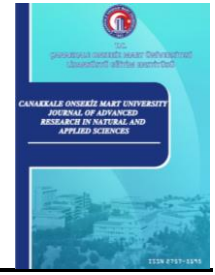
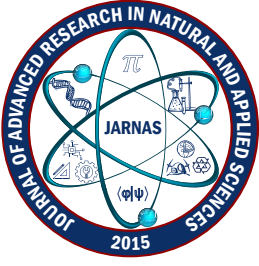
References

- [1] N. Yılankırkan, H. Doğan, *Turkey's energy outlook and primary energy supply projection for 2023*, Batman University Journal of Life Sciences 10 (2) (2020) 77–92.
- [2] Enerji ve Tabii Kaynaklar Bakanlığı (ETKB), *Tabii Kaynaklar, Kömür* (2023), <https://enerji.gov.tr/bilgimerkezi-tabiiKaynaklar-komur>, Accessed 27 Oct 2023.
- [3] Yüktevzibilgisistemi, https://ytbsbilgi.teias.gov.tr/ytbsbilgi/frm_istatistikler.jsf, Accessed: 10 May 2024.
- [4] R. N. Hendri, A. F. Lubis, *Characteristics of medium-low rank coal blending on performance and efficiency steam power plant*, IOP Conference Series: Materials Science and Engineering 1173 (2021) 012001 6 pages.
- [5] O. Erbaş, M. A. Rahim, *Low quality lignites uses as fuel in ultra super critical boilers*, Journal of Science and Technology of Dumlupınar University (018) (2009) 83–90.
- [6] M. Gorokhovski, Z. Jankoski, F. Lockwood, E. Karpenko, V. Messerle, A. Ustimenko, *Enhancement of*

- pulverized coal combustion by plasma technology*, Combustion Science and Technology 179 (10) (2007) 2065–2090.
- [7] A. R. Kvrivishvili, S. A. Samokhin, T. N. Morozova, A. V. Gruznov, A. I. Tsepenok, F. A. Serant, I. Yu. Belorutskii, A. A. Lavrinenko, *Primorskaya thermal power plant: Construction of modern pulverized coal-fired boilers*, Power Technology and Engineering 52 (2018) 197–206.
- [8] A. Peakman, T. Bennett, K. Fitzgerald, R. Gregg, G. Rossiter, *Nexus framework for whole-core fuel performance: current applications and future trends*, EPJ Web of Conferences 247 (2021) 12001 8 pages.
- [9] T.C Enerji ve Tabii Kaynaklar Bakanlığı, 2022 Yılı Taşkömürü Sektör Raporu (2022), <https://www.taskomuru.gov.tr/ttk/iglaglov/2023/05/2022YiliTaskomuruSektorRaporu..pdf>, Accessed: 10 May 2024.
- [10] F. Yurdakul, C. Erdoğan, *Determinants of current account deficit in Türkiye: The conditional and partial Granger causality approach*, Procedia Economics and Finance 26 (2015) 92–100.
- [11] M. Bilen, S. Yılmaz, *The relationship of unburned carbon in coal fired power plants with pulverized coal size distribution and volatile matter content*, BEU Journal of Science 9 (4) (2020) 1745–1755.
- [12] Türkiye: Çevre ve Orman Bakanlığı, Çevre ve Orman Bakanlığı, Büyük Yakma Tesisleri Yönetmeliği (2010), <https://www.resmigazete.gov.tr/eskiler/2010/06/20100608-4.htm>, Accessed 10 May 2024.
- [13] G. O. Odu, *Weighting methods for multicriteria decision-making technique*, Journal of Applied Sciences and Environmental Management 23 (8) (2019) 1449–1457.
- [14] J. P. Brans, Ph Vincke, B. Mareschal, *How to select and how to rank project: The Promethee Method*, European Journal of Operational Research 24 (2) (1986) 228–238.
- [15] R. Watrionthos, W. A. Ritonga, A. Rengganis, A. Wanto, M. I. Indrawan, *Implementation of Promethee-GAIA method for lecturer performance evaluation*, Journal of Physics: Conference Series (2021) 012067 7 pages.
- [16] J. P. Brans, Ph Vincke, *A preference ranking organization method*, Management Science 31 (6) (1985) 647–656.
- [17] M. Altın Karataş, A. R. Motorcu, E. Ekici, *Evaluating the optimum abrasive water jet machinability for CARALL composites with fiber orientations*, Polymer Composites 45 (11) (2024) 10050–10068.
- [18] S. Sammarchi, J. Li, D. Izikowitz, Q. Yang, D. Xu, *China’s coal power decarbonization via CO₂ capture and storage and biomass co-firing: A LCA case study in Inner Mongolia*, Energy 261 (PartA) (2022) 125158 13 pages.
- [19] Y. Wang, W. Nian, H. Li, J. Yuan, *Life cycle analysis of integrated gasification combined cycle power generation in the context of southeast Asia*, Energies 11 (6) (2018) 1587 18 pages.
- [20] Y. Zhu, D. Tian, F. Yan, *Effectiveness of entropy weight method in decision-making*, Mathematical Problems in Engineering 2020 (2020) Article ID 3564835 5 pages.
- [21] L. Abdullah, V. Chan, A. Afshari, *Application of PROMETHEE method for green supplier selection: A comparative result based on preference functions*, Journal of Industrial Engineering International 15 (2018) 271–285.
- [22] A. C. Gök, S. Perçin, *Performance measurement with integrated entropy-vikor methods in information technology sector*, The International Journal of Economic and Social Research 14 (1) (2018) 14 pages.
- [23] J. P. Brans, Ph Vincke, B. Mareschl, *How to select and how to rank projects: The PROMETHEE method*, European Journal of Operational Research 24 (1986) 228–238.
- [24] C. Rodrigues, A. P. Lopes, *Multicriteria decision support model for selection of fiberglass suppliers: A*

case study in a wind industry company, in: A. P. Lopes (Ed.), *Cases on Supply Chain Management and Lessons Learned From COVID-19*, IGI Global, 2022, Ch. 6, pp. 119-145.

- [25] C. Güney, *Evaluation of sectors in terms of investors with visual PROMETHEE*, TURAN-CSR International Scientific Peer-Reviewed and Refereed Journal 9 (34) (2017) 177–187.
- [26] A. Şahin, G. C. Akkaya, *An application on creating a portfolio with PROMETHEE ranking method*, Journal of Economics and Management Research 2 (2) (2013) 67–81.



Blood Vessel Segmentation and Classification of Diabetic Retinopathy with Machine Learning-Based Ensemble Model

Cihan Akyel¹ , Bünyamin Ciyilan² 

¹Department of Computer Engineering, Graduate School of Natural and Applied Sciences, Gazi University, Ankara, Türkiye

²Department of Computer Engineering, Faculty of Technology, Gazi University, Ankara, Türkiye

Article Info

Received: 10 May 2024

Accepted: 12 Jun 2024

Published: 30 Sep 2024

Research Article

Abstract – The incidence of diabetes has increased in recent times due to factors such as obesity and genetic predisposition. Diabetes wears out the eye vessels over time. Diabetic retinopathy (DR) is a serious disease that leads to vision problems. DR can be diagnosed by specialists who examine the fundus images of the eye at regular intervals. With 537 million diabetics in 2021, this method can be time-consuming, costly and inadequate. Artificial intelligence algorithms can provide fast and cost-effective solutions for DR diagnosis. In this study, the noise of blood vessels in fundus images was eliminated using the LinkNet-RCB7 model, and diabetic retinopathy was categorized into five classes using a machine learning-based ensemble model. Artificial intelligence-based classification training using images as input takes a long time and requires high resource requirements such as Random Access Memory (RAM) and Graphics Processing Unit (GPU). By using Gray Level Cooccurrence Matrix (GLCM) attributes in the classification phase, a lower resource requirement was aimed for. A Dice coefficient of 85.95% was achieved for the segmentation of blood vessels in the Stare dataset, in addition to 97.46% accuracy for binary classification and 96.10% accuracy for classifying DR into five classes in the dataset APTOS 2019.

Keywords – Diabetic retinopathy, ensemble learning, classification, segmentation, information systems

1. Introduction

Diabetes occurs in high glucose levels because of insufficient secretion or ineffective use of the hormone insulin. Nowadays, the incidence of diabetes is increasing due to factors such as obesity, lack of exercise, and genetic predisposition. In 2021, there will be around 537 million diabetics in all countries. According to forecasts, it will be 783 million by 2045 [1].

Diabetes affects many different organs in the human body via the bloodstream. If the amount of glucose in the blood transported to these organs increases, the organs can be damaged. One of the organs affected by diabetes is the eye. Diabetic retinopathy (DR) develops in the eye due to diabetes. In DR, the blood vessels are damaged by the effects of glucose. As a result, patients may experience visual impairment and blindness. In view of this situation, it is necessary to detect this disease at an early stage [2].

For the diagnosis of DR, patients' fundus images should be regularly examined by experts. The fundus image is an imaging technique that can display and archive the condition of the fundus structures, such as the optic nerve, macula, retina, blood vessels, and vitreous in color. There are around 40 thousand ophthalmologists in China. Compared to the number of diabetes patients, there is one specialist for every 3,000 patients. Moreover,

¹cihan.akyel@gmail.com.tr (Corresponding Author); ²bciylan@gazi.edu.tr

diagnosis in this way is time-consuming and costly [3]. There are two approaches to classification in the literature. These are non-proliferative DR (NPDR) and proliferative DR (PDR). NPDR stands for phases of DR in which it is relatively benign. It is divided into three stages: mild, moderate, and severe. PDR refers to the advanced stage of the disease. On this basis, it is divided into normal, mild, moderate, severe, and PDR [4].

Thanks to the development of computer-aided technologies, image-based rapid diagnosis is now possible. Information systems using these methods are used for noise removal, segmentation, and classification of images. Numerous studies can be found in the literature using these methods for DR. Removing blood vessel noise on fundus images is essential for diagnosing DR. Classification of images from which the blood vessel noise has been removed can be performed with higher accuracy. In addition, images from which the blood vessel noise has been removed can be more easily examined and diagnosed by experts. Considering the number of ophthalmologists per patient, the fact that success depends on the skills of the specialist, and the costly and lengthy diagnosis, the importance of computerized studies for the diagnosis of DR becomes clear. This study used LinkNet-RCB, which provides successful results in the segmentation of medical images. Unlike in the literature, the dataset APTOS 2019 was cleaned of blood vessel noise utilizing this model and segmented into five classes using the Xception-based Convolutional Neural Network (CNN) algorithm. This will contribute to the diagnostic process by presenting noise-free images of blood vessels to experts and categorizing the images into five classes.

Blood vessel noise in fundus images can be removed using image processing algorithms. However, this solution has a low success rate, as an optimal threshold cannot be found for every image. Instead, the noise can be cleaned using deep learning with noise mask data and the results can be corrected with image processing. Cleaning up blood vessel noise in fundus images using deep learning methods involves some difficulties, such as the long duration of training, finding suitable datasets, and developing an effective model. In artificial intelligence-based approaches where the images are used as input during the classification phase, resources such as Graphics Processing Unit (GPU) and Random Access Memory (RAM) are used more, and the training time is extended. The relatively new LinkNetRCB7 model in this domain achieved high success rates in the segmentation phase to overcome these difficulties. A new ensemble learning approach based on machine learning was proposed in the classification phase. With this approach, successful results were achieved with fewer resources.

The purpose is explained in the introductory part of the study, and a literature study on this topic is carried out. In the second part, the phases of the study, the data sets, and the methods used are described in detail. The results are presented in the third part and commented on in the fourth part. Figure 1 shows the proposed approach. In summary, it can be said that in the study context.

1. The LinkNet-RCB7 model is used for blood vessel segmentation. Preprocessing was applied to input images. The prediction results were corrected with image processing.
2. Images cleared of blood vessel noise are divided into five and two classes with the proposed approach.
3. In order to consume less GPU, RAM, and Central Process Unit (CPU) resources, an ensemble method using Gray Level Cooccurrence Matrix (GLCM) features in the classification phase was proposed.

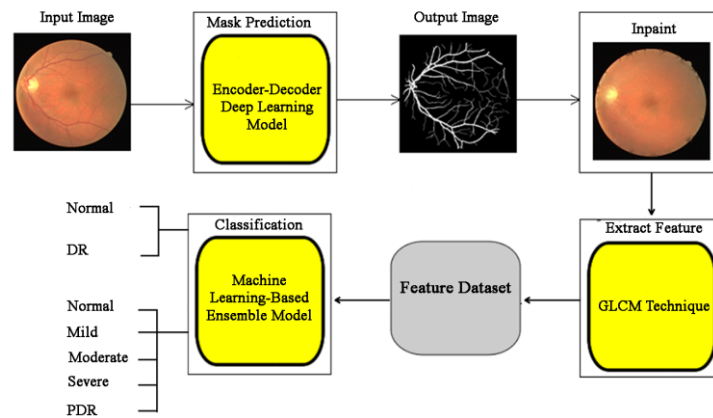


Figure 1. Proposed approach

Blood vessels must first be segmented to remove the noise of the blood vessels from the image. Masks and noise resulting from the segmentation can then be removed from the image using functions similar to inpaint. A literature review shows that blood vessel noise removal, optic disk segmentation, and DR classification play a role in the studies. Since the study focused on removing blood vessel noise and classification, the studies in this area were examined in the literature. In the vessel noise removal phase, the vessels in the images are segmented. Image segmentation algorithms from the literature can be used to segment the vessels. Some studies show that image processing or deep learning alone is used to segment the vessels. However, using these two methods together seems more advantageous as the accuracy can be increased by correcting the estimated masks. The images can also be preprocessed with image processing before being trained with deep learning. This way, the visibility of noise and areas on the image's increases.

There are studies in which the images are subjected to various preprocessing steps during the segmentation of blood vessels. The visibility of vein noise in the image varies depending on the channels in the Red-Green-Blue (RGB) color space. Tan et al. [5] show that the green color channel is more effective in determining blood vessel noise. In diagnosing DR with fundus images, the destruction of vessels causes noise in the image. Since the classification is performed with these images, the green color channel can be selected in the images that serve as input for deep learning training. The green channel has the highest contrast compared to the others. This situation was highlighted in the study by Long et al. [6], in which they attempted to detect microaneurysms. Tang et al. [7] used a new approach to remove blood vessel noise. In their study, image preprocessing was performed using the median filter. In this way, unnecessary background elements are removed from the grayscale image. Subsequently, each pixel of the image is classified as blood vessel noise or not, and the segmentation of the vessels is completed. The study favored the blue channel, where the vessel noise is most visible. The nearest neighbor algorithm is used to classify the pixels. This study's accuracy is 96.11% and 81.74% for the Digital Retinal Images for Vessel Extraction (DRIVE) and Structured Analysis of the Retina (STARE) databases, respectively.

In the work of Guo et al. [8], the vessel noise was removed using an Fully Convolutional Network (FCN)-based deep learning algorithm. In the segmentation performed with deep learning, an f1 score of 82.49% was achieved using only the rigid dataset. In another study [9] on blood vessel segmentation, the Clahe and Bottom Hat techniques were used with deep learning. These methods are used to increase the visibility of noise. A UNet-based model was proposed using driving data, and a training accuracy of 98.19% was achieved using this model. Laibacher et al. [10] proposed a UNet-based model called M2UNet. This model uses the residual blocks (RB) used in Residual Network (ResNet). The image size is kept the same at the inputs and outputs of the RBs. With this model, a cube accuracy of 80.91% was achieved in the Drive dataset and 80.06% in the Retinal Vessel Reference Dataset (Chase_DB1) dataset for the segmentation of blood vessels. Aurangzeb et al. [11] proposed a new algorithm called Anam-Net based on the decoder architecture. This model achieved a training accuracy of 96.60%, 97.28%, and 97.46% in Chase_DB1, Drive, and Stare. Diabetic retinopathy is a preventable disease if detected early. Experts can diagnose DR by examining images. However, there are many

challenges in observing diabetic retinopathy, such as expertise, contrast differences, image noise, and financial constraints [12]. In the study by Sikder et al. [13], the images were categorized into five classes using the Extra Tree algorithm (a type of decision tree method) and a training accuracy of 91.07%, a prediction accuracy of 90.40%, and a sensitivity accuracy of 89.54% were achieved for the dataset The Asia Pacific Tele-Ophthalmology Society 2019 (APTOS 2019).

EfficientNet is a model offered by Google and has different types. Although the long training time is considered a disadvantage, it is a model with great accuracy. An example of the use of this algorithm is provided by Liu et al. [14]. In the study, DR was categorized into five classes using EfficientNetB5. As a result of the training, the study achieved a training accuracy of 84.88%. Majumder et al. [15] proposed a study on the classification of fundus images (five classes). They used the datasets APTOS and EyePACS for their research. They used SEDenseNet, a modified Dense Convolutional Network (DenseNet) algorithm. The training accuracy, sensitivity, and F1-score values were 85%, 70%, and 72%, respectively.

Modi and Kumar [16] divided the images of DR into two classes. They used random forest in their study. The accuracy rate of binary classification is 89.64% with the Messidor dataset. Wang et al. [17] presented a model based on InceptionV3 and achieved a training accuracy of 63.23% when students were categorized into five classes. In another study, using the Visual Geometry Group 16 (VGG16) model and CNN, a training accuracy of 73.83% was achieved for the DRISTHI dataset. The images were categorized into five classes in the study by Nagaraj et al. [18]. Wu et al. [19] presented a classification model called CF-DRNET based on CNN. They observed an accuracy of 86.61% with the Kaggle dataset.

By extracting the GLCM features of the images, DR classification can be performed, which provides faster results than classification with images. An example is the study by Rahman et al. [20]. In this study, binary classification was performed using the GLCM features (mean, energy, contrast, similarity, maximum, homogeneity, entropy). Binary classification using Support Vector Machine (SVM) achieved an accuracy of 94.59%. Sikder et al. [21] classified DR into five classes using GLCM features. In the study using the XGBoost method, an accuracy value of 94.20% was achieved with the dataset APTOS. The images were cropped to better display the relevant area. The images were sharpened, and the contrast was increased. In the study presented by Ishtiaq et al., the eyePACS dataset was divided into five classes with a hybrid model using DR CNN and ResNET50 models as an ensemble. An accuracy value of 98.85% was observed in the study. It was performed on the Kaggle EyePACS dataset; a five-fold classification of DR was performed by extracting the features of the images. LBP was used to extract the features. Classification with SVM yielded an accuracy of 98.63%, sensitivity of 98.628, prediction of 98.67, specificity of 99.656, and F1 value of 98.622 [22]. DR was separated into two classes using GLCM features and SVM by Foady et al. [23]. Energy, entropy, homogeneity, contrast, and correlation values were selected as features in the images that underwent preprocessing steps, such as histogram equalization and optic disc elimination. When classified as PDR and NPDR, 92.86% accuracy, 100% sensitivity, and 91.67% specificity were achieved with 0 degrees GLCM. Ensemble models can provide more successful results than self-contained models.

An example is the study presented by Deepa et al. [24]. The study uses a separate data set. Two inception and two Xception models were used together. SVM was preferred for the final estimation. The study has four classes: pedunculated, mild, moderate, and PDR. An accuracy value of 96.20% was achieved.

In successful models in the literature, more successful results can be obtained by changing parameters such as activation function and number of layers. Kılıçarslan presented an example of this. The HardSReLU activation function proposed in the study achieved 1.13% higher success with the VGG19 model than the standard Rectified Linear Unit (ReLU) [25]. Different combinations of activation and optimizer can offer different success values. ReLU activation function and AdaMax optimizer showed the highest value for glaucoma diagnosis in the study of Kılıçarslan [26]. This duo was also preferred in our research.

2. Materials and Methods

There are two phases in the study. These are blood vessel segmentation and DR classification. In the first phase, the model was run at 500 epochs. The hyper-parameters used in the training phase are shown in Table 1. For the classification phase, default parameters that belong to models were used. The datasets used in the study were divided into 80% training and 20% test.

Table 1. Hyper-parameters

Parameter	Blood vessel segmentation
Batch size	8
Weight decay	0.025
Epoch number	500
Input size	256x256
Optimizer	AdamW
Loss function	MSE+dice loss
Output function	Sigmoid
Learning rate	0.0001

2.1. Datasets and Image Preprocessing

For the segmentation phase, the data sets stare (20 images – 700 x 605) [27] and drive (20 images - 584 x 565) [28] were combined and used. This data set is referred to as the blood vessel data set (BVDS – 40 images and ground truth of the blood vessels). The green color channel is preferred as it increases the visibility of the vessel noise. The green color channel selection, grayscale conversion, normalization, Clahe filter, and Gaussian filter were applied to this dataset. Clahe is used to improve the contrast between the background and the vessels. The dataset APTOS 2019 [29] for DR classification was preferred in the training phase. The noise of the blood vessels in the dataset APTOS is adjusted by training. APTOS 2019 training dataset was split into 80% training and 20% test. The data distribution of APTOS 2019 can be seen in Table 2. All datasets used in this study are publicly available.

Table 2. APTOS 2019 distribution for two classes

Dataset	Class	Count	New Classes	Train (80%)	Test (20%)
APTOS 2019	Normal	1805	Normal	1444	361
	Soft	370			
	Mild	999	DR	1485	372
	Moderate	193			
	PDR	295			
TOTAL		3662		2929	733

2.2. Blood Vessel Segmentation Model

The LinkNet-RCB7 model, which showed high accuracy in image segmentation, was preferred at this phase. This model uses the EfficientNetB7 algorithm in coding blocks [30] (Figure 2). LinkNet-RB7 is a modified version of LinkNet-B7 [31]. Before the last layer, the ResNetC model was added. ResNetC is a more successful parallel model than ResNet [32]. The architecture of ResNetC can be seen in Figure 3. LinkNet-RCB7 is a model based on an encoder-decoder architecture. The encoder-decoder architecture is widely used in the literature due to its successful results in medical image segmentation. LinkNet-RCB7 has four encoder and decoder blocks. The decoder block is identical to the original LinkNet model. The encoder block contains different layers of EfficientNetB7. In this way, the number of extracted features is increased. Using ResNetC, LinkNet-RCB7 shows higher accuracy [30]. In this phase, the input images were divided into 36 layers with a

resolution of 256x256. In this way, the input images could be used as 1024x1024. In this way, pixel losses that occur when images are resized are reduced. Morphological operations corrected the prediction results.

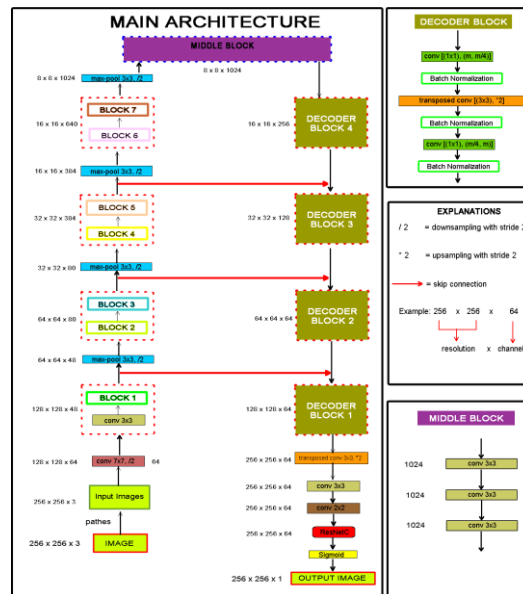


Figure 2. LinkNet-RCB7 architecture [30]

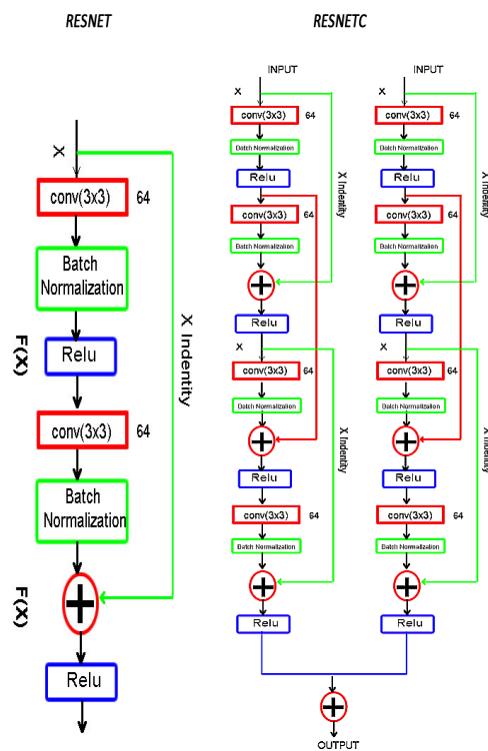


Figure 3. ResNetC architecture [32]

2.3. DR Classification Model

At this phase, the DR was classified into two and five classes. The binary classification has two classes: normal and DR. Normal, mild, moderate, severe, and PDR were used to classify DR into five classes. The number of data given in Table 2 was used for classification in binary classification. In classifying DR into five classes, the number of images was balanced by smote data balancing. Table 3 shows the dataset used for the five classes.

Table 3. APTOS 2019 distribution for five classes

Dataset	Class	Count	Balanced Train (80%)	Test (20%)
APTOS 2019	Normal	1805	1454	351
	Soft	370	1454	68
	Mild	999	1454	213
	Moderate	193	1454	36
	PDR	295	1454	65
TOTAL		3662	7270	733

An ensemble learning-based method was used for classification. This method uses stacking and includes base classifiers and meta-classifiers. Each base classifier produces a prediction result. Then, the meta classifier selects the best result by voting. The stacking classifiers in the Sklearn library were used for the final prediction. Decision Tree, K nearest neighbor (KNN), Random Forest, and SVM were selected as base classifiers based on their success in classification. XGBoost is a metaclassifier. It provides parallel tree boosting. Figure 4 shows the proposed approach.

The features that belong to images were achieved using GLCM. The images were resized to 256x256. The dissimilarity, energy, correlation, homogeneity, contrast, and Angular Second Moment (ASM) features were used at 0, 45, 90, and 135 degrees. The training dataset, therefore contained a total of 30 features.

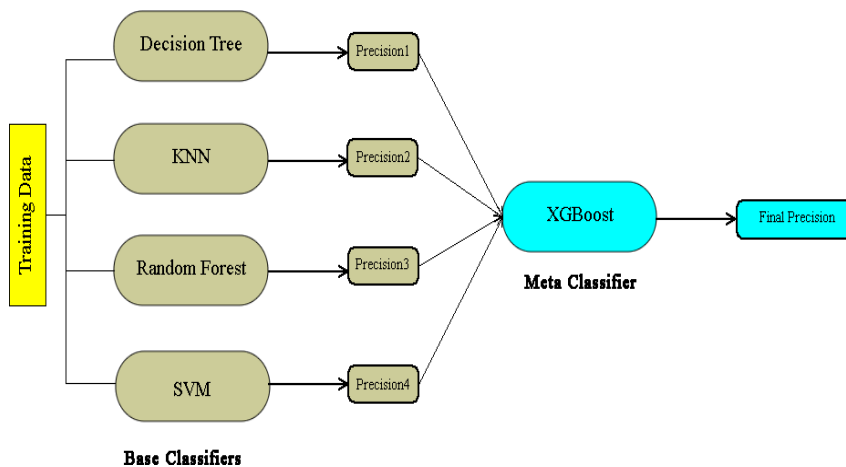


Figure 4. The architecture of the classification approach

3. Results and Discussion

The results obtained in the segmentation of the blood vessels are shown in Table 4. At this phase, the noise in the estimated masks was corrected by morphological operations, median filters, and the removal of independent segments from the image. Figure 5 shows example results. Table 5 shows the results of the study trained on different datasets.

Table 4. Blood vessel segmentation

Study	Model	Acc (%)	DA (%)	F1-Score (%)	Dataset
[7]	KNN	96.11	-	-	Drive
[8]	FCN	-	-	82.49	Rigid
[9]	UNET	98.19	-	-	Drive
[10]	M2UNET	-	80.91	-	Drive
[11]	Anam-NET	96.60	-	-	Drive
[30]	LinkNet-RCB7	98.50	85.75	86.50	Stare
Proposed Model	LinkNet-RCB7	98.56	85.95	86.54	Stare
Proposed Model	LinkNet-RCB7	98.10	85.48	86.33	Drive
Proposed Model	LinkNet-RCB7	98.08	85.65	85.96	BVDS

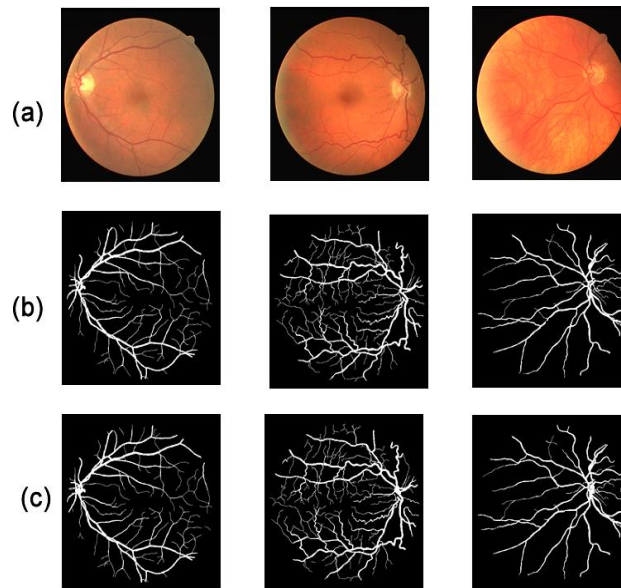


Figure 5. Sample results of blood vessel segmentation

The results obtained in the classification phase are presented in Table 4 in comparison with other studies based on the datasets. The results show that the study succeeded in classifying DR into two and five classes. We have used "accuracy_score(y_pred,y_test):0.2f}" with the training dataset for results.

Table 5. DR classification

Study	Model	Acc (%)	Recall (%)	Precision (%)	F1	Dataset/Number of classes
[13]	Extra Tree	91.07	89.54	90.40	89.97	APTOS/five classes
[14]	EfficientNetB5	86.34	-	90.94	93.90	APTOS + Kaggle + EyePACS/five classes
[15]	DenseNet	85.00	70.00	75.00	72.00	EyePACS/five classes
[16]	Random Forest	89.64	-	-	90.41	Messidor/ two classes
[17]	InceptionV3	63.23	-	-	-	EyePACS/five classes
[18]	VGG16	73.83	-	-	-	DRISTHI/five classes
[19]	CNN-Based	86.61	-	-	-	Kaggle/five classes
[20]	GLCM+SVM	94.59	-	-	-	APTOS/ five classes
[21]	GLCM+XGBoost	94.34	92.69	-	-	EyePACS/ five classes
[22]	GLCM+ Hybrid Model	98.63	-	99.65	98.62	EYEPACS/five classes
[23]	GLCM+SVM	92.86	-	91.67	-	Special (44 images-10 normal and 34 DR) /two classes
[24]	Ensemble Model	96.20	-	-	-	Special / four classes
Proposed Ensemble Model		97.46	97.00	96.00	97.00	APTOS/two classes
Proposed Ensemble Model		96.10	94.80	95.90	96.00	APTOS/five classes

Table 6 shows the cross-validation results obtained by selecting the k value as 5. We have used cross-validation from the sklearn library for binary and multi-classifications. With cross-validation, the data set was divided into 5 parts, and one was selected as validation in each training, while the remaining ones were used as the training set. The purpose is to measure the model's effectiveness on data it has never seen.

Table 6. Cross-validation results

Model	Fold	Acc (%)	Recall (%)	Precision (%)	F1	Dataset/Number of classes
Proposed Ensemble Model	1	91.807	90.25	92.37	91.30	APTOS/two classes
Proposed Ensemble Model	2	94.10	91.56	95.00	93.25	APTOS/two classes
Proposed Ensemble Model	3	94.25	95.57	94.12	93.34	APTOS/two classes
Proposed Ensemble Model	4	93.07	92.90	92.00	92.45	APTOS/two classes
Proposed Ensemble Model	5	92.57	94.25	91.54	92.87	APTOS/two classes
Proposed Ensemble Model	1	86.58	85.50	87.60	86.00	APTOS/five classes
Proposed Ensemble Model	2	88.13	86.00	89.00	88.70	APTOS/five classes
Proposed Ensemble Model	3	88.83	87.72	89.40	89.20	APTOS/five classes
Proposed Ensemble Model	4	88.18	88.00	89.32	89.10	APTOS/five classes
Proposed Ensemble Model	5	90.38	89.90	90.00	90.00	APTOS/five classes

4. Conclusion

In this study, the noise of the blood vessels in fundus images was eliminated, and the images were classified into two and five classes. Examination of the results obtained shows that the study presented has high accuracy values. Especially in the classification phase, the accuracy distribution between the classes is balanced. This can be seen in Table 4.

In the blood vessel segmentation phase, it is important to pre-treat the images by image processing and correct the estimated masks before inputting them into the system. The image was divided into 36 layers to reduce pixel loss. These processes are effective in achieving high accuracy with LinkNet-RCB7.

This study divides DR into two and five classes using ensemble learning. This is to help decision-makers in the diagnosis phase of DR. In the ensemble learning approach proposed in the study, SVM, Random Forest, Decision Tree, and KNN were used as base classifiers and XGBoost as meta-classifiers. The accuracy values achieved were 97.46% in two classes and 96.10% in five. In future studies, comparisons can be made with different datasets by performing cross-training. The fact that other datasets from the literature were not used in the study can be considered a limitation.

As a result, the existing LinknetRCB7 model was used in the grain noise removal stage by dividing the input images into 36 slices instead of 16. At this stage, increasing the total resolution of the images taken as input greatly improved success. In the classification stage, the main goal was determined as achieving similar success with less resource use rather than achieving higher success than existing studies, and this goal was achieved. In addition, hybridizing existing machine learning methods with an ensemble model in the classification stage has been observed to give successful results. In future studies, success can be increased with parameters and models such as different activation functions and optimizers.

Author Contributions

The first author conducted the experiments, analyzed the results, and wrote the article. The second author planned for the tables, graphs, and figures used in the study. The second author also contributed to the creation of the methods used in the study. All authors read and approved the final version of the paper. This paper is derived from the first author's master's thesis, supervised by the second author.

Conflicts of Interest

All the authors declare no conflict of interest.

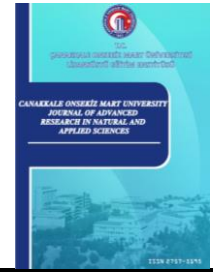
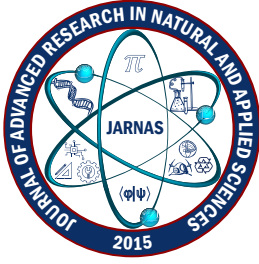
Ethical Review and Approval

No approval from the Board of Ethics is required.




References

- [1] M. J. Hossain, M. Al-Mamun, M. R. Islam, *Diabetes mellitus, the fastest growing global public health concern: Early detection should be focused*, Health Science Reports 7 (3) (2024) 1–5.
- [2] S. İnan, *Diabetic retinopathy and etiopathogenesis*, Kocatepe Medical Journal 15 (2) (2014) 207–217.
- [3] L. Dai, L. Wu, H. Li, C. Cai, Q. Wu, H. Kong, R. Liu, X. Wang, X. Hou, Y. Liu, X. Long, Y. Wen, L. Lu, Y. Shen, Y. Chen, D. Shen, X. Yang, H. Zou, B. Sheng, W. Jia, *A deep learning system for detecting diabetic retinopathy across the disease spectrum*, Nature Communications 12 (2021) 3242 11 pages.
- [4] Y. B. Özçelik, A. Altan, Ö. Canbolat, Ş. Ekenler, Ü. Polat, *Deep learning-based classification of fundus images for the diagnosis of diabetic retinopathy*, European Journal of Science and Technology (29) (2021) 156–167.
- [5] X. Tan, S. Lai, M. Zhang, *Green channel guiding denoising on Bayer image*, The Scientific World Journal 2014 (2014) 1–9.
- [6] S. Long, J. Chen, A. Hu, H. Liu, Z. Chen, D. Zheng, *Microaneurysms detection in color fundus images using machine learning based on directional local contrast*, BioMedical Engineering Online 19 (21) (2020) 1–23.
- [7] Z. Tang, J. Zhang, W. Gui, *Selective search and intensity context-based retina vessel image segmentation*, Journal of Medical Systems 41 (3) (2017) 1–12.
- [8] S. Guo, K. Wang, H. Kang, Y. Zhang, Y. Gao, T. Li, *BTS-DSN: Deeply supervised neural network with short connections for retinal vessel segmentation*, International Journal of Medical Informatics 126 (2019) 105–113.
- [9] H. Boudegga, Y. Elloumi, M. Akil, M. H. Bedoui, R. Kachouri, A. B. Abdallah, *Fast and efficient retinal blood vessel segmentation method based on deep learning network*, Computerized Medical Imaging and Graphics 90 (2021) 101902 12 pages.
- [10] T. Laibacher, T. Weyde, S. Jalali, *M2U-Net: Effective and efficient retinal vessel segmentation for real-world applications*, in: L. O'Conner (Ed.), IEEE/CVF Conference on Computer Vision and Pattern Recognition Workshops (CVPRW), Long Beach, 2019, pp. 1–10.
- [11] K. Aurangzeb, S. I. Haider, M. Alhussein, *Retinal vessel segmentation based on the anam-net model*, Elektronika ir Elektrotechnika 28 (3) (2022) 54–63.
- [12] G. Zhang, B. Sun, Z. Chen, Y. Gao, Z. Zhang, W. Yang, L. Li, *Diabetic retinopia grading by deep graph correlation network on retinal images without manual annotations*, Frontiers in Medicine 9 (2022) 1–9.
- [13] N. Sikder, M. S. Chowdhury, A. S. Mohammad, A. A. Nahid, *Early blindness detection based on retinal images using ensemble learning*, 22nd International Conference on Computer and Information Technology (ICCIT), Dhaka, 2019, pp. 1–6.
- [14] H. Liu, K. Yue, S. Cheng, C. Pan, J. Sun, W. Li, *Hybrid model structure for diabetic retinopathy classification*, Internet of Medical Things for Healthcare Engineering 2020 (2020) Article ID 840174 9 pages.
- [15] S. Majumder, N. Kehtarnavaz, *Multitasking deep learning model for detection of five stages of diabetic retinopathy*, IEEE Access 9 (2021) 123220–123230.
- [16] P. Modi, Y. Kumar, *Smart detection and diagnosis of diabetic retinopathy using bat-based feature selection algorithm and deep forest technique*, Computers & Industrial Engineering 182 (2023) 109364 21 pages.
- [17] X. Wang, Y. Wang, W. Chen, *Diabetic retinopathy stage classification using convolutional neural*

- networks*, in: R. Bilof (Ed.), 2018 IEEE International Conference on Information Reuse and Integration (IRI), UT, 2018, pp. 465–471.
- [18] G. Nagaraj, S. C. Simha, H. G. R. Chandra, M. Indiramma, *Deep learning framework for diabetic retinopathy diagnosis*, 3rd International Conference on Computing Methodologies and Communication (ICCMC), Erode, 2019, pp. 648–653.
- [19] Z. Wu, G. Shi, Y. Chen, F. Shi, X. Chen, G. Coatrieux, J. Yang, L. Luo, S. Li, *Coarse-to-fine classification for diabetic retinopathy grading using convolutional neural network*, Artificial Intelligence in Medicine 108 (2020) 1–19.
- [20] K. Rahman, M. Nador, A. Imran, *Automatic screening of diabetic retinopathy using fundus images and machine learning algorithms*, Diagnostics 12 (9) (2022) 2262–2274.
- [21] N. Sikder, M. Masud, A. Bairagi, A. Arif, A. Nahid, H. A. Alhumyani, *Severity classification of diabetic retinopathy using an ensemble learning algorithm through analyzing retinal images*, Symmetry 13 (4) (2021) 670–696.
- [22] U. Ishtiaq, E. Abdullah, Z. Ishtiaque, *A hybrid technique for diabetic retinopathy detection based on ensemble-optimized CNN and texture features*, Diagnostics 13 (10) (2023) 1–21.
- [23] A. Z. Foady, D. C. R. Novitasari, A. H. Asyhar, M. Firmansjah, *Automated diagnosis system of diabetic retinopathy using GLCM method and SVM classifier*, in: A. Yudhana, Zulfatman, D. Stiawan, M. A. Riyadi, I. M. I. Subroto, A. E. Minarno, C. S. K. Aditya (Eds.), 5th International Conference on Electrical Engineering, Computer Science and Informatics (EECSI), Malang, 2018, pp. 153–160.
- [24] V. Deepa, S. Kumar, T. Cherian, *Ensemble of multi-stage deep convolutional neural networks for automated grading of diabetic retinopathy using image patches*, Journal of King Saud University - Computer and Information Sciences 34 (8) (2022) 6255–6265.
- [25] A. Hoover, V. Kouznetsova, M. Goldbaum, *Locating blood vessels in retinal images by piecewise threshold probing of a matched filter response*, IEEE Transactions on Medical Imaging 19 (3) (2000) 203–210.
- [26] S. Kılıçarslan, *A novel nonlinear hybrid HardSReLU activation function in transfer learning architectures for hemorrhage classification*, Multimedia Tools Applications 82 (2023) 6345–6365.
- [27] C. Közkurt, A. Diker, A. Elen, S. Kılıçarslan, E. Dönmez, F. B. Demir, *Trish: An efficient activation function for CNN models and analysis of its effectiveness with optimizers in diagnosing glaucoma*, The Journal of Supercomputing 2024 (2024) 1–32.
- [28] J. Staal, M. D. Abramoff, M. Niemeijer, M. A. Viergever, B. Van Ginneken, *Ridge-based vessel segmentation in color images of the retina*, IEEE Transactions on Medical Imaging 23 (4) (2004) 501–509.
- [29] K. Dane, M. Dane, S. Dane, APTOS 2019 Blindness Detection (2019), <https://kaggle.com/competitions/aptos2019-blindness-detection>, Accessed 1 May 2024.
- [30] C. Akyel, N. Arıcı, *Decision support system for blood vessel and optic disc segmentation*, Gazi Journal of Engineering Sciences, 9 (1) (2023) 12–26.
- [31] C. Akyel, N. Arıcı, *LinkNet-B7: Noise removal and lesion segmentation in images of skin cancer*, Mathematics 10 (5) (2022) 736–751.
- [32] C. Akyel, N. Arıcı, *Hair removal and lesion segmentation with FCN8-ResNetC and Image processing in images of skin cancer*, Journal of Information Technologies 15 (2) (2022) 231–238.



Evaluation of Recombinant Antibody Production Efficiency in CHO Cells with Sleeping Beauty Transposon Vector System

Pelin Kolçak Yaşlı¹ , Seda Savranoğlu Kulabaş² , Evren Doruk Engin³ 

¹Basic Biotechnology Graduation Program, Biotechnology Institute & SİSBİYOTEK, Ankara University, Ankara, Türkiye

²Department of Basic Medical Sciences, Faculty of Medicine, Çanakkale Onsekiz Mart University, Çanakkale, Türkiye

³Department of Biotechnology, Biotechnology Institute & SİSBİYOTEK, Ankara University, Ankara, Türkiye

Article Info

Received: 09 May 2024

Accepted: 14 Jun 2024

Published: 30 Sep 2024

Research Article

Abstract – Chinese hamster ovary (CHO) mammalian cell lines are widely used as cell platforms in biopharmaceutical productions. Different transfection systems are employed for the integration of the target gene cassette into the cell genome and have limitations, such as (i) the integration region in the genome, (ii) the size of the target cassette, and (iii) long selection periods for stable expression. Transposon systems can be utilized to overcome the limitations mentioned in the efficient production of commercially significant recombinant proteins. This study aims to demonstrate the differences in production potential and selection periods by using a specially designed vector system for random genome integration in CHODG44 DHFR ^{-/-} cells and the Sleeping Beauty (SB) transposon system. In this context, the optimal transfer ratio between the donor and the helper plasmid was determined for the most efficient co-transfection in the SB transposon system. According to the results, the pools obtained using the SB transposon system had titers ranging from 1300 to 2600 mg/L in 13-day fed-batch studies, while the pool obtained using the random transfer system had a titer of 0.056 mg/L. Additionally, stable cell pools obtained using the transposon system underwent selection in a short period of 52 days, compared to over 100 days for the pool obtained through random transfer. Considering all these results together, it is demonstrated that stable CHO pools obtained using the optimal SB transposon system can achieve high-efficiency monoclonal antibody production in a short period, making it an optimal production platform in the biopharmaceutical field.

Keywords – *Sleeping Beauty transposon, gene integration, expression level, CHO cells, industrial production*

1. Introduction

Immunological surveillance and tumoricidal activity towards newly formed tumor cells are the primary defense against cancer formation. Thus, cancer immunotherapy started appealing to attention for therapeutic purposes. One such therapeutic strategy involves the blockade of the PD1 - PDL1/2 axis. Antibodies directed to either T-cell receptor PD1 or its ligand PDL-1 are gaining popularity to overcome this mode of immune evasion in various malignancies, including metastatic melanoma, non-small cell lung cancer (NSCLS), renal cell carcinoma and bladder cancer [1].

In the last 30 years, over 170 therapeutic monoclonal antibodies have received approval from administrative authorities worldwide. Most of these complex recombinant proteins are produced in mammalian expression systems. Chinese hamster ovary (CHO) cells have become one of the most favored platforms to express recombinant mAbs, providing protein folding and processing capabilities comparable to human cells. Owing

¹plnkolcak@gmail.com; ²sedasavranoglu@gmail.com; ³edoruk@gmail.com (Corresponding Author)

to established cell lines, vectors, and broad experience, it is not unusual to reach several grams per liter yields [2]. Development and characterization of stable cell lines with desired production capacity and product quality are the most critical parameters of this workflow. The mode of gene transfer is closely related to the expression efficiency. Conventional methods for transformation usually involve chemicals like polycationic substances or calcium phosphate. These methods typically provide a random integration of the target gene into chromosomal sites, which may be transcriptionally inactive. Intense effort is required to select productive clones that retain a high expression profile from a heterogeneous pool of cells. Low and variable yields with long-term stability issues are not uncommon for these random integrants.

On the other hand, naturally occurring vertebrate transposons have been engineered for efficient gene delivery systems. PiggyBac (PB), Tol2, and Sleeping Beauty (SB) are the most popular commercialized transposon-based gene delivery systems. Despite the diverse ancestral origins, all three systems are highly efficient in generating producer cell pools.

Therefore, creating low-cost production platforms with high quality and production capacity is increasingly necessary to meet the growing demand in the biopharmaceutical market. The first stage of protein-specific production involves transferring the target protein gene to the host cell using gene transfer systems. However, this process can affect the physicochemical and functional quality of the monoclonal antibody and product production efficiency, so pharmaceutical R&D needs to make applications to increase efficiency at this stage. The target gene transfer systems used at these stages can be divided into viral or non-viral systems. While viral vectors provide effective integration, deoxyribonucleic acid (DNA)-based plasmids, usually non-immunogenic and can carry large amounts of target genes, are used despite their limitations in transferring large genes due to their poor transfection and integration abilities compared to viral vectors [3]. Techniques mainly involve optimizing CHO cells and expression vectors by promoting the expression of the target gene to ensure efficient expression of the transgene. However, inefficient stable integration occurs due to the random integration of one to five copies into the host genome [4-6]. Consequently, protein expression in producer cell lines generated by random integration results in unpredictable, variable, and often unstable protein levels [7]. Transposon vector systems, which enable efficient integration of the target gene to overcome this problem by inserting it into a transcriptionally active region, can allow the production of expression-challenging recombinant proteins such as monoclonal antibodies in stable cell pools suitable for large-scale production [8].

Transposons are genetic elements primarily consisting of transposase genes and inverted repeat (ITR) sequences. Transposases bind to directed repeat sequences in the ITR and function by cutting the transposon sequence into the host DNA genome to insert these transposon fragments. Non-homologous end-joining, a DNA double-helix repair system, is used to repair the resulting open DNA ends [9]. The most used transposon systems in mammalian cells are PiggyBac (PB), Tol2, and Sleeping Beauty (SB). While all three systems are effective, PB and SB transposon vector systems are more successful than Tol2 transposon systems in obtaining stable and efficient producer cell lines [10-12]. Therefore, these transposon systems offer a valuable alternative to random genome integration for generating stable and efficient producer cell lines, providing an effective and practical approach to creating a producer cell platform. In order to enhance the proficiency of the dual-vector transposon system in delivering the target gene into the host genome, it is necessary to implement optimizations such as determining the optimal proportions of the two vectors and the transposase enzyme, which can be developed through engineering technologies. In this study, the utilization of optimized transposase enzymes, such as SB100X, demonstrated 100-fold greater transposition activity compared to the wild-type SB transposase [13, 14].

Moreover, the effectiveness of the transposase and transposon plasmid ratio on transposition efficiency is not the sole determinant of success. Direct optimization of the transposon donor also plays a significant role in transposition. The circular or linear form of the target DNA can impact the efficiency of SB and PB transposon systems and the duration of subsequent cell pool selections [8, 15, 16].

This research study primarily aimed to evaluate the pool selection times and production performance of SB100X transposon-generated anti-PD-1 hIgG producer CHODG44 cell pools. We sought the optimal donor

and helper plasmid ratio and determined whether linear or circular transposon donor plasmid worked better. We compared the overall efficiency of the transposon system to a transgene random integration strategy.

2. Materials and Methods

2.1. Construction and Transformation of Expression Vectors

Mammalian expression vectors pExpV-antiPD-1 and pSBbiHYG-antiPD-1 were constructed to investigate the impact of random and transposon-mediated integration strategies, respectively. Both vectors carried a tricistronic design in which anti-PD-1 hIgG4 light chain (LC), heavy chain (HC), and dihydrofolate reductase (DHFR) open reading frames were joined by intervening FMDV internal ribosomal entry sites (IRES).

Insert DNA segments in this study were generated by using PCR amplification. Reaction mixtures contained 10 mM Tris-HCl (pH 8.8 at 25°C), 50 mM potassium chloride, 0.2 mM dNTP, 2 mM magnesium chloride, 0.5 μ M of each oligonucleotide primer, 1 unit of Phusion high-fidelity DNA polymerase and 1 ng of template DNA. Following the initial denaturation at 98°C for 2 min, the amplifications were performed for 30 cycles of denaturation at 98°C for 10 s, annealing at 70°C for 30 s, and extension at 72°C. The amplicons were analyzed on 1.5% (w/v) agarose gels stained with SYBR Safe (Invitrogen, S33102). Before proceeding to the subsequent steps, products were spin column purified from agarose gels (Macherey Nagel, 740609)

Exp-Cassette-F and Exp-Cassette-R oligonucleotide primer pair was used to amplify a codon-optimized synthetic DNA segment anti-PD-1 hIgG4 LC-IRES (wt)-HC-IRES (att) (Geneart, Thermo). The mammalian selection marker DHFR open reading frame was amplified using pGEM-T-DHFR-ORF (SinoBiological, HG14365-G) DNA template with DHFR-F and DHFR-R oligonucleotide primers. The primer sequences are outlined in Table 1.

The random integration vector backbone pExpV (Figure 1A) was custom-designed to allow CMV promoter-driven expression of the insert DNA (Geneart, Thermo). The SLiCE cloning method was used to assemble and ligate the amplicons into the SmaI linearized pExpV DNA with the specified order described by Zhang et al. [17].

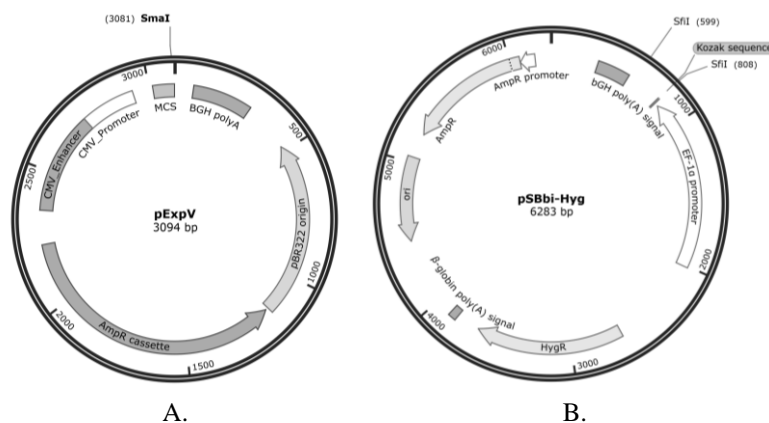


Figure 1. Vectors used in expression vector construction: A) pExpV vector map, B) pSBbiHYG vector map

Transposon mediated integration vector has been built on backbone pSBbi-Hyg (AddGene #60524). For this purpose, we used SfiI-Anti-PD-1-F and SfiI-DHFR-R oligonucleotide primer pair to amplify LC-IRES (wt)-HC-IRES (att)-DHFR insert from pExpV-antiPD-1 (in this study) plasmid DNA template. Following digestion with SfiI endonuclease, insert DNA and pSBbi-Hyg segments were ligated using T4 DNA ligase (Thermo Scientific, K1422). We transformed *Escherichia coli* Stb13 cells with pExpV-antiPD-1 and pSBbiHYG-antiPD-1 ligation products using the TSS method, as described by Chung et al. [18]. We performed a screening PCR following overnight incubation to determine insert positive colonies were present. Each 25 μ l reaction tube included 10 mM Tris-HCl (pH 8.8 at 25°C), 50 mM potassium chloride, 0.2 mM dNTP, 2 mM magnesium chloride, 0.5 μ M of each primer, 0.5 U Taq DNA polymerase and 5 μ l of colony suspension. We used CMV-

F and BGH-R or EF1a-F and BGH-R primer pairs to scan pExpV-antiPD-1 and pSBbiHYG-antiPD-1 transformants, respectively. Following initial denaturation at 95°C for 5 mins, target DNAs were amplified for 30 cycles of denaturation at 95°C for 30 s, annealing at 60°C for 1 minute, and extension at 68°C for 5 min. The primer sequences are depicted in Table 1. Midiprep plasmid isolation was performed to insert positive colonies using a kit (NucleoBond Xtra Midi Columns-Macherey Nagel, 740410).

Table 1. Sequences of the primers for construction of pExpV-antiPD-1 and pSBbiHYG-antiPD-1

Primer Name - Gene	Sequences (5' – 3')
Exp-Cassette-F	5'-CGGGCCCGGATCCACCGGTGCCGCCACCATGAAATGG -3'
Exp-Cassette-R	5'-AGTTCAATGGTCAACCATGGAATTCGATCCTCATC-3'
DHFR-F	5'-GATGAGGATCGAATTCATGGTTCGACCATTGAACT-3'
DHFR-R	5'-CTAGAGTCGCGGCCGCTTTATTAGTCTTTCTTCTCGTAGACTTC-3'
SfiI-Anti-PD-1-F	5'-GCTGGCCTCTGAGGCCGCCACCATGAAATGGGTCACCTT-3'
SfiI-DHFR-R	5'-GCTTGGCCTGACAGGCCTTATTAGTCTTTCTTCTCGTAGACTTC-3'
CMV-F	5'-CGCAAATGGGCGGTAGGCGTG-3'
EF1a-F	5'-TCAAGCCTCAGACAGTGGTTC-3'
BGH-R	5'-TAGAAGGCACAGTCGAGG-3'

2.2. Cell Culture and Standard Cultivation

Serum free-suspension culture adapted CHO DG44 DHFR *-/-* cells were a kind gift from Dr. Lawrence Chasin (Columbia University, NY). The cells were propagated in either 6-well plates (TPP, 92106) or 125 ml shaking flasks (Thermo Scientific, 4115-0125). The media used for routine subculturing, transfection, and selection is listed in Table 2. After every 2 - 3 days of cultivation, the cells were transferred to a fresh media at a 3 - 5 x 10⁵ cells/ml density. All cultures were incubated at 36.8°C with 7.5% CO₂ (v/v) (HERAcell 240, Thermo Scientific, US). Flask cultures were shaken at 110 rpm (Celltron, Infors HT shaker, Denmark).

Table 2. Cell culture media compositions

Composition of media for CHO DG44 (DHFR <i>-/-</i>) wild-type cells (Media A1)	
96.8 %	eCHO Basal Media (Lonza, BEBP12-933Q)
3 %	L-Glutamine (200 mM) (Sigma Aldrich, G7513)
0.2 %	HT Supplement 100X (Thermo Scientific, 11067030)
Composition of media for CHO DG44 cells transfection (Media A2)	
97 %	BalanCD Transfectory CHO Media (Irvine Scientific, 91147)
3 %	L-Glutamine (200 mM) (Sigma Aldrich, G7513)
10 % (after 24 Hours)	Transfectory Supplement (Irvine Scientific, 91148)
Composition of media for CHO DG44 cells transfected with semi-targeted integration system and CHO DG44 cells selection	
97 %	eCHO Basal Media (Lonza, BEBP12-933Q)
3 %	L-Glutamine (200 mM) (Sigma Aldrich, G7513)
Composition of media for CHO DG44 cells transfected with random integration system and CHO DG44 cells selection	
97 %	eCHO Basal Media (Lonza, BEBP12-933Q)
3 %	L-Glutamine (200 mM) (Sigma Aldrich, G7513)
25 nM	Methotrexate Hydrate (Sigma Aldrich, M8407)

2.3. Transfection and Sub-Cultivation

Stable pools of anti-PD-1 hIgG4 producer CHO cells were generated by random integration vector pExpV-antiPD-1 or transposon vector pSBbiHYG-antiPD-1. Prior to the transfection process, 60 µg of pExpV-antiPD-1 vector was linearized using restriction enzyme digestion with SspI (NEB, R3132S) and PvuI (NEB, R3150S) and then purified using a plasmid isolation/purification kit (Macherey Nagel, 740490).

Logarithmic phase 2x10⁶ CHO DG44 cells were transfected with 2 µg of linearized plasmid DNA by using a 4D Nucleofector system (Core and X Unit, Lonza Amaxa) with X kit L (Lonza, V4XC-2012) and DU-158 program, following the manufacturer's instructions. The transfection procedure was carried on by seeding the cells in 6-well plates at 2x10⁶ cells/well in media A2. After 24 hours, 10% (v/v) transfection supplement was added to each well to improve the transfection efficiency. Cells were counted 48 hours after transfection using

Vicell XR (Beckman Coulter). To establish stably transfected cell populations, the cell cultures were transferred to media A3 and incubated under standard conditions with media changes every 2-3 days until cell viability reached 95% (30 days of hypoxanthine and thymidine (HT) selection). Following HT selection, methotrexate (MTX)-driven gene amplification was performed by seeding and passaging at a concentration of $0.5 - 0.8 \times 10^6$ cells/ml according to standard conditions in media A4 supplemented with 50, 100, 200, 400, and 800 nM MTX, respectively. The concentration of metotrexat (MTX) in the culture media increased after cell viability reached above 80%. To ensure genetic stability, the decision was to employ selective media A4 containing 25 nM MTX rather than discontinuing MTX treatment in subsequent passages of selected cell cultures. This served to maintain selection pressure.

In order to establish a semi-integrated transfection system based on the transposon system, 50 μ g of the pSBbiHYG-antiPD-1 vector was linearized through digestion with BamHI and then isolated using a gel and PCR isolation kit (Macherey Nagel, 740609). The linearized and circular forms of the donor plasmid encoding the target gene and the helper plasmid encoding the transposase (SB100X) were then transfected into CHO cells at three different ratios (1:2, 1:3, and 1:4) using media A2. This was done to determine the optimal transposon condition. After 24 hours post-transfection, a 10% (v/v) transfection supplement was added to each well to enhance transfection efficiency. To establish stable transfected pools 48 hours after transfection, cell populations were seeded in HT-free media A3 under standard conditions until cell viability reached at least 90%. The cell populations were then passaged every 2-3 days using the fresh medium at $0.5 - 0.8 \times 10^6$ cells/ml concentration. All media compositions are outlined in Table 2.

2.4. Fed-Batch Cultivation and Protein Quantification

For the fed-batch study, 25 ml of Excell Advanced CHO Fed-Batch media (Sigma Aldrich, 14366C) supplemented with 6.0 mM of L-glutamine (Sigma Aldrich, G7513) were inoculated into shaking flasks at a concentration of 300,000 viable cells/ml. The cultures were maintained under standard conditions using nutrient media consisting of CHO Feed 1 - with glucose (Sigma Aldrich, 24367C) and CHO Feed 1 - without glucose (Sigma Aldrich, 24368C) at a concentration of 28.0 g/L, as well as glucose (Thermo Scientific, A2494001) prepared according to the manufacturer's instructions. The daily glucose concentration was adjusted to between 4.5 and 7.0 g/L, and when the daily Feed-1 supplementation exceeded 10% by volume, the remaining glucose requirement was supplemented with 200 g/L of glucose solution. The cell concentration and viability were determined using the Vi-Cell XR (Beckman Coulter).

The Anti-PD-1 Human IgG4 protein was quantified in the cultures using ACQUITY UPLC (Waters) Protein A chromatography with a Bio-Monolith Protein A column (Agilent, 5069-3639). The analysis parameters are listed in Table 3, and the gradient information is listed in Table 4.

Table 3. Protein A chromatography quantitative analysis parameters

Autosampler Temperature: 10°C	
Mobil Phase A	50 mM Sodium Phosphate pH: 7,4
Mobil Phase B	100 mM Citrate pH: 2,8
Column	Agilent Bio-Monolith Protein A, 5.2 mm x 4.95mm
Column Temperature	25°C
UV	280 nanometer
Injection Volume	50 μ L

Table 4. Protein A chromatography gradient system parameters

Time (Minute)	Flow rate (μ L/dk)	Solvent A (%)	Solvent B (%)	Curve
0.00	0.5	100	0	Initial
2.00	0.5	100	0	6
2.01	0.5	0	100	6
6.00	0.5	0	100	6
6.01	0.5	100	0	6
8.00	0.5	100	0	6

2.5. Statistical Analysis

The results were analyzed by applying Student's t-test or One-Way ANOVA, nonparametric Mann-Whitney U, Tukey and Dunnett tests according to the suitability of the parameters. For this purpose, the GraphPad (version 8) program was used, and $p < 0.05$ values were considered statistically significant.

3. Results and Discussion

3.1. Construction of A Random Integration Vector Expressing Anti-PD-1 Human IgG4

Random integration vector pExpV-anti-PD-1 carried a CMV promoter-driven tricistronic expression cassette. We used PCR to generate the 3367 bp long LC-IRES (wt)-HC-IRES (att) and 601 bp long DHFR gene (Figure 3B). SLiCE ligated these segments with SmaI linearized (Figure 3C) pExpV. We performed a colony PCR to screen the insert positive bacterial transformants. Plasmid isolation was performed from insert positive colonies (Figure 3.D). Restriction mapping was done to confirm pExpV-anti-PD-1 constructs. Eco321/XhoI and BamHI/NotI enzyme pairs generated 2539/4431 bp and 3890/3080 bp long bands, respectively (Figure 3E). The band observed around 6900 bp was likely caused by the incomplete digestion of one of the enzymes.

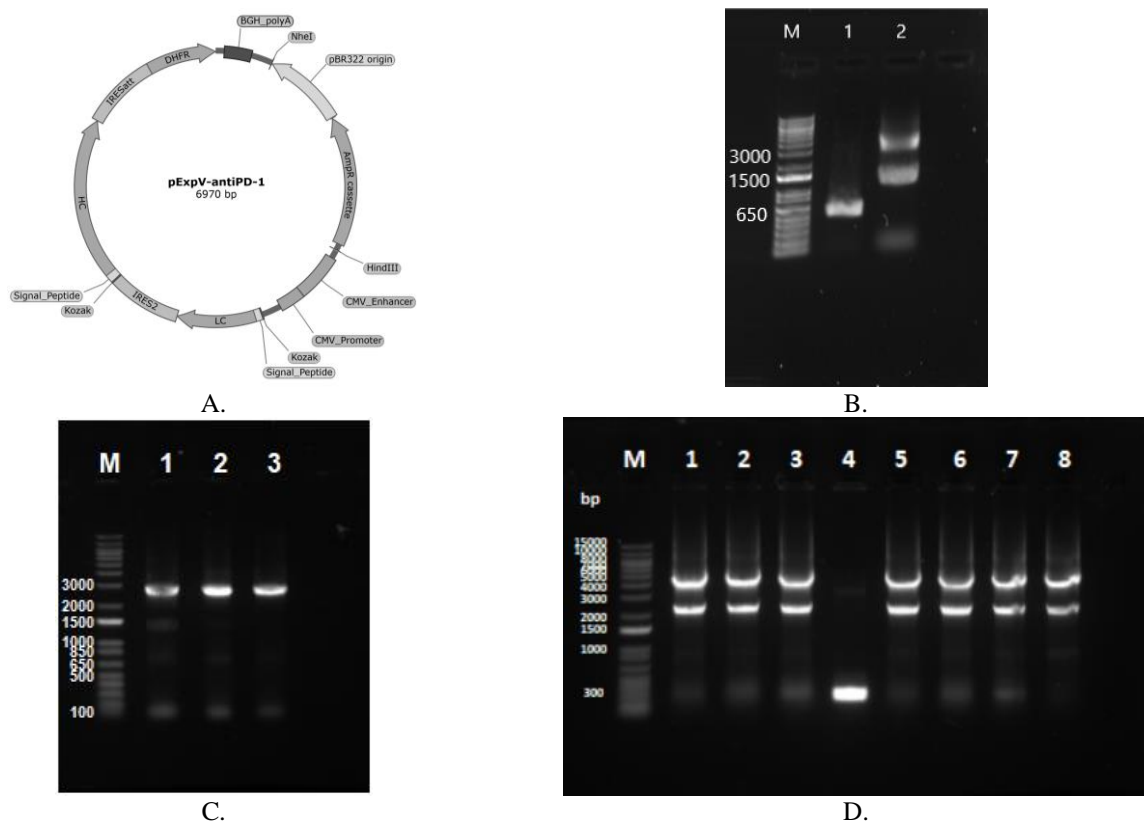


Figure 2. Design and construction of pExpV-antiPD-1. A) Random integration vector pExpV-antiPD-1 map. B) Expression cassette gene segments, Lane M: MW standard, Lane-1: DHFR amplicon (601 bp), Lane-2: LC-IRES-HC-IRES segment (3367 bp) C) SmaI linearized pExpV vector, Lane M: MW standard, Lane 1-3: SmaI treated pExpV backbone (3094 bp). D) Colony screening PCR products, M: Marker, 1–8: 4166 and 300 bp products amplified from insert positive and negative colonies, respectively. E) Restriction endonuclease mapping of pExpV-antiPD-1 vector, Lane M: MW Standard, Lane 1: Colony-1 BamHI/NotI digestion, Lane 2: Colony-1 Eco321/XhoI digestion, Lane 3: Colony-2 BamHI/NotI digestion, Lane 4: Colony-2 Eco321/XhoI digestion. Expected fragment sizes for BamHI/NotI are 2539/4431 bp, and Eco321/XhoI are 3890/3080 bp. F) 1 kb DNA MW Standard. Expected fragment sizes for BamHI/NotI and XhoI/Eco32I digestion are 3077/3893 and 2538/4432 bp, respectively

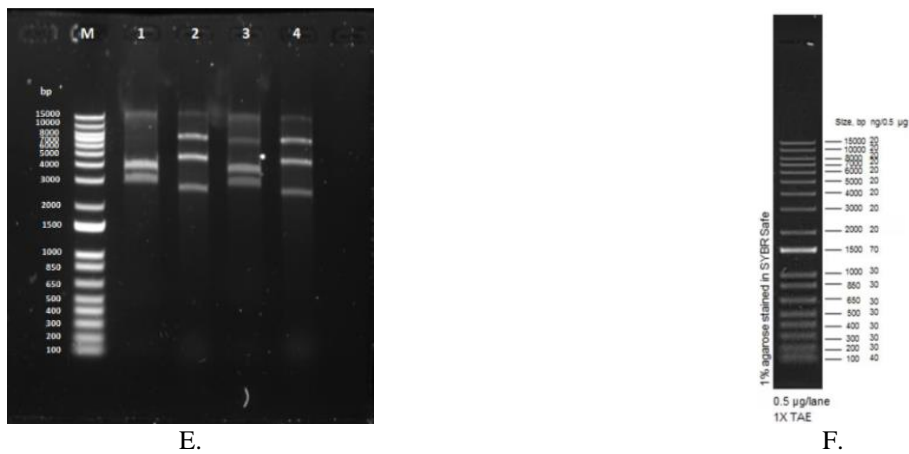


Figure 3. (Continued) Design and construction of pExpV-antiPD-1. A) Random integration vector pExpV-antiPD-1 map. B) Expression cassette gene segments, Lane M: MW standard, Lane-1: DHFR amplicon (601 bp), Lane-2: LC-IRES-HC-IRES segment (3367 bp) C) SmaI linearized pExpV vector, Lane M: MW standard, Lane 1-3: SmaI treated pExpV backbone (3094 bp). D) Colony screening PCR products, M: Marker, 1–8: 4166 and 300 bp products amplified from insert positive and negative colonies, respectively. E) Restriction endonuclease mapping of pExpV-antiPD-1 vector, Lane M: MW Standard, Lane 1: Colony-1 BamHI/NotI digestion, Lane 2: Colony-1 Eco321/XhoI digestion, Lane 3: Colony-2 BamHI/NotI digestion, Lane 4: Colony-2 Eco321/XhoI digestion. Expected fragment sizes for BamHI/NotI are 2539/4431 bp, and Eco321/XhoI are 3890/3080 bp. F) 1 kb DNA MW Standard. Expected fragment sizes for BamHI/NotI and XhoI/Eco32I digestion are 3077/3893 and 2538/4432 bp, respectively

3.2. Construction of SB Transposon Vector Expressing Anti-PD-1 Human IgG4

Previously constructed pExpV-antiPD-1 served as a template for the LC-IRES (wt)-HC-IRES (att)-DHFR segment. Agarose gel purified amplicon (Figure 5B) was ligated to the SfiI digested transposon donor vector (Figure 5C) in order to build pSBbiHYG-antiPD-1 (Figure 5A). We screened bacterial transformants for insert positive colonies (Figure 5.D) and performed a restriction endonuclease mapping using BamHI/FseI and Sall/FseI enzyme pairs to confirm the constructs. Agarose gel electrophoresis revealed the expected band pattern of 2015/2063/4985 and 2500/7463 bp for respective digestion products (Figure 5E).

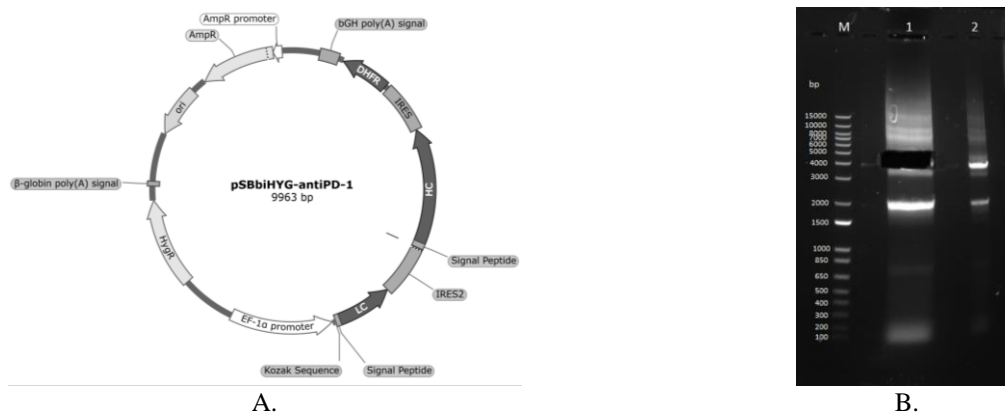


Figure 4. Design and construction of pSBbi-HYG-antiPD-1. A) Transposon-mediated integration vector pSBbi-HYG-antiPD-1 map. B) LC-IRES (wt)-HC-IRES (att)-DHFR amplicon, agarose gel electrophoresis. Lane M: MW standard, Lane 1: 3903 bp band excised from agarose gel, Lane 2: amplification products. C) SfiI digest of pSBbiHYG. D) Colony screening PCR products. Lane M: MW standard, Lane 1-8: 4025 bp products amplified from insert positive colonies. E) Restriction endonuclease mapping of pSBbiHYG-antiPD-1 vector. Lane M: MW standard, Lane 1: BamHI/FseI digestion products with expected band profile of 2015/2063/4985 bp, Lane 2: Sall/FseI digestion products with expected 2500/7463 bp band profiles. F) 1 kb DNA MW Standard

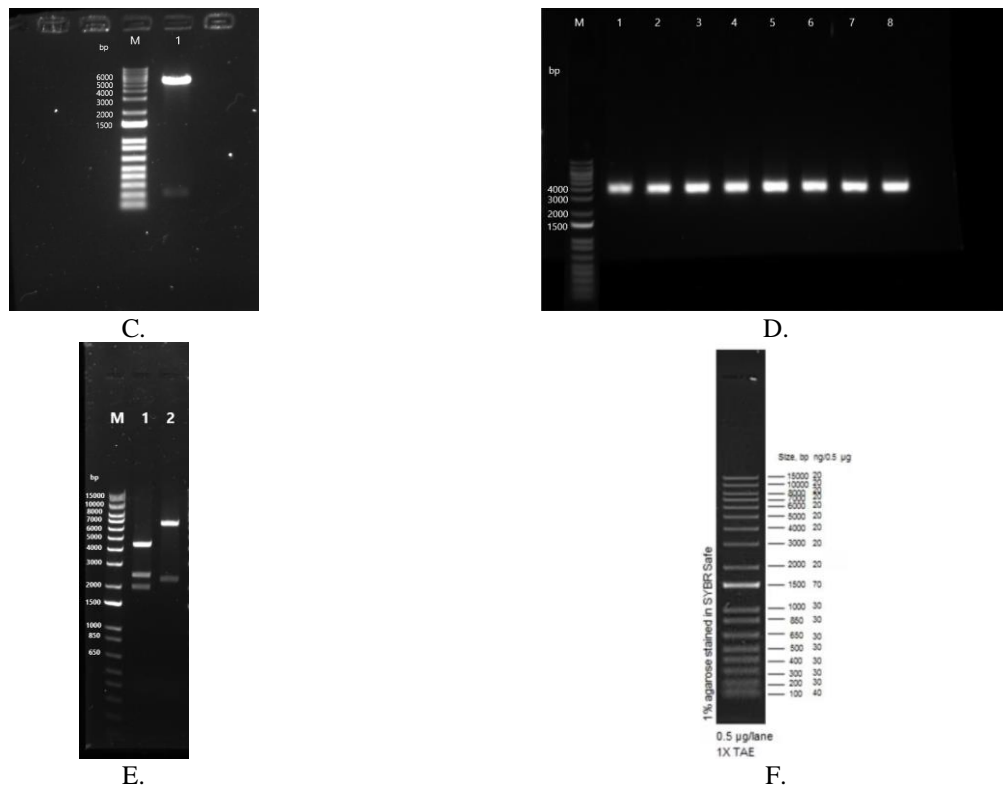


Figure 5. (Continued) Design and construction of pSBbi-HYG-antiPD-1. A) Transposon-mediated integration vector pSBbi-HYG-antiPD-1 map. B) LC-IRES (wt)-HC-IRES (att)-DHFR amplicon, agarose gel electrophoresis. Lane M: MW standard, Lane 1: 3903 bp band excised from agarose gel, Lane 2: amplification products. C) SfiI digest of pSBbiHYG. D) Colony screening PCR products. Lane M: MW standard, Lane 1-8: 4025 bp products amplified from insert positive colonies. E) Restriction endonuclease mapping of pSBbiHYG-antiPD-1 vector. Lane M: MW standard, Lane 1: BamHI/FseI digestion products with expected band profile of 2015/2063/4985 bp, Lane 2: SalI/FseI digestion products with expected 2500/7463 bp band profiles. F) 1 kb DNA MW Standard

3.3. Generation and Evaluation of CHO-DG44 Cell Pools Stably Expressing Anti PD-1 Human IgG4

3.3.1. Producer Pools Generated with Sleeping Beauty Transposon System

We digested pSBbiHYG-antiPD-1 with BamHI to cut out the 2015 bp long ampicillin resistance cassette. The linearized transposon donor vector segment was agarose gel purified and recovered at a concentration of 0.862 $\mu\text{g}/\mu\text{l}$ (Macherey Nagel, 740609) (Figure 6).

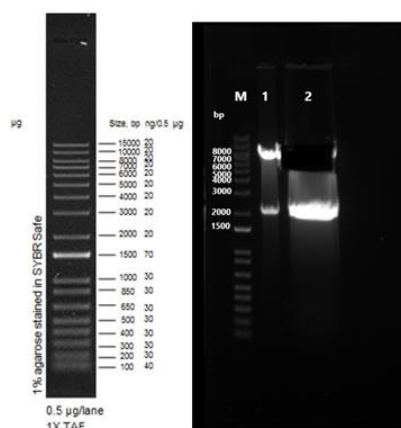


Figure 6. Agarose gel electrophoresis of BamHI digested pSBbiHYG-antiPD-1. M: MW standard, Lane 1: 7948/2015 bp digestion products, Lane 2: 7948 bp transposon donor segment excised from the gel

We determined the optimal transposon: transposase vector ratio. CHO DG44-DHFR^{-/-} cells were co-transfected with transposon encoding vector pSB100X and either with linearized or circular pSBbiHYG-antiPD-1 transposon donor vector DNA at ratios 1:2, 1:3, and 1:4. Upon hypoxanthine and thymidine depletion, cell viability rapidly declined for the first 20 days of incubation. Under selective pressure, pool-3 (linear vector, 1:4 ratio) reached 90% cell viability as early as day 44. This was followed by pool-2 (linear vector, 1:3 ratio) and pool-6 (circular vector, 1:4) on day 52 (Figure 7) ($p < 0.01$). Comparing all six cell pools, linear donor plasmid favors faster recovery of the cell viability, regardless of the transposon: transposase vector ratio.

In this study, we also showed that increasing the transposon donor vector ratio positively affected the selection times and production potentials of the cell pools. This may be attributed to more efficient transposition. As an autoregulatory control, an overabundance of mariner transposase drastically decreases the excision activity over its target. Specifically, keeping SB transposase expression constant and low is critical to avoid the phenomenon of overproduction inhibition (OPI), as previously reported [19-21]. Our findings were consistent with other studies, which favored a higher transposon donor vector over the SB transposase ratio [22, 23].

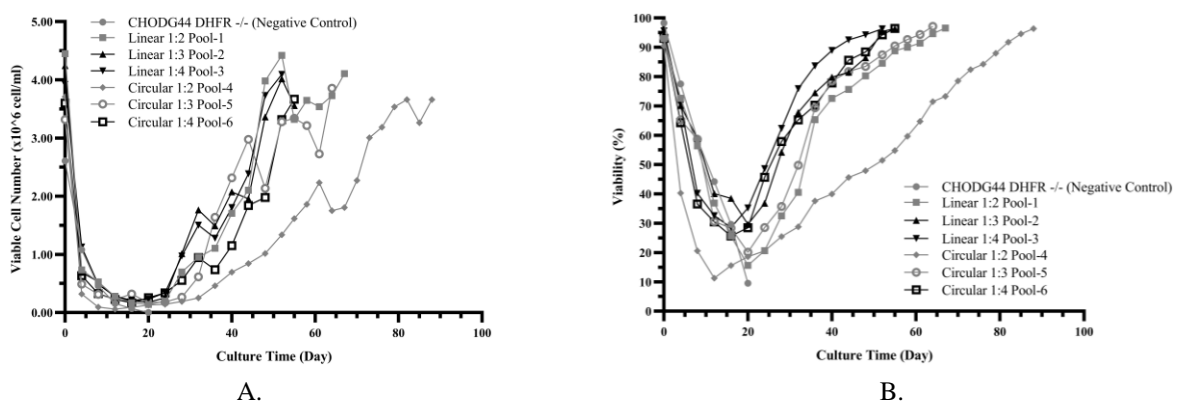


Figure 7. Selection of SB transposon-generated cell pools by HT depletion A) percent cell viability (%), B) viable cell count (x10⁶ cells/ml) over days of selection

3.3.2. Producer Pool Generated by Random Integration

The random integration vector pExpV-antiPD-1 was digested by SspI/PvuI restriction endonucleases (Figure 8). Linearized product was used to nucleofactor CHO DG44 DHFR^{-/-} cells.

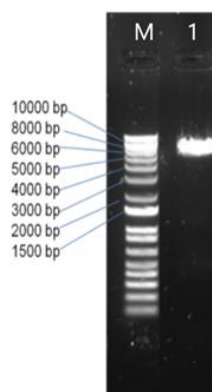


Figure 8. Agarose gel image of linearized random integration vector. M: MW standard, Lane 1: SspI/PvuI digestion product of pExpV-antiPD-1

The cells were allowed to recover for the first 48 hours. Subsequently, we transferred the cells to the HT-depleted selection medium until the non-integrants were killed, and later, the cell viability was restored. By day 30, the cell viability reached 90%, and the pool was subjected to gradually increasing MTX concentrations up to 800 nM to pick up cells with amplified copy numbers of the expression cassette. After 85 days of

consequent selection and amplification, a stable cell pool expressing human antiPD-1 was obtained (Figure 9). Generating stable producer cells through random integration vectors is well-known for being labor-intensive and time-consuming. Similar workflows and time courses were described in previous studies [23].

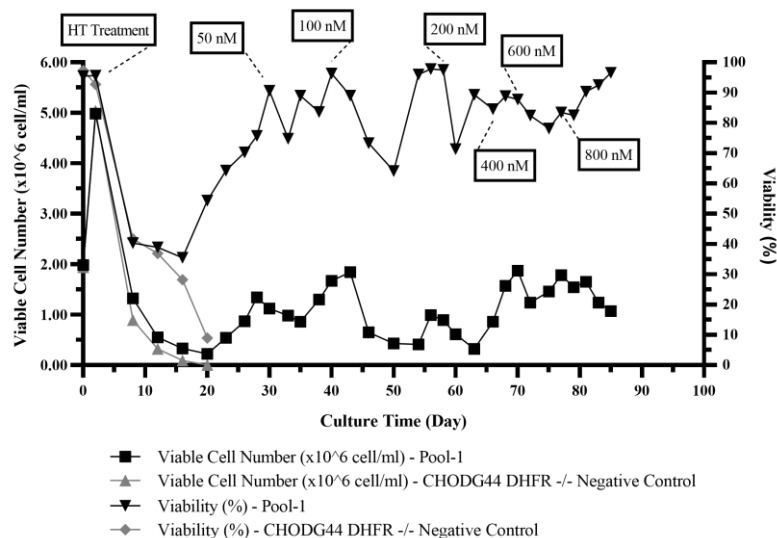


Figure 9. Viable cell counts ($\times 10^6$ cells/ml) and percent viability (%) of random integration cell pool subjected to consequent HT selection and MTX-mediated gene amplification

3.3.3. Fed-Batch Culture Study in Pools and Evaluation of Anti-PD-1 Human IgG4 Production Performance

A fed-batch culture was conducted with random and transposon-generated pools to investigate the performance of biomass throughput, cell viability, essential metabolic parameters, and protein production. The random integration pool reached a peak density of 9.5×10^6 cells/ml, with a steady decrease in cell viability. By day 10, this pool had lost $>20\%$ viability and entered the death phase. The cell counts of transposon-generated pools ranged between $12 - 20 \times 10^6$ cells/ml with $>90\%$ viability at the end of the active growth phase. Among these, pool 3 was the best-performing pool, reaching the plateau phase on day 6 with 19.7×10^6 cells/ml and the highest overall cell viability. Pools 4, 5, and 6 showed similar growth kinetics with marginally lower cell counts and cell viability ratios (Figure 10AB). Transposon-generated pools 1 and 2 behaved like a random integration pool, entering the death phase immediately after reaching a peak cell density. We also observed a premature decline in cell viability in those pools.

We evaluated glucose utilization and lactate accumulation of random integration and transposon-generated pools. We observed gradually increasing glucose uptake in the exponential phase of the cultures (Figure 10.D). CHO cells are renowned for utilizing glucose as a carbon and energy source to sustain rapid growth rates and release lactic acid into the medium. Later, the cells start to consume lactic acid to drive the tricarboxylic acid cycle (TCA) cycle to supply anabolic intermediary substrates and energy for the biosynthesis of the recombinant product. Lactic acid builds up had also occurred in our pools. Upon reaching the stationary phase, we observed decreased lactic acid concentrations in certain cell pools (Figure 10C). The pools following the sequential glucose and lactic acid metabolism pattern displayed high recombinant product yields (Figure 11). Random integration pool formed the smallest cell mass with sub-optimal glucose utilization. Concerning the biomass size, this pool over-accumulated lactic acid in the rapid growth phase without valorizing in the stationary phase. Random integration vectors may cause insertional silencing of certain critical host genes and become detrimental to cellular functions.

Furthermore, subsequent MTX gene amplification may form repeated arrays of transgene and trigger epigenetic silencing of the expression cassette. Once seeded, epigenetic reprogramming may spread hundreds

of thousands of bases away from the initial target. Most probably, these contagious modifications that result in heterochromatin formation may have a negative impact on the overall robustness of the cell physiology.

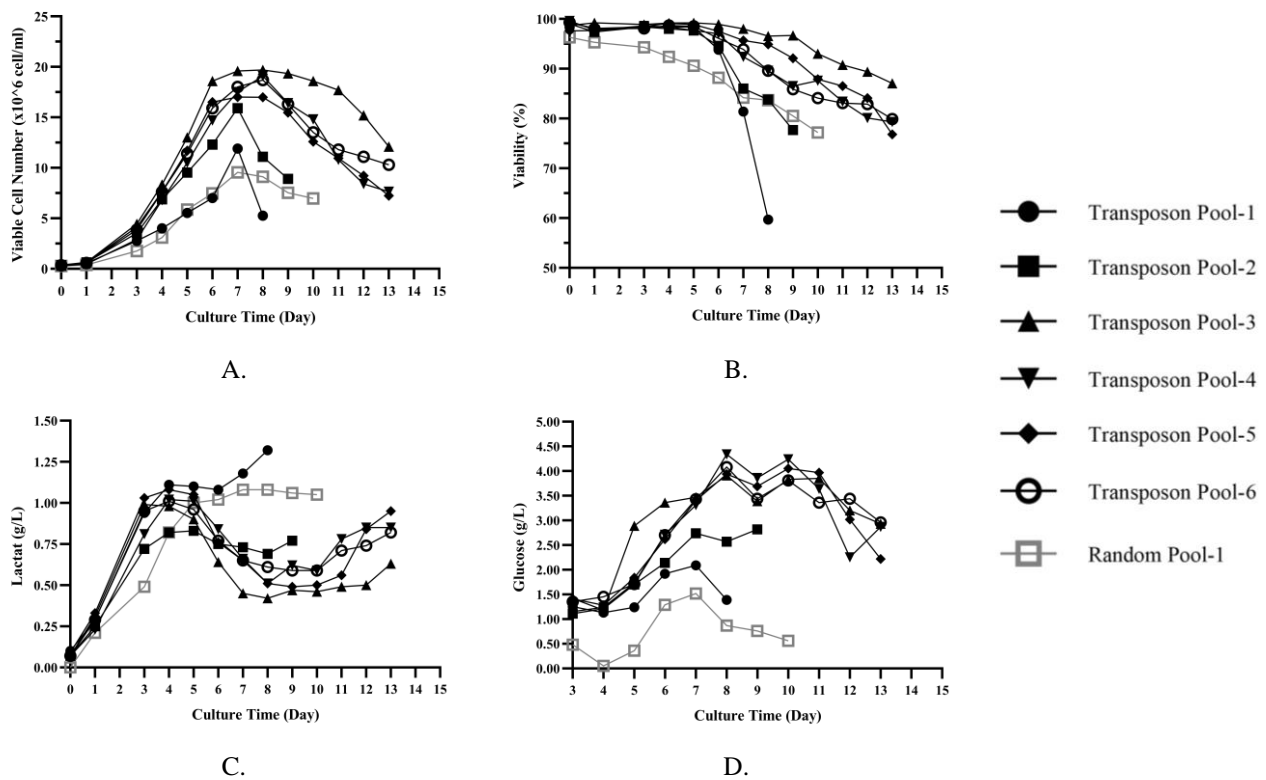


Figure 10. Growth and metabolic characteristics of fed-batch cultures of random and transposon integration pools. A) Viable cell count ($\times 10^6$ cells/ml). B) Cell viability ratio (%). C) Lactate production (g/l). D) Glucose consumption (g/l)

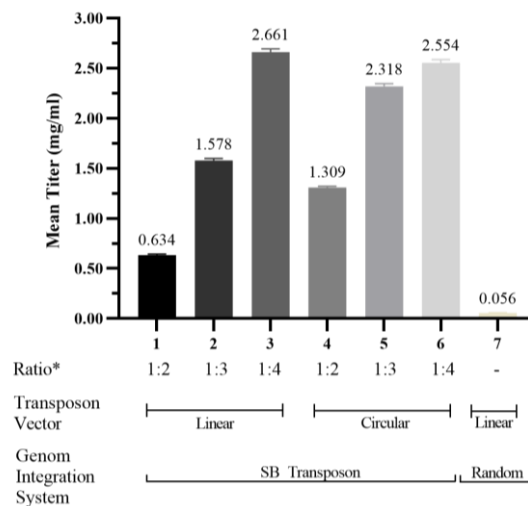


Figure 11. Titer of antiPD-1 human IgG4 production in fed-batch pools (mg/ml)

Transposon vector technology, which is employed to create recombinant cell lines utilized in the industrial production of biological drugs, vaccines, and viral vector particles, presents a more advantageous delivery system than random integration techniques [8]. Random integration systems have the potential to produce unforeseeable and occasionally controversial effects on gene expression, such as gene silencing and activation or disruption of endogenous genes. However, using random integration for industrial purposes can result in unpredictable cell line behavior, unbalanced and inefficient gene expression, and potentially irreproducible outcomes [24]. In contrast, the transposon-mediated cut-and-paste style of gene delivery ensures a single copy of the transgene per insertion site. Therefore, transgene concatemer-induced epigenetic silencing is much more

unlikely. Nevertheless, all transposon systems are subject to events such as undesired integration, continuous transposition, or insufficient transposition due to the continuous expression of the transposase gene as a result of stable transfection of the transposase vector and the suboptimal ratio between the transposase vector and transposon vector [12, 25]. Consequently, genetic instability may occur, leading to inadequate or loss of production in recombinant cell lines obtained and selected using the transposon system.

Transposon vector systems have successfully been used for creating industrial cell lines to manufacture biological drugs, vaccines, and viral vector particles. Commonly used transposases PiggyBac, Sleeping Beauty, and Tol2 are engineered to operate in non-native mammalian host cells, such as CHO, HEK293, and HeLa. An enhanced version of Sleeping Beauty transposase, SB100X can transpose 10% of transfected mammalian cells. This is 10 times more efficient than Tol2 and approximately 3 times more efficient than PiggyBac [19]. Contrastingly, transfection via random integration vectors tends to stabilize at several magnitudes of lower frequencies [24, 26]. Therefore, transposase-mediated integration could offer a starting blend of cell populations that may evolve through the adaptation landscape to reach a new fitness maxima. Consequently, more productive cell pools become generated in much shorter time frames. In our study, the top producer cell pool was achieved in the shortest selection time of 44 days.

In this research study, we sought to rapidly produce high-potential cell pools using the transposon system, increasing both productivity and efficiency in commercial production. We applied effective optimization techniques to develop producer cell lines to achieve this. Specifically, we used host CHO-DG44 recombinant cell pools and evaluated their potential for target protein production using random transfers and the SB transposon system. Additionally, we examined the impact of optimal vector ratios on anti-PD-1 human IgG4 expression through the batch culture of stable cell pools selected from transfection of the donor vector with the transposase vector in either linear or circular form at various ratios within the SB transposon system.

Tests were conducted to compare the performance of the optimized transposon with that of the random transfer method in the SB transposon system. Various transposase and transposon vector ratios were used to thoroughly examine their effects on productivity. In our study, transposon-generated pools 3, 6, and 5 yielded the best antiPD-1 hIgG4 titers (Figure 11). However, in the fed-batch process, pools 1 and 2 abruptly lost viability following the exponential growth phase (Figure 10B). Nonetheless, these underperforming pools were still 10 - 30 times more productive than the random integration pool. The results also revealed that the 1:4 ratio (transposase to transposon) was the optimal ratio, with a protein content of 2.6 mg/ml (Figure 11), regarding production efficiency and the shortest selection time of 44 days. In our findings on different transfer rates, we observed that increasing the transposon vector (donor vector) ratio positively impacted production potential and selection due to efficient transposition. Specifically, we kept the ratio of the donor vector expressing the SB transposon enzyme constant and low to avoid the phenomenon of overproduction inhibition, as stated in previous studies [20, 21]. The high production amount was compatible with the low lactate level and high glucose consumption observed in fed-batch studies of the pools. Studies have shown that 90% of the glucose taken into cell metabolism is used for glycosylation due to the high amount of precursor glycans required, especially in producing glycoproteins such as monoclonal antibodies [2, 27]. Additionally, the low amount of lactate measured may indicate that the pools utilize the lactate produced to replenish the TCA cycle and meet the energy demand from high production [28-30].

Circular and linear donor vector transfections were performed on cell pools to evaluate the effect of donor vector transfection on production and selection. The results indicated that the average production trend was higher in pools obtained with circular donor vectors, regardless of the ratios (Figure 11). This finding is consistent with previous literature on the PB system, which showed that transposition on linear substrates is less efficient than on circular ones in the SB system. Studies have found that linear donor molecules impair transposition. However, there are examples where linear donor DNA can be transformed into circular form using recombinases inside the cell [16, 31, 32]. Additionally, the position of the donor DNA in the chromosome, whether in a circular or linear form, can affect the frequency of transposition due to chromatin status [33].

The results of the current study demonstrated that random transformation, compared to the transposon system with a low protein production amount measured as 0.056 mg/ml, can obtain more efficient results with cells developed with the transposon system, especially in accordance with industrial productions. CHO cell systems, frequently preferred in industrial production, are highly prone to genetic instability (chromosomal instability, haploidy/polyploidy, gene loss, etc.) [34-36]. Due to this genetic plasticity, the structural instability and uncertain chromosomal location of transgenes with random integration leads to unstable production when using CHO cell lines, requiring extensive and time-consuming colony screening during cell line development to identify a small number of stable colonies from an inefficient pool. Considering these findings, the transposon system is more advantageous than random integration.

The utilization of transposon vectors in this study has demonstrated the potential to enhance the production of recombinant proteins in CHO cells when transfected at optimal rates. The amount and form of the donor vector employed directly influence the efficiency of the process. These findings offer valuable insights for future system optimization, particularly to produce complex proteins such as monoclonal antibodies using the SB transposon system. In addition, the genome-wide distribution of insertion sites for transposon and retroviral systems shows varying bias. SB transposase exhibits limited preference towards specific chromatin states and insertional hot spots compared to other systems. SB-mediated insertions' near-random nature may have the least detrimental effect on nearby genes [37].

4. Conclusion

In this study, we aimed to generate stable and highly productive antiPD-1 hIgG4-expressing CHO cell pools. We compared the performance of SB100X transposase to random integration in terms of stable pool selection time, metabolic robustness, biomass, and recombinant protein yields.

SB transposase is well known for the overproduction inhibition effect (OPI). Our data confirmed that keeping the transposase vector constant at a minimum concentration and co-transfecting it with an increased transposon donor vector favors the selection of better-performing producer cell pools in a shorter period. SB100X transposase enabled us to select the most productive stable cell pool in as early as 44 days (Figure 7). In contrast, a random integration vector required 85 days of selection with HT depletion and MTX amplification (Figure 9). Despite the lengthy selection time, most transposon-generated pools surpassed this pool regarding growth potential, glucose, and lactic acid metabolic profile. Moreover, the recombinant protein yields of transposon pools were far superior to the random integration pool in the 1 - 2 orders of magnitude range (as illustrated in Figure 10 and Figure 11). However, it is notable that transposon pools 1 and 2 experienced an abrupt loss of viability before the random integration pool in batch culture conditions (Figure 10B).

Transposons have proved useful as an expansion to the molecular biology toolbox. Functional genomics studies, gene therapy, and cell factory technologies have benefited greatly from transposon-mediated gene delivery.

The versatility of the SB transposon system may give superpowers to researchers and industrial cell line developers. Highly productive, stable cell pools and lines can be developed with proper optimization in considerably shorter periods. Moreover, the resulting cell pools have exceptionally high recombinant product yields compared to traditional cell factory engineering techniques like random integration vectors. Taking advantage of these benefits, the SB transposon system offers an accelerated research and development phase and a more efficient and cost-effective upstream process.

Author Contributions

The third author directed the project and supervised this study's findings. The second and first authors devised the main conceptual ideas and performed the experiment and statistical analyses. The first author wrote the manuscript with support from the second and third authors. All authors reviewed and edited the paper. All

authors read and approved the final version of the paper. This paper is derived from the first author's doctoral dissertation thesis supervised by the third author.

Conflicts of Interest

All the authors declare no conflict of interest.

Ethical Review and Approval

No approval from the Board of Ethics is required.

Acknowledgment

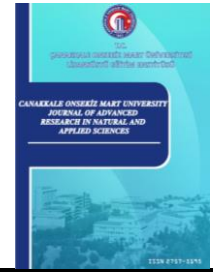
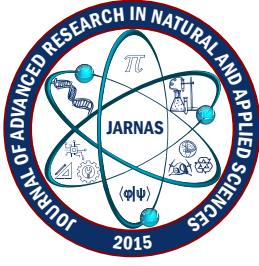
We extend our gratitude to Dr. İrfan Çinkaya for his invaluable support. This study received generous sponsorship and backing from Deva Pharmaceutical Biotechnology. The authors would like to thank the Deva upstream/downstream process team and the analytical group for their assistance during the molecular biology, cell culture studies, and analysis. The authors sincerely thank Prof. Dr. Tuğba Tümer for their invaluable contribution to editing this paper.

References

- [1] A. Naimi, *Tumor immunotherapies by immune checkpoint inhibitors (ICIs); the pros and cons*, Cell Communication and Signaling 20 (2022) 44 pages.
- [2] S. Luo, B. Zhang, *Benchmark glycan profile of therapeutic monoclonal antibodies produced by mammalian cell expression systems*, Pharmaceutical Research 41 (1) (2024) 29–37.
- [3] Y. H. Chen, M. S. Keiser, B. L. Davidson, *Viral vectors for gene transfer*, Current Protocols in Mouse Biology 8 (4) (2018) 7 pages.
- [4] S. H. Jazayeri, A. Amiri-Yekta, S. Bahrami, H. Gourabi, M. H. Sanati, M. R. Khorramizadeh, *Vector and cell line engineering technologies toward recombinant protein expression in mammalian cell lines*, Applied Biochemistry and Biotechnology 185 (4) (2018) 986–1003.
- [5] S. Puttini, *MAR-mediated integration of plasmid vectors for in vivo gene transfer and regulation*, BMC Molecular Biology 14 (1) (2013) 26 pages.
- [6] J. Chusainow, Y. S. Yang, J. H. M. Yeo, P. C. Toh, P. Asvadi, N. S. C. Wong, M. G. S. Yap, *A Study of monoclonal antibody-producing CHO cell lines: What makes a stable high producer?*, Biotechnology and Bioengineering 102 (4) (2009) 1182–1196.
- [7] S. W. Shin, J. S. Lee, *CHO cell line development and engineering via site-specific integration: Challenges and opportunities*, Biotechnology and Bioprocess Engineering 25 (5) (2020) 633–645.
- [8] M. Wei, C.-L. Mi, C.-Q. Jing, T.-Y. Wang, *Progress of transposon vector system for production of recombinant therapeutic proteins in mammalian cells*, Frontiers in Bioengineering and Biotechnology 10 (2022) 10 pages.
- [9] N. Tschorn, K. Berg, J. Stitz, *Transposon vector-mediated stable gene transfer for the accelerated establishment of recombinant mammalian cell pools allowing for high-yield production of biologics*, Biotechnology Letters 42 (7) (2020) 1103–1112.
- [10] D. Balciunas, K. J. Wangensteen, A. Wilber, J. Bell, A. Geurts, S. Sivasubbu, X. Wang, P. B. Hackett, D. A. Largaespada, R. S. McIvor, S. C. Ekker, *Harnessing a high cargo-capacity transposon for genetic applications in vertebrates*, PLoS Genetics 2 (11) (2006) 11 pages.

- [11] M. Sato, E. Inada, I. Saitoh, S. Watanabe, S. Nakamura, *PiggyBac-based non-viral in vivo gene delivery useful for production of genetically modified animals and organs*, *Pharmaceutics* 12 (3) (2020) 277–290 pages.
- [12] S. Balasubramanian, Y. Rajendra, L. Baldi, D. L. Hacker, F. M. Wurm, *Comparison of three transposons for the generation of highly productive recombinant CHO cell pools and cell lines*, *Biotechnology and Bioengineering* 113 (6) (2016) 1234–1243.
- [13] L. Mátés, Z. Izsvák, Z. Ivics, *Technology transfer from worms and flies to vertebrates: Transposition-based genome manipulations and their future perspectives*, *Genome Biology* 8 (1) (2007) Article Number S1 19 pages.
- [14] F. Voigt, L. Wiedemann, C. Zuliani, I. Querques, A. Sebe, L. Mates, Z. Izsvak, Z. Ivics, O. Barabas, *Sleeping Beauty transposase structure allows rational design of hyperactive variants for genetic engineering*, *Nature Communication* 7 (1) (2016) Article Number 11126 8 pages.
- [15] S. R. Yant, A. Ehrhardt, J. G. Mikkelsen, L. Meuse, T. Pham, M. A. Kay, *Transposition from a gutless adeno-transposon vector stabilizes transgene expression in vivo*, *Nature Biotechnology* 20 (10) (2002) 10 pages.
- [16] H. Nakanishi, Y. Higuchi, S. Kawakami, F. Yamashita, M. Hashida, *Comparison of piggybac transposition efficiency between linear and circular donor vectors in mammalian cells*, *Journal of Biotechnology* 154 (4) (2011) 205–208.
- [17] Y. Zhang, U. Werling, W. Edelmann, *SLiCE: A novel bacterial cell extract-based DNA cloning method*, *Nucleic Acids Research* 40 (8) (2012) 10 pages.
- [18] C. T. Chung, S. L. Niemela, R. H. Miller, *One-step preparation of competent Escherichia coli: Transformation and storage of bacterial cells in the same solution*, *Proceedings of the National Academy of Sciences of the United States of America* 86 (7) (1989) 2172–2175.
- [19] I. Grabundzija, M. Irgang, L. Mátés, E. Belay, J. Matrai, A. Gogol-Döring, K. Kawakami, W. Chen, P. Ruiz, M. K. L. Chuah, T. Vanden Driessche, Z. Izsvák, Z. Ivics, *Comparative analysis of transposable element vector systems in human cells*, *Molecular Therapy* 18 (6) (2010) 1200–1209.
- [20] A. R. Lohe, D. L. Hartl, *Autoregulation of mariner transposase activity by overproduction and dominant-negative complementation*, *Molecular Biology and Evolution* 13 (4) (1996) 549–555.
- [21] T. Sumiyoshi, N. G. Holt, R. P. Hollis, S. Ge, P. M. Cannon, G. M. Crooks, D. B. Kohn, *Stable transgene expression in primitive human CD34+ hematopoietic stem/progenitor cells, using the Sleeping Beauty Transposon System*, *Human Gene Therapy* 20 (12) (2009) 1607–1626.
- [22] H. Zayed, Z. Izsvák, O. Walisko, Z. Ivics, *Development of hyperactive Sleeping Beauty transposon vectors by mutational analysis*, *Molecular Therapy: The Journal of the American Society of Gene Therapy* 9 (2) (2004) 292–304.
- [23] T. Yoshikawa, F. Nakanishi, Y. Ogura, D. Oi, T. Omasa, Y. Katakura, M. Kishimoto, K. Suga, *Amplified gene location in chromosomal DNA affected recombinant protein production and stability of amplified genes*, *Biotechnology Progress* 16 (5) (2000) 710–715.
- [24] A. Stadermann, M. Gamer, J. Fieder, B. Lindler, S. Fehrmann, M. Schmidt, P. Schulz, I. H. Gorr, *Structural analysis of random transgene integration in cho manufacturing cell lines by targeted sequencing*, *Biotechnology and Bioengineering* 119 (3) (2022) 868–880.
- [25] K. Berg, V. N. Schäfer, N. Tschorn, J. Stitz, *Advanced establishment of stable recombinant human suspension cell lines using genotype-phenotype coupling transposon vectors*, *Genotype-Phenotype Coupling: Methods and Protocols*, Humana Press, New York, 2020.
- [26] C. Gorman, R. Padmanabhan, B. H. Howard, *High-efficiency DNA-mediated transformation of primate*

- cells, *Science* 221 (4610) (1983) 4610 551–553.
- [27] B. Liu, M. Spearman, J. Doering, E. Lattová, H. Perreault, M. Butler, *The availability of glucose to CHO cells affects the intracellular lipid-linked oligosaccharide distribution, site occupancy and the N-glycosylation profile of a monoclonal antibody*, *Journal of Biotechnology* 170 (2014) 17–27.
- [28] L. Zhang, A. Castan, J. Stevenson, N. Chatzissavidou, F. Vilaplana, V. Chotteau, *Combined effects of glycosylation precursors and lactate on the glycoprofile of IgG produced by CHO cells*, *Journal of Biotechnology* 289 (2019) 71–79.
- [29] H. Le, S. Kabbur, L. Pollastrini, Z. Sun, K. Mills, K. Johnson, G. Karypis, W. S. Hu, *Multivariate analysis of cell culture bioprocess data—lactate consumption as process indicator*, *Journal of Biotechnology* 162 (2) (2012) 210–223.
- [30] M. Torres, C. Altamirano, A. J. Dickson, *Process and metabolic engineering perspectives of lactate production in mammalian cell cultures*, *Current Opinion in Chemical Engineering* 22 (2018) 184–190.
- [31] S. R. Yant, L. Meuse, W. Chiu, Z. Ivics, Z. Izsvák, M. A. Kay, *Somatic integration and long-term transgene expression in normal and haemophilic mice using a DNA transposon system*, *Nature Genetics* 25 (1) (2000) 35–41.
- [32] Z. Izsvák, Z. Ivics, *Sleeping Beauty transposition: Biology and applications for molecular therapy*, *Molecular Therapy* 9 (2) (2004) 147–156.
- [33] A. J. Dupuy, S. Fritz, D. A. Largaespada, *Transposition and gene disruption in the male germline of the mouse*, *Genesis* 30 (2) (2001) 82–88.
- [34] M. J. Wurm, F. M. Wurm, *Naming CHO cells for bio-manufacturing: Genome plasticity and variant phenotypes of cell populations in bioreactors question the relevance of old names*, *Biotechnology Journal* 16 (7) (2021) 24 pages.
- [35] C. Frye, R. Deshpande, S. Estes, K. Francissen, J. Joly, A. Lubiniecki, T. Munro, R. Russell, T. Wang, K. Anderson, *Industry view on the relative importance of 'Clonality' of biopharmaceutical-producing cell lines*, *Biologicals* 44 (2) (2016) 117–122.
- [36] G. Walsh, *Biopharmaceutical benchmarks 2018*, *Nature Biotechnology* 36 (12) (2018) 1136–1145.
- [37] J. Yoshida, K. Akagi, R. Misawa, C. Kokubu, J. Takeda, K. Horie, *Chromatin states shape insertion profiles of the piggyBac, Tol2 and Sleeping Beauty transposons and murine leukemia virus*, *Scientific Report* 7 (1) (2017) Article Number 43613 18 pages.



Particle Shape-Based Evaluation of the Leaching of Sphalerite Ore in Dilute Acid Solutions

Tuğba Deniz Tombal¹ , İlgin Kurşun² , Mert Terzi³ 

¹Department of Mining Engineering, Faculty of Engineering, Adana Alparslan Türkeş Science and Technology University, Adana, Türkiye

^{2,3}Department of Mining Engineering, Faculty of Engineering, İstanbul University-Cerrahpaşa, İstanbul, Türkiye

Abstract – In this study, the effects of changes in particle shapes on dissolution efficiencies in zinc (Zn) recovery from a lead-zinc (Pb-Zn) ore by acid leaching method were investigated. In the experiments with nitric acid (HNO₃), sulfuric acid (H₂SO₄), and hydrochloric acid (HCl), particle size (75-106-150 µm), solids ratio (5-10-15-20-25%), leaching time (30-60-120-180-240 min), acid dosage (0.25-0.5-1-2-5 M) and pulp temperature (30-40-50-60-70 °C) parameters were analyzed. Optimum results were obtained under the conditions of 75 µm particle size, 15% solids ratio, 120 min leaching time, 0.5 M acid dosage, and 50°C pulp temperature for H₂SO₄; 106 µm particle size, 25% solids ratio, 60 min leaching time, 0.5 M acid dosage, and 70°C pulp temperature for HCl; 75 µm particle size, 20% solids ratio, 60 min leaching time, 1 M acid dosage, and 50°C pulp temperature for HNO₃. As a consequence of the tests performed under these optimized conditions, 97.32%, 96.38% and 96.06% Zn dissolution efficiencies were obtained. Within the context of particle shape factor research, microscope images of the leaching residues were obtained from the experiments in which the pulp temperature, acid dosage, and leaching time parameters were examined. The samples obtained from the experiments with all three acids were compared with the ore samples, and the impacts of changes in circularity, roundness, and solidity values on dissolution efficiencies were interpreted.

Article Info

Received: 12 Mar 2024

Accepted: 21 Jun 2024

Published: 30 Sep 2024

Research Article

Keywords – Sphalerite, chemical dissolution, particle shape factor analysis

1. Introduction

Morphology is a common term for the detailed description of an object and is considered to have two main sides: shape and surface texture. Shape relates to large and medium-scale aspects of an object's morphology, while surface texture refers to small-scale surface features related to the object's size. Particle morphology, including size and shape, is an important factor that significantly affects the physical and chemical properties of the material. Basic information about the nature and origin of granular material can often be obtained from the particles' shape, form, and/or surface shape [1-3]. Shape is a basic characteristic of all objects, even sedimentary particles, but it remains one of the most challenging processes to measure and characterize. Despite a huge bibliography on the topic, there continues to be a pervasive misunderstanding about the importance and relative value of various measurements of particle shape. Different researchers have used various terms to describe the external geometric expression of particles, including shape, morphology, and form. While several shape dimensions can be defined, four are particularly important: form, roundness, roughness, and sphericity [4-7].

¹ttombal@atu.edu.tr (Corresponding Author); ²ilginkur@iuc.edu.tr; ³mert.terzi@iuc.edu.tr

Particle circularity is a measure of the extent to which the shape of a particle resembles a circle. This dimensionless value ranges from 0 to 1, with 1 indicating a perfect circle. The circularity of a particle is calculated from the ratio of the area of the particle projection to its circumference. A rough particle surface leads to low numerical values of the circularity parameter. The particle circularity is one of the most common shape factors used in particle analysis [8, 9]. Roundness is a measure of the extent to which the corners and edges of a particle are eroded. Particle roundness is also an important aspect of particle morphology and is directly related to granular materials' mechanical response and strength [10, 11]. Particle solidity, one of the parameters used to characterize the shape of particles, is a measure of the overall concavity of a particle. It is described as the ratio of a particle's area to its convex body's area. Solidity is a dimensionless value ranging from 0 to 1; 1 indicates a completely hard object with no concavity, while 0 indicates an object with infinite concavity. Solidity is used to evaluate particles' performance and understand their physical properties [12].

Leaching processes play an important role in industries ranging from mining to environmental remediation. The efficiency of leaching processes depends on several factors, including particle size, surface area, and particle shape. While great emphasis has been placed on particle size and surface area, the importance of particle shape in leaching remains a topic of debate and research. One of the key factors affecting leaching kinetics is the surface area of solid particles. It is assumed that particles with larger surface area have more contact with the leaching solution, resulting in faster leaching. However, the role of particle shape complicates this relationship. Irregularly shaped particles may have higher surface areas than spherical particles of similar size, potentially enhancing leaching kinetics.

In contrast, sharp edges and crevices in irregularly shaped particles can impede mass transfer, leading to non-uniform leaching and lower efficiencies. Particle shape can also influence the hydrodynamics of the leaching system, affecting the transport of reactants and products to the particle surface and the distribution of the leach solution around the particles. Irregularly shaped particles can lead to inhomogeneous leaching behavior. Despite advances in modeling and simulation techniques, accurately predicting the behavior of irregularly shaped particles in leaching processes remains a significant challenge [13-16].

The purpose of this study is to understand how the morphology of ore particles impacts the leaching process and to determine how it affects the efficiency when exposed to dilute sulfuric acid (H_2SO_4), hydrochloric acid (HCl), and nitric acid (HNO_3) solutions while optimizing the leaching process by determining the most effective conditions to maximize zinc (Zn) extraction. In this context, controlled leaching experiments with varying parameters were conducted to determine optimum dissolution. Additionally, the effect of particle shape on leaching kinetics was evaluated by microscopy investigations to analyze the circularity, roundness, and solidity factors of sphalerite ore particles. Moreover, the relationship between particle shape and the efficiency of sphalerite dissolution in dilute acid solutions was investigated. Based on the results obtained from this study, the effects of particle shape factor on leaching efficiency were examined to shed light on future studies.

2. Materials and Methods

The representative samples used in this study were taken from Esan Eczacıbaşı Inc. Balya Lead-Zinc plant located in the Balya district of Balıkesir province, Türkiye. First, the number of representative samples weighing approximately 100 kg was reduced using coning-quartering and sample grid methods. Then, the size reduction was performed gradually using a jaw crusher (Baz Machinery, Türkiye). Finally, the samples crushed below 2 mm were ground using a ball mill-sieve closed circuit system to the appropriate size for leaching experiments. An agate mortar (Retsch, RM 200, Germany) was used for sample preparation for elemental analysis and density experiments. Moisture analysis was performed in an oven (Mettler, Uf450) at 105°C to characterize the sample's moisture content. Density experiments were carried out in 50 ml pycnometers using distilled water. Moisture and density analyses were performed according to American Society for Testing and Materials (ASTM) standards. As a result of the experiments, the moisture value was 0.069%, and the density value was 4.89 g/cm³. Particle size analysis was performed using the wet sieving method with the Retsch sieve

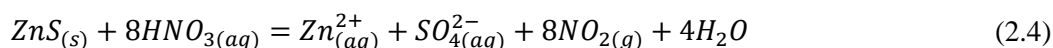
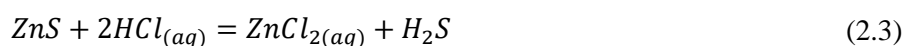
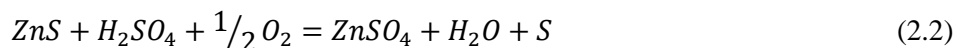
series. According to the results of the particle size analysis of the sample, the d_{10} , d_{50} , and d_{80} dimensions of the sample were found to be 0.21 mm, 1.4 mm, and 3.55 mm, respectively. Inductively coupled plasma optical emission spectroscopy (ICP-OES) analysis revealed that the sample contained 2.14% Zn. ICP-OES analyses were carried out at the Department of Mineral Analysis and Technology, General Directorate of Mineral Research and Exploration.

Within the scope of mineralogical studies, X-Ray Diffraction (XRD) analysis (Rigaku, MiniFlex 600, Japan) was first performed, and it was observed to contain quartz, dolomite, albite, and sphalerite. Sphalerite (ZnS), low amounts of galena (PbS), and trace amounts of pyrite (FeS₂) were observed in the sample within the scope of polished section studies. Galena formations are observed in fractured formations, non-euhedral, and isotropic. Limestone is observed in an anisotropic form as gangue minerals to represent the waste rock. Apart from limestone, iron sulfides are also observed as inclusions in the gangue as small pseudomorphs.

The effect of H₂SO₄, HCl, and HNO₃ leaching processes on the dissolution efficiency of Zn recovery was investigated within the scope of leaching experiments. The pH values were checked periodically during the experiments, and a variation of $< \pm 0.1$ was observed. For the leaching experiments, 98% pure H₂SO₄ (Sigma-Aldrich), 37% pure HCl (Sigma-Aldrich), and 55% pure HNO₃ (Sigma-Aldrich) were used. Solid-liquid separation after leaching experiments was carried out using Whatman (4 μm) filter papers. The leaching tailings obtained after solid-liquid separation were washed with 1% acid solution in 2 stages, and then Zn contents were analyzed by the Inductively coupled plasma mass spectrometry (ICP-MS) method. The dissolution efficiency was calculated according to (2.1):

$$\% \text{ Efficiency} = \frac{\text{Zn (in run - of - mine)} - \text{Zn (in tailings)}}{\text{Zn (in run - of - mine)}} * 100 \quad (2.1)$$

The following reactions (2.2)-(2.4) are thought to occur during leaching processes [17-19]:



In the leaching experiments, the effects of solvent concentration, pulp temperature, solids ratio, dissolution time, and particle size parameters on the dissolution of the sample were examined, and the optimum values for each parameter were determined.

Within the scope of the particle shape factor studies, at least 10 photographs were taken with a digital microscope (IronX). At least 300 data were collected for each run-of-mine sample and the leachate sample to be analyzed for shape factors. The total counted particle number was within the range of previous studies where the particles were counted manually [20].

These photographs were then analyzed through the ImageJ program, and the average values of circularity, roundness, and solidity were determined by the data obtained from all photographs. Then, microscope photographs were taken of the leach samples from the experiments in which the pulp temperature, acid dosage, and leaching time parameters were tested, and the optimum values were determined. The values obtained from the ore sample were compared with those obtained from the leachate samples, interpreted by utilizing the data in Tables 1 and 2, and the effects of changes in particle shapes on dissolution efficiency were revealed.

Table 1. [7] Alternative roundness classification schemes based on Wadell's [21] measurement method

	Russel and Taylor [22]		Pettijohn [23]		Powers [24]		Blott and Pye [7]	
	CL	AM	CL	GM	CL	GM	CL	GM
Very Angular	-	-	-	-	0.12-0.17	0.14	-	-
Angular	0.00-0.15	0.075	0.00-0.15	0.125	0.17-0.25	0.21	0-0.13	0.09
Sub-angular	0.15-0.30	0.225	0.15-0.25	0.200	0.25-0.35	0.30	0.13-0.25	0.18
Sub-rounded	0.30-0.50	0.400	0.25-0.40	0.315	0.35-0.49	0.41	0.25-0.50	0.35
Rounded	0.50-0.70	0.600	0.40-0.60	0.500	0.49-0.70	0.59	0.50-1.00	0.71
Well rounded	0.70-1.00	0.850	0.60-1.00	0.800	0.70-1.00	0.84	-	-

CL: Class limits, AM: Arithmetic Mean, GM: Geometric Mean

Table 2. [7] Proposed classification scheme for particle circularity (when used in two dimensions) or particle sphericity (when applied in three dimensions), measured using the method of Riley [25]

	CL	GM
Very high circularity/sphericity	0.894-1.000	0.949
High circularity/sphericity	0.775-0.894	0.837
Moderate circularity/sphericity	0.632-0.775	0.707
Low circularity/sphericity	0.447-0.632	0.548
Very low circularity/sphericity	0.000-0.447	0.316

3. Results and Discussion

The parameter ranges tested in the leaching experiments, the dissolution efficiencies and the optimum parameters are presented in Table 3. The dissolution efficiencies in the experiments with all three acids were between 92.69% and 97.63%. The final highest dissolution efficiency was obtained in the experiment with H₂SO₄.

Table 3. Data of the leaching experiments

Acid	Experiment	Parameters	Dissolution Efficiency (%)	Optimum Parameter
H ₂ SO ₄	Particle size (µm) (d ₁₀₀)	75, 106, 150	97.12	106
	Solids ratio (%)	5, 10, 15, 20, 25	97.27	15
	Leaching time (min)	30, 60, 90, 120, 180, 240	96.25	120
	Acid dosage (M)	0.25, 0.5, 1, 2, 5	97.63	0.5
	Pulp temperature (°C)	30, 40, 50, 60, 70	97.32	50
HCl	Particle size (µm) (d ₁₀₀)	75, 106, 150	95.59	106
	Solids ratio (%)	5, 10, 15, 20, 25	96.56	25
	Leaching time (min)	30, 60, 90, 120, 180, 240	92.69	60
	Acid dosage (M)	0.25, 0.5, 1, 2, 5	95.90	0.5
	Pulp temperature (°C)	30, 40, 50, 60, 70	96.38	70
HNO ₃	Particle size (µm) (d ₁₀₀)	75, 106, 150	93.24	75
	Solids ratio (%)	5, 10, 15, 20, 25	96.44	20
	Leaching time (min)	30, 60, 90, 120, 180, 240	93.09	60
	Acid dosage (M)	0.25, 0.5, 1, 2, 5	97.21	1
	Pulp temperature (°C)	30, 40, 50, 60, 70	96.06	50

Since the optimum values for the leaching experiments were obtained at particle sizes of 106 µm and 75 µm, firstly, microscope photographs were taken of the samples with these particle sizes (Figure 1). The average particle shape factor value (AV), standard deviation (SD), minimum (Min), and maximum (Max) values for the roundness, circularity, and solidity values of each sample were calculated by performing particle shape factor analysis using ImageJ analysis program (Table 4).

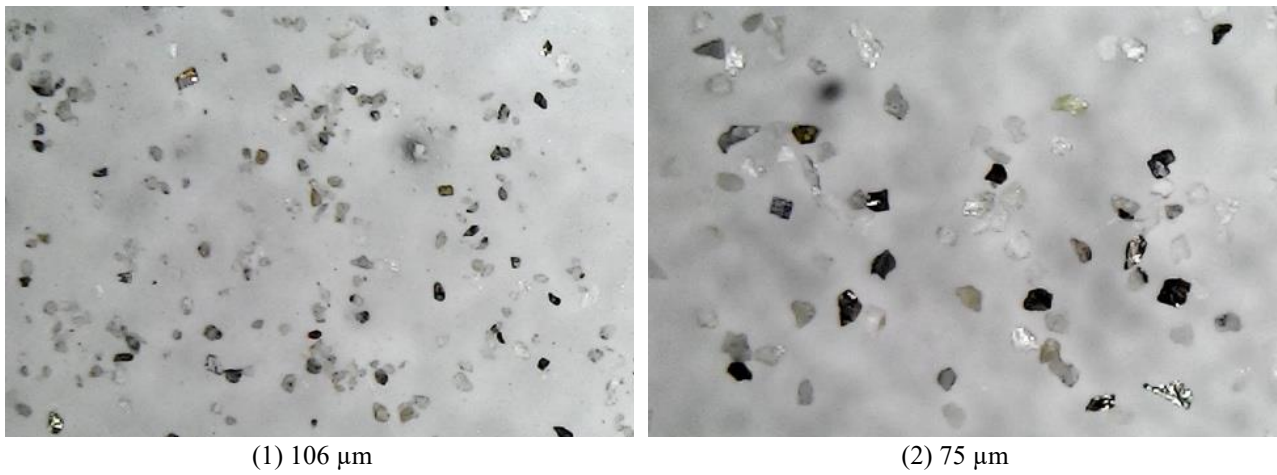


Figure 1. Microscope photographs of the run-of-mine samples

Table 4. Results of ImageJ analysis of run-of-mine samples

	Circularity				Roundness				Solidity			
	AV	SD	Min	Max	AV	SD	Min	Max	AV	SD	Min	Max
(1)	0.633	0.211	0.161	0.998	0.650	0.164	0.162	0.989	0.808	0.101	0.448	0.974
(2)	0.525	0.228	0.086	0.917	0.649	0.171	0.170	0.969	0.776	0.138	0.366	0.952

Subsequently, the leaching residual samples for which optimum values were obtained for the pulp temperature, acid dosage, and leaching time experiments where dissolution efficiencies were examined were photographed, and particle shape factor analysis was performed using the ImageJ analysis program. The AV, SD, Min, and Max values of each sample's roundness, circularity, and solidity values were calculated. The results obtained were compared with the data from the run-of-mine samples, and the effects of particle shape factor on dissolution kinetics were attempted to uncover. Table 5 shows the codes assigned to the samples for each experiment within the scope of particle shape factor studies.

Table 5. The codes assigned to the samples for each experiment within the scope of particle shape factor studies

Sample code	Experiment
Zn _{lt} H ₂ SO ₄	Leaching time (H ₂ SO ₄)
Zn _{ad} H ₂ SO ₄	Acid dosage (H ₂ SO ₄)
Zn _{pt} H ₂ SO ₄	Pulp temperature (H ₂ SO ₄)
Zn _{lt} HCl	Leaching time (HCl)
Zn _{ad} HCl	Acid dosage (HCl)
Zn _{pt} HCl	Pulp temperature (HCl)
Zn _{lt} HNO ₃	Leaching time (HNO ₃)
Zn _{ad} HNO ₃	Acid dosage (HNO ₃)
Zn _{pt} HNO ₃	Pulp temperature (HNO ₃)

The results obtained by photographing the leaching samples (Figure 3, Figure 5, Figure 7) of the optimum values acquired as a result of the tests performed with H₂SO₄, HCl, and HNO₃ at various value ranges for pulp temperature, acid dosage, and leaching time parameters, and analyzing the particle shape factor in ImageJ analysis program were presented in Table 6.

Table 6. ImageJ analysis results of optimum leaching residual samples

	Circularity				Roundness				Solidity			
	AV	SD	Min	Max	AV	SD	Min	Max	AV	SD	Min	Max
Zn _{lt} H ₂ SO ₄	0.613	0.193	0.134	0.914	0.709	0.151	0.286	0.949	0.848	0.083	0.579	0.943
Zn _{ad} H ₂ SO ₄	0.621	0.199	0.168	0.926	0.694	0.151	0.288	0.974	0.821	0.098	0.557	0.953
Zn _{pt} H ₂ SO ₄	0.619	0.222	0.072	0.976	0.687	0.150	0.279	0.981	0.816	0.128	0.321	0.950
Zn _{lt} HCl	0.678	0.180	0.129	0.996	0.671	0.165	0.216	0.995	0.832	0.083	0.330	0.950
Zn _{ad} HCl	0.622	0.219	0.126	0.985	0.639	0.173	0.173	0.977	0.805	0.110	0.439	0.971
Zn _{pt} HCl	0.605	0.226	0.121	0.988	0.648	0.170	0.059	0.989	0.790	0.123	0.363	0.967
Zn _{lt} HNO ₃	0.607	0.219	0.139	0.976	0.662	0.160	0.168	0.977	0.808	0.119	0.407	0.947
Zn _{ad} HNO ₃	0.669	0.213	0.107	0.990	0.674	0.167	0.191	0.978	0.834	0.110	0.341	0.968
Zn _{pt} HNO ₃	0.620	0.212	0.142	0.994	0.649	0.162	0.200	0.984	0.795	0.103	0.327	0.952

3.1. Investigation of Leaching Residues of Experiments Performed with H₂SO₄

ImageJ analyses of the optimum leaching residual samples are shown in Figure 2; optical microscope photographs and ImageJ outputs are seen in Figure 3.

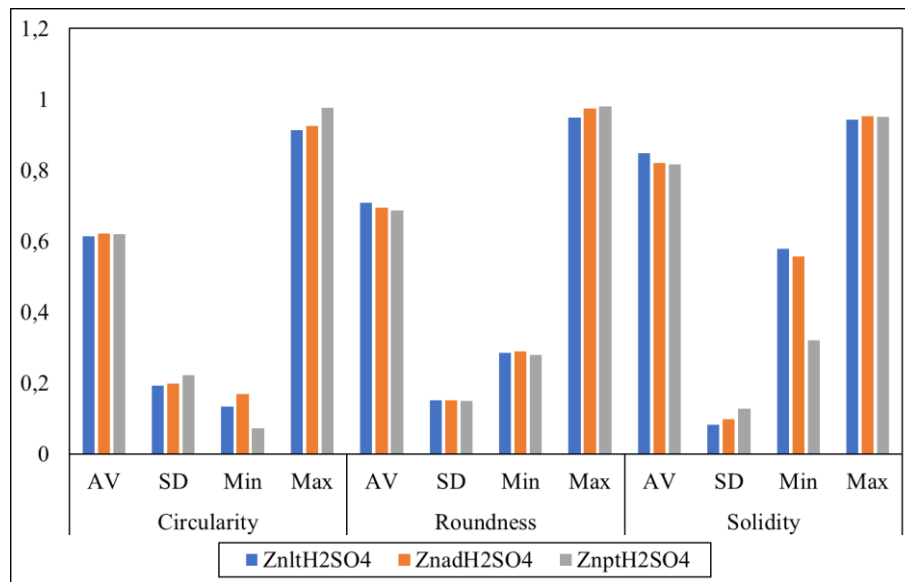


Figure 2. ImageJ analysis results of optimum leaching residual samples (Leaching time: 120 min, Acid dosage: 0.5 M, Pulp temperature: 50 °C)

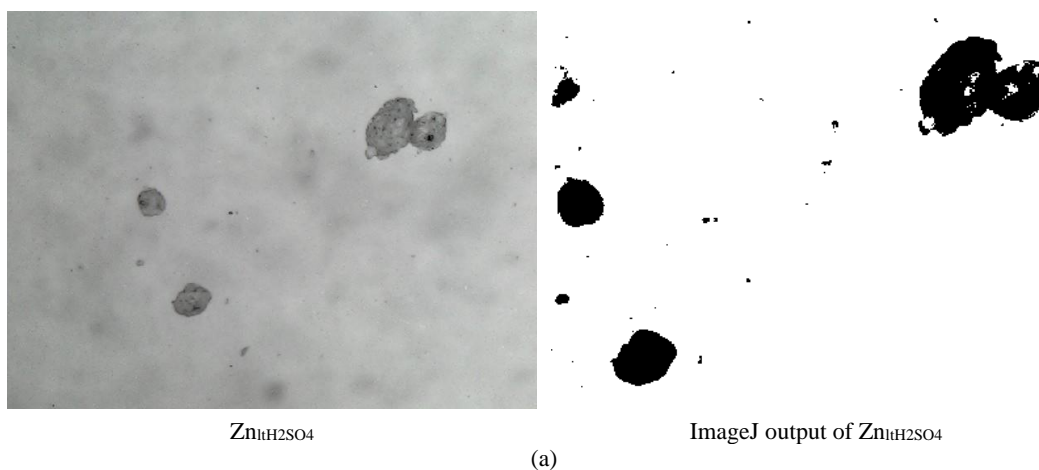


Figure 3. Optical microscope photographs and ImageJ outputs of (a) Zn_{lt}H₂SO₄, (b) Zn_{ad}H₂SO₄, and (c) Zn_{pt}H₂SO₄

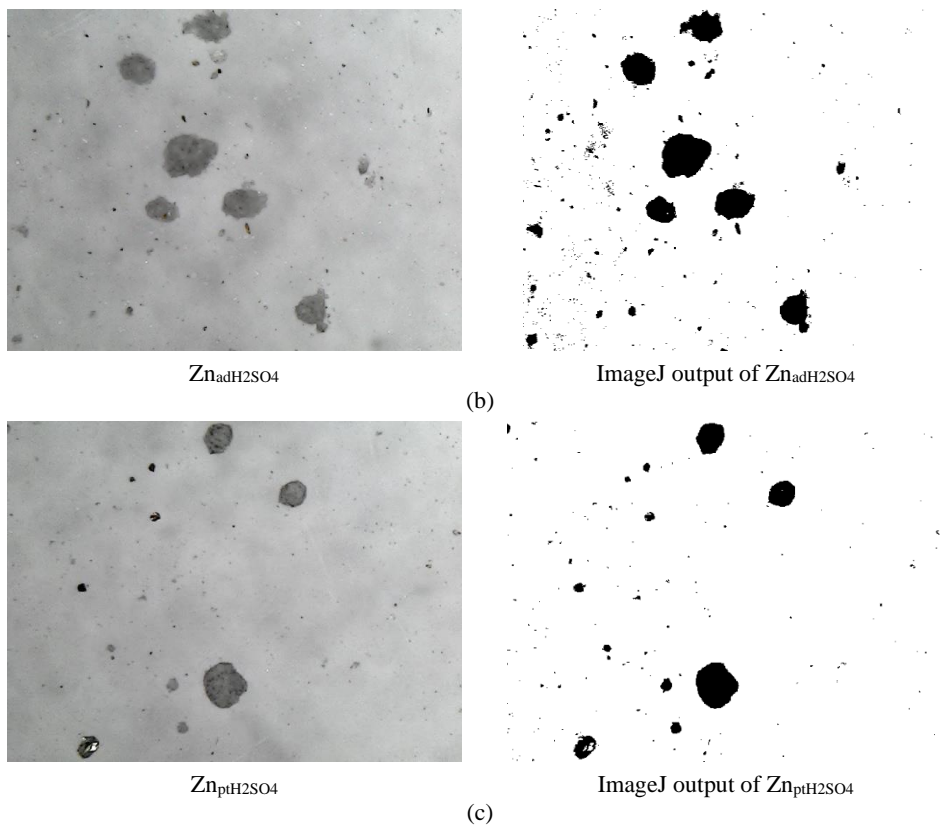


Figure 3. (Continued) Optical microscope photographs and ImageJ outputs of (a) $Zn_{ad}H_2SO_4$, (b) $Zn_{ad}H_2SO_4$, and (c) $Zn_{pt}H_2SO_4$

As a result of H_2SO_4 leaching, circularity values of all three samples decreased, while roundness and solidity values increased. According to the circularity values given in Table 2, all three samples were within the "low circularity" class limit. According to the roundness values given in Table 1, it was observed that the $Zn_{ad}H_2SO_4$ sample belonged to the "well-rounded" class limit according to Russel and Taylor [22], Powers [24], and Pettijohn [23] and to the "rounded" class limit according to Blott and Pye [7]. $Zn_{ad}H_2SO_4$ and $Zn_{pt}H_2SO_4$ samples were found to be within the "rounded" class limit according to Russel and Taylor [22], Powers [24], and Blott and Pye [7], and within the "well rounded" class limit according to Pettijohn [23].

3.2. Investigation of Leaching Residues of Experiments Performed with HCl

ImageJ analysis results of the optimum leaching residual samples are given in Figure 4, and optical microscope photographs and ImageJ outputs are seen in Figure 5.

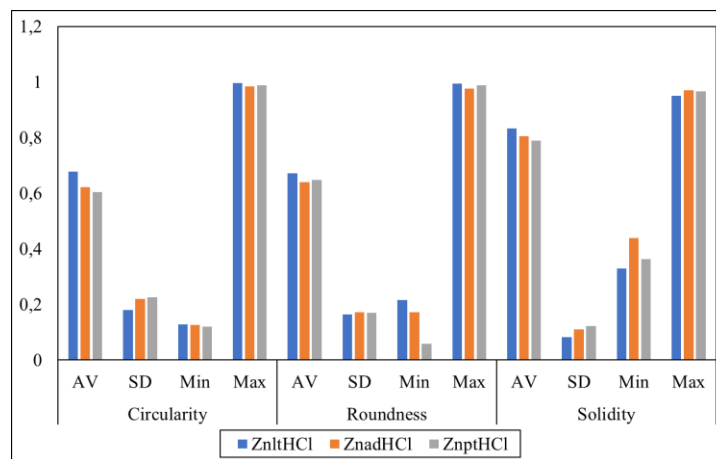


Figure 4. ImageJ analysis results of optimum leaching residual samples (Leaching time: 60 min, Acid dosage: 0.5 M, Pulp temperature: 70 °C)

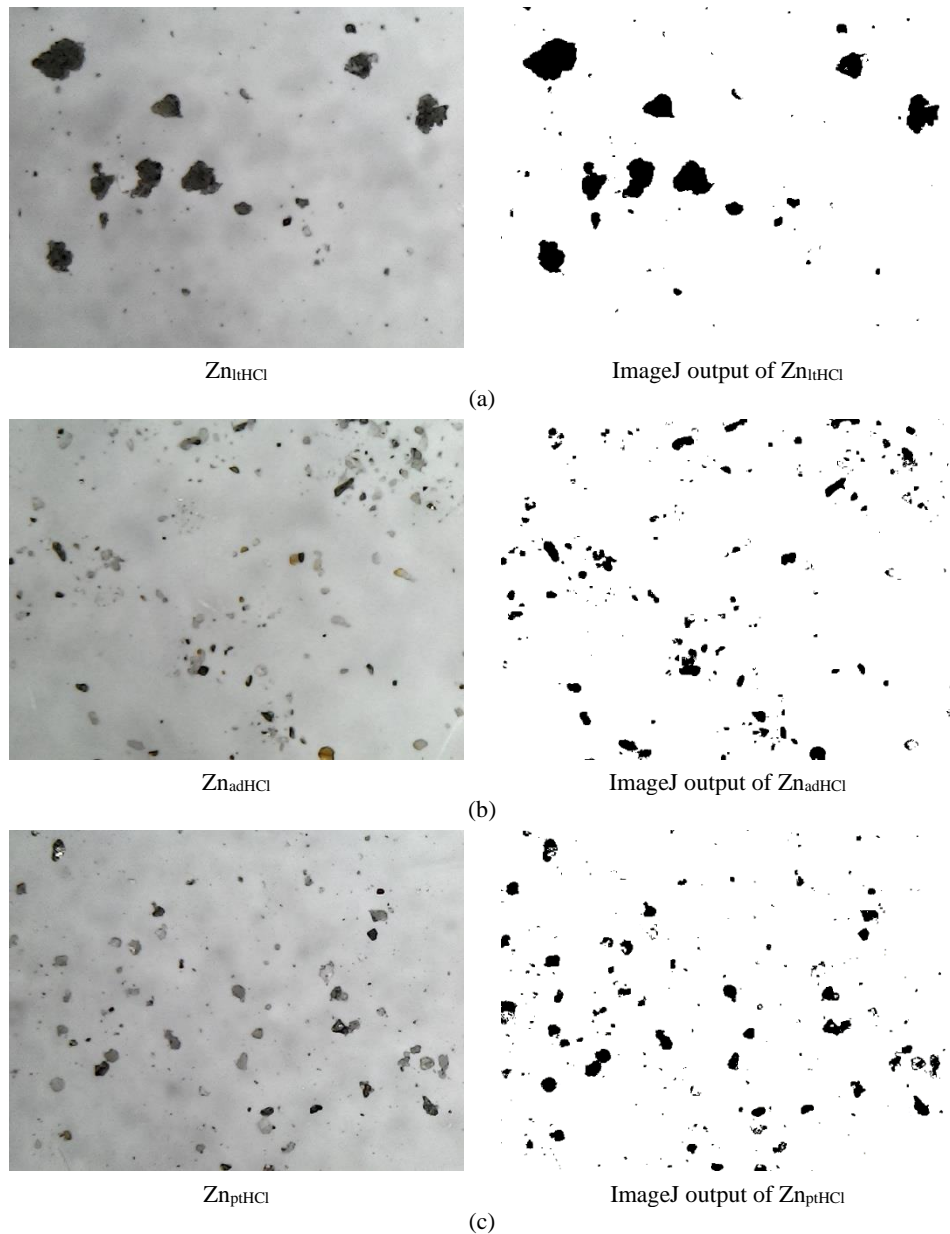


Figure 5. Optical microscope photographs and ImageJ outputs of (a) Zn_{1HCl} , (b) Zn_{adHCl} , and (c) Zn_{ptHCl}

It was noticed that the circularity values of each of the three samples increased due to HCl leaching. While the roundness value of Zn_{1HCl} increased, the roundness values of Zn_{adHCl} and Zn_{ptHCl} decreased. When the solidity values were analyzed, it was noticed that the solidity values of all three specimens significantly increased. According to the circularity values given in Table 2, the Zn_{1HCl} sample was within the "moderate circularity" class limit, and the Zn_{adHCl} and Zn_{ptHCl} samples were within the "low circularity" class limits. According to the roundness values given in Table 1, it was found that Zn_{1HCl} , Zn_{adHCl} , and Zn_{ptHCl} samples were included in the "rounded" class limit according to Russel and Taylor [22], Powers [24], and Blott and Pye [7], and in the "well rounded" class limit according to Pettijohn [23].

3.3. Investigation of Leaching Residues of Experiments Performed with HNO_3

ImageJ analysis results of the optimum leaching residual samples are shown in Figure 6, and optical microscope photographs and ImageJ outputs are seen in Figure 7.

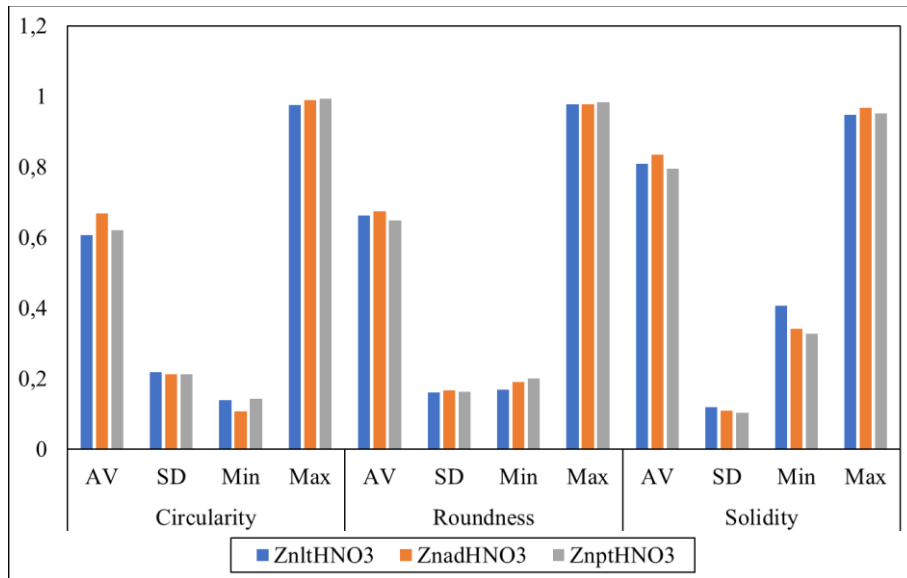


Figure 6. ImageJ analysis results of optimum leaching residual samples (Leaching time: 60 min, Acid dosage: 1 M, Pulp temperature: 50 °C)

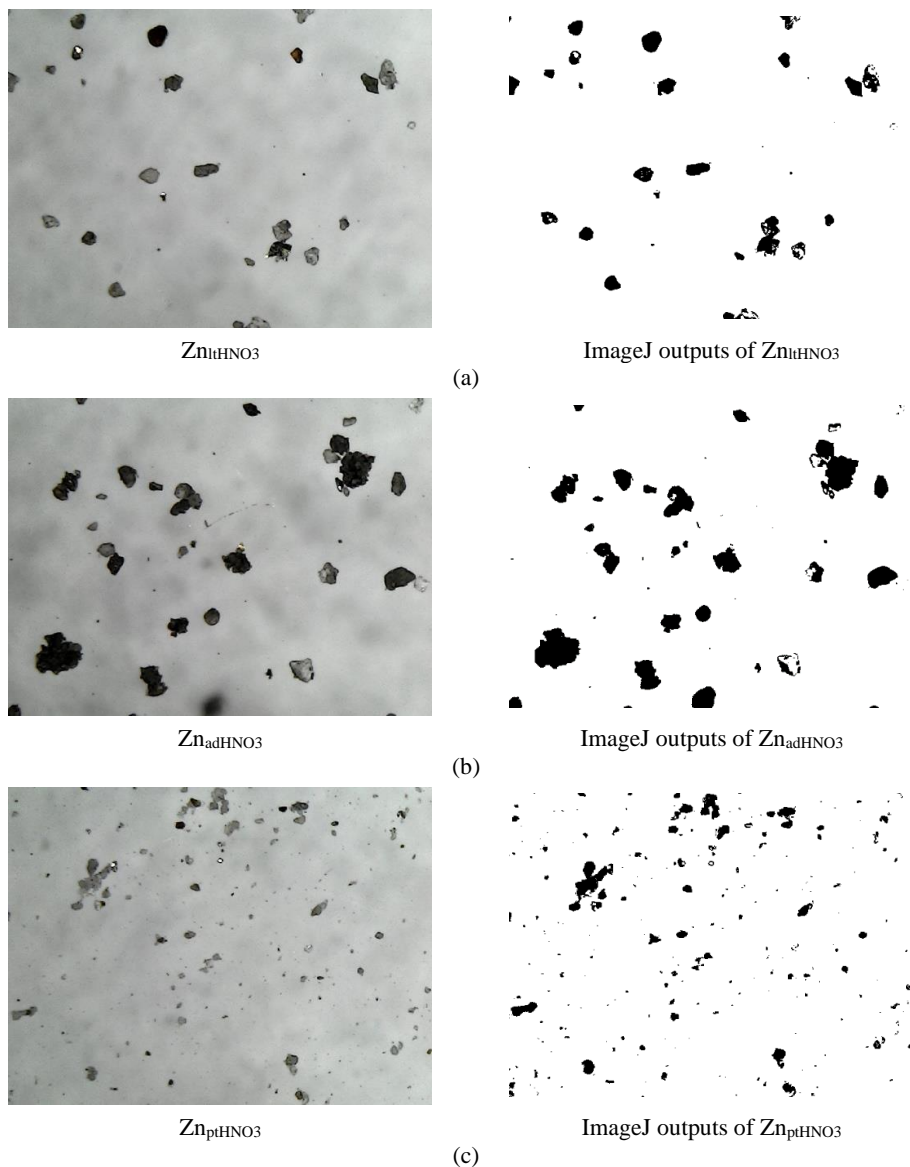


Figure 7. Optical microscope photographs and ImageJ outputs of (a) $Zn_{lt}HNO_3$, (b) $Zn_{ad}HNO_3$, and (c) $Zn_{pt}HNO_3$

As a result of HNO₃ leaching, the circularity values of the Zn_{liHNO₃} and Zn_{ptHNO₃} samples decreased, but the circularity value of the Zn_{adHNO₃} sample increased. Whereas the roundness values of Zn_{liHNO₃} and Zn_{adHNO₃} samples increased, the roundness value of Zn_{ptHNO₃} sample decreased. The solidity value of the Zn_{liHNO₃} sample had a stable value, but the Zn_{adHNO₃} sample had an increased solidity value, and the Zn_{ptHNO₃} sample had a decreased solidity value. According to the circularity values given in Table 2, it was seen that Zn_{liHNO₃} and Zn_{ptHNO₃} samples were in the range of "low circularity" class limits, and the Zn_{adHNO₃} sample was in the range of "moderate circularity" class limit. According to the roundness values given in Table 1, it was observed that Zn_{liHNO₃}, Zn_{adHNO₃}, and Zn_{ptHNO₃} samples were within the "rounded" class limit according to Russel and Taylor [22], Powers [24], and Blott and Pye [7], and within the "well rounded" class limit according to Pettijohn [23]. The results of the particle shape factor studies are summarized in Table 7.

Table 7. The summary of particle shape factor studies

Experiment	Circularity	Roundness	Solidity	Based on Table 2	Russel and Taylor [22]	Pettijohn [23]	Powers [24]	Blott and Pye [7]
Zn _{liH₂SO₄}	Decreased	Increased	Increased	Low circularity	Well rounded	Well rounded	Well rounded	Rounded
Zn _{adH₂SO₄}	Decreased	Increased	Increased	Low circularity	Rounded	Well rounded	Rounded	Rounded
Zn _{ptH₂SO₄}	Decreased	Increased	Increased	Low circularity	Rounded	Well rounded	Rounded	Rounded
Zn _{liHCl}	Increased	Increased	Increased	Moderate circularity	Rounded	Well rounded	Rounded	Rounded
Zn _{adHCl}	Increased	Decreased	Increased	Low circularity	Rounded	Well rounded	Rounded	Rounded
Zn _{ptHCl}	Increased	Decreased	Increased	Low circularity	Rounded	Well rounded	Rounded	Rounded
Zn _{liHNO₃}	Decreased	Increased	Stable	Low circularity	Rounded	Well rounded	Rounded	Rounded
Zn _{adHNO₃}	Increased	Increased	Increased	Moderate circularity	Rounded	Well rounded	Rounded	Rounded
Zn _{ptHNO₃}	Decreased	Decreased	Decreased	Low circularity	Rounded	Well rounded	Rounded	Rounded

Sulfuric acid, hydrochloric acid, and nitric acid all belong to strong mineral acids. Despite differences in their chemical structures and properties, they share common functional groups (sulfonic, chloride, and nitrate groups, respectively) [26-28]. These functional groups probably determine similar interactions with the metal ore during dissolution, leading to comparable shape parameters. However, sulfuric, hydrochloric, and nitric acid's high reactivities can facilitate similar chemical processes during ore dissolution, resulting in dissolution residues with similar shapes and properties. This is due to these acids' strong oxidizing and complexing abilities, which enable them to effectively break down and dissolve various minerals and ore [29-35]. In this study, particle shape's effect on dissolution was observed in a limited manner due to the complex structure of the material. Therefore, it is recommended to carry out experimental studies on pure selected particles to eliminate the effect of heterogeneity in future studies.

The particle shape factor can influence the leaching mechanisms. For example, in the study by Ghorbani et al. on the progression of zinc leaching from large sphalerite ore particles, the authors found that the leaching mechanisms differed significantly between particles with different shapes. They observed that leaching from large particles led to near complete conversion near the surface but only partial conversion in the zones closer to the center of the particles. This suggests that the particle shape can influence the distribution of leaching agents and the reaction rates within the particles [36]. Another research study emphasized the significant role of particle shape in influencing transient fluid flow dynamics during particle adsorption and dispersion. This was highlighted through Particle Image Velocimetry (PIV) measurements, suggesting that different particle shapes could lead to varied fluid flow dynamics around the particles, which might influence the leaching rates and efficiencies [37]. This could be particularly relevant in processes where the interface between the particle surface and the leachate solution critically determines the overall reaction kinetics. This research highlights the importance of particle shape in Zn leaching experiments and suggests that further investigation is needed

to understand its full implications for advanced plant applications. By investigating the effects of particle shape on dissolution efficiencies in zinc recovery through acid leaching, the study sheds light on an aspect of mineral processing that has not been extensively explored. By analyzing microscope images of leaching residues and comparing them with ore samples, the study provides insights into the impact of particle circularity, roundness, and solidity on dissolution efficiencies. This understanding can guide future research in particle morphology and its influence on various processes.

4. Conclusion

Particle roundness, circularity, and solidity can impact ore beneficiation processes, as they can affect particulate materials' behavior and the particles' surface properties. The decrease in particle roundness is thought to cause the particles to rotate less despite a higher displacement value, as stated in [38]. The study's findings supported the relationship between more spherical particles, shorter disintegration time and higher dissolution rate [39]. This is because, as stated in [40], it is thought that the specific surface area of the particle increases with decreasing particle size, leading to an increase in the dissolution rate. From these, it can be concluded that circularity may indirectly affect dissolution efficiency through its effect on particle size and surface area. Particle circularity and solidity can affect the homogeneity and quality of the final product. Particle solidity can significantly impact leaching by affecting the rate of chemical reactions, permeability, and infiltration.

Since particle morphology is still poorly understood to evaluate the success of chemical dissolution and intergranular interactions, it is necessary to identify, model, and determine the mechanisms affecting dissolution through various measurements in combination with chemical dissolution experiments and dissolution kinetics analysis. Although there is a wide range of shape factors, the main purpose of prioritizing the roundness, circularity, and solidity values in this study is to search the effect of particle shape on chemical dissolution processes by considering the changes in these values. When the results obtained were analyzed, it was seen that changes in particle shape could be a control factor in Zn leaching experiments. The study established the relationship between particle shape and leaching efficiency in a limited manner. It is recommended to carry out experimental studies on pure selected particles in milder conditions in order to eliminate the effect of heterogeneity and to see the particle-specific effects more clearly in future studies, as particle morphology is a process that still requires further research and development for advanced plant applications.

Author Contributions

The first author contributed to the experimental studies and writing of the manuscript. The second author contributed to the design of experimental studies, manuscript writing, and interpretation of findings. The third author contributed to the writing of the manuscript and interpretation of the findings. All authors read and approved the final version of the paper.

Conflicts of Interest

All the authors declare no conflict of interest.

Ethical Review and Approval

No approval from the Board of Ethics is required.

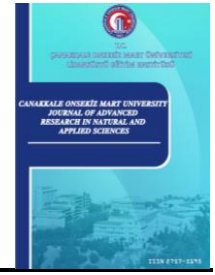
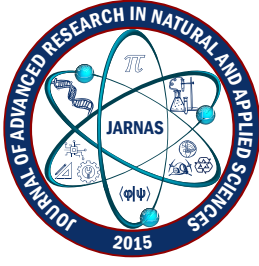
References

- [1] Z. Lu, X. Hu, Y. Lu, *Particle morphology analysis of biomass material based on improved image*

- processing method*, International Journal of Analytical Chemistry Special issue (2017) Article ID 5840690 9 pages.
- [2] Upstate Medical University, Particle Morphology (2018), http://www.upstate.edu/pathenvi/basics/particle_morphology.php, Accessed 30 Jan 2018.
- [3] Chulalongkorn University, Particle Morphology (2018), http://www.geo.sc.chula.ac.th/courses/2307223/2307223_02-particle_morphology.pdf, Accessed 30 Jan 2018.
- [4] A. R. Yudhbir, *Quantification of particle shape and angularity using the image analyzer*, Geotechnical Testing Journal 14 (3) (1991) 296–308.
- [5] E. T. Bowman, K. Soga, T. W. Drummond, *Particle shape characterisation using Fourier Analysis*, Géotechnique 51 (6) (2001) 545–554.
- [6] M. Uzuntaş, *Investigation of crusher type effect on the particle shape by image analysis method*, Master's Thesis Eskişehir Osmangazi University (2007) Eskişehir.
- [7] S. J. Blott, K. Pye, *Particle shape: a review and new methods of characterization and classification*, Sedimentology 55 (1) (2008) 31–63.
- [8] J. R. Grace, A. Ebneyamini, *Connecting particle sphericity and circularity*, Particuology 54 (2021) 1–4.
- [9] U. Ulusoy, H. Kurşun, İ. Erdoğan, *Statistical significance testing of the particle circularity values from various products of sphalerite column flotation beneficiation with ultrasonic pretreatment*, in: A. İşman, Ş. Dündar (Eds.), International Science and Technology Conference, Berlin, 2017, pp.524–539.
- [10] N. Roy, P. Vangla, J. D. Frost, G. M. Latha, *An enhanced automated particle angularity measurement method*, Journal of Testing and Evaluation 50 (2) (2021) 1060–1078.
- [11] W. Wang, L. Xu, Z. Liu, R. Huang, Y. Lai, Y. Liu, D. Ruping, *Comparison and application of three quantitative methods to describe sedimentary particle shapes*, Geological Review (3) (2013) 553–562.
- [12] L. E. Liem, D. Smith, S. J. Stanley, *Particle reduction study of flocculation mixing by means of grids*, Canadian Journal of Civil Engineering 26 (1999) 251–261.
- [13] F. Faraji, A. Alizadeh, F. Rashchi, N. Mostoufi, *Kinetics of leaching: A review*, Reviews in Chemical Engineering 38 (2) (2022) 113–148.
- [14] Y. Ghorbani, M. Becker, A. Mainza, J. P. Franzidis, J. Petersen, *Large particle effects in chemical/biochemical heap leach processes – A review*, Minerals Engineering 24 (11) (2011) 1172–1184.
- [15] Y. Li, N. Kawashima, J. Li, A. P. Chandra, A. R. Gerson, *A review of the structure, and fundamental mechanisms and kinetics of the leaching of chalcopyrite*, Advances in Colloid and Interface Science 197–198 (2013) 1–32.
- [16] J. MacCarthy, A. Nosrati, W. Skinner, J. Addai-Mensah, *Effect of mineralogy and temperature on atmospheric acid leaching and rheological behaviour of model oxide and clay mineral dispersions*, Powder Technology 286 (2015) 420–430.
- [17] A. A. Baba, F. A. Adekola, *Hydrometallurgical processing of a Nigerian sphalerite in hydrochloric acid: Characterization and dissolution kinetics*, Hydrometallurgy 101 (2010) 69–75.
- [18] M. Çopur, *Solubility of ZnS concentrate containing pyrite and chalcopyrite in HNO₃ solutions*, Chemical and Biochemical Engineering Quarterly 15 (4) (2001) 181–184.
- [19] R. J. Jan, M. T. Hepworth, V. G. Fox, *A kinetic study on the pressure leaching of sphalerite*, Metallurgical Transactions B 7B (1976) 353–361.
- [20] W. Yin, Z. Zhu, B. Yang, Y. Fu, J. Yao, *Contribution of particle shape and surface roughness on the*

- flotation behavior of low-ash coking coal*, Energy Sources, Part A: Recovery, Utilization, and Environmental Effects, 41 (5) (2019) 636–644.
- [21] H. Wadell, *Volume, shape, and roundness of rock particles*, The Journal of Geology 40 (5) (1932) 443–451.
- [22] R. D. Russell, R. E. Taylor, *Roundness and shape of Mississippi River sands*, The Journal of Geology 45 (3) (1937) 225–267.
- [23] F. J. Pettijohn, *Sedimentary rocks*, Harper and Brothers, New York, 1949.
- [24] M. C. Powers, *A new roundness scale for sedimentary particles*, Journal of Sedimentary Research 23 (1953) 117–119.
- [25] N. A. Riley, *Projection sphericity*, Journal of Sedimentary Research 11 (2) (1941) 94–97.
- [26] O. M. Longworth, C. J. Bready, M. S. Joines, G. C. Shields, *The driving effects of common atmospheric molecules for formation of clusters: The case of sulfuric acid, nitric acid, hydrochloric acid, ammonia, and dimethylamine*, Environmental Science: Atmospheres 3 (2023) 1335–1351.
- [27] C. Tsau, P. Lee, *Microstructures of Al_{7.5}Cr_{22.5}Fe₃₅Mn₂₀Ni₁₅ high-entropy alloy and its polarization behaviors in sulfuric acid, nitric acid and hydrochloric acid solutions*, Entropy 18 (8) (2016) 288 12 pages.
- [28] F. E. Critchfield, J. B. Johnson, *Differential, alkalimetric determination of sulfuric acid-hydrochloric acid and sulfuric acid-nitric acid mixtures*, Analytical Chemistry 26 (1954) 1803–1806.
- [29] A. V. Dubenko, M. V. Nikolenko, O. Pasenko, A. Kostyniuk, B. Likozar, *Intensification of sulfuric acid leaching of altered ilmenite via adding fluoride activator*, Processes 9 (11) (2021) 1922 16 pages.
- [30] Y. Mubarak, *Kinetics of hydrochloric acid leaching of copper from its ore*, International Journal of Emerging Trends in Engineering Research 8 (9) (2020) 5006–5015.
- [31] A. Mukhachev, D. Yelatontsev, O. A. Kharitonova, *Physical and chemical foundations of the extraction refining of natural uranium*, Problems of Atomic Science and Technology 53 (25) (2022) 106–110.
- [32] S. Teimouri, J. H. Potgieter, L. van Dyk, C. Billing, *The kinetics of pyrite dissolution in nitric acid solution*, Materials 15 (12) (2022) 4181 19 pages.
- [33] A. Azizi, S. M. Ghasemi, *A comparative analysis of the dissolution kinetics of lead from low grade oxide ores in HCl, H₂SO₄, HNO₃ and citric acid solutions*, Revue De Metallurgie-cahiers D Informations Techniques 114 (4) (2017) 406 12 pages.
- [34] S. M. Ghasemi, A. Azizi, *Investigation of leaching kinetics of zinc from a low-grade ore in organic and inorganic acids*, I Journal of Mining and Environment 8 (2016) 579–591.
- [35] B. E. Widyanto, S. W. Putri, *Corrosion behavior of ASTM A1008 carbon steel in mixtures of HNO₃, H₂SO₄, and HCl using immersion and polarization methods*, Materials Transactions 60 (15) (2019) 732–736.
- [36] Y. Ghorbani, J. Petersen, M. Becker, A. N. Mainza, J. P. Franzidis, *Investigation and modelling of the progression of zinc leaching from large sphalerite ore particles*, Hydrometallurgy 131-132 (2013) 8–23.
- [37] N. A. Musunuri, P. Singh, I. S. Fischer, *PIV measurement of the transient fluid flow due to the adsorption of particles*, ASME 2014 4th Joint US-European Fluids Engineering Division Summer Meeting collocated with the ASME 2014 12th International Conference on Nanochannels, Microchannels, and Minichannels, Chicago, 2014, 10 pages.
- [38] M. Wu, L. Xiong, J. Wang, *DEM study on effect of particle roundness on biaxial shearing of sand*, Underground Space 6 (6) (2021) 678–694.

- [39] J. Li, Z. Wang, H. Xiu, X. Zhao, F. Ma, L. Liu, C. Yi, M. Zhang, E. Kozliak, Y. Ji, *Correlation between the powder characteristics and particle morphology of microcrystalline cellulose (MCC) and its tablet application performance*, Powder Technology 39 (2022) 117194 13 pages.
- [40] K. R. Chu, E. Lee, S. H. Jeong, E. S. Park, *Effect of particle size on the dissolution behaviors of poorly water-soluble drugs*, Archives of Pharmacal Research 35 (2012) 1187–1195.



Seismic Risk Evaluation of Existing Reinforced Concrete Buildings: A Case Study for Çanakkale-Türkiye

Muhammed Benek¹ , Selen Aktan² 

¹Department of Risk Management of Natural Disasters, School of Graduate Studies, Çanakkale Onsekiz Mart University, Çanakkale, Türkiye

^{2,3}Department of Civil Engineering, Faculty of Engineering, Çanakkale Onsekiz Mart University, Çanakkale, Türkiye

Article Info

Received: 09 Apr 2024

Accepted: 02 Jul 2024

Published: 30 Sep 2024

Research Article

Abstract – Türkiye is in an important earthquake zone, and most of the population is under seismic hazard. The high loss of lives in the past earthquakes indicates that our existing building stock is vulnerable. In this study, a field survey was carried out to determine the existing earthquake risks of reinforced concrete buildings in İsmetpaşa, Barbaros, Cevatpaşa, Kemalpaşa, Namikkemal, Esenler, and Fevzipaşa Neighborhoods of Çanakkale city center. This study was conducted to specify the regional distribution of risky buildings to be examined by the street survey method called "Simplified methods that can be used to determine the regional risk distribution of buildings" in the implementation regulation of Law No. 6306. For this purpose, 585 reinforced concrete buildings were examined with this method, and the earthquake performance scores of these buildings were determined. The performance scores calculated as a result of reflecting the number of stories, earthquake hazard zone, type of structural system, and structural irregularities of the buildings were evaluated based on different parameters. It was seen that soft stories with values ranging from 50% to 100% and heavy overhangs with values ranging from 37% to 63% were the most common irregularities in existing buildings in Çanakkale.

Keywords – Çanakkale, seismic risk, Law no. 6306, street survey method, building stock

1. Introduction

Just as many destructive earthquakes have occurred in our country in the past, it is known that such severe earthquakes will occur in a wide area in the future. Buildings to be constructed in earthquake-risk areas must be highly earthquake-resistant and in accordance with current earthquake codes. In addition, the existing structures need to be strengthened or demolished and rebuilt to ensure earthquake safety and avoid the loss of life.

To reveal the collapse risk of a building, it is necessary first to determine the soil and material parameters; then model and analyze the structure. However, determining the earthquake safety of various buildings is time-consuming and expensive. For this reason, the necessity of determining the situation with applicable and realistic approaches arises. It is considered a reasonable approach to use gradual assessment methods, which are done in developed countries that are vulnerable to similar risks, such as earthquakes [1]. There are evaluation methods developed by America and Japan [2-6]. The incompatibilities between the project area and parameters, such as the building stock in these countries and the seismic characteristics of the area to be investigated, require the adaptation of these methods [1]. Studies have been carried out by examining these

¹muhammed_benek84@hotmail.com; ²saktan@comu.edu.tr (Corresponding Author)

methods and presenting new methods in Türkiye to determine the earthquake resistance of existing buildings in recent years [7-23]. In the studies [7, 11, 14], the authors presented a simplified method of ranking low to mid-rise, monolithic reinforced concrete (RC) buildings according to their vulnerability to seismic damage. Ersoy and Özcebe [8] presented the research carried out by Middle East Technical University related to seismic rehabilitation emphasizing infilled frames, a system extensively used in Türkiye. In the studies [9, 15], the authors developed a computer program using the DURTES algorithm to analyze existing structures' earthquake risk. Ilki et al. [10] applied the first stage of the seismic index method on 4 buildings located in Istanbul and Izmit. In the studies [12, 17, 18], the authors proposed a two-level risk assessment procedure in which the first level is based on recording building parameters from the street, and in the second level, these are extended by structural parameters measured by entering the ground story. In the studies [13, 19, 21], the authors presented an assessment method to rapidly scan existing buildings to prevent loss of life in an earthquake. Boduroğlu and Çağlayan [16] developed a rapid screening method called the Seismic Safety Screening Method, an adaptation of the Japanese Seismic Index Method. Inel et al. [20] carried out a seismic risk assessment for a typical mid-size city based on building inventory from a field study. Özçelik et al. [22] discussed the details of the "multiple decision tree" method used to prioritize buildings in terms of risks. Köksal and Yıldız [23] conducted a sampling study in 54 buildings to estimate the possibility of physical damage. These studies have contributed to creating forms and methods for evaluating existing buildings in our country.

The existence of natural disasters, especially earthquakes, and the state of the existing building stock have made it necessary to initiate the urban transformation process. In this context, Law No. 6306, The Transformation of Areas Under Disaster Risk [24], was published in 2012. The law contains methods and principles for transforming buildings, either on an individual building basis or collectively on an area basis. A section in the law allows risk prioritization in areas containing a significant number of buildings and the examination of the buildings in areas with high-risk priorities according to the results. This section, titled "Simplified methods that can be used to determine the regional risk distribution of buildings," is referred to as Appendix A in the study. After the law was published, some studies using the method were carried out [25-29]. This study is the first and most comprehensive study conducted for Çanakkale.

In this article, after mentioning the previous studies in this field, information about the earthquake risk of the study area was given. The method parameters in the law were introduced, and the works carried out in the study area were explained. Finally, it was evaluated how the results of this method could be used by interpreting the obtained data.

2. Materials and Methods

This section presents the basic definitions needed in the method in the Appendix-A of Law No. 6306 [24].

2.1. Earthquake Hazard of the Study Area

Çanakkale is in the western part of Türkiye, as seen in Figure 1. In the figure, the black frame indicates the maximum ground acceleration values of Çanakkale Province in the earthquake hazard map [30]. The maximum acceleration value of 475-year Çanakkale Province is in the range of 0.3-0.7. These values show that the seismicity of the region is very high.

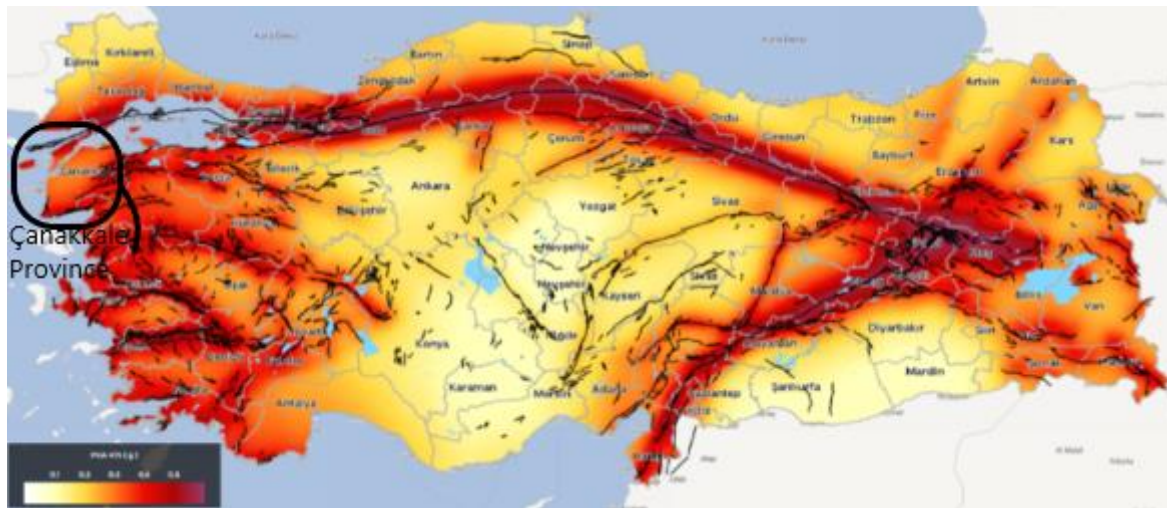


Figure 1. Türkiye earthquake hazard map [30]

The surface area of the central district of Çanakkale is about 94900 hectares. Figure 2 specifies the borders of the study area.



Figure 2. Satellite image of the study area [31]

Fault lines, each extending 50-100 km from Çanakkale city center and causing earthquakes at certain periods, threaten the city. Local conditions that may cause an increase in the earthquake effect in the city center can be listed as follows: high groundwater levels, liquefaction problems, and coastal areas consisting of filled areas.

Saroz-Gaziköy, Etili, Çan-Biga Zone, Sarıköy, and Yenice-Gönen Fractures located around Çanakkale are known as active faults due to the earthquakes they caused [32]. Many earthquakes of different magnitudes have been recorded where the Saros-Gaziköy Fault is located. Among these earthquakes, the most destructive was the Şarköy-Mürefte earthquake in 1912, with a magnitude of $M_S = 7.4$. An earthquake of magnitude $M_S=6.4$ was recorded in the Çan-Biga Fault Zone in 1935. The Yenice-Gönen Fault is one of the Biga Peninsula's most important active tectonic structures. On March 18, 1953, a destructive earthquake ($M_W=7.2$) occurred on this fault, considered part of the southern branch of the North Anatolian Fault Zone [33]. Four moderate size earthquakes hit Ayvacık district of Çanakkale Province on February 6, 2017, $M_W=5.2$ and $M_W=5.1$, February 7, 2017, $M_W=5.2$, February 12, 2017, $M_W=5.3$ [34]. In addition, the $M_W=6.9$ earthquake occurred on May 24, 2014, in the west of Gökçeada Island, in the northern Aegean Sea, and the earthquake caused moderate damage to about 300 buildings (50 of them in Çanakkale city and 200 of them located in Gökçeada Island) [35]. The North Aegean Sea earthquake with a magnitude of $M_W=5.7$, which occurred on January 8, 2013, and with a magnitude of $M_L= 5.3$, which occurred on July 30, 2013, were the earthquakes felt

in Çanakkale. Finally, the Tartışık-Ayvacic earthquake with a magnitude of $M_w=5.0$ on February 20, 2019, the Beypınar Lapseki earthquake with a magnitude of $M_L=4.5$ on February 27, 2024, and the Karasu Yenice earthquake with a magnitude of $M_L=4.9$ on March 4, 2024, shows that earthquakes occur frequently in this region. These earthquakes are shown in Table 1.

Table 1. Earthquakes in the region

Date	Magnitude	Location
09.08.1912	$M_S=7.4$	Şarköy-Mürefte
10.08.1912	$M_S=6.2$	Şarköy-Mürefte
10.08.1912	$M_S=5.3$	Şarköy-Mürefte
04.01.1935	$M_S=6.4$	Çan –Biga zone
18.03.1953	$M_w=7.2$	Yenice-Gönen
08.01.2013	$M_w=5.7$	North Aegean Sea
30.07.2013	$M_L=5.3$	North Aegean
24.05.2014	$M_w=6.9$	Aegean Sea
06.02.2017	$M_w=5.2$	Ayvacic
06.02.2017	$M_w=5.1$	Ayvacic
07.02.2017	$M_w=5.2$	Ayvacic
12.02.2017	$M_w=5.3$	Ayvacic
20.02.2019	$M_w=5.0$	Tartışık-Ayvacic
27.02.2024	$M_L=4.5$	Beypınar-Lapseki
04.03.2024	$M_L=4.9$	Karasu-Yenice

2.2. Parameters of the Method

The parameters required in the evaluation method for RC buildings in Appendix-A are as follows: type of structural system, number of stories, apparent quality, soft or weak story, vertical irregularity, heavy overhangs, irregularity in plan torsion, short column, building adjacency, topographic effects, and local soil conditions. These parameters for each building can be determined with approximately 15 minutes of street survey.

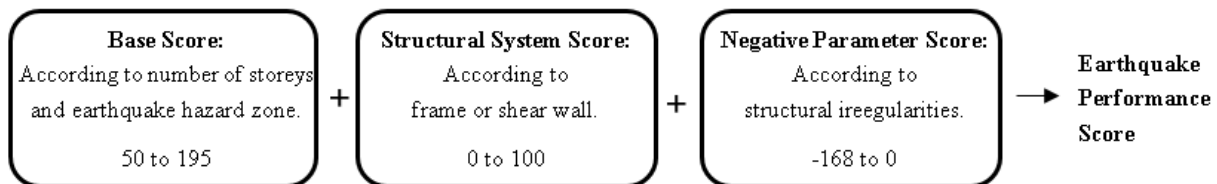


Figure 3. Flowchart of earthquake performance score

The data collected from the buildings was recorded using a form. The earthquake performance score was calculated for each building after evaluating the data. When calculating the performance scores of buildings, (+) points depending on the type of structural system, number of stories and hazard zone, and negative parameter scores in (-) points due to the effect of irregularities in the structural system are evaluated together (Figure 3). The performance scores can be used to determine the risk priorities of the regions. A short description of these irregularities is given below.

2.2.1. Number of Stories

Due to the increase in the number of stories, the building mass and the effects of earthquake forces increase. As a result of many observations and studies, it turns out that there is an almost linear relationship between the number of stories and structural damage in RC structures.

2.2.2. Soft or Weak Story

Many buildings in our country's building stock had soft or weak story irregularities. If the ground floor is used as a shop or store, the infill walls on this floor are usually removed or reduced. Based on the height difference of the floors, a significant difference in the rigidities of stories and soft or weak story damage occurs in such

buildings. It will be determined observationally by considering the difference in floor height and the apparent stiffness between floors.

2.2.3. Heavy Overhangs

One of the most significant features of buildings in Türkiye is the difference between the floor area of the ground floor and the floors above. Heavy overhang occurs by creating a larger area on the upper floors of the building. The presence of heavy overhangs causes mass and stiffness irregularities in the structure.

2.2.4. Short Column

Frames with partial infills lead to the formation of short columns, which sustain heavy damage since they are not designed for the high shear forces due to the shortened heights that will result from a strong earthquake [36].

2.2.5. Apparent Quality

The strength of building materials and the importance given to the quality of workmanship directly affect the performance of the building.

2.2.6. Building Adjacency

Since each structure has different vibration periods, structures built without sufficient clearance may result in damage during the earthquake.

2.2.7. Topographic Effects

Building a structure on a hill with a slope of more than 30° will slightly increase the effects of the earthquake load due to the height differences in the structural system elements.

2.2.8. Vertical Irregularity

The presence of discontinuous frames, columns, and shear walls along the height is very risky regarding load transfer during an earthquake.

2.2.9. Irregularity in Plan Torsion

In RC buildings, an unsymmetrical plan and distribution of vertical structural elements may cause additional loadings. As a result of the fact that the center of mass and the center of rigidity of a building do not coincide, torsion occurs due to eccentricity.

2.2.10. Type of Structural System

RC structural systems consist of frames or shear wall+frames. Shear walls are the major earthquake resisting members; therefore, there is an advantage to the shear wall+frame structures.

Using these parameters, 585 RC buildings in all the neighborhoods in Çanakkale city center were selected randomly and recorded in data collection forms. While making these selections, care was taken to reflect a certain distribution. Figure 4 indicates the distribution of building locations in the study. Figure 5 shows two building examples from the study.

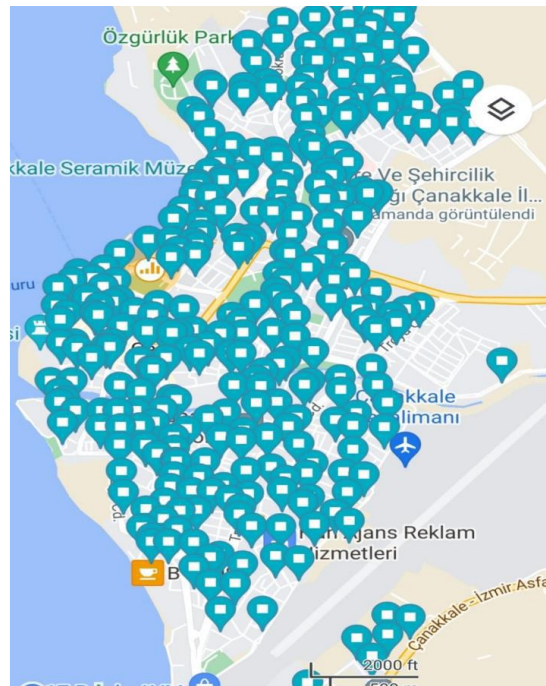


Figure 4. Distribution of building locations



Figure 5. Building examples

In order to obtain the local soil classes of the existing buildings, the data obtained from the geological and geotechnical studies previously carried out for the Çanakkale city center were obtained from Çanakkale Municipality. The vector and raster data obtained from the Çanakkale Municipality were transferred to the ArcGIS application [37], and the average shear wave velocity values for the top 30 meters of depth (V_s)₃₀ values were revealed by obtaining the grid code for each parcel (Figure 6). In the study area, (V_s)₃₀ values are lowest at 152 m/s and highest at 544 m/s. According to these values, according to the Turkish Building Seismic Code, there are ZC, ZD, and ZE local soil classes in the study areas in Çanakkale city center [38]. These soil classes and the coordinates of the buildings were entered into the earthquake hazard maps interactive web application [30]. The hazard zone was determined with the Short Period Design Spectral Acceleration Coefficient values found in the web application, and they were used to determine the base scores of the buildings. DD-2 ground motion level was used in the method. As a result of evaluating the data collected by applying the method to the buildings, a performance score was calculated for each building. Risk priorities between regions can be determined by sorting the calculated performance scores from largest to smallest.

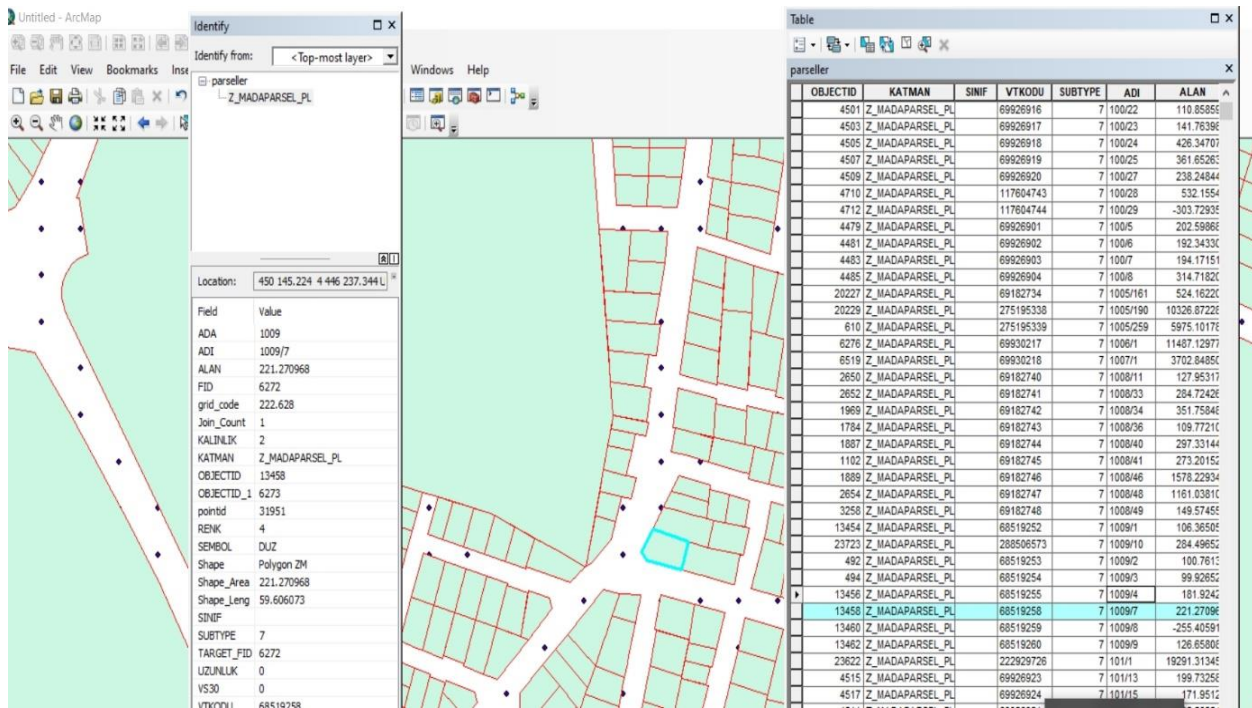


Figure 6. Grid codes from the ArcGIS application

Analyses were made in the Statistical Package for the Social Sciences (SPSS) program [39] with the values obtained by filling in the data collection forms of 585 buildings in the city center of Çanakkale. By entering all the collected data into the SPSS program, it was aimed to obtain the most accurate results with the fewest errors.

3. Results and Discussion

The distribution of randomly selected buildings in the city center of Çanakkale according to neighborhoods and the total number of buildings in the neighborhoods are shown in Table 2. The number of evaluated buildings was intended to be compatible with the total number of buildings.

Table 2. Number of buildings [40]

Name of Neighborhood	Total Number of Buildings	Evaluated Number of Buildings
Barbaros	3826	169
İsmetpaşa	2215	88
Cevatpaşa	1508	105
Kemalpaşa	655	54
Namıkkemal	432	50
Esenler	1232	77
Fevzipaşa	578	42

The performance scores were classified according to neighborhoods and number of stories (Figure 7). The graph shows that the total score of the buildings decreases as the number of stories increases. The reason is that the base score, considered when calculating the total score, is high in low-rise buildings but decreases as the number of stories increases. In addition, it is seen that as the number of stories increases, there are lower scores in the negativity parameter score, which evaluates the current irregularity in buildings.

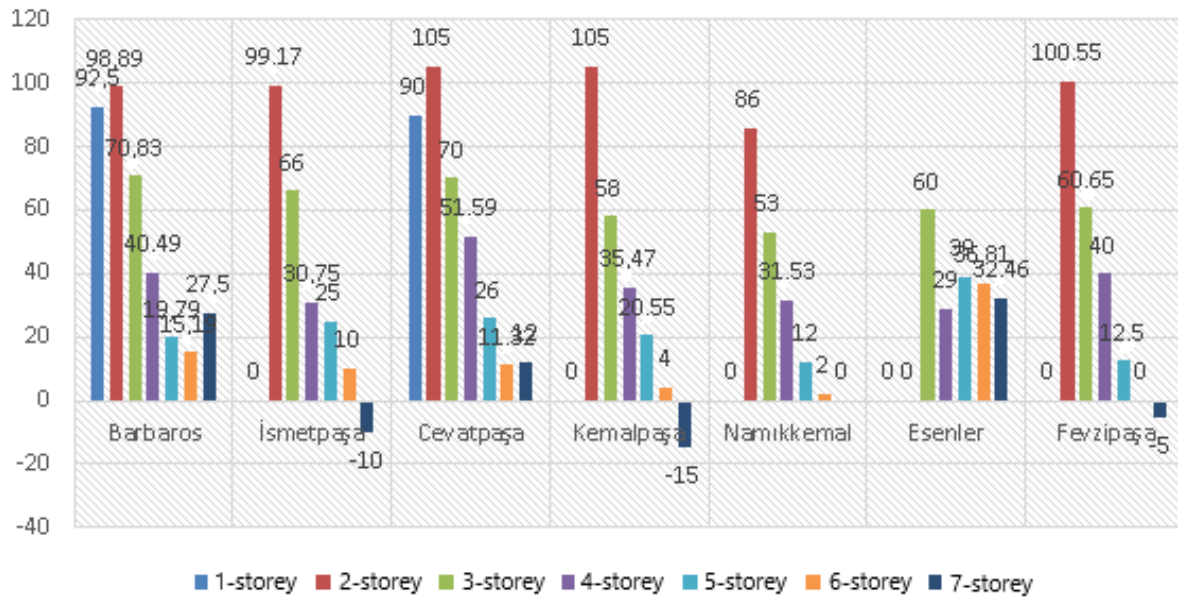


Figure 7. Average scores according to neighborhoods and number of stories

Figure 8 compares the average score calculated for Çanakkale city center and the average score of each neighborhood. The average score of total buildings was found to be 38.56. It is seen that the calculated average scores of the buildings in Cevatpaşa, Kemalpaşa, and Esenler are below the general average score. The reasons can be said to be that there are many structural irregularities in Cevatpaşa; moreover, Cevatpaşa is the region with the highest natural ground slope. In Kemalpaşa, there is a high concentration of workplaces; most buildings are adjacent, and soft stories are present in all the buildings. Esenler is a newly built area, and there are many high-rise buildings. Additionally, 46 of the 77 buildings have heavy overhangs. In Fevzipaşa, where the average score is significantly above the general score average, most existing buildings are low-rise.

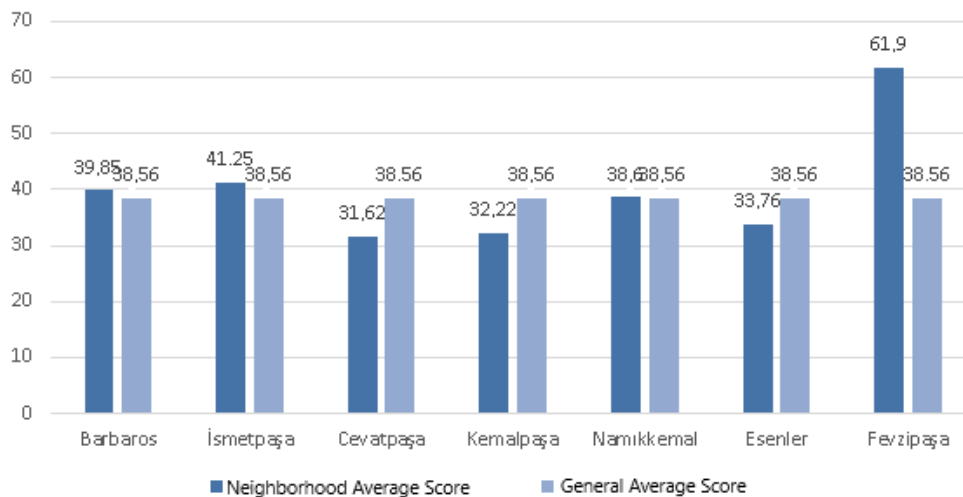


Figure 8. Comparison of the general average score and average score of each neighborhood

Figure 9 indicates the apparent quality distribution according to neighborhoods. When the results are evaluated as a percentage, the percentage with good apparent quality was calculated as 92% in Esenler, 76% in Barbaros, 70% in Cevatpaşa, 67% in İsmetpaşa, 61% in Kemalpaşa, 57% in Fevzipaşa and 40% in Namikkemal. This ranking was largely accurate regarding the construction process for Çanakkale city center.

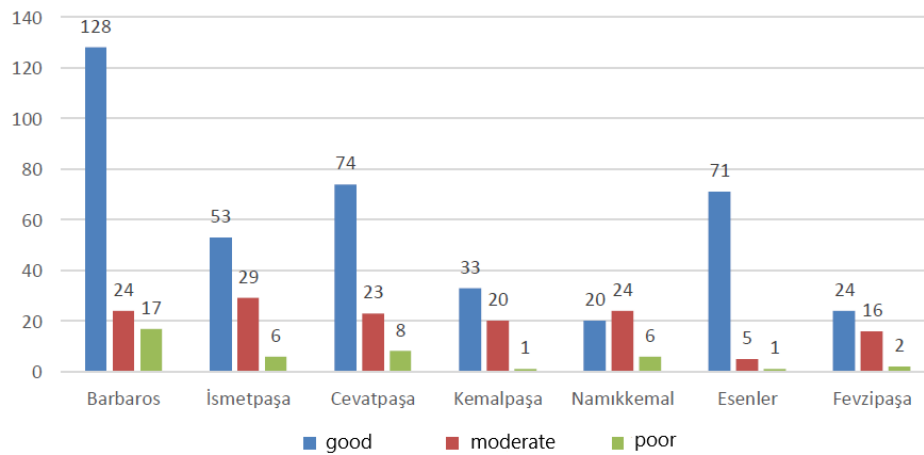


Figure 9. Building apparent quality according to neighborhoods

The distribution of soft or weak stories according to neighborhoods is seen in Figure 10. The soft or weak story rate was calculated as 100% in Kemalpaşa and Namikkemal, 76% in İsmetpaşa, 69% in Fevzipaşa, 57% in Esenler, 54% in Barbaros and 50% in Cevatpaşa. Looking at these ratios, it is possible to say that a soft or weak story is the type of irregularity that is generally the most common. In the Kemalpaşa and Namikkemal Neighborhoods, shops and stores are on the ground floors of all buildings, as seen in Figure 10.

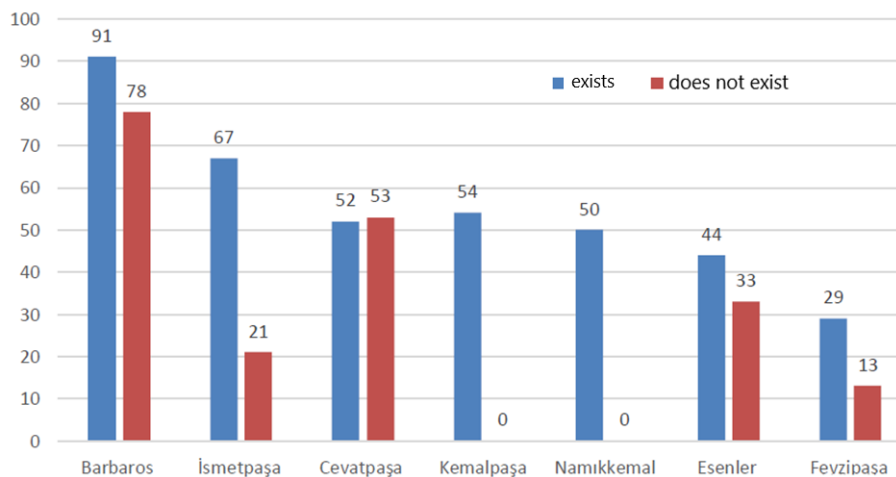


Figure 10. Soft/Weak story based on neighborhoods

Figure 11 shows the distribution of heavy overhangs according to neighborhoods. The percentage of buildings with heavy overhangs was calculated as 63% in Barbaros, 60% in Esenler, 51% in Cevatpaşa, 47% in İsmetpaşa, 45% in Fevzipaşa, 42% in Namikkemal and 37% in Kemalpaşa Neighborhoods. Based on the ratios, heavy overhang irregularity is the most common irregularity after a soft or weak story.

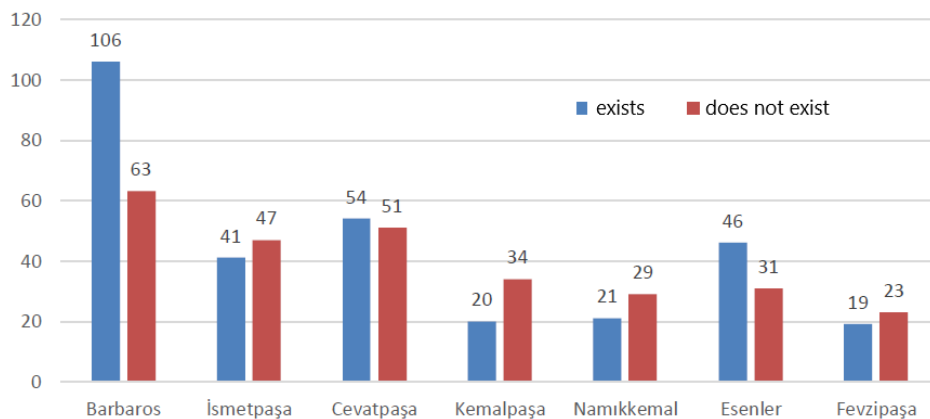


Figure 11. Heavy overhangs, according to neighborhoods

The distribution of irregularities in plan torsion according to neighborhoods is seen in Figure 12. There is an irregularity in the plan at a rate of 22% in Esenler, 21% in Barbaros, 12% in Namıkkemal, 11% in Kemalpaşa, 9% in Cevatpaşa, 7% in Fevzipaşa and 6% in İsmetpaşa Neighborhoods. Compared to other irregularities, it is seen that the rates of irregularity in the plan torsion are low.

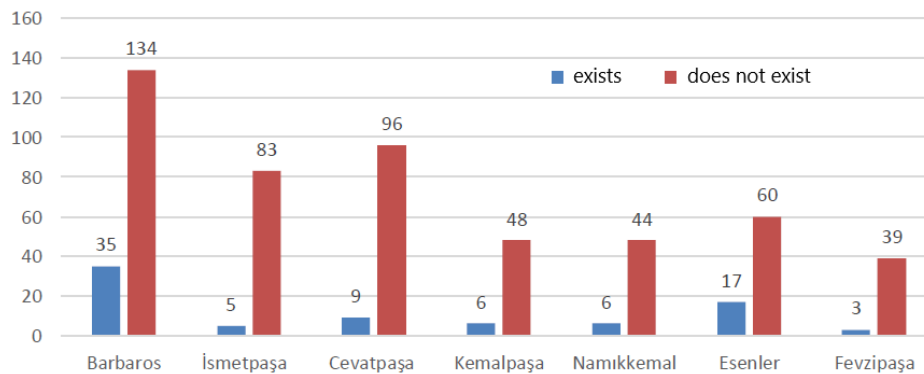


Figure 12. Irregularity in plan torsion according to neighborhoods

Figure 13 shows the existence of short columns in the buildings. The rates are 22% in Esenler, 20% in Kemalpaşa, 14% in Namıkkemal, 11% in Barbaros, 7% in Fevzipaşa, 5% in Cevatpaşa and 1% in İsmetpaşa. Compared to other irregularities, the short column appears to be low.

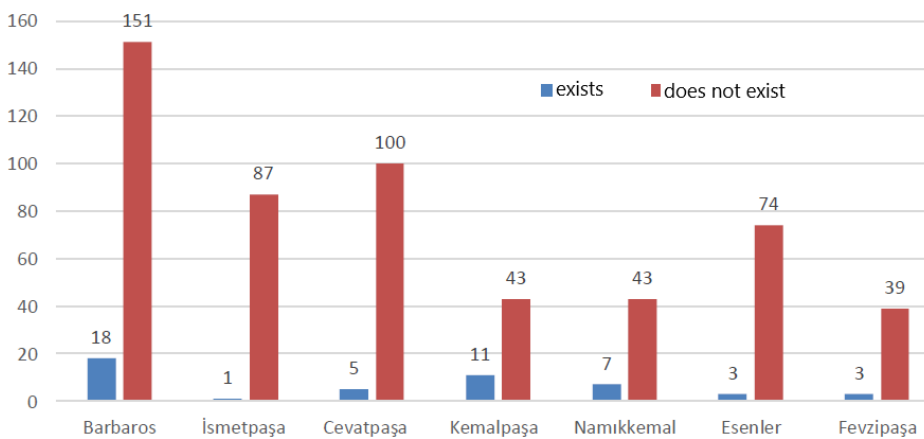


Figure 13. Short columns according to neighborhoods

4. Conclusion

A rapid seismic assessment was conducted in 585 selected RC buildings in the city center of Çanakkale using Appendix-A of Law No. 6306 [24]. In this method in Law No. 6306, building adjacency, short column, and topographic effects have the same negativity value for all heights of buildings. However, the impact of the negativities from building apparent quality, soft or weak story, vertical irregularity, heavy overhangs, and irregularity in plan torsion is considered greater in high-rise buildings. These irregularities increase the risk of earthquakes, especially in buildings with four or more floors. They were evaluated in this way because it is known that they caused more damage and destruction in the past earthquakes.

Our study found soft stories with values ranging from 50% to 100% and heavy overhangs ranging from 37% to 63% were the most common irregularities in existing buildings according to neighborhoods. Soft story, especially with significantly higher story heights, may cause sudden collapse during an earthquake. Buildings with both low-performance scores and also soft stories can be prioritized.

Similar results were found in other studies using this method in the literature. Street survey results showed that 79% of concrete buildings have a pounding effect, 65% have a soft story, and 37% have heavy overhangs [27]. 24% have a soft story, and 22% have a heavy overhang of the 487 RC buildings, and they specified that these

buildings must be subjected to a more detailed assessment [25]. Among the total 1550 RC buildings in the study area [26], 36% have short column effect, 28% have heavy overhangs, 28% have a soft story, and 139 buildings with a performance score of below 40 points are considered to have a high-risk level. They should be addressed primarily in the disaster risk assessment studies to be carried out. It has been understood that this method in the law gives much more general results than other rapid assessment methods. It is a suitable method for comparing risky areas rather than buildings [28]. The main aim is not to decide a definitive conclusion about building seismic risk but to identify priority buildings in detailed investigations [27].

Finally, it has been observed that this method is suitable for making a general and rapid evaluation based on existing buildings in a certain region. The results can be evaluated in terms of a wide range of results with statistical programs. Local authorities can consider them within the scope of evaluating existing structures. Until the study is completely accomplished, the results may not make much sense. Considering there are approximately 15000 buildings in Çanakkale city center, it will be important to carry out the work quickly, supporting the more efficient implementation of urban transformation works. Renovating priority buildings should be the most important goal for reducing the loss of life in earthquakes.

Author Contributions

This paper is derived from the first author's master's thesis and supervised by the second author. Both authors devised the main conceptual ideas and developed the theoretical framework. The first author performed the study and analyses under the supervision of the second author. The second author wrote the article. The authors read and approved the final version of the paper.

Conflicts of Interest

All the authors declare no conflict of interest.

Ethical Review and Approval

No approval from the Board of Ethics is required.

Acknowledgment

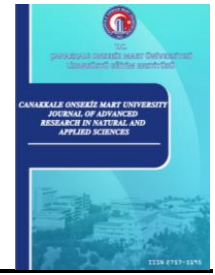
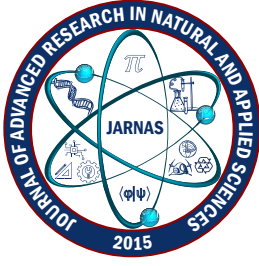
We would like to thank the Çanakkale Municipality for the support.

References

- [1] S. Kahraman, T. Baran, Ö. Özçelik, A. Saatçi, S. Mısır, S. C. Girgin, *Building stock inventory studies: İzmir Balçova and Seferihisar pilot projects*, 2nd Conference on Earthquake Engineering and Seismology, Hatay, 2013, pp. 1-10.
- [2] Applied Technology Council (ATC) 21, Rapid visual screening of buildings for potential seismic hazards - A handbook (FEMA 154 Report), second edition, California, USA, 2002.
- [3] Federal Emergency Management Agency (FEMA) 273, NEHRP Guidelines for the seismic rehabilitation of buildings, (FEMA 273 Report), Federal Emergency Management Council, Washington DC, USA, 1997a.
- [4] Federal Emergency Management Agency (FEMA) 302, NEHRP Recommended provisions for the seismic regulations for new buildings and other structures and commentary, (FEMA 302 Report), Federal Emergency Management Council, Washington DC, USA, 1997b.
- [5] Federal Emergency Management Agency (FEMA) 310, Handbook for the seismic evaluation of buildings

- A prestandard (FEMA 310 Report), Federal Emergency Management Council, New York, USA, 1998.
- [6] The Japan Building Disaster Prevention Association (JBDPA). Standard for Seismic Evaluation of Existing Reinforced Concrete Buildings, Tokyo, Japan, 2001.
- [7] A. F. Hassan, M. A. Sözen, *Seismic vulnerability assessment of low rise buildings in regions with infrequent earthquakes*, ACI Structural Journal 94 (1) (1997) 31-39.
- [8] U. Ersoy, G. Özcebe, *Lessons from recent earthquakes in Türkiye and seismic rehabilitation of buildings*, in: S. Sheikh, O. Bayrak (Eds), S. M. Uzumeri Symposium - Behavior and Design of Concrete Structures for Seismic Performance, SP-197, ACI International, 2002, pp. 105-126.
- [9] E. Damcı, B. Yıldızlar, G. Gürsoy, N. K. Öztörün, T. Çelik, *An algorithm for situational determination of structures throughout Türkiye, specifically in Bakırköy*, 5th Conference on National Earthquake Engineering, İstanbul, 2003, pp. 71-73.
- [10] A. İlki, H. Boduroğlu, Ö. Pınar, F. Baysan, C. Demir, S. Şirin, *Comparison of seismic index method and structural analysis results for existing and strengthened structures*, 5th Conference on National Earthquake Engineering, İstanbul, 2003, pp. 69-71.
- [11] G. Özcebe, M. S. Yüçemen, A. Yakut, V. Aydoğan, *Seismic vulnerability assessment procedure for low-to medium-rise reinforced concrete buildings*, Structural Engineering Research Unit (SERU) report no: 03/02, TUBITAK-METU, Ankara, 2003.
- [12] H. Sucuoğlu, U. Yazgan, *Simple survey procedures for seismic risk assessment in urban building stocks, seismic assessment and rehabilitation of existing buildings*, NATO Science Series (IV/29) (2003) 97-118.
- [13] S. S. Tezcan, M. Gürsoy, E. Kaya, İ. E. Bal, *Project to prevent loss of life in earthquakes*, Kocaeli'99 Emergency Conference, İstanbul, 2003, pp. 146-153.
- [14] A. Yakut, V. Aydoğan, G. Özcebe, M. S. Yüçemen, *Preliminary seismic vulnerability assessment of existing reinforced concrete buildings in Türkiye-Part II: Inclusion of site characteristics*, NATO Science Series (IV/29) (2003) 43-58.
- [15] R. Temür, *Developing a rapid analysis technique and related software*, Master's Thesis İstanbul University (2006) İstanbul.
- [16] M. H. Boduroğlu, P. Ö. Çağlayan, *A screening method for the evaluation of existing buildings*, 6th Conference on National Earthquake Engineering, İstanbul, 2007, pp. 157-166.
- [17] H. Sucuoğlu, *A screening procedure for seismic risk assessment in urban building stocks*, 6th Conference on National Earthquake Engineering, İstanbul, 2007, pp. 267-284.
- [18] H. Sucuoğlu, U. Yazgan, A. Yakut, *A screening procedure for seismic risk assessment in urban building stocks*, Earthquake Spectra 23 (2) (2007) 441-458.
- [19] İ. E. Bal, F. G. Gülay, S. S. Tezcan, *A new approach for the preliminary seismic assessment of RC buildings: P25 scoring method*, The 14th World Conference on Earthquake Engineering, Beijing, China, 2008, pp. 219-226.
- [20] M. İnel, Ş. M. Senel, S. Toprak, Y. Manav, *Seismic risk assessment of buildings in urban areas: A case study for Denizli, Türkiye*, Natural Hazards (46) (2008) 265-285.
- [21] F. G. Gülay, K. Kaptan, İ. E. Bal, S. S. Tezcan, *P25-scoring method for the collapse vulnerability assessment of R/C buildings*, Procedia Engineering (14) (2011) 1219-1228.
- [22] Ö. Özçelik, S. Mısır, T. Baran, S. Kahraman, A. Saatçi, S. C. Girgin, *Results of the building stock inventory and earthquake safety preliminary assessment project carried out in Balçova and Seferihisar districts*, 2nd İzmir City Symposium, İzmir, 2013, pp. 1-10.

- [23] H. O. Köksal, S. Yıldız, *Micro scale physical vulnerability assessment study for the city center of Çanakkale*, 4th Conference on International Earthquake Engineering and Seismology, Eskişehir, 2017, pp. 1-8.
- [24] Law No. 6306, Law on transformation of areas under disaster risk, 2012.
- [25] H. Bilici, E. Işık, H. M. Özlük, *The evaluation of urban buildings stocks in Adilcevaz district*, Dicle University Journal of the Institute of Natural and Applied Sciences 3 (1) (2014) 1-12.
- [26] Z. Tozlu, *The implementation of rapid assessment method within Law no. 6306 to determine risk condition of existing buildings*, Master's Thesis Gazi University (2015) Ankara.
- [27] U. Albayrak, M. Canbaz, G. Albayrak, *A rapid seismic risk assessment method for existing building stock in urban areas*, Procedia Engineering (118) (2015) 1242-1249.
- [28] Ç. Çırak, *Evaluation of seismic performance of existing buildings obtained from rapid and detailed performance assessment methods*, Master's Thesis Pamukkale University (2016) Denizli.
- [29] E. Güler, M. Canbaz, *Determination of earthquake risk of structures by street screening method*, Journal of Engineering and Architecture Faculty of Eskişehir Osmangazi University 28 (3) (2020) 227-234.
- [30] Disaster and Emergency Management Presidency (AFAD), *Türkiye Earthquake Hazard Maps Interactive Web Application*, 2018.
- [31] Google Maps, 2022.
- [32] B. Akol, *Earthquake risk assessment of Çanakkale and its vicinity*, Master's Thesis Çanakkale Onsekiz Mart University (2009) Çanakkale.
- [33] A. Kürçer, A. Chatzipetros, S. Z. Tutkun, S. Pavlides, Ö. Ateş, S. Valkaniotis, *The Yenice–Gönen active fault (NW Türkiye): Active tectonics and paleoseismology*, Tectonophysics (453) (2008) 263-275.
- [34] E. Görgün, D. Kalafat, K. Kekovalı, *Source mechanisms and stress field of the 2017 Ayvacık/Çanakkale earthquake sequence in NW Türkiye*, Annals of Geophysics, (2020) 63 (3) SE332 23 pages.
- [35] Ö. Karagöz, K. Chimoto, H. Yamanaka, O. Ozel, S. Citak, *Broadband ground-motion simulation of the 24 May 2014 Gokceada (North Aegean Sea) earthquake (Mw 6.9) in NW Türkiye considering local soil effects*, Bulletin of Earthquake Engineering 16 (1) (2018) 23-43.
- [36] G. Özcebe, H. Sucuoglu, M. S. Yüçemen, A. Yakut, J. Kubin, *Seismic risk assessment of existing building stock in Istanbul a pilot application in Zeytinburnu District*, Proceedings of the 8th U.S. National Conference on Earthquake Engineering, California, USA, 2006, paper no. 1737.
- [37] Geographic Information System (ArcGIS), Enterprise GIS Mapping Platform, Environmental Systems Research Institute, 2022.
- [38] Turkish Building Seismic Code, Disaster and Emergency Management Presidency, 2018.
- [39] Statistical Package for the Social Sciences (SPSS), IBM Corp. Version 28.0. Armonk, New York, USA, 2021.
- [40] Çanakkale Municipality, 2022.



Cost and Benefit Analysis of Different Buildings Through Reuse of Treated Greywater

Elif Ayyüce Kılınç¹ , Asude Hanedar² , Ayşe Gül Tanık³ , Erdem Görgün⁴ 

^{1,3,4}Department of Environmental Engineering, Faculty of Civil Engineering, Istanbul Technical University, İstanbul, Türkiye

²Department of Environmental Engineering, Çorlu Faculty of Engineering, Tekirdağ Namık Kemal University, Tekirdağ, Türkiye

Article Info

Received: 29 Apr 2024

Accepted: 08 Jul 2024

Published: 30 Sep 2024

Research Article

Abstract – The fact that the impacts of climate change cannot be prevented in the short term has increased the importance of climate change adaptation activities, and many national and international studies have been initiated in this regard. Greywater reuse (GWR) activities have become important methods recommended by the Intergovernmental Panel on Climate Change (IPCC) for adaptation to climate change. This study selects GWR from 3 different real typologies, a hotel, a residential building, and an industrial plant planned in Izmir Province of Türkiye, to design greywater systems followed by cost-benefit analyses. The applicability of GWR systems in these typologies has been analyzed, and comparisons have been made. GWR systems at the project design stage eliminate the need for installation modifications. Therefore, it is concluded that new buildings should be designed to integrate these alternative water resource systems. Recovered water through the installation of GWR systems is recommended to be used as flushing water, and the excess for garden irrigation, car washing and cleaning. The payback periods were calculated as 12 years for the hotel and industrial plant and 6 years for the residential building. The water savings were calculated as 46% for the hotel, 44% for the residential building, and 29% for the industrial plant. The results put forth the feasibility of this alternative water resource.

Keywords – Alternative water resources, buildings, cost and benefit analysis, greywater reuse, water saving

1. Introduction

In developing countries, rapid urbanization caused some complications over time. In the future, urbanization is expected to increase more with the effects of climate change, and this will require the rapid implementation of sustainable management strategies, especially in water use. The final declaration of the Climate Council organized by the Turkish Ministry of Environment, Urbanization and Climate Change (MoEUCC) [1] in February 2022 states the country's road map for combating climate change in which two issues related to water use were emphasized:

- i. Legislation regarding water efficiency in buildings should be established, greywater reuse (GWR) should be encouraged, and the use of rainwater and the establishment of a zero-waste system should be made mandatory.
- ii. Rainwater harvesting (RWH) and GWR should be disseminated, and guiding legislation should be developed for this purpose. Wastewater treated in wastewater treatment plants should be reused.

When we look at the components of domestic water use, it is observed that at least 34% of it (30% flushing water, 4% garden irrigation) does not require potable quality water. Moreover, greywater/rainwater can be preferred in laundries and cleaning works, which account for 16% of domestic water use, by ensuring the need

¹elifkilinc@iocevre.com; ²ahanedar@nku.edu.tr (Corresponding Author); ³tanika@itu.edu.tr; ⁴gorgune@itu.edu.tr

for treatment and water quality [2]. In short, RWH and GWR are the possibilities to be used in buildings, especially for flushing toilets, garden irrigation, car washing, and laundries and are regarded as alternative water resources. As such, around 50% of tap water can be saved [3-4]. These alternative uses have become even more feasible and remarkable due to the negative effects of climate change on existing water resources, as emphasized by [5-6].

Greywater is a large volume of wastewater with high reuse potential and applicability. It is domestic wastewater from showers, hand washing sinks, laundries, and kitchen water, excluding toilet and food waste from garbage disposals, known as black water [7]. The source and composition of greywater depend on living standards, demographical status, social and cultural habits, number of people living in the household, chemicals used in the household, availability of water, and climatic conditions that differ from one country to another [8].

This study on cost and benefit analyses of different buildings through the reuse of greywater was realized in real cases that have provided comprehensive examples to be followed by other scientists and practitioners interested in similar water reuse efforts in different parts of the world. Three building typologies are selected from the Izmir Province of the country: a hotel, a residential area (housing), and an industrial plant. All these buildings are in the planning stage. Calculations based on these real cases' design criteria and installation plans enabled detailed preparation of investment and operating costs along with depreciation periods.

Characteristics of greywater: Greywater contains easily degradable organic matter with less suspended solids (SS) and nitrogen (N) and more phosphorus (P) than typical domestic wastewater. Ammonia and total kjeldahl nitrogen (TKN) concentrations are approximately 10 times lower than in municipal wastewater. The metal and organic contaminant content in greywater is generally low, with lower levels of zinc and mercury than in mixed wastewater, and the rate of pathogens is relatively low [10-11]. The contaminants that cause pollution in greywater result from used personal hygiene products, detergents, dirty clothes, and body dirt. While greywater from showers and sinks contains low concentrations of bacteria and chemicals, wastewater from kitchen sinks and laundries contains high concentrations of bacteria, solids, chemicals, and oils [12]. For this reason, greywater sources are divided into low-load sources (bathtubs, showers, and hand sinks) and high-load sources (laundry rooms and kitchens). Pollutants that vary according to the different sources of greywater are given in Table 1.

Table 1. Sources of greywater and polluting parameters [12]

Source of greywater	Polluting parameters
Washing machine	SS, organic matter, oil/grease, salinity, sodium, nitrate, P (from detergents), bleach
Dishwasher	SS, organic matter, oil/grease, increasing salinity, bacteria and detergent
Bathtub-Shower	Bacteria, hair, SS, organic matter, oil/grease, soap, shampoo residues
Sink (including kitchen)	Bacteria, SS, organic matter, oil/grease, soap, shampoo residues

Typical greywater volume varies between 60 L-120 L/person/day, depending on user behavior, demographics, traditions and habits, plumbing, and water availability [13]. Method of using treated greywater includes indoor reuse, such as flush toilets, and outdoor reuse, such as garden watering, car washing, and cleaning. Treated greywater may also be used as agricultural irrigation water when it meets the required health and environmental standards [14]. When we look at the European Union (EU) regulations, we see that there is currently no directive regulating water reuse. The European Plan for the Protection of Water Resources stated in 2012, emphasizes the importance of water reuse in irrigation and industry in line with the Water Framework Directive (WFD). Still, there is no clear directive [15]. EU tools on water reuse were prepared in 2016 [16], and the main idea behind these statements and efforts underlined the sustainable management of water, as water resources become scarce over time due to the effects of climate change. Water Reuse in EU Member States was proposed

by the Commission on Environment, Climate Change, and Energy in 2018; however, this recommendation was mainly based on the reuse of treated wastewater for irrigation within the scope of river basin management plans [17].

On the other hand, water recycling is increasingly being incorporated into the policy framework and development of guidelines to help alleviate demand for drinking water in a water-stressed country, Australia. Implementation rules for GWR were established in 2010. Various states in the United States of America (USA) offer various incentives to users of GWR systems. However, as with RWH, this practice varies from country to country, state to state, and city to city [18].

Greywater treatment requirement for reuse and applicable technologies: When determining the collected greywater's quality and intended use after treatment, the required treatment level should be considered. While greywater can be used after being treated, it also has sample applications where it is reused without being treated. There are some practices where it is used directly in the garden and directly in toilet reservoirs [19]. In such applications as the greywater transfer system in Australia and the USA, greywater from sinks, washing machines, and dishwashers is used as flushing water in toilet reservoirs without being treated. In addition to the water savings achieved in both applications, storage problems are eliminated, and cost is low. However, untreated greywater in toilets leaves tints on the toilet bowl and requires sensitivity when flushing. Using untreated greywater in garden irrigation can accumulate salts, surfactants, oil, and grease in the soil in the long term. Therefore, when determining the need to treat greywater in its area of use, its environmental impacts should be considered.

Types of treatment may include one or more of the following substeps [12, 20]:

- i.* Physical treatment: sedimentation/flotation via sedimentation tanks, large particle filtration by sieving, mechanical fine filtration by membrane filtration,
- ii.* Biological treatment: such as constructed wetland (CW), rotating biological contactor (RBC), sequential batch reactor (SBR), membrane bioreactor (MBR) technologies,
- iii.* Chemical treatment: such as precipitation, electrocoagulation, photocatalytic oxidation, ion exchangers and granular activated carbon,
- iv.* Disinfection: such as ultraviolet (UV) radiation chlorination.

The most important greywater treatment technologies mentioned by Üstün and Tırpancı (2015) are given in Figure 1a-d [21-23].



Figure 1. Greywater treatment technologies: a) Constructed wetland [21], b) Rotary biological reactors [12], c) Sequential batch reactors [22], and d) Membrane bioreactors [23]

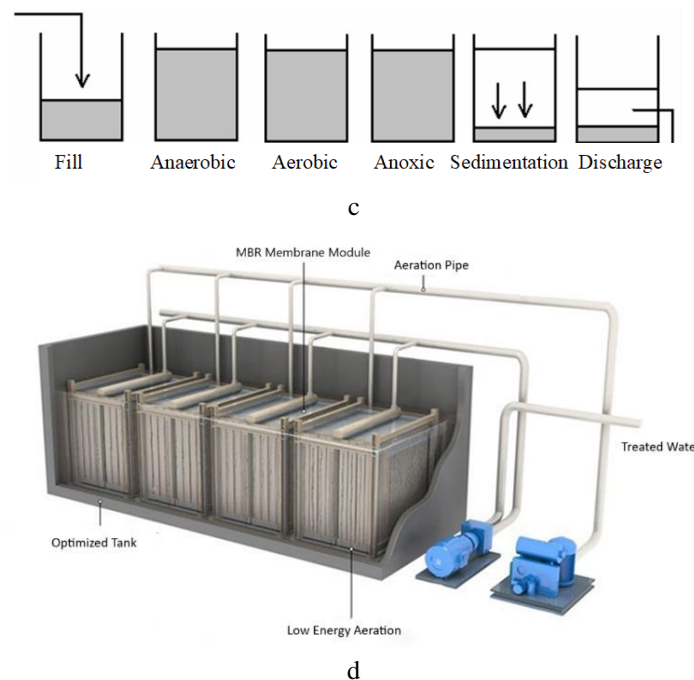


Figure 1. (Continued) Greywater treatment technologies: a) Constructed wetland [21]; b) Rotary biological reactors [12], c) Sequential batch reactors [22], and d) Membrane bioreactors [23]

National legislation: Although there is no statement in our country's legislation that requires the implementation of GWR systems, there are some encouraging principles. Regulation on Amendments to the Water Pollution Control Regulation prepared by MoEUCC put into force through publication in the Official Gazette dated 17.12.2022 and numbered 32046. With Article 4 under the title of Principles on Water Protection of the Regulation, the phrases "*Encouraging recycling and reuse in wastewater management in accordance with circular economy principles*" and "*Establishing an infrastructure suitable for the reuse of greywater*" are dictated. In Article 28, under the title of Reuse of Treated Wastewater of the same regulation, the phrase "*It is essential to evaluate the reuse opportunities of greywater and rainwater*" was added. In addition, within the scope of Article 28, "*In regions where irrigation water is scarce and has economic value, wastewater treated up to the irrigation water quality criteria given in the Communiqué on Wastewater Treatment Facilities Technical Procedures published in the Official Gazette dated 20.03.2010 and numbered 27527 should be used as agricultural irrigation water*". These phrases encourage the public the use alternative water resources. The Communiqué on Technical Procedures for Wastewater Treatment Facilities, which came into force after being published in the Official Gazette dated 20.03.2010 and numbered 27257, covers the technology selection of wastewater treatment plants related to the treatment of wastewater originating from settlements, design criteria, disinfection of treated wastewater, reuse and treatment options with deep sea discharge. It was prepared by the repealed Ministry of Environment and Forestry to regulate the basic technical procedures and practices to be used to dispose of the sludge generated during the process. In the 7th section of the Communiqué on Technical Procedures for Wastewater Treatment Facilities, regulations have been made regarding the areas of use of treated wastewater, location of the wastewater recovery facility, storage of treated wastewater, technology selection for wastewater recovery and irrigation water use criteria of treated wastewater.

Later, the Communiqué on Amendments to the Technical Procedures Communiqué on Wastewater Treatment Facilities was published in the Official Gazette dated 25.10.2022 and numbered 31994. In this context, by referring to Article 22/C added to the Communiqué after Article 22, Criteria and explanations regarding reusing greywater as urinals and flush water with closed circuit systems are given under the heading 7.4 in Annex 7. Accordingly, "*In the reuse of greywater as closed-circuit urinals and flush water, disinfection and removal of microorganisms and suspended solids are sufficient*" has been added. The debate on the need to treat greywater for use as flush water has been answered through the phrase added to the legislation.

The Turkish Standard titled TS EN 16941-2 Onsite non-potable water systems - Part 2: Systems for the use of treated greywater (sink wastewater), published by the Turkish Standards Institute (TSE) in February 2021, is one of the important steps taken in the implementation of GWR systems. TS 16941-2 Standard covers greywater systems' design, sizing, installation, commissioning, and maintenance principles for onsite use [20].

2. Materials and Methods

2.1. Calculating the Amount of Greywater to be Recycled

Reference values used to calculate the amount of greywater that can be recovered in the greywater systems designed within the scope of this study are given in Tables 2, 3, and 4 [20]. The values reflect the average, and it is recommended to check the model standards of the vitrified fixtures used for each building of concern.

Equation 2.1 calculates the amount of greywater from sinks, showers, and bathtubs.

$$\text{Amount of greywater} \frac{lt}{day} = \text{Flow rate} \frac{lt}{min} * \text{Flow time, min} * \text{times of use} \frac{\text{times. person}}{\text{day}} * \text{number of people} \quad (2.1)$$

Table 2. Typical average daily greywater yield and demand [20]

Fullness	Efficiency ^a (L/day)	Demand (L/day)		
		Toilets	Laundry	Other non-potable uses ^c
1 person	60	35	15	10

a) Efficiency from showers, baths, or sinks.

b) These figures are based on average daily demand. It should be noted that a washing machine usually uses 30 - 60 L per cycle.

c) For example, garden irrigation.

Table 3. Reference value ranges for water use [20]

Water Use	Range	Unit
The volumetric flow of the shower	5-15	L/min
Water volume per tub use	70-200	L
Sink	5-10	L/min
Water volume for washing machine per operating cycle	30-60	L/cycle
Water volume for dishwasher per operating cycle	10-20	L/cycle

Table 4. Flow times of bathroom fixtures [20]

Water Use	Value	Unit
Shower	5	minute
Sink	15	second
Bathtub	15	minute

2.2. Components of Greywater System

Greywater should be collected in a separate wastewater drainage pipe and allowed to flow by gravity from collection devices to the greywater system. The use of greywater for flush water, green area irrigation water, car washing, and cleaning purposes was evaluated for the buildings studied. While the system was being set up, it was accepted that only greywater from the sink, shower, and bathtub would come to the treatment plant. Various methods can be used to meet the need for treatment in selected use areas. The recovery of weak greywater (sinks, showers, and bathtubs) was evaluated in the studied cases.

Many studies cited in the literature indicate that biological treatment is needed to treat mixed and strong greywater. It has been stated that treatment systems that include combinations of physical or chemical treatment processes will be sufficient to treat weak greywater [24-26]. Direct membrane filtration alternative is considered convenient, consisting of pre-chlorination, sand filter, active carbon filter, ultrafiltration and disinfection-chlorination units [27]. In order to determine the components and costs of the greywater treatment system in this study, local companies were contacted, and local market prices of highly applicable systems

were obtained. The greywater treatment system selected within this study consists of the following units: greywater collection tank, system feeding booster, stainless steel bag filter, fully automatic multilayer sand filter, fully automatic active carbon filter, filtered water tank, filtration system backwash booster, greywater package ultrafiltration system, automatic chlorine dosing unit, and treated water tank.

Prior to the cost-benefit analysis, the necessary data regarding the structure where the systems will be applied and the area where the system is located were obtained. In this context, the current situation of Izmir in terms of population, land use, water unit price, water supply and demand, and seasonal norms was examined, and its impact on the applicability of the systems was evaluated. Floor plans and plumbing projects were also discussed, necessary information was obtained, and calculations were made. The amount of recoverable greywater in selected areas, water needed in alternative use areas, potential water savings, and economic gain if the systems are implemented, were calculated. Since the selected buildings are in the planning phase and construction has not started, actual water consumption amounts were unavailable. As such, the amount of water needed was calculated by making certain assumptions for values, such as the number of people/visitors using the building and the number of days the building was used. Using the membrane filtration method in the greywater treatment system was preferred. Only greywater from the sinks and showers of the buildings will be collected, and wastewater produced from any areas other than these will not mix with the system.

In the selected cases, the location of the systems and the connection lengths for the installation floor column have been determined. The Bill of quantities was shaped by removing all investment cost items required to implement the systems, and unit costs for all necessary equipment and fittings were calculated according to local market prices. Average unit prices were reached by taking offers from companies close to Izmir. Regarding operating costs, electricity, and maintenance-repair costs were considered. The electricity cost was calculated using the unit prices per kWh of the distribution companies in the province based on the energy consumption of the pump operating in the system. The average prices suggested by maintenance service and system supply companies are the basis for maintenance repair costs. The repayment periods were calculated after calculating the benefits that the systems can provide and the investment and operating costs required.

In the benefit part, the savings on water bills using greywater instead of tap water were taken as the basis. Accordingly, the economic feasibility of the systems was determined based on the calculated payback periods. The payback period calculated within the benefit-cost analysis scope is an important criterion in evaluating the investment. The net Present Value (NPV) criterion was used to calculate the payback period and analyze the profitability of the GWR system to be implemented. NPV refers to the difference obtained by deducting investment expenses from the present value of the return provided by the GWR system investment throughout its economic life. The present value is calculated based on a certain capital cost discount. The discount rate was taken as 5%. The system's payback period was calculated by finding the annual net benefits. The payback period shows how many years it takes to recoup the investment made for the GWR system. The year in which NPV is positive was determined as the payback period [27].

Table 5 presents the water tariffs per subscriber in Izmir. These values were used in the selected typologies' cost calculations of GWR systems.

Table 5. İzmir Metropolitan Municipality 2023 water tariffs

Subscriber Types	Stages (m ³ /month)	Water Price (TL/m ³)	Wastewater Price (TL/m ³)	Total (TL/m ³)
Housing	0~10	22.09	11.04	33.13
Housing	11~20	28.25	14.12	42.37
Housing	21~Above	52.89	26.44	79.33
Non-Residential	0~10	44.18	22.08	66.26
Non-Residential	11~20	56.50	28.24	84.74
Non-Residential	21~Above	105.78	52.88	158.66
Government offices	stepless	33.13	16.56	49.69
Park and Cemetery	stepless	32.71		32.71
Organized Industry	stepless	41,15	20,57	61.72
NATO and Embassy	stepless	62,22	31,10	93.32

2.3. Designing GWR Systems

The methodology followed in the design is explained through the Izmir Hotel example. It is accepted that 23 personnel work in the hotel, which serves as a tourist facility. The maximum number of guests (staying) is 60 people, and the number of visitors (participating in the various activities) is 455. The amount of greywater that could be recycled in the hotel's bedrooms and living room floors was calculated through investigating the possible water usage habits. By means of inspecting the hotel's floor plans, all water usage areas resulting from greywater were analyzed and the number of existing fixtures was determined (Table 6). In the hotel, which also has washing machines and dishwashers, it was predicted that greywater from bathtubs and sinks will be collected, as the pollution load is thought to be lower than others. Greywater from bathtubs and sinks will be treated and fed to 53 toilets. In calculating the amount of greywater that can be collected, the water consumption of the people in the building and the reference values of the fixtures were considered (Table 7).

Table 6. Fixture types and quantity

Fixture type	Total number
Number of Tubs	53
Number of Sinks	67
Number of Toilet Bowls	53

Table 7. Amount of greywater that can be collected in the Hotel

Amount of Collectable Greywater		
Sinks		
Flow time	1	minute
flow rate	2.5	L/min
Number of guest usages	5	times/day
Number of personnel usage	10	times/day
Number of visitor usage	1	times/day
Sinks greywater flow rate	2.46	m ³ /day
Bathtubs		
Flow time	15	minute
flow rate	10	L/min
Number of guest usages	0,5	times/day
Number of personnel usage	0.1	times/day
Number of visitor usage*	0.5	times/day
Bathtub greywater flow rate	6.72	m ³ /day
Total amount of greywater from sinks and bathtubs	9.18	m³/day

*Only visitors to the gym are allowed.

The monthly maximum collectible greywater amount was calculated by multiplying the hotel's monthly occupancy rates. A comparison was made between the amount of greywater that could be collected and the water needed in areas where the treated greywater could be reused. The entire flush water requirement (5.22 m³/day) can be met by the amount of collectible greywater (9.18 m³/day) at the maximum capacity of the Hotel. Laterion, excess water remains, and that amount can be used for garden irrigation, car washing, and cleaning purposes. Therefore, a greywater treatment system with a capacity of 10 m³/day was chosen for the hotel. The selected booster system and pump features for the greywater system with a capacity of 10 m³/day are given in Table 8. In order to find the electricity cost during the operation of the greywater system, the annual energy cost was calculated by taking into account the daily operating times of the feed booster and pumps in the system with electrical power (Table 9).

Table 8. Greywater booster system and pump features

Parameter	Value	Unit
Pump pressure operating range	65.63-80.63	mSS
Pump capacity	3.67	m ³ /hr
Booster tank capacity	139	L

Table 9. Energy cost of the greywater treatment system under operation

Parameter	Value	Unit
Average daily operating time of the system	8	hour
Daily electricity consumption	14	kWhr
Electricity tariff fee	279	kr/ kWhr
Annual electricity operating cost	14.143	TL/year

Greywater systems require periodic maintenance and control. Thus, annual maintenance and repair costs were included in the operating cost. According to the prices received from the companies supplying the greywater system, 26.000 TL/year was taken for the greywater system with a capacity of 10 m³/day. Investment cost components of the GWR system are listed as piping, mechanical equipment, installation, and treatment. Investment costs, together with the operation costs of the system, are given in detail in Table 10.

Table 10. Cost items and fees of Izmir Hotel GWR system

Cost Items	Meter survey (m)	Unit cost (TL)	Total Cost (TL)
Pipe need			
DN15	198	17	3.366
DN25	198	50	9.900
DN32	100	67	6.700
PVC70	198	34	6.732
PVC100	198	50	9.900
PVC125	100	67	6.700
Mechanical equipment			
Shut-off valve	33	83	2.739
Collector	2	415	830
Package booster system	1	30.240	30.240
Booster tank	1	6.840	6.840
Installation			
DN15	198	9	1.782
DN25	198	25	4.950
DN32	100	34	3.400
PVC70	198	17	3.366
PVC100	198	25	4.950
PVC125	100	34	3.400
Shut-off valve	33	42	1.386
Collector	2	208	416
Installation cost (manometer, pressure)	1	8.000	8.000
Treatment			
10 m ³ greywater treatment system	1	507.000	507.000
Total Investment Cost			622.597
Operation cost (electricity)			14.143
Maintenance and Operation Cost			26.000

3. Results and Discussion

The methodology used is given in detail for the Izmir Hotel case. The amount of greywater that can be recycled in the hotel, open 365 days with a daily amount of 5.8 m³ greywater treatment, was calculated as 1.667,24 m³/year. It has been determined that the annual economic savings of 222.078 TL can be achieved in the Izmir province, where the water unit price was 66.26 TL/m³ for non-residential subscribers. The benefit-cost analysis for the Hotel performed with the NPV formula is given in Table 11.

Table 11. Cost and benefit analysis of the Izmir Hotel GWR system

Cost and Benefits	0. year (TL)	12 th year calculated with NPV (TL)
Investment cost	622.597	592.950
Operation cost	40.143	355.795
Annual benefit	110.471	979.135
Annual net benefit	70.329	707

Based on this calculation, the investment cost of the GWR system in the hotel, where a 10 m³/day greywater system will be treated and reused, is paid back after 12 years. The same methodology was used for the two other typologies, housing and industrial plants, and the findings are summarized below.

3.1. Residential Building

The corresponding GWR system design and feasibility analysis results are given in Table 12. The water recovered with the GWR system designed for the residential building is predicted to be used as flush water. In this residential building where 450 people reside, 90% of the flush water need can be met by recycling 7.300 m³/year of greywater. Greywater treatment system capacity was determined as 20 m³/day. The subscriber tariff is lower than the other subscriber types and is determined as 33.13 TL/m³. Accordingly, the water bill had an annual economic saving of 241.849 TL. On the other hand, the initial investment cost was 853.540 TL. As a result of the benefit-cost analysis, the repayment period was found to be 6 years.

Table 12. Residential building greywater system

Parameters used	Values	Unit
Building typology	Housing	
Number of living people	450	person
Number of guests	45	person
Green areas	750	m ²
Water tariff	33,13	TL/m ³
Collected amount of greywater	7.300	m ³ /year
Capacity of the selected treatment system	20	m ³ /day
Demand for flushing	7.873	m ³ /month
Water saving potential	90	%
Economic saving (annual benefit)	241.849	TL/year
Investment cost	853.540	TL
Operation cost	53.973	TL/year
Annual net benefit	187.876	TL/year
Repayment period	6	year

3.2. Industrial Plant

The results of the industrial facility in Izmir, where the GWR system design and feasibility analysis were performed, are given in Table 13. Since there are no showers or bathtubs in the industrial facility with 400 personnel, only the amount of greywater resulting from the sinks was calculated. In the facility, where 5.25 m³ of greywater is produced from daily sink use, the greywater treatment system capacity is determined as 10 m³/day. By recycling 1.890 m³/year of greywater in the industrial facility, 42% of the flush water need can be met. The industrial facility subscriber tariff is higher than residential subscribers and is determined as 66.26 TL/m³. Accordingly, the water bill has an economic saving of 117.445 TL per year. As a result of the benefit-cost analysis of the system, whose initial investment cost was 611.514 TL and operating cost was 44.844 TL/year, the payback period was found as 12 years.

Table 13. Industrial facility greywater system

Parameters	Values	Unit
Building typology	Industrial plant	
Number of people	400	person
Number of guests	20	person
Green areas	500	m ²
Water tariff	66,26	TL/m ³
Collected amount of greywater	1.890	m ³ /year
Capacity of the selected treatment system	10	m ³ /day
Demand for flushing	4.356	m ³ /year
Water saving potential	42	%
Economic saving (annual benefit)	117.445	TL/year
Investment cost	611.513	TL
Operation cost	44.844	TL/year
Annual net benefit	72.600	TL/year
Repayment period	12	year

Table 14 summarizes the total water consumption in the analyzed buildings and water savings from the tap water that can be achieved with the GWR System. Water-saving rates were 46%, 44%, and 29% for the hotel, residential building, and industrial plant. These values show that utilizing alternative water resources like greywater reuse gains back a considerable amount of water. As mentioned previously, the selected typologies were in the planning stage. If these were already built and put into operation, installing a greywater system would require some demolition-production costs. The effect of such costs on the payback period of these buildings was also considered. Table 15 illustrates the effect of the demolition-production cost on the payback periods. The payback periods will, as expected, increase by 1 year in the case of the residential building and the industrial plant and 4 years in the hotel. However, such periods are considered acceptable and feasible compared to the benefits gained.

Table 14. Total water consumption in the studied buildings and water saving rates that can be achieved with the GWR System

Building typology	Recovered greywater (m ³ /year)	Flushing water (m ³ /year)	Garden irrigation (m ³ /year)	Car washing (m ³ /year)	Cleaning (m ³ /year)	Water Use Reference Value (L/person.day)	Number of people	Total Water Consumption in the Building (m ³ /year)	Water Saving Rate (%)
Hotel	1.667	733	731	4.32	230	150	83	3.663	46
Housing	7.300	7.873		-	-	100	450	16.425	44
Industrial plant	1.890	4.536	1.218	432	115	45	400	6.570	29

Table 15. The effect of the demolition-production cost on the payback period in selected typologies

Building typologies	When Applied During the Project Phase		When Applied During the Use Phase	
	Investment cost (TL)	Repayment period (year)	Investment cost (TL)	Repayment period (year)
Hotel	622.597	12	749.797	16
Housing	853.540	6	973.540	7
Industrial plant	611.514	12	649.914	13

On a university campus in Northeastern Mexico, where GWR strategies were implemented coupled with RWH, the payback period was found to be 6 years [28]. India is experiencing a water shortage due to the demand brought by its rapidly growing population. Aybuga and Isildar [29] calculated the repayment period of both RWH and GWR systems in Ankara, Türkiye, as approximately 5 years at the household level. An applied case study was conducted on both systems in a single-family house in Durban, Kwa-Zulu Natal Province, South Africa, and the corresponding payback period was found to be 4.39 years [30]. Another interesting study on the cost-effectiveness of RWH and GWR systems was recently conducted in detached houses in 8 different countries. The results varied widely depending on access to fresh water, water price, water quality, climate change, and the city's precipitation regime. However, the general result of the study revealed

the reality of the approach that such new technologies and their financial indicators will provide benefits in the long term, regardless of the location of the building [31]. According to the results of the surveys conducted in 8 different European cities within the scope of the same study, it is seen that RWH systems were relatively more preferred than GWR systems. This finding highlights a societal problem regarding the questionable hygienic conditions of GWR systems. This situation is consistent with [18], which underlines the need to provide some financial incentives to GWR systems to encourage the use of the GWR system. Finally, [32-33] summarized information on social acceptance of reuse practices. It offers a systematic perspective on general reuse experiments and social isolations for water reuse, considering water source, technology, and end-use elements. Therefore, taking inspiration from reuse practices is not just a technological and financial aspect; it also manages a socio-economic understanding that requires dissemination activities to be carried out across the country.

4. Conclusion

Cost and benefit analyses on installing GWR systems to 3 different building typologies in İzmir Province of Türkiye were the main intention of this study. These 3 buildings were real cases under planning. The investment and operation costs were calculated, and payback periods were determined. In addition to payback periods, it has been observed that the water savings achieved with GWR applications are significant in areas that do not require potable water quality, such as toilet flushing, irrigation, cleaning, and car washing. Since these systems generally require a treatment plant, they need more technical details than RWH systems. Nowadays, packaged membrane modules are supplied by manufacturers, and they also provide technical support during the entire system's operation. In addition, since greywater is produced continuously, there is no water flow problem, and it can be used safely to flush toilets after disinfection. As a result, using recovered water will provide undeniable water savings. Water savings will also protect receiving water resources and reduce the pollution load of wastewater treatment facilities. There will also be a financial benefit as water bills will be greatly reduce.

Savings in total water consumption through GWR were calculated as 46% for the hotel, 44% for the residential building, and 29% for the industrial plant. As seen from the water and economic savings values, high benefits can be achieved with these applications, and thus, freshwater resources can be used more effectively, especially in urbanized areas. Finally, raising public awareness and increasing interest in the great benefits provided by this alternative system is another issue that should be emphasized as much as the implementation by the government and local governments. Its practices could also be further encouraged by providing certain tax benefits similar to those undertaken by some countries as an important adaptation action against climate change.

Author Contributions

The third author directed the project and supervised this study's findings. The second and third authors devised the main conceptual ideas and developed the theoretical framework. The first and second authors performed the data analyses. The first author wrote the manuscript with support from the second, third, and fourth authors. The third author reviewed and edited the paper. All authors read and approved the final version of the paper. This paper is derived from the first author's master's thesis, supervised by the third author.

Conflicts of Interest

All the authors declare no conflict of interest.

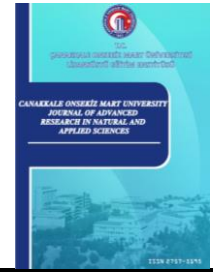
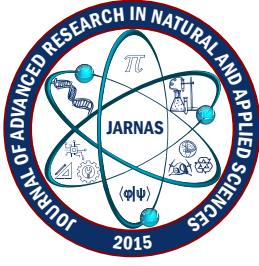
Ethical Review and Approval

No approval from the Board of Ethics is required.






References

- [1] Turkish Ministry of Environment, Urbanization and Climate Change (MoEUCC), <https://ab.csb.gov.tr/turkiye-nin-ilk-iklim-surasi-konyada-toplandi-haber-267396>, Accessed 10 December 2023.
- [2] Marmara Municipalities Union (MMU), Yapılar ve iç mekânda yağmur suyundan yararlanma yöntemleri, <https://marmara.gov.tr/uploads/old-site/2021/03/Aysegul-Baysal-Tanik.pdf>, Accessed 10 December 2023.
- [3] United States Environmental Protection Agency (EPA), Water recycling and reuse: The environmental benefits. Available at: <http://www.epa.gov/region9/water/recycling/>, Accessed 05 October 2022.
- [4] P. Vieira, C. Jorge, D. Covas, *Assessment of household water use efficiency using performance indices*, Resource Conservation Recycling 116 (2017) 94–106.
- [5] V. Novotny, *Water-energy nexus: Retrofitting urban areas to achieve zero pollution*, Building Research and Information 41 (5) (2013) 589–604.
- [6] S. Eslamian, *Urban water reuse handbook*, USA: CRC Press, Taylor and Francis Group 1141 2016.
- [7] P. A. Wilderer, *Applying sustainable water management concepts in rural and urban areas: Some thoughts about reasons, means and needs*, Water Science Technology 4 (2004) 7–16.
- [8] H. Filali, N. Barsan, D. Souguir, V. Nedeff, C. Tomozei, M. Hachicha, *Greywater as an alternative solution for a sustainable management of water resources-a review*, Sustainability 14 (2) (2022) 665.
- [9] V. Lazarova, S. Hills, R. Birks, *Using recycled water for non-potable, urban uses: A review with particular reference to toilet flushing*, Water Science Technology Water Supply 3(4) (2003) 69–77.
- [10] S. Potivichayanon, N. Sittitooon, B. Vinneras, *Exposure assessment of treated greywater reused for irrigation*, Water Science Technology Water Supply 21 (8) (2021) 4404–4417.
- [11] I. N. Shaikh, M. M. Ahammed, *Granular media filtration for onsite treatment of greywater: A review*, Water Science Technology 86 (5) (2022) 992–1016.
- [12] G. E. Üstün, A. Tırpancı, *Greywater Treatment and Reuse*, Uludağ University Journal of The Faculty of Engineering 20 (2) (2015).
- [13] M. A. L. Zavala, R. C. Vega, R. A. L. Miranda, *Potential of rainwater harvesting and greywater reuse for water consumption reduction and wastewater minimization*, Water 8 (2016) 264.
- [14] N. Rodda, L. Salukazanaa, S. A. F. Jackson, M. T. Smith, *Use of domestic greywater for small-scale irrigation of food crops: Effects on plants and soil*, Physics and Chemistry of the Earth A/B/C 36 (2011) 1051-1062.
- [15] U. Stein, Water reuse and water quality aspects in Europe, CAPACITIE Training Course. Berlin: Ecologic Institute, https://www.ecologic.eu/sites/default/files/event/2015/22_steinwaterreusewaterquality_0.pdf, Accessed 15 November 2022.
- [16] European Commission: Directorate-General for Environment, Cherrier, V., Farmer, A., Jarrit, N., Delacamera, G. et al., EU-level instruments on water reuse – Final report to support the Commission's impact assessment, Publications Office, 2016, <https://data.europa.eu/doi/10.2779/974903>, Accessed 1 March 2022.

- [17] European Committee of the Regions: Commission for the Environment, Climate Change and Energy, Gancheva, M., McNeill, A. and Muro, M., Water reuse – Legislative framework in EU regions, European Committee of the Regions, 2018, <https://data.europa.eu/doi/10.2863/846239>, Accessed 5 March 2022.
- [18] Z. L. T. Yu, J. R. De Shazo, M. K. Stenstrom, Y. Cohen, *Cost–benefit analysis of onsite residential greywater recycling: A case study on the city of Los Angeles*, Journal American Water Works Association 108 (2016) E436–E444.
- [19] Ecohome, <https://www.ecohome.net/guides/1561/greywater-recycling-never-looked-better/>, Accessed 15 December 2023.
- [20] *Yerinde içilemez su sistemleri- Bölüm 2: Arıtılmış grisuyun (lavabo atık suyu) kullanımına yönelik sistemler (TS EN 16941-2)*, Turkish Standards Institution 2021.
- [21] Eurosan, <https://eurosan.com.tr/mbr-sistemleri/>, Accessed 15 December 2023.
- [22] SlidePlayer, <https://slideplayer.biz.tr/slide/9141315/>, Accessed 15 December 2023.
- [23] Simurg Peyzaj, <https://simurgpeyzaj.com/yapay-sulak-alanlar-ve-biyolojik-golet/>, Accessed 15 December 2023.
- [24] L. Fangyue, K. Wichmann, R. Otterpohl, *Review of the technological approaches for greywater treatment and reuses*, Science of the Total Environment 407 (2009) 3439–3449.
- [25] W. H. F. Chin, F. A. Roddick, J. L. Harris, *Greywater treatment by UVC/H₂O₂*, Water Research 43 (16) (2009) 3940-3947.
- [26] M., Sanchez, M. J., Rivero, I. Ortiz, *Photocatalytic oxidation of greywater over titanium dioxide suspensions*, Desalination 262 (1-3) (2010) 141-146.
- [27] *Türkiye Kıyılarında Yüzme Suyu Profillerinin Belirlenmesi Projesi, Bileşen 2: Turizmde Çevre Dostu Atıksu Yönetim Modelinin Oluşturulması – Fizibilite Raporu*, TÜBİTAK Marmara Research Center (MAM), Turkish Ministry of Environment, Urbanization and Climate Change (MoEUCC) (2014).
- [28] M. A. L. Zavala, R. C. Vega, R. A. L. Miranda, *Potential of rainwater harvesting and greywater reuse for water consumption reduction and wastewater minimization*, Water 8 (2016) 264.
- [29] K. Aybuga, G. Y. Isıldar, *An evaluation of rain water harvesting and greywater reuse potential for Ankara*, Sigma Journal of Engineering and Natural Sciences 8 (3) (2017) 209–216.
- [30] L. Zhang, A. Njepu, X. Xia, *Minimum cost solution to residential energy-water nexus through rainwater harvesting and greywater recycling*, Journal of Cleaner Production 298 (2021) 126742.
- [31] A. Stec, D. Slys, *Financial and social factors influencing the use of unconventional water systems in single-family houses in eight European countries*, Resources 11 (2022) 16.
- [32] M. Al-Saidi, *From acceptance snapshots to the social acceptability process: Structuring knowledge on attitudes towards water reuse*, Frontiers in Environmental Science 9 (2021) 633841.
- [33] I. A. Al-Khatib, A. A. H. U. Al Shami, G. R. Garcia, I. Celik, *Social acceptance of greywater reuse in rural areas*, Journal of Environmental Public Health (2022) 1–11.



Effects of Pervari Honey from Türkiye on Proliferation, Oxidative Stress, and Apoptosis of Human Breast Cancer Cells

Muazzez Derya-Andeden¹ , Pınar Altın-Çelik² , Mustafa Çakır³ , Ramazan Üzen⁴ ,
Hamiyet Dönmez-Altuntaş⁵ 

^{1,2,4,5}Department of Medical Biology, Faculty of Medicine, Erciyes University, Kayseri, Türkiye

³Department of Medical Biology, Faculty of Medicine, Van Yüzüncü Yıl University, Van, Türkiye

Article Info

Received: 21 Mar 2024

Accepted: 08 Jul 2024

Published: 30 Sep 2024

Research Article

Abstract – Breast cancer is one of the most common causes of deaths worldwide. Major obstacles to treatment have contributed to the increasing popularity of complementary or alternative therapies. Although recent results support the mechanism that honey induces cell death, the full mechanisms are still unknown. This study investigates the potential use of Pervari honey (PH) as an in vitro therapeutic agent in breast cancer. Firstly, the antioxidant capacity and total phenolic content of PH were tested. In addition, MCF-7 and MDA-MB-231 breast cancer cells treated with PH were examined for cell viability, reactive oxygen species production, oxidative deoxyribonucleic acid (DNA) damage, and apoptosis. Our results show that PH treatment decreased cell viability dose-dependently and increased reactive oxygen species (ROS) levels, oxidative DNA damage, and apoptosis rate. The present study suggests that honey is a promising source to produce pharmaceuticals and nutraceuticals for breast cancer therapy.

Keywords – Antioxidant, apoptosis, cancer, honey, oxidative deoxyribonucleic acid (DNA) damage, reactive oxygen species

1. Introduction

Cancer is a disease that disrupts the natural mechanisms that control cell survival, proliferation, and differentiation. The process of cancer progression involves irreversible deoxyribonucleic acid (DNA) damage caused by the accumulation of mutant DNA, the excessive growth of mutant cells and the accumulation of abnormal cells in the form of tumors as a result of advanced genomic alterations, and finally, the spread of cancer cells during the metastatic process [1]. Although almost every organ in the body is susceptible to cancer, the most commonly affected are the liver, colon, and breast. Breast cancer is the most common cancer in women worldwide, with 2.3 million new cases in 2020 and 685,000 deaths [2]. However, most of the chemotherapeutic agents currently in use are not very effective. They may lose their efficacy due to the emergence of resistance and their numerous side effects [3]. Scientists have focused on the potential use of natural products to develop fewer toxic alternatives to chemotherapy and radiation for cancer.

There are numerous molecular subtypes of breast cancer cells, such as triple negative or positive [4]. The cells lacking the expression of both steroid receptors are the source of triple-negative breast cancer cells [5]. Human triple-negative breast cancer cells are modeled by the MDA-MB-231 cell line [6]. MCF-7 cells, on the other hand, are hormone-dependent triple-positive breast cancer cells that have estrogen receptors on the cell surface

¹derya.muazzez@gmail.com (Corresponding Author); ²pnar.altinclk@gmail.com; ³cakirmustafa32@gmail.com; ⁴r-uzen@yandex.com;

⁵donmez@erciyes.edu.tr

[7]. The proliferation of these cells is induced by estrogen [8]. The ER-positive subtype of breast cancer is the most common form of the disease. Due to its high estrogen receptor (ER) expression and extreme hormone sensitivity, MCF-7 is the most commonly used breast cancer cell line in research [9]. These two cell lines were used in our study to examine both subtypes of breast cancer.

Recently, many natural products containing a wide variety of molecular targets, including transcription factors, cytokines, chemokines, adhesion molecules, growth factor receptors, and inflammatory enzymes, and exhibiting novel structural features and mechanisms of action have been intensively studied in a variety of cancer cell lines because of their potential to be a good and cost-effective source of novel pharmacological structures [10-12]. In addition, combining natural products with established chemotherapeutic treatments has significantly improved patient survival as cancer cells respond better to chemotherapy and radiotherapy [13]. Honey, used as a natural ingredient in complementary and alternative medicine, stands out as a valuable bee product that contains many biologically active compounds with high antioxidant capacity and other health properties that make it a suitable source for exploring medicinal potential [14, 15]. In recent years, several benefits of honey have been reported, such as anti-inflammatory [16, 17], antimicrobial [18, 19], and antioxidant [20, 21] effects. In addition, the anticancer effects of honey have been demonstrated in various cancers, including renal [22], prostate [23], endometrial [24], cervical [25], and breast [26, 27] cancers.

Research into honey as a possible preventive and therapeutic supplement is gaining momentum. Numerous studies investigate the anticancer properties of different types of honey from different sources against various cancer cell lines and tissues [28]. The bioactive components of honey are generally consistent with its chemopreventive abilities. Certain studies have demonstrated the interference of bioactive chemicals in honey with pro-apoptotic, antioxidant, and anti-proliferative cell signaling pathways; however, the exact mechanism underlying this interference remains unclear [29].

The biochemical composition and pharmacological activity of honey varies from country to country and even from region to region within the same country due to geographic conditions, climate, and floral sources [30]. In Türkiye, which is the second largest honey producer in the world, with a production of 104.08 thousand tons in 2020 [31], there are different types of honey, such as chestnut, acacia, pine, and flower honey, due to the rich biodiversity of flora. Pervari honey (PH), produced by bees feeding on the rich flora consisting of hundreds of endemic plants such as clover, sage, and thyme and given at altitudes between 1600 meters and 2000 meters, is considered one of the best quality honey in Türkiye [32]. Although there are many studies in the literature on the anticancer properties of honey from different parts of the world [1], the number of studies on the anticancer and apoptotic effects of honey from Türkiye is limited [23]. This is the first study to investigate the cytotoxic effect of PH and its ability to induce apoptosis in human breast cancer cell lines. In this study, we hypothesize that PH has an apoptotic effect on breast cancer cells and can be used in the treatment plan for breast cancer.

2. Materials and Methods

2.1. Honey Sample

PH sample was kindly obtained from Erkan Bilen, Pervari Honey Cooperative, Siirt, Türkiye. The honey was stored in the dark at room temperature. PH was freshly dissolved in the complete Dulbecco's Modified Eagle Medium (DMEM) supplemented with 10% fetal bovine serum and 2% penicillin/streptomycin at a final concentration of 100 mg/mL and sterilized with a 0.2 µm syringe filter before being added to cells.

2.2. Total Phenolic Content

The total phenolic content of PH was measured using the Folin-Ciocalteu method described by Singleton and Rossi [33]. Briefly, 20 µL of the honey solution (100 mg/mL in distilled water) was combined with 100 µL of Folin-Ciocalteu reagent (1:10) and followed by 80 µL of 15% sodium carbonate. After mixing the ingredients,

the absorbance at 700 nm was measured. The results were reported as milligram gallic acid equivalents per kilogram honey (mg GAE/kg honey) following (2.1) using a standard gallic acid concentration (5-500 µg/mL) curve.

$$C = (C1 \times V) \div m \quad (2.1)$$

Here, C is total phenolic content (mg GAE / kg honey), $C1$ is gallic acid concentration obtained from the standard curve graph (mg/mL), V is honey solution volume (mL), and m is the honey weight (kg).

2.3. DPPH Assay

The antioxidant activity of PH was determined using the 2,2-diphenyl-1-picrylhydrazyl hydrate radical (DPPH) assay, according to Cheng et al. [34]. The honey sample was diluted in methanol at 1.5 to 100 mg/mL concentrations, and 0.1 mL from each dilution was mixed with 0.1 mL of DPPH (0.2 mM in methanol). The mixtures were left in the dark at room temperature for 30 minutes after gently shaking, and the absorbance was determined at 517 nm. The radical scavenging activity (RSA) of the honey (100 mg/mL) was calculated according to the following (2.2) and expressed as percent inhibition. Butyl hydroxytoluene (BHT) (100 mg/mL) was used as a positive control.

$$\% \text{ Radical scavenging activity} = (1 - As/Ac) \times 100 \quad (2.2)$$

Here, As is the absorbance of the honey sample, and Ac is the absorbance of the control.

2.4. Cell Culture

Human breast adenocarcinoma cell lines, MCF-7 and MDA-MB-231, were obtained from the American Type Culture Collection (ATCC, Manassas, VA, and USA). They were propagated in DMEM/F12, supplemented with 10% fetal bovine serum and 2% penicillin/streptomycin. The cells were maintained at 37°C in a 5% CO₂ humidified atmosphere. All cell passages used were between passages 20 and 30.

2.5. Cell Viability

Anti-proliferative activity of PH as a cytotoxic agent in MCF-7 and MDA-MB-231 cells was assessed by 3-(4,5-dimethylthiazol-2-yl)-2,5-diphenyltetrazolium bromide (MTT) assay [35]. Briefly, cells were seeded in a culture medium at a density of 5×10^3 cells/well in 96 flat-bottomed well plates. After 24 hours of plating, honey samples were added at final concentrations ranging from 10-60 mg/mL in DMEM. After 48 hours of incubation, the medium was replaced with MTT dissolved in the medium at a final concentration of 0.5 mg/mL for a further 4 hours at 37°C. Then, the MTT-formazan was solubilized in DMSO, and the optical density was measured at 570 nm and a reference wavelength of 620 nm. Cytotoxic activity was calculated from the following (2.3):

$$\% \text{ Cell viability} = (As \div Ac) \times 100 \quad (2.3)$$

Here, As is the absorbance of the PH-treated cells, and Ac is the absorbance of the untreated cells. The viability of the control cells was assumed to be 100%, and the viability of PH-treated cells was compared with that of the control, and the IC₅₀ values of PH were determined for MCF-7 and MDA-MB-231 cells.

2.6. Flow Cytometric Analysis of Apoptosis

The FITC Annexin V Apoptosis Detection Kit with 7-AAD detected apoptotic cells (Biolegend, 640922). The cells were seeded in a 24-well plate with a density of 5×10^4 cells per well and treated with the IC₅₀ doses of PH and Doxorubicin for 48 hours. Doxorubicin was used as a standard cytotoxic agent. Cells were harvested

and rinsed with $1 \times$ PBS after incubation. The cells were resuspended in 200 μ L of Annexin V Binding Buffer and transferred to a new test tube with 100 μ L of cell suspension. Cells were gently vortexed and kept for 15 minutes at room temperature in the dark after adding 5 μ L of FITC Annexin V and 5 μ L of 7-AAD viability staining solutions. Finally, 400 μ L of Annexin V Binding Buffer was added to each tube, and a flow cytometer was used to analyze the cells (FACS Aria III, BD Biosciences, USA). The results were expressed as a percentage of early, late, and total apoptotic cells.

2.7. Intracellular ROS Production

The intracellular ROS generation levels were determined using dichlorodihydrofluorescein diacetate (DCFH-DA), a fluorescent probe. The cells were seeded at a density of 1×10^4 cells per well in a 96-well plate. They were subsequently given the IC₅₀ doses of PH and Doxorubicin for 48 hours. Doxorubicin was used as a standard cytotoxic agent. After incubation, the medium was removed, and cells were treated with 10 μ M DCFH-DA for 30 minutes at 37 °C. The fluorescence intensity was measured using a microplate reader at 485 nm for excitation and 530 nm for emission wavelengths. The results are expressed as a percentage of the untreated control value, with the mean absorbance normalized. H₂O₂, a well-known ROS-inducing toxin, was used as a positive control to ensure the assay provided the predicted results.

2.8. Oxidative DNA Damage

The 8-hydroxy-2'-deoxyguanosine (8-OHdG) ELISA kit (Fine Test, #EU2548, Wuhan Fine Biotech Co., Ltd., China) was used for quantitative detection of 8-OHdG in the supernatant of the cells. After the cells were treated with IC₅₀ doses of PH and Doxorubicin for 48 hours, the ELISA assay was performed according to the manufacturer's protocol. Doxorubicin was used as a standard cytotoxic agent. The target concentration of the samples was interpolated from the standard curve obtained from the measurement of 450 nm absorbance.

2.9. Statistical Analysis

The cell viability (%) for each concentration of PH was calculated and expressed as a percentage relative to the control response. IC₅₀ values of PH were also calculated. All values are expressed as the mean \pm standard deviation of three (MTT assay) measurements. Statistical analysis was performed using a t-test two-tailed distribution, assuming two-sample unequal variance. $p < 0.05$ value was considered statistically significant (* $p < 0.05$, ** $p < 0.01$, and *** $p < 0.001$). Data was analyzed using GraphPad Prism 8 (GraphPad Software Inc., San Diego, CA, USA).

3. Results and Discussion

3.1. Total Phenolic Content

Phenolic compounds can inhibit cell proliferation and induce cell death in various cancer cell lines [36-39]. In this study, phenolic contents were expressed as total phenolic acid contents. The total phenolic content in PH was found to be 0.71 mg GAE/g honey by plotting the gallic acid standard calibration curve ($R^2=0.9995$). When comparing the contents with other studies, the content determined for PH is quite higher than those of other Turkish honey such as multifloral, chestnut, acacia, rhododendron (0.02-0.26 mg GAE/g honey; [20]), clover, lavender, lime, astragalus (0.25-0.53 mg GAE/g honey; [40]), and lower than those of others such as chestnut, cedar, pine honey (31.6-98.6 mg GAE/g honey; [41]), chestnut, heather, oak (0.98-1.20 mg GAE/g honey; [40]), pine, thyme, citrus honey (0.88- 10.93 mg GAE/g honey; [42]). Considering these studies, it is clear that the phenolic content of honey samples varies in quality and quantity depending on the botanical origin and nectar source.

3.2. Antioxidant Activity

Antioxidants are important reducing substances that scavenge ROS. They have been reported to inhibit the growth of various cancer cells [43]. Honey samples from different regions have been shown to have antioxidant activity. Still, the number of antioxidants they contain is influenced by their botanical origin, variety, processing, handling, and storage [44, 45]. In this study, the antioxidant activity of PH was determined using the DPPH radical scavenging assay. PH showed higher activity ($IC_{50}=41.33$ mg/mL) than the positive control BHT ($IC_{50}=58$ mg/mL). In a study in which 16 different types of honey from Brazil were examined, the results of the DPPH test varied between 8.20 ± 0.16 and 62.12 ± 0.13 mg/mL IC_{50} value [21]. One recent study reported that the DPPH assay of chestnut honey samples from different regions in Türkiye was found between 6.32 ± 0.35 and 17.06 ± 1.30 mg/mL IC_{50} value [46]. Therefore, it can be concluded that honey's antioxidant effect can vary depending on the phytochemical content, flower source, and geographical origin.

3.3. The Effect of Pervari Honey on the Proliferation of MCF-7 and MDA-MB-231 Cells

The effect of PH on the viability of MCF-7 and MDA-MB-231 cells was determined using the MTT assay, which indirectly measures the effect of a substance or extracts on cell survival and proliferation. The use of PH on MCF-7 and MDA-MB-231 cells at different concentrations over 48 hours caused decreased cell viability in a dose-dependent manner (Figure 1). PH treatment resulted in a significant decrease in cell viability at 50 and 55 mg/mL (IC_{50} doses) concentrations in MCF-7 and MDA-MB-231 cells, respectively, compared to the control group.

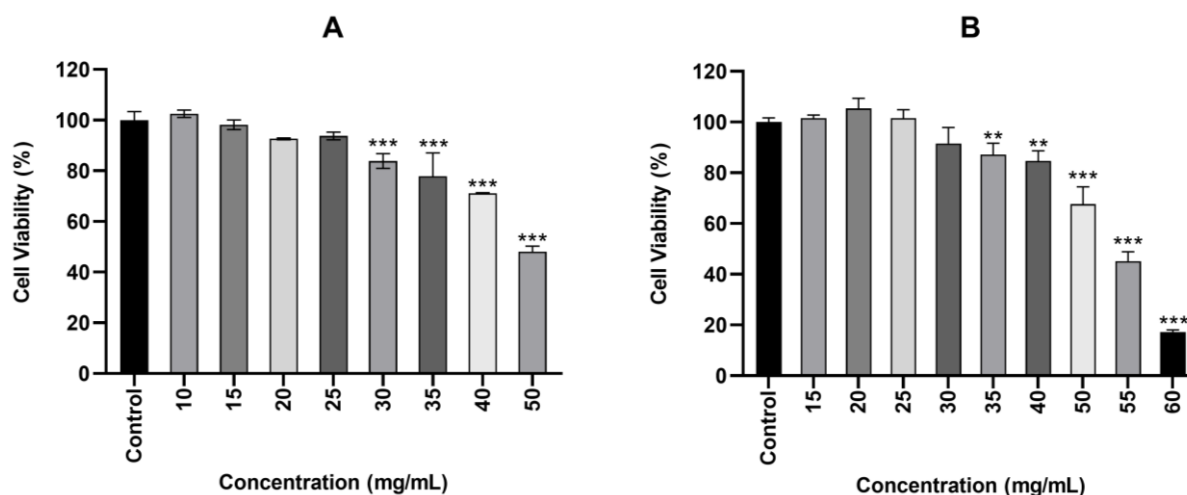


Figure 1. (A) Cytotoxicity evaluation of Pervari honey on MCF-7 cells using MTT assay. (B) Cytotoxicity evaluation of Pervari honey on MDA-MB-231 cells using MTT assay. Untreated cells served as control. All the values are presented as mean \pm SEM (n=3). The significance of difference is demonstrated as ** $p < 0.01$ and *** $p < 0.001$ in comparison to the control group

Based on conclusive data from previous studies investigating the cytotoxic effects of different types of honey on breast cancer cell lines, we performed a PH treatment for 48 hours [41, 47]. In view of studies showing that polyphenols and phenolic acids inhibit cancer-related signaling pathways and processes [48, 49], the chemical composition of honey could be responsible for the different effects of various types of honey on viability/proliferation.

3.4. Apoptosis Rate by Flow Cytometry Analysis

Apoptosis is a gene-controlled and programmed cell death characterized by physical changes such as the breakage of chromosomal DNA, swelling of the plasma membrane, and shrinkage of the cell. One of the most important mechanisms of cancer drugs is the induction of apoptosis. For this reason, researchers have focused

on the potential use of natural and synthetic chemicals for novel cancer treatments to increase the sensitivity and efficacy of drug-induced apoptosis. In flow cytometric analyses, propidium iodide, which binds to cellular DNA to detect apoptotic and necrotic cells at a very late stage, and the fluorescent antibody annexin V, which binds to phosphatidylserine, were used to detect apoptotic cells. In this study, after treatment with 50 and 55 mg/mL PH for 48 hours, PH mostly induced early apoptosis of 33.7% and 10.5% in MCF-7 and MDA-MB-231 cells, respectively.

In contrast, the percentage of apoptosis in the control group was 15.3% and 1.46% in MCF-7 and MDA-MB-231 cells, respectively, as shown in Figure 2. Doxorubicin treatment was more effective than PH in inducing apoptosis, with 59.6% and 29.5% early apoptosis rates for MCF-7 and MDA-MB-231 cells, respectively. Low necrotic cell rates (<4 %) were also observed in all cell groups (Figure 2).

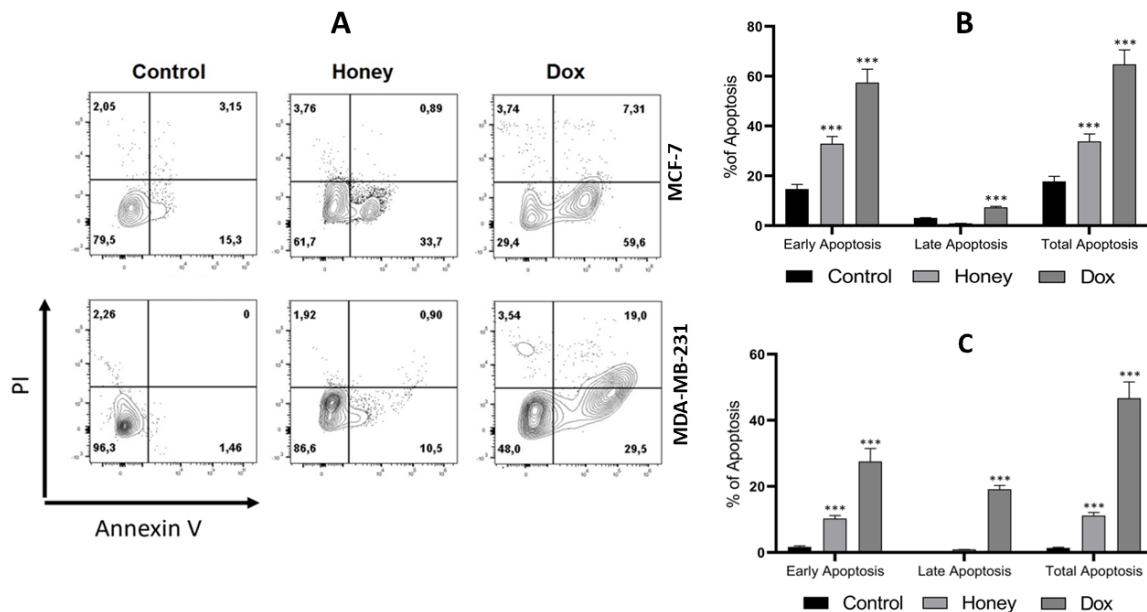


Figure 2. Apoptotic effect of Pervari honey treatment on breast cancer cells by flow cytometry. (A) The histogram represents the percentage of viable (left bottom), early apoptotic (right bottom), late apoptotic (right-top), and necrotic cells (left top). (B) The apoptotic ratio for MCF-7 cells after treatment with 50 mg/mL PH for 48 hours. (C) The apoptotic ratio for MDA-MB-231 cells after treatment with 55 mg/mL PH for 48 hours. The apoptotic ratio was determined by Annexin V FITC/PI assay. The bars represent mean values \pm SEM of three independent experiments. The significance of the differences compared to the control group is indicated with *** $p < 0.0001$

It has previously been reported that a Malaysian honey, Tualang, significantly reduced the proliferation of human breast cancer cells MCF-7 (55.6%) and MDA-MB-231 (51.2%) and there was not much difference between the total apoptosis rate of the two cell lines [47]. However, in our study, the total apoptosis rate of MCF cells (34.6 %) was significantly higher than that of the MDA-MB-231 cell line (11.4 %). While the apoptotic effect of PH and Tualang honey was similar in MCF-7 cells, Tualang honey showed a significantly stronger apoptotic effect in MDA-MB-231 cells. Many research groups have studied the anticancer effect of honey from different regions of Türkiye on breast cancer cell lines [50, 51]. The study conducted by Seyhan et al. [41] showed that 85 % and 90 % of MCF-7 cells died after 48 hours of treatment with chestnut honey at a dose of 2.5 and 5 μ g/mL, respectively, whereas 34.6% apoptotic cell death was observed in MCF-7 cells at PH dose of 50 mg/mL in our study. These studies show that honey's doses and effects vary depending on the source and geographical region from which it is obtained.

3.5. ROS Production

This study investigated the effect of PH on ROS production in breast cancer cells using the DCFH-DA assay. PH treatment with IC₅₀ doses of PH and Doxorubicin for 48 hours significantly increased ROS production in

both cell lines (Figure 3). In normal cells, low levels of ROS contribute to cell proliferation [52]. Previous studies have shown that elevated ROS levels cause oxidative damage and trigger cancer cell death in many cancers, including breast cancer [53]. Therefore, the inhibitory effect of PH on cancer cell proliferation may be partly mediated by ROS-dependent mechanisms. Furthermore, PH caused higher ROS levels in MCF-7 cells than in MDA-MB-231 cells, and high ROS levels may also be associated with higher apoptosis rates in MCF-7 cells (Figure 2B). This result was similar to previous findings reported that cell apoptosis could be induced by stimulated ROS overexpression [54,55].

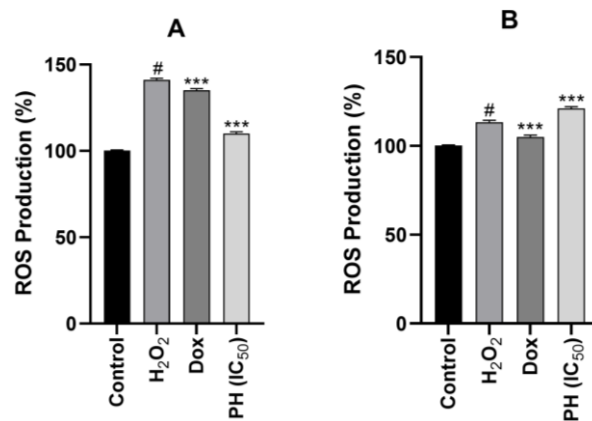


Figure 3. (A) Effect of treatment with Pervari honey on ROS production in MCF-7 cells. (B) Effect of treatment with Pervari honey on ROS production in MDA-MB-231 cells. Untreated cells served as control. All the values are presented as mean \pm SEM (n=3). The significance of the difference is demonstrated as #p < 0.001 compared to the control group and *** p < 0.001 compared to the H₂O₂ group

Reactive oxygen species (ROS) are by-products of mitochondrial metabolism and redox signaling [56]. If ROS homeostasis becomes unbalanced due to an excessive accumulation of ROS, this can lead to the development of various diseases, such as neurodegenerative diseases, cardiovascular diseases, and cancer. Depending on their concentration, ROS have a dual effect on cancer. Higher levels of ROS have been found to play a role in tumorigenesis and have a chemotherapeutic effect in suppressing cancer growth by promoting apoptosis and cell death [57].

Honey may also prevent cancer growth by regulating oxidative stress, i.e., by enhancing or inducing oxidative stress. The anticancer effects of honey, which it exerts via antioxidants or pro-oxidants, appear to depend entirely on the level of oxidative stress in cancer cells. If cancer cell survival depends on low levels of ROS and oxidative stress, honey acts as a pro-oxidant, thereby increasing ROS and oxidative stress [58]. In addition, few studies have addressed the effect of honey on intracellular ROS production to induce apoptotic cell death in cancer cell lines [59–61].

3.6. Oxidative DNA Damage

The increased level of 8-hydroxyguanosine (8-OHdG) indicates oxidative DNA damage [62]. Oxidative stress was triggered either by the production of ROS or by the depletion of intracellular antioxidant defense mechanisms. Antioxidants protect against oxidative stress and can effectively scavenge free radicals [63]. In the present study, after treatment with IC50 doses of PH and Doxorubicin for 48 hours, PH was found to increase 8-OHdG levels by causing oxidative DNA damage in MCF-7 and MDA-MB-231 cells. In both cell lines, 8-OHdG levels were close to each other in the PH-treated group, 49 and 51.5 ng/mL for MCF-7 and MDA-MB-231 cells, respectively.

Furthermore, compared to the control group, the increase in the MDA-MB-231 cells (p < 0.001) was significantly higher than in the MCF-7 cells (p < 0.05) (Figure 4). Contrary to our results, Musarrat et al. [64] found that the ER-positive cell line MCF-7 showed a 9.3-fold higher 8-OHdG level than the ER-negative cell line MDA-MB 231. The changes in the genome of breast cells are probably caused by the oxidative attack of

ROS resulting from estrogen-induced oxidative stress in combination with the receptor-mediated proliferation of the damaged cells [65]. However, the higher amount of oxidative DNA damage in MDA-MB-231 cells suggests that the stimulation of proliferation in triple-negative breast cancer with poor prognosis may be associated with non-estrogen factors, although estrogens stimulated proliferation and DNA damage in breast cancer [66]. Moreover, PH-induced elevated 8-OHdG levels in MCF-7 and MDA-MB-231 cells could contribute to increased apoptotic rates in these cells, and PH may have potential in the treatment of breast cancer.

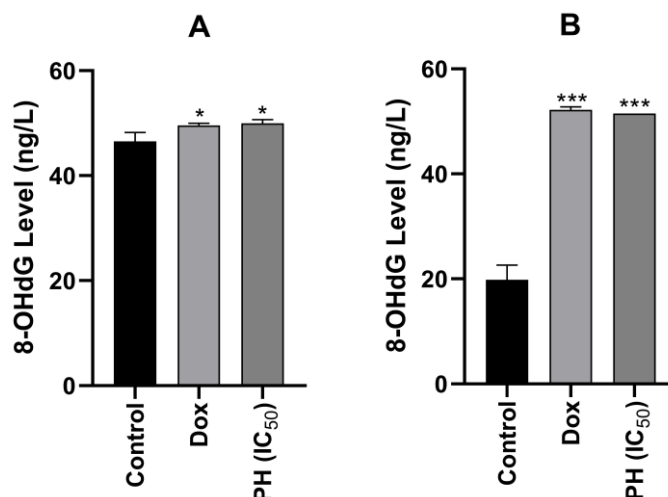


Figure 4. (A) Effect of Pervari honey on oxidative DNA damage in MCF-7 cells. (B) Effect of Pervari honey on oxidative DNA damage in MDA-MB-231 cells. 8-OHdG ELISA assay was performed to measure oxidative DNA damage. Untreated cells served as control. All the values are presented as mean \pm SEM (n=3). The significance of the difference is demonstrated as * $p < 0.05$ and *** $p < 0.001$ in comparison to the control group

4. Conclusion

PH is the best-selling honey in Türkiye. However, the effect of PH on breast cancer is still unknown, and there is no information about the phenolic profiles of the honey. This study investigated the anticancer effects and phenolic profiles of PH for the first time. PH may be a promising candidate for studies to develop targeted therapies and reduce certain excessive adverse effects of current approaches. These results suggest that PH has great potential for preventive and rehabilitative use for treatment and further experiments are needed to explore the signaling pathways.

Author Contributions

The first and second authors devised the main conceptual ideas and developed the theoretical framework. The first, second, and third authors performed the experiment and statistical analyses. The fourth author supported the study for methodology and software usage. The fifth author directed and supervised this study. The first author wrote the manuscript with support from the second and fifth authors. The fifth author reviewed and edited the paper. All authors read and approved the final version of the paper.

Conflicts of Interest

All the authors declare no conflict of interest.

Ethical Review and Approval

No approval from the Board of Ethics is required.

References

- [1] T. Eteraf-Oskouei, M. Najafi, *Uses of natural honey in cancer: An updated review*, *Advanced Pharmaceutical Bulletin* 12 (2) (2022) 23 pages.
- [2] World Health Organization, <https://www.who.int/news-room/fact-sheets/detail/breast-cancer>, Accessed: 27 May 2022.
- [3] A. Wellstein, *General principles in the pharmacotherapy of cancer*, Goodman & Gilman's: The Pharmacological Basis of Therapeutics, 13th Edition, McGraw-Hill Education, New York, 2015, Ch. 65.
- [4] A. Rezano, F. Ridhayanti, A. R. Rangkuti, T. Gunawan, G. N. A. Winarno, I. Wijaya, *Cytotoxicity of simvastatin in human breast cancer MCF-7 and MDA-MB-231 cell lines*, *Asian Pacific Journal of Cancer Prevention* 22 (2021) 33–42.
- [5] K. N. Stevens, C. M. Vachon, F. J. Couch, *Genetic susceptibility to triple-negative breast cancer*, *Cancer Research* 73 (7) (2013) 2025–2030.
- [6] A. Kabała-Dzik, A. Rzepecka-Stojko, R. Kubina, M. Iriti, R. D. Wojtyczka, E. Buszman, J. Stojko, *Flavonoids, bioactive components of propolis, exhibit cytotoxic activity and induce cell cycle arrest and apoptosis in human breast cancer cells MDA-MB-231 and MCF-7-A comparative study*, *Cellular and Molecular Biology* 64 (8) (2018) 10 pages.
- [7] B. Westley, H. Rochefort, *Estradiol induced proteins in the MCF7 human breast cancer cell line*, *Biochemical and Biophysical Research Communications* 90 (2) (1979) 410–416.
- [8] B. S. Katzenellenbogen, K. L. Kendra, M. J. Norman, Y. Berthois, *Proliferation, hormonal responsiveness, and estrogen receptor content of MCF-7 human breast cancer cells grown in the short-term and long-term absence of estrogens*, *Cancer Research* 47 (1987) 4355–4360.
- [9] D. L. Holliday, V. Speirs, *Choosing the right cell line for breast cancer research*, *Breast Cancer Research* 13 (2011) Article Number 215 7 pages.
- [10] A. R. M. R. Amin, O. Kucuk, F. R. Khuri, D. M. Shin, *Perspectives for cancer prevention with natural compounds*, *Journal of Clinical Oncology* 27 (16) (2009) 14 pages.
- [11] W. Park, A. R. M. Ruhul Amin, Z. G. Chen, D. M. Shin, *New perspectives of curcumin in cancer prevention*, *Cancer Prevention Research* 6 (5) (2013) 20 pages.
- [12] A. Haque, D. Brazeau, A. R. Amin, *Perspectives on natural compounds in chemoprevention and treatment of cancer: An update with new promising compounds*, *European Journal of Cancer* 149 (2021) 165–183.
- [13] M. K. Shanmugam, J. H. Lee, E. Z. P. Chai, M. M. Kanchi, S. Kar, F. Arfuso, A. Dharmarajan, A. P. Kumar, P. S. Ramar, C. Y. Looi, M. R. Mustafa, V. Tergaonkar, A. Bishayee, K. S. Ahn, G. Sethi, *Cancer prevention and therapy through the modulation of transcription factors by bioactive natural compounds*, *Seminars in Cancer Biology* 40-41 (2016) 35–47.
- [14] S. Ahmed, S. A. Sulaiman, A. A. Baig, M. Ibrahim, S. Liaqat, S. Fatima, S. Jabeen, N. Shamim, N. H. Othman, *Honey as a potential natural antioxidant medicine: An insight into its molecular mechanisms of action*, *Oxidative Medicine and Cellular Longevity* 2018 (2018) Article ID 8367846 19 pages.
- [15] R. J. Masad, S. M. Haneefa, Y. A. Mohamed, A. Al-Sbiei, G. Bashir, M. J. Fernandez-Cabezudo, B. K. al-Ramadi, *The immunomodulatory effects of honey and associated flavonoids in cancer*, *Nutrients* 13 (4) (2021) 15 pages.
- [16] F. C. Biluca, B. da Silva, T. Caon, E. T. B. Mohr, G. N. Vieira, L. V. Gonzaga, L. Vitali, G. Micke, R. Fett, E. M. Dalmarco, A. C. O Costa, *Investigation of phenolic compounds, antioxidant and anti-inflammatory activities in stingless bee honey (Meliponinae)*, *Food Research International* 129 (2020)

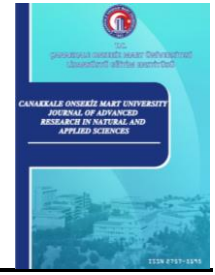
108756 9 pages.

- [17] H. R. El-Seedi, N. Eid, A. A. A. El-Wahed, M. E. Rateb, H. S. Afifi, A. F. Algethami, C. Zhao, Y. Al Nagggar, S. M. Alsharif, H. E. Tahir, B. Xu, K. Wang, S. A. M. Khalifa, *Honey bee products: Preclinical and clinical studies of their anti-inflammatory and immunomodulatory properties*, *Frontiers in Nutrition* 8 (2022) 19 pages.
- [18] N. Ecem Bayram, M. O. Yüzer, S. Bayram, *Melissopalynology analysis, physicochemical properties, multi-element content and antimicrobial activity of honey samples collected from Bayburt, Turkey*, *Uludağ Bee Journal* 19 (2) (2019) 16 pages.
- [19] S. Mežnarić, I. B. Karaconji, G. Crnkovic, A. Lesar, T. Pavlesic, D. Vuckovic, I. Gobin, *Combined inhibitory effect of fir (Abies alba Mill.) honeydew honey and probiotic bacteria lactiplantibacillus plantarum on the growth of salmonella enterica serotype typhimurium*, *Antibiotics* 11 (2) (2022) 13 pages.
- [20] N. Akgün, Ö. F. Çelik, L. Kelebekli, *Physicochemical properties, total phenolic content, and antioxidant activity of chestnut, rhododendron, acacia and multifloral honey*, *Journal of Food Measurement and Characterization* 15 (4) (2021) 8 pages.
- [21] D. S. Pena Júnior, C. A. Almeida, M. C. F. Santos, P. H. V. Fonseca, E. V. Menezes, A. F. de M. Junior, M. M. Brandao, D. A. de Oliveira, L. F. de Souza, J. C. Silva, V. de A. Royo, *Antioxidant activities of some monofloral honey types produced across Minas Gerais (Brazil)*, *PLoS One* 17 (1) (2022) 12 pages.
- [22] S. Samarghandian, J. T. Afshari, S. Davoodi, *Honey induces apoptosis in renal cell carcinoma*, *Pharmacogn Mag* 7 (25) (2011) 8 pages.
- [23] B. Kaya, A. Yıldırım, *Determination of the antioxidant, antimicrobial and anticancer properties of the honey phenolic extract of five different regions of Bingöl province*, *Journal of Food Science and Technology* 58 (6) (2021) 2420–2430.
- [24] Y. He, Y. Shi, Y. Yang, H. Huang, Y. Feng, Y. Wang, L. Zhan, B. Wei, *Chrysin induces autophagy through the inactivation of the ROS-mediated Akt/mTOR signaling pathway in endometrial cancer*, *International Journal of Molecular Medicine* 48 (3) (2021) 13 pages.
- [25] D. Bose, A. Chaudhary, M. Padmavati, J. Chatterjee, R. Banerjee, *In vitro evaluation of anti-proliferative activity of protein from Litchi chinensis honey against human cervical cancer cell line (HeLa)*, *Journal of Herbal Medicine* 31 (2022) 100518 8 pages.
- [26] E. M. Halawani, *Potential effects of Saudi Shaoka (Fagonia bruguieri) honey against multi-drug-resistant bacteria and cancer cells in comparison to Manuka honey*, *Saudi Journal of Biological Sciences* 28 (12) (2021) 11 pages.
- [27] A. N. Fauzi, N. S. Yaacob, *Cell cycle and apoptosis pathway modulation by Tualang honey in ER-dependent and -independent breast cancer cell lines*, *Journal of Apicultural Research* 55 (5) (2016) 11 pages.
- [28] M. Sakač, P. Jovanov, A. Marić, D. Četojević-Simin, A. Novaković, D. Plavšić, D. Škrobot, R. Kovač, *Antioxidative, antibacterial and anti-proliferative properties of honey types from the western Balkans*, *Antioxidants* 11 (6) (2022) 1120 14 pages.
- [29] M. A. Al-Kafaween, M. Alwahsh, A. B. Mohd Hilmi, D. H. Abulebdah, *Physicochemical characteristics and bioactive compounds of different types of honey and their biological and therapeutic properties: A comprehensive review*, *Antibiotics* 12 (2) (2023) 337 34 pages.
- [30] L. D. O. Sant'Ana, A. B. Buarque Ferreira, M. C. A. Lorenzon, R. L. L. Berbara, R. N. Castro, *Correlation of total phenolic and flavonoid contents of Brazilian honey with colour and antioxidant capacity*, *International Journal of Food Properties* 17 (1) (2014) 30 pages.

- [31] Statista (2022), <https://www.statista.com/statistics/812172/global-top-producers-of-honey/>, Accessed 17 Oct 2022.
- [32] E. Demirhan, *Siirt'ten şifa kaynağı: Pervari balı*, Türk Tarım Orman Dergisi 270 (2022) 82–85.
- [33] V. L. Singleton, J. A. Rossi, *Colorimetry of total phenolics with phosphomolybdic-phosphotungstic acid reagents*, American Journal of Enology and Viticulture 16 (3) (1965) 144–158.
- [34] Z. Cheng, J. Moore, L. Yu, *High-throughput relative DPPH radical scavenging capacity assay*, Journal of Agricultural and Food Chemistry 54 (20) (2006) 7429–7436.
- [35] T. Mosmann, *Rapid colorimetric assay for cellular growth and survival: Application to proliferation and cytotoxicity assays*, Journal of Immunological Methods 65 (1–2) (1983) 55–63.
- [36] S. Kiokias, V. Oreopoulou, *A review of the health protective effects of phenolic acids against a range of severe pathologic conditions (Including coronavirus-based infections)*, Molecules 26 (17) (2021) 5405 18 pages.
- [37] M. Z. Mumtaz, F. Kausar, M. Hassan, S. Javaid, A. Malik, *Anticancer activities of phenolic compounds from Moringa oleifera leaves: in vitro and in silico mechanistic study*, Beni-Suef University Journal of Basic and Applied Sciences 10 (1) (2021) 11 pages.
- [38] J. Duan, H. Guo, Y. Fang, G. Zhou, *The mechanisms of wine phenolic compounds for preclinical anticancer therapeutics*, Food & Nutrition Research 65 (2021) 15 pages.
- [39] I. C. da S. Haas, D. J. Marmitt, I. M. T. Fedrigo, M. I. Goettert, M. T. Bordignon-Luiz, *Evaluation of anti-proliferative and anti-inflammatory effects of non-pomace sediment of red grape juices (Vitis labrusca L.) in healthy and cancer cells after in vitro gastrointestinal simulation*, PharmaNutrition 13 (2020) 100204 31 pages.
- [40] Z. Can, O. Yildiz, H. Sahin, E. Akyuz Turumtay, S. Silici, S. Kolayli, *An investigation of Turkish honeys: Their physico-chemical properties, antioxidant capacities and phenolic profiles*, Food Chemistry 180 (2015) 133–141.
- [41] M. F. Seyhan, E. Yılmaz, Ö. Timirci Kahraman, N. Saygılı, H. İ. Kısakesen, A. P. Eronat, A. B. Ceviz, S. B. Gazioğlu, H. Yılmaz Aydoğan, O. Öztürk, *Anatolian honey is not only sweet but can also protect from breast cancer: Elixir for women from Artemis to present*, IUBMB Life 69 (9) (2017) 12 pages.
- [42] H. Sipahi, G. Aydogan, S. Helvacioğlu, M. Charehsaz, E. Guzelmeric, A. Aydin, *Antioxidant, anti-inflammatory and antimutagenic activities of various kinds of Turkish honey*, Fabad Journal of Pharmaceutical Sciences 42 (1) (2017) 7–13.
- [43] M. Ozcan, D. Aydemir, M. Bacanlı, H. G. Anlar, N. N. Ulusu, Y. Aksoy, *Protective effects of antioxidant chlorophyllin in chemically induced breast cancer model in vivo*, Biological Trace Element Research 199 (12) (2021) 4475–4488.
- [44] J. Bertoneclj, U. Doberšek, M. Jamnik, T. Golob, *Evaluation of the phenolic content, antioxidant activity and colour of Slovenian honey*, Food Chemistry 105 (2) (2007) 822–828.
- [45] A. Alves, A. Ramos, M. M. Gonçalves, M. Bernardo, B. Mendes, *Antioxidant activity, quality parameters and mineral content of Portuguese monofloral honey*, Journal of Food Composition and Analysis 30 (2) (2013) 130–138.
- [46] M. Taş-Küçükaydın, G. Tel Çayan, F. Çayan, S. Küçükaydın, B. H. Çiftçi, Ö. Ceylan, M. E. Duru, *Chemometric classification of chestnut honey from different regions in Turkey based on their phenolic compositions and biological activities*, Food Chemistry 415 (2023) 135727 10 pages.
- [47] A. N. Fauzi, M. N. Norazmi, N. S. Yaacob, *Tualang honey induces apoptosis and disrupts the mitochondrial membrane potential of human breast and cervical cancer cell lines*, Food and Chemical

- Toxicology 49 (4) (2011) 871–878.
- [48] J. S. Câmara, B. R. Albuquerque, J. Aguiar, R. C. G. Corrêa, J. L. Gonçalves, D. Granato, J. A. M. Pereira, L. Barros, I. C. F. R. Ferreira, *Food bioactive compounds and emerging techniques for their extraction: Polyphenols as a case study*, *Foods* 10 (1) (2021) 34 pages.
- [49] M. Samtiya, R. E. Aluko, T. Dhewa, J. M. Moreno-Rojas, *Potential health benefits of plant food-derived bioactive components: An overview*, *Foods* 10 (4) (2021) 25 pages.
- [50] E. Kurtdede, M. E. Alçıgır, A. M. Alperen, B. Baran, O. K. Karaca, E. Gülendağ, *Evaluation of the combined effects of Turkish mad honey and 5-Fluorouracil in colon cancer model in rats*, *Veterinary Journal of Ankara University* 70 (4) (2023) 427–435.
- [51] T. Ozdal, G. Sari-Kaplan, E. Mutlu-Altundag, D. Boyacioglu, E. Capanoglu, *Evaluation of Turkish propolis for its chemical composition, antioxidant capacity, anti-proliferative effect on several human breast cancer cell lines and proliferative effect on fibroblasts and mouse mesenchymal stem cell line*, *Journal of Apicultural Research* 57 (5) (2018) 12 pages.
- [52] F. L. Sarmiento-Salinas, A. Perez-Gonzalez, A. Acosta-Casique, A. Ix-Ballote, A. Diaz, S. Treviño, N. H. Rosas-Murrieta, L. Millán-Perez-Peña, P. Maycotte, *Reactive oxygen species: Role in carcinogenesis, cancer cell signaling and tumor progression*, *Life Sciences* 284 (2021) 119942 13 pages.
- [53] M. L. Balestrieri, A. Dicitore, R. Benevento, M. di Maio, A. Santoriello, S. Canonico, A. Giordano, P. Stiuso, *Interplay between membrane lipid peroxidation, transglutaminase activity, and Cyclooxygenase 2 expression in the tissue adjoining to breast cancer*, *Journal of Cellular Physiology* 227 (2012) 1577–1582.
- [54] X. Zhang, Y. Xiao, Q. Huang, *The cellular uptake of Cordyceps sinensis exopolysaccharide-selenium nanoparticles and their induced apoptosis of HepG2 cells via mitochondria- and death receptor-mediated pathways*, *International Journal of Biological Macromolecules* 247 (2023) 125747 14 pages.
- [55] X. Y. Tang, S. J. Yu, X. M. Guo, H. Li, M. S. Chen, T. Zhang, C. Y. Lei, Z. G. Zhao, H. C. Meng, *Betacyanins functionalized selenium nanoparticles inhibit HepG2 cells growth via mitochondria-mediated pathway*, *Journal of Functional Foods* 78 (2021) 104359 11 pages.
- [56] M. Hornsveld, T. B. Dansen, *The hallmarks of cancer from a redox perspective*, *Antioxidants and Redox Signaling* 25 (6) (2016) 26 pages.
- [57] G. Y. Liou, P. Storz, *Reactive oxygen species in cancer*, *Free Radical Research* 44 (5) (2010) 479–496.
- [58] A. Alamri, *A review of the anticancer properties of bee products and their molecular mechanisms: An overview on lung cancer*, *Tropical Journal of Pharmaceutical Research* 20 (8) (2021) 1765–1774.
- [59] S. K. Jaganathan, M. Mandal, *Involvement of non-protein thiols, mitochondrial dysfunction, reactive oxygen species and p53 in honey-induced apoptosis*, *Invest New Drugs* 28 (5) (2010) 624–633.
- [60] S. Afrin, T. Y Forbes-Hernandez, M. Gasparrini, S. Bompadre, J. L. Quiles, G. Sanna, N. Spano, F. Giampieri, M. Battino, *Strawberry-tree honey induces growth inhibition of human colon cancer cells and increases ros generation: A comparison with manuka honey*, *International Journal of Molecular Sciences* 18 (3) (2017) 19 pages.
- [61] D. Cianciosi, T. Y. Forbes-Hernández, S. Afrin, M. Gasparrini, J. L. Quiles, E. Gil, S. Bompadre, J. Simal-Gandara, M. Battino, F. Giampieri, *The influence of in vitro gastrointestinal digestion on the anticancer activity of manuka honey*, *Antioxidants* 9 (1) (2020) 20 pages.
- [62] X. Zhao, A. Abulikemu, S. Lv, Y. Qi, J. Duan, J. Zhang, R. Chen, C. Guo, Y. Li, Z. Sun, *Oxidative stress- and mitochondrial dysfunction-mediated cytotoxicity by silica nanoparticle in lung epithelial cells from metabolomic perspective*, *Chemosphere* 275 (2021) 129969 14 pages.

- [63] A. L. Becerrilsánchez, B. Quintero-Salazar, O. Dublán-García, H. B. Escalona-Buendía, *Phenolic compounds in honey and their relationship with antioxidant activity, botanical origin, and color*, *Antioxidants* 10 (11) (2021) 23 pages.
- [64] J. Musarrat, J. Arezina-Wilson, A. A. Wani, *Prognostic and aetiological relevance of 8-hydroxyguanosine in human breast carcinogenesis*, *European Journal of Cancer Part 32A* (7) (1996) 1209–1214.
- [65] J. S. Helm, R. A. Rudel, *Adverse outcome pathways for ionizing radiation and breast cancer involve direct and indirect DNA damage, oxidative stress, inflammation, genomic instability, and interaction with hormonal regulation of the breast*, *Archives of Toxicology* 94 (5) (2020) 39 pages.
- [66] J. Wunder, D. Pemp, A. Cecil, M. Mahdiani, R. Hauptstein, K. Schmalbach, L. N. Geppert, K. Ickstadt, H. L. Esch, T. Dandekar, L. Lehmann, *Influence of breast cancer risk factors on proliferation and DNA damage in human breast glandular tissues: Role of intracellular estrogen levels, oxidative stress and estrogen biotransformation*, *Archives of Toxicology* 96 (2) (2022) 673–687.



Composite Sand–Clay Infrastructural Soil Fills: Characteristic Consolidation and Hydraulic Properties

Tanay Karademir¹ , Burcu Dışkaya² 

¹Department of Civil Engineering, Faculty of Engineering and Natural Sciences, İstanbul Bilgi University, İstanbul, Türkiye

²Department of Construction Technology, Vocational School, Beykent University, İstanbul, Türkiye

Article Info

Received: 28 Dec 2023

Accepted: 09 Jul 2024

Published: 30 Sep 2024

Research Article

Abstract – In the design construction of infrastructural projects comprised of geotechnical applications, including composite soil fill layers, compacted sand-clay soil fills are widely preferred as barrier layers, particularly in solid waste landfills, to minimize leakage, to prevent leachate from entering into groundwater. When bentonite clay with high water absorption capacity and low hydraulic conductivity is mixed with sand possessing relatively enhanced frictional properties, greater shear strength capacity, an effective fill material exhibiting low sensitivity to frost, and low volume change in case of wetting, drying can be obtained. On the other hand, when montmorillonite clay is loaded, due to highly critical volumetric contraction or dilation characteristics (high compressibility nature of clay), the soil fill composed of sand-clay will significantly consolidate. This situation may cause differential settlement problems of infrastructural fills employed in geotechnical applications. In this regard, the load conditions (mechanical effects) and the environmental conditions (physicochemical effects) in the field control compressibility characteristics and consolidation properties of sand-bentonite clay mixtures. This will ultimately impact the desired stability conditions of sand-clay soil layers built for constructed infrastructural fill, resulting in a deviation from anticipated performance conditions. To this end, in this study, the specimens of sand-bentonite clay mixtures prepared with different contents of sand-bentonite clay were subjected to one-dimensional consolidation tests to investigate the effect of bentonite content used in the mixture on consolidation behavior, hydraulic properties, and effect of sand amount on rate of consolidation and on resulting compressive strength behavior.

Keywords – Sand-clay mixtures, infrastructural soil fills, consolidation characteristics, hydraulic properties

1. Introduction

The engineered infrastructural soil fills, designed and constructed by mixing and compacting sand and bentonite clayey soils, are nowadays used as clay lining layers in solid waste storage landfills and as a barrier protection layer in high-grade nuclear waste storage areas, and additionally, used frequently in ponds where mine waste is stored as well as for the construction of dams. The primary reason for selecting layers including clay in constructing these infrastructures is that the lining layer built by soil fill containing clay, having very low permeability, provides impermeability to this barrier layer. On the other hand, the soil fill, including the clay lining layer, should be able to maintain its strength and bearing capacity when subjected to the stresses under the action of surficial loads that the infrastructural application will be exposed to during its service life, and besides, should not exhibit time-dependent settlement problems under long-term loading.

¹tanay.karademir@bilgi.edu.tr (Corresponding Author); ²burcudiskaya@beykent.edu.tr

Under loads, imposed forces, and induced stresses, all soils will settle, causing the settlement of structures and infrastructures founded on and within them. If the settlement is not kept to a tolerable limit, the desired use of the structure or infrastructure might be impaired, and the design life of the structure or infrastructure could be reduced. Structures or infrastructures might settle uniformly or nonuniformly. The latter condition is called differential settlement and is often the crucial design consideration. In general, the development of plastic consolidation settlement usually leads to the mobilization of hazardous differential settlement resulting in risky design issues. As a response and meet this important phenomenon, in order to extend understanding of the characteristics of consolidation deformation and the resulting settlement properties as well as the hydraulic conductivity behavior of soil fills constructed using sand-clay mixtures, within the scope of this research study, a comprehensive experimental program including a series of consolidation tests were carried out in the laboratory on the sand-bentonite admixtures with different sand contents by means of which the consolidation behavior and hydraulic conductivity characteristics of those soil mixtures were investigated.

2. Relevant Literature and Background

The bentonite clay, which consists of a large amount of montmorillonite minerals, provides high water absorption capacity and low hydraulic permeability to the barrier layer. At the same time, the sand soil increases the strength properties of the layer constructed by mixing and compacting sand and clay. The hydraulic conductivity of the compacted clays is generally less than 10^{-7} cm/s. In the condition that sandy soils with high hydraulic conductivity are mixed with fine-grained soils such as bentonite clay with low permeability, their conductivity properties decrease considerably [1]. Therefore, in constructing infrastructural fills, in case there is insufficient clayey soil to be utilized nearby, the compressed sand-bentonite mixtures will be a good alternative for barrier layers conventionally constructed using only compressed clay [2].

Bentonite is a clay type containing montmorillonite group mineral. The metamorphosis of volcanic ash forms montmorillonite minerals, and its mineralogical structure is composed of a gibbsite layer between two silica layers. Small amounts of cations and large amounts of water molecules exist between each montmorillonite layer [3]. High cation exchange capacity, low hydraulic conductivity, high swelling potential, and large surface area constitute the characteristic structure of the montmorillonite mineral [4]. Due to the very weak bonds between the Montmorillonite layers, excessive volume changes are observed in the clays containing this mineral when they take in water. Therefore, bentonites containing this mineral have a high swelling potential. Since it contains Montmorillonite minerals, bentonite clay has high water absorption capacity and low hydraulic permeability. In addition, the interaction of pore water and grains surrounding bentonite grains greatly affects the bentonite behavior [1].

The materials to be used in the clay coating layer in modern solid waste landfills should have low hydraulic conductivity, low compression tendency, sufficient swelling potential, high strength, and the quality to prevent water leakage [5]. The most important factor determining the time-dependent performance of these infrastructures is how long the substances in the leachate are delivered to the natural ground or groundwater under the barrier layer. Therefore, hydraulic imperviousness is the most important physical property that determines the performance of barrier layers [6]. Another feature of clay layers that should be considered in modern landfills is the long-term compressibility of the clay layer under load. In these infrastructures, serious settlement problems may occur under prolonged loading. Examining the consolidation properties of the bentonite-sand mixtures is important for the settlement analysis of the infrastructure. In addition, the physical, chemical, and mineralogical properties of bentonite clay affect the consolidation properties of bentonite soil mixtures [7].

For this reason, to date, consolidation parameters such as compression index (C_c), coefficient of consolidation (c_v), and reloading index (C_r) of bentonite-soil mixtures have been studied by many researchers. Furthermore, Mishra et al. [7] applied consolidation tests on 15 different bentonite-soil samples prepared by using various types of bentonites to investigate the effect of physical, chemical, and mineralogical properties of bentonite on bentonite-soil mixtures. As a result of the experimental program, they observed that the C_c increased directly

proportional to the plasticity index (PI), and the c_v for all bentonite types, for which the experiment was performed, decreased with the increasing liquid limit (LL) value. They also observed an increase in c_v under increasing consolidation pressure. They explained and reasoned this with experimental findings that bentonite-soil mixtures were consolidated at a higher rate under a higher load.

In another study examining the consolidation properties of bentonite-soil mixtures, they investigated the changes in volumetric compression coefficient (m_v), consolidation coefficient (c_v), and recompression index (C_r) in the presence of different concentrations of NaCl and CaCl₂ salt solutions in the environment. They observed that when the salt concentration in the environment was increased, the C_c and m_v decreased, whereas the c_v increased. Further, it has been stated that the c_v decreases under increasing consolidation pressure without considering the salt concentration. The m_v increases under increasing consolidation pressure until a certain maximum value is reached and decreases after this maximum value. They attributed the decrease in the consolidation coefficient, c_v , under increasing pressure to the mechanisms controlling the compression behavior of bentonite-soil mixtures [8].

Moreover, a study examining the consolidation behavior of different clayey soils containing montmorillonite, kaolinite, and illite minerals detected that the m_v decreased with the increase in consolidation pressure [9]. Furthermore, a recent research study [10] showed that the compressive strength of the admixture soils mixed with pond ash, including sand, enhanced with an additional contribution to improving hydraulic characteristics. Another important research work [11] demonstrated that as the coral sand content increased in the admixture soils, including fine and course materials, the peak shear strength and the critical state shear strength decreased marginally. Moreover, the influence of sustainable utilization of chemically depolymerized polyethylene terephthalate (PET) on the sand-bentonite clay liners was revealed by Alok and Sumi [12]. The findings of this study suggested that a mechanism of interaction exists between sand-bentonite admixtures and the chemically depolymerized form of polietilen tereftalat (PET) polymers.

Further, an insightful research study to extend understanding of the volume change behavior of binary sand-clay mixtures was conducted by Sun et al. [13]. The volumetric contraction was reported to increase with increased stress level or fine content such as clay proportion in the mixture. Lastly, one-dimensional cyclic loading tests on sand-clay mixtures were performed by Khoshghalb et al. [14] to examine the settlement of the test samples. Their research findings revealed that the admixture soil settlement decreases while the time required to complete the primary consolidation increases. In light of the research findings until the present time discussed throughout the introduction and literature review section herein, to this end, a purpose is to fill the gaps among those earlier studies as well as to explore contradictions and uncover discrepancies; in this current study, an extensive laboratory testing program has been conducted such that a series of consolidation tests were applied to sand-bentonite mixtures containing different sand content ranging from 10% up to 40% by dry weight. This way, sand-bentonite admixture soils' consolidation behavior, properties, and hydraulic permeability characteristics were investigated. Additionally, a further statistical analysis was comparatively carried out on the test results and experimental findings to investigate the correlational binary behavior of the resulting engineering properties and design parameters. This was intentionally conducted to quantitatively evaluate the resulting behavior detected and examine important engineering characteristics of sand-clay mixtures based on the increased amount of granular soil (i.e., sand) in the admixture soils.

3. Experimental Materials and Methods

3.1. Testing Materials

The sandy soil preferred to be used in the laboratory experimental program was natural beach sand and an industrial bentonite was selected to be utilized as clayey soil. Figure 1 shows the images of the testing materials, including beach sand and bentonite clay.



Figure 1. Soil types used in the testing program: (a) Bentonite clay, (b) Beach sand

The bentonite clay used in the experimental program is an absorbent swelling clay consisting mostly of montmorillonite. It is classified as high plasticity clay (CH) based on the Unified Soil Classification System (USCS) soil classification system. As such, the powdered form sodium bentonite clay tested in the laboratory program comprises the montmorillonite group of minerals. The physical and index properties of the bentonite clay utilized in the testing program consist of specific gravity (G_s) of 2.74, liquid limit (LL) of 295%, plastic limit (PL) of 57%, plasticity index (PI) of 238%.

A Sieve analysis test was performed for the sand soil to determine the grain size distribution of the sand sample that constitutes the sand-clay admixture specimens to be subjected to the consolidation test. After preparing dry test specimens with the predetermined sand and bentonite content (i.e., dry weight proportions), the admixture specimens were ready for the consolidation test by kneading (plasticizing) with water. The experimental program took a substantial amount of time such that each consolidation test was completed in six days. The important index properties of sand and clay soils are provided in Table 1 below.

Table 1. Important index properties of sand and clay soils

Soil	PL	LL	e_{min}	e_{max}	G_s
Sand	–	–	0.59	0.76	2.80
Clay	57%	295%	1.9	18.2	2.74

3.2. Experimental Device

Consolidation is the time-dependent settlement of soils resulting from water expulsion from the soil pores. This important plastic deformation response (i.e., settlement behavior) of particularly fine-grained soils, including clays, can be measured. The resulting detected behavior can be evaluated using an oedometer (i.e., 1D consolidation device). That is to say, a floating ring cell consolidometer in which the ring containing the soil sample is unrestrained in the container is utilized in the laboratory to perform consolidation tests on clayey soil and admixture specimens (Figure 2). A linear variable differential transformer (LVDT) was employed in the system to measure vertical displacement in evaluating the deformations developing in the soil specimen under the application of load during the tests. Enclosed in a stiff metal ring, a disk of soil was placed between two porous stones in a cylindrical container filled with water (Figure 2b). A metal load platen mounted on top of the upper porous stone transmits the applied vertical stress to the soil sample. In this way, the soil specimen inside the ring was loaded and the resulting vertical displacement was measured and recorded in the computer by testing controller program.



Figure 2. Consolidation device: (a) General view, (b) Close up view

3.3. Experimental Procedures

3.3.1. Sieve Analysis

Before preparing the sand - clay mixtures, sieve analysis was performed to draw the sand sample's grain size distribution curve and determine the grain size criteria [15]. ASTM sieves, including 4.76 mm (No.4), 2 mm (No.10), 1 mm (No.40), 0.420 mm, 0.250 mm (No.60), and 0.076 mm (No.200) were used in the tests. Test specimens of 200 g were partitioned off from the sand sample by following the quartering method before starting the dry sieving process. The test specimens were kept in water to which Sodium Hexameta Phosphate ($\text{NaPO}_3)_6$ was added for one day and washed under clean water on a 0.076 mm sieve to remove possible salt and lime. The sand test specimens, left to dry for 24 hours in an oven heated at 110°C , were subjected to sieving. A sieve shaker device was used during the sieving process followed by manual sieving by hand to ensure particle sorting perfectly for better rating. After the weight of the soil remaining on the sieves, which were arranged with the largest mesh opening at the top, was measured on an electronic scale with 0.1 g precision as specified in the relevant regulation, the percentage of the sample passing through each sieve (% P) was calculated. Figure 3 shows the grain size distribution curve of the sand sample tested. Based on the results of sieve analysis tests performed in the laboratory, the sample was determined as SP (poorly graded sand) according to the ASTM classification system. Further, the grain size distribution properties of sand specimens used in the laboratory experimental program are tabulated in Table 2.

Furthermore, the tests with soil admixtures at specific proposed dry weight proportions are generally performed with laboratory-constituted specimens. A special soil mixer achieved relatively uniform and homogeneous soil specimen admixtures. Accordingly, the test specimen preparation technique of air pluviation is an extensively and commonly preferred methodology among other different sample preparation techniques developed to simulate in-situ field conditions. Moreover, the air pluviation methodology provides more uniform and homogeneous specimens than the other techniques [16]. Similarly, Rad and Tumay [17] concluded that air pluvial compaction is the best reconstitution method for soil admixtures, including granular soils such as sand and cohesive soils such as clay, to simulate the formation of soil admixture deposits in the field.

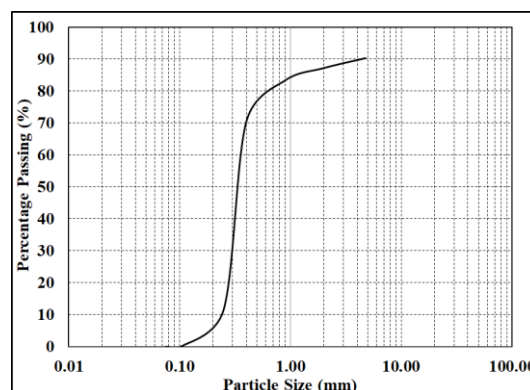


Figure 3. Particle size distribution for sand specimen tested

Table 2. Grain size distribution properties of sand specimen

D ₁₀ (mm)	D ₅₀ (mm)	C _u	C _c
0.22	0.31	2.27	0.87

3.3.2. Oedometer Test and Testing Program

The physical, chemical, and mineralogical properties of bentonite clay influence consolidation properties and, hence, the settlement behavior of sand-bentonite mixtures. This study performed a series of one-dimensional consolidation tests in the laboratory to determine the settlement properties and consolidation engineering parameters (c_v , m_v , α_v , C_c , and C_r) of sand-bentonite mixtures [18, 19]. Based on Terzaghi's one-dimensional consolidation theory, the one-dimensional consolidation experiment aims to find the consolidation parameters by providing vertical drainage under the controlled, increased vertical stress in the soil specimen where the horizontal deformation is prevented [20-23]. Sand-bentonite soil admixtures were mixed with distilled water and kneaded, and thereafter, the test specimens with a thickness of 2.50 cm and a diameter of 6.0 cm were prepared. Test mixture specimens prepared from sand-bentonite admixture samples were taken into the consolidation ring, the inner wall coated with Vaseline to minimize the lateral friction effect. The top and bottom of the test specimens in the consolidation ring were enclosed by filter papers and porous stones and kept in purified water for 24 hours to ensure purification from air voids and dirt residue. The floating ring consolidation cell is filled with purified water to enable full saturation of the test specimen after the placement of the consolidometer cell in the experimental set-up prior to the initiation of the test. The measurement intervals followed during the consolidation tests and the dry mass proportions of sand-bentonite mixtures tested are given in Tables 3 and 4, respectively.

Table 3. Data acquisition time intervals during consolidation tests

Reading No.	1	2	3	4	5	6	7	8	9	10	11	12	13	14	15	16	17
Time (min.)	0.05	0.1	0.2	0.25	0.5	1	2	4	8	15	30	60	120	240	480	960	1440

Table 4. Dry mass proportions of sand-bentonite mixtures

Mass Proportions	1	2	3	4
Sand	10%	20%	30%	40%
Bentonite	90%	80%	70%	60%

4. Results and Discussion

Figure 4 shows the variation of the coefficient of consolidation (c_v) found for different sand contents under increasing consolidation pressure. In all mixtures, the c_v increased with increasing load while t_{90} decreased. Samarasinghe et al. [24] reported that the value of c_v for pure bentonite clay containing montmorillonite-type minerals decreases under increasing pressure, while it increases for sandy clay. Additionally, Mishra et al. [7] observed increased c_v as the consolidation pressure increased due to the consolidation tests performed on 15 different bentonite-soil samples. This can be explained by pure bentonite and sand-bentonite mixtures' consolidation behavior is completely different due to micro-structural inherent characteristics.

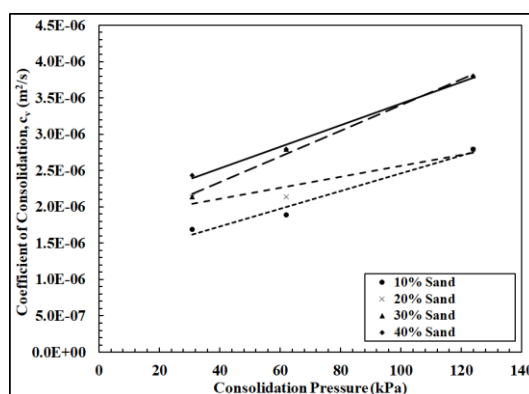


Figure 4. The variation of the coefficient of consolidation (c_v) with the consolidation pressure

Furthermore, while the consolidation behavior of pure bentonite depends on long-term repulsive and attractive forces based on physicochemical factors, the consolidation behavior of sand-bentonite mixtures mostly depends on mechanical effects that can result in c_v changing directly proportional to the increasing consolidation pressure [9]. Therefore, the results obtained from most of the specimens in this study are compatible and can be related and concerned with the aforementioned mechanical effects. Regardless of sand content, a linear increase in the values of c_v was observed with an increment in pressure. As such, the higher the sand content for the specimens containing 30% and 40% sand by dry mass, the larger the increase in the values of c_v exhibited, while the relatively smaller increase in the values of c_v displayed for the lower sand content specimens including 10% and 20% sand by dry mass. This concurs with the prevailing observations of previous researchers, including Robinson and Allam [9] and Mishra et al. [7]. In a purpose to investigate the compressibility characteristics of sand-clay mixtures at different dry weight proportions (10%-90%, 20%-80%, 30%-70%, and 40%-60%), the void ratio (e) on linear scale versus pressure (σ) (i.e., normal stress) on logarithmic scale semi-logarithmic curves were developed as a result of the obtained experimental measurement data from the entire testing phases of oedometer tests as presented in Figure 5. Accordingly, the compressibility characteristics of clayey soils containing various sand contents varying from 10% up to 40% and the compressibility response under increasing pressure can be deeply understood from the curves shown in Figure 5.

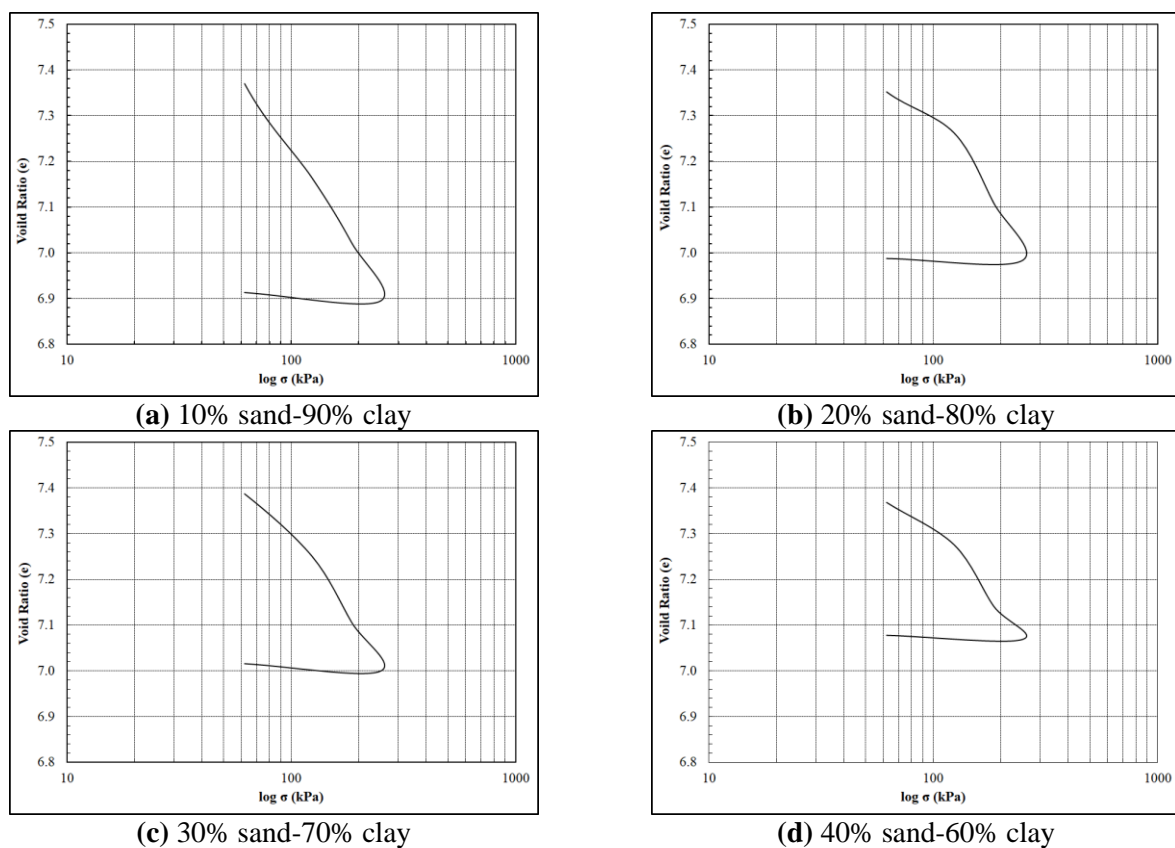


Figure 5. Void ratio (e) versus $\log(\sigma)$ curves: Compressibility characteristics of sand-clay mixtures at different dry mass proportions

For one-dimensional consolidation, the volumetric strain controlling consolidation settlement in the field is analogous and equivalent to the vertical strain governed by the change in void ratio under induced load. In this regard, the e versus $\log(\sigma)$ curves have been developed and utilized to extend understanding of the compressibility properties and, thus, consolidation settlement characteristics and load response. Furthermore, the decrease in the void ratio (Δe) resulted from incremental pressure - that could be related to the volumetric strain (ϵ_v) mobilized under loading reduced owing to the increasing sand content in clayey soil, and thus, enabling relatively greater bearing resistance against loading as well as providing higher strength response. This is attributed to the micro-inherent characteristics of admixtures such that relatively improved graded grain

distribution of sandy clays as compared to pure clays containing one predominant soil mineral size facilitates the re-orientation of sand-particles and clay minerals for the ease and reformed re-organization of admixture micro-structure. In this way, the relatively denser soil is obtained with increasing sand proportion, resulting in less decrease in void ratio under identical pressure increment which controls the degree and severity of consolidation settlement through the volumetric strain displayed under loading in the field. Additionally, the increase in mass proportion of relatively rigid sand particles compared to weak, powerless clay minerals in the admixture enhances the sandy clays' overall bearing capacity, including greater sand contents.

5. Further Statistical Analysis on Experimental Findings

Consolidation is a time-dependent soil settlement resulting from water expulsion from the soil pores. As such, consolidation is the change in the volume of fine-grained soil caused by the expulsion of water from the voids and the transfer of stress from the excess pore-water pressure to the soil particles that result in the mobilization and progression of settlement of soil fills in the field for particularly designed and constructed in infrastructural applications. In this regard, the ultimate magnitude as well as the rate of consolidation settlement initiated, progressed, and augmented inside soil fills in the field within the body of infrastructural applications are technically governed and can quantitatively be evaluated by accurately identifying consolidation engineering design parameters such as Δe , ε_v , C_c , C_r , α_v , m_v , c_v , and k and properly investigating their variation with increasing sand content so as that the consolidation characteristics and hydraulic behavior of soil fill under loading, most of which are designed and constructed by utilizing sandy clays in the field, could be unveiled. Within this context, the variation in compressibility properties of sand-clay mixtures as a function of sand content are presented in Figure 6 to provide statistical analysis on the detected behavior with a change in the amount of sand available in clayey soil.

After load application, the onset of a decrease in the volume of void space occurs in the soil that can be measured and quantified by the change in void ratio (Δe). The degree and severity of this variation in Δe with an increase in sand content is shown in Figure 6a such that an exponential decrease in the resulting value of Δe displayed as a function of sand dry weight proportion. The change in the void ratio (Δe) is related to the volumetric strain (ε_v) developed in the soil due to load application, and that is concerned with the extent and intensity of consolidation settlement mobilized in the field under forces or stresses. In order to extend the understanding of the amount of consolidation deformation taking place within sandy clays in the field, the variation in volumetric strain (ε_v) with increasing sand content is demonstrated in Figure 6b such that an exponential decrease with an increase in sand dry weight proportion in the admixture exhibited.

As previously mentioned, the compression index (C_c) is the slope of the virgin line in the semi-logarithmic void ratio versus the pressure plot. The term expresses and demonstrates the consolidation settlement and compressibility that will occur under the applied pressure in the vertical direction. Accordingly, the compression index (C_c), as well as the recompression index (C_r), were determined from the generated e - $\log(\sigma)$ curves as earlier presented in Figure 5. The variation in C_c and C_r with increasing sand content in clayey soil is shown in Figures 6c and 6d, respectively. It was observed that there occurs a linearly decreasing behavior in the values of both C_c and C_r with an increment in sand content from 10% up to 40%. The decrease in compression indices with increasing sand content indicates the reduction in compressibility in sandy, clayey soils when the weight proportion of sand becomes larger within the admixture.

The statistical analysis of the detected behavior revealed an inverse proportionality between the compressibility engineering parameters, including Δe , ε_v , C_c , C_r , and the amount of sand available in clayey soil. This highlights how the consolidation characteristics of clayey soils are changed owing to sand inclusion in such a way that the compressibility of clayey soils reduces and becomes relatively more resistant against loading in the field, enabling less consolidation settlement and lower magnitude of deformations mobilized under stresses. Therefore, due to increased sand content, the sandy soil will provide greater bearing capacity and facilitate larger strength and durability against the induced forces/loads in the infrastructural applications. As seen in Figures 6a through 6d, the results of statistical analysis for the behavior investigated for the

compressibility engineering parameters such as Δe , ϵ_v , C_c , and C_r are in good agreement between distinct data points and continuous regression with relatively high values of coefficient of determination (R^2) are demonstrated. Further, the detected values of Δe , ϵ_v , C_c , and C_r at different sand contents (i.e., dry weight proportions) are tabulated in Table 5.

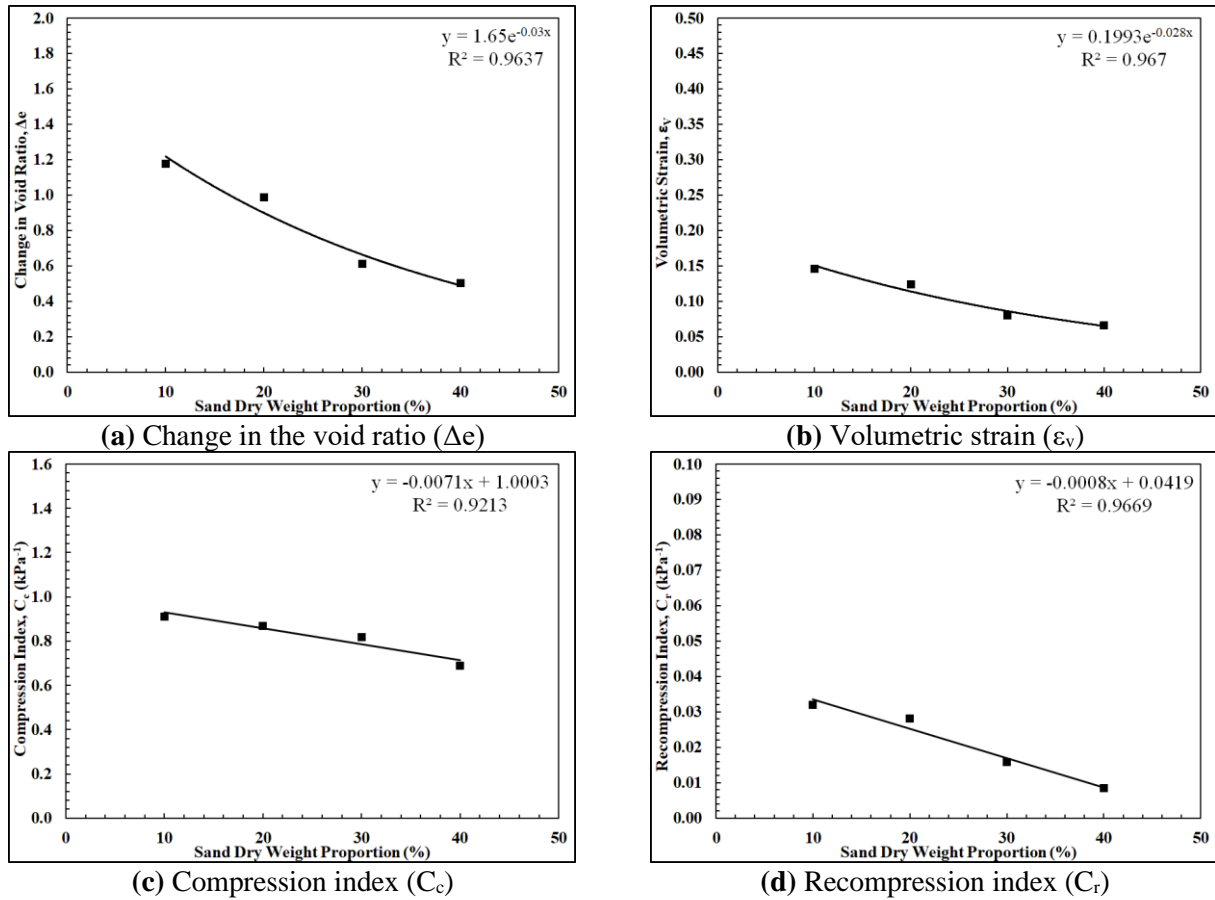


Figure 6. The variation in compressibility engineering parameters of sand-clay mixtures per sand content: statistical analysis on the detected behavior

Table 5. The detected values of Δe , ϵ_v , C_c , and C_r at different sand contents

Sand Content (%)	Δe	ϵ_v	C_c (kPa ⁻¹)	C_r (kPa ⁻¹)
10	1.1761	0.1457	0.9108	0.0320
20	0.9875	0.1239	0.8682	0.0281
30	0.6113	0.0803	0.8190	0.0158
40	0.5017	0.0663	0.6892	0.0084

The change in the void ratio (Δe) developed and, similarly, the volumetric strain (ϵ_v) generated during consolidation settlement reduced 50% to 60% owing to the addition of sand up to 40% by dry weight. Furthermore, the compression index (C_c) and the recompression index (C_r) diminished by 35% and 65%, respectively, due to the inclusion of sand up to 40% by dry weight into the clayey soil.

The variation in consolidation characteristics and hydraulic properties of sand-clay mixtures per sand content is presented in Figure 7 for various consolidation and hydraulic conductivity engineering design parameters based on further statistical analysis of the investigated behavior as a function of sand dry weight proportion. Accordingly, the compressibility coefficient (α_v) is the ratio of the reduction in the volume of void space (Δe) to the change in vertical pressure (i.e., load per unit area) detected from the plot of void ratio versus pressure curves. The change in α_v as a function of sand weight proportion in the admixture is given in Figure 7a. The statistical analysis of the investigated behavior has shown an exponential decrease with a relatively high coefficient of determination ($R^2 = 0.9637$) due to an increase in sand content in the sandy clay exhibited.

Furthermore, the coefficient of volume compressibility (m_v) defines and represents the volumetric strain developed corresponding to the unit stress increase in the consolidating clay soil layer. The variation in m_v concerning the amount of sand available in the admixture is shown in Figure 7b such that an exponential decrease in the detected values of m_v was observed while the sand weight proportion in the mixture increases. Similar to that α_v of, the distinct data points depict a very good agreement along with a continuous regression curve, which results in obtaining the relatively high value of $R^2 = 0.9666$, indicating that the investigated behavior is accurate and precise. The resulting behaviors (i.e., exponential decreases) observed for two important characteristics of consolidation compressibility properties point out that the consolidation deformational settlement exhibited in sandy soils employed in infrastructural applications can be reduced by including a greater amount of sand into the admixture soil fill in the field.

The variation of the coefficient of consolidation (c_v) (i.e., characterizing the rate and duration of consolidation settlement and deformation, respectively), as well as the coefficient of permeability [hydraulic conductivity] (i.e., identifying hydraulic properties) depending on the sand content, is shown in Figures 7c and 7d, respectively. The coefficient of permeability (k) based on the coefficient of consolidation (c_v) was calculated by following Terzaghi's one-dimensional consolidation theory. Since consolidation settlement of soil is a time-dependent process that depends on the hydraulic conductivity and the drainage conditions. The c_v governing the rate and speed of consolidation settlement for infrastructural soil fills in the field as well as the k controlling the drainage and expulsion of excess pore-water pressure from void space, resulting in the increase of vertical effective stress within the soil body against forces and stresses in order to provide larger bearing capacity under loading conditions are two critical and crucial engineering design properties to help us further understand consolidation characteristics and hydraulic properties of sandy clay soil fills in the geotechnical infrastructural applications. To this end, the variation of c_v and k concerning an increase in sand content of the admixture soil are shown in Figures 7c and 7d, respectively.

It can be observed that the coefficient of consolidation (c_v) (Figure 7c) increased, whereas the compression index (Figure 6c) decreased in the admixture test specimens with increased sand content. This reveals that the consolidation rate increases when coarse grain material (i.e., sand) increases in those admixture samples. Accordingly, the increase in sand weight proportion of sandy clay soil displayed an increase in the detected values of c_v with a decreasing rate at greater sand contents particularly above 30% up to 40% sand fraction by dry weight in the mixture. This depicts a behavior consisting of a power model for the measured and determined values of c_v as a function of increasing sand content in the admixture soil. The proximity obtained between distinct data points and the continuous regression curve of the power model remarks the relatively good agreement between the individual data points experimentally measured and defined and the power model curve analytically developed and generated.

Additionally, the proximity attained results in acquiring a relatively high value of $R^2 = 0.9294$, which indicates the accuracy and precision of statistical analysis to unveil the behavior investigated due to the laboratory testing program for the change in c_v with an increase in sand content. Consequently, this extends the understanding of the increment in the rate of consolidation deformation with increasing sand mass proportion in sandy clays such that the consolidation settlement will ease, speed up, and accelerate owing to greater sand proportion in the admixture soil fill in the field. This could be advantageous for achieving settlement process under loading, force and stresses within relatively short time duration in soil fills employed in geotechnical infrastructures so that the soil fill will possess a larger bearing capacity facilitating higher strength and resistance against forces and stresses mobilizing within infrastructural fill. Further, it was investigated that the coefficient of permeability (k) increased as the amount of coarse-grained soil (i.e., sand) increased in the mixture. As such, an exponential increase ($R^2 = 0.9770$) in the values of k with increasing sand content is exhibited, as shown in Figure 7d. This is attributed to the improved hydraulic conductivity properties of sand when included in clayey soil to facilitate the enhanced drainage of excess pore-water pressure - built up due to external loads and forces exerted to infrastructural fill - from clayey soil owing to the inclusion of more and more sand amount into the admixture soil particularly above 30% up to 40% by dry mass proportion of sand. This will ease and expedite the progression of consolidation deformation. Hence, long-term settlement is accomplished within a relatively

short period in soil fills designed and constructed by utilizing sandy clays in the infrastructural applications to reach higher bearing capacities quickly. Further, the computed values of α_v , m_v , c_v , and k at different sand contents (i.e., dry weight proportions) are tabulated in Table 6.

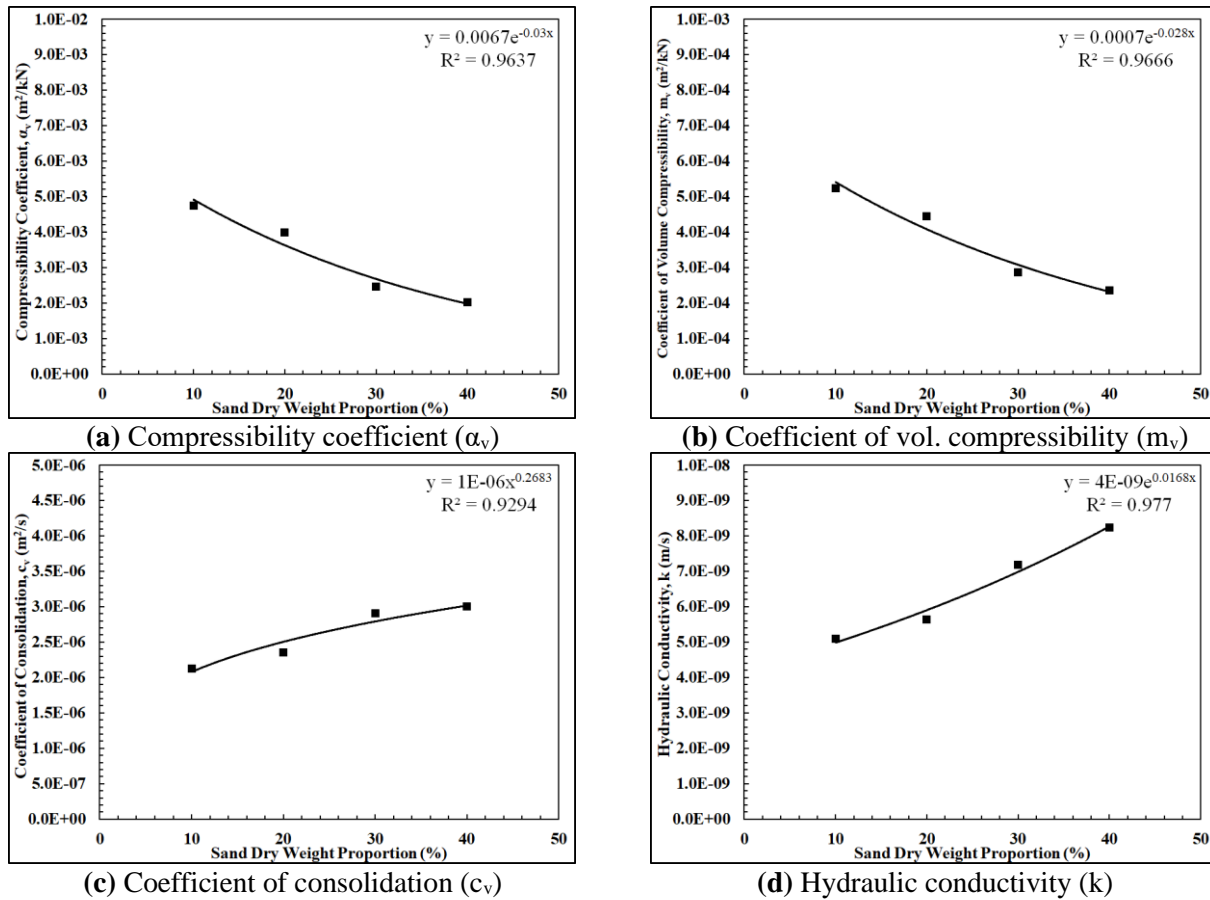


Figure 7. The variation in consolidation characteristics and hydraulic properties of sand-clay mixtures per sand content: statistical analysis on the investigated behavior

Table 6. The computed values of α_v , m_v , c_v , and k at different sand contents

Sand Content (%)	α_v (m ² /kN)	m_v (m ² /kN)	c_v (m ² /s)	k (m/s)
10	0.00475	0.00052	2.1243x10 ⁻⁶	5.09x10 ⁻⁹
20	0.00399	0.00044	2.3552x10 ⁻⁶	5.64x10 ⁻⁹
30	0.00247	0.00029	2.9092x10 ⁻⁶	7.19x10 ⁻⁹
40	0.00203	0.00024	3.0074x10 ⁻⁶	8.23x10 ⁻⁹

The compressibility coefficient (α_v) and the coefficient of volume compressibility (m_v) decreased by 65% and 60%, respectively, owing to the inclusion of sand up to 40% by dry weight. Moreover, the coefficient of consolidation (c_v) and the hydraulic conductivity (k) increased by 55% and 75%, respectively, due to the addition of sand up to 40% by dry weight into the clayey soil.

To sum up, the amount of vertical deformation detected governs the degree of consolidation settlement and, thus, is related to the magnitude of displacement measured in the vertical direction in the specimen. The vertical displacement measured in the specimens increased with increasing normal load. In contrast, it decreased with increasing sand content owing to the larger inherent strength characteristics of sand particles compared to weak and sensitive clay minerals. Therefore, it is further noted that the compressibility properties of clayey soil have been improved by including sandy soil that exhibits smaller vertical deformation under the same loading conditions. Regardless of loading conditions, either low, medium, or high, the magnitude of vertical displacement has reduced with an increase in sand content.

Further, it was seen that the decrease in void ratio resulted from incremental pressure - that could be related to the volumetric strain mobilized under loading reduced owing to the increasing sand content in clayey soil, thus enabling relatively greater bearing resistance against loading as well as providing higher strength response. This is attributed to the micro-inherent characteristics of admixtures such that relatively improved graded grain distribution of sandy clays as compared to pure clays containing one predominant soil mineral size facilitates the re-orientation of sand-particles and clay minerals for the ease and reformed re-organization of admixture micro-structure. In this way, the relatively denser soil is obtained with increasing sand proportion, resulting in less decrease in void ratio under identical pressure increment which controls the degree and severity of consolidation settlement through the volumetric strain displayed under loading in the field. Additionally, the increase in mass proportion of relatively rigid sand particles compared to weak, powerless clay minerals in the admixture enhances the sandy clays' overall bearing capacity, including greater sand contents. Further, analogous test results of laboratory experimental programs were likewise published by Iravanian and Bilsel [3], Mishra et al. [7], and Dutta and Mishra [8] for consolidation compressibility properties of sand-clay admixture soils in terms of extensive comparative analysis carried out to examine the changes in C_c , C_r , α_v , m_v as a result of the increase or decrease in sand weight proportion in the fine-grained cohesive soils such as bentonite clay. Furthermore, similar research findings were also revealed by Chalermyanont and Arrykul [1], Gleason et al. [4], Kockar et al. [5], and Robinson and Allam [9] for hydraulic characteristics of sand-clay admixtures in terms of comprehensive analysis conducted to observe the variations in c_v , k owing to the change in sand content in the fine-grained cohesive soils including bentonite.

6. Comparative Analysis of Correlation Behavior of Engineering Properties

Further comparative analyses have been carried out to investigate correlation and the resulting behavior among distinct consolidation characteristics and hydraulic properties detected and determined due to the testing program conducted on sandy clays, including various sand contents ranging from 10% to 40%. The developed correlation models between various engineering design parameters to comparatively reveal the behavioral relationship are presented in Figure 8. It was obtained a linear relationship between the change in void ratio (Δe) and the volumetric strain (ϵ_v) with a very high value of coefficient of determination ($R^2 = 0.9944$) (Figure 8a). The ϵ_v is linearly related to Δe through the initial volume of the soil. This was realized and confirmed due to a laboratory testing program in which consolidation tests were performed on sandy clays containing different sand contents. Likewise, a linear correlation was displayed between the compressibility coefficient (α_v) and the coefficient of volume compressibility (m_v) by showing a very high value of $R^2 = 0.9956$ (Figure 8b). Similarly, m_v is linearly interrelated to α_v through the initial volume of the soil. This was again attained and verified from the results of the testing program.

Figure 8c shows the relation between two important compressibility engineering design parameters: the compression index (C_c) and the recompression index (C_r). The mathematical model obtained as a result of statistical analysis is in the form of a natural logarithmic relationship with a relatively very high value of $R^2 = 0.9655$ such that the rate of increase in C_c gets smaller than that of C_r . This specifies that although there was a gradual decrease in the detected values of both C_c and C_r with an increase in sand content up to 20%, a sharp decline commenced to be exhibited for the observed values of both C_c and C_r for the sand contents, particularly above 20%. Additionally, even though the amount of reduction displayed in the values of C_r was 70% with increasing sand content up to 40%, only a 25% reduction was seen in the values of C_c , indicating that the inclusion of sand into clays benefits comparatively more the clayey soils under reconsolidation pressures by relatively greater improving their compressibility characteristics in providing larger strength response, and hence, greater bearing capacity against loading.

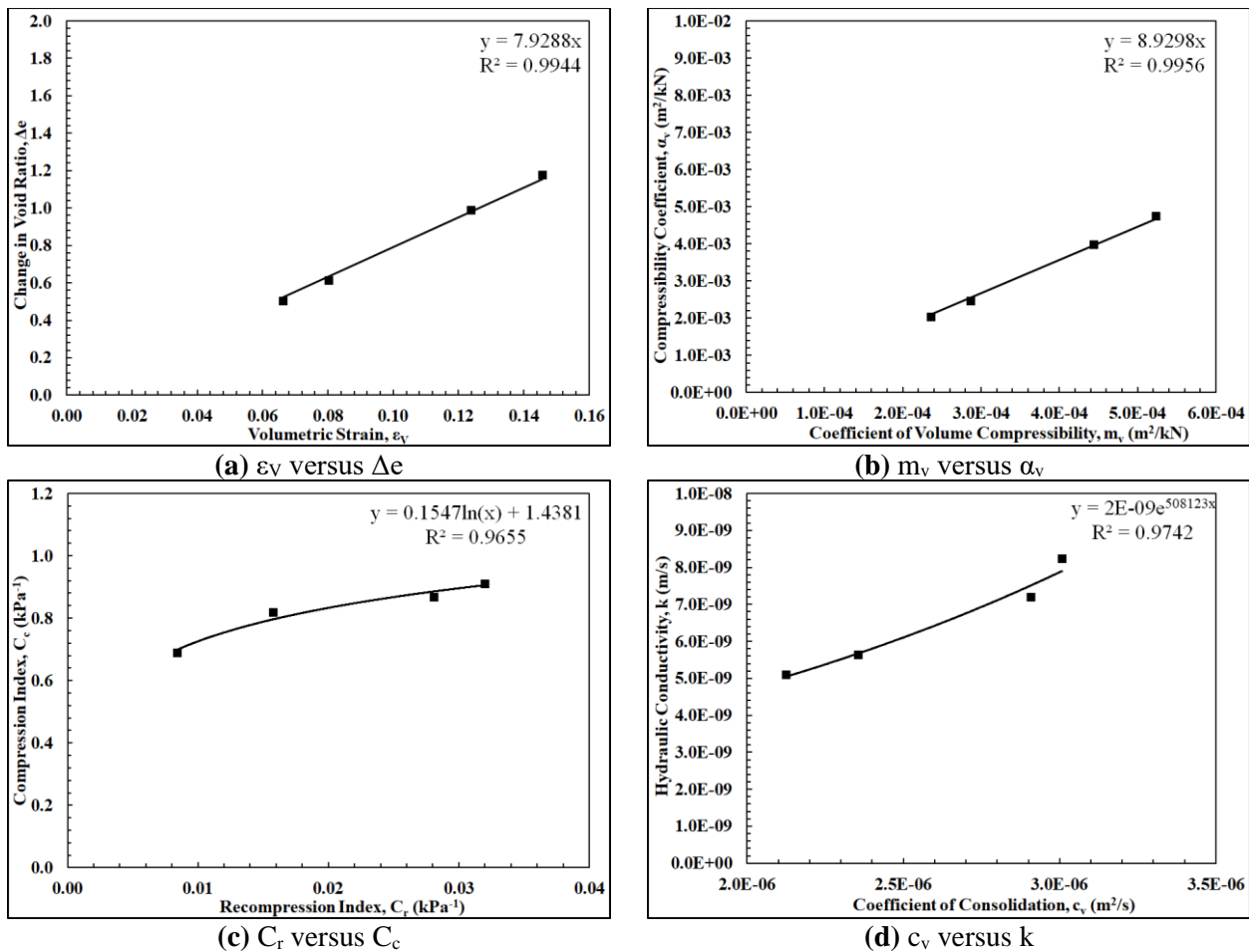


Figure 8. Correlation behavior between engineering design parameters to comparatively investigate consolidation and hydraulic conductivity characteristics

A statistical analysis has been conducted to analyze the variation in hydraulic conductivity properties (k) concerning the time rate of consolidation response (c_v - a characteristic utilized engineering design parameter), such that the correlation behavior between k and c_v is presented in Figure 8d. The values of k increase exponentially as a function of c_v with an attained very high value of $R^2 = 0.9742$, which points out that although the inclusion of sand into clay up to 20% - 30% augments the hydraulic conductivity as progressively increasing manner, subsequently beyond 30% up to 40% sand content, the rate of increment becomes greater that the further addition of sand enhances the hydraulic conductivity as sharply increasing fashion owing to superior conductivity characteristics of sand. This ensures a relatively improved time rate of consolidation response as a result of accelerated expulsion (i.e., escape) of excess pore-water pressure and, thus, speedy (i.e., fast) consolidation deformation mobilized due to loads, forces, or stresses. Thereby, rapid and quick settlement progressed within soil fill-in infrastructural applications to expedite construction activities by shortening the overall duration of building. To sum up, as explicitly seen in Figures 8a through 8d, the proximity gained between the distinct data points and the continuous regression curves of analytical models developed from further statistical analysis specifies and remarks very good agreement, validity investigated in the developed correlation behavior between both consolidations as well as hydraulic conductivity engineering design parameters.

The degree of volumetric strain (ϵ_v) experienced by the soil during consolidation deformation because of load application, external forces, or internal stresses is important to clearly understand and deeply figure out the settlement mechanism initiating, mobilizing, and advancing extended. To this end, the change in consolidation engineering design characteristic parameters such as Δe , C_c , α_v , m_v , and c_v with the severity and concerning the magnitude of volumetric strain (ϵ_v) the sandy clayey soil has undergone is presented in Figure 9. As seen in Figure 9a, the variation in void ratio with a change in volumetric strain (ϵ_v) is indirectly relevant fashion such that a linear relationship having a zero intercept in both x and y axes with a very high value of $R^2 = 0.9944$

exhibited as a result of statistical analysis. This demonstrates that the results of the experimental findings achieve and ratify the consolidation theory such that the Δe is directly proportional to the ϵ_v through a constant being the initial volume of the soil for the sandy clay admixtures containing various sand contents ranging from 10% up to 40%. Moreover, the alteration in compression index (C_c) as a function of the change in volumetric strain (ϵ_v) is given in Figure 9b. The behavior based on statistical analysis displays a mathematical model of natural logarithmic variation with a good value of $R^2 = 0.8690$, indicating that the rate of increment in the measured and determined value of C_c decreases with the increasing value of ϵ_v . This points out that even though the amount of volumetric strain increases considerably, particularly for the sandy clay soils, including less and less sand content, especially below 20%, the degree and the magnitude of compressibility based on C_c increases only marginally to a slight extent. This moderate increase to a limited extent/degree is attributed to the clayey soil's inherent characteristics that depend on the repulsive and attractive forces based on physicochemical factors.

Furthermore, the compressibility coefficient (α_v) increases linearly with increasing volumetric strain (ϵ_v) (Figure 9c), as confirmed by the analytical model (with an excellent $R^2 = 0.9998$) developed per the further statistical analysis performed on the experimental data. This was anticipated that the α_v directly related to Δe due to the intensity of stress increase ($\Delta\sigma'$) within the soil is directly proportional to ϵ_v the soil has undergone due to the severity of loading and imposed forces. Hence, the magnitude of α_v changes linearly concerning the increased degree of ϵ_v . The sandy, clayey soil has been subjected to a lack of sufficient sand content, particularly for low sand amounts (i.e., 10%).

Lastly, Figure 9d presents the inversely proportional nonlinear (i.e., exponential) relationship between the coefficient of consolidation (c_v) and the volumetric strain (ϵ_v). The statistical analysis results provided an excellent $R^2 = 0.9944$, demonstrating that there is very good agreement and proximity among distinct data points and continuous regression behavior curve. This is concerned with the observed characteristics of sandy clay soil mixtures. The increase in sand content leads to the reduced volumetric strain experienced by the sand-clay mixture becoming relatively larger resistant against loads and, hence, possessing greater bearing capacity under induced forces or stresses. Therefore, this is also relevant to the improvement of the consolidation properties, and thus, the enhancement of the time rate of consolidation (i.e., c_v) leading to the moderate expulsion of excess pressure and the accelerated escape of excess pore-water as a result of having higher hydraulic conductivity features owing to the increment in c_v and hence, the increase in k at greater sand contents in sandy, clayey soil. To sum up, the consolidation parameters, including Δe , C_c , α_v have depicted directly proportional behavior, whereas the c_v has shown inversely proportional response as a function of volumetric strain (ϵ_v).

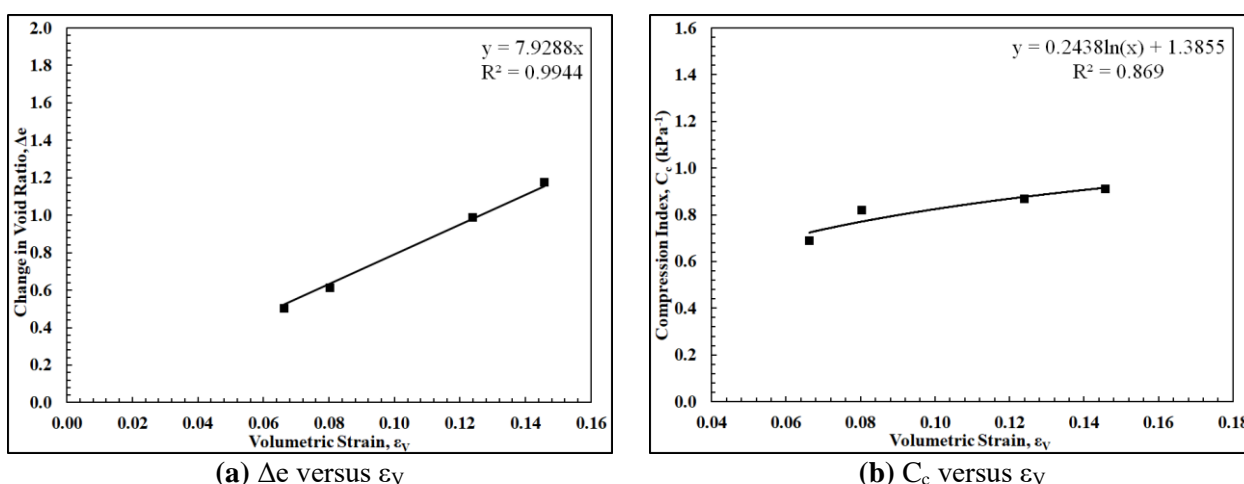


Figure 9. Variation of consolidation engineering design properties with the degree of volumetric strain (ϵ_v) sand-clay mixture experienced

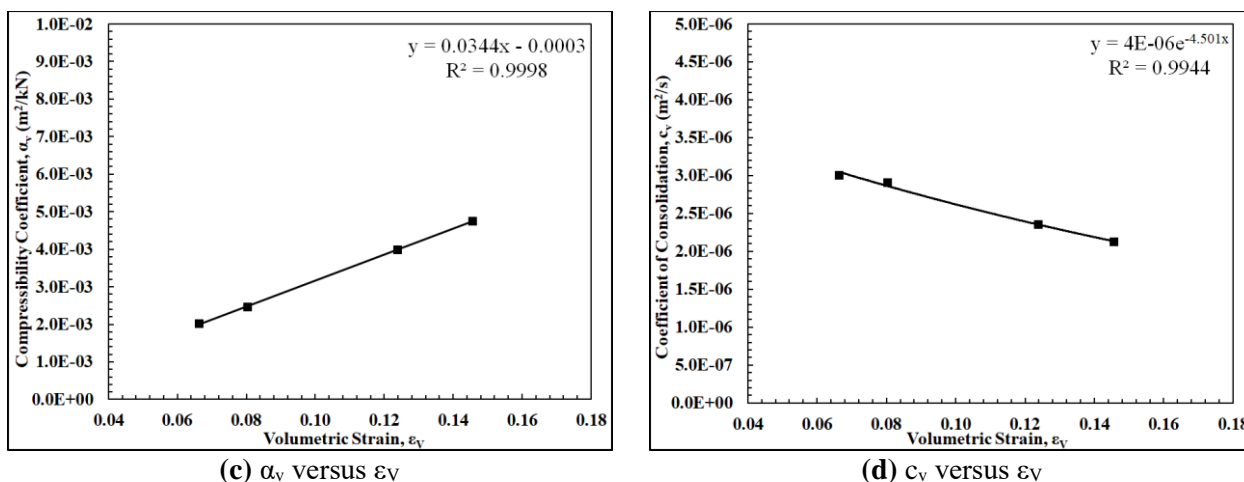


Figure 9. (Continued) Variation of consolidation engineering design properties with the degree of volumetric strain (ϵ_v) sand-clay mixture experienced

The relationship based on the relativeness of consolidation engineering design properties and the resulting developed mathematical models for the detected behavior according to the performed statistical analysis is presented in Figure 10. The alteration of an important compressibility design parameter (i.e., C_c) governing the magnitude of final consolidation settlement concerning the change in the rate of consolidation engineering property (i.e., c_v) controlling the speed and progression of consolidation deformation is shown in Figure 10a. It was obtained that the C_c decreases while the c_v increases, indicating that an inverse correlational behavior with an inversely linear model between C_c and c_v is exhibited. This specifies that the amount of decrease in C_c is relevant and comparatively proportional to the amount of increase in c_v owing to the additional inclusion of sand into sandy, clayey soil by further increasing sand content so that the admixture soil will undergo lower consolidation settlement per having relatively higher bearing capacity/resistance properties against loading as well as will possess improved and superior characteristics in allowing the quick escape of pore-water, and thereby, rapid reduction and decay of excess pore pressure so as that the time rate for the continued consolidation deformation is sped up and accelerated that could be towards the benefit and advantage of construction activities of soil fills composed of sandy clays in the field.

The correlative relationship between the coefficient of volume compressibility (m_v) (i.e., governing compressibility characteristics) and coefficient of consolidation (c_v) (i.e., controlling the rate/speed of consolidation) is displayed in Figure 10b such that an exponential behavior with an attained high value of $R^2 = 0.9843$ was obtained. As such, the rate of decline in the measured and determined value of m_v decreases with increasing the detected value of c_v . This is a consequence of sand inclusion into clayey soil that the rate/speed of consolidation rises substantially owing to relatively enhanced hydraulic properties of coarse-grained material (sand). At the same time, the reduction in magnitude of m_v is limited even though the sand fraction in the mixture is further increased above 20% by dry weight. However, the improvement in compressibility properties is considerable, such that the decrease in the m_v is important. This shows and remarks that the load resistance capability of clayey soil is boosted by the addition of sand, providing that the degree and the amount of the resulting consolidation deformation progressed in soil under loads/forces, stresses diminish, aiding in accomplishing smaller extent and magnitude of consolidation settlement mobilized and observed in the field for the infrastructural applications constructed by utilizing sandy clays.

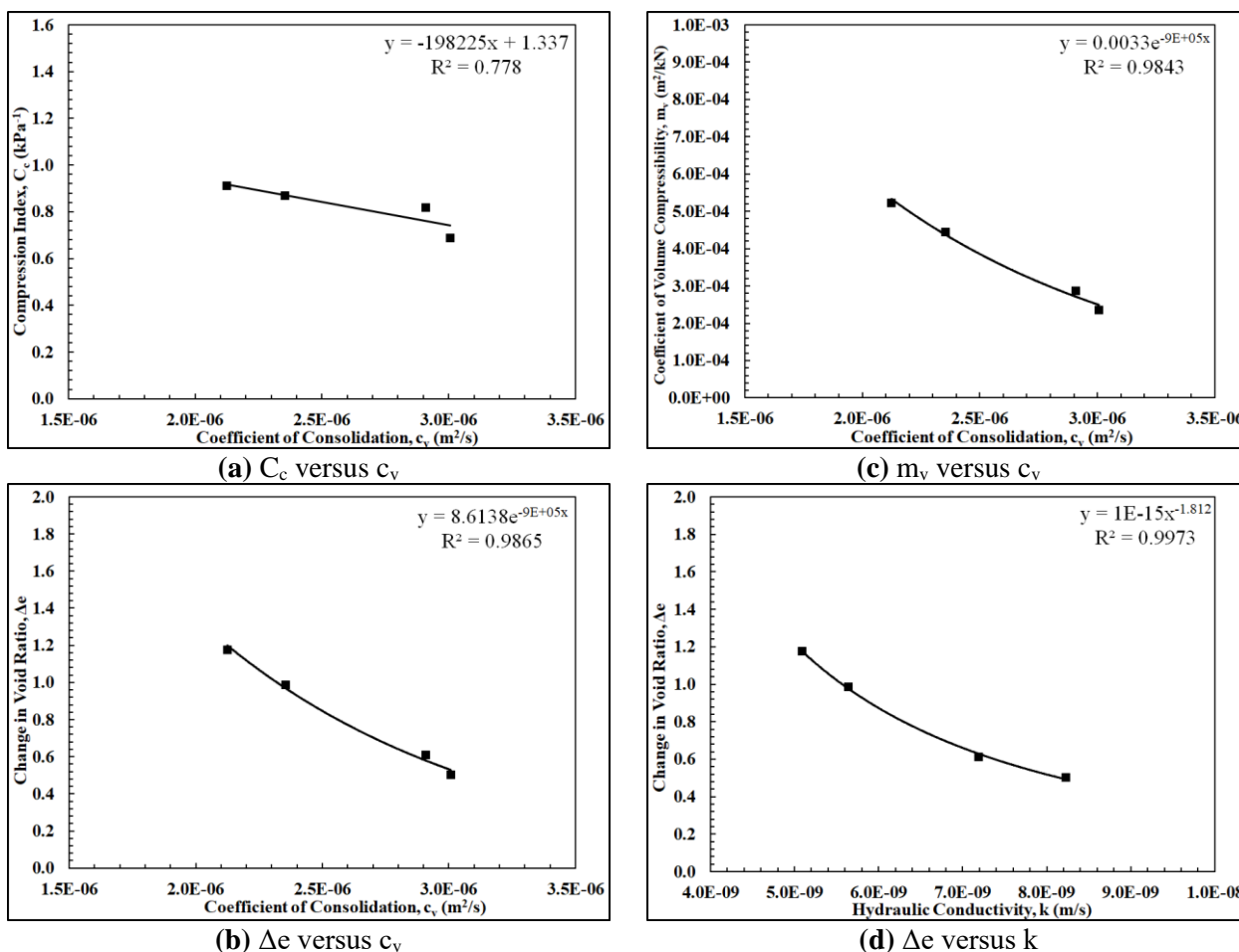


Figure 10. Relativeness of consolidation engineering design parameters and the resulting mathematical model for the behavior based on statistical analysis

The relativeness and the mathematical model between two important consolidation properties, change in the void ratio (Δe) and coefficient of consolidation (c_v), are presented in Figure 10c. There occurs an exponential decline in the measured values of Δe with increasing detected values of c_v such that the analytical model developed as a result of statistical analysis provided a very high $R^2 = 0.9865$ value. This shows a very good proximity among distinct experimentally attained data points and a statistically developed model. Under load application, the void ratio reduction becomes smaller owing to sand inclusion. As known, the resulting magnitude of consolidation settlement experienced in the field for the soils subjected to loads, forces, and stresses is governed by the degree of reduction in void ratio. As such, fine-grained soils (pure clays) generally exhibit much larger changes in void ratio when exposed to loads. However, the inclusion of sand into clay benefits not only the increment for the consolidation rate (c_v) for facilitating accelerated consolidation but also the diminish generated for the void ratio (Δe) so that the sandy soil has become relatively stronger by possessing greater strength and bearing capacity. Finally, the variation between the change in void ratio (Δe) and the coefficient of permeability (k) is given in Figure 10d. An inverse power model with an excellent $R^2 = 0.9973$ was investigated such that the Δe decays nonlinearly with an increase in k due to sand inclusion into clay, which improves hydraulic conductivity properties and enhances strength characteristics under loads. The resulting observed behavior between Δe and k eventually specifies that sandy soils' consolidation characteristics and hydraulic properties are intensified and rehabilitated, respectively. Consequently, the soil fills designed and constructed utilizing sand-clay mixtures in geotechnical infrastructural applications will become robust and durable due to sand inclusion during construction.

7. Conclusion

The resulting consolidation behaviors and compression responses detected by means of the most important characteristics of consolidation compressibility properties, including C_c , C_r , α_v , m_v , Δe , and ε_v pointed out that the consolidation deformational settlement exhibited in sandy soils employed in infrastructural applications can be reduced by inclusion of greater amount of sand into the admixture soil fill in the field. Furthermore, the variation of the coefficient of consolidation (c_v) (i.e., characterizing the rate and duration of consolidation settlement and deformation, respectively) as well as the coefficient of permeability (k) [hydraulic conductivity] (i.e., identifying hydraulic properties) depending on the sand content showed that the coefficient of consolidation (c_v) increased whereas the compression index decreased in the admixture test specimens with increased sand content. This reveals that the consolidation rate increases when coarse grain material (i.e., sand) increases in those admixture samples. Accordingly, the increase in sand weight proportion of sandy clay soil displayed an increase in the detected values of c_v with a decreasing rate at greater sand contents particularly above 30% up to 40% sand fraction by dry weight in the mixture. Consequently, this extends the understanding of the increment in the rate of consolidation deformation with increasing sand mass proportion in sandy clays such that the consolidation settlement will ease, speed up, and accelerate owing to greater sand proportion in the admixture soil fill in the field. This could be advantageous for achieving settlement process under loading, force and stresses within relatively short time duration in soil fills employed in geotechnical infrastructures so that the soil fill will possess a larger bearing capacity facilitating higher strength and resistance against forces and stresses mobilizing within infrastructural fill. It was also investigated that the coefficient of permeability (k) increased as the amount of coarse-grained soil (i.e., sand) increased in the mixture. This is attributed to the improved hydraulic conductivity properties of sand when included in clayey soil to facilitate the enhanced drainage of excess pore-water pressure - built up due to external loads and forces exerted to infrastructural fill - from clayey soil owing to the inclusion of more and more sand amount into the admixture soil particularly above 30% up to 40% by dry mass proportion of sand. This will ease and expedite the progression of consolidation deformation. Hence, long-term settlement is accomplished within a relatively short period in soil fills designed and constructed by utilizing sandy clays in the infrastructural applications to reach higher bearing capacities in a short time interval.

To conclude, in projects where sandy clay soil fills are designed and constructed, in addition to the size (i.e., magnitude) and severity of possible settlements, the speed (i.e., rate) of the deformation to occur and its progress development over time are also crucial for the performance and service life of geotechnical infrastructural projects. To this end, the different ratios of sand additives, the variation in the related consolidation engineering parameters, and the change in the dependent hydraulic properties were comprehensively studied and investigated in this research study consisting of a wide-spectrum laboratory testing program. Besides, several different contrary factors work in the opposite direction, resulting in reverse effects for the mobilization as well as progression and continuation of consolidation settlement, primarily plastic deformation. In this regard, the higher the hydraulic conductivity in the 40% sand mixture, the shorter the time duration to allow the pore-water to leave/escape out of the body of soil mixture (i.e., the expulsion of excess pore-water to subside high pressure developed within the soil as a result of loading) which triggers and initiates the rapid development of consolidation settlement through the progress and advancement of quick short-term sudden deformation that is in immediate elastic mode resulting in the improvement of rate as well as the enhancement of speed of consolidation displacement being in long-term permanent plastic mode. In this way, the characteristics of consolidation behavior change and evolve from predominantly/mainly irreversible long-term plastic nature of settlement to principally elastoplastic type exhibiting considerable reversible short-term elastic form of deformation (i.e., vertical displacement).

Further, rapid and speedy deformation is generally a consequence of elastic behavior and can be directly related to the stiffness of the soil. The sample including 40% sand has a stiffer and relatively rigid micro-, meso-, and macro-structure compared to the sample containing 10% sand. To sum up, the stiffness of coarser and harder solid sand particles is much higher as compared to very small and weak, sensitive clay particles of microscopic

size, and as its ratio in the mixture increases, it shows greater strength and resistance against consolidation loading which displays an effect and demonstrates a role in minimizing the occurrence of large extent of deformation, and hence, the progression of great extent of settlement.

Author Contributions

The first author directed the project and supervised this study's findings. The first and the second authors devised the main conceptual ideas and developed the theoretical framework. The second author performed the experiments, and the first author conducted the statistical analyses. The first author wrote the manuscript. All authors read and approved the final version of the paper.

Conflicts of Interest

All the authors declare no conflict of interest.

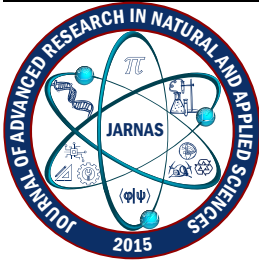
Ethical Review and Approval

No approval from the Board of Ethics is required.

References

- [1] T. Chalermyanont, S. Arrykul, *Compacted sand-bentonite mixtures for hydraulic containment liners*, Songklanakarin Journal of Science and Technology 27 (2) (2005) 313–323.
- [2] A. Iravanian, H. Bilsel, *Tensile strength properties of sand-bentonite mixtures enhanced with cement*, Procedia Engineering 143 (2016) 111–118.
- [3] A. Iravanian, H. Bilsel, *Strength characterization of sand-bentonite mixtures and the effect of cement additives*, Marine Georesources & Geotechnology 34 (3) (2016) 210–218.
- [4] M. H. Gleason, D. E. Daniel, G. R. Eykhole, *Calcium and sodium bentonite for hydraulic contaminant applications*, Journal of Geotechnical and Geoenvironmental Engineering 123 (5) (1997) 438–445.
- [5] M. K. Kockar, H. Akgün, Ö. Aktürk, *Preliminary evaluation of a compacted bentonite/sand mixture as a landfill liner material*, The Journal of Solid Waste Technology and Management 31 (4) (2005) 182–187.
- [6] İ. Bozbey, S. Saltı, *Evaluation of Turkey's solid waste control regulations from a "performance-based approach" perspective*, ZMGM 14th National Conference, Isparta, 2012, pp. 931–940.
- [7] A. K. Mishra, M. Ohtsubo, L. Y. Li, T. Higashi, *Influence of the bentonite on the consolidation behaviour of soil-bentonite mixtures*, Carbonates and Evaporites 25 (1) (2010) 43–49.
- [8] J. Dutta, A. K. Mishra, *Consolidation behaviour of bentonites in the presence of salt solutions*, Applied Clay Science 120 (1) (2016) 61–69.
- [9] R. G. Robinson, M. M. Allam, *Effect of clay mineralogy on coefficient of consolidation*, Clays and Clay Minerals 46 (5) (1998) 596–600.
- [10] N. Kantesaria, D. Chotani, H. Ganvit, *Evaluation of geotechnical properties of pond ash-bentonite mixture as a potential landfill liner material*, in: S. Kolathayar, N. Vinod Chandra Menon, K. S. Sreekesava (Eds.), International Conference on Interdisciplinary Approaches in Civil Engineering for Sustainable Development, Bangalore, 2024, pp. 191–199.
- [11] C. Jiang, X. Ding, H. Fang, Q. Ou, L. Niu, *The undrained shear behavior of clean coral silt and coral silt-sand mixtures*, ASTM Journal of Testing and Evaluation 51 (5) (2023) 3596–3611.

- [12] A. Chandra, S. Siddiqua, *Sustainable utilization of chemically depolymerized polyethylene terephthalate (PET) waste to enhance sand-bentonite clay liners*, Waste Management 166 (1) (2023) 346–359.
- [13] Z. Sun, Y. Xiao, M. Meng, H. Liu, J. Shi, *Thermally induced volume change behavior of sand-clay mixtures*, Acta Geotechnica 18 (5) (2023) 2373–2388.
- [14] A. Khoshghalb, J. Li, B. Shahbodagh, *One-dimensional cyclic loading tests on saturated and unsaturated sand-clay mixtures*, in: M. Bardanis (Ed.), 8th International Conference on Unsaturated Soils, UNSAT 2023, Milos, 2023, Article Number 03008 6 pages.
- [15] ASTM D422-63, Standard test method for particle-size analysis of soils, ASTM International, West Conshohocken, PA, Reapproved 63 (2007) 1–8.
- [16] J. D. Frost, J. -Y. Park, *A critical assessment of the moist tamping technique*, ASTM Geotechnical Testing Journal 26 (1) (2003) 57–70.
- [17] N. S. Rad, M. T. Tumay, *Factors affecting sand specimen preparation by raining*, ASTM Geotechnical Testing Journal 10(1) (1987) 3–37.
- [18] ASTM D2435-65T, Standard test method for one-dimensional consolidation properties of soils, ASTM International, West Conshohocken, PA, 4(August) (1990) 196–205.
- [19] ASTM D2435M-11, Standard test methods for one-dimensional consolidation properties of soils using incremental loading, ASTM International, West Conshohocken, PA, 4(June) (2020) 1–10.
- [20] R. Shenbaga, R. Kaniraj, V. Gayathri, *Permeability and consolidation characteristics of compacted fly ash*, Journal of Energy Engineering 130 (1) (2004) 18–43.
- [21] D. W. Taylor, Fundamentals of soil mechanics, John Wiley & Sons, New York, 1948.
- [22] A. Önalp, E. Arel, S. Sert, Geotechnical knowledge 1 (in Turkish), Birsen Publication, İstanbul, 2010.
- [23] B. A. Porbaha, T. B. S. Pradhan, N. Yamane, *Time effect on shear strength and permeability of fly ash*, Journal of Energy Engineering 126 (1) (2000) 15–31.
- [24] V. P. D. Samarasinghe, A. Mahinda, H. Huang Yang, *Permeability and consolidation of normally consolidated soils*, Journal of Geotechnical Engineering, 108 (1982) 835–850.



Effects of *Pleurotus Eryngii* (DC.) Quél. Mushroom Extracts on Cell Proliferation in Breast and Colon Cancer Cell Lines

Ferah Cömert Önder¹ , Gülce Davutlar² , Alper Önder³ , Hakan Allı⁴ , Mehmet Ay⁵ 

¹Department of Medical Biology, Faculty of Medicine, Çanakkale Onsekiz Mart University, Çanakkale, Türkiye

²Department of Medical System Biology, School of Graduate Students, Çanakkale Onsekiz Mart University, Çanakkale, Türkiye

^{3,5}Natural Products and Drug Research Laboratory, Department of Chemistry, Faculty of Science, Çanakkale Onsekiz Mart University, Çanakkale, Türkiye

⁴Department of Biology, Faculty of Science, Muğla Sıtkı Koçman University, Muğla, Türkiye

Abstract – This study was aimed to collect *Pleurotus eryngii* (DC.) Quél. edible/medicinal mushroom from Çanakkale/Kumkale and to evaluate the antiproliferative effects of alcoholic extracts on breast and colon cancer cell lines. For this purpose, the Soxhlet method prepared methanol and ethanol:H₂O (70:30) extracts by gradually increasing solvent polarities. Then, breast (MDA-MB-231, BT-549, BT-20, MCF-7) and colon (HT-29) cancer cell lines were treated with the extracts in increasing concentrations (0.05-0.5 mg/mL) for 48 h. In conclusion, methanol and aqueous ethanol extracts exhibited significant antiproliferative effects in cancer cell lines, according to the MTT assay. The cell viability in the triple-negative breast cancer (TNBC) MDA-MB-231 cell line was highly decreased by methanol extract at a very low concentration (0.1 mg/mL). Furthermore, methanol extract at 0.3 mg/mL reduced the percentage of cell viability in the HT-29 cell line. Aqueous ethanol extract showed antiproliferative activity in breast and colon cancer cell lines at 0.25 mg/mL concentration for 48 h applications. In addition, some bioactive components such as 4-hydroxy flavone, chrysin, and tannic acid of aqueous ethanol extract have been determined by High-Performance Liquid Chromatography (HPLC) analysis. As a result, this study may increase interest in the studies on the anticancer activities and the mechanisms of *P. eryngii* mushroom.

Article Info

Received: 11 Jun 2024

Accepted: 22 Jul 2024

Published: 30 Sep 2024

Research Article

Keywords – *Pleurotus eryngii* (DC.) Quél., mushroom, antiproliferation, natural products, cancer

1. Introduction

There are many natural resources, such as edible/medicinal mushrooms in nature for human health. The use of fungi as medicine and food has existed since time immemorial. Since fungi have chitin in their cell walls, they are included in an independent class called Mycota [1]. More than 14,000 species of mushrooms exist in nature, and 2,200 of them are edible [2]. Approximately 650 species are known for health and medicinal usage [2]. The fungal cell wall contains chitin, glucans, and glycoproteins [3]. Moreover, fungi contain bioactive compounds such as polyphenols, terpenoids, polysaccharides, and proteins [4]. Fungal compounds fight cancers by modulating various immune systems [5]. Since cancer-related deaths are estimated to increase to 13 million by 2030, efforts to find effective and better treatments to fight the disease are increasing [6]. Nevertheless, modern anticancer therapy causes various adverse effects, including impairment of the immune system [7, 8]. Nowadays, there is a need for alternative therapies to regulate cancer cells and, at the same time,

¹ferahcomertonder@comu.edu.tr (Corresponding Author); ²gulcedavutlarr@gmail.com; ³alperonder@outlook.com;

⁴ahakan@mu.edu.tr; ⁵mehmetay@comu.edu.tr

reinforce the immune system [5]. It was reported that mushroom extracts exhibited anticancer effects and positively affected human health [9].

Several edible/medicinal mushrooms have been reported for their anticancer effects *on breast cancer in vitro and in vivo* and evaluated for their mechanisms [9]. Furthermore, several mushrooms were studied in Phase clinical trials to treat breast, colon, and prostate cancers. It was reported that most *in vitro* studies were performed on breast, lung, and colon cancer cell lines [10]. Considering these explanations, mushrooms have been reported to be associated with the treatment of various types of cancer, including breast, colorectal, ovarian, stomach, skin, lung, cervical, liver, bladder, prostate, and leukemia [11].

Pleurotus species have been reported for their medicinal properties, such as anti-tumor, hepatoprotective, and hypolipidemic [12-14]. *P. eryngii* is a well-known edible/medicinal mushroom [12, 15-18]. *P. eryngii* grows in three villages of Türkiye (Muğla, Çanakkale, and İzmir). *P. eryngii* was called "körek mushroom" in the Egea region and "çakşır mushroom" in Anatolia of Türkiye [19]. In one of the reported studies, *P. eryngii* collected from Muğla was conducted for its fatty acid content [19]. In another study, its extracts were studied on bone metabolism [20]. Moreover, the researchers reviewed its role in biotechnological processes [21]. In the previously reported study, the *P. eryngii* mushroom was used for the mycosynthesis of silver nanoparticles in biomedical applications. Then, AgNPs were analyzed for deoxyribonucleic acid (DNA) damage, antioxidant activity, and lipid peroxidation [22].

In this study, it was the first time, *P. eryngii* mushroom was collected from Çanakkale/Kumkale of Türkiye. This study aimed to investigate *in vitro* antiproliferative effects of the alcoholic extracts of mushrooms on various cancer cell lines. Therefore, methanol and aqueous ethanol extracts of *P. eryngii* mushroom were gradually obtained by Soxhlet extraction. Then, these extracts were applied to breast and colon cancer cell lines to reduce cell proliferation. According to our findings, the proliferation of various cancer cells decreased in the increasing doses of the applications in dose- and time-dependent manner studies.



Figure 1. *P. eryngii* mushroom collected from Çanakkale/Kumkale (The photos were taken by G.D.)

2. Materials and Methods

2.1. Materials

All solvents, including *n*-hexane, ethyl acetate (EtOAc), methanol (MeOH), ethanol (EtOH), and dimethyl sulfoxide (DMSO), were obtained from Sigma and Merck with HPLC grade. MTT (3-(4,5-dimethylthiazol-2-yl)-2,5-diphenyltetrazolium bromide) was purchased from Cayman Chemical. DMEM/F12 (Dulbecco's Modified Eagle Medium) (Thermo, Gibco), Penicillin-streptomycin (PS) (Thermo, Gibco), fetal bovine serum (FBS) (Serox), and 0.25% trypsin-EDTA (Thermo, Gibco) were used. A rotary evaporator (IKA RV10) and a microplate reader (Thermo) were used in the experiments.

2.2. Collection and Identification of *P. Eryngii* Mushrooms and Preparation of its Extracts

P. eryngii mushroom was collected from Çanakkale-Kumkale. Then, the mushrooms were identified and kept at the Department of Biology Muğla Sıtkı Koçman University in Fungarium. The edible mushrooms were divided into small pieces, and water was removed at 50-60 °C. The dried samples were taken into the grinder. The extraction process was carried out by the traditional Soxhlet method. At this stage, it was carried out gradually with the help of various solvents. The extraction was carried out with *n*-hexane, EtOAc, MeOH, and EtOH: water (EtOH:H₂O) (70:30) solvents, respectively. Then, a rotary evaporator was used to remove the solvents at reduced pressure under vacuum. The obtained extracts were dried at room temperature. Then, it was weighed and stored in the refrigerator at +4 °C. The freshly prepared intermediate solutions were prepared from stock solutions (10 mg/mL) before use in *in vitro* cell culture assay [23].

2.3. Cell Culture Conditions

The human breast (MDA-MB-231, BT-549, BT-20, MCF-7) and colon (HT-29) cancer cell lines were used in cell culture studies. The cells were incubated in DMEM/F12 at 37°C in an incubator containing 5% CO₂. PS (1%) and FBS (10%) were used. Passaging was performed using 0.25% trypsin-EDTA at appropriate passage times [23].

2.4. Antiproliferative Activity

To determine the antiproliferative effects of the mushroom extracts on different cancer cell lines, MTT assay was used according to a reported study [23]. A representative workflow is shown in Figure 2. Thus, this assay was applied for 48 h treatments in the increasing dose-dependent manner studies. After incubation, the MTT solution (10 µL) was added and incubated for 3-4 h in an incubator at 37 °C. The absorbances at 570 nm were measured in a 96-well plate following the addition of dimethyl sulfoxide (DMSO) (100 µL). The percentage of cell viability (%) graphs were formed against DMSO as a control. Statistically significant results were taken and indicated with an asterisk [23].

2.5. HPLC Analysis

30% of Aqueous ethanol (EtOH) extract was used in this analysis. The detailed instrument conditions and injection volume, flow rate, solvent system, wavelengths, and standards were given in a previously reported study [23].

2.6. Statistical Analysis

Statistical analysis was performed using the Welch t-test of the GraphPad Prism program. Significant results of $p < 0.05$ were evaluated.



Figure 2. A representative workflow for this study

3. Results and Discussion

3.1. *P. Eryngii* Mushroom Extracts Show Antiproliferative Effect on Human Cancer Cell Lines

This study tested the antiproliferative effects of methanol (MeOH) and aqueous EtOH extracts obtained from *P. eryngii* mushroom by MTT assay. In the increasing concentrations (0.05-0.5 mg/mL), their effects on short-term cell proliferation against MDA-MB-231, BT-549, BT-20, MCF-7, and HT-29 cell lines were evaluated. According to our findings, it has been determined that MeOH extract significantly decreased the cell viability of MDA-MB-231 cells at 0.1 mg/mL for 48 h treatments (Figure 3a). Unlike this, it was determined that MeOH extract showed an antiproliferative effect on the HT-29 cells at 0.3 mg/mL (Figure 3e). The effect of the MeOH extract on TNBC BT-549 and BT-20 cell lines exhibited similar results at 0.1 mg/mL concentration of the extract (Figure 3b,c).

Although aqueous EtOH extract displayed a significant antiproliferative effect on breast cancer cells between 0.125 mg/mL and 0.5 mg/mL concentrations. (Figure 4a-d). It was determined that the cell viability of MDA-MB-231 cells was decreased with the treatments of the aqueous EtOH extract at 0.25 mg/mL (Figure 4a). IC₅₀ values were obtained at 0.375 mg/mL and 0.25 mg/mL on BT-549 and BT-20 cell lines, respectively (Figure 4b,c). The percentage of cell viability was significantly reduced on MCF-7 cells at 0.25 mg/mL, as shown in Figure 4d. Moreover, in Figure 4e, the extract was highly cytotoxic on HT-29 cells at 0.25 mg/mL concentration.

According to previously reported studies of the mushroom extracts, water extracts of the fruiting bodies of *Agaricus blazei* Murill (AbM), a species of mushroom, induce interleukin-8, TNF-alpha, and nitric oxide production, and it was also reported to suppress tumor growth *in vivo* [24]. *Ganoderma lucidum* inhibited

tumor growth in *in vitro* and *in vivo* studies [25]. In addition, *G. lucidum* and *G. tsugae* extracts have been reported to inhibit the growth of colorectal cancer cells *in vitro* [26].

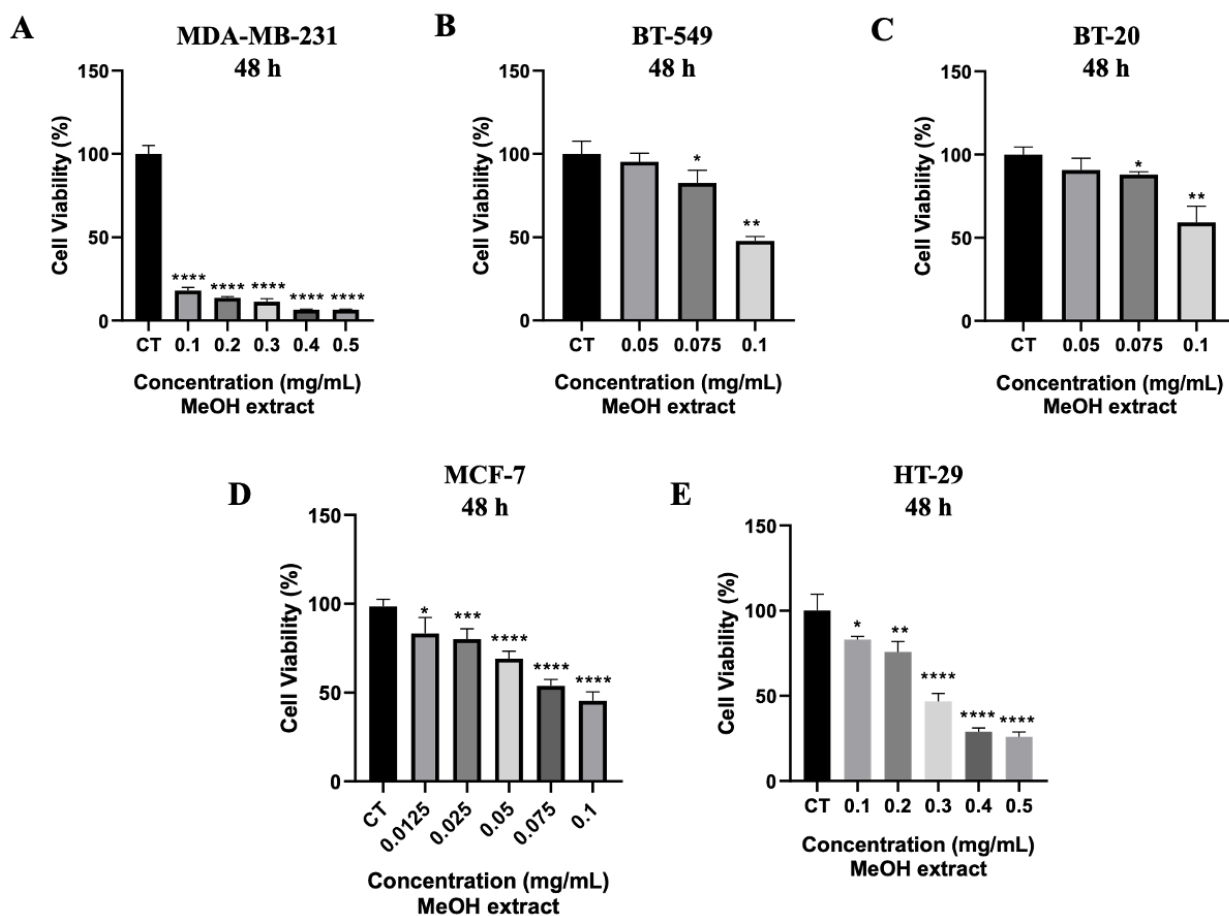


Figure 3. The effect of *P. eryngii* mushroom extracts on breast and colon cancer cell lines. The MeOH extracts showed an antiproliferative effect on A) MDA-MB-231, B) BT-549, C) BT-20, D) MCF-7, and E) HT-29 cell lines after 48 h treatments

According to the reported studies, proteoglycans of TCM mushrooms are associated with the apoptosis process, antiangiogenesis, reversal of drug resistance, and antimetastasis and immune system [27]. In a different study with gold nanoparticles, gold nanoparticles (AuNPs) were isolated from *Commiphora wightii* using an aqueous extract of *Cladosporium* sp., breast cancer cell line (MCF-7), and showed enhanced apoptotic activity [28]. An ethyl acetate fraction of *Lentinula edodes* mushroom induced apoptosis in MCF-7 and MDA-MB-453 cell lines, and the anticancer effect of its isolated bioactive component in MDA-MB-231 and MCF-7 cells was reported [9].

TNBC is identified by the absence of estrogen, progesterone, and Her2 receptors (ER-/PR-/HER2-). The most important feature of these tumors is breast cancer, which is very aggressive and has the lowest patient survival [29]. Therefore, effective and safe treatments against TN breast cancers must be developed due to the lack of targeted therapies. Because of limited response to standard chemotherapeutics and rapid development of resistance, early relapse and lack of therapeutic options are the most important factors that cause high patient mortality rates in TNBC [30]. Colon cancer is the second and third most frequently diagnosed cancer in women and in men, respectively, in the world [31]. Therefore, new sources or therapeutics are needed to discover and develop to fight cancers. These mushroom products from different geographical regions must be deeply evaluated [32].

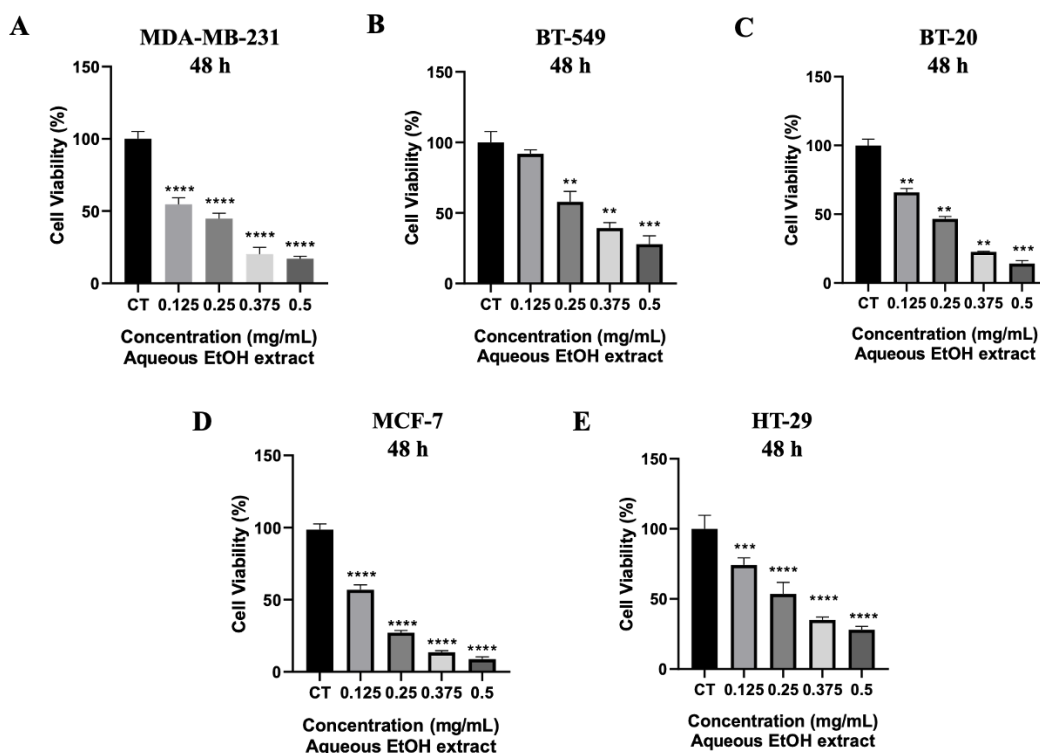


Figure 4. The effect of *P. eryngii* mushroom extracts on breast and colon cancer cell lines. The aqueous EtOH extract showed an antiproliferative effect on A) MDA-MB-231, B) BT-549, C) BT-20, D) MCF-7, and E) HT-29 cell lines after 48 h treatments

3.2. HPLC Analysis

The aqueous EtOH extract was analyzed using high-performance liquid chromatography (HPLC). As given in HPLC chromatograms (Figure 5a-c), the retention times (minutes) of the components were determined at 4.371 (gallic acid), 8.166 (tannic acid), 13.989 (4-hydroxybenzoic acid), 32.463 (salicylic acid), 37.728 (apigenin), 38.033 (4-hydroxy flavone), and 39.092 (chrysin). Gallic acid and 4-hydroxybenzoic acid from the ethanolic and aqueous methanol (80:20) extracts of *P. eryngii* mushroom were identified in reported studies [15, 33]. Furthermore, most phenolics, tocopherols, and carotenoids were determined from ethanolic extracts of *P. eryngii* fruiting bodies by HPLC analysis [15].

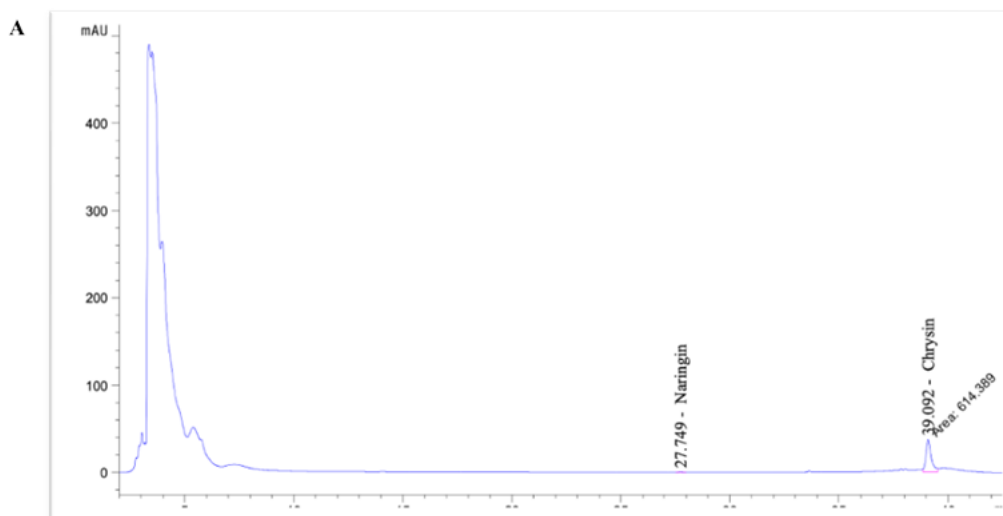


Figure 5. HPLC chromatogram of aqueous EtOH extract of *P. eryngii*

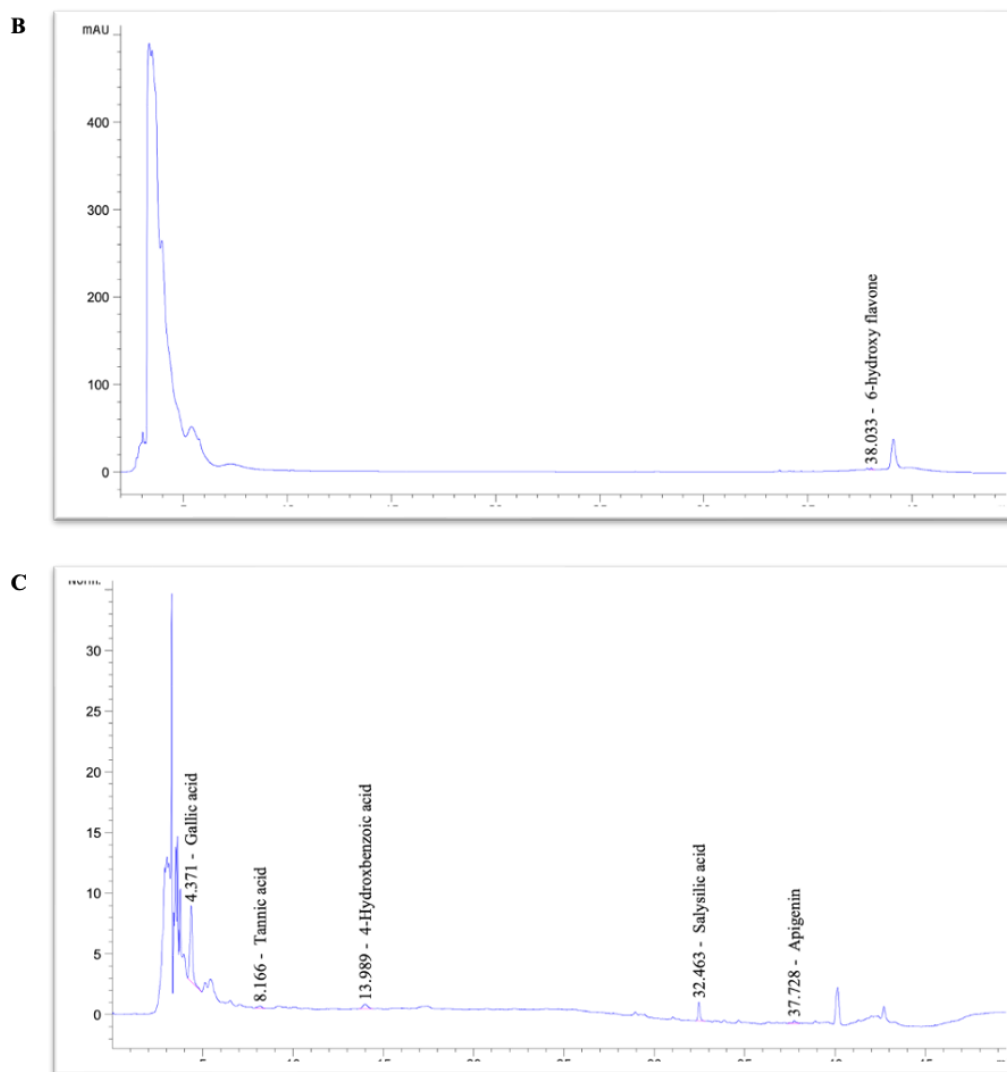


Figure 5. (Continued) HPLC chromatogram of aqueous EtOH extract of *P. eryngii*

4. Conclusion

Edible/medicinal mushrooms are an attractive source for treating human diseases due to their effective bioactive components. Thus, several mushrooms have been used in traditional medicine [10]. Edible *P. eryngii* mushroom collected from Çanakkale was reported for the first time in this study. Therefore, this study focused on investigating the antiproliferative effects of the extracts of *P. eryngii* mushroom against various cancer cell lines. The promising results on cancer cell lines have been obtained following the dose-response treatments. These findings showed that the extracts of *P. eryngii* mushroom were effective at very low concentrations, such as 0.1 mg/mL, on breast cancer cell lines. As indicated in the literature, a bioactive protein and polysaccharides isolated from *P. eryngii* fruiting bodies have been studied on different cancer cell lines and shown significant cytotoxic activity [12, 34]. Consequently, it is thought that there is a need for investigations on edible/medicinal mushroom species with *in vitro* or *in vivo* studies. Thus, these reported studies may lead to the determination of new and effective bioactive components such as polysaccharides, proteins, or phenolics to be used in treating human diseases for further studies.

Author Contributions

All authors analyzed the experiments. All authors contributed to the writing of the manuscript. The first, third, fourth, and fifth authors reviewed and edited the manuscript. All authors read and approved the final version of the manuscript.

Conflicts of Interest

All authors declare no conflicts of interest.

Ethical Review and Approval

No approval from the Board of Ethics is required.

Acknowledgment

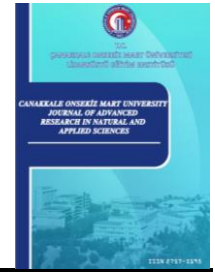
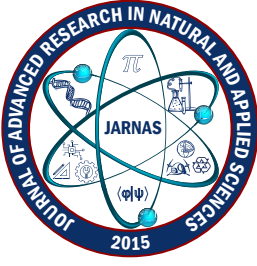
The cancer cell lines were provided by Erciyes University and Çanakkale Onsekiz Mart University. We would like to thank Ahmet Davutlar for collecting *Pleurotus eryngii* mushroom in Kumkale/Çanakkale and Çanakkale Onsekiz Mart University Experimental Research Application and Research Center (ÇOMÜDAM) for laboratory facilities, and Iğdır University Research Laboratory Practice and Research Center (ALUM) for HPLC analysis. A representative workflow was generated with the help of <https://www.biorender.com>.

References

- [1] K. Kumar, R. Mehra, R. P. F. Guiné, M. J. Lima, N. Kumar, R. Kaushik, N. Ahmed, A. N. Yadav, H. Kumar, *Edible mushrooms: A comprehensive review on bioactive compounds with health benefits and processing aspects*, National Library of Medicine 10 (12) (2021) 2996.
- [2] G. Anusiya, U. Gowthama Prabu, N.V. Yamini, N. Sivarajasekar, K. Rambabu, G. Bharath, F. Banat, *A review of the therapeutic and biological effects of edible and wild mushrooms*, Bioengineered 12 (2) (2021) 11239-11268.
- [3] R. Garcia-Rubio, H. C. de Oliveira, J. Rivera, N. Trevijano-Contador, *The fungal cell wall: Candida, cryptococcus and aspergillus species*, Frontiers in Microbiology 10 (2020) 2993.
- [4] A. Assemie, G. Abaya, *The effect of edible mushroom on health and their biochemistry*, International Journal of Microbiology 2022 (2022) 8744788.
- [5] P. A. Ayeka, *Potential of mushroom compounds as immunomodulators in cancer immunotherapy: A review*, Evidence Based Complementary and Alternative Medicine (2018) 7271509.
- [6] R. L. Siegel, K. D. Miller, N. S. Wagle, A. Jemal, *Cancer statistics*, CA Cancer Journal for Clinicians 73 (1) (2023) 17-48.
- [7] M. Borówka, S. Łacki-Zynzeling, M. Nicze, S. Kozak, J. Chudek, *adverse renal effects of anti-cancer immunotherapy: A review*, Cancers Basel 14 (17) (2022) 4086.
- [8] H. S. Chen, Y. F. Tsai, S. Lin, C. C. Lin, K. H. Khoo, C. H. Lin, C. H. Wong, *Studies on the immunomodulating and anti-tumor activities of Ganoderma lucidum (Reishi) polysaccharides*, Bioorganic Medicinal Chemistry 12 (21) (2004) 5595-5601.
- [9] M. B. Gariboldi, E. Marras, N. Ferrario, V. Vivona, P. Prini, F. Vignati, G Perletti, *Anti-cancer potential of edible/medicinal mushrooms in breast cancer*, International Journal of Molecular Sciences 24 (12) (2023) 10120.
- [10] S. K. Panda, G. Sahoo, S. S. Swain, W. Luyten, *Anti-cancer activities of mushrooms: A neglected source for drug discovery*, Pharmaceuticals Basel 15 (2) (2022) 176.
- [11] S. P. Wasser, *Medicinal mushrooms as a source of anti-tumor and immunomodulating polysaccharides*, Applied Microbiology and Biotechnology 60 (3) (2002) 258–274.
- [12] A. M. Mariga, F. Pei, W. J. Yang, L. Y. Zhao, Y. N. Shao, D. K. Mugambi, Q. H. Hu, *Immunopotential of Pleurotus eryngii (DC. ex Fr.) quel*, Journal of Ethnopharmacology 153 (3) (2014) 604-14.

- [13] X. Shi, Y. Zhao, Y. Jiao, T. Shi, X. Yang, *ROS-dependent mitochondria molecular mechanisms underlying anti-tumor activity of Pleurotus abalonus acidic polysaccharides in human breast cancer MCF-7 cells*, PLoS One 8 (5) (2013).
- [14] M. C. Radhakrishnan, N. Peter, *Biological Properties of silver nanoparticles from β (1–3) glucan isolated from the edible mushroom Pleurotus florida*, Letters Applied NanoBioScience 10 (2020) 2096–2106.
- [15] J-T. Lin, C-W. Liu, Y-C. Chen, C-C. Hu, L-D. Juang, C-C. Shiesh, D-J. Yang, *Chemical composition, antioxidant and anti-inflammatory properties for ethanolic extracts from Pleurotus eryngii fruiting bodies harvested at different time*, LWT - Food Science and Technology 55 (2014) 374–382.
- [16] C. Sánchez, *Cultivation of Pleurotus ostreatus and other edible mushrooms*, Applied Microbiology and Biotechnology 85 (2010) 1321–1337.
- [17] R. C. G. Corrêa, T. Brugnari, A. Bracht, R. M. Peralta, I. C. F. R. Ferreira, *Biotechnological, nutritional and therapeutic uses of Pleurotus spp. (Oyster mushroom) related with its chemical composition: A review on the past decade findings*, Trends in Food Science and Technology 50 (2016) 103–117.
- [18] D. Sande, G. P. de Oliveira, M. A. F. Moura, B. de Almeida Martins, M. T. N. S. Lima, J. A. Takahashi, *Edible mushrooms as a ubiquitous source of essential fatty acids*, Food Research International 125 (2018) 108524.
- [19] H. Allı, S. Özderin, İ. Kıvrak, *Ege bölgesinde yetişen körek mantarı (Pleurotus eryngii (DC.) quél.)'nin yağ asidi içeriğinin belirlenmesi*, Mantar Dergisi 13 (3) (2022) 26-31.
- [20] S. W. Kim, H. G. Kim, B. E. Lee, H. H. Hwang, D. H. Baek, S. Y. Ko, *Effects of mushroom, Pleurotus eryngii, extracts on bone metabolism*, Clinical Nutrition 25 (1) (2006) 166–170.
- [21] M. Stajić, J. Vukojević, V. Sonja, *Biology of Pleurotus eryngii and role in biotechnological processes: A review*, Critical Reviews in Biotechnology 29 (1) (2009) 55–66.
- [22] Y. Kocak, I. Meydan, T. Gur Karahan, F. Sen, *Investigation of mycosynthesized silver nanoparticles by the mushroom Pleurotus eryngii in biomedical applications*, International Journal of Environmental Science and Technology 20 (2023) 4861–4872.
- [23] F. Cömert Önder, S. Kalın, Ö. Maraba, A. Önder, P. Ilgın, E. Karabacak, *Anti-cancer, antioxidant, antimicrobial activities, and HPLC analysis of alcoholic extracts of Parthenocissus quinquefolia l. plant collected from Çanakkale*, Journal of Advanced Research in Natural and Applied Sciences 10 (1) (2024) 116-133.
- [24] K. Sorimachi, K. Akimoto, Y. Ikehara, K. Inafuku, A. Okubo, S. Yamazaki, *Secretion of TNF- α , IL-8 and nitric oxide by macrophages activated with Agaricus blazei Murill fractions in vitro*, Cell Structure and Function 26 (2) (2001) 103–108.
- [25] B. S. Min, J. J. Gao, N. Nakamura, M. Hattori, *Triterpenes from the spores of Ganoderma lucidum and their cytotoxicity against Meth-A and LLC tumor cells*, Pharmaceutical Bulletin 48 (7) (2000) 1026–1033.
- [26] S. C. Hsu, C. C. Ou, J. W. Li, T.C. Chuang, H. P. Kuo, J. Y. Liu, C. S. Chen, S. C. Lin, C. H. Su, M. C. Kao, *Ganoderma tsugae extracts inhibit colorectal cancer cell growth via G2/M cell cycle arrest*, Journal of Ethnopharmacology 120 (3) (2008) 394–401.
- [27] L. Li, Y. Wang, *Progress on experimental research and clinical application of trametes robiniophila*, China Cancer 16 (2006) 110–113.
- [28] U. Munawer, V. B. Raghavendra, S. Ningaraju, K. L. Krishna, A. R. Ghosh, G. Melappa, A. Pugazhendhi, *Biofabrication of gold nanoparticles mediated by the endophytic Cladosporium species: Photodegradation, in vitro anti-cancer activity and in vivo anti-tumor studies*, International Journal of Pharmaceutics 588 (2020).

- [29] M. van Barele, B. A. M. Heemskerk-Gerritsen, Y. V. Louwers, M. B. Vastbinder, J. W. M. Martens, M. J. Hooning, A. Jager, *Estrogens and progestogens in triple negative breast cancer: do they harm?*, *Cancers Basel* 13 (11) (2021) 2506.
- [30] Q. Wu, S. Siddharth, D. Sharma, *Triple negative breast cancer: A mountain yet to be scaled despite the triumphs*, *Cancers Basel* 13 (15) (2021) 3697.
- [31] F. T. Kolligs, *Diagnostics and epidemiology of colorectal cancer*, *Visceral Medicine* 32 (3) (2016) 158-64.
- [32] M. P. Pathak, K. Pathak, R. Saikia, U. Gogoi, M. Z. Ahmad, P. Patowary, A. Das, *Immunomodulatory effect of mushrooms and their bioactive compounds in cancer: A comprehensive review*, *Biomedicine and Pharmacotherapy* 149 (2022) 112901.
- [33] F. S. Reis, A. Martins, L. Barros, I. C. Ferreira, *Antioxidant properties and phenolic profile of the most widely appreciated cultivated mushrooms: A comparative study between in vivo and in vitro samples*, *Food and Chemical Toxicology* 50 (5) (2012) 1201-1227.
- [34] D. Ren, N. Wang, J. Guo, L. Yuan, X. Yang, *Chemical characterization of *Pleurotus eryngii* polysaccharide and its tumor-inhibitory effects against human hepatoblastoma HepG-2 cells*, *Carbohydrate Polymers* 138 (2016) 123-133.



Multi-Focus Image Fusion Using Energy Valley Optimization Algorithm

Harun Akbulut¹ 

¹Department of Computer Engineering, Faculty of Engineering and Architecture, Nevşehir Hacı Bektaş Veli University, Nevşehir, Türkiye

Article Info

Received: 04 Jun 2024

Accepted: 25 Jul 2024

Published: 30 Sep 2024

Research Article

Abstract – When a natural scene is photographed using imaging sensors commonly used today, part of the image is obtained sharply while the other part is obtained blurry. This problem is called limited depth of field. This problem can be solved by fusing the sharper parts of multi-focus images of the same scene. These methods are called multi-focus image fusion methods. This study proposes a block-based multi-focus image fusion method using the Energy Valley Optimization Algorithm (EVOA), which has been introduced in recent years. In the proposed method, the source images are first divided into uniform blocks, and then the sharper blocks are determined using the criterion function. By fusing these blocks, a fused image is obtained. EVOA is used to optimize the block size. The function that maximizes the quality of the fused image is used as the fitness function of the EVOA. The proposed method has been applied to commonly used image sets. The obtained experimental results are compared with the well-known Genetic Algorithm (GA), Differential Evolution Algorithm (DE), and Artificial Bee Colony Optimization Algorithm (ABC). The experimental results show that EVOA can compete with the other block-based multi-focus image fusion algorithms.

Keywords – Multi-focus image fusion, energy valley optimizer, block-based image fusion, comparison of meta-heuristic algorithms

1. Introduction

Image fusion methods have recently become more useful in human perception and computer vision applications. Image fusion can obtain a single image containing more information from multiple images of the same scene. These images of the same scene can be obtained from a single sensor whose perceptual parameters can be changed or from different sensors. The first method is called single-sensor image fusion, while the other is called multi-sensor image fusion. The fused images are used more efficiently in many fields, from health to military fields [1-3].

Imaging sensors commonly used today cannot display the entire natural scene. Sensors focus on an object in the natural scene and photograph the focused area. The area outside the focus area is displayed as blurry. Due to these limitations of the sensors, some of the obtained images are clear, while the other parts are blurred. This problem can be solved by combining clear parts of multi-focus images of the same scene. These methods are called multi-focus image fusion (MFIF). MFIF methods can be examined in four groups: transformation domain, spatial domain, deep learning, and hybrid-based methods [4].

In transformation-based methods, the source images are first transferred to the transformation space using a transformation algorithm. Then, by applying the fusion rule, the source images are combined in the

¹harun.akbulut@nevsehir.edu.tr (Corresponding Author)

transformation space. Then, the fused image is obtained by applying the inverse transformation process. Transform-based multi-focus image fusion methods have been presented using many transformation algorithms such as discrete wavelet transform [5], Laplacian transform [6], Curvelet transform [7], Contourlet transform [8], and Shearlet transform [9]. In these methods, artificial images may appear in the fused image because any possible error in the transformation space will be reflected in the entire image. In addition, transformation and reverse transformation processes take a long time. These problems are seen as disadvantages of transformation-based methods.

Another method for MFIF is spatial-based methods. These methods can be examined in two parts: pixel and region based. Pixel-based methods aim to transfer sharp pixels in the source images to the fused image [10]. The sharpness function used in this method for selecting sharp pixels is important. The sharpening criterion function directly affects the method's performance [11]. This method provides more effective results than the transformation-based method because the sharp pixels in the source images are directly transferred to the fused image. However, since this method only deals with the pixel's attribute and not the neighboring pixel values around it, undesirable situations may arise in the fused image. In addition, this method will take a longer calculation time since all pixel values will be processed separately [12].

Due to the above-mentioned disadvantage of the pixel-based method, region-based MFIF methods have been proposed. The basic idea of these methods is to move sharper pixel groups to the fused image by taking advantage of the sharpness information of both a pixel and the relevant pixel and neighboring pixels. Region-based methods have less computational cost, and the obtained results are more satisfactory because they also consider neighboring pixel values. The first block-based multi-focal image fusion method is proposed by Li et al. [13]. The proposed method first divides the source images into identical blocks. Then, the sharper blocks are identified using the spatial frequency criterion function and moved into the merged image. Another method that is based on combining the focus maps obtained by block-based focus measures and employing a multi-matting model with weight maps is proposed by Chen et al. [14]. Based on the optimal placing of the blocks multi-focal method is proposed by Toprak and Aslantaş [15]. Using a differential evolution algorithm based on point distribution functions of source images multi-focus image fusion method is presented by Aslantaş and Toprak [16]. Using a genetic algorithm, multi-focus image fusion is presented by Kong et al. [17]. Aslantaş and Kurban suggest a multi-focus method based on optimizing block size using a differential evolution algorithm [1].

Despite numerous studies on multi-focus image fusion in the literature, there remains a critical need for enhancing the quality of fused images obtained. Particularly noteworthy is the recent utilization of artificial intelligence techniques that have effectively solved various non-linear problems [18, 19]. Therefore, evaluating current problems with recently proposed artificial intelligence techniques is crucial. This article proposes a method using Energy Valley Optimization Algorithm (EVOA) for block-based multi-focus image fusion. EVOA is used to optimize the block size of the source images. For the fitness function of EVOA, the function that maximizes the variance value of the fused image is used. The method is applied to commonly used test data sets. The objective and subjective evaluation results show that EVOA provides satisfactory results for multi-focal image fusion. EVOA has demonstrated that it can compete with commonly used meta-heuristic algorithms such as Genetic Algorithm (GA), Evolution Algorithm (DE), and Artificial Bee Colony Optimization Algorithm (ABC). The contribution of the study is as follows:

- i.* In this study, EVOA is used for multi-focus image fusion for the first time,
- ii.* The proposed method is applied to commonly used datasets,
- iii.* The obtained fused images are evaluated with quality metrics to obtain numerical results,
- iv.* Numerical results are compared with a well-known meta-heuristic optimization algorithm: GA, DE, and ABC.

In the remaining part of our study, the proposed method and quality metrics are mentioned in the second part, the Energy Valley Optimization Algorithm. In the third section, the results of the conducted experiments are given. Finally, the results and discussion section are provided.

2. Block-based Multi-focus Image Fusion Using Energy Valley Optimization Algorithm

2.1. Energy Valley Optimization Algorithm

EVOA is a meta-heuristic optimization algorithm proposed by Azizi et al. [18] in 2023. EVOA aims to solve optimization problems inspired by advanced physics principles. In this context, meta-heuristic algorithms belong to the class of physics-based meta-heuristic optimization algorithms. EVOA mimics the degradation process caused by different particles in nature. In EVOA, each particle with varying levels of stability represents a possible solution. The algorithm first starts with the creation of the initial population. The initial population is created using (2.1).

$$x_i^j = x_{i,min}^j + rand \cdot (x_{i,max}^j - x_{i,min}^j), \quad i \in \{1,2,3, \dots, n\} \text{ and } j \in \{1,2,3, \dots, d\} \quad (2.1)$$

Here, n refers to the number of pieces in the solution space, and d refers to the problem size. $x_{i,min}^j$ and $x_{i,max}^j$ represent the lower and upper bounds of the problem, respectively. The second step calculates the neutron enrichment level using (2.2).

$$EB = \frac{\sum_{i=1}^n NEL_i}{n}, \quad i \in \{1,2,3, \dots, n\} \quad (2.2)$$

Here, NEL_i i -th represents the neutron enrichment level of the particle, and EB refers to the enrichment limit of the particles. The stability levels of the particles are calculated using (2.3).

$$SL_i = \frac{NEL_i - BS}{WS - BS}, \quad i \in \{1,2,3, \dots, n\} \quad (2.3)$$

Here, SL_i i -th. BS and WS represent the stability level of the particle, and BS and WS represent the best and worst particle stability levels, respectively. In EVOA, a new particle is generated using (2.4).

$$x_i^{New1} = x_i(x_{BS}(x_i^j)), \quad i \in \{1,2,3, \dots, n\} \text{ and } j = \text{Alpha Index II} \quad (2.4)$$

Here, x_i^{New1} represents the newly produced particle, x_i represents the position of the current particle and x_{BS} represents the best particle in the solution space. Particles in the universe interact with each other by emitting rays. Accordingly, the second new individual is created using (2.5) based on neighbor interaction.

$$x_i^{New2} = x_i(x_{NG}(x_i^j)), \quad i \in \{1,2,3, \dots, n\} \text{ and } j = \text{Gamma Index II} \quad (2.5)$$

Here, x_i^{New2} represents the newly produced particle and x_{NG} represents the neighboring particles that emit photons. If the stability level of a particle is lower than the stability limit, its degradation is considered to have occurred. Thus, the stability level of these particles is updated to the particle with the best stability level and to the center of the particles using (2.6).

$$x_i^{New1} = x_i + \frac{\left(r_1 x_{BS} - r_2 \frac{\sum_{i=1}^n x_i}{n}\right)}{SL_i}, \quad i \in \{1,2,3, \dots, n\} \quad (2.6)$$

Here, $r_1, r_2 \in [0,1]$ and SL_i represents the stability level of the particle in the i -th iteration. To increase the exploration and exploitation speed of the algorithm, a location update is performed using (2.7).

$$x_i^{New2} = x_i + (r_3 \cdot x_{BS} - r_4 \cdot x_{NG}), \quad i \in \{1,2,3, \dots, n\} \quad (2.7)$$

Here, $r_3, r_4 \in [0,1]$ and x_{NG} denote the stability level of the neighboring particle. If the stability level of a particle is less than the neutron enrichment limit, the position update is performed randomly using (2.8).

$$x_i^{New} = x_i + r, \quad i \in \{1,2,3, \dots, n\} \quad (2.8)$$

Here, $r \in [0,1]$, x_i denotes the current position and x_i^{New} denotes the new position. Position updates of the particles are made throughout the algorithm's main loop. Thus, it is aimed to reach the best solution. The basic steps of EVOA are shown in Figure 1.

2.2. Block-based Multi-focus Image Fusion Using Energy Valley Optimization Algorithm

In block-based MFIF methods, the source images are first divided into $m \times n$ -sized blocks. Then, using the sharpness criterion function, sharper blocks are detected and moved to the fused image to obtain the fused image. Since each image will have its attributes, a block method with a fixed $m \times n$ size will not give good results for every image. Thus, the $m \times n$ block size must be determined by researchers for each image. The determined block size will directly affect the performance of the method. Optimization algorithms can be used effectively to compute the optimal block size. The flow chart of the optimized block-based method is shown in Figure 2 [4].

As shown in Figure 2, the source images are first divided into $m \times n$ -sized blocks. The optimization algorithm starts the cycle with random $m \times n$ block size generation. During each cycle, blocks with $m \times n$ block size are compared using the sharpness criterion function. Blocks with greater sharpness criterion function are transferred to the fused image. This study uses the spatial frequency (SF) [19] criterion function as the sharpness criterion function. SF is a criterion function that measures overall activity in the image by highlighting differences between neighboring pixels. The sharpness value of each block is calculated using (2.9)-(2.11).

$$SF = \sqrt{R^2 + C^2} \quad (2.9)$$

$$R = \sqrt{\frac{1}{m \times n} \sum_i \sum_j [f(i, j) - f(i - 1, j)]^2} \quad (2.10)$$

$$C = \sqrt{\frac{1}{m \times n} \sum_i \sum_j [f(i, j) - f(i, j - 1)]^2} \quad (2.11)$$

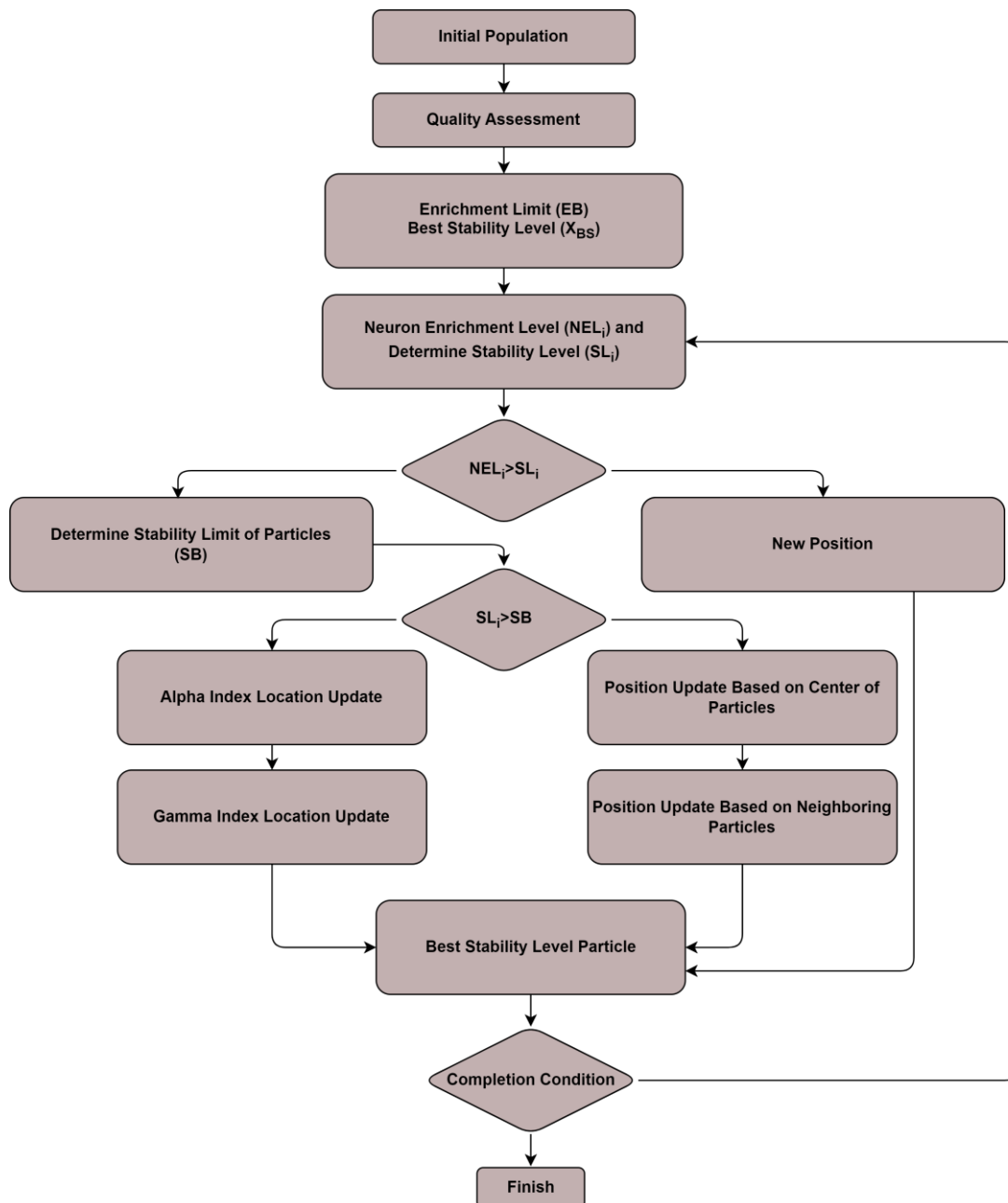


Figure 1. EVOA flowchart

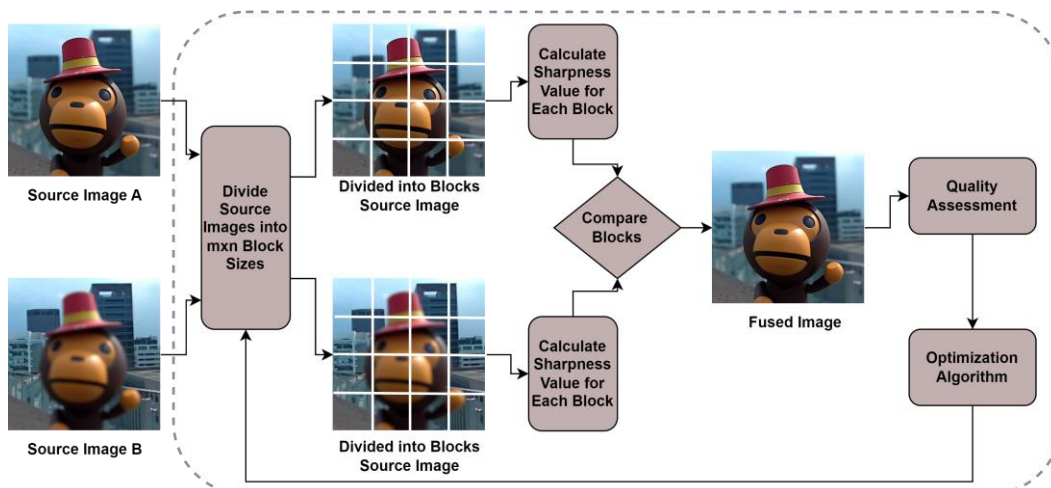


Figure 2. Multi-focus image fusion flowchart by optimization algorithm

Blocks with higher SF values are moved to the fused image. F represents the fused image, and Cr represents the criterion function. Sharper blocks are selected using (2.12) and moved to the fused image.

$$F_i = \begin{cases} A_i, & Cr_i^A \geq Cr_i^B \\ B_i, & \text{otherwise} \end{cases} \quad (2.12)$$

Then, the fused image is obtained. The quality of the fused image is evaluated using the variance (QM_{var}) [22] quality metric. The QM_{var} value of the fused image is calculated using (2.13), where μ is the average value of the F and $m \times n$ is the size of the F.

$$QM_{var}(F) = \frac{1}{m \times n} \sum_{(i,j)} (F(i,j) - \mu)^2 \quad (2.13)$$

The function that maximizes the variance value of the fused image is used as the fitness function of the optimization algorithm. In this study, EVOA, proposed in recent years, is used as the optimization algorithm.

2.3. Compared Optimization Algorithms

Information about the metaheuristic optimization algorithms that are GA, DE, and ABC is provided in this section. These well-known, widely used, and meta-heuristic optimization algorithms give good results in optimization problems. GA belongs to the evolutionary, DE numerical, and ABC belongs to the intelligent swarm metaheuristic class of optimization algorithms. Thus, EVOA is compared with algorithms representative of many classes of metaheuristic optimization algorithms.

2.3.1. Genetic Algorithm (GA)

GA [23] is a population-based optimization algorithm developed by Holland and colleagues in 1975, widely used for solving multidimensional and non-linear problems, and known for delivering effective results. GA solves optimization problems by employing genetic operators such as selection, crossover, and mutation. The selection genetic operator ensures the survival of individuals with high solution quality during the algorithm's iterations while gradually eliminating individuals with low solution quality. The crossover genetic operator aims to produce higher-quality individuals by combining pairs of randomly selected individuals from the solution pool. The mutation genetic operator seeks to generate new individuals from randomly selected ones in the solution pool to create individuals with potentially better solution quality.

2.3.2. Differential Evolution Algorithm (DE)

DE [24] is a stochastic, population-based metaheuristic algorithm introduced by Storn and Price, known for being fast and stable and delivering effective results in optimizing multidimensional and non-linear problems, especially in numerical optimization. Since DE is a stochastic evolution algorithm, it generates the initial population randomly. DE employs a unique mutation method that creates a new individual by adding the weighted difference of two randomly selected individuals from the solution pool, determined by a parameter F specified by the researcher, to the value of a third individual.

2.3.3. Artificial Bee Colony Optimization Algorithm (ABC)

ABC algorithm [25], developed by Karaboga and Basturk, is a recent optimization algorithm based on swarm intelligence that models the intelligent foraging behavior of honeybees for numerical optimization problems. The ABC algorithm mathematically models the aforementioned intelligent behaviors of honeybee colonies in nature, yielding effective results in solving numerical optimization problems. In the ABC algorithm, food source regions represent potential solution values for the problem to be solved. Once scout bees detect food

sources, employed bees are sent to these sources. Employed bees evaluate the quality of the food sources they work on and the neighboring sources, gravitating towards the source with better solution quality. When an employed bee with a current solution and new location information returns to the hive, it communicates this information to the onlooker bees through a dance. When the food quantity is depleted, reaching the threshold specified by the limit parameter of the ABC algorithm, the employed bee becomes a scout bee and continues searching again.

2.4. Quality Metrics

In image fusion, quality metrics play a crucial role in evaluating the effectiveness of the fusion process, which aims to integrate information from multiple images into a single fused image with improved visual quality and information content. These metrics provide quantitative measures to assess various aspects such as spatial resolution, spectral fidelity, contrast, and overall perceptual quality of the fused image. However, a single quality metric that considers all images' quality has not yet been developed. Therefore, it is necessary to evaluate the quality of an image using multiple quality metrics. This section includes a variety of quality metrics for the objective assessment of fused images. These metrics have been selected from commonly used quality metrics in image fusion. Variance (QM_{var}) and Spatial Frequency (QM_{SF}) are mentioned in (2.13) and (2.9)-(2.11), respectively.

2.4.1. Entropy (QM_E)

Entropy [26] is a quality metric that measures the content information of a fused image. As the entropy value increases, the quality of the fused image increases. Entropy is calculated using (2.14).

$$QM_E(F) = - \sum_{i=0}^L h_f(i) \log_2 h_f(i) \quad (2.14)$$

Here, L is the number of gray tones, h_f is the normalized histogram of the fused image.

2.4.2. Standard Deviation (QM_{SD})

Standard deviation [27] is a quality metric measuring the fused image's contrast. As the QM_{SD} value increases, the quality of the fused image increases. QM_{SD} is calculated using (2.15).

$$QM_{SD}(F) = \sqrt{\sum_{i=0}^L (i - \bar{i})^2 \log_2 h_f(i)} \quad (2.15)$$

Here, L is the number of gray tones, h_f is the normalized histogram of the fused image.

2.4.3. Edge Based Quality Metric (QM_{ABF})

QM_{ABF} [28] is a quality metric that calculates the quality of the image by using edge information. QM_{ABF} is computed using (2.16).

$$QM_{ABF}(F) = \frac{\sum_{n=1}^N \sum_{m=1}^M Q^{AF}(n, m) w^A(n, m) + Q^{BF}(n, m) w^B(n, m)}{\sum_{n=1}^N \sum_{m=1}^M (w^A(n, m) + w^B(n, m))} \quad (2.16)$$

Here, $Q^{A/BF}$ denotes weighted by $w^{A/B}(n, m)$.

2.4.4. Chen-Blum Metric (QM_{CB})

QM_{CB} [29] is a quality metric that calculates the quality of the image using a saliency map. As the QM_{CB} value increases, the quality of the image increases. QM_{CB} is calculated using (2.17).

$$QM_{CB}(F) = Sm_A(x, y)Q_{AF}(x, y) + Sm_B(x, y)Q_{BF}(x, y) \quad (2.17)$$

Here, $Sm_A(x, y)$ denotes a global quality map.

2.4.5. Mutual Information (QM_{MI})

QM_{MI} [30] is a quality metric measuring the similarity information between the fused and the source images. QM_{MI} is calculated using (2.18).

$$QM_{MI}(F) = \sum_{i=1}^L \sum_{j=1}^L h_{sf}(i, j) \log_2 \frac{h_{sf}(i, j)}{h_s(i, j)h_f(i, j)} \quad (2.18)$$

Here, h_s and h_f denotes the normalized histogram of the source and fused image, respectively. L represents the number of gray tones.

2.4.6. Sum of the Correlations of Differences (QM_{SCD})

QM_{SCD} [31] is a quality metric that determines the quality of the image according to the correlation coefficient between the fused image and the different images. SCD is calculated using (2.19).

$$QM_{SCD}(F) = c(D_A, F) + c(D_B, F) \quad (2.19)$$

Here, c denotes the correlation coefficient, $D_{A/F}$ denote the different images.

3. Experimental Results

This study proposes a method based on block size optimization for multi-focus image fusion using EVOA. Several experiments are conducted to test the performance of the method. The experiments use a laptop with Windows 7 operating system, 8 GB RAM, Intel Core 2.3 features and MATLAB r2019a. Experiments are carried out on the 512x512 color Lytro dataset. EVOA has been run independently thirty times. Max, mean, and standard deviation values of experiments are obtained. Numerical results are obtained using the eight quality functions used for image quality evaluation in the literature. Figure 3 shows test images taken from the Lytro [10] dataset where the experiments are carried out. To ensure fairness, common parameter values for optimization algorithms, namely a population size of 10 and a maximum iteration count of 100, have been selected. These values were chosen based on insights from the literature and preliminary experiments conducted.

The parameter values used for GA, DE, and ABC are those commonly used in the literature and generally observed to yield good results. For GA, the selection strategy is roulette wheel selection, with single-point crossover and a crossover rate of 0.8. The mutation strategy is a uniform mutation with a mutation rate of 0.2. A crossover rate of 0.6 and an F value of 0.9 were chosen for DE. The number of onlooker bees equals the population size for ABC, and the L parameter value is set to 100. EVOA does not have its unique control parameter.

In Tables 1-4, the obtained numerical results in the experiments carried out using optimization algorithms are given comparatively. Max, mean, and standard deviation quality metric values are obtained for each

optimization algorithm. QM_{Var} , QM_E , QM_{SF} , QM_{SD} , QM_{ABF} , QM_{CB} , QM_{MI} , and QM_{SCD} in each column, respectively, is given.

Table 1 shows the numerical results of the experiments conducted for the 1st image. When Table 1 is examined, it is seen that GA and EVOA achieve the best value in a single quality metric for the 1st image. It can be said that while DE gives the best results in four quality metrics, ABC provides the best in three. As a result, it can be said that ABC achieved the best result for the first image, followed by DE.

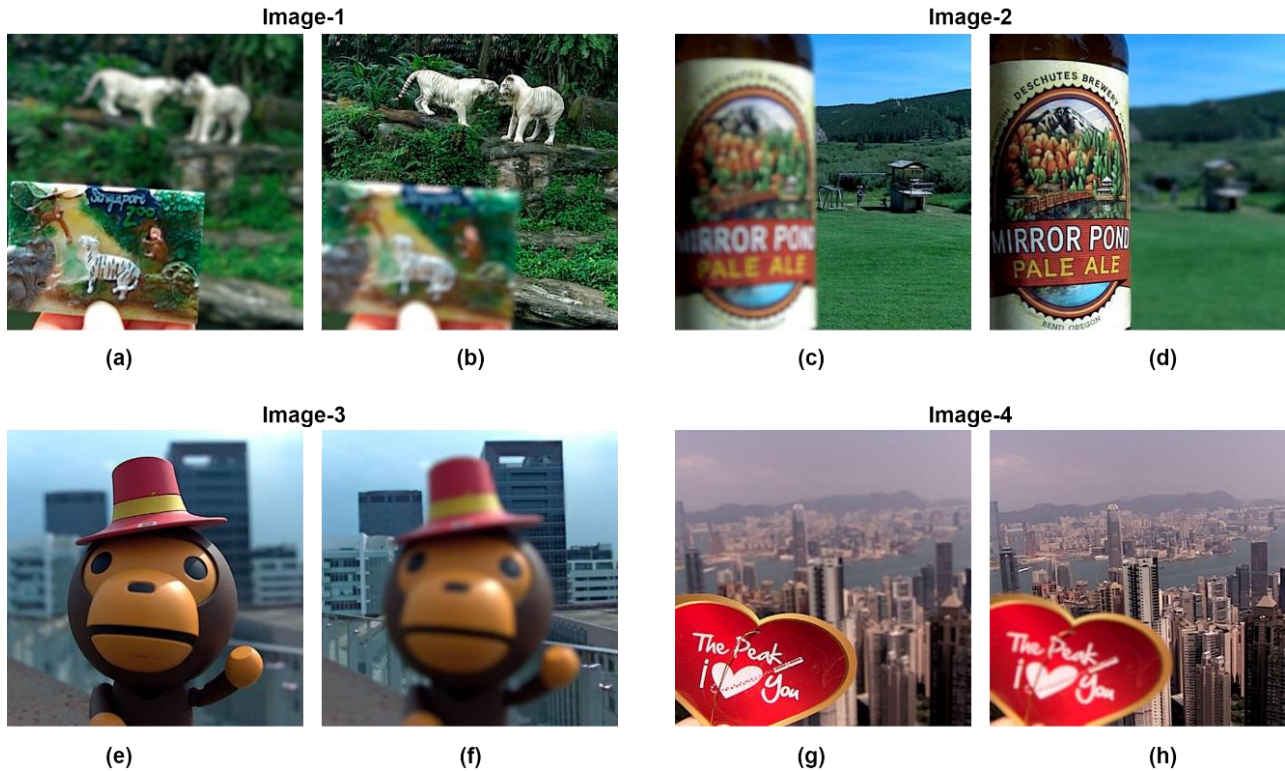


Figure 3. Experimental data sets

Table 1. Experimental results for Image 1

	QM_{Var}	QM_E	QM_{SF}	QM_{SD}	QM_{ABF}	QM_{CB}	QM_{MI}	QM_{SCD}
GA								
Max	3818,6295	7,5106	7,0564	61,7950	0,7994	0,8627	0,8564	0,6483
Mean	3813,7821	7,4613	7,0072	61,2006	0,7951	0,8582	0,8524	0,6436
SD	3,1457	0,0333	0,0337	0,2853	0,0033	0,0036	0,0032	0,0030
DE								
Max	3824,0571	7,5098	7,0659	61,8389	0,8013	0,8635	0,8561	0,6554
Mean	3819,3852	7,4654	7,0214	61,3595	0,7964	0,8582	0,8528	0,6504
SD	3,2401	0,0307	0,0311	0,3212	0,0032	0,0034	0,0025	0,0033
ABC								
Max	3816,5063	7,5120	7,0891	61,7778	0,8009	0,8638	0,8559	0,6479
Mean	3811,4401	7,4583	7,0402	61,2467	0,7960	0,8591	0,8512	0,6422
SD	2,9729	0,0328	0,0296	0,2614	0,0031	0,0033	0,0032	0,0030
EVOA								
Max	3818,1955	7,5118	7,0670	61,7915	0,8002	0,8615	0,8559	0,6511
Mean	3812,9763	7,4711	7,0199	61,3342	0,7951	0,8571	0,8516	0,6467
SD	3,1362	0,0285	0,0307	0,3113	0,0034	0,0032	0,0033	0,0029

Boldfaced values indicate the "best" performances.

Table 2 shows the numerical results of the experiments conducted for the second image. When Table 2 is examined, ABC gives the best result in seven quality metrics for the 2nd image. Other algorithms provide the best results in one quality metric. Thus, it can be said that ABC has a superior performance compared to others for this image.

Table 2. Experimental results for Image 2

	QM _{Var}	QM _E	QM _{SF}	QM _{SD}	QM _{ABF}	QM _{CB}	QM _{MI}	QM _{SCD}
GA								
Max	4955,6490	7,5740	5,1673	70,3963	0,7957	0,8539	0,8926	0,4765
Mean	4950,7864	7,5258	5,1178	69,9621	0,7907	0,8491	0,8882	0,4718
SD	3,1543	0,0352	0,0271	0,2744	0,0031	0,0032	0,0035	0,0036
DE								
Max	4959,8559	7,5755	5,1695	70,4262	0,7964	0,8530	0,8925	0,4809
Mean	4953,8459	7,5329	5,1117	69,9503	0,7924	0,8486	0,8871	0,4756
SD	2,7059	0,0289	0,0295	0,3262	0,0036	0,0034	0,0033	0,0033
ABC								
Max	4965,5762	7,5753	5,1939	70,4668	0,8010	0,8541	0,8925	0,4816
Mean	4961,1913	7,5382	5,1572	70,0680	0,7967	0,8494	0,8882	0,4771
SD	2,7592	0,0224	0,0320	0,2814	0,0027	0,0032	0,0033	0,0034
EVOA								
Max	4959,8559	7,5755	5,1695	70,4262	0,7964	0,8530	0,8925	0,4809
Mean	4954,3476	7,5203	5,1260	69,9727	0,7917	0,8482	0,8880	0,4752
SD	3,0449	0,0337	0,0318	0,2889	0,0036	0,0029	0,0037	0,0036

Boldfaced values indicate the "best" performances.

Table 3 shows the numerical results of the experiments conducted for the 3rd image. When Table 3 is examined, DE achieves the best result in six quality metrics for the 3rd image. Then, ABC achieves the best result in two quality metrics, while EVOA achieves the best result in a single quality metric. Thus, it can be said that DE performs superiorly to the others in this image. Also, it can be said that EVOA can also compete with ABC.

Table 4 shows the numerical results of the experiments conducted for the 4th image. When Table 4 is examined, GA produces the best results for the four-quality metrics for the 4th image. It produces the best results in two quality metrics, DE and EVOA. ABC, on the other hand, produces the best result for a quality metric. It can be said that GA performs better than the others for this image. Also, it can be said that DE and EVOA perform equally well.

Table 3. Experimental results for Image 3

	QM _{Var}	QM _E	QM _{SF}	QM _{SD}	QM _{ABF}	QM _{CB}	QM _{MI}	QM _{SCD}
GA								
Max	4796,5094	7,7837	2,3946	69,2568	0,6968	0,7704	0,9297	0,1626
Mean	4791,8393	7,7421	2,3402	68,9532	0,6921	0,7660	0,9242	0,1573
SD	2,9967	0,0315	0,0304	0,2574	0,0031	0,0031	0,0028	0,0035
DE								
Max	4847,6539	7,7788	2,4482	69,6251	0,7112	0,7790	0,9297	0,2141
Mean	4842,7669	7,7243	2,4051	69,0841	0,7069	0,7737	0,9251	0,2096
SD	3,4452	0,0271	0,0297	0,2590	0,0036	0,0033	0,0033	0,0033
ABC								
Max	4822,3318	7,7839	2,4096	69,4430	0,6993	0,7746	0,9296	0,1868
Mean	4818,0853	7,7436	2,3638	68,9429	0,6944	0,7690	0,9244	0,1814
SD	2,5065	0,0271	0,0326	0,3278	0,0028	0,0031	0,0033	0,0034
EVOA								
Max	4831,1246	7,7812	2,4191	69,5062	0,7069	0,7742	0,9300	0,1945
Mean	4825,9793	7,7312	2,3778	69,0992	0,7013	0,7696	0,9250	0,1900
SD	3,2322	0,0279	0,0296	0,2586	0,0034	0,0031	0,0036	0,0035

Boldfaced values indicate the "best" performances.

Table 4. Experimental results for Image 4

	QM _{var}	QM _E	QM _{SF}	QM _{SD}	QM _{ABF}	QM _{CB}	QM _{MI}	QM _{SCD}
GA								
Max	3895,2398	7,6520	4,3443	62,4118	0,7365	0,7876	0,8946	0,3913
Mean	3891,2508	7,6083	4,3000	61,8875	0,7314	0,7834	0,8906	0,3865
SD	3,4083	0,0309	0,0280	0,3245	0,0036	0,0031	0,0032	0,0035
DE								
Max	3894,1864	7,6525	4,3472	62,4034	0,7364	0,7874	0,8946	0,3923
Mean	3888,9185	7,5978	4,3040	61,8967	0,7315	0,7826	0,8898	0,3870
SD	3,2738	0,0300	0,0327	0,2882	0,0037	0,0032	0,0033	0,0030
ABC								
Max	3893,0045	7,6524	4,3484	62,3939	0,7354	0,7874	0,8949	0,3903
Mean	3888,0230	7,5997	4,3049	61,9339	0,7297	0,7826	0,8898	0,3861
SD	3,1932	0,0298	0,0328	0,3137	0,0034	0,0035	0,0027	0,0030
EVOA								
Max	3890,6701	7,6522	4,3539	62,3752	0,7365	0,7873	0,8949	0,3892
Mean	3885,7726	7,6043	4,2940	61,8454	0,7317	0,7823	0,8897	0,3847
SD	3,1889	0,0319	0,0320	0,3215	0,0033	0,0033	0,0029	0,0034

Boldfaced values indicate the "best" performances.

When Table 1-4 is generally examined, it can be said that the optimization algorithms compared based on quality metrics give similar results. It can be said that DE and ABC produce the best results regarding more quality metrics. Thus, it can be said that DE and ABC give similar results, and GA and EVOA give similar results.

Figure 4-7 shows the fused images obtained within the scope of the experiments carried out for the images and the zoom images of these images. The first row for each image shows the fused images obtained with GA, DE, ABC, and EVOA, respectively. In the second line, the zoom of the fused images is respectively demonstrated, to make a subjective evaluation.

Figure 4 shows the fused images obtained for image 1. As shown in Figure 4, when the zoomed images are examined carefully, it is seen that ABC and EVOA give similar and better results than the other algorithms. When DE and GA are compared, it can be said that DE gives better results. In the numerical results in Table 1, DE and ABC gave better results than the others. Thus, it can be said that only numerical evaluation is insufficient and may give meaningless results in some cases.

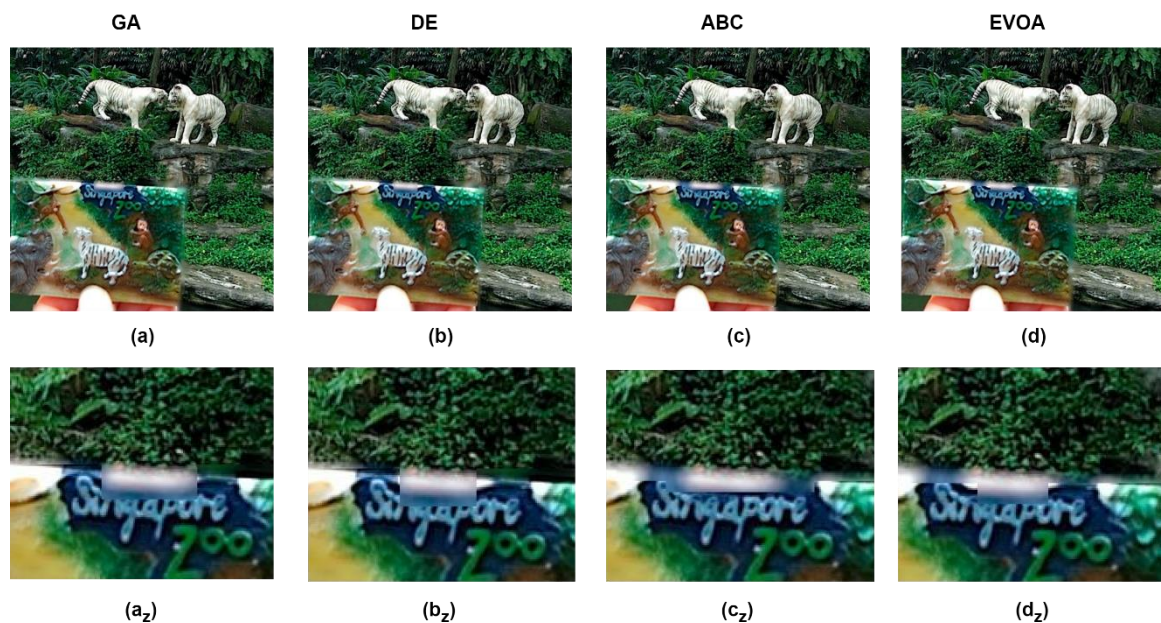


Figure 4. The obtained fused image for image 1

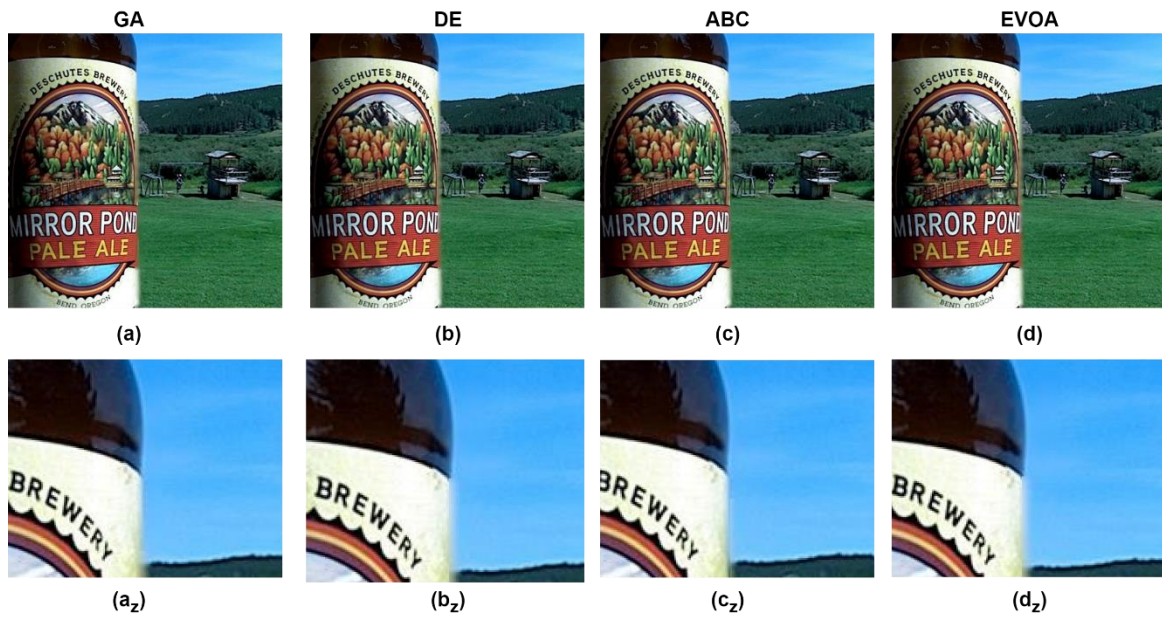


Figure 5. The obtained fused image for image 2

Figure 5 shows the fused images obtained for image 2. When Figure 5 is examined, it is seen that all optimization algorithms give similar results. In the numerical data of Table 2, the ABC algorithm achieves the best result based on seven quality metrics. However, there is no significant difference between the algorithms in subjective evaluation.

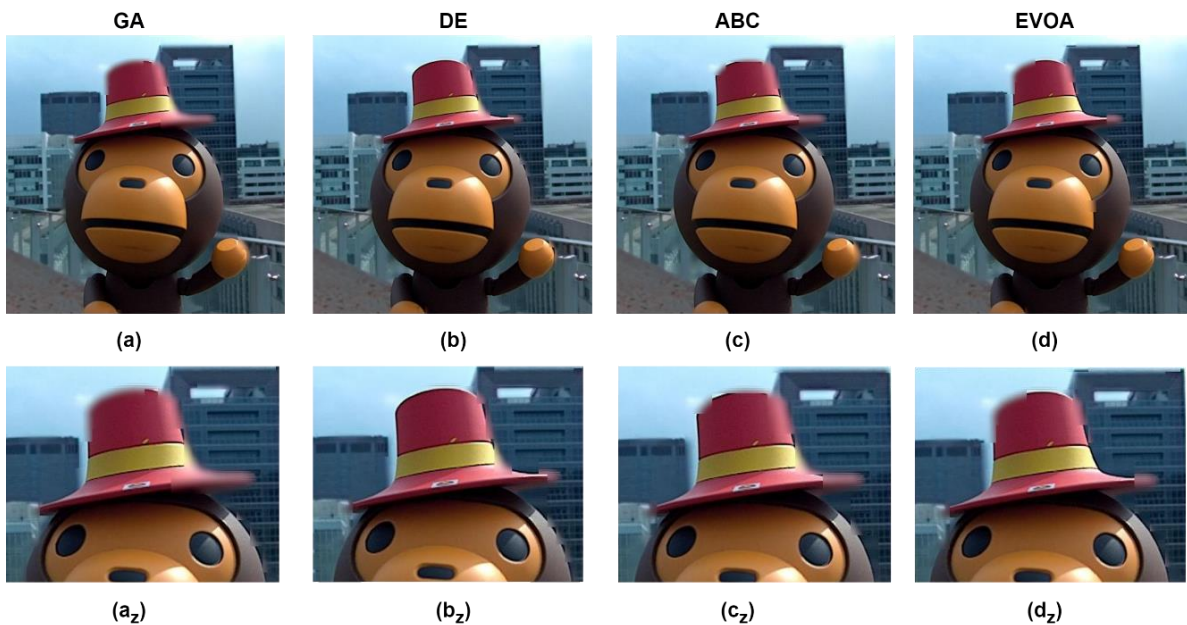


Figure 6. The obtained fused image for image 3

Figure 6 shows the fused images obtained for image 3. When Figure 6 is examined, it is obvious that the method's performance decreases and makes incorrect fusing in photographs containing non-linear objects. The main disadvantage of block-based multi-focus image fusion methods is seen in Figure 6. As seen in Figure 6, DE gives better results than the others. Then, while ABC and EVOA obtain similar results, it is seen that GA performs the worst fusing process. When evaluated together with the numerical results obtained in Table 3 for this image, it is seen that a result equivalent to the subjective evaluation is reached.



Figure 7. The obtained fused image for image 4

Figure 7 shows the fused images obtained for image 4. When Figure 7 is examined, although the image has non-linear objects, the optimization algorithms obtained well-fused images close to each other. When Figure 4-7 is generally reviewed, it is seen that the algorithms give similar results and can compete with each other.

4. Conclusion

This work proposes using the recently proposed energy valley optimization algorithm (EVOA) for multi-focus image fusion. Multi-focus image fusion is the method of obtaining a clear image on all sides by combining multi-focus images of the same scene. These fused images are widely used in many fields, from the military to the medical field. EVOA is a new meta-heuristic optimization algorithm presented by Azizi et al. in 2023. EVOA is used to calculate optimal block sizes. The method is applied to commonly used image sets. Despite the development of numerous quality assessment metrics in the literature, evaluating fused images remains challenging. While one quality metric may yield favorable results for an image, another metric may produce less favorable outcomes for the same image. Thus, relying on a single quality metric may be insufficient for objective assessment.

Consequently, multiple quality metrics are employed for objective evaluation. In addition to objective assessment, conducting subjective evaluations is also crucial. Both objective and subjective evaluations are made to evaluate the quality of the resulting fused images. When the results are compared with the well-known GA, DE and ABC, it was seen that EVOA showed a performance close to the others.

In this study, EVOA is used to optimize the block size. By changing the parameter values of EVOA, experiments can be conducted, and the results compared. Experiments can be run using different current meta-heuristic optimization algorithms, and the results can be compared. Optimized block-based image fusion is used in this study. Other optimization algorithms can be used for region-based multi-focus image fusion methods and the performance of these algorithms can be evaluated.

Author Contributions

The author read and approved the final version of the paper.

Conflicts of Interest

The author declares no conflict of interest.

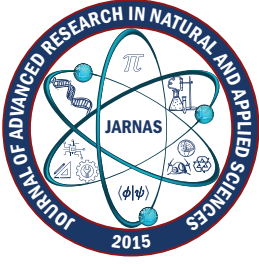
Ethical Review and Approval

No approval from the Board of Ethics is required.

References

- [1] V. Aslantas, R. Kurban, *Fusion of multi-focus images using differential evolution algorithm*, Expert Systems with Applications 37 (12) (2010) 8861–8870.
- [2] C. Akyel, *Diagnosis of oral cancer from histopathological images with xception*, Journal of Advanced Research in Natural and Applied Sciences 9 (2) (2023) 283–290.
- [3] H. Avcı, J. Karakaya, *Effect of different parameter values for pre-processing of using mammography images*, Journal of Advanced Research in Natural and Applied Sciences 9 (2) (2023) 345–354.
- [4] F. Çakıroğlu, R. Kurban, A. Durmuş, E. Karaköse, *Multi-focus image fusion by using swarm and physics based metaheuristic algorithms: A comparative study with Archimedes, atomic orbital search, equilibrium, particle swarm, artificial bee colony and jellyfish search optimizers*, Multimedia Tools and Applications 82 (29) (2023) 44859–44883.
- [5] G. Pajares, J. M. De La Cruz, *A wavelet-based image fusion tutorial*, Pattern Recognition 37 (9) (2004) 1855–1872.
- [6] P. Burt, E. Adelson, *The Laplacian Pyramid as a compact image code*, IRE Transactions on Communications Systems 31 (4) (1983) 532–540.
- [7] S. Li, B. Yang, *Multifocus image fusion by combining curvelet and wavelet transform*, Pattern Recognition Letters 29 (9) (2008) 1295–1301.
- [8] M. N. Do, M. Vetterli, *The contourlet transform: An efficient directional multiresolution image representation*, IEEE Transactions on Image Processing 14 (12) (2005) 2091–2106.
- [9] Q.-G. Miao, C. Shi, P.-F. Xu, M. Yang, Y.-B. Shi, *A novel algorithm of image fusion using shearlets*, Optics Communications 284 (6) (2011) 1540–1547.
- [10] M. Nejati, S. Samavi, S. Shirani, *Multi-focus image fusion using dictionary-based sparse representation*, Information Fusion 25 (2015) 72–84.
- [11] M. Nejati, S. Samavi, N. Karimi, S. M. R. Soroushmehr, S. Shirani, I. Roosta, K. Najarian, *Surface area-based focus criterion for multi-focus image fusion*, Information Fusion 36 (2017) 284–295.
- [12] S. Bhat, D. Koundal, *Multi-focus image fusion techniques: A survey*, Artificial Intelligence Review 54 (8) (2021) 5735–5787.
- [13] S. Li, J. T. Kwok, Y. Wang, *Combination of images with diverse focuses using the spatial frequency*, Information Fusion 2 (3) (2001) 169–176.
- [14] Y. Chen, J. Guan, W.-K. Cham, *Robust Multi-Focus image fusion using Edge model and Multi-Matting*, IEEE Transactions on Image Processing 27 (3) (2018) 1526–1541.
- [15] A. N. Toprak, V. Aslantas, *Fusion of multi-focus image by blocks optimal positions*, in: E. Adalı, Ş. Sağıroğlu (Eds.), 3rd International Conference on Computer Science and Engineering (UBMK), Sarayova, 2018, pp. 471–476.
- [16] V. Aslantas, A. N. Toprak, *Multi focus image fusion by differential evolution algorithm*, in: J. Filipe, O.

- Gusikhin (Eds), 11th International Conference on Informatics in Control, Automation and Robotics (ICINCO), Vienna, 2014, pp. 312–317.
- [17] J. Kong, K. Zheng, J. Zhang, X. Feng, *Multi-focus image fusion using spatial frequency and genetic algorithm*, International Journal of Computer Science and Network Security 8 (2) (2008) 220–224.
- [18] R. Özdemir, M. Taşyürek, V. Aslantaş, *Improved Marine Predators Algorithm and Extreme Gradient Boosting (XGBoost) for shipment status time prediction*, Knowledge-Based Systems 294 (2024) 111775 20 pages.
- [19] M. Taşyürek, M. Erat, *Determining the best meter reading route using ant colony and genetic algorithm methods*, Dicle University Journal of Engineering 13 (3) (2022) 405–412.
- [20] M. Azizi, U. Aickelin, H. A. Khorshidi, M. B. Shishehgharkhaneh, *Energy valley optimizer: A novel metaheuristic algorithm for global and engineering optimization*, Scientific Reports 13 (1) (2023) Article Number 226 23 pages.
- [21] M. Eskicioglu, P. S. Fisher, *Image quality measures and their performance*, IEEE Transactions on Communications 43 (12) (1995) 2959–2965.
- [22] V. Aslantas, R. Kurban, *A comparison of criterion functions for fusion of multi-focus noisy images*, Optics Communications 282 (16) (2009) 3231–3242.
- [23] J. H. Holland, *An introductory analysis with applications to biology, control and artificial intelligence, Adaptation in Natural and Artificial System*, MIT Press, Cambridge, 1992, Ch. 1-14, 211 pages.
- [24] R. Storn, K. Price, *Differential evolution - A simple and efficient heuristic for global optimization over continuous spaces*, Journal of Global Optimization 11 (4) (1997) 341–359.
- [25] D. Karaboga, B. Basturk, *A powerful and efficient algorithm for numerical function optimization: Artificial bee colony (ABC) algorithm*, Journal of Global Optimization 39 (3) (2007) 459–471.
- [26] K. Ma, N. K. Zeng, N. Z. Wang, *Perceptual quality assessment for multi-exposure image fusion*, IEEE Transactions on Image Processing 24 (11) (2015) 3345–3356.
- [27] Y. Liu, S. Liu, Z. Wang, *A general framework for image fusion based on multi-scale transform and sparse representation*, Information Fusion 24 (2015) 147–164.
- [28] C. S. Xydeas, V. Petrovic, *Objective image fusion performance measure*, Electronics Letters 36 (4) (2000) 308 3 pages.
- [29] Y. Chen, R. S. Blum, *A new automated quality assessment algorithm for image fusion*, Image and Vision Computing 27 (10) (2009) 1421–1432.
- [30] B. Wei, X. Feng, K. Wang, B. Gao, *The Multi-Focus-Image-Fusion method based on convolutional neural network and sparse representation*, Entropy 23 (7) (2021) 827 16 pages.
- [31] V. Aslantas, E. Bendes, *A new image quality metric for image fusion: The sum of the correlations of differences*, AEÜ. International Journal of Electronics and Communications 69 (12) (2015) 1890–1896.



Multi-Band Optical Variability of Blazar 1ES 2344+514 on Diverse Time-Scales

Aykut Özdönmez¹

¹Department of Astronomy and Space Science, Faculty of Science, Atatürk University, Erzurum, Türkiye

Article Info

Received: 13 May 2024

Accepted: 29 Jul 2024

Published: 30 Sep 2024

Research Article

Abstract— This study presents the results of multi-band observations from 2022 to 2024 and Zwicky Transient Facility (ZTF) observations from 2018 to 2023, examining the flux variability of the blazar 1ES 2344+514 on diverse time-scales in the optical bands. The blazar has mild short-term variability (STV) and long-term variability (LTV), with small amplitudes of ~ 0.7 mag and 0.4 mag for the host subtracted- and included-light curves, respectively. The power-enhanced F-test and the nested Analysis of Variance (ANOVA) statistical tests of the six intra-day light curves show that the blazar has no minute-scale variability. The multiband color behavior analysis revealed a moderate redder-when-brighter (RWB) trend on intra-day time scales, while the LTV shows no detectable color behavior. We found a strong correlation between the ZTF optical light curves without any time lag, but no detectable correlations for the optical band emissions. From our periodicity searches using WWZ and LS methods, three significant quasi-periodic oscillation (QPO) signals in the ZTF light curves are found at about 1.02, 1.3, and 2.85 years. The observational results indicate that the blazar 1ES 2344+514 has a complex variability while emphasizing the need for future observations to unravel its underlying mechanisms.

Keywords — *Galaxies general, galaxies active, bl lacertae objects general, bl lacertae objects individua 1ES 2344+514*

1. Introduction

One class of Active Galactic Nuclei (AGNs) called a blazar consists of an accretion disc, a supermassive black hole at the galaxy's centre, and a relativistic jet oriented in the direction of the observer. Blazars show flux variations, strong polarisation, superluminal velocity, non-thermal emission, and high-energy gamma-ray radiation [1,2]. A double-hump structure is seen in the spectral energy distribution (SED) of the blazars. Synchrotron emission from relativistic electrons in the jet's magnetic field produces the low-energy peak, while the inverse Compton process in the MeV–TeV range produces the high-energy peak in the SED [3,4]. Blazars are divided into flat-spectrum radio quasars (FSRQs) and BL Lacertae objects (BL Lacs). Broad emission lines are seen in the optical spectrum of FSRQs, and very faint or nonexistent emission lines are seen in the optical spectrum of BL Lacs [5,6]. Analyzing intra-day variability (IDV), short-term variability (STV), and long-term variability (LTV) of blazar flux is the most common way to study its nature. While STV takes days to months and LTV lasts months to years, IDV occurs rapidly over minutes to hours (e.g. [7–9]). Many models have been used to try

¹aykut.ozdonmez@atauni.edu.tr (Corresponding Author)

to explain the variations, such as shocks-in-jet [10], gravitational microlensing [11], and variations in Doppler factor [12]. However, there is ongoing debate about many details of the model [13].

Variations in their optical color and spectral characteristics also reveal the emission mechanisms of blazars. The Bluer-When-Brighter (BWB) trend, most commonly observed in BL Lac objects, is often associated with the shock-in-jet hypothesis and variations in the Doppler factor (e.g., [14–17]). Contrarily, additional radiation out from the accretion disk or host galaxy causes the redder-when-brighter (RWB) trend, which is commonly observed in FSRQs (e.g., [18, 19]). When the color behavior is not detectable or significant, achromatic behavior is also seen in the blazars [15]. However, it is difficult to fully understand the underlying mechanisms causing these trends due to the complexity of color changes across different time-scales and observational datasets. [20–23]. The interaction between the core engine and the surrounding environment, as well as the jet structure has a significant effect on the color trend and flux variability of blazars.

In many studies, periodic or quasi-periodic flux variability ranging from minutes to decades have been detected in numerous blazars. Many models have been suggested for periodic flux variation-driven mechanisms (e.g. [24–35]). Such models include jet precession, helically moving plasma blobs or shocks within the jet, and binary supermassive black hole systems. Shorter time-scale oscillations, such as those with periodicities of minutes or days, are typically associated with the central emission region, which includes the black hole and accretion disk.

The blazar 1ES 2344+514 is highly variable and an extreme high-frequency-peaked blazar (EHBL), which has a redshift of $z = 0.044$ [36]. Since its discovery in 1995, it has had many GeV-TeV outbursts. Its radio to very high energy emissions have been studied with data from several telescopes, especially during flares [37–42]. There have also been studies of the optical variability of 1ES 2344+514. On September 20, 1996, early observations revealed a 0.08 mag BVR filter microvariability [43]. [44] recorded a 26-minute V-band IDV of 0.14 mag. Many studies have researched LTV and IDVs, but no noteworthy IDV has been found on a time-scale of hours or less [45–48]. However, [49] found a flux variation of 0.69 ± 0.16 mag over 79 min, matching the X-ray variability [50]. LTV was observed in [51], which also included 19 intra-day observations; however, no significant IDV was detected. The authors also reported that the spectral index alpha values of 1.77 and 1.61 remained consistent regardless of whether the host galaxy contribution was included or not. They concluded that the optical emission from this source is likely only affected by non-thermal radiation originating from another region in the relativistic jet. Recently, [48] observed an IDV of $\Delta R = 0.155$ mag over $\Delta T = 12.99$ minutes, indicating a link between magnetic field strength and IDV occurrence. They also reported LTV periodicities of 2.72, 1.61, and 1.05 years.

The scope of this study is to use multi-color observations from intra-day to long-term time-scales to examine the optical flux variations, correlations between various optical bands, color behavior, and periodicity of the blazar 1ES 2344+514 in order to understand its nature and structure.

2. Data

Utilising a 60 cm RC robotic telescope (T60) and a 1.0 m RC telescope (T100) at the Scientific and Technological Research Council of Türkiye (TUBITAK) National Observatory (TUG), we carried out optical observations in the BVRI bands between July 2022 and January 2024. We took a total of 1366 frames over the duration of 75 nights of data collection. Depending on the band and brightness of the source, the exposure times ranged from 20 to 180 seconds. We subtracted the bias, applied flat-fielding, and eliminated cosmic rays as part of the usual CCD reduction procedure. As reported in [52], the host galaxy contributes significantly to the total optical flux with 90%. They suggested

that the contribution of the host galaxy depends on the aperture radius during photometry, and they determined a host galaxy brightness of 14.90 mag in R-band for a 5" aperture. Thus, we used the same fixed aperture radius for photometry to account for the host contamination. From the chart provided by [53], we chose star C2 as the reference due to its proximity to the blazar's position, brightness, and color, and stars C1 and 1 were used as comparisons for the instrumental magnitude evaluation. To obtain the flux of the central region, we first corrected the magnitudes of the Galactic extinction using the A_λ values obtained from the NASA/IPAC Extragalactic. Then, we converted the R-magnitude to flux density as given in [54]. Thus, we subtracted the contribution of the host galaxy and obtained the source flux density based on the aperture radii and brightness given in [52]. Finally, we determined the flux and magnitude in the R-band, either with the host flux subtracted or included. The R-band flux of the host galaxy is also used to determine the corresponding contribution in the B, V, and I bands for the given galaxy colors [55].

In addition to our observational data, we collected Zwicky Transient Facility (ZTF) light curve data between May 2018 and October 2023 in the gr-bands from the ZTF. To maintain the ZTF light curve's quality, we selected 1333 ZTF data points with catflags = 0 and $\chi < 4$. It should be noted that since both the galaxy colors in the ZTF bands and used aperture size are not known, the host subtraction is not applied for ZTF fluxes.

3. Flux Variability

Studying the flux variability of blazars at different wavelengths and time-scales, from the shortest to the longest, is crucial to understand the nature of the emission regions and the underlying radiative processes. Our observations of the blazar 1ES 2344+514 allowed us to study the flux and color variability on diverse time-scales, as well as the role of the host galaxy in these phenomena. Figure 1 shows the corresponding intra-day light curves of the multi-band (BVRI) data obtained from all six nights with at least one hour of observations.

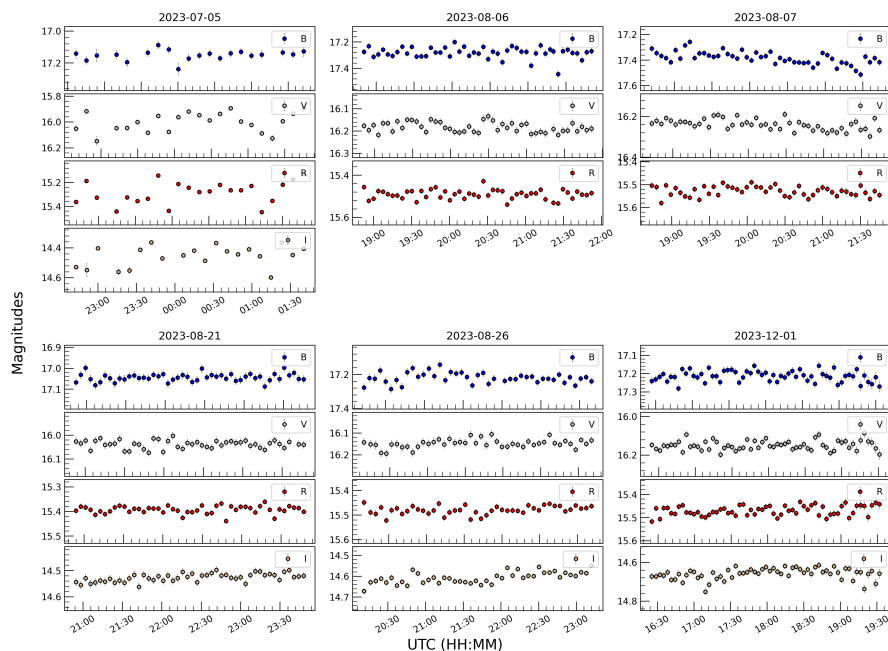


Figure 1. Intra-day light curves of blazar 1ES 2344+514 in the optical *BVRI* bands. For better visualization, the blue, green, gray and dark red circles represent the B-, V-, R- and I-band magnitudes, respectively, with a labeled offset. The dates of the observations are given at the top of each plot

To detect variability in the optical BVRI bands of the blazar 1ES 2344+514, two common statistical tests were used [9, 56–59]: the power-enhanced F-test and the nested analyzes of variance (ANOVA) test. The power-enhanced F-test compares the variance of the blazar’s light curve to the total variance of comparison stars using the formula $F_{enh} = \frac{s_{bl}^2}{s_c^2}$ [60]. s_{bl}^2 represents the blazar’s differential variance, and s_c^2 represents the total variance of the comparison stars. The formulas for the degrees of freedom (DOF) are $u_{bl} = N - 1$ and $u_c = k(N - 1)$. For the variability hypothesis to be valid, the F_{enh} is expected to be equal to or greater than the critical value ($F_{critical}$), which is calculated at a 99% confidence level ($\alpha = 0.01$). In our study, we calculated the F_{enh} values by analyzing the differential light curves from all ten comparison stars and the reference star (field star C2 from the mentioned chart). We then compared these values with the crucial value (F_c) for each ID lightcurve. Nested ANOVA, a modified version of ANOVA, is used to assess mean group variations in the blazar’s differential light curves by employing multiple reference stars. Using nested ANOVA has the advantage of not relying on a specific comparison star, allowing any available field stars to serve as reference stars for the study. In our investigation, we constructed differential light curves (LCs) for the blazar using eleven standard stars (including star C2). We created five data points per group from these differential LCs. The mean square of the groups (MS_G) and the nested observations within the groups (MS_{O_G}) were computed using the methods described in [61] and [56] as well. The resulting ratio, $F = MS_G/MS_{O_G}$, has $a(b - 1)$ and $(a - 1)$ degrees of freedom in the denominator and numerator, respectively, and is distributed according to a F distribution. Hypothesis tests on the variability of Blazar’s light curve were validity tested at a significance level of $\alpha = 0.01$. Table 1 presents the results of the nested ANOVA tests and the F_{enh} -tests. If the F -statistic in both tests is equal or greater than the critical value (F_c), the ID light curve is considered variable (V); otherwise, it is considered non-variable (NV). The six intra-day LCs showed no significant variability on minute-time scales. Although the standard deviation and mean error of our ID data are both less than 0.03 mag, we could not detect any significant IDV in the LCs similar to the $\Delta R = 0.155$ mag detected by [48], except for a few scatter points. It should be considered that the probability of detecting IDV increases with observational time. [62] found that blazars are variable on intra-day time-scales for $\sim 60 - 65\%$ when observed for < 6 hours and $\sim 80 - 85\%$ when observed for more than 8 hours. However, the observational data in our light curve spans one to three hours. Given this discrepancy in observation time, it is possible that any potential variability in the ID LCs of the blazar may not have been fully captured.

Table 1. The test results of IDV of the blazar 1ES 2344+51.4

Obs. date yyyy-mm-dd	Band	Average Magnitude	t_{obs} hours	Power-enhanced F-test			Nested ANOVA test			Status	Variability Amplitude (%)
				DOF(ν_1, ν_2)	F_{enh}	F_c	DOF(ν_1, ν_2)	F	F_c		
2023-07-05	B	16.38	3.10	(19, 190)	0.08	2.00	(3, 16)	0.05	5.29	NV	6.51
	V	15.32	3.10	(21, 210)	0.02	1.94	(3, 16)	1.68	5.29	NV	13.30
	R	14.61	3.10	(21, 210)	0.06	1.94	(3, 16)	0.99	5.29	NV	17.21
	I	13.83	2.96	(19, 190)	0.30	2.00	(3, 16)	0.91	5.29	NV	12.89
2023-08-06	B	16.45	3.00	(48, 480)	0.56	1.58	(8, 36)	0.48	3.05	NV	10.62
	V	15.42	3.00	(47, 470)	0.69	1.59	(8, 36)	2.70	3.05	NV	3.66
	R	14.72	3.00	(47, 470)	0.93	1.59	(8, 36)	2.56	3.05	NV	5.23
2023-08-07	B	16.49	3.02	(48, 480)	1.24	1.58	(8, 36)	5.33	3.05	NV	10.88
	V	15.45	3.02	(48, 480)	0.55	1.58	(8, 36)	3.49	3.05	NV	4.81
	R	14.74	3.02	(48, 480)	0.63	1.58	(8, 36)	1.31	3.05	NV	4.06
2023-08-21	B	16.33	2.89	(47, 470)	0.57	1.59	(8, 36)	0.71	3.05	NV	3.98
	V	15.35	2.89	(46, 460)	1.02	1.59	(8, 36)	1.71	3.05	NV	3.23
	R	14.67	2.89	(47, 470)	1.12	1.59	(8, 36)	0.97	3.05	NV	3.76
	I	13.87	2.89	(47, 470)	0.39	1.59	(8, 36)	4.11	3.05	NV	3.07
2023-08-26	B	16.42	2.93	(41, 410)	0.80	1.63	(7, 32)	0.98	3.26	NV	6.29
	V	15.40	3.02	(43, 430)	0.74	1.62	(7, 32)	2.05	3.26	NV	3.89
	R	14.71	3.02	(43, 430)	0.85	1.62	(7, 32)	2.72	3.26	NV	3.29
2023-12-01	I	13.91	3.02	(43, 430)	0.51	1.62	(7, 32)	30.67	3.26	NV	6.26
	B	16.41	3.10	(60, 600)	0.89	1.51	(11, 48)	1.49	2.64	NV	5.32
	V	15.40	3.11	(60, 600)	1.06	1.51	(11, 48)	0.90	2.64	NV	5.18
	R	14.71	3.11	(60, 600)	0.96	1.51	(11, 48)	1.32	2.64	NV	3.86
	I	13.94	3.11	(60, 600)	1.02	1.51	(11, 48)	1.79	2.64	NV	6.63

Figure 2 displays the long-term optical light curves for the ZTF gr- and BVRI-bands, based on all observational data. The analyzes for BVRI data was performed with and without host subtraction, while the analyzes for ZTF data was done only for fluxes with host galaxy light. Table 2 provides a summary of the LTV light curves, including the minimum, maximum, and mean magnitudes. In addition, we estimated the variability amplitude (A) as given by [63], in which it is defined to quantify the actual variation in a light curve after correcting for the observational errors. The formula for the variability amplitude (A) is $A = 100 \times \sqrt{(A_{\max} - A_{\min})^2 - 2\sigma^2} \%$. Here, A_{\max} represents the maximum magnitude, A_{\min} represents the minimum magnitude of the LTV light curve, and σ denotes the average error.

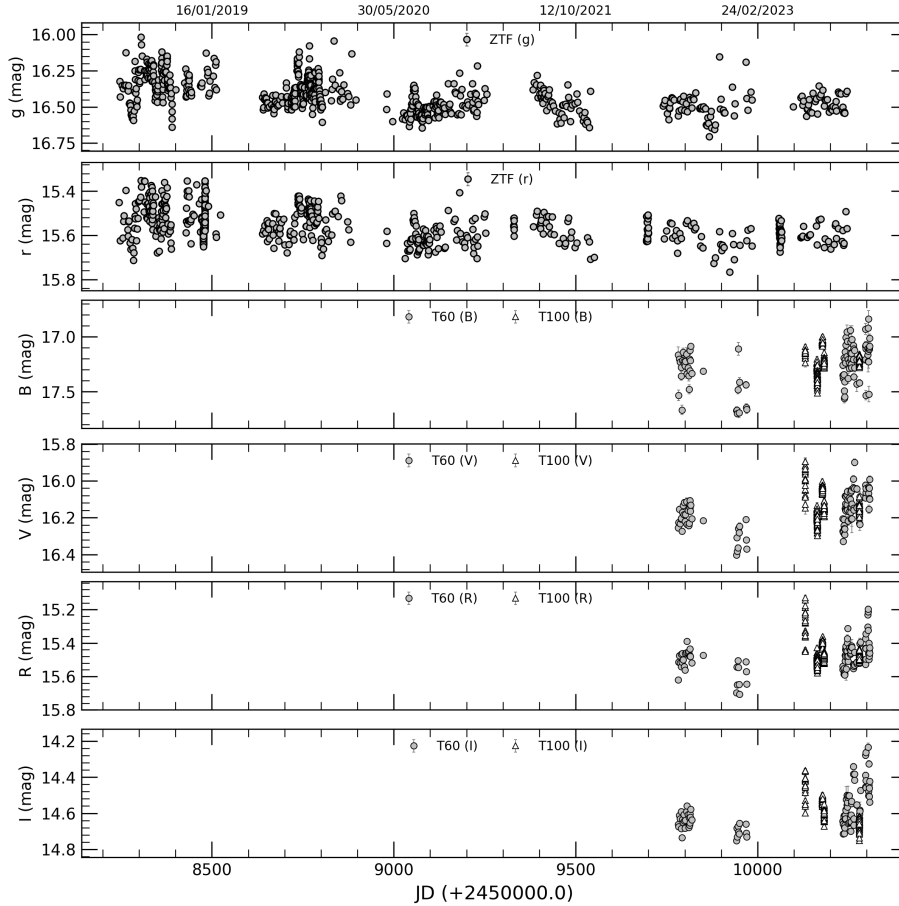


Figure 2. Long-term light curves of the blazar 1ES 2344+51.4 in the optical ZTF gri bands and BVRI bands. The BVRI light curves are the host-subtracted but ZTF light curves includes host contribution

Table 2. Results of the LTV analyzes of the blazar. Lower given values for BVRI bands includes host galaxy light

Band	Brightest magnitude/MJD	Faintest magnitude/MJD	Average magnitude	Variability amplitude (%)
B	$16.836 \pm 0.073 / 60305.24014$	$17.699 \pm 0.033 / 59944.20939$	17.232 ± 0.026	86.252
	16.216 ± 0.073	16.619 ± 0.033	16.420 ± 0.026	40.108
V	$15.894 \pm 0.014 / 60131.53178$	$16.403 \pm 0.015 / 59942.21587$	16.147 ± 0.016	50.843
	15.266 ± 0.014	15.522 ± 0.015	15.400 ± 0.016	25.477
R	$15.128 \pm 0.016 / 60131.57453$	$15.707 \pm 0.013 / 59950.19463$	15.463 ± 0.012	57.815
	14.525 ± 0.016	14.818 ± 0.013	14.703 ± 0.012	29.305
I	$14.235 \pm 0.024 / 60303.27906$	$14.752 \pm 0.015 / 60280.21487$	14.585 ± 0.014	51.582
	13.698 ± 0.024	13.983 ± 0.015	13.897 ± 0.014	28.414
zg	$16.018 \pm 0.014 / 58304.9748$	$16.703 \pm 0.016 / 59866.72145$	16.415 ± 0.015	68.564
zr	$15.351 \pm 0.011 / 58304.90155$	$15.767 \pm 0.011 / 59922.78525$	15.555 ± 0.011	41.608

The long-term light curve exhibits varying behavior, with amplitudes ranging from 25% to 70% depending on the band. Host subtraction increases the variability amplitude by about a factor of two. The variability in brightness can vary by up to 0.4 mag within a few days, or even within a single day, for light curves. During our observations, the brightest magnitude was measured to be $R = 14.525$ mag, while the faintest brightness was $R = 14.818$ mag. Meanwhile, the mean R-band magnitude was 14.703 ± 0.012 mag, with a calculated variability amplitude of 29%. The ZTF observations show the brightest magnitude at $r = 15.351$ and the faintest at $r = 15.767$ mag, resulting in a mean magnitude of 16.415 and a variability amplitude of 42%. Throughout both observations, no flare was detected.

3.1. The Multiband Color Behavior and the Correlation Analyzes

Blazars show rapid variations in both flux and spectral characteristics, which are caused by the combination of thermal emission from the accretion disc and non-thermal synchrotron radiation from the relativistic jet. Given that the color variability of blazars mirrors their spectral variations, we conducted a comprehensive analyzes of the correlations between magnitudes and colors through intra-day and long-term time-scales. For the intra-day time-scales, we focused on the $B - R$ and $V - R$ indices with respect to the R magnitude. The color-magnitude plots are shown in Figure 3, and the results of the linear regressions are listed in Table 3. We identified moderate correlations ($r < -0.6$ and $p < 0.05$) for both the $B - R$ and $V - R$ color indices, regardless of the presence of host contributions. The negative slope indicates RWB trend.

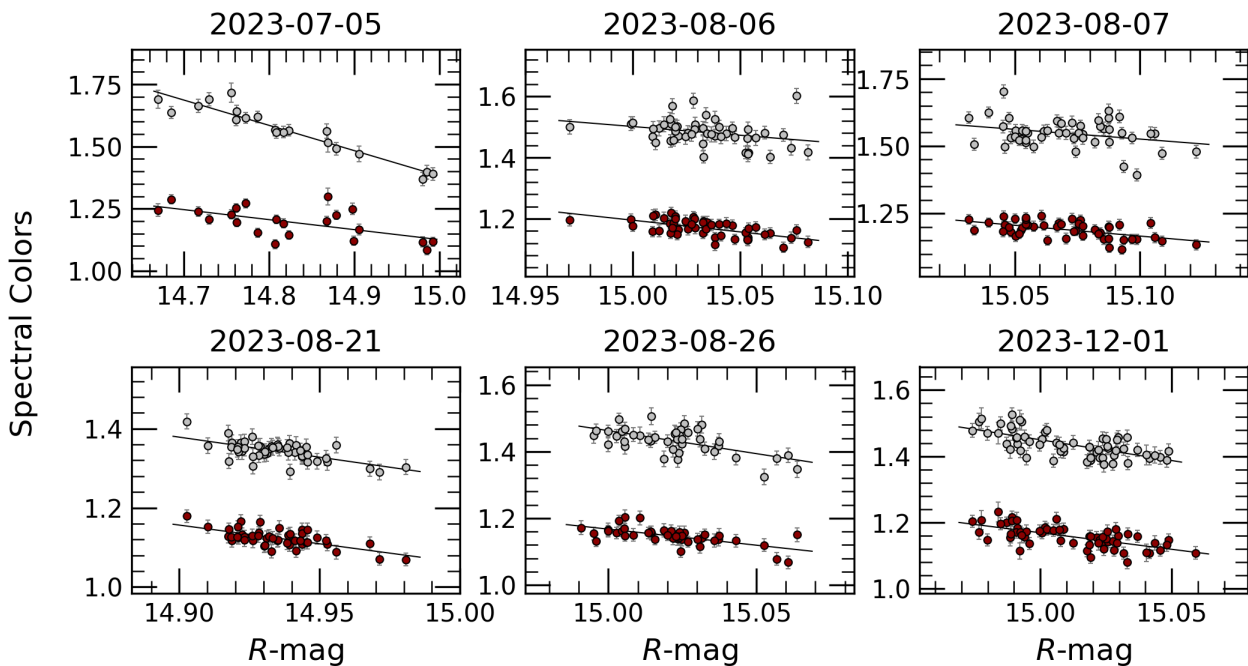


Figure 3. The intra-day color–magnitude plots of the blazar 1ES 2344+51.4 obtained from host-subtracted fluxes. The date are presented above each plot. The silver and dark red dots represent $B - R$ and $V - R$ color indices. Black lines represent linear fits. For better representation, the offset value of 0.6 are added to $V - R$ colors

Table 3. Correlation between the color indices and R-band magnitude for multiband IDV data

Date	color	slope	r	p
2023-07-05	$B - R$	-1.02 ± 0.08	-0.95	1.22e-10
	$V - R$	-0.40 ± 0.12	-0.60	2.85e-03
	* $B - R$	-1.01 ± 0.07	-0.96	3.08e-11
	* $V - R$	-0.40 ± 0.12	-0.61	2.69e-03
2023-08-06	$B - R$	-0.57 ± 0.27	-0.30	4.16e-02
	$V - R$	-0.76 ± 0.14	-0.62	3.17e-06
	* $B - R$	-0.60 ± 0.25	-0.33	2.13e-02
	* $V - R$	-0.76 ± 0.15	-0.61	4.17e-06
2023-08-07	$B - R$	-0.72 ± 0.34	-0.30	3.94e-02
	$V - R$	-0.80 ± 0.18	-0.55	4.92e-05
	* $B - R$	-0.75 ± 0.31	-0.33	2.03e-02
	* $V - R$	-0.80 ± 0.18	-0.55	5.01e-05
2023-08-21	$B - R$	-1.01 ± 0.18	-0.64	1.10e-06
	$V - R$	-0.94 ± 0.16	-0.66	4.96e-07
	* $B - R$	-1.01 ± 0.18	-0.63	1.42e-06
	* $V - R$	-0.94 ± 0.17	-0.65	9.31e-07
2023-08-26	$B - R$	-1.37 ± 0.29	-0.61	2.09e-05
	$V - R$	-0.96 ± 0.17	-0.65	1.94e-06
	* $B - R$	-1.37 ± 0.28	-0.62	1.46e-05
	* $V - R$	-0.96 ± 0.18	-0.64	2.82e-06
2023-12-01	$B - R$	-1.25 ± 0.18	-0.67	5.42e-09
	$V - R$	-1.00 ± 0.15	-0.65	1.43e-08
	* $B - R$	-1.24 ± 0.18	-0.68	2.57e-09
	* $V - R$	-1.00 ± 0.15	-0.64	2.24e-08

* The results are obtained from for the colors including host contribution

For the long-term multiband data from ZTF and our observations, the color magnitude plots are shown in Figure 4. We observed very weak correlations for all color indices, with a correlation coefficient of $|r| < 0.3$, and the slope errors are similar to the slope values (Table 4). Thus, the color relation for LTV is not significant; i.e. achromatic trend.

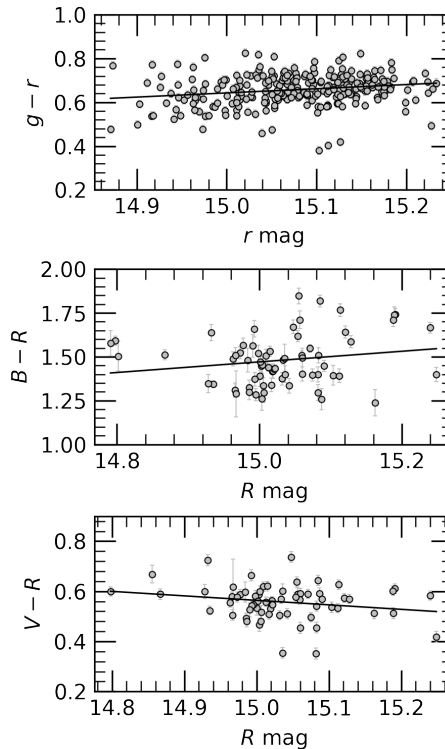


Figure 4. The color-magnitude diagram of the blazar 1ES 2344+51.4 on long-term time-scale obtained from ZTF gr-band magnitudes which includes host light and from host subtracted BVR magnitudes Black lines represent the linear fits

Table 4. The results of the linear regression between the colors and the corresponding magnitude on the long-term time-scales

Model	slope	intercept	r-value	p-value
R vs $B - R$	$+0.303 \pm +0.201$	-3.070 ± 3.024	+0.183	1.373e-01
R vs $V - R$	$-0.179 \pm +0.104$	$+3.255 \pm 1.563$	-0.211	8.927e-02
* r vs $g - r$	0.191 ± 0.055	-2.221 ± 0.834	0.206	6.43e-04
* R vs $B - R$	$+0.163 \pm 0.184$	-0.916 ± 2.623	+0.110	3.774e-01
* R vs $V - R$	-0.176 ± 0.106	$+3.086 \pm 1.510$	-0.204	1.011e-01

* The results are obtained from for the fluxes including host contribution

Understanding the correlations between different spectral bands is critical because any identified time lag implies spatial differences between the corresponding emission regions. Thus, we used the Discrete Correlation Function (DCF), which is an effective statistical tool for investigating unevenly distributed time series of multiband light curves ([64] and references therein). The calculation of the DCF involves using the unbinned DCF (UDCF), which is expressed as:

$$UDCF_{ij}(\tau) = \frac{(a_i - \bar{a})(b_j - \bar{b})}{\sqrt{(\sigma_{a^2} - e_{a^2})(\sigma_{b^2} - e_{b^2})}} \tag{3.1}$$

Here, \bar{a} and \bar{b} are the mean values of the respective time-series datasets, while $\sigma_{a,b}$ and $e_{a,b}$ are their standard deviations and errors. The time delay between two data points is denoted by $\Delta t_{ij} = (t_{bj} - t_{ai})$. The DCF is then found by taking the average of the UDCF values over the interval $\tau - \frac{\Delta\tau}{2} \leq \tau_{ij} \leq \tau + \frac{\Delta\tau}{2}$ as given in [65]:

$$DCF(\tau) = \frac{\sum_{k=1}^m UDCF_k}{M} \tag{3.2}$$

Here, "M" denotes the number of pairwise time lag values within the specified τ interval.

In the examination of the long-term light curves, weighted mean magnitudes and mean Julian dates (JD) were computed from nightly binned observations. The DCF analyzes (see Figure 5) were applied to each pair combination of the nightly binned ZTF *gri* and optical *VRI* long-term light curves using a time binning value of 10 days. We found a strong correlation between the g- and r-band LCs, but this correlation is not significant for the other multi-band pairs. For all pairs, the maximum DCF values were found to be at $\tau = 0$ days, which implies that the optical emission regions are likely co-spatial.

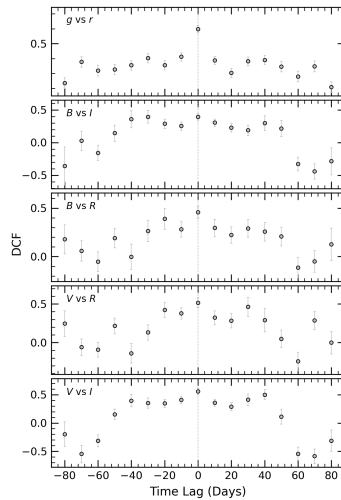


Figure 5. Cross-correlation analyzes for the ZTF *gri* and optical *BVRI* bands using Discrete Correlation Function for the entire monitoring period

3.1.1. Optical Quasi-Periodic Oscillations

In order to identify any underlying periodicity or optical quasi-periodic oscillation (QPO) of flux variability on long-term time-scales, we used the ZTF light curves of 1ES 2344+514, which consist of longer and continuous observational data. We employed two widely recognised methods: the Lomb-Scargle (LS) periodogram [66, 67], and the Weighted Wavelet Z-transform (WWZ; [68]). The LS periodogram is a Fourier transform method used to detect periodic patterns in time series data by integrating sinusoidal components based on likelihood minimisation. Utilising the Python Astropy package, the LS periodogram provided a detailed analysis of quasi-periodic signals within the corresponding time series. The WWZ method represents an enhanced version of the wavelet transform, designed to detect periodic or quasi-periodic signals in unevenly sampled time series data and evaluate their consistency over the observation period. The signal is simultaneously decomposed into both the frequency and time domains, and this method employs wavelet functions to model the observation rather than sinusoidal components. We performed a thorough WWZ analysis of the light curves over the entire observation period. Accurately estimating the significance of potential detections is crucial to avoid misinterpreting noise-induced peaks as periodic signals in the power spectrum. To ensure robust analysis, we generated 10,000 simulated light curves reflecting the power spectral density of the blazar light curve, following the methodology outlined in [69]. By performing identical period analysis using WWZ and LS on the simulated light curves, as was done on the Blazar light curve, we obtained significance levels of 99% and 99.9% of red noise for each frequency.

The resulting plots of the WWZ and LS analysis for the ZTF *r*-band light curve are shown in Figure 6, including the WWZ power map corresponding to the periodicity and time, the periodogram of the time-averaged WWZ power, and the LS periodogram. The WWZ analysis revealed two significant signals at a periodicity of 373^{+89}_{-74} and 1041^{+351}_{-127} days in the WWZ periodogram, spanning the entire observation time in the WWZ power map and exceeding the significant level at 99%, almost at 99.9%. The LS periodogram also exhibited two similar peak signals at 479^{+173}_{-74} days and 1065^{+258}_{-193} days. First peak surpasses the significance level at 99%, but significance of the second peak is at about 98%. Notably, similar results were obtained for the ZTF *g*-band light curve. We also checked the periodicity for our BVRI light curves only, but found no significant signal for the STV periodicity.

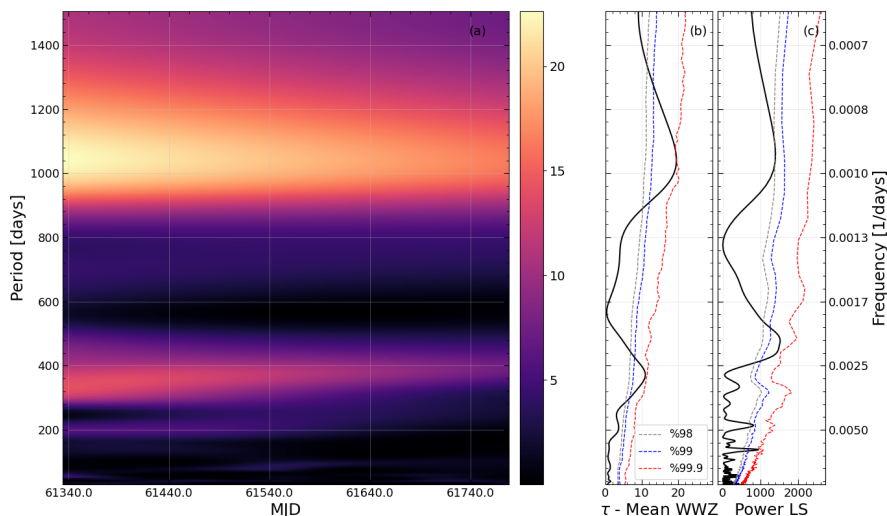


Figure 6. (a) 2D plane contour plot of the WWZ power over time and frequency domain, (b) Time averaged WWZ power periodogram, and (c) the Lomb-Scargle periodogram of the combined ZTF *r* band light curve. Dotted brown and red lines represent the significance level of 98, 99 and 99.9 percent, respectively

4. Conclusion

This study presents the results of our multi-band observations from 2022 to 2024 and ZTF observations from 2018 to 2023, examining the flux variability of the blazar 1ES 2344+514 on diverse time-scales in optical bands. The blazar 1ES 2344+514 has mild STV and LTV, with a small amplitude of ~ 0.7 mag and 0.4 mag for host subtracted- and included-light curves, respectively. During whole observation period, no flare was recorded. For a 10-day time binning with the optical datasets in this study, the obtained correlation between ZTF LCs suggests that the optical emission region is likely to be co-spatial or that any spatial differences are too small to detect. Statistical analyzes on the six multi-band ID light curves show that the blazar has no minute-scale variability. Moreover, the IDV has been reported only for a few nights in the literature, as well. The detected IDV fraction for this blazar is significantly less than that of typical BL Lac objects [70–72]. As a point source, a substantial emission from the host galaxy is known to dilute the underlying IDV [48]. Even though the host galaxy contribution is subtracted from the total flux, we didn't detect IDV. The absence of IDV in a blazar can be attributed to the presence of a powerful magnetic field that prevents or delays the occurrence of instability. This instability is likely responsible for the significant change in the jet's morphology, which could explain the observed rapid variability [73]. This explanation is plausible for Blazar 1ES 2344+514 because to its magnetic field strength beyond the crucial value, as reported by [48]. It is worth noting that 1ES 2344 + 514 is classified as a HBL source, but low-energy-peaked blazars are more likely to exhibit IDV than HBLs [70, 72].

The multiband color behavior analyzes indicated that a typically moderate and detectable RWB trend for intra-day time-scales exists, but no detectable color behavior is found for the LTV. The RWB trend is more commonly detected in FSRQs and is thought to be caused by additional contributions from the accretion disc or other emission regions (e.g. [18]). The color trend of the blazars is determined by several parameters, including the synchrotron peak frequency, the width of optical wavelengths, and the intensity of thermal blue emission compared to jet emission. We know that the host galaxy mostly contaminates thermal emissions [16]. Therefore, an RWB trend and color saturation can be observed in the blazar when the jet and other emission regions, such as the host galaxy and the accretion disc, contribute varying amounts of thermal emission over time. Variations in the Doppler factor are commonly used to explain achromatic behavior. The geometric scenarios provide the most plausible explanation for these differences.

Blazars frequently exhibit periodic variation in their light curves, such in case of 1ES 2344+514. Our results suggest three significant QPO signals in ZTF light curves at around 1.02, 1.3, and 2.85 years. These signals are very similar with the reported periodicities of 1.05, 1.61, and 2.72 years by [48], in which binary black hole system is considered for the explanation of these periodicities. In case of blazars, it is proposed that the most likely reasons for the year-scale periodicity are binary black hole in the central region, and helical-jet structure. The presence of closely orbiting binary black holes or warped accretion discs can cause the jet precession phenomenon when a blazar is involved in a binary SMBH system (e.g. [74–76]). Depending on the angle of the jet axis to the observer's line of sight and the jet's Lorentz factor, this mechanism is likely to produce QPOs at year-like time-scales, as found in this study. On the other hand, helical structures are common in blazars [77, 78]. The Doppler boosting effect due to helical or non-ballistic motions of relativistic blobs or shocks within blazar jets could be responsible for the QPO in blazar LCs (e.g. [79, 80]). The simplest leptonic one-zone model suggests that the viewing angle of the blob with respect to the line of sight (ϕ_{obs}) changes periodically with time due to the postulated helical motion of the blob, and the Doppler factor (δ) varies with viewing angle as $\delta = 1/[\Gamma(1 - \beta \cos \theta(t))]$. Here, $\Gamma = 1/\sqrt{1 - \beta^2}$ is the bulk Lorentz factor of the blob

motion with $\beta = v_{jet}/c$. Given this scenario, the periodicity in the rest frame of the blob is given by $P_{rf} = P_{obs}/(1 - \beta \cos \psi \cos \phi)$. For typical values of the pitch angle of the helical path $\phi = 2^\circ$, the angle of the jet axis with respect to the line of sight $\psi = 2^\circ$, and Doppler factor $\Gamma = 10$, the periodicities in the rest frame of the blob are calculated as $\sim 164, 209$, and 458 years for the observed periodicities (see for methodology [81–83]). During these rest frame periodicities, the blob traverses distances as $D = c\beta P_{rf} \cos \phi \simeq 50, 64$, and 139 pc, respectively. It is physically more plausible that the jet has a significantly lower curvature, which explains these length scales and is consistent with the observed periodogram (see for discussion [84]).

To improve our understanding of the complex variability of the blazar 1ES 2344+514, simultaneous multi-wavelength observations as well as the determination of host contamination over time, complemented by theoretical modelling on the underlying mechanisms of blazar variability, are needed.

Author Contributions

The author read and approved the final version of the paper.

Conflicts of Interest

The author declares no conflict of interest.

Ethical Review and Approval

No approval from the Board of Ethics is required.

Acknowledgement

This study was supported by Scientific and Technological Research Council of Turkey (TUBITAK) under the Grant Number 121F427. The authors thank to TUBITAK for their supports. We thank the team of TUBITAK National Observatory (TUG) for a partial support in using the T60 and T100 telescopes with project numbers: 22AT60-1907 and 23AT100-2006.

References

- [1] C. M. Urry, P. Padovani, *Unified schemes for radio-loud active galactic nuclei*, Publications of the Astronomical Society of the Pacific 107 (1995) 803.
- [2] J. H. Woo, C. M. Urry, *Active galactic nucleus black hole masses and bolometric luminosities*, Astrophysical Journal 579 (2) (2002) 530–544.
- [3] A. A. Abdo, M. Ackermann, I. Agudo, M. Ajello, H. D. Aller, M. F. Aller, E. Angelakis, A. A. Arkharov, M. Axelsson, U. Bach, L. Baldini, J. Ballet, G. Barbiellini, D. Bastieri, B. M. Baughman, K. Bechtol, R. Bellazzini, E. Benitez, A. Berdyugin, B. Berenji, R. D. Blandford, E. D. Bloom, M. Boettcher, E. Bonamente, A. W. Borgland, J. Bregeon, A. Brez, M. Brigida, P. Bruel, T. H. Burnett, D. Burrows, S. Buson, G. A. Caliandro, L. Calzoletti, R. A. Cameron, M. Capalbi, P. A. Caraveo, D. Carosati, J. M. Casandjian, E. Cavazzuti, C. Cecchi, O. Çelik, E. Charles, S. Chaty, A. Chekhtman, W. P. Chen, J. Chiang, G. Chincarini, S. Ciprini, R. Claus, ..., M. Ziegler, *The spectral energy distribution of fermi bright blazars*, Astrophysical Journal 716 (1) (2010) 30–70.
- [4] M. Sikora, L. Stawarz, R. Moderski, K. Nalewajko, G. M. Madejski, *Constraining emission models of luminous blazar sources*, Astrophysical Journal 704 (1) (2009) 38–50.

- [5] M. J. M. Marcha, I. W. A. Browne, C. D. Impey, P. S. Smith, *Optical spectroscopy and polarization of a new sample of optically bright flat radio spectrum sources*, Monthly Notices of the Royal Astronomical Society 281 (2) (1996) 425–448.
- [6] V. Beckmann, C. R. Shrader, Active galactic nuclei, Wiley-VCH, 2012, Ch. 6, pp. 209–231.
- [7] G. Z. Xie, S. B. Zhou, K. H. Li, H. Dai, L. E. Chen, L. Ma, *CCD photometric studies of rapid variability in eight blazars*, Monthly Notices of the Royal Astronomical Society 348 (3) (2004) 831–845.
- [8] A. C. Gupta, J. H. Fan, J. M. Bai, S. J. Wagner, *Optical intra-day variability in blazars*, The Astronomical Journal 135 (4) (2008) 1384–1394.
- [9] A. Agarwal, A. Pandey, A. Özdönmez, E. Ege, A. Kumar Das, V. Karakulak, *Characterizing the optical nature of the blazar S5 1803+784 during Its 2020 flare*, Astrophysical Journal 933 (1) (2022) 42.
- [10] A. P. Marscher, J. P. Travis, *Synchrotron self-Compton interpretation of multiwaveband observations of gamma-ray bright blazars*, Astronomy and Astrophysics Supplement 120 (1996) 537–540.
- [11] P. Schneider, A. Weiss, *A gravitational lens origin for AGN-variability ? Consequences of microlensing*, Astronomy and Astrophysics 171 (1987) 49–65.
- [12] C. M. Raiteri, M. Villata, J. A. Acosta-Pulido, I. Agudo, A. A. Arkharov, R. Bachev, G. V. Baida, E. Benítez, G. A. Borman, W. Boschin, V. Bozhilov, M. S. Butuzova, P. Calcidese, M. I. Carnerero, D. Carosati, C. Casadio, N. Castro-Segura, W. Chen, G. Damljanić, F. D’Ammando, A. Di Paola, J. Echevarría, N. V. Efimova, S. A. Ehgamberdiev, C. Espinosa, A. Fuentes, A. Giunta, J. L. G. Gómez, T. S. G. Grishina, M. A., D. Hiriart, H. Jermak, B. Jordan, S. G. Jorstad, M. Joshi, E. N. Kopatskaya, K. Kuratov, O. M. Kurtanidze, S. O. Kurtanidze, A. Lähteenmäki, V. M. Larionov, E. G. Larionova, L. V. Larionova, C. Lázaro, C. S. Lin, M. P. Malmrose, A. P. Marscher, K. Matsumoto, B. McBreen, R. Michel, ..., A. A. V. O. Vasilyev, *Blazar spectral variability as explained by a twisted inhomogeneous jet*, Nature 552 (7685) (2017) 374–377.
- [13] G. Bhatta, *Characterizing long-term optical variability properties of γ -ray-bright blazars*, Astrophysical Journal 923 (1) (2021) 19 pages.
- [14] G. Ghisellini, M. Villata, C. M. Raiteri, S. Bosio, G. de Francesco, G. Latini, M. Maesano, E. Massaro, F. Montagni, R. Nesci, G. Tosti, M. Fiorucci, E. Pian, L. Maraschi, A. Treves, C. A., M. Mignoli, *Optical-IUE observations of the gamma-ray loud BL Lacertae object S5 0716+714: data and interpretation*, Astronomy and Astrophysics 327 (1997) 61–71.
- [15] M. Villata, C. M. Raiteri, O. M. Kurtanidze, M. G. Nikolashvili, M. A. Ibrahimov, I. E. Papadakis, K. Tsinganos, K. Sadakane, N. Okada, L. O. Takalo, A. Sillanpää, G. Tosti, S. Ciprini, A. Frasca, E. Marilli, R. M. Robb, J. C. Noble, S. G. Jorstad, V. A. Hagen-Thorn, V. M. Larionov, R. Nesci, M. Maesano, R. D. Schwartz, J. Basler, P. W. Gorham, H. Iwamatsu, T. Kato, C. Pullen, E. Benítez, J. A. de Diego, M. Moilanen, A. Oksanen, D. Rodriguez, A. C. Sadun, M. Kelly, M. T. Carini, H. R. Miller, S. Catalano, D. Dultzin Hacyan, J. H. Fan, R. Ishioka, H. Karttunen, P. Keinänen, N. A. Kudryavtseva, M. Lainela, L. Lanteri, E. G. Larionova, K. Matsumoto, J. R. Mattox, F. Montagni, ..., M. G. Sobrito Uemura, *The WEBT BL Lacertae campaign 2000*, Astronomy and Astrophysics 390 (2002) 407–421.
- [16] B. Rani, A. C. Gupta, A. Strigachev, R. Bachev, P. J. Wiita, E. Semkov, E. Ovcharov, B. Mihov, S. Boeva, S. Peneva, B. Spassov, S. Tsvetkova, K. Stoyanov, A. Valcheva, *Short-term flux and*

- colour variations in low-energy peaked blazars*, Monthly Notices of the Royal Astronomical Society 404 (4) (2010) 1992–2017.
- [17] A. Agarwal, S. A. Cellone, I. Andruchow, L. Mammana, M. Singh, G. C. Anupama, B. Mihov, A. Raj, L. Slavcheva-Mihova, A. Özdönmez, E. Ege, *Multiband optical variability of 3C 279 on diverse time-scales*, Monthly Notices of the Royal Astronomical Society 488 (3) (2019) 4093–4105.
- [18] M. Villata, C. M. Raiteri, T. J. Balonek, M. F. Aller, S. G. Jorstad, O. M. Kurtanidze, F. Nicastro, K. Nilsson, H. D. Aller, A. Arai, A. Arkharov, U. Bach, E. Benítez, A. Berdyugin, C. S. Buemi, M. Böttcher, D. Carosati, R. C. Casas, A., W. P. Chen, P. Chiang, Y. Chou, S. Ciprini, J. M. Coloma, G. Di Rico, C. Díaz, N. V. Efimova, C. Forsyth, A. Frasca, L. Fuhrmann, B. Gadway, S. Gupta, V. A. Hagen Thorn, J. Harvey, J. Heidt, H. Hernandez Toledo, F. Hroch, C. P. Hu, R. Hudec, M. A. Ibrahimov, A. Imada, M. Kamata, T. Kato, M. Katsuura, T. Konstantinova, E. Kopatskaya, D. Kotaka, Y. Y. Kovalev, Y. A. Kovalev, T. P. Krichbaum, ..., S. Voss, B. Wortel, *The unprecedented optical outburst of the quasar ASTROBJ 3C 454.3 ASTROBJ. The WEBT campaign of 2004-2005*, Astronomy and Astrophysics 453 (3) (2006) 817–822.
- [19] M. F. Gu, Y. L. Ai, *The optical variability of flat-spectrum radio quasars in the SDSS stripe 82 region*, Astronomy and Astrophysics 528 (A95) (2011) 8 pages.
- [20] A. C. Gupta, A. Agarwal, J. Bhagwan, A. Strigachev, R. Bachev, E. Semkov, H. Gaur, G. Damljanovic, O. Vince, P. J. Wiita, *Multiband optical variability of three tev blazars on diverse time-scales*, Monthly Notices of the Royal Astronomical Society 458 (1) (2016) 1127–1137.
- [21] J. C. Isler, C. M. Urry, P. Coppi, C. Bailyn, M. Brady, E. MacPherson, M. Buxton, I. Hasan, *A consolidated framework of the color variability in blazars: Long-term optical near-infrared observations of 3C 279*, Astrophysical Journal 844 (107) (2017) 8 pages.
- [22] A. Agarwal, B. Mihov, I. Andruchow, S. A. Cellone, G. C. Anupama, V. Agrawal, S. Zola, L. Slavcheva-Mihova, A. Özdönmez, E. Ege, A. Raj, L. Mammana, L. Zibecchi, E. Fernández-Lajús, *Multi-band behaviour of the tev blazar PG 1553+113 in optical range on diverse timescales. Flux and spectral variations*, Astronomy and Astrophysics 645 (2021) A137.
- [23] V. Negi, R. Joshi, K. Chand, H. Chand, P. Wiita, L. C. Ho, R. S. Singh, *Optical flux and colour variability of blazars in the ZTF survey*, Monthly Notices of the Royal Astronomical Society 510 (2) (2022) 1791–1800.
- [24] A. Sillanpaa, S. Haarala, M. J. Valtonen, B. Sundelius, G. G. Byrd, *OJ 287: Binary pair of supermassive black holes*, Astrophysical Journal 325 (1988) 628–634.
- [25] S. G. Jorstad, A. P. Marscher, J. R. Mattox, A. E. Wehrle, S. D. Bloom, A. V. Yurchenko, *Multiepoch very long baseline array observations of EGRET-detected quasars and BL Lacertae objects: Superluminal motion of gamma-ray bright blazars*, Astrophysical Journal Supplement Series 134 (2) (2001) 181–240.
- [26] C. M. Raiteri, M. Villata, H. D. Aller, M. F. Aller, J. Heidt, O. M. Kurtanidze, L. Lanteri, M. Maesano, E. Massaro, F. Montagni, R. Nesci, K. Nilsson, M. G. Nikolashvili, P. Nurmi, L. Ostorero, T. Pursimo, R. Rekola, A. Sillanpää, L. O. Takalo, H. Teräsanta, G. Tosti, T. J. Balonek, M. Feldt, A. Heines, C. Heisler, J. Hu, M. Kidger, J. R. Mattox, E. J. McGrath, A. Pati, R. Robb, A. C. Sadun, P. Shastri, S. J. Wagner, X. Wei, J. Wu, *Optical and radio variability of the BL Lacertae object ASTROBJ AO 0235+16 ASTROBJ: A possible 5-6 year periodicity*, Astronomy and Astrophysics 377 (2001) 396–412.

- [27] M. A. Ibrahimov, I. E. Papadakis, T. P. Krichbaum, A. Kraus, A. Witzel, H. Ungerechts, U. Lisenfeld, U. Bach, G. Cimò, S. Ciprini, L. Fuhrmann, G. N. Kimeridze, L. Lanteri, M. Maesano, F. Montagni, L. Nucciarelli, G. Ostorero, *Optical and radio behaviour of the BL Lacertae object ASTROBJ 0716+714 ASTROBJ*, *Astronomy and Astrophysics* 402 (2003) 151–169.
- [28] A. C. Gupta, A. K. Srivastava, P. J. Wiita, *Periodic oscillations in the intra-day optical light curves of the blazar S5 0716+714*, *Astrophysical Journal* 690 (1) (2009) 216–223.
- [29] M. Villata, C. M. Raiteri, V. M. Larionov, M. G. Nikolashvili, M. F. Aller, U. Bach, D. Carosati, F. Hroch, M. A. Ibrahimov, S. G. Jorstad, Y. Y. Kovalev, A. Lähteenmäki, K. Nilsson, H. Teräsranata, G. Tosti, H. D. Aller, A. A. Arkharov, A. Berdyugin, P. Boltwood, C. S. Buemi, R. Casas, P. Charlot, J. M. Coloma, A. di Paola, G. di Rico, G. N. Kimeridze, T. S. Konstantinova, E. N. Kopatskaya, Y. A. Kovalev, O. M. Kurtanidze, L. Lanteri, E. G. Larionova, L. V. Larionova, J. F. Le Champion, P. Leto, E. Lindfors, A. P. Marscher, K. Marshall, J. P. McFarland, I. M. McHardy, H. R. Miller, G. Nucciarelli, M. P. Osterman, M. Pasanen, T. Pursimo, J. A. Ros, A. C. Sadun, L. A. Sigua, L. Sixtova, ..., S. B. Zhou, *The correlated optical and radio variability of ASTROBJ BL Lacertae ASTROBJ. WEBT data analysis 1994-2005*, *Astronomy and Astrophysics* 501 (2) (2009) 455–460.
- [30] J. Y. Wang, W. A. An, T. and Baan, X. L. Lu, *Periodic radio variabilities of the blazar 1156+295: Harmonic oscillations*, *Monthly Notices of the Royal Astronomical Society* 443 (1) (2014) 58–66.
- [31] A. Sandrinelli, S. Covino, A. Treves, E. Lindfors, C. M. Raiteri, K. Nilsson, L. O. Takalo, R. Reinthal, A. Berdyugin, V. Fallah Ramazani, V. Kadenius, T. Tuominen, P. Kehusmaa, A. Bachev, R. Strigachev, *Gamma-ray and optical oscillations of 0716+714, MRK 421, and BL Lacertae*, *Astronomy and Astrophysics* 600 (2017) 7 pages.
- [32] A. Roy, V. R. Chitnis, A. C. Gupta, P. J. Wiita, G. E. Romero, S. A. Cellone, A. Chatterjee, J. A. Combi, C. M. Raiteri, A. Sarkar, M. Villata, *Detection of a quasi-periodic oscillation in the optical light curve of the remarkable blazar AO 0235+164*, *Monthly Notices of the Royal Astronomical Society* 513 (4) (2022) 5238–5244.
- [33] X. Chang, T. F. Yi, D. R. Xiong, C. X. Liu, X. Yang, H. Z. Li, Y. L. Gong, W. W. Na, Y. Li, Z. H. Chen, J. P. Chen, L. S. Mao, *Multicolour optical variability monitoring of blazars with high time resolution*, *Monthly Notices of the Royal Astronomical Society* 520 (3) (2023) 4118–4133.
- [34] S. Kishore, A. C. Gupta, P. J. Wiita, *Detection of quasiperiodic oscillations in the blazar S4 0954+658 with TESS*, *Astrophysical Journal* 943 (1) (2023) 16 pages.
- [35] A. Tripathi, K. L. Smith, P. J. Wiita, R. V. Wagoner, *Optical quasi-periodic oscillations in the TESS light curves of three blazars*, *Monthly Notices of the Royal Astronomical Society* 527 (3) (2024) 9132–9144.
- [36] E. S. Perlman, J. T. Stocke, J. F. Schachter, M. Elvis, E. Ellingson, C. M. Urry, M. Potter, P. Impey, C. D. Colchinsky, *The Einstein slew survey sample of BL Lacertae objects*, *Astrophysical Journal Supplement Series* 104 (1996) 251–285.
- [37] M. Catanese, C. W. Akerlof, H. M. Badran, S. D. Biller, I. H. Bond, P. J. Boyle, S. M. Bradbury, J. H. Buckley, A. M. Burdett, J. Bussons Gordo, D. A. Carter Lewis, M. F. Cawley, V. Connaughton, D. J. Fegan, J. P. Finley, J. A. Gaidos, T. Hall, A. M. Hillas, F. Krennrich, R. C. Lamb, R. W. Lessard, C. Masterson, J. E. McEnery, G. Mohanty, J. Quinn, A. J. Rodgers, H. J. Rose, F. W. Samuelson, M. S. Schubnell, G. H. Sembroski, R. Srinivasan, T. C. Weekes, C. W.

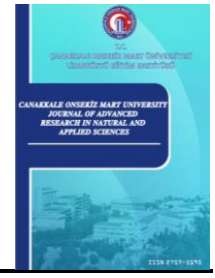
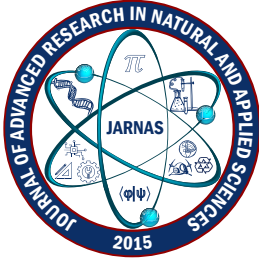
- Z. J. Wilson, *Discovery of gamma-ray emission above 350 GeV from the BL Lacertae object 1ES 2344+514*, *Astrophysical Journal* 501 (2) (1998) 616–623.
- [38] J. Albert, E. Aliu, H. Anderhub, P. Antoranz, A. Armada, C. Baixeras, J. A. Barrio, H. Bartko, D. Bastieri, J. K. Becker, W. Bednarek, K. Berger, C. Bigongiari, A. Biland, R. K. Bock, P. Bordas, V. Bosch-Ramon, T. Bretz, I. Britvitch, M. Camara, E. Carmona, A. Chilingarian, S. Ciprini, J. A. Coarasa, S. Commichau, J. L. Contreras, J. Cortina, M. T. Costado, V. Curtef, V. Danielyan, F. Dazzi, A. De Angelis, C. Delgado, R. de los Reyes, B. De Lotto, E. Domingo-Santamaría, D. Dorner, M. Doro, M. Errando, M. Fagiolini, D. Angelis, D. Ferenc, E. Fernández, R. Firpo, J. Flix, M. V. Fonseca, L. Font, M. Fuchs, N. Galante, R. García-López, ..., J. Zapatero, *Observation of very high energy γ -rays from the AGN 1ES 2344+514 in a low emission state with the magic telescope*, *Astrophysical Journal* 662 (2) (2007) 892–899.
- [39] V. A. Acciari, E. Aliu, T. Arlen, T. Aune, M. Beilicke, W. Benbow, D. Boltuch, V. Bugaev, A. Cannon, L. Ciupik, P. Cogan, P. Colin, R. Dickherber, A. Falcone, S. J. Fegan, J. P. Finley, P. Fortin, L. F. Fortson, A. Furniss, D. Gall, G. H. Gillanders, J. Grube, R. Guenette, G. Gyuk, D. Hanna, J. Holder, D. Horan, C. M. Hui, T. B. Humensky, A. Imran, P. Kaaret, N. Karlsson, M. Kertzman, D. Kieda, J. Kildea, A. Konopelko, H. Krawczynski, F. Krennrich, M. J. Lang, S. LeBohec, P. Maier G., and Moriarty, R. Mukherjee, R. A. Ong, A. N. Otte, D. Pandel, J. S. Perkins, A. Pichel, M. Pohl, J. Quinn, ..., B. Zitzer, *Multiwavelength observations of the very high energy blazar 1ES 2344+514*, *Astrophysical Journal* 738 (2) (2011) 8 pages.
- [40] J. Aleksić, L. A. Antonelli, P. Antoranz, M. Asensio, M. Backes, U. Barres de Almeida, J. A. Barrio, W. Bednarek, K. Berger, E. Bernardini, A. Biland, O. Blanch, R. K. Bock, A. Boller, S. Bonnefoy, G. Bonnoli, D. Borla Tridon, T. Bretz, E. Carmona, A. Carosi, D. Carreto Fidalgo, P. Colin, E. Colombo, J. L. Contreras, J. Cortina, L. Cossio, S. Covino, P. Da Vela, F. Dazzi, A. De Angelis, G. De Caneva, B. De Lotto, C. Delgado Mendez, M. Doert, A. Domínguez, D. Dominis Prester, D. Dorner, M. Doro, D. Eisenacher, D. Elsaesser, D. Ferenc, M. V. Fonseca, L. Font, C. Fruck, R. J. García López, M. Garczarczyk, D. Garrido Terrats, M. Gaug, G. Giavitto, N. Godinović, ..., J. Wilms, *The simultaneous low state spectral energy distribution of 1ES 2344+514 from radio to very high energies*, *Astronomy and Astrophysics* 556 (2013) 28 pages.
- [41] C. Allen, S. Archambault, A. Archer, W. Benbow, R. Bird, E. Bourbeau, R. Brose, M. Buchovecky, J. H. Buckley, V. Bugaev, J. V. Cardenzana, M. Cerruti, X. Chen, J. L. Christiansen, M. P. Connolly, W. Cui, M. K. Daniel, J. D. Eisch, A. Falcone, Q. Feng, M. Fernandez Alonso, J. P. Finley, H. Fleischhack, A. Flinders, L. Fortson, A. Furniss, G. H. Gillanders, S. Griffin, J. Grube, M. Hütten, N. Håkansson, D. Hanna, O. Herve, J. Holder, G. Hughes, T. B. Humensky, C. A. Johnson, P. Kaaret, P. Kar, N. Kelley-Hoskins, M. Kertzman, D. Kieda, M. Krause, F. Krennrich, S. Kumar, M. J. Lang, G. Maier, S. McArthur, A. McCann, K. Meagher, ..., D. A. Williams, *Very high energy γ -ray observations of the blazar 1ES 2344+514 with veritas*, *Monthly Notices of the Royal Astronomical Society* 471 (2) (2017) 2117–2123.
- [42] H. Abe, S. Abe, V. A. Acciari, I. Agudo, T. Aniello, S. Ansoldi, L. A. Antonelli, A. Arbet Engels, C. Arcaro, M. Artero, K. Asano, D. Baack, A. Babić, A. Baquero, U. Barres De Almeida, I. Batković, J. Baxter, J. Becerra González, E. Bernardini, J. Bernete, A. Berti, J. Besenrieder, C. Bigongiari, A. Bil and, O. Blanch, G. Bonnoli, n. Bošnjak, I. Burelli, G. Busetto, A. Campoy-Ordaz, A. Carosi, R. Carosi, M. Carretero-Castrillo, A. J. Castro-Tirado, Y. Chai, A. Cifuentes, S. Cikota, E. Colombo, J. L. Contreras, J. Cortina, S. Covino, G. D’Amico, F. D’Ammando, V. D’Elia, P. Da Vela, F. Dazzi, A. De Angelis, B. De Lotto, A. Del Popolo, M. Delfino, ..., S. Lombardi, *Multi-year characterisation of the broad-band emission from the intermittent extreme BL*

lac 1ES 2344+514, Astronomy and Astrophysics 682 (2024) 26 pages.

- [43] H. R. Miller, A. B. Daya, E. C. Ferrara, *The character of the microvariability of three tev blazars*, BL Lac Phenomenon ASP Conference Series 159 (1999) 75–78.
- [44] B. Z. Dai, G. Z. Xie, K. H. Li, S. B. Zhou, W. W. Liu, Z. J. Jiang, *Rapid optical variability of gamma ray loud blazars*, The Astronomical Journal 122 (6) (2001) 2901–2912.
- [45] G. Z. Xie, S. B. Zhou, B. Z. Dai, E. W. Liang, K. H. Li, J. M. Bai, S. Y. Xing, W. W. Liu, *Photometric monitoring of 12 BL Lacertae objects*, Monthly Notices of the Royal Astronomical Society 329 (4) (2002) 689–699.
- [46] J. H. Fan, O. M. Kurtanidze, M. G. Nikolashvili, A. C. Gupta, J. S. Zhang, Y. H. Yuan, *Optical photometric observations of γ -ray loud blazars*, Chinese Journal of Astronomy and Astrophysics 4 (2004) 133–142.
- [47] A. Pandey, A. C. Gupta, G. Damljanovic, P. J. Wiita, O. Vince, M. D. Jovanovic, *Optical variability of three extreme tev blazars*, Monthly Notices of the Royal Astronomical Society 496 (2) (2020) 1430–1444.
- [48] J. T. Cai, S. O. Kurtanidze, Y. Liu, O. M. Kurtanidze, M. G. Nikolashvili, H. B. Xiao, J. H. Fan, *Long-term optical monitoring of the tev BL Lacertae object 1ES 2344 + 514*, Astrophysical Journal Supplement Series 260 (2) (2022) 14 pages.
- [49] L. Ma, G. Z. Xie, T. F. Yi, S. B. Zhou, K. H. Li, X. Zhang, H. Dai, *CCD photometry of five x-ray selected BL Lacertae objects*, Astrophysics and Space Science 327 (1) (2010) 35–58.
- [50] P. Giommi, P. Padovani, E. Perlman, *Detection of exceptional x-ray spectral variability in the tev BL lac 1ES 2344+514*, Monthly Notices of the Royal Astronomical Society 317 (4) (2000) 743–749.
- [51] H. Gaur, A. C. Gupta, A. Strigachev, R. Bachev, E. Semkov, P. J. Wiita, S. Peneva, S. Boeva, L. Slavcheva Mihova, B. Mihov, U. S. Latev, G. Pandey, *Optical flux and spectral variability of blazars*, Monthly Notices of the Royal Astronomical Society 425 (4) (2012) 3002–3023.
- [52] K. Nilsson, T. Pursimo, L. O. Takalo, A. Sillanpää, H. Pietilä, J. Heidt, *Two-dimensional photometric decomposition of the tev BL Lacertae objects Markarian 421, Markarian 501, and 1ES 2344+514*, Publications of the Astronomical Society of the Pacific 111 (764) (1999) 1223–1232.
- [53] V. T. Doroshenko, Y. S. Efimov, G. A. Borman, N. G. Pulatova, *BVRI CCD-photometry of comparison stars in the fields of galaxies with active nuclei. VII*, Astrophysics 57 (2) (2014) 176–196.
- [54] M. S. Bessell, F. Castelli, B. Plez, *Model atmospheres broad-band colors, bolometric corrections and temperature calibrations for O - M stars*, Astronomy and Astrophysics 333 (1998) 231–250.
- [55] M. Fukugita, K. Shimasaku, T. Ichikawa, *Galaxy colors in various photometric band systems*, Publications of the Astronomical Society of the Pacific 107 (716) (1995) 945–958.
- [56] J. A. de Diego, J. Polednikova, A. Bongiovanni, A. M. Pérez García, M. A. De Leo, T. Verdugo, J. Cepa, *Testing microvariability in quasar differential light curves using several field stars*, The Astronomical Journal 150 (2) (2015) 10 pages.
- [57] H. Gaur, A. C. Gupta, R. Bachev, A. Strigachev, E. Semkov, M. Böttcher, P. J. Wiita, J. A. Diego, M. F. Gu, H. Guo, R. Joshi, B. Mihov, N. Palma, S. Peneva, A. Rajasingam, L. S. Mihova, *Nature of intranight optical variability of BL Lacertae*, Monthly Notices of the Royal Astronomical Society 452 (4) (2015) 4263–4273.

- [58] A. Pandey, A. C. Gupta, P. J. Wiita, S. N. Tiwari, *Optical flux and spectral variability of the tev blazar PG 1553+113*, *Astrophysical Journal* 871 (2) (2019) 8 pages.
- [59] Z. R. Weaver, K. E. Williamson, S. G. Jorstad, A. P. Marscher, V. M. Larionov, C. M. Raiteri, M. Villata, J. A. Acosta-Pulido, R. Bachev, G. V. Baida, T. J. Balonek, E. Benítez, G. A. Borman, V. Bozhilov, M. I. Carnerero, D. Carosati, W. P. Chen, G. Damjanovic, V. Dhiman, D. J. Dougherty, S. A. Ehgamberdiev, T. S. Grishina, A. C. Gupta, M. Hart, D. Hiriart, H. Y. Hsiao, S. Ibryamov, M. Joner, G. N. Kimeridze, E. N. Kopatskaya, O. M. Kurtanidze, S. O. Kurtanidze, E. G. Larionova, K. Matsumoto, R. Matsumura, M. Minev, D. O. Mirzaqulov, D. A. Morozova, A. A. Nikiforova, M. G. Nikolashvili, E. Ovcharov, N. Rizzi, A. Sadun, S. S. Savchenko, E. Semkov, J. J. Slater, K. L. Smith, M. Stojanovic, A. Strigachev, Y. V. Troitskaya, ..., A. V. Zhovtan, *Multiwavelength variability of BL Lacertae measured with high time resolution*, *Astrophysical Journal* 900 (2) (2020) 26 pages.
- [60] J. A. de Diego, *On the reliability of microvariability tests in quasars*, *The Astronomical Journal* 148 (5) (2014) 16 pages.
- [61] D. Montgomery, *Nested and split-plot designs*, *Design and Analysis of Experiments*, 8th Edition, John Wiley & Sons Incorporated, United State, 2012, Ch. 14, pp. 604–637.
- [62] A. C. Gupta, U. C. Joshi, *Intra-night optical variability of luminous radio quiet QSOs*, *Astronomy and Astrophysics* 440 (3) (2005) 855–865.
- [63] J. Heidt, S. J. Wagner, *Statistics of optical intraday variability in a complete sample of radio-selected BL Lacertae objects*, *Astronomy and Astrophysics* 305 (1) (1996) 42–52.
- [64] A. Agarwal, A. C. Gupta, *Multiband optical variability studies of BL Lacertae*, *Monthly Notices of the Royal Astronomical Society* 450 (1) (2015) 541–551.
- [65] R. A. Edelson, J. H. Krolik, *The discrete correlation function: A new method for analyzing unevenly sampled variability data*, *Astrophysical Journal* 333 (1988) 646–659.
- [66] N. R. Lomb, *Least squares frequency analysis of unequally spaced data*, *Astrophysics and Space Science* 39 (2) (1976) 447–462.
- [67] J. D. Scargle, *Studies in astronomical time series analysis. II. Statistical aspects of spectral analysis of unevenly spaced data.*, *Astrophysical Journal* 263 (1982) 835–853.
- [68] G. Foster, *Wavelets for period analysis of unevenly sampled time series*, *The Astronomical Journal* 112 (1996) 1709–1729.
- [69] S. O’Neill, S. Kiehlmann, A. C. S. Readhead, M. F. Aller, R. D. Blandford, I. Liodakis, M. L. Lister, P. J. Mróz, C. P. O’Dea, T. J. Pearson, V. Ravi, M. Vallisneri, K. A. Cleary, M. J. Graham, K. J. B. Grainge, M. W. Hodges, T. Hovatta, A. Lähteenmäki, J. W. Lamb, T. J. W. Lazio, W. Max Moerbeck, V. Pavlidou, T. A. Prince, R. A. Reeves, M. Tornikoski, J. A. Vergara de la Parra, P. Zensus, *The unanticipated phenomenology of the blazar PKS 2131-021: A unique supermassive black hole binary candidate*, *Astrophysical Journal* 926 (2) (2022) 21 pages.
- [70] G. E. Romero, S. A. Cellone, J. A. Combi, I. Andruchow, *Optical microvariability of EGRET blazars*, *Astronomy and Astrophysics* 390 (2002) 431–438.
- [71] R. Sagar, C. S. Stalin, K. Gopal, P. J. Wiita, *Intranight optical variability of blazars*, *Monthly Notices of the Royal Astronomical Society* 348 (1) (2004) 176–186.

- [72] K. Gopal, A. Goyal, S. Joshi, C. Karthick, R. Sagar, P. J. Wiita, G. C. Anupama, D. K. Sahu, *Rapid optical variability of tev blazars*, Monthly Notices of the Royal Astronomical Society 416 (1) (2011) 101–117.
- [73] G. E. Romero, S. A. Cellone, J. A. Combi, *Optical microvariability of southern AGNs*, Astronomy and Astrophysics Supplement 135 (1999) 477–486.
- [74] M. J. Valtonen, H. J. Lehto, K. Nilsson, J. Heidt, L. O. Takalo, A. Sillanpää, C. Villforth, M. Kidger, G. Poyner, T. Pursimo, S. Zola, J. H. Wu, X. Zhou, K. Sadakane, M. Drozd, D. Koziel, D. Marchev, W. Ogloza, C. Porowski, M. Siwak, G. Stachowski, M. Winiarski, V. P. Hentunen, M. Nissinen, A. Liakos, S. Dogru, *A massive binary black-hole system in OJ287 and a test of general relativity*, Nature 452 (7189) (2008) 851–853.
- [75] M. J. Graham, S. G. Djorgovski, D. Stern, A. J. Drake, A. A. Mahabal, C. Donalek, E. Glikman, S. Larsen, E. Christensen, *A systematic search for close supermassive black hole binaries in the catalina real-time transient survey*, Monthly Notices of the Royal Astronomical Society 453 (2) (2015) 1562–1576.
- [76] G. Bhatta, S. Zola, L. Stawarz, M. Ostrowski, M. Winiarski, W. Ogłóza, M. Drózd, M. Siwak, A. Liakos, D. Koziel Wierzbowska, K. Gazeas, B. Debski, T. Kundera, V. S. Stachowski, G. Paliya, *Detection of possible quasi-periodic oscillations in the long-term optical light curve of the BL lac object OJ 287*, Astrophysical Journal 832 (1) (2016) 7 pages.
- [77] M. Villata, C. M. Raiteri, *Helical jets in blazars. I. The case of MKN 501*, Astronomy and Astrophysics 347 (1999) 30–36.
- [78] F. M. Rieger, *On the geometrical origin of periodicity in blazar-type sources*, Astrophysical Journal 615 (1) (2004) L5–L8.
- [79] M. Camenzind, M. Krockenberger, *The lighthouse effect of relativistic jets in blazars. A geometric origin of intraday variability*, Astronomy and Astrophysics 255 (1992) 59–62.
- [80] P. Mohan, A. Mangalam, *Kinematics of and emission from helically orbiting blobs in a relativistic magnetized jet*, Astrophysical Journal 805 (2) (2015) 20 pages.
- [81] E. Sobacchi, M. C. Sormani, A. Stamerra, *A model for periodic blazars*, Monthly Notices of the Royal Astronomical Society 465 (1) (2017) 161–172.
- [82] J. Zhou, Z. Wang, L. Chen, P. J. Wiita, J. Vadakkumthani, N. Morrell, P. Zhang, J. Zhang, *A 34.5 day quasi-periodic oscillation in γ -ray emission from the blazar PKS 2247-131*, Nature Communications 9 (2018) 6 pages.
- [83] A. Banerjee, V. Negi, R. Joshi, N. Kumar, P. J. Wiita, H. Chand, N. Rawat, X. Wu, L. C. Ho, *Probable low-frequency quasi-periodic oscillations in blazars from the ZTF survey*, Monthly Notices of the Royal Astronomical Society 526 (4) (2023) 5172–5186.
- [84] A. Roy, A. Sarkar, A. Chatterjee, A. C. Gupta, V. Chitnis, P. J. Wiita, *Transient quasi-periodic oscillations at γ -rays in the tev blazar PKS 1510-089*, Monthly Notices of the Royal Astronomical Society 510 (3) (2022) 3641–3649.



Unlocking Cognitive Horizons by Exploring the Influence of Maps on Primary School Pupils: An Examination Conducted in North Macedonia

Edmond Jonuzi¹ , Hüseyin Zahit Selvi² 

^{1,2}Department of Geomatics Engineering, Faculty of Engineering, Necmettin Erbakan University, Konya, Türkiye

Article Info

Received: 12 May 2024

Accepted: 12 Aug 2024

Published: 30 Sep 2024

Research Article

Abstract – This study thoroughly investigates the effects of utilizing maps as educational tools for children, aiming to enhance pupils' cognitive abilities and improve the overall educational system within primary schools. By exploring the potential benefits of incorporating cartographic materials into the curriculum, this research sheds light on their positive impact on children's intellectual growth and the educational framework at the elementary level, such as primary schools. The primary aim of this investigation is to deliver an interactive and compelling educational resource tailored for pupils aged between 7 and 10 years old. Pre-test and post-test were conducted with 377 primary school pupils in Tetovo, North Macedonia. Employing a comprehensive mixed-methods approach and through a meticulous analysis of the potential benefits of integrating maps into the pedagogical framework, this study aims to provide valuable insights into the positive effects they can have on children's skill acquisition and the overall efficacy of the educational system. Ultimately, the findings of this study are expected to inform educational stakeholders by furnishing empirical evidence on the advantages of incorporating maps into the learning process for young learners, thus contributing to more effective educational practices. The study's findings demonstrate a predominantly favorable reception, emphasizing the efficacy and educational utility of the maps and atlases among young pupils. The analysis shows that employing the maps and atlas led to an average enhancement in pupils' learning abilities, with an approximate mean increase of 31.45%.

Keywords – Map utilization, children's skill development, cognitive development, educational system improvement, map use

1. Introduction

Cartography is a potent and influential medium for effective communication [1]. Maps serve as the primary embodiments of cartographic representation. Maps are ubiquitously available and find utility across various fields and disciplines [2]. Maps enjoy substantial popularity widespread appeal, and serve as visual depictions [3,4], and they can be utilized by a diverse range of individuals [5]. Maps are additionally employed within the educational system to support various pedagogical endeavors. Cartographers possess the specialized knowledge and skills required to facilitate the education of educators and other influential stakeholders, including parents, who play a vital role in fostering children's appreciation and comprehension of maps [6]. The contemporary young learners of the present have the potential of map users, map compilers and map designers of the future. Designing assistive technologies specifically catered to the requirements of children, encompassing maps as well, presents considerable challenges [7]. It is essential to provide young learners with the necessary skills. Educators or teachers play a crucial role in guiding pupils to articulate their thoughts explicitly, assisting pupils in elucidating and refining their reasoning within the framework of the norms and

¹edmondjonuzi1@gmail.com (Corresponding Author); ²hzelvi@erbakan.edu.tr

criteria [8]. There is a consensus among researchers that children at a young age, specifically in the early stages of primary school, possess the cognitive capacity to comprehend maps [9]. Comprehending maps presents a viable avenue for exploring children's grasp of spatial relationships [10]. It has been hypothesized that children and adults perceive maps and interpret spatial information differently [11-13]. The identified and purported disparities in comprehension between adults and children have engendered a proliferation of maps meticulously tailored for children by publishers and cartographers, deviating from those originally intended for adult audiences [14]. Curriculum developers may need to address the inclusion of explicit geographical and cartographic vocabulary within the educational framework [15]. Within the educational realm, maps are widely regarded as indispensable communication tools [9]. The exploration of color within maps has been the subject of comprehensive inquiry in cartographic research, representing one of the most extensively examined aspects of map design [16-24]. The expressive capabilities of young children are not fully developed; thus, it is more advantageous for them to communicate their genuine emotions and thoughts through non-verbal means such as pictures, charts, concept maps, and semantic networks [25]. Geographical education has always been concerned with systematically teaching and learning map skills [26]. Children's proficiency in map-reading skills offers significant insights into a particular form of representational competence [27]. Maps convey information through the utilization of signs and symbols, augmented by additional details presented through the inclusion of words, letters, and numbers, facilitating the process of decoding and interpretation [26]. Cartographers have recognized that maps do not provide a direct and unambiguous portrayal of the world; rather, maps function as representations that offer diverse interpretations of reality, allowing human cognition to perceive distinct versions of truth [28]. Piaget's theory of cognitive development elucidates the process through which a child constructs a cognitive framework, or mental model, to comprehend the world [29]. Jean Piaget dedicated approximately five decades of his career to investigating children's cognitive development [30]. According to Piaget's theory, pupils and students require a curriculum that fosters their cognitive development by facilitating the acquisition of concepts and logical reasoning skills [31]. An important implication of Piaget's theory is the need to adapt instruction to the learner's developmental level, ensuring that the content aligns with their stage of development. In this context, the educator or teacher plays a crucial role in facilitating learning by offering diverse experiences that allow learners to explore, experience, and develop new understandings [32]. Cognitive development is explicated through a succession of hierarchical skill structures known as levels, accompanied by transformation rules that establish the interrelationships between these levels [33]. Cartography and cartographers shoulder substantial responsibilities in creating maps that are customarily crafted to cater to children's unique requirements, align with educational curricula, and correspond to the cognitive development levels of children [3]. In recent years, enhanced maps that adhere to more comprehensive standards and are being introduced into the market have notably emerged. This trend has also affected atlases. An increasing number of atlas projects are being undertaken for educational purposes, encompassing diverse subject matter and content [34-37]. The utilization of maps as pedagogical tools in primary education has gained significant attention due to its potential influence on children's cognitive development and the overall effectiveness of the educational system. By incorporating cartographic materials into the curriculum, educators seek to engage pupils in spatial thinking, enhance their problem-solving skills, and foster a deeper understanding of geographical concepts. However, despite the widespread use of maps in primary schools, limited empirical research has systematically examined their impact on pupils' abilities and the educational framework. Several comparative studies have been conducted across various nations, focusing on promoting cartographic literacy among elementary school pupils by utilizing maps and atlases. In different studies, it is also seen that map use starts at different ages in different countries: 2nd grade (7 years) in Hungary [38], 1st grade (6 years) in Bulgaria [39], 2nd grade (7 years) in Azerbaijan [40]. Integrating maps and atlases into geography education is also widespread in Bulgaria; a child's acquaintance with cartography begins with the first map they see; children often see maps in books and thus try to read them [5]. Kramáreková et al. (2016) [41] state that pupils in the Czech Republic acquire their first cartographic knowledge and skills already in primary school education, mainly through social science textbooks. The course 'Nature and Society' is part of the national education program in education and is taught in the second, third, and fourth grades of primary schools. According to Buğdaycı and Bildirici [42], it is possible to find three groups of atlases in the education

system in Turkey: the first atlas for grades 4,5 (ages 10, 11), the middle atlas for grades 6,7,8 (ages 12-14) and the basic atlas for grades 9,10,11,12 (ages 15-19). According to the study project of Reyes Nunez et al. [38], in Hungary, pupils are first introduced to elementary map concepts between the 3rd and 5th grades of primary school. As they grow older, in grade 6, students use maps more frequently in related subjects such as geography and history. By grade 7, according to the authors, students should have practical experience with thematic maps and general maps. Safaraliyeva et al. [40] produced educational maps in the first Geography textbooks, which constitute the beginning of teaching map concepts in Azerbaijani schools. Map-related concepts are included in the curriculum under the 'Life Science' course from grade 2 to grade 5, followed by the geography course from grade 6 to grade 11. This study aims to address this gap in the literature by investigating the effects of utilizing maps for children, highlighting the potential benefits they offer to both pupils and the primary school education system. The study seeks to provide empirical evidence on the advantages of incorporating maps into the learning process for young learners, thus contributing to more effective educational practices and informing educational stakeholders. The findings of this study are expected to contribute to educational practices by providing valuable insights into the positive effects of incorporating maps in primary education. These insights will inform educational stakeholders, enabling them to make informed decisions and enhance the overall efficacy of the educational system. Ultimately, the research strives to create a foundation for evidence-based educational practices that maximize pupils' cognitive abilities and promote a comprehensive understanding of geographical concepts. The main assumption posits that this integration enhances children's learning. Subsidiary assumptions include the assertion that maps as pedagogical tools increase engagement in spatial thinking and problem-solving skills, improve knowledge acquisition of geographical concepts and specifics about North Macedonia, and that effectiveness varies across grades due to developmental cognitive differences. The study seeks to validate these assumptions through rigorous analysis of pre- and post-atlas test results among primary school pupils in North Macedonia, aiming to provide empirical evidence supporting the educational benefits of using maps in classrooms. This study is situated within the framework of a project focused on the compilation and design of an atlas intended for primary school pupils in the Republic of North Macedonia. The atlas project constitutes an integral component of the diploma study research pursued by the corresponding author of this article.

2. Materials and Methods

A comprehensive mixed-methods research design was employed to investigate the impact of map usage on children's development and the educational system. This study aims to thoroughly understand the effects of incorporating maps and atlases as educational tools in primary education. Developing the pre-atlas and post-atlas tests was an integral part of the overall process involved in creating and designing maps for the dedicated atlas aimed at primary school pupils in the Republic of North Macedonia. The maps and the accompanying content of the atlas, such as symbols and population-related tables, were meticulously tailored to align with the cognitive abilities, age range, and spatial reasoning skills of primary school pupils. Extensive testing of the pre-atlas test and post-atlas test, which encompassed both general knowledge about the Republic of North Macedonia and the maps specifically compiled and designed for inclusion in the atlas, were conducted with primary school pupils. The pre-test aimed to assess pupils' overall knowledge regarding the Republic of North Macedonia, encompassing its geography, culture, history, tourism, and economy.

Conversely, the post-test aimed to appraise the influence of newly developed maps within the "Atlas of North Macedonia for primary school pupils" initiative, specifically their role in enhancing the efficiency and effectiveness of learning, thereby contributing to the broader improvement and advancement of education quality. Prior to conducting the pre- and post-tests, relevant authorities, including the Ministry of Education and Science of the Republic of North Macedonia and the Municipality of Tetovo, in collaboration with the regional office of the Ministry of Education and Science at the municipal level, were duly informed. Pupil assessments were conducted anonymously; pupils indicated only their class without providing personal identifiers such as first and last names. A similar anonymized approach was employed for teacher questionnaires, where respondents indicated only their teaching assignment without disclosing personal

details. The primary objective of this testing phase was to ensure that the maps and accompanying information were clear, comprehensible, and suitable for the intended users. In assessing the significance of observed disparities among distinct groups within our sample, t-tests were employed and computed via Microsoft Excel. The utilization of t-tests is pivotal in gauging the impact of an experimental intervention. This statistical methodology, supported by Excel, enhances the robustness and credibility of our results, thereby establishing a firm foundation for the conclusions drawn in this scholarly investigation. The findings of this research will contribute to the field of primary education by providing empirical evidence on the advantages and challenges of utilizing maps as educational tools. Educators, curriculum developers, and policymakers can leverage these findings to inform their decision-making processes and improve teaching practices. Ultimately, this study seeks to enhance the learning experiences of young learners and promote the effective integration of maps into the primary education system.

2.1. Participants

A cohort of 377 primary school pupils, aged 7 to 10 years, actively participated in pre- and post-atlas assessment phases, which comprised evaluations featuring specially crafted maps for the Atlas and general knowledge pertaining to North Macedonia. The demographic breakdown encompassed 84 pupils from third, 140 from fourth, and 153 from fifth. To mitigate potential confounding variables such as socio-economic status and environmental factors, four comparable schools were meticulously chosen within the municipality of Tetovo, situated in the northwestern precinct of North Macedonia. Three of these selected educational institutions were situated within urban settings, while one was in a rural village on the city's outskirts. This deliberate selection process aimed to ensure a comprehensive and varied representation of contexts for the assessment phase.

2.2. Designed and Compiled Tests

The pre-atlas test consists of 15 general questions specifically designed to assess the knowledge of primary school pupils in the lower grades, ranging from 7 to 10 years of age. These questions primarily revolve around various aspects concerning the Republic of North Macedonia. The selection and design of these questions were tailored to align with the target age group's cognitive abilities and educational level. Also, the post-atlas test consists of 15 general questions specifically designed to assess the knowledge of primary school pupils in the lower grades, ranging from 7 to 10 years of age. These questions primarily revolve around various aspects concerning the Republic of North Macedonia. The selection and design of these questions were tailored to align with the target age group's cognitive abilities and educational level. The questions formulated for both the pre- and post-atlas tests are directly linked to the maps compiled and designed specifically for the Atlas, including general information. These questions are designed to assess the pupils' understanding and interpretation of the information presented on the maps within the Atlas. The content of the questions is aligned with the geographic features, symbols, and thematic elements depicted on the maps, ensuring that the pupils' knowledge and comprehension of the map content are effectively evaluated. By analyzing the outcomes of the pre-atlas test and the post-atlas test, a comparison can be drawn to assess the impact of the atlas on the enhancement of general knowledge, which allows us to present the results indicating the improvement achieved.

3. Results and Discussion

3.1. Results

Analyzing both the pre-atlas test data and post-atlas test data will provide valuable insights into the correlation between map usage and pupils' skill development and cognitive development as well as the educational system's positive impact and overall efficacy. Pre-atlas and post-atlas tests will offer numerical findings on

pupils' spatial reasoning abilities, problem-solving skills, and academic performance, providing a statistical basis for understanding the impact of map utilization. These tests will explore the benefits of using cartographic materials, such as increased pupil engagement, motivation, and the facilitation of interdisciplinary learning. Additionally, the tests will shed light on the challenges faced by educators, including resource limitations and the need for adequate training. By combining these test data, this study aims to provide a comprehensive perspective on the advantages, challenges, and potential improvements related to integrating maps into primary education. The tables below represent the pre-atlas test and post-atlas test questions administered to the pupils:

Table 1. An overview of the pre-atlas test questions administered to primary school pupils

Questions No.	Questions
Question 1	Which of these states does the Republic of North Macedonia not share a border with?
Question 2	What is the number of regions in the Republic of North Macedonia?
Question 3	In which region of North Macedonia does the city of Bitola belong?
Question 4	What is the number of cities in the Republic of North Macedonia?
Question 5	What is the capital city of the Republic of North Macedonia?
Question 6	What is the number of municipalities in the Republic of North Macedonia?
Question 7	How many natural lakes does North Macedonia have?
Question 8	What is the largest natural lake in North Macedonia?
Question 9	What is the largest river in North Macedonia?
Question 10	What is the highest mountain in North Macedonia?
Question 11	What is the symbol of the city of Skopje?
Question 12	Which state does North Macedonia share a border with the east?
Question 13	What is the largest plain in the Republic of North Macedonia?
Question 14	The relief of the Republic of North Macedonia is predominantly characterized by?
Question 15	What is the resident population count in the Republic of North Macedonia?

Table 2. An overview of the post-atlas test questions administered to primary school pupils

Questions No.	Questions
Question 1	In which region does the skiing center "Mavrova" belong?
Question 2	How many countries border the Republic of North Macedonia?
Question 3	In which region of North Macedonia does the city of Debar belong?
Question 4	The Museum of the Alphabet of the Albanian Language is located in the city of?
Question 5	In which region is the highest mountain of the Republic of North Macedonia, Mount Korabi?
Question 6	What is the largest ethnic group in the Republic of North Macedonia?
Question 7	Which is the most populated region in the Republic of North Macedonia?
Question 8	Based on the maps and the atlas, the state border of the Republic of North Macedonia is represented by?
Question 9	Trofta fish is characteristic of the city of?
Question 10	In which city of North Macedonia is the Monument of Ilinden - Makedonium?
Question 11	Sharr's dog is characteristic of the region of?
Question 12	The old/ancient city of Stobi is located in the region of?
Question 13	Which of these elements is considered a historical element in Tetova?
Question 14	In which city of the Republic of North Macedonia is rice grown?
Question 15	Matka Canyon and Mustafa Pasha Mosque are part of the city of?

3.1.1. Pre-Atlas Test

A thorough preliminary assessment concerning general knowledge related to the Atlas was administered, involving 84 third-grade pupils from a primary school who participated in an atlas presentation, forming the experimental group. It is essential to underscore that the percentages in the following table represent the ratio of accurate affirmative responses the pupils gave. Following the completion of the preliminary assessment for primary school pupils, the outcomes derived from this evaluation are delineated in the subsequent table:

Table 3. An overview of the pre-atlas test questions administered to third-grade primary school pupils who actively engaged in the Atlas presentation and associated exercises, along with the corresponding success percentages

Questions	Success Percentages %
Question 1	34.52 %
Question 2	40.48 %
Question 3	10.71 %
Question 4	20.24 %
Question 5	51.19 %
Question 6	16.67 %
Question 7	26.19 %
Question 8	70.24 %
Question 9	36.91 %
Question 10	13.10 %
Question 11	50.00 %
Question 12	20.24 %
Question 13	11.91 %
Question 14	27.38 %
Question 15	21.43 %

As per the information in the provided tabular data, it can be inferred that question number 8 manifests the highest mean percentage of accurate responses, reaching 70.24%. In contrast, question number 3 illustrates the lowest mean percentage of accurate responses, registering at 10.71%.

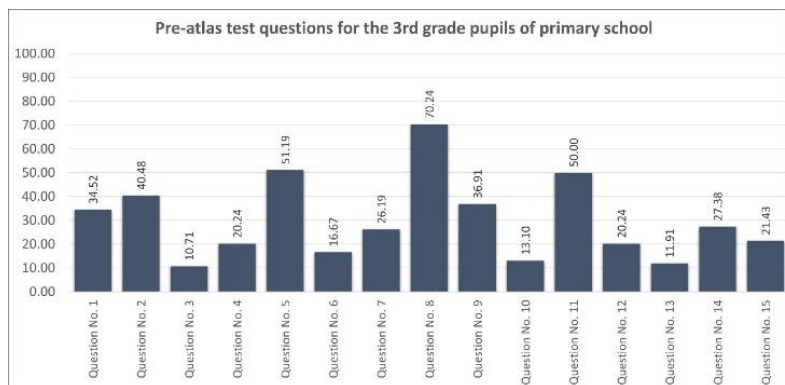


Figure 1. Pre-atlas test questions for the 3rd-grade pupils who did participate in the Atlas presentation and the success percentages are represented with a chart

The ensuing pre-atlas test was carried out on third-grade pupils, involving 15 carefully formulated inquiries. These questions were categorized into three domains: A) Concepts related to Maps and Atlases, B) Comprehension of Directions, geographical regions, and neighboring areas, and C) Understanding of Tourism and Economy in North Macedonia. The subsequent table offers a detailed summary of the outcomes corresponding to these specific categories for third-grade pupils:

Table 4. An overview of the pre-atlas test questions of categories administered to third-grade primary school pupils who actively engaged in the Atlas presentation and associated exercises, along with the corresponding success percentages

Questions	Success Percentages %
Category A	21.43 %
Category B	29.21 %
Category C	50.00 %

Derived from the information delineated in the presented tabular data, it is discernible that inquiries falling under Category C showcase the most elevated mean accuracy, attaining a value of 50.00%. Subsequently,

queries classified under Category B also showcase a notable accuracy rate, totaling 29.21%. In contrast, questions categorized under Category A exhibit the lowest mean accuracy, sustaining a rate of 21.43%.

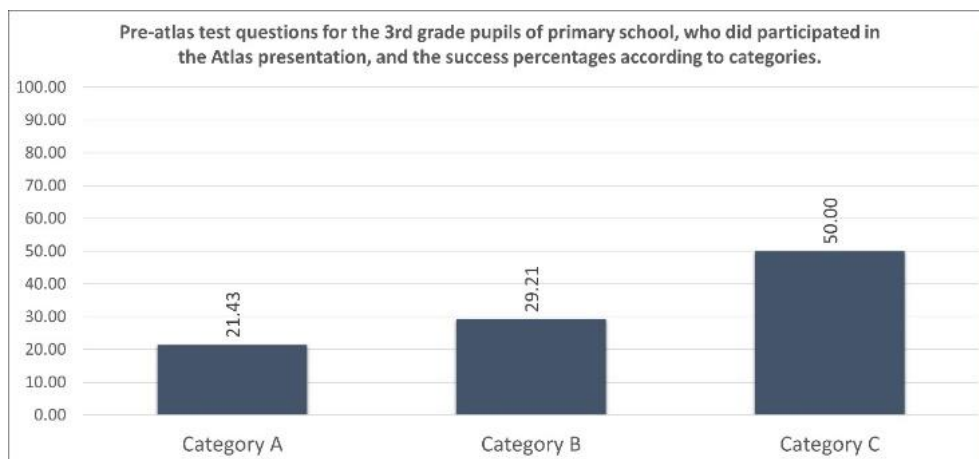


Figure 2. Pre-atlas test questions for the 3rd-grade pupils according to categories, who did participate in the Atlas presentation, and the success percentages are represented with a chart

Considering the outcomes presented in the preliminary tables pertaining to the pre-atlas assessment, it is evident that the cohort of female pupils in the third-grade cohort attained an accuracy rate of 30.33%, while their male counterparts in the same grade achieved a slightly lower accuracy rate of 29.70%.

A comprehensive preliminary examination focusing on fundamental knowledge regarding the Atlas was undertaken, involving the engagement of 140 fourth-grade pupils from a primary school who participated in an atlas presentation, forming the experimental cohort. It is paramount to highlight that the percentages illustrated in the subsequent table represent the ratio of accurate affirmative responses supplied by the pupils. Following the conclusion of the preliminary evaluation for primary school pupils, the findings derived from this assessment are elucidated in the ensuing table:

Table 5. An overview of the pre-atlas test questions administered to fourth-grade primary school pupils who actively engaged in the Atlas presentation and associated exercises, along with the corresponding success percentages

Questions	Success Percentages %
Question 1	66.43 %
Question 2	48.57 %
Question 3	20.71 %
Question 4	20.71 %
Question 5	77.86 %
Question 6	12.86 %
Question 7	37.86 %
Question 8	77.86 %
Question 9	46.43 %
Question 10	25.00 %
Question 11	57.14 %
Question 12	29.29 %
Question 13	16.43 %
Question 14	45.71 %
Question 15	17.86 %

As per the information presented in the provided tabular data, it can be inferred that questions number 5 and number 8 manifest the highest mean percentage of accurate responses, reaching 77.86%. In contrast, question 6 illustrates the lowest mean percentage of accurate responses, registering at 12.86%.

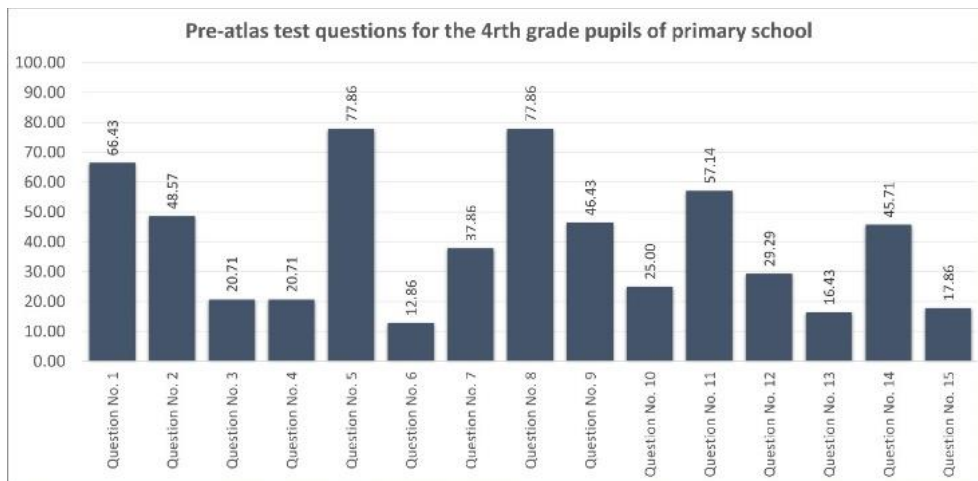


Figure 3. Pre-atlas test questions for the 4rth grade pupils who did participate in the Atlas presentation and the success percentages are represented with a chart

The ensuing pre-atlas test was carried out on fourth-grade pupils, involving 15 carefully formulated inquiries. These questions were categorized into three domains: A) Concepts related to Maps and Atlases, B) Comprehension of Directions, geographical regions, and neighboring areas, and C) Understanding of Tourism and Economy in North Macedonia. The subsequent table offers a detailed summary of the outcomes corresponding to these specific categories for fourth-grade pupils:

Table 6. An overview of the pre-atlas test questions of categories administered to fourth-grade primary school pupils who actively engaged in the Atlas presentation and associated exercises, along with the corresponding success percentages

Questions	Success Percentages %
Category A	17.86 %
Category B	40.44 %
Category C	57.14 %

Derived from the information delineated in the presented tabular data, it is discernible that inquiries falling under Category C showcase the most elevated mean accuracy, attaining a value of 57.14%. Subsequently, queries classified under Category B also showcase a notable accuracy rate, totaling 40.44%. In contrast, questions categorized under Category A exhibit the lowest mean accuracy, sustaining a rate of 17.86%.

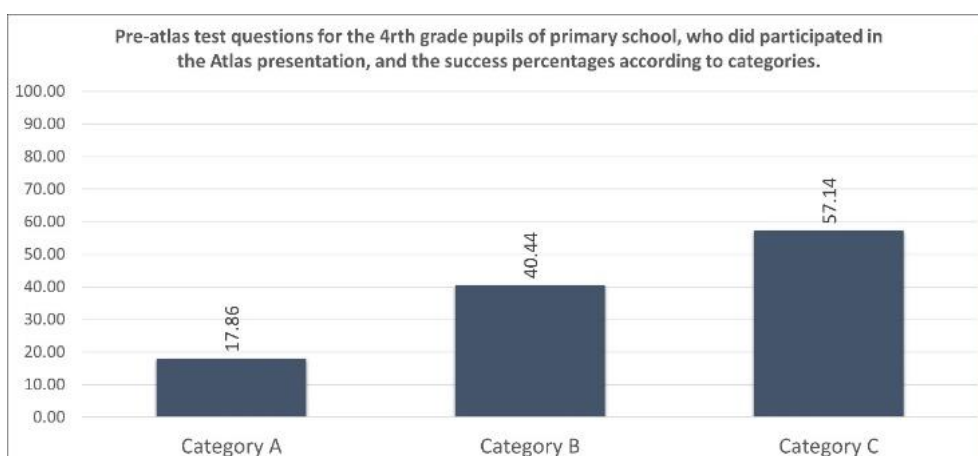


Figure 4. Pre-atlas test questions for the 4rth grade pupils who did participate in the Atlas presentation, according to categories, and the success percentages are represented with a chart

Considering the outcomes presented in the preliminary tables pertaining to the pre-atlas assessment, it is evident that the cohort of female pupils in the fourth-grade cohort attained an accuracy rate of 40.81%, while their male counterparts in the same grade achieved a slightly lower accuracy rate of 39.37%.

A thorough initial assessment focusing on basic knowledge related to the Atlas was carried out, including 153 fifth-grade pupils from a primary school who actively participated in an atlas presentation, forming the experimental cohort. It is essential to underscore that the percentages in the subsequent table signify the proportion of accurate affirmative responses the pupils gave. Following the conclusion of the preliminary assessment for primary school pupils, the outcomes derived from this evaluation are delineated in the ensuing table:

Table 7. An overview of the pre-atlas test questions administered to fifth-grade primary school pupils who actively engaged in the Atlas presentation and associated exercises, along with the corresponding success percentages

Questions	Success Percentages %
Question 1	74.51 %
Question 2	19.61 %
Question 3	25.49 %
Question 4	43.14 %
Question 5	74.51 %
Question 6	20.92 %
Question 7	39.22 %
Question 8	64.71 %
Question 9	69.28 %
Question 10	54.90 %
Question 11	65.36 %
Question 12	25.49 %
Question 13	22.22 %
Question 14	38.56 %
Question 15	16.99 %

As per the information presented in the provided tabular data, it can be inferred that questions number 1 and number 5 manifest the highest mean percentage of accurate responses, reaching 74.51%. In contrast, question 15 illustrates the lowest mean percentage of accurate responses, registering at 16.99%.

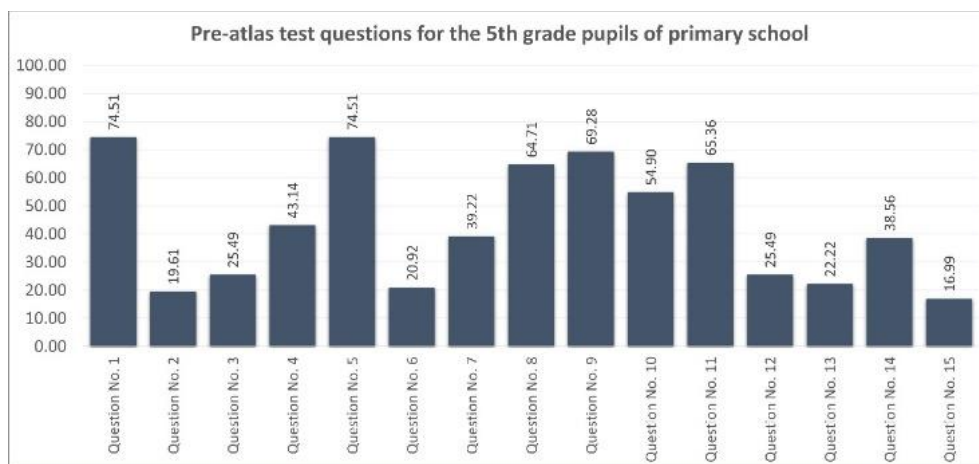


Figure 5. Pre-atlas test questions for the 5th grade pupils who did participate in the Atlas presentation and the success percentages are represented with a chart

The ensuing pre-atlas test was carried out on fourth-grade pupils, involving 15 carefully formulated inquiries. These questions were categorized into three domains: A) Concepts related to Maps and Atlases, B) Comprehension of Directions, geographical regions, and neighboring areas, and C) Understanding of Tourism and Economy in North Macedonia. The subsequent table offers a detailed summary of the outcomes corresponding to these specific categories for fifth-grade pupils:

Table 8. An overview of the pre-atlas test questions of categories administered to fifth-grade primary school pupils who actively engaged in the Atlas presentation and associated exercises, along with the corresponding success percentages

Questions	Success Percentages %
Category A	16.99 %
Category B	44.04 %
Category C	65.36 %

Derived from the information delineated in the presented tabular data, it is discernible that inquiries falling under Category C showcase the most elevated mean accuracy, attaining a value of 65.36%. Subsequently, queries classified under Category B also showcase a notable accuracy rate, totaling 44.04%. In contrast, questions categorized under Category A exhibit the lowest mean accuracy, sustaining a rate of 16.99%.

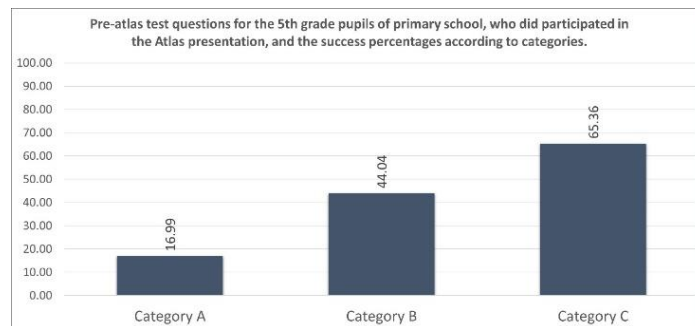


Figure 6. Pre-atlas test questions for the 5th-grade pupils who did participate in the Atlas presentation, according to categories, and the success percentages are represented with a chart

Considering the outcomes presented in the preliminary tables pertaining to the pre-atlas assessment, it is evident that the cohort of female pupils in the fifth-grade cohort attained an accuracy rate of 46.04%, while their male counterparts in the same grade achieved a slightly lower accuracy rate of 41.44%.

In this study, a comprehensive sample comprising 377 primary school pupils actively involved in the Atlas presentation and associated activities, from third to fifth grade and aged between 7 to 10 years, participated in a preliminary assessment designed to gauge their comprehensive understanding of the Atlas. These pupils also formed the experimental group that engaged in the atlas presentation. It is important to highlight that the percentages in the subsequent table are derived from the pupils' accurate affirmative responses. After the conclusion of the preliminary assessment for primary school pupils, the following table presents the outcomes obtained from this evaluation:

Table 9. An overview of the pre-atlas test questions administered to all primary school pupils (from 3rd grade to 5th grade) who actively engaged in the Atlas presentation and associated exercises, along with the corresponding success percentages

Questions	Success Percentages %
Question 1	58.49 %
Question 2	36.22 %
Question 3	18.97 %
Question 4	28.03 %
Question 5	67.85 %
Question 6	16.81 %
Question 7	34.42 %
Question 8	70.93 %
Question 9	50.87 %
Question 10	30.40 %
Question 11	57.50 %
Question 12	25.01 %
Question 13	16.85 %
Question 14	37.22 %
Question 15	18.76 %

As per the information in the provided tabular data, it can be inferred that question number 8 manifests the highest mean percentage of accurate responses, reaching 70.93%. In contrast, question 6 illustrates the lowest mean percentage of accurate responses, registering at 16.81%.

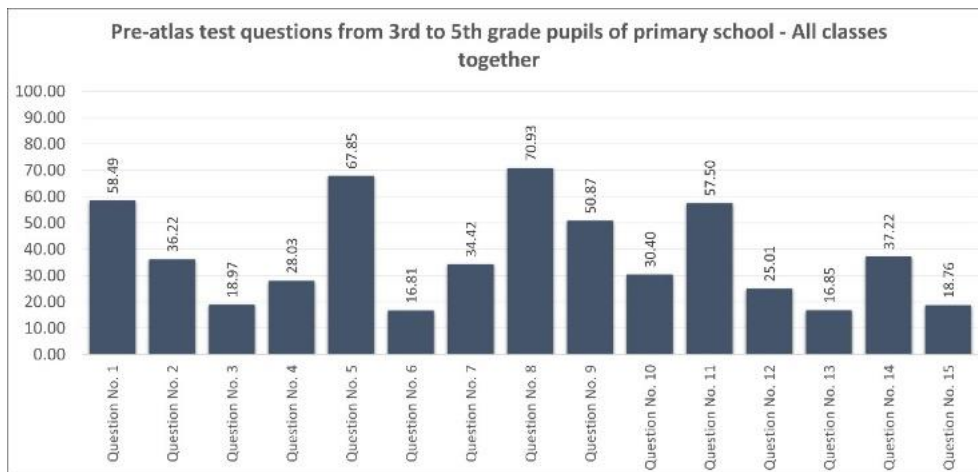


Figure 7. Pre-atlas test questions for all classes together (3rd to 5th-grade pupils) who did participate in the Atlas presentation and the success percentages are represented with a chart

The ensuing pre-atlas test was carried out on pupils from 3rd to 5th grade, involving 15 carefully formulated inquiries. These questions were categorized into three domains: A) Concepts related to Maps and Atlases, B) Comprehension of Directions, geographical regions, and neighboring areas, and C) Understanding of Tourism and Economy in North Macedonia. The subsequent table offers a detailed summary of the outcomes corresponding to these specific categories for fifth-grade pupils:

Table 10. An overview of the pre-atlas test questions of categories administered to all primary school pupils (from 3rd to 5th grade) who actively engaged in the Atlas presentation and associated exercises, along with the corresponding success percentages

Questions	Success Percentages %
Category A	18.76 %
Category B	37.90 %
Category C	57.50 %

Derived from the information delineated in the presented tabular data, it is discernible that inquiries falling under Category C showcase the most elevated mean accuracy, attaining a value of 57.50%. Subsequently, queries classified under Category B also showcase a notable accuracy rate, totaling 37.90%. In contrast, questions categorized under Category A exhibit the lowest mean accuracy, sustaining a rate of 18.76%.

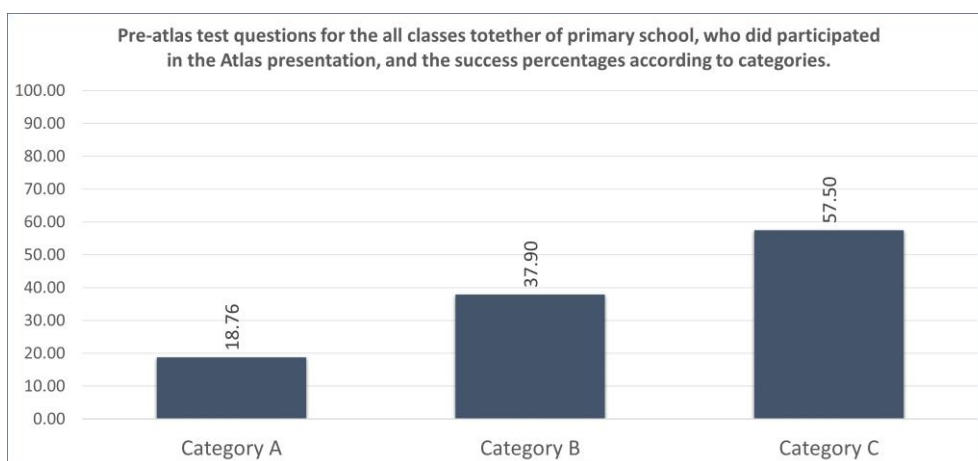


Figure 8. Pre-atlas test questions for all classes together (3rd to 5th-grade pupils) who did participate in the Atlas presentation, according to categories and the success percentages are represented with a chart

Considering the outcomes presented in the preliminary tables pertaining to the pre-atlas assessment, it is evident that the cohort of female pupils from the third to fifth grade cohort attained an accuracy rate of 39.06%, while their male counterparts in the same grade achieved a slightly lower accuracy rate of 36.84%.

3.1.2. Post-Atlas Test

A thorough post-atlas examination regarding general knowledge related to the Atlas was administered to a cohort of 84 third-grade primary school pupils who actively participated in the atlas presentation, forming the experimental group. These pupils were actively involved in the post-atlas test, which aimed to evaluate their overall understanding of the Atlas. It is crucial to emphasize that the percentages depicted in the subsequent table represent the outcomes obtained from accurate positive responses provided by the pupils. Following the conclusion of the pre-atlas test for primary school pupils, the results obtained from this identical assessment are presented in the tables below:

Table 11. An overview of the post-atlas test questions administered to third-grade primary school pupils who actively engaged in the Atlas presentation and associated exercises, along with the corresponding success percentages

Questions	Success Percentages %
Question 1	70.23 %
Question 2	55.95 %
Question 3	26.19 %
Question 4	53.57 %
Question 5	35.71 %
Question 6	60.71 %
Question 7	51.19 %
Question 8	52.38 %
Question 9	75.00 %
Question 10	32.14 %
Question 11	52.38 %
Question 12	21.43 %
Question 13	69.05 %
Question 14	47.62 %
Question 15	51.19 %

As per the information in the provided tabular data, it can be inferred that question number 9 manifests the highest mean percentage of accurate responses, reaching 75.00%. In contrast, question 12 illustrates the lowest mean percentage of accurate responses, registering at 21.43%.

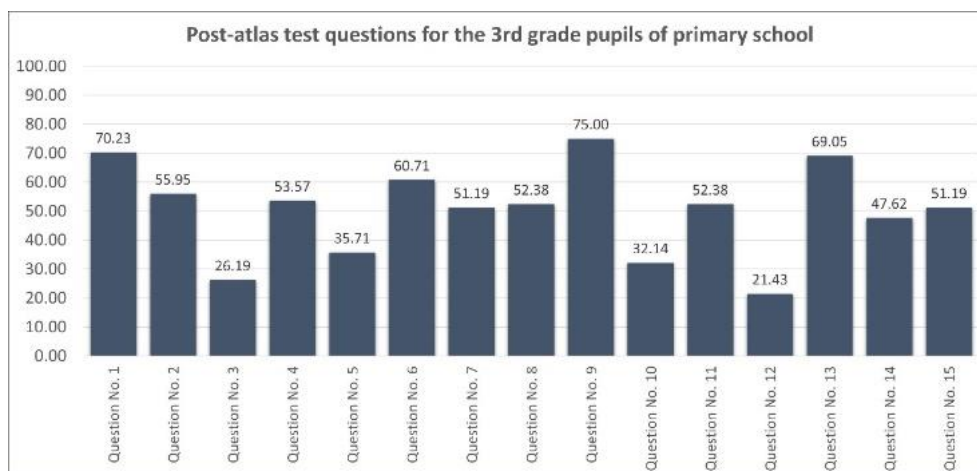


Figure 9. Post-atlas test questions for the 3rd-grade pupils who did participate in the Atlas presentation and the success percentages are represented with a chart

The ensuing post-atlas test was carried out on third-grade pupils, involving 15 carefully formulated inquiries. These questions were categorized into three domains: A) Concepts related to Maps and Atlases, B) Comprehension of Directions, geographical regions, and neighboring areas, and C) Understanding of Tourism and Economy in North Macedonia. The subsequent table offers a detailed summary of the outcomes corresponding to these specific categories for third-grade pupils:

Table 12. An overview of the post-atlas test questions of categories administered to third-grade primary school pupils who actively engaged in the Atlas presentation and associated exercises, along with the corresponding success percentages

Questions	Success Percentages %
Category A	54.76 %
Category B	48.33 %
Category C	49.83 %

Derived from the information delineated in the presented tabular data, it is discernible that inquiries falling under Category A showcase the most elevated mean accuracy, attaining a value of 54.76%. Subsequently, queries classified under Category C also showcase a notable accuracy rate, totaling 49.83%. In contrast, questions categorized under Category B exhibit the lowest mean accuracy, sustaining a rate of 48.33%.

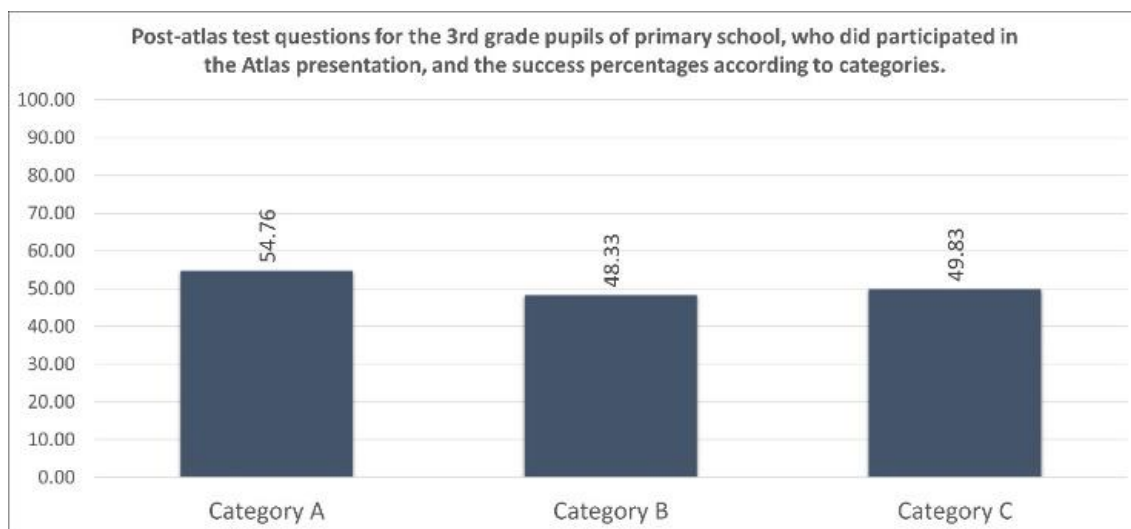


Figure 10. Post-atlas test questions for the 3rd-grade pupils who did participate in the Atlas presentation, according to categories, and the success percentages are represented with a chart

Considering the outcomes presented in the preliminary tables pertaining to the post-atlas assessment, it is evident that the cohort of female pupils in the third-grade cohort attained an accuracy rate of 57.67%, while their male counterparts in the same grade achieved a slightly lower accuracy rate of 57.21%.

An extensive post-atlas assessment regarding fundamental knowledge associated with the Atlas was carried out among 140 fourth-grade primary school pupils, all participated in the atlas presentation and comprised the experimental group. These pupils actively participated in the post-atlas test, which aimed to gauge their overall comprehension of the Atlas. It is vital to emphasize that the percentages depicted in the subsequent table represent the outcomes derived from accurate positive responses provided by the pupils. Following the conclusion of the pre-atlas test for primary school pupils, the results obtained from this identical assessment are presented in the tables below:

Table 13. An overview of the post-atlas test questions administered to fourth-grade primary school pupils who actively engaged in the Atlas presentation and associated exercises, along with the corresponding success percentages

Questions	Success Percentages %
Question 1	69.29 %
Question 2	95.00 %
Question 3	44.29 %
Question 4	96.43 %
Question 5	88.57 %
Question 6	82.14 %
Question 7	92.14 %
Question 8	92.14 %
Question 9	87.86 %
Question 10	80.71 %
Question 11	85.00 %
Question 12	49.29 %
Question 13	90.00 %
Question 14	95.71 %
Question 15	90.00 %

As per the information in the provided tabular data, it can be inferred that query number 4 manifests the highest mean percentage of accurate responses, reaching 96.43%. In contrast, query number 3 illustrates the lowest mean percentage of accurate responses, registering at 44.29%.

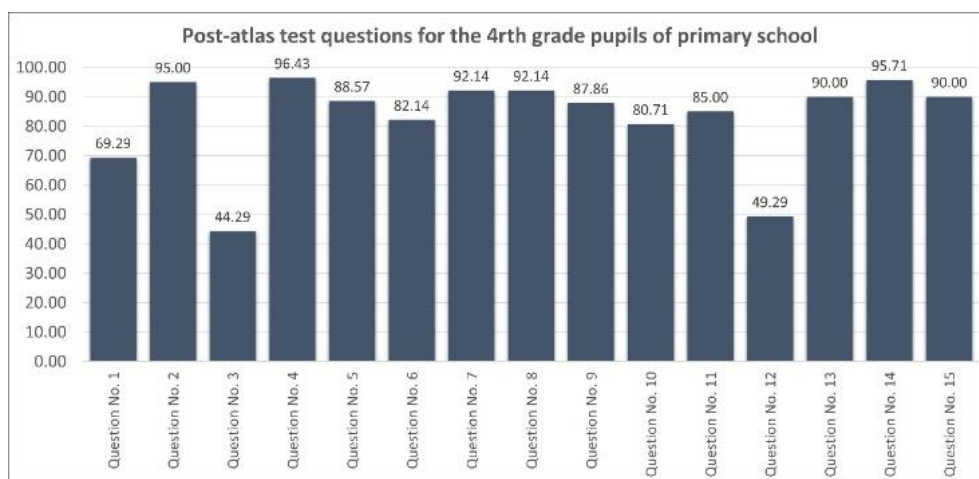


Figure 11. Post-atlas test questions for the 3rd-grade pupils who did participate in the Atlas presentation, according to categories, and the success percentages are represented with a chart

The ensuing post-atlas test was carried out on fourth-grade pupils, involving 15 carefully formulated inquiries. These questions were categorized into three domains: A) Concepts related to Maps and Atlases, B) Comprehension of Directions, geographical regions, and neighboring areas, and C) Understanding of Tourism and Economy in North Macedonia. The subsequent table offers a detailed summary of the outcomes corresponding to these specific categories for fourth-grade pupils:

Table 14. An overview of the post-atlas test questions of categories administered to fourth-grade primary school pupils who actively engaged in the Atlas presentation and associated exercises, along with the corresponding success percentages

Questions	Success Percentages %
Category A	88.81 %
Category B	78.71 %
Category C	82.65 %

Derived from the information delineated in the presented tabular data, it is discernible that inquiries falling under Category A showcase the most elevated mean accuracy, attaining a value of 88.81%. Subsequently, queries classified under Category C also showcase a notable accuracy rate, totaling 82.65%. In contrast, questions categorized under Category B exhibit the lowest mean accuracy, sustaining a rate of 78.71%.

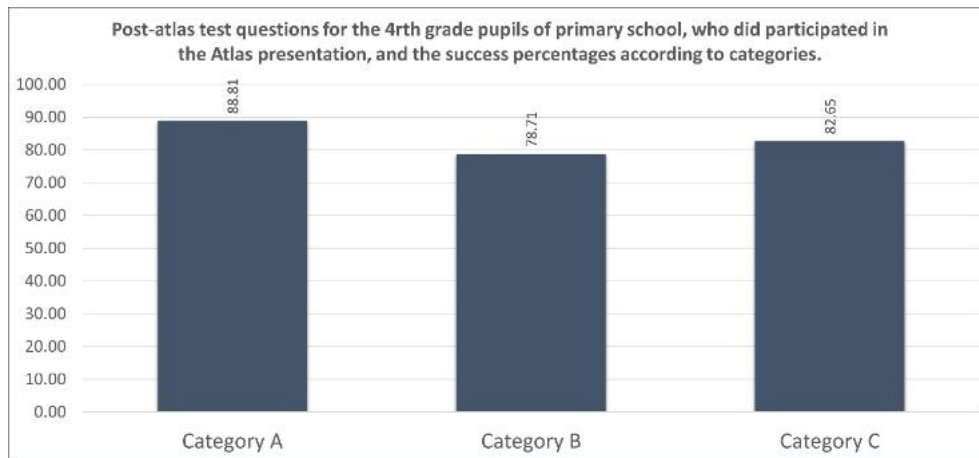


Figure 12. Post-atlas test questions for the 3rd-grade pupils who did participate in the Atlas presentation, according to categories, and the success percentages are represented with a chart

Considering the outcomes presented in the preliminary tables pertaining to the post-atlas assessment, it is evident that the cohort of female pupils in the fourth-grade cohort attained an accuracy rate of 83.64%, while their male counterparts in the same grade achieved a slightly lower accuracy rate of 81.62%.

A thorough post-atlas assessment concerning general knowledge associated with the Atlas was administered to 153 fifth-grade primary school pupils who participated in the atlas presentation, constituting the experimental group. These pupils actively participated in the post-atlas test to evaluate their overall understanding of the Atlas. It is crucial to emphasize that the percentages depicted in the subsequent table represent the outcomes derived from accurate positive responses provided by the pupils. Following the completion of the pre-atlas test for primary school pupils, the results obtained from this identical assessment are presented in the tables below:

Table 15. An overview of the post-atlas test questions administered to fifth-grade primary school pupils who actively engaged in the Atlas presentation and associated exercises, along with the corresponding success percentages

Questions	Success Percentages %
Question 1	71.24 %
Question 2	92.16 %
Question 3	48.37 %
Question 4	96.73 %
Question 5	54.90 %
Question 6	81.05 %
Question 7	90.20 %
Question 8	82.35 %
Question 9	87.58 %
Question 10	45.75 %
Question 11	75.16 %
Question 12	28.11 %
Question 13	92.81 %
Question 14	90.17 %
Question 15	92.16 %

As per the information in the provided tabular data, it can be inferred that query number 4 manifests the highest mean percentage of accurate responses, reaching 96.73%. In contrast, query 12 illustrates the lowest mean percentage of accurate responses, registering at 28.11%.

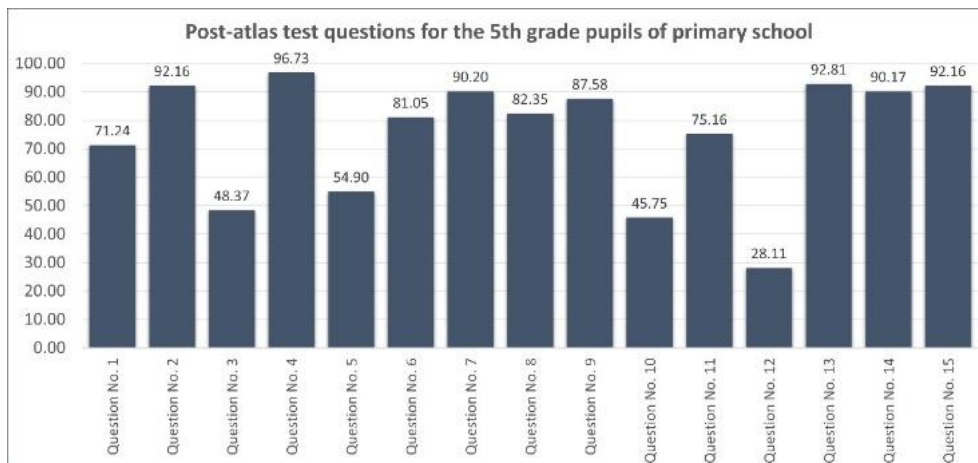


Figure 13. Post-atlas test questions for the 5th-grade pupils who did participate in the Atlas presentation and the success percentages are represented with a chart

The ensuing post-atlas test was carried out on fifth-grade pupils, involving 15 carefully formulated inquiries. These questions were categorized into three domains: A) Concepts related to Maps and Atlases, B) Comprehension of Directions, geographical regions, and neighboring areas, and C) Understanding of Tourism and Economy in North Macedonia. The subsequent table offers a detailed summary of the outcomes corresponding to these specific categories for fourth-grade pupils:

Table 16. An overview of the post-atlas test questions of categories administered to fifth-grade primary school pupils who actively engaged in the Atlas presentation and associated exercises, along with the corresponding success percentages

Questions	Success Percentages %
Category A	84.53 %
Category B	72.68 %
Category C	73.11 %

Derived from the information delineated in the presented tabular data, it is discernible that inquiries falling under Category A showcase the most elevated mean accuracy, attaining a value of 84.53%. Subsequently, queries classified under Category C also showcase a notable accuracy rate, totaling 73.11%. In contrast, questions categorized under Category B exhibit the lowest mean accuracy, sustaining a rate of 72.68%.

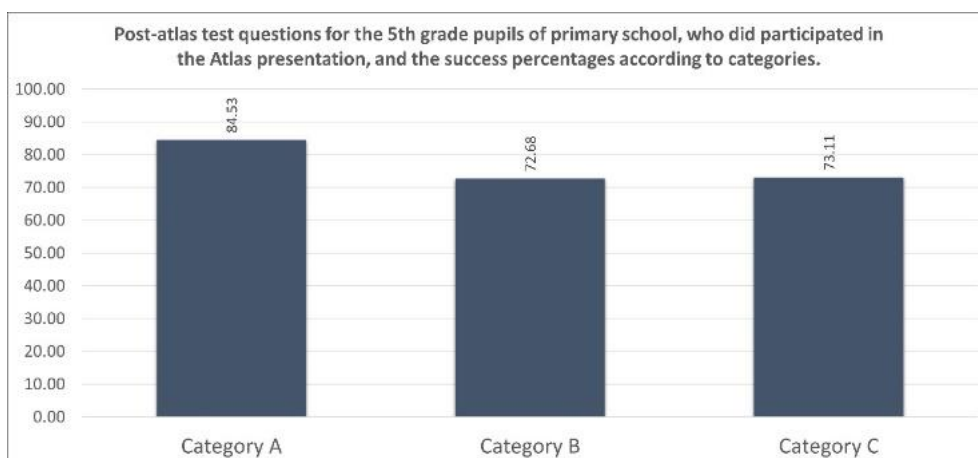


Figure 14. Post-atlas test questions for the 5th-grade pupils who did participate in the Atlas presentation and the success percentages are represented with a chart

Considering the outcomes presented in the preliminary tables pertaining to the post-atlas assessment, it is evident that the cohort of female pupils in the fifth-grade cohort attained an accuracy rate of 75.95%, while their male counterparts in the same grade achieved a slightly lower accuracy rate of 74.60%.

In this study, a comprehensive sample comprising 377 primary school pupils actively involved in the Atlas presentation and related activities, from the third to fifth grade and aged between 7 to 10 years, participated in a post-atlas test to evaluate their comprehensive understanding of the Atlas. These pupils also formed the experimental group that engaged in the atlas presentation. It is important to note that the percentages depicted in the subsequent table are derived from the pupils' accurate affirmative responses. Following the completion of the post-atlas test for primary school pupils, the following table presents the outcomes obtained from this evaluation:

Table 17. An overview of the post-atlas test questions administered to all primary school pupils (from 3rd grade to 5th grade) who actively engaged in the Atlas presentation and associated exercises, along with the corresponding success percentages

Questions	Success Percentages %
Question 1	70.26 %
Question 2	81.04 %
Question 3	39.61 %
Question 4	82.24 %
Question 5	59.73 %
Question 6	74.63 %
Question 7	77.84 %
Question 8	75.63 %
Question 9	83.48 %
Question 10	52.87 %
Question 11	70.85 %
Question 12	32.94 %
Question 13	83.95 %
Question 14	77.84 %
Question 15	77.78 %

As per the information in the provided tabular data, it can be inferred that query number 13 manifests the highest mean percentage of accurate responses, reaching 83.95%. In contrast, query 12 illustrates the lowest mean percentage of accurate responses, registering at 32.94%.

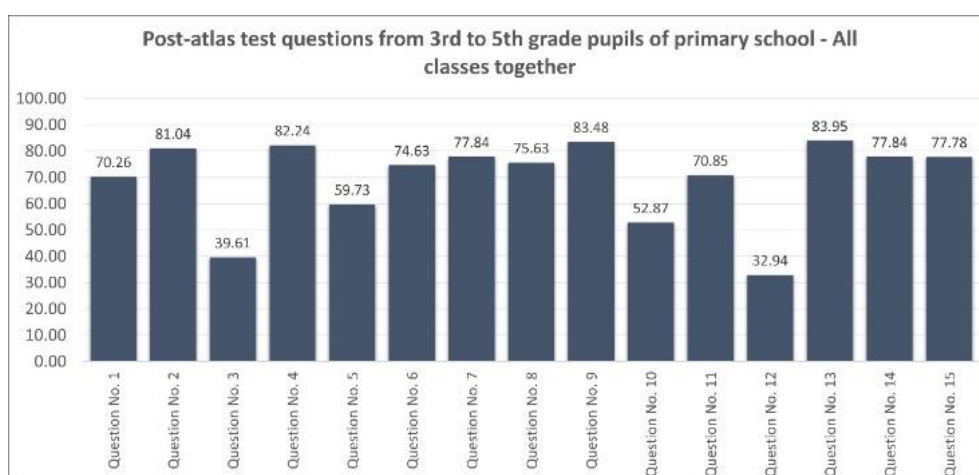


Figure 15. Post-atlas test questions for the 5th-grade pupils who did participate in the Atlas presentation and the success percentages are represented with a chart

The ensuing post-atlas test was carried out on pupils from 3rd to 5th grade, involving 15 carefully formulated inquiries. These questions were categorized into three domains: A) Concepts related to Maps and Atlases, B) Comprehension of Directions, geographical regions, and neighboring areas, and C) Understanding of Tourism

and Economy in North Macedonia. The subsequent table offers a detailed summary of the outcomes corresponding to these specific categories for fifth-grade pupils:

Table 18. An overview of the post-atlas test questions of categories administered to all primary school pupils (from 3rd to 5th grade) who actively engaged in the Atlas presentation and associated exercises, along with the corresponding success percentages

Questions	Success Percentages %
Category A	76.03 %
Category B	66.58 %
Category C	68.53 %

Derived from the information delineated in the presented tabular data, it is discernible that inquiries falling under Category A showcase the most elevated mean accuracy, attaining a value of 76.03%. Subsequently, queries classified under Category C also showcase a notable accuracy rate, totaling 68.53%. In contrast, questions categorized under Category B exhibit the lowest mean accuracy, sustaining a rate of 66.58%.

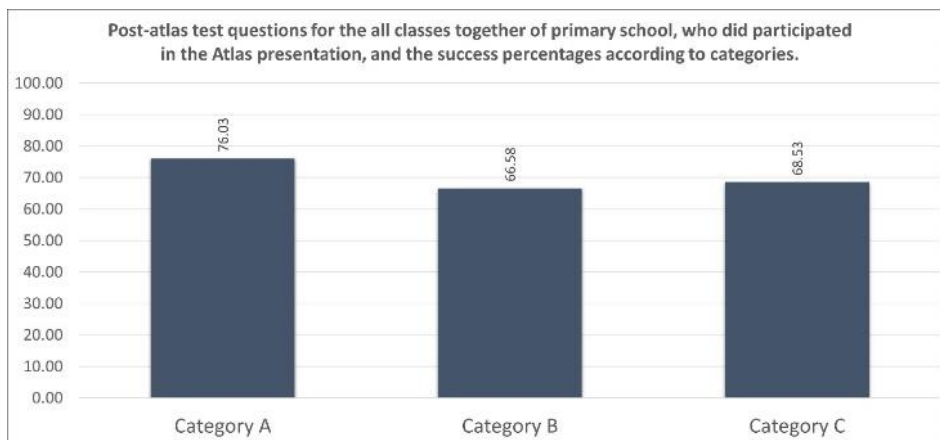


Figure 16. Post-atlas test questions for the 5th-grade pupils who did participate in the Atlas presentation and the success percentages are represented with a chart

Considering the outcomes presented in the preliminary tables pertaining to the post-atlas assessment, it is evident that the cohort of female pupils from the third to fifth grade cohort attained an accuracy rate of 72.42%, while their male counterparts in the same grade achieved a slightly lower accuracy rate of 70.84%.

T-tests were employed and calculated using Microsoft Excel to rigorously examine the significance of observed differences between distinct groups within our sample. The application of t-tests was pivotal in evaluating the effectiveness of the experimental intervention. This statistical approach, facilitated by Excel, enhances the reliability and validity of our findings, providing a robust basis for the conclusions drawn in this academic investigation. The following tables and descriptive texts related to the tables are presented as follows:

Table 19. Discoveries pertaining to the outcomes of pre-atlas and post-atlas assessments for third-grade pupils in primary education

Groups	Number of Pupils (N)	Arithmetic Average(X) (out of 100)	Standard Deviation (SD)	t value	P value
Pre Atlas	84	30.08	17.10	2.15	0.002
Post Atlas	84	50.32	15.78		

The table presents a comparative analysis of academic performance before and after implementing the Atlas program in a primary school setting. Prior to the program, the average score among 377 pupils was 30.08 out of 100, with a standard deviation of 17.10. Post-implementation, there was a substantial increase in the average score to 50.32, accompanied by a higher standard deviation of 15.78. The calculated t-value of 2.15 indicates a statistically significant difference between pre-Atlas and post-Atlas test results, further supported by a p-value of 0.002, confirming the significance of the findings. These results underscore the efficacy of the Atlas program in enhancing pupil learning outcomes and highlight its importance in driving positive educational outcomes in primary school settings.

Table 20. Discoveries pertaining to the outcomes of pre-atlas and post-atlas assessments for third-grade pupils in primary education

Groups	Number of Pupils (N)	Arithmetic Average(X) (out of 100)	Standard Deviation (SD)	t value	P value
Pre Atlas	140	40.05	22.16	2.15	0.00001
Post Atlas	140	82.57	16.12		

The provided table offers a comparative examination of academic performance metrics before and after the introduction of the Atlas program in a primary school context. Prior to the program, among 377 pupils, the average score was 40.05 out of 100, with a standard deviation of 22.16. Following the intervention, there was a notable enhancement in academic achievement, with the average score surging to 82.57 out of 100 and a decrease in the standard deviation to 16.12. The computed t-value of 2.15 indicates a statistically significant difference between pre-Atlas and post-Atlas assessment results, further supported by a p-value of 0.00001, affirming the substantial nature of the observed improvements. These findings highlight the efficacy of the Atlas program in augmenting pupil learning outcomes and emphasize its pivotal role in fostering positive educational advancements within primary school environments.

Table 21. Discoveries pertaining to the outcomes of pre-atlas and post-atlas assessments for third-grade pupils in primary education

Groups	Number of Pupils (N)	Arithmetic Average(X) (out of 100)	Standard Deviation (SD)	t value	P value
Pre Atlas	153	43.66	21.67	2.15	0.002
Post Atlas	153	75.25	21.16		

The table presents a comparative analysis of academic performance before and after implementing the Atlas program in a primary school setting. Prior to the program, the average score among 377 pupils was 43.66 out of 100, with a standard deviation of 21.67. Post-implementation, there was a substantial increase in the average score to 75.25, accompanied by a higher standard deviation of 21.16. The calculated t-value of 2.15 indicates a statistically significant difference between pre-Atlas and post-Atlas test results, further supported by a p-value of 0.002, confirming the significance of the findings. These results underscore the efficacy of the Atlas program in enhancing pupil learning outcomes and highlight its importance in driving positive educational outcomes in primary school settings.

Table 22. Discoveries pertaining to the outcomes of pre-atlas and post-atlas assessments for third-grade pupils in primary education

Groups	Number of Pupils (N)	Arithmetic Average(X) (out of 100)	Standard Deviation (SD)	t value	P value
Pre Atlas	377	37.93	18.72	2.15	0.0001
Post Atlas	377	69.38	15.98		

The provided table offers a comparative examination of academic performance metrics before and after the introduction of the Atlas program in a primary school context. Prior to the program, among 377 pupils, the average score was 37.93 out of 100, with a standard deviation of 18.72. Following the intervention, there was a notable enhancement in academic achievement, with the average score surging to 69.38 out of 100 and a decrease in the standard deviation to 15.98. The computed t-value of 2.15 indicates a statistically significant difference between pre-Atlas and post-Atlas assessment results, further supported by a p-value of 0.0001, affirming the substantial nature of the observed improvements. These findings highlight the efficacy of the Atlas program in augmenting pupil learning outcomes and emphasize its pivotal role in fostering positive educational advancements within primary school environments.

The findings presented based on the pre-test and post-test results with pupils that were part of the atlas presentation, through rigorous statistical analyses, underscore the effectiveness of the Atlas program in significantly improving academic performance among primary school pupils across multiple grade levels. The observed increases in average scores post-test implementation and notable decreases in standard deviations indicate a consistent pattern of enhanced learning outcomes attributed to the program. Furthermore, the statistically significant differences between pre-Atlas and post-Atlas test results, as evidenced by low p-values,

substantiate the impact of the intervention on fostering positive educational advancements. These results emphasize the pivotal role of the Atlas program in driving meaningful improvements in pupil learning outcomes and highlight its potential to contribute positively to educational practices within primary school settings. Future research endeavors should delve deeper into the mechanisms underlying these observed improvements to inform more targeted and effective educational interventions.

3.2. Discussion

By employing a comprehensive mixed-methods research design, this study seeks to thoroughly understand the effects of incorporating maps as educational tools in primary education. The development and testing of the pre-atlas and post-atlas tests ensure that the maps and accompanying information are suitable for primary school pupils, aligning with their cognitive abilities and spatial reasoning skills. The findings of this research will contribute empirical evidence on the advantages and challenges of using maps as educational tools, enabling educators, curriculum developers, and policymakers to make informed decisions and improve teaching practices. The pre-atlas and post-atlas tests are designed to assess pupils' knowledge and comprehension of the information presented on the maps within the Atlas. By analyzing the outcomes of these tests, a comparison can be drawn to assess the impact of the atlas on the enhancement of general knowledge, allowing for the presentation of results indicating the improvement achieved. This analysis provides valuable insights into the correlation between map usage and pupils' skill development, cognitive abilities, and overall academic performance. Furthermore, the analysis of the pre-atlas and post-atlas test data offers numerical findings that contribute to a statistical basis for understanding the impact of map utilization on spatial reasoning abilities, problem-solving skills, and pupil engagement and motivation. Additionally, the tests shed light on the challenges faced by educators, such as resource limitations and the need for adequate training. By combining these test data, this study aims to provide a comprehensive perspective on the advantages, challenges, and potential improvements related to integrating maps into primary education. Overall, the findings of this study are expected to inform educational practices, enhance the learning experiences of young learners, and promote the effective integration of maps into the primary education system. By establishing an evidence-based foundation, this research strives to maximize pupils' cognitive abilities, foster a comprehensive understanding of geographical concepts, and contribute to the overall efficacy of the educational system. With the conclusion of both the pre-atlas and post-atlas tests, the obtained results offer valuable insights into the evolving geographic awareness of primary school pupils, providing a foundation for informed pedagogical strategies and curricular improvements in geography education regarding the Republic of North Macedonia. The pre-test results revealed variations in the success percentages across different questions and categories. Remarkably, question number 8 consistently exhibited the highest average of correct answers among all the classes, reaching 70.93%, while question number 6 consistently demonstrated the lowest average at 16.81%. Additionally, analyzing the results based on category and grade levels showcased intriguing trends. Category C (Tourism and Economy in North Macedonia) consistently exhibited the highest mean accuracy at 47.50%. These findings contribute valuable insights into the geographic knowledge proficiency of primary school pupils and can inform future educational interventions to enhance geographical awareness and understanding. The post-test results also revealed variations in the success percentages across different questions; question number 13 consistently exhibited the highest average of correct answers between all the classes, reaching 83.95%, while question number 12 consistently demonstrated the lowest average at 32.94%. The highest mean accuracy was observed in questions pertaining to Map and Atlas concepts (Category A), with an average success rate of 76.03%. Conversely, questions categorized under Directions, geographical regions, and neighboring areas (Category B) demonstrated a comparatively lower mean accuracy of 66.58%. The study further identified notable differences in performance between female and male pupil groups, emphasizing the importance of considering gender dynamics in educational assessments. Overall, the findings underscore the need for targeted interventions to enhance geographic knowledge among primary school pupils, specifically focusing on areas with lower proficiency levels. Based on the findings derived from the pre-atlas test, it can be inferred that the academic performance of third-grade pupils exhibited a notable improvement of 20.24%.

Similarly, the fourth-grade pupils demonstrated a comparable improvement of 42.52% in their results. Furthermore, the fifth-grade pupils displayed a significant advancement of 31.59% in their academic outcomes. The results show that the collective progress or advancement of all the classes involved amounts to approximately 31.45%. Previous research by different authors has also aimed to demonstrate similar impacts. For instance, in Türkiye, Erol, in 2020 [43], conducted a study involving 206 pupils, where the mean score of pupils or students in public schools was reported as 38.12. Buğdaycı and Selvi conducted a study in 2021 [2] involving primary school pupils, revealing a notable enhancement of approximately 40% in children's knowledge performance following the utilization of maps and atlases. Furthermore, Buğdaycı and Çetinkaya [44] conducted one of the initial investigations in the field of cartography pertaining to Türkiye, focusing on enhancing disaster awareness among children. Their findings indicate a significant increase of approximately 39% in the knowledge levels of pupils following the intervention, as evidenced by test results. The observed improvements in academic performance among third-, fourth-, and fifth-grade pupils following the implementation of the Atlas program underscore its potential to enhance educational outcomes across multiple grade levels. These results suggest that incorporating interactive geographical tools like maps boosts pupils' spatial reasoning and problem-solving skills and increases their engagement and motivation in learning. Policymakers could consider these findings when designing curriculum frameworks prioritizing interactive and experiential learning methodologies. Policymakers can foster a more inclusive and effective educational environment by investing in similar educational interventions that cater to diverse learning styles and promote hands-on learning experiences. Moreover, the study highlights the importance of continuous teacher training and resource allocation to support the successful integration of innovative educational tools like maps into classroom instruction. These insights could guide future policymaking decisions aimed at improving educational quality and equitability across primary schools in North Macedonia, ultimately contributing to a more robust educational system capable of nurturing well-rounded and informed young learners.

4. Conclusion

This study aims to contribute significantly to the field of primary education by examining the impact of utilizing maps as educational tools for pupils or children. By providing empirical evidence on the positive effects of incorporating cartographic materials into the curriculum, the findings foster cognitive development and lead to improvements in the overall educational system. This research informs educators, curriculum developers, and policymakers about the benefits and challenges associated with integrating maps, guiding their efforts to enhance primary school education. Ultimately, the study seeks to promote effective teaching practices and enrich the learning experiences of young learners through the thoughtful implementation of maps as pedagogical resources. The findings can potentially drive positive change and advancements in primary education, benefiting pupils and the educational community.

In conclusion, using maps as pedagogical tools in primary education holds great potential for enhancing children's cognitive development and the overall effectiveness of the educational system. Incorporating maps into the curriculum can engage pupils in spatial thinking, improve problem-solving skills, and deepen their understanding of geographical concepts. However, limited empirical research has systematically examined the impact of maps on pupils' abilities and the educational framework. Therefore, this study addresses this gap by investigating the effects of utilizing maps for children and highlighting their potential benefits for both pupils and the primary school education system. This study was conducted as part of a project focused on compiling and designing an atlas for primary school pupils between the ages of 7 and 10 in the Republic of North Macedonia. 377 primary school pupils, ranging from third to fifth grade, participated in this study.

Additionally, including a diverse sample of primary school pupils spanning grades 3 to 5 and stratified by gender allowed for a comprehensive analysis of geographic knowledge acquisition, shedding light on gender dynamics in educational assessments and the importance of considering these dynamics in pedagogical strategies. The testing process took place in four different schools in the city of Tetovo, North Macedonia, comprising three urban schools and one school in a peripheral village surrounding the city. The results obtained

from the pre-atlas test and post-atlas test were positive. Based on the outcomes of these tests, it can be concluded that incorporating maps into the educational system and lessons enhances learning and proficiency among pupils by around 31.45%. Additionally, it increases the effectiveness and efficiency of the learning process. Using cartographic materials such as maps and atlases in the classroom improves the quality of education and fosters pupils' engagement and participation. The empirical evidence presented in this study supports the effective integration of maps as educational tools in primary education, offering valuable insights for educators, curriculum developers, and policymakers. By fostering a comprehensive understanding of geographical concepts and maximizing pupils' cognitive abilities, the integration of maps holds great potential to enhance the learning experiences of young learners and contribute to the overall efficacy of the educational system.

Author Contributions

All the authors equally contributed to this work. This paper is derived from the first author's master's thesis, supervised by the second author. They all read and approved the final version of the paper.

Conflicts of Interest

All the authors declare no conflict of interest.

Ethical Review and Approval

No approval from the Board of Ethics is required.

Acknowledgment

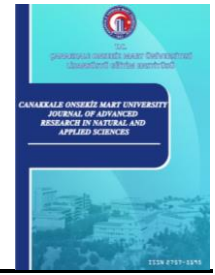
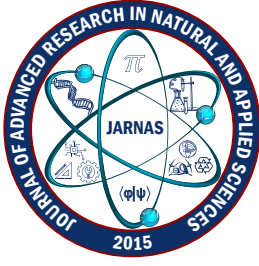
This work was supported by the Office of Scientific Research Projects Coordination at Necmettin Erbakan University, Grand number: 23YL19002.

References

- [1] T. Bandrova, *A cartographic atlas created for and with the help of children*, in: Proceedings of the Joint Seminar on Discovering Basic Concepts, Canada, 1999, pp. 45–49.
- [2] I. Bugdayci, H. Z. Selvi, *Teaching map concepts in social science education: An evaluation with undergraduate students*, in: IOP Conference Series: Earth and Environmental Science IOP Publishing, Prague, 2017, 7 pages.
- [3] I. Bugdayci, H. Z. Selvi, *Do maps contribute to pupils' learning skills in primary schools?*, The Cartographic Journal 58 (2) (2021) 135–149.
- [4] M. Robertson, R. Gerber, *The child's world: Triggers for learning*, Australian Council for Education Research, Camberwell, 1999.
- [5] T. Bandrova, A. Deleva, *Contemporary cartography for children in Bulgaria*, in: J. M. Anderson, E. Krzywicka-Blum (Eds.), *The Joint Seminar Maps for Special Users*, Wroclaw, 1998, pp. 59–78.
- [6] J. M. Anderson, R. Vasconcellos, *Maps for and by children: Possible contributions by cartographers*, in: 17th International Cartographic Conference, Barcelona, Spain, 1995, 9 pages.
- [7] E. Brule, G. Bailly, A. Brock, F. Valentin, G. Denis, C. Jouffrais, *MapSense: Multi-sensory interactive maps for children living with visual impairments*, in: J. Kaye, A. Druin (Eds.), *Proceedings of the 2016 CHI Conference on Human Factors in Computing Systems*, San Jose, 2016, pp. 445–457.
- [8] A. Okada, S. Buckingham Shum, *Evidence-based dialogue maps as a research tool to investigate the*

- quality of school pupils' scientific argumentation*, International Journal of Research and Method in Education 31 (3) (2008) 291–315.
- [9] M. Myridis, A. Christodoulou, E. Kalyva, N. Karanikolas, P. Lafazani, *Cartography and children: Designing a multimedia educational tool*, in: I. Drecki (Ed.), 23rd International Cartographic Conference, Moscow, 2007, 12 pages.
- [10] M. Peter, J. Glück, W. Beiglböck, *Map understanding as a developmental marker in childhood*, Journal of Individual Difference 31 (2) (2010) 64–67.
- [11] B. Bartz, *Map design for children*, Field Research Corporation, Chicago, 1965.
- [12] P. Sorrell, *Map design with the young in mind*, The Cartographic Journal 11 (2) (1974) 82–90.
- [13] R. Gerber, *Factors affecting the competence and performance in map language for children at the concrete level of map-reasoning*, Cartography 13 (3) (1984) 205–213.
- [14] B. Buckingham, M. Harrower, *The role of color saturation in maps for children*, Cartographic Perspectives (58) (2007) 28–47.
- [15] D. Owen, *Primary children's collaborative cartography: Communication and mapping processes*, Education, Computer Science, Geography (2005) 10 pages.
- [16] A. Robinson, *The looks of maps: An examination of cartographic design*, Madison, University of Wisconsin Press, Madison, 1952.
- [17] G. Jenks, D. Knos, *The use of shading patterns in graded series*, Annals Association of American Geographers 51 (3) (1961) 316–334
- [18] P. Crawford, *Perception of grey-tone symbols*, Annals of the Association of American Geographers 61 (4) (1971) 721–735.
- [19] J. Kimerling, *Color specification in cartography*, American Cartographer 7 (2) (1980) 139–153.
- [20] J. Olson, *Spectrally encoded two-variable maps*, Annals Association of American Geographers 71 (2) (1981) 259–276.
- [21] E. Imhof, *Cartographic Relief Presentation*, De Gruyter, New York, 1982.
- [22] A. M. MacEachren, *How maps work: Representation, visualization and design*, Guilford, New York, 1995.
- [23] B. Dent, *Thematic map design*, WCB/McGraw-Hill, Boston, 1999.
- [24] C. A. Brewer, G. Hatchard, M. A. Harrower, *ColorBrewer in print: A catalog of color schemes for maps*, Cartography and Geographic Information Science 30 (1) (2003a) 5–32.
- [25] W. C. Wang, C. C. Lee, Y. C. Chu, *A brief review on developing creative thinking in young children by mind mapping*, International Business Research 3 (3) (2010) 6 pages.
- [26] P. Weeden, *Learning through maps*, in: D. Tilbury, M. Williams (Eds.), *Teaching and Learning Geography*, Routledge, London, 1997, Ch. 16, pp. 168–179.
- [27] D. H. Uttal, H. M. Wellman, *Young children's representation of spatial information acquired from maps*, Developmental Psychology 25 (1) (1989) 128–138.
- [28] D. R. Montello, *Cognitive map-design research in the twentieth century: Theoretical and empirical approaches*, Cartography and Geographic Information Science 29 (3) (2002) 283–304.
- [29] S. McLeod, *Jean Piaget's theory of cognitive development*, Simply Psychology 18 (3) (2018) 1–9.
- [30] Z. Babakr, P. Mohamedamin, K. Kakamad, *Piaget's cognitive developmental theory: Critical review*, Education Quarterly Reviews 2 (3) (2019) 8 pages.

- [31] B. Lefa, *The Piaget theory of cognitive development: An educational implication*, Educational Psychology 1 (1) (2014) 1–8.
- [32] J. Piaget, *Piaget's theory*, Handbook of Child Psychology, Wiley, New York, 1983.
- [33] K. W. Fischer, *A theory of cognitive development: The control and construction of hierarchies of skills*, Psychological Review 87 (6) (1980) 477–531.
- [34] P. Wiegand, *Oxford international primary atlas*, 2nd Edition, Oxford University Press, Oxford, 2011.
- [35] P. Wiegand, *Oxford school atlas*, 3rd Edition, Oxford University Press, Singapore, 2012a.
- [36] P. Wiegand, *Oxford student atlas*, 4th Edition, Oxford University Press, Singapore, 2012b.
- [37] P. Wiegand, *Oxford international student's skills workbook*, 3rd Edition, Oxford University Press, New York, 2012c.
- [38] J. J. Reyes Nuñez, C. E. Juliarena de Moretti, E. Gallé, A. M. Garra, C. A. Rey, M. V. Alves de Castro, A. S. Dibiase, *Reading thematic maps in Argentine and Hungarian schools*, in: XXII International Cartographic Conference ICC2005, A Coruña, 2005, pp. 9–16.
- [39] T. Bandrova, C. Dinev, *The new cartographic products in Bulgaria-modern school atlases*, In CD Proceedings of the XXII International Cartographic Conference ICC2005, A Coruña, Spain, 2005, 8 pages.
- [40] N. Safaraliyeva, N. Al Hosani, J. J. Reyes Nunez, *Teaching basic map concepts in three countries: Azerbaijan, Hungary and United Arab Emirates*, International Journal of Cartography 5 (2-3) (2019) 285–303.
- [41] H. Kramáreková, M. Nemčíková, M. Vojtek, A. Dubcová, B. Gajdošíková, M. Konečný, *Comparison of cartographic language of pupils in the 4th grade of primary school case study of the Slovak republic and Czech republic*, in: T. Bandrova, M. Konecny (Eds.), 6th International Conference on Cartography and GIS, Albena, 2016, pp. 13–17.
- [42] İ. Buğdaycı, I. O. Bildirici, *Map use, map user and map maker: An evaluation of the current education material containing maps for pupils in Turkey*, in: 3rd International Conference on Cartography and GIS, Nessebar, 2010, 9 pages.
- [43] H. Erol, *8th grade students' positioning skills on the map*, Eurasian Journal of Educational Research 20 (88) (2020) 67–86.
- [44] I. Buğdaycı, E. Cetinkaya, *Designing teaching materials with disaster maps and evaluating its effectiveness for primary students*, Open Geosciences 14 (1) (2022) 675–690.



Effect of Sound Absorption on Noise Reduction in the Automotive Industry

Muammer Yaman¹ , Cüneyt Kurtay² 

¹Department of Architecture, Faculty of Architecture, Ondokuz Mayıs University, Samsun, Türkiye

²Department of Architecture, Faculty of Fine Arts, Design and Architecture, Başkent University, Ankara, Türkiye

Article Info

Received: 24 Jul 2024

Accepted: 12 Sep 2024

Published: 30 Sep 2024

Research Article

Abstract – Industrial noise is one of the most common physical factors that cause annoyance and damage to workers' health in the long term. Precautions should be taken to reduce noise and to improve acoustic performance in industrial working environments. This paper aims to analyze the acoustic performance of the automotive industry contributes to the global outcomes of sustainability and develop strategies for improving the quality of the working environment through improvement scenarios. For this purpose, the automotive industry in Türkiye was examined as a case study. In-situ acoustic measurements were made in the seat manufacturing unit of an automotive factory, and the current situation was transferred to the simulation program. The effects of acoustic improvements on A-weighted sound pressure level and reverberation time at mid-frequencies (500, 1000, 2000 Hz) were investigated through three scenarios. In the investigations, noise distributions were carried out through noise mapping. The A-weighted sound pressure levels in the automotive industry were reduced by approximately 15 dB. As a result of the study, suggestions for noise control precautions and their effects on the automotive industry seat manufacturing unit are presented.

Keywords – *Acoustics simulation, automotive industry, industrial noise control, noise reduction, sound absorption*

1. Introduction

Industrial noise has been one of the important physical risk factors for employee health. Noise has physical, physiological, and psychological effects on workers and major effects on worker productivity [1-3]. Noise affects people's nervous system and hearing, weakens workers' concentration, and reduces attention and reaction skills [4-5]. However, the productivity and efficiency of employees, which vary due to noise, have been important factors affecting the overall performance of any organization, from small to large companies [6]. Since the 90s, interest in the relationship between the working environment and productivity has increased, and, in this context, research has focused on employee job satisfaction, and reforms and improvements have been made.

The automotive industry is one of the most developed industries in the world and is the engine of the economy of many states. The automotive industry is characterized by high consumption of raw materials to produce cars, trucks, and buses. Some companies have units with a full production cycle, and several companies only deal with the assembly and production of automobile parts [7, 8]. Employee productivity in the automotive industry needs to be increased by improving health and safety conditions in the workplace. Occupational noise in the automotive industry has been a detailed area evaluated and studied.

Depending on various production processes in the automotive industry, different noise levels occur and the

¹mimar.myaman@gmail.com (Corresponding Author); ²cuneytkurtay@baskent.edu.tr

noise exposure levels of employees vary. However, it has been determined that indoor noise levels are high according to the regulations of the relevant countries in the measurements made in automotive factories [9-14]. A hierarchy of noise control steps should be followed in controlling production area noise in factories. Within the scheme, precautions should be taken and implemented from the highest to the lowest impact (Figure 1). In the hierarchy of noise control, it is generally necessary to take various precautions at the source, transmission path, and receiver [15-17]. The most effective and expected noise control is achieved through engineering control precautions at the source and the transmission path. Different approaches to engineering control methods exist in factories [18, 19]. Variables such as industrial sector, production process, machine and human interactions, and plant characteristics effectively determine the noise control precautions that can be taken. Simultaneously, the noise control precautions should be compatible with other working conditions and not harm the production process. For this reason, using absorptive materials, noise barriers, and enclosures creates effective engineering noise control precautions in industrial plants [20-22]. Moreover, noise control by absorption and enclosure of the source are effective noise control mechanisms in the transmission path. Research on noise control in automotive factories is quite limited.

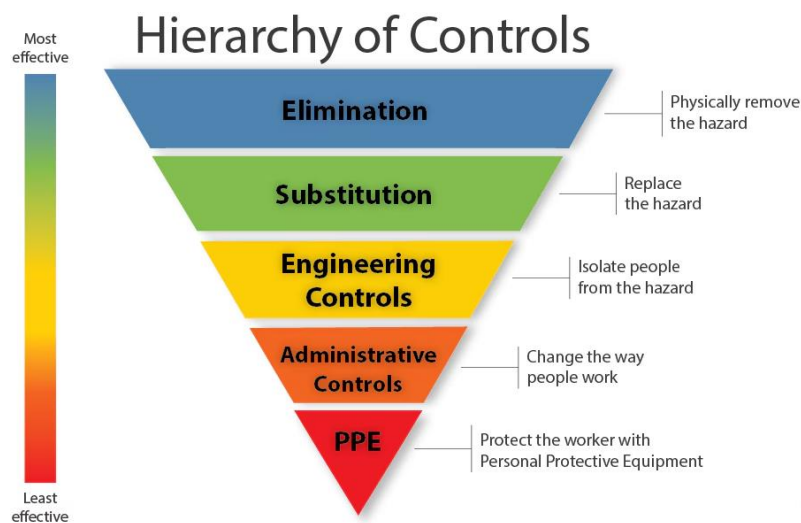


Figure 1. Hierarchy of noise control [17]

This study aims to perform acoustic measurements in the seat manufacturing unit, a part of the automotive industry with high sound pressure levels, and to determine the effects of the precautions that can be taken depending on the absorption of sound and the enclosure of the source on noise reduction. The effects of the precautions that can be applied in noise reduction are analyzed in a simulation environment, and their distributions are shown by the noise mapping method. A-weighted sound pressure levels, noise reduction values, and reverberation times at mid-frequency bands (500, 1000, 2000 Hz) for different scenarios were determined. Mid-frequency bands were used in the study since the sound level the human ear can hear sensitively occurs at mid-frequency bands.

2. Material and Methods

2.1. Case Study

The research selected the seat manufacturing unit of an automotive factory in Türkiye as a case study. The automotive factory is divided into main production halls, storage units, technical spaces, and administrative units. In the seat manufacturing unit, which is within the scope of the main production halls, fabric, foam, and coating processes are carried out for seat sets. The unit has an area of 2000 m², measuring approximately 50 m x 40 m. In the factory, the floor (lean concrete + coating), walls (metal panel), and ceiling (metal panel) are created with materials with high sound reflectivity. Accordingly, the hall in the case study creates an acoustic environment with high sound-reflecting properties. Additionally, the unit has a two-stage production process at ground and platform levels (Figure 2).

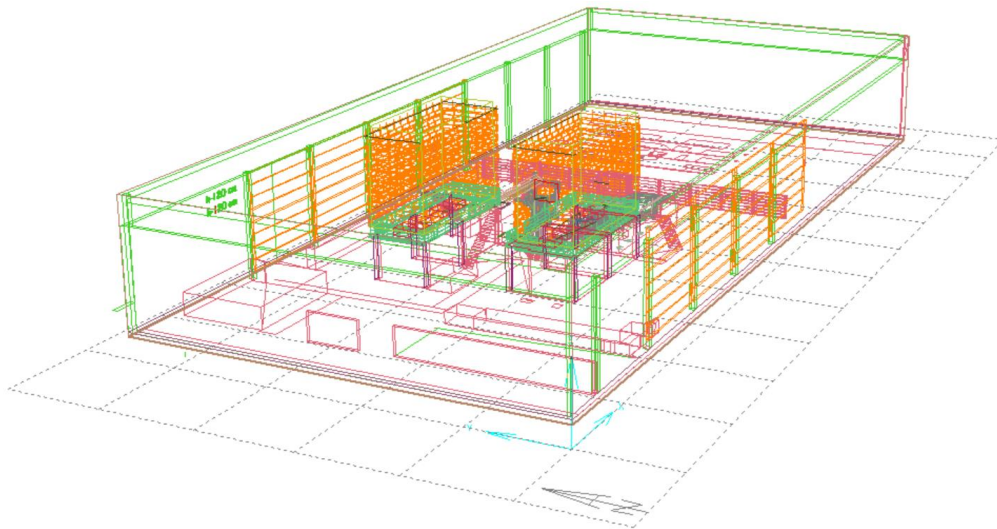


Figure 2. Seat manufacturing unit in the automotive industry

2.2. Acoustics Data Analysis and Simulations

Interior acoustic measurements were made in the seat manufacturing unit of the automotive factory. A sound level meter (testo 816-1, IEC 61672-1 Class 2) was used for acoustic measurements. Acoustic measurements were made in the seat manufacturing unit by ISO 9612:2009 standard, and A-weighted sound pressure levels were determined [23].

The seat manufacturing unit was modeled in the 3D computer environment. Existing machines (polyurethane filling machines, machines on platforms, vacuuming machines, and conveyors) were transferred to the model as sound sources. The acoustic environment of the unit was transferred to the simulation program (calibration) based on the sound pressure levels determined by acoustic measurements and the sound power levels in the catalog information of the existing machines. In the simulation program, surface sound absorption coefficients were defined following the properties of the finish materials of the building elements. Autodesk Ecotect v.5.20, a Building Information Modeling (BIM) software, was used as the simulation program. The simulation program used, Autodesk Ecotect, creates many random rays and examines the damping of the rays [24, 25]. This data generates the average damping curve for each frequency band in the spectrum distribution, and the environment's sound pressure level and reverberation time are calculated.

Various scenarios were created to reduce the A-weighted sound pressure levels, which are currently high. The effects of the scenarios on the indoor sound pressure level, the noise reductions, and reverberation times at mid-frequencies (500, 1000, 2000 Hz) were investigated. Existing ceiling materials were retained in the scenarios (due to intervention limitations). In the geometrical acoustic analysis investigated by simulation, 20000 beams with 12 reflections were used. The data obtained were analyzed using sound-absorbing panels on the wall and interior planes and by enclosing the machines on the platform and the results were evaluated.

A weighted sound pressure level used to compare the results of different scenarios expresses the relative loudness of sounds the human ear perceives. A-weighting first adjusts the measured octave-band decibel levels to account for human decreased sensitivity to sound levels at low frequencies, then uses decibel addition of the newly weighted sound level values at each octave band [26, 27]. Within the scope of the research, an A-weighted sound pressure level was used to determine the sound level of the current situation, and the simulation results were used to determine the ambient sound levels. Simultaneously, the simulation results were used as the difference between the current situation and the result in calculating the effect of simulation results on noise reduction.

The reverberation time used to determine the effect of surface absorption on acoustic comfort is determined by the volume of the space and the sound absorption coefficients and surface areas of the finish materials used [28]. Wallace C. Sabine (1868-1919) determined the examination of reverberation time in the control of room

acoustic performance and made acoustic evaluations to strengthen the effect of auditory performances [29]. Different calculations approaches, and application areas have been developed in the historical process to determine the reverberation time. However, Sabine's equation is especially preferred and used in architectural and room acoustics [30, 31]. In this research, Sabine's equation analyzes the change of reverberation time at mid-frequencies (500, 1000, and 2000 Hz) over different noise reduction scenarios to be applied in the automotive industry. Using the optimum reverberation time for any parameter in industrial facilities is impossible. However, the change of reverberation time depending on the surface absorption is an effective parameter in noise reduction.

3. Results and Discussion

3.1. Acoustic Measurements

Sound pressure level measurements were made at various points (for employee positions) in the seat manufacturing unit of the automotive factory. Acoustic measurements revealed a sound pressure level distribution of 70-88 dBA on the floor and 60-80 dBA on the platform. It was observed that sound pressure levels increased in the sections close to the engines of the machines. With this situation, it has been determined that high noise exposure levels occur when machine and employee interaction is considered. Reducing sound pressure levels with rational and appropriate interventions in the indoor environment is necessary.

3.2. Acoustic Simulations

In the seat manufacturing unit of the automotive factory, solutions were developed to cover the structural elements with high sound reflective properties with materials with high sound absorption properties and to enclose the machines with high sound power levels in an insulated enclosure. For this purpose, a material with a high sound absorption coefficient ($\alpha_w=1$, ISO 11654) was selected and used in acoustic simulations [32] (Figure 3). An important criterion was that the material should be non-combustible (A2 - A) according to EN 13501-1 and ASTM E84 [33, 34]. Additionally, the material used in the automotive industry is impact-resistant and long-lasting.

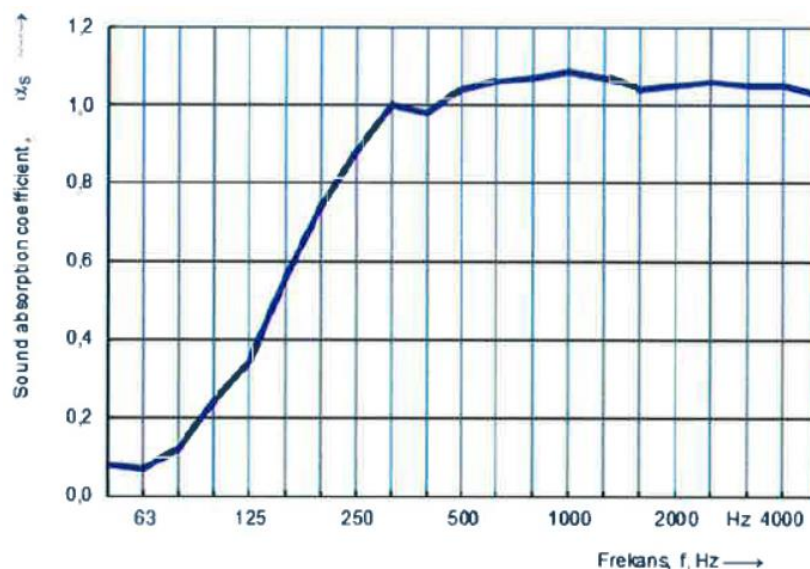


Figure 3. The sound absorption coefficient of the new material

Three different possible action scenarios for reducing sound pressure levels in the existing unit were developed, and their effects on indoor sound pressure levels, noise reduction, and reverberation times at mid-frequencies (500, 1000, 2000 Hz) on the ground and platform were investigated. The acoustic environment created by the rational solutions for the employees on the floor and platform was analyzed (Table 1).

Table 1. Scenarios for noise reduction and their effects on the acoustic environment

	Properties	SPL dB(A)	Noise Reduction (dB)	Reverberation Time, s		
				500 Hz	1000 Hz	2000 Hz
Current Situation	Seat manufacturing unit of the automotive factory with high reflective properties	Ground: 70-88 Platform: 60-80	-	13,03	16,70	9,64
Scenario 1	<ul style="list-style-type: none"> - Use of sound-absorbing materials on the walls surrounding the production unit (up to 9,20 m) - Enclosure with sound-absorbing material on the platform - the top is covered (h: 5 m) - Use of sound-absorbing material on the sides of the mold cleaning bench (h: 2 m)* - Use of sound-absorbing material on conveyor sides (h: 2 m)* 	Ground: 50-65 Platform: 55-75	Ground: 20-23 Platform: 5	0,24	0,24	0,24
Scenario 2	<ul style="list-style-type: none"> - Use of sound-absorbing materials on the walls surrounding the production unit (up to 8 m) - Enclosure with sound-absorbing material on the platform - the top is uncovered (h: 3 m) - Use of sound-absorbing material on the sides of the mold cleaning bench (h: 2 m)* - Use of sound-absorbing material on conveyor sides (h: 2 m)* 	Ground: 50-68 Platform: 55-70	Ground: 20 Platform: 5-10	1,74	1,75	1,67
Scenario 3	<ul style="list-style-type: none"> - Use of sound-absorbing materials on the walls surrounding the production unit (up to 8 m) - Enclosure with sound-absorbing material on the platform - the top is covered (h: 2 m) - Use of sound-absorbing material on the sides of the mold cleaning bench (h: 2 m)* - Use of sound-absorbing material on conveyor sides (h: 2 m)* 	Ground: 54-72 Platform: 56-73	Ground: 16 Platform: 4-7	1,88	1,89	1,81

* Precautions that are the same in all scenarios are described.

In Scenario 1, it was determined that the A-weighted sound pressure levels were 50-65 dBA on the floor and 55-75 dBA on the platform by covering the walls surrounding the production area with sound-absorbing material (up to 9,20 m), enclosing the platform in an enclosure with sound-absorbing material (h: 5 m), covering the sides of the mold cleaning bench with sound-absorbing material (h: 2 m), covering the conveyor sides with sound-absorbing material (h: 2 m). The noise control methods applied for Scenario 1 and the resulting noise map were prepared (Figure 4). Noise reduction was approximately 20 dB on the ground and 5 dB on the platform. Reverberation times were 0,24 s for 500 Hz, 0,24 s for 1000 Hz, and 0,24 s for 2000 Hz.

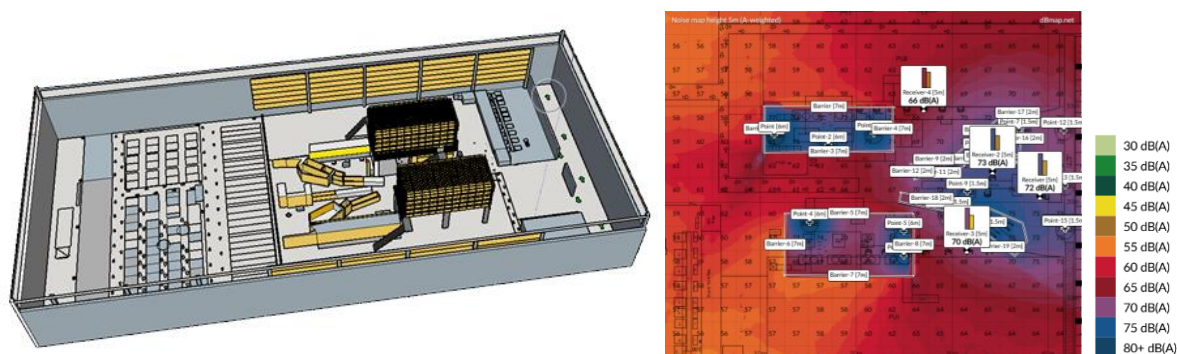


Figure 4. Noise control methods in Scenario 1 and the noise map created at a height of 1,5 m

In Scenario 2, it was determined that the A-weighted sound pressure levels were 50-68 dBA on the floor and 55-70 dBA on the platform with the processes of covering the walls surrounding the production area with sound-absorbing material (up to 8.00 m), enclosing the platform in an open cell with sound-absorbing material (h: 3 m), covering the sides of the mold cleaning bench with sound-absorbing material (h: 2 m), covering the conveyor sides with sound-absorbing material (h: 2 m). The noise control methods applied for Scenario 2 and the resulting noise map were prepared (Figure 5). Noise reduction was determined as 20 dB on the ground and

approximately 5-10 dB on the platform. Reverberation times were 1,74 s for 500 Hz, 1,75 s for 1000 Hz, and 1,67 s for 2000 Hz.

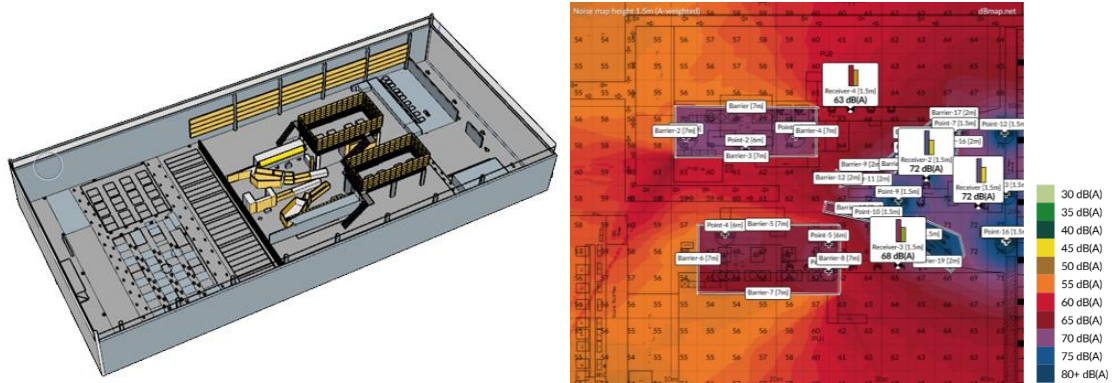


Figure 5. Noise control methods in Scenario 2 and the noise map created at a height of 1,5 m

In Scenario 3, it was determined that the A-weighted sound pressure levels were 54-72 dBA on the floor and 56-73 dBA on the platform with the processes of covering the walls surrounding the production area with sound-absorbing material (up to 8,00 m), enclosing the platform in an open cell with sound-absorbing material (h: 2 m), covering the sides of the mold cleaning bench with sound-absorbing material (h: 2 m), covering the conveyor sides with sound-absorbing material (h: 2 m). The noise control methods applied for Scenario 2 and the resulting noise map were prepared (Figure 6). Noise reduction was determined as 16 dB on the ground and approximately 4-7 dB on the platform. Reverberation times were 1,88 s for 500 Hz, 1,89 s for 1000 Hz, and 1,81 s for 2000 Hz.

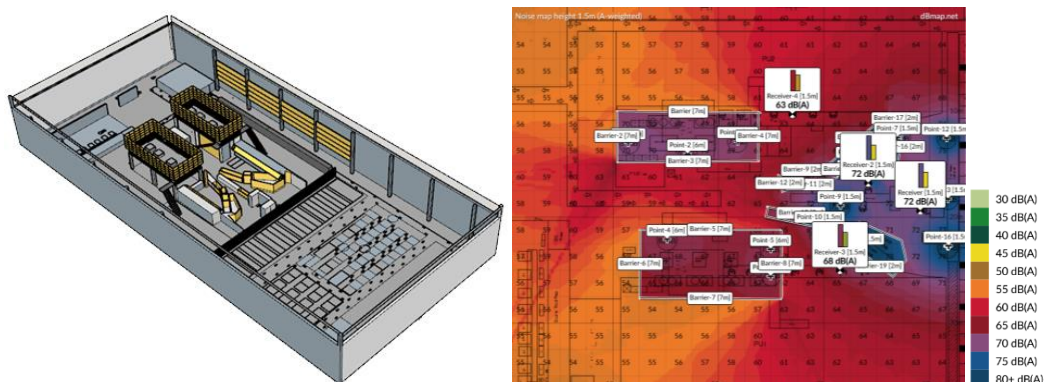


Figure 6. Noise control methods in Scenario 3 and the noise map created at a height of 1,5 m

Sound pressure level controls were carried out in two steps in the seat manufacturing unit of the automotive factory. In enclosed room conditions, it is aimed to prevent sound waves from increasing the sound pressure level in the environment by reflections. Accordingly, a suitable acoustic environment was created by reducing the reverberation time. Scenario 1 was created with the noise control methods on the current situation, possible interventions and variables were applied, and scenario 2 and scenario 3 were obtained. The precautions applied on the floor for noise control achieved a success of over 15 dB. However, the noise control measures applied on the platform achieved only 5-10 dB. The location of the machines (sound sources) close to the platform and the fact that the ceiling could not be intervened in the case study effectively achieved these results.

Additionally, noise reduction with sound absorption in the enclosure method yielded effective results. Using the enclosure as a noise barrier with sound absorption properties has created an effective sound absorption property in the enclosure method. The noise levels inside the enclosure evidence are higher than the existing environment in the noise maps. It has been observed that in the enclosure method, the closed top and the enclosure's high height provide the most effective sound absorption. Accordingly, the reverberation time at mid-frequencies is greatly decreased. Compared to planar sound-absorbing panels inside the room, it was observed that enclosing sound sources in isolated enclosures provides more effective results.

4. Conclusion

Seat manufacturing units in automotive factories create noisy working environments with high sound pressure levels. Precautions need to be taken to protect employees' health and eliminate noise. For this purpose, various noise control precautions are applied at the source, transmission path, and receiver. However, the most applicable methods for existing buildings are detailed with precautions to be taken directly in the transmission path. Intervening in the reverberant sound field with the principle of sound absorption is sufficient to provide the required reduction values on the floor and platform in the unit. The use of sound-absorbing materials in the room and the enclosure of sound sources effectively create a suitable and quieter acoustic environment. Preventing the spread of sound into the space with the enclosure method and absorbing it inside the enclosure plays an important role in shaping the sound pressure level distribution of the environment. It should be known that the reverberation time, which cannot be used as a direct objective parameter in factories, may vary according to the sound absorption capacity of the environment. It is planned to test alternative scenarios in different simulation tools and analyze the success rates of simulation results by creating the scenario results in the facilities. Moreover, it is recommended to investigate the acoustic characteristics of other automotive industry units and the effects of different noise control precautions on the acoustic environment in various units.

Author Contributions

The first and second authors devised the main conceptual ideas and developed the theoretical framework. The first and second authors performed the experiment and simulation analyses. The first author wrote the manuscript with support from the second author. The second author reviewed and edited the paper. All authors read and approved the final version of the paper.

Conflicts of Interest

All the authors declare no conflict of interest.

Ethical Review and Approval

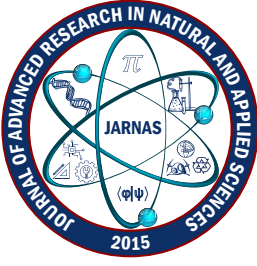
No approval from the Board of Ethics is required.

References




- [1] I. Alimohammadi, F. A. Kanrash, J. Abolaghasemi, H. Afrazandeh, K. Rahmani, *Effect of chronic noise exposure on aggressive behavior of automotive industry workers*, International Journal of Occupational Environmental Medicine 9 (2018) 170–175.
- [2] Y. Chen, M. Zhang, W. Qiu, X. Sun, X. Wang, Y. Dong, Z. Chen, W. Hu, *Prevalence and determinants of noise-induced hearing loss among workers in the automotive industry in China: A pilot study*, Journal of Occupational Health 61 (5) (2019) 387–397.
- [3] M. Yaman, C. Kurtay, G. Ulukavak Harputlugil, *Acoustical environments in the textile industry facilities: A case study of Malatya Province, Türkiye*, In Proceedings of INTER-NOISE 2023, Chiba, Greater Tokyo, Japan, 2023.
- [4] E. Atmaca, I. Peker, A. Altin, *Industrial noise and its effects on humans*, Polish Journal of Environmental Studies 14 (6) (2005) 721–726.
- [5] M. D. Fernández, S. Quintana, N. Chavarría, J. A. Ballesteros, *Noise exposure of workers of the construction sector*, Applied Acoustics 70 (2009) 753–760.

- [6] C. Rinjea Costache, O. R. Chivu, A. I. Țăpîrdea, A. Feier, L. Dascălu, A. C. Firu, C. Babis, *Professional exposure to noise in the automotive industry*, Journal of Research and Innovation for Sustainable Society 2 (2) (2020) 37–42.
- [7] S. I. Monye, S. A. Afolalu, S. L. Lawal, T. T. Gisanrin, O. A. Oluwatoyin, A. G. Adeyemi, *Now and future challenges of the automobile industry in the developing world*, In Proceedings of E3S Web of Conferences, 430, ICMPC, 2023.
- [8] H. M. V. Montemayor, R. H. Chanda, *Automotive industry's circularity applications and industry 4.0*, Environmental Challenges 12 (2023) 100725.
- [9] Z. Wang, J. Liang, X. Rong, H. Zhou, C. Duan, W. Du, Y. Liu, *Noise hazard and hearing loss in workers in automotive component manufacturing industry in Guangzhou, China*, Chinese Journal of Industrial Hygiene and Occupational Diseases 33 (12) (2015) 906–909.
- [10] L. Luo, J. Jiang, S. L. Huang, J. He, J. M. Li, *Analysis on characteristics of hearing loss in occupational noise-exposed workers in the automotive manufacturing industry*, Chinese Journal of Industrial Hygiene and Occupational Diseases 36 (6) (2018) 445–448.
- [11] D. P. Duan, L. X. Bai, C. X. Qiu, T. Y. Huang, S. H. Tang, Y. M. Liu, *Combined effect of noise and hand-transmitted vibration on noise-induced hearing loss in the automobile manufacturing industry*, Chinese Journal of Industrial Hygiene and Occupational Diseases 38 (6) (2020) 420–423.
- [12] Y. X. Tang, Y. R. Li, C. W. Duan, S. F. Hou, J. Y. Wang, Y. M. Liu, *Characteristics at different frequencies of hearing loss in noise exposure workers of the automobile manufacturing industry*, Chinese Journal of Industrial Hygiene and Occupational Diseases 39 (4) (2021) 266–269.
- [13] N. A. M. Zulkefli, M. F. Rusli, A. A. Rahman, *Predictors of knowledge, attitude, and practice of noise induced hearing loss among workers in an automotive industry in Malaysia*, Malaysian Journal of Medicine and Health Sciences 13 (1) (2017) 61–68.
- [14] Ü. Taş, E. Pak, B. Uğur, *Recent engineering applications for noise reduction in an automotive industry*, Journal of Advanced Research in Natural and Applied Sciences 10 (1) (2024) 207–217.
- [15] W. W. Lang, G. C. Maling, *Noise as a technological and policy challenge*, The Bridge National Academy of Engineering 37 (3) (2007) 4–10.
- [16] A. D. Bies, C. H. Hansen, *Engineering noise control theory and practice*, 3rd Edition, London, New York, E and FN Spon Press, 2003.
- [17] NIOSH, National Institute for Occupational Safety and Health, Url: <https://www.cdc.gov/niosh/hierarchy-of-controls/about/index.html> Accessed 18 July 2024
- [18] M. Mokhtar, S. Kamaruddin, Z. A. Khan, Z. Mallick, *A study on the effects of noise on industrial workers in Malaysia*, Jurnal Teknologi 46 (A) (2007) 17–30.
- [19] E. K. Putro, S. Mangkoedihardjo, N. Karnaningroem, E. S. Pandabessi, A. D. Syafei, *Industrial noise mapping: Literature review, designed for new plant operation*, In Proceedings of E3S Web of Conferences, ICENIS 2023, 448, 03059, (2023).
- [20] N. Ilgürel, *Effectiveness of the total absorption on noise reduction in industrial plants*, Noise Control Engineering Journal 61 (1) (2013) 11–25.
- [21] R. Golmohammadi, M. R. Monazzam, Z. Hashemi, S. M. B. Fard, *Pattern evaluation of noise propagation at various units of a textile industry*, Caspian Journal of Applied Sciences Research 3 (6) (2014) 1–8.
- [22] M. Kavraz, and R. Abdulrahimov, *A study comparing the noise reduction behavior of variously shaped barriers of limited size in indoor spaces*, Indoor and Built Environment 18 (6) (2009) 541–552.

- [23] ISO 9612:2009 Acoustics - Determination of occupational noise exposure engineering method, International Organization for Standardization, Genève, 2009.
- [24] A. Tokuc, *Building energy simulation tools and selection criteria*, Dokuz Eylül University Faculty of Engineering Journal of Science and Engineering 11 (2) (2009) 19–30.
- [25] G. Riether, T. Butler, *Simulation space: A new design environment for architects*. In Proceedings of Section 03: Prediction and Evaluation 1 - eCAADe 26 (2008) 133–142 2008.
- [26] M. Ermann, *Architectural acoustics illustrated*, John Wiley and Sons, Inc., 2015, pp. 17--22.
- [27] K. Genuit, W. Bray, G. Caspary, *Comparison of a-weighted sound pressure level (dB(A)), loudness-level weighted sound pressure level (dB(EQL)), and loudness with respect to environmental noise assessment*, The Journal of the Acoustical Society of America 128 (4) (2010) 2469.
- [28] C. Kurtay, G. Harputlugil, M. Yaman, *Effects of sound absorption materials on reverberation time according to their positions in the square plan and high ceiling rooms*, Journal of the Faculty of Engineering and Architecture of Gazi University 36 (4) (2021) 2069-2080.
- [29] W. C. Sabine, *Collected papers on acoustics*, London, Humphrey Milford, Oxford University Press, England, 1922.
- [30] L. L. Beranek, *Analysis of Sabine and Eyring equations and their application to concert hall audience and chair absorption*, The Journal of the Acoustical Society of America 120 (2006) 1399–1410.
- [31] A. Nowoświat, and M. Olechowska, *Investigation studies on the application of reverberation time*, Archives of Acoustics 41 (1) (2016) 15–26.
- [32] EN ISO 11654, Acoustics - Sound absorbers for use in buildings - Rating of sound absorption, International Organization for Standardization, Genève, 1997.
- [33] EN 13501-1:2018, Fire classification of construction products and building elements - Part 1: Classification using data from reaction to fire tests, European Committee for Standardization, Brussels, 2018.
- [34] ASTM E84, Standard test method for surface burning characteristics of building materials, American Society for Testing and Materials, U.S. Department of Defense, USA.



AeroRunway: Diverse Weather and Time of Day Aerial Dataset for Autonomous Landing Training

Nesil Bor¹ , Nergis Pervan-Akman² , Ali Berkol³ 

^{1,2,3}BITES Defense and Information Systems, Ankara, Türkiye

Abstract – Acquiring a sufficient amount of diverse and accurate real-world data poses a significant challenge in advancing autonomous systems, which are becoming increasingly popular. Despite the aerospace industry's keen practical and economic interest in autonomous landing systems, readily available open-source datasets containing aerial photographs are scarce. To address this issue, we present a dataset named AeroRunway, comprising high-quality aerial photos designed to aid in runway recognition during the approach and landing stages. The dataset is composed of images using X-Plane, a flight simulator software developed by Laminar Research. It is a highly realistic and detailed flight simulation program that allows users to experience the sensation of piloting various aircraft in a virtual environment. These synthetic images were collected mostly in variable weather conditions above 5000 feet to supplement existing satellite imagery that can be used for extreme situations. This dataset was created from 28 different airports in different weather conditions, such as foggy and rainy, at various times of the day, such as day and night, and consists of 3880 images and is approximately 13.3 GB in size.

Article Info

Received: 14 Jun 2024

Accepted: 19 Sep 2024

Published: 30 Sep 2024

Research Article

Keywords – *Aerodrome detection, spatial awareness, artificial intelligence, deep learning, machine learning*

1. Introduction

Maintaining situational awareness is paramount for pilots, especially during critical phases of flight such as approach and landing. Visual cues aid pilots' orientation and decision-making processes, providing essential information about their surroundings and facilitating safe navigation. However, visually identifying aerodromes amidst diverse and often rapidly changing environments presents significant challenges. Spatial disorientation, a phenomenon where pilots may misinterpret their spatial position and orientation relative to the ground, poses a considerable risk during flight. This can be exacerbated by poor visibility, inclement weather conditions, or complex terrain features. Additionally, aerodromes exhibit varying characteristics and visual appearances, ranging from large international airports with distinctive runway layouts to smaller regional airfields nestled amidst rural landscapes.

In response to these challenges, the study introduces a dataset designed to leverage the power of Deep Learning (DL) algorithms for real-time aerodrome detection from aircraft. By harnessing the capabilities of machine learning and computer vision, this dataset offers a revolutionary solution to enhance pilots' situational awareness and improve flight safety. The dataset comprises a comprehensive collection of high-resolution aerial images capturing diverse aerodrome environments worldwide. These images are meticulously annotated with precise aerodrome boundaries, runway configurations, taxiway markings, and other distinctive features,

¹nesil.bor@bites.com.tr (Corresponding Author); ²nergis.pervan@bites.com.tr; ³ali.berkol@bites.com.tr

facilitating robust training and validation of DL models.

By training DL algorithms on this dataset, pilots can benefit from advanced onboard systems capable of autonomously detecting and identifying aerodromes in real time, even under challenging conditions. This technology promises to revolutionize cockpit instrumentation, providing pilots with invaluable assistance in navigating complex airspace environments and mitigating the risks associated with visual navigation errors. Incorporating DL-based aerodrome detection systems into aircraft avionics represents a significant leap forward in enhancing flight safety and efficiency. By empowering pilots with cutting-edge technology, this initiative aims to redefine the standards of situational awareness in aviation, ensuring safer skies for passengers and crew alike. These methods employ neural networks to extract pertinent features and have demonstrated effectiveness in computer vision applications [1].

Northwestern Polytechnical University (NWPU) created the NWPU-RESISC45 dataset [2], a standard for Remote Sensing Image Scene Classification (RESISC). There are 700 photos in each of the 45 scene classifications in this dataset's 31,500 photographs. The NWPU-RESISC45 proposal includes a large number of scene classes and total images. It has significant changes in translation, spatial resolution, perspective, object posture, lighting, background, and occlusion and has a high level of both within-class and between-class variability.

10 classes of openly accessible geographic object identification NWPU VHR-10 dataset [3-5] is another resource we can reach in this field. An aircraft, ship, storage tank, baseball diamond, tennis court, basketball court, running track on the ground, harbor, bridge, and vehicle are among the ten categories. This collection consists of 800 Very High-resolution (VHR) remote sensing photos that specialists carefully annotated after being clipped from the Vaihingen and Google Earth datasets. This 10-class dataset for geographic object recognition may be used to find both single-class and multi-class items. A total of 800 VHR optical Remote Sensing Images (RSIs) were used to create this dataset, from which 477 vehicles, 757 airplanes, 302 ships, 655 storage tanks, 390 baseball diamonds, 524 tennis courts, 159 basketball courts, 163 ground track fields, 224 harbors, and 124 bridges were manually annotated with axis-aligned bounding boxes. 715 color images from Google Earth were acquired with spatial resolutions ranging from 0.5 to 2 meters, and 85 pan-sharpened Color Infrared (CIR) images from Vaihingen data [6] were acquired with a spatial resolution of 0.08 meters.

A diverse dataset [7] is constructed by collecting RGB imagery using Google Earth technology. This collection consists of a total of 3092 images measuring approximately 4800 x 2703 pixels each. This was achieved by sourcing photographs from renowned international airports such as Paris-Charles de Gaulle, John F. Kennedy International Airport, and Frankfurt Airport, among others, and aircraft boneyards such as Davis-Monthan Air Force Base. To properly label each photograph's aircraft, they used the help of HyperLabel software where they manually created individual bounding boxes surrounding them, which included quality control measures using external independent visual inspectors who maintained accuracy during this process. This led them to label a staggering amount of about eighteen thousand four hundred seventy-seven airplanes overall. Once labeled, their dataset was portioned into three smaller sets with different usage criteria. These subsets were separated accordingly into training (70%, 2166 images), validation (20%, 615 images), and testing (10%, 311 images) to cover all bases respectfully. The DIOR dataset [8] for object detection in optical remote sensing images consists of 20 object classes, 23463 images, and 192518 object instances annotated with horizontal bounding boxes. DIOR-R is an expanded version of DIOR that uses the same images as DIOR but is annotated with orientated bounding boxes. Images in the collection are 800 by 800 pixels in size, with spatial resolutions varying from 0.5 to 30 meters. Similar to most current datasets, this one was gathered from Google Earth (Google Inc.) by specialists in interpreting earth observation data. As opposed to dataset NWPU VHR-10, which has only 800 images, the 23463 remote sensing images in the proposed DIOR collection span over eighty countries. These images are carefully gathered in various weather situations, seasons, imaging settings, and image quality. As a result, for each object class in the DIOR dataset, there are richer variations in perspective, translation, lighting, backdrop, object position and appearance, occlusion, etc.

Military Aircraft Recognition dataset (MAR20) [9] is a publicly accessible remote sensing image collection intended solely for research. This collection consists of 22341 instances, 20 categories, and 3842 images with orientated and horizontal bounding boxes annotated.

A large-scale Dataset for Object Detection in Aerial images (DOTA) [10] collects 2806 aerial images from different sensors and platforms. Each image is around 4000 by 4000 pixels and includes items with a broad range of sizes, orientations, and forms. Experts in aerial image interpretation then annotate these DOTA images using 15 common item categories. There are 188,282 occurrences in the completely annotated DOTA images, and each one is given a random (8 d.o.f.) quadrilateral label.

Scene semantic categories are used to identify the 10 million scene images in the Places Database [11], which provides a comprehensive catalog of the many sorts of surroundings seen across the globe. The Place Database's data-collecting procedure is comparable to the picture collection in other widely used datasets, such as ImageNet [12] and COCO [13]. Based on the synset of WordNet [14], the categories for the ImageNet dataset have been defined. Using the collection of WordNet synonyms, potential images are retrieved from several image search engines. Contrarily, the COCO dataset focuses on adding additional scene information to the object instances inside the images. Places database as a benchmark has four subsets: Places205, Places88, Places365-Standard, and Places365-Challenge.

FAIR1M [15] is another benchmark dataset for recognizing fine-grained objects in high-resolution remote sensing images. It contains more than 1 million instances and more than 15,000 images. From several stations dispersed throughout numerous nations and regions, remote sensing images with resolutions ranging from 0.3 to 0.8 meters are gathered. All items in the FAIR1M dataset have oriented bounding boxes that annotate them about 5 categories and 37 subcategories.

Comparing the FAIR1M dataset to other datasets, it has several unique traits. The first thing that makes it unique is its vastly increased number of samples and pictures, which offers more thorough, fine-grained category information. The collection includes items from remote sensing photographs, which offer useful geographic data like latitude and longitude. Another important aspect is the dataset's high resolution, attained through a careful data-cleaning process that guarantees superior image quality.

Another method uses an open-source virtual globe to replicate the surroundings around airport runways. Virtual globes have been employed in many research projects over the past ten years as common instruments for data collecting, exploration, and modeling [16]. Google Earth Studio [17, 18], a sophisticated animation tool for obtaining and creating Google satellite pictures, is considered in this work. Landings of civil aircraft are represented by the Landing Approach Runway Detection (LARD) dataset [19]. So, based on the information supplied by aviation standards, we first define a general landing approach cone. It next designs a method to create a dataset of images with appropriate labels from this description. It consists of 14.433 images with a resolution of 2448x2648 that were collected from a total of 32 runways at 16 distinct airports. Approximately 451 images are taken for each approach (or runway). Although most of the dataset is made up of artificial pictures, they include hand-tagged photos from actual landing footage to provide the detection job with a more realistic context. They provide a generator to create these artificial front-view images and automatically annotate the runway corners using geometric transformations.

This paper is structured to comprehensively address developing and utilizing a synthetic dataset for runway recognition, which is crucial for enhancing autonomous landing systems in aviation. It begins with an introduction that highlights the significance of the problem and the motivation behind the research. The methodology section details the X-Plane simulator's data collection process, including the specific conditions and parameters considered, such as weather variations and different altitudes. Following this, the results and discussion section presents the findings from the dataset, emphasizing the impact of weather conditions, day/night operations, and altitude on runway recognition. High-resolution images and their standardized dimensions are also discussed to underline the dataset's precision and applicability. The conclusion synthesizes the key insights and underscores the potential of machine learning in improving autonomous landing systems,

advocating for the value of large datasets in facilitating advanced algorithms. Finally, the paper includes author contributions, conflict of interest statements, and a references section to ensure comprehensive attribution and context for further research.

2. Data Description

Today, object detection studies are integrated into our lives in many areas. It has an important place in aviation as pilot assist systems. To contribute to these studies, many dataset studies are presented. In our study, a dataset study was conducted to contribute to this literature. The images were systematically created for 16 airports. These airports included Adana Incirlik Airport (LTAG), Adiyaman Airport (LTCP), Alanya Gazipasa Airport (LTFG), Ankara Esenboga Airport (LTAC), Antalya Airport (LTAI), Balikesir Koca Seyit Airport (LTFD), Çanakkale Airport (LTBH), Chios Island Airport (LGHI), Diyarbakir Airport (LTCC), Elazığ Airport (LTCA), Erzincan Airport (LTCD), Erzurum Airport (LTCE), Hatay Airport (LTDA), Istanbul Airport (LTFM), Istanbul Ataturk Airport (LTBA), Izmir Adnan Menderes Airport (LTBJ), Kayseri Erkilet Airport (LTAU), Kocaeli Cengiz Topel Airport (LTBQ), Konya Airport (LTAN), Malatya Airport (LTAT), Nevsehir Kapadokya Airport (LTAZ), Rhodes Diagoras Airport (LGRP), Şanlıurfa Airport (LTCS), ,Sırnak Airport (LTCV), Tekirdag Airport (LTBU), Trabzon Airport (LTCG), Van Airport (LTCI), Zonguldak Çaycuma Airport (LTAS). When we examined the studies in the literature in which artificial intelligence was used in this field, we saw that most of the datasets used were on clear images regardless of weather conditions. That's why we wanted to make a different contribution and add difficult weather conditions to our dataset for the development of algorithms. It was seen that the same situation was valid for the altitude parameter. Thus the lower altitude status was preferred to the higher altitude status. The images were taken for different weather conditions, such as clear, cirrus, scattered, broken, foggy, and stormy at different altitudes. Hereafter, 'altitude' refers to the height above an aerodrome. High-altitude images were taken above 10000 feet. Lower-altitude images were taken between 5000 and 10000 feet. Images were not included for altitudes below 5000 feet because other public datasets, like the Places dataset, contained most such low-altitude images. The altitudes were combined with different distances from the aerodrome to the aircraft approximately between 2 and 70 nautical miles, such that the aerodrome was visible from the aircraft. The weather conditions included precipitation variations, cumulus cloud varieties, cirrus clouds, and stratus clouds. The images were taken from different camera angles to create diversity. Figure 1 shows images taken at different times, such as day and night. In contrast, Figure 2 shows examples of images in different weather conditions, such as foggy and rainy, respectively. In Figure 3, low and high-altitude images of the same airport are shown, respectively.

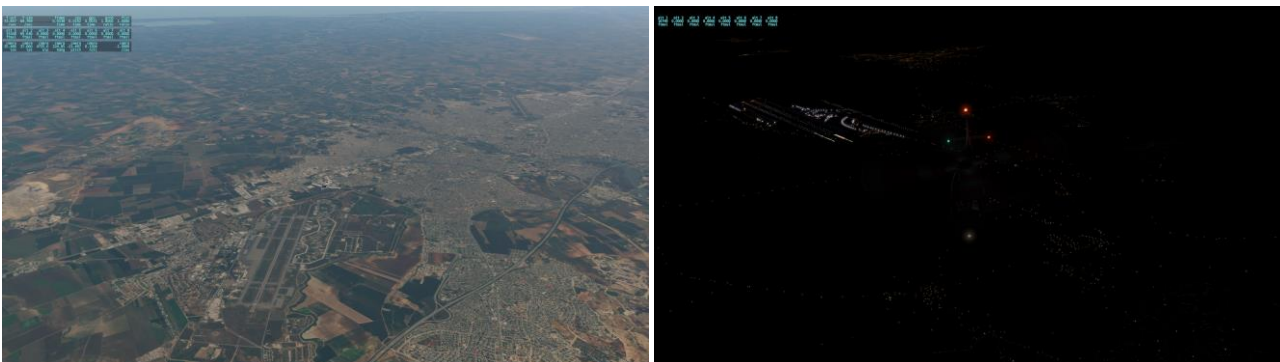


Figure 1. The left side of the figure represents a daytime image, and the right side represents a nighttime image

In addition to helping the algorithms acquire better features, adjusting the camera angle also makes the detection independent of the location of the mounted camera. Images were captured from the sides and as the aircraft approached an airfield in the direction of each runway. Images are captured with the entire airport visible in each view, and partial views of the airport and rotations of views are included. Because bad weather conditions, such as foggy weather are also considered. To use it for aerodrome detection even in closed weather

conditions such as foggy rain, attention was paid to the fact that a part of the runway, if not the whole, was visible while creating the dataset.



Figure 2. The left side of the figure represents a foggy image, and the right side represents a rainy image

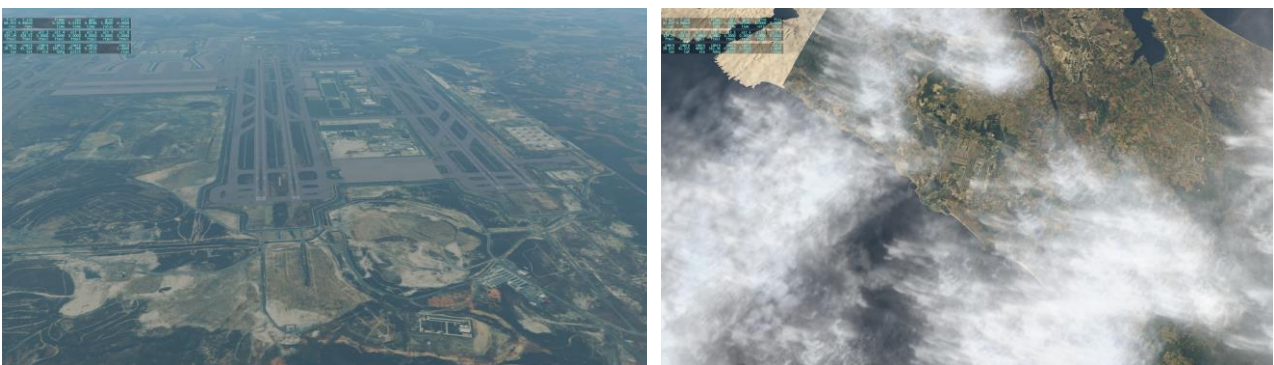


Figure 3. The left side of the figure represents a low-altitude image, and the right side represents a high-altitude image

3. Image Acquisition

This dataset was collected using X-Plane 11, a sophisticated flight simulation software developed by Laminar Research, renowned for its realistic flight physics based on "blade element theory". Widely used by aviation enthusiasts and professionals, it offers detailed global scenery, customizable environments, and a wide range of aircraft models. The simulator supports multiple platforms, including Windows, macOS, and Linux, and even offers Virtual Reality (VR) capabilities for an immersive experience. Additionally, X-Plane 11 is recognized by the Federal Aviation Administration (FAA) for its high level of realism, making it suitable for professional flight training and certification purposes. Simulations were run on equipment featuring an NVIDIA GeForce RTX 3060 GPU and an AMD Ryzen 7 6800H with Radeon Graphics CPU. Ortho4XP v1.15 was combined with X-Plane to create overlays and custom scenery. It is a tool widely used by flight simulation enthusiasts to enhance the realism of X-Plane by creating custom, photo-realistic ground textures. It allows users to generate detailed scenery by downloading satellite imagery and integrating it with elevation data, producing high-resolution orthophotos that accurately represent real-world landscapes. Designed specifically for X-Plane, Ortho4XP replaces the default terrain textures with these realistic images, significantly improving the visual experience of the simulator. Supported by an active community, the tool enables users to customize and enhance specific regions, making flights in X-Plane more immersive and visually accurate. The images were exported by taking screenshots at multiple angles and heights, ensuring the frame rate was above 50. In each image, values such as height, camera angle, frame rate, etc., are displayed in the upper left corner by the sensor opened in the image.

When the literature was reviewed, it was observed that there was a lack of image dataset studies in extreme weather conditions, particularly in Türkiye, in datasets created with X-Plane, as stated in this article. This

dataset offers several key advantages compared to existing ones, particularly regarding its diversity and relevance to autonomous landing systems. One of the primary benefits is the inclusion of images captured under challenging weather conditions such as fog, rain, and storms. This is significant because many existing datasets predominantly feature clear weather scenarios, which restricts the performance of trained models in adverse conditions. The trained models' robustness is enhanced by including these challenging scenarios, enabling better performance in real-world situations with varying visibility and weather conditions.

Additionally, a wide range of altitudes, from 5,000 to 70,000 feet, is covered by this dataset, which is crucial for simulating different phases of approach and landing. This variation allows models to be trained on images representing both low and high-altitude approaches, improving their ability to recognize runways from various distances and perspectives.

The superiority of this method is underscored by these enhancements, which provide a more representative and challenging dataset for training deep learning models. These benefits are believed to significantly advance the field of autonomous landing systems and offer a valuable resource for improving model performance in real-world conditions.

The effectiveness of the dataset is further contributed to by the high-resolution images and diverse aircraft types used in the simulations. By capturing images from multiple aircraft and camera angles, various perspectives and viewpoints are ensured, enhancing the generalization capabilities of the models.

In this dataset, 3880 images of 28 different airports around Türkiye are taken with different angles, weather conditions, and aircraft. The total size of this dataset is approximately 13.3 GB. Lighting is important in airport and runway determinations, as it becomes difficult to detect the landforms from the air after dark, that is, at night. In addition, for the sake of diversity and being closer to reality, multiple aircraft were used to obtain the images. This distribution can be seen in the pie chart in Figure 4. The largest part of the data set, which is approximately a quarter slice, was obtained with the CirrusSF50 type aircraft model, and the other large slices consist of Cessna_172SP, Cessna_172SP_G1, and L5_Sentinel type model aircraft. There is not much difference between the number of images obtained from the remaining aircraft models and they are proportionally close to each other.

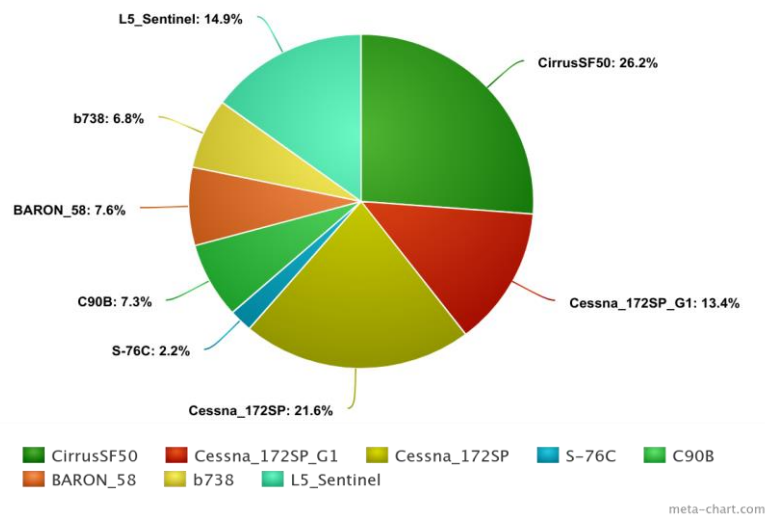


Figure 4. Distribution of aircraft types

To be close to real scenarios and to cover extreme conditions, images containing these weather conditions were also obtained, apart from clear images. The detailed table showing the number distributions of these parameters is included in Table 1. When the distribution of the number of images taken from 28 different airports is examined, it is seen that the airport with the most images is Adiyaman Airport, with 202 images, and the airport with the least images is Ankara Esenboga Airport, with 37 images.

In addition to the weather conditions, the number distribution of the feet where the flights are made and the day/night conditions during the flights according to the airports are shown in Table 2 in more detail. When the distribution is made by considering the feet parameter, the observability of the airport generally increases at low feet, and the observability decreases with higher feet as one moves away from the airport. Considering the literature, since there are not many sources at high altitudes, adding high-altitude images to the dataset is important.

While obtaining images of existing airports, it was imperative to ensure a minimum actual frame rate (f-act) of 50 frames per second (FPS) on the video card, guaranteeing smooth and accurate rendering of the dynamic airport environments. This requirement is crucial for various applications, including real-time air traffic monitoring, surveillance, and security measures, where even minor delays or lags can have significant implications for operational efficiency and safety.

The images' diversity spans from ground level to an impressive altitude of 70,000 feet. It extends up to 70 nautical miles in range, providing a comprehensive aerial perspective of the airport surroundings. This extensive coverage enables comprehensive monitoring and analysis of airport infrastructure, surrounding terrain, and airspace dynamics, offering valuable insights for airspace management, flight planning, and emergency response procedures.

Table 1. Image counts in each airport folder

Airports	Image Count
Adana İncirlik Airport (LTAG)	173
Adiyaman Airport (LTCP)	202
Alanya Gazipaşa Airport (LTFG)	148
Ankara Esenboğa Airport (LTAC)	37
Antalya Airport (LTAI)	184
Balikesir Koca Seyit Airport (LTFD)	155
Canakkale Airport (LTBH)	113
Chios Island Airport (LGHI)	154
Diyarbakir Airport (LTCC)	157
Elazığ Airport (LTCA)	148
Erzincan Yıldırım Akbulut Airport (LTCD)	150
Erzurum Airport (LTCE)	126
Hatay Airport (LTDA)	142
Istanbul Airport (LTFM)	180
Istanbul Ataturk Airport (LTBA)	48
Izmir Adnan Menderes Airport (LTBJ)	136
Kayseri Erkilet Airport (LTAU)	130
Kocaeli Cengiz Topel Airport (LTBQ)	117
Konya Airport (LTAN)	105
Malatya Airport (LTAT)	165
Nevşehir Kapadokya Airport (LTAZ)	43
Rhodes Diagoras Airport (LGRP)	188
Şanlıurfa GAP Airport (LTCS)	130
Şırnak Şerafettin Elçi Airport (LTCV)	161
Tekirdağ Çorlu Airport (LTBU)	152
Trabzon Airport (LTCG)	160
Van Ferit Melen Airport (LTCI)	140
Zonguldak Caycuma Airport (LTAS)	136
Total	3880

High-resolution imaging techniques were employed to ensure optimal image quality and facilitate the easy detection of landforms and infrastructural details. High-resolution images offer enhanced clarity and precision, enabling precise identification of runway markings, terminal buildings, navigation aids, and other critical elements essential for air traffic management and airport operations. To achieve this, rendering options were meticulously configured to operate at the highest settings, maximizing image fidelity and detail resolution.

The images in the dataset adhere to standardized dimensions, with pixel values of 1920 in width and 1080 in height. Standardizing image dimensions ensures consistency and compatibility across various visualization and analysis platforms, facilitating seamless integration into airport planning, simulation, and management software systems. This standardized approach streamlines data processing and analysis, enabling efficient extraction of relevant insights and actionable information from the vast repository of airport imagery.

While 803 flights are categorized under 'Not Clear' conditions at 28 airports, indicating adverse weather conditions such as fog, rain, or snow, the number of flights marked as 'Clear' stands at 394. This discrepancy highlights the significant impact that weather conditions can have on flight operations, underscoring the importance of robust safety protocols and the expertise of air traffic controllers and pilots in navigating challenging weather scenarios to ensure passenger safety.

In addition to weather conditions, the distinction between Day and Night operations also plays a crucial role in aviation. The fact that 730 flights were conducted during the day compared to 467 flights during the night emphasizes the preference for daytime operations, which often offer better visibility and favorable weather conditions, contributing to smoother and safer flights. However, it's essential to note the vital role of nighttime operations, particularly in facilitating cargo transportation and accommodating international flight schedules across different time zones.

Moreover, altitude is another critical factor influencing flight operations. Of the total flights, 817 were operated at High Altitude, exceeding 10,000 feet above sea level. High-altitude flights typically involve long-haul routes and require specialized equipment and training due to reduced oxygen levels and lower temperatures. Conversely, 409 flights were conducted below the 10,000 feet threshold at Low Altitudes.

Table 2. Table of situations

Airport	Clear	Not Clear	Day	Night	High Alt	Low Alt	Total
LTAG	106	67	139	34	123	50	173
LTCP	143	59	170	32	165	37	202
LTFG	109	39	111	37	49	99	148
LTAC	20	17	11	26	31	6	37
LTAI	112	72	112	72	130	54	184
LTFD	82	73	115	40	64	91	155
LTBH	68	45	88	25	63	50	113
LGHI	90	64	116	38	33	121	154
LTCC	64	93	125	32	106	51	157
LTCA	89	59	115	33	109	39	148
LTCD	62	88	117	33	111	39	150
LTCE	21	105	105	21	112	14	126
LTDA	38	104	123	19	95	47	142
LTFM	101	79	135	45	112	68	180
LTBA	11	37	30	18	26	22	48
LTBJ	94	42	107	29	56	80	136
LTAU	81	49	105	25	111	19	130
LTBQ	65	52	97	20	69	48	117
LTAN	32	73	76	29	83	22	105
LTAT	42	123	118	47	142	23	165
LTAZ	1	42	43	0	42	1	43
LGRP	110	78	142	46	133	55	188
LTCS	19	111	121	9	95	35	130
LTCV	41	120	135	26	102	59	161
LTBU	40	112	127	25	94	58	152
LTCG	82	78	117	43	83	77	160
LTCI	72	68	111	29	128	12	140
LTAS	69	67	87	49	67	69	136
TOTAL	394	803	730	467	817	409	3880

Low-altitude flights often encompass short-haul journeys, regional routes, and flights approaching or departing from airports, necessitating different navigation procedures and considerations for air traffic management and terrain clearance.

The 28 airports and the aircraft type of the obtained images were named in Figure 5 to be read systematically. The airport's ICAO code is made up of four letters. These codes are created using divisions made between nations and regions. The first letter identifies the geographical area where the airport is located, while the second letter identifies the nation. Usually, the other two letters are given in alphabetical sequence. The first part of naming the images is to provide an ICAO code of which airports they belong to. For example, naming the images of ADANA INCIRLIK Airport, ALANYA GAZIPASA Airport, ANKARA ESENBOGA Airport, ANTALYA Airport, BALIKESIR KOCA SEYIT Airport, and CANAKKALE Airport airports start with LTAG, LTFG, LTAC, LTAI, LTFD, and LTBH respectively. After the ICAO part, naming is done according to aircraft types. Finally, the sample number concat and forms the image name. According to all these rules mentioned above, the file name of the first image of the "ADANA INCIRLIK Airport" species and with the "CirrusSF50" aircraft will be "LTAG_CirrusSF50_01.png". Figure 6 shows the structure of the dataset.

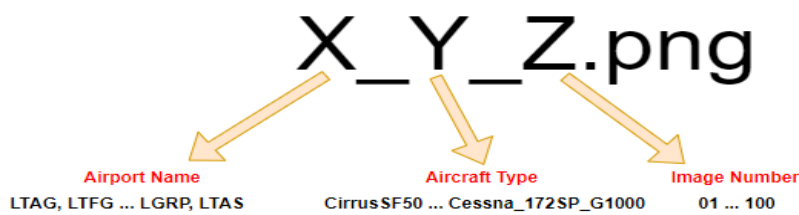


Figure 5. Renaming files

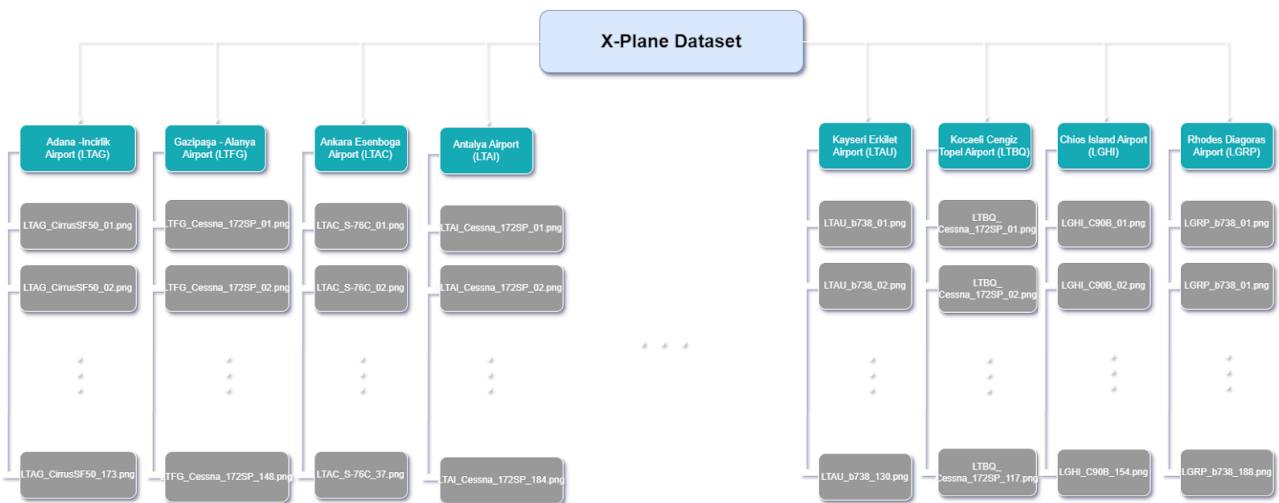


Figure 6. File structure of the dataset

4. Conclusion

As autonomous systems gain popularity, a significant hurdle lies in acquiring enough relevant real-world data. The aerospace industry, particularly autonomous landing systems, has a strong practical and economic interest. However, open-source datasets are scarce, specifically focused on aerial images. To solve this problem, we offer a collection of aerial images for runway recognition during the approach and landing phases. The collection consists of synthetic images from the X-Plane simulator, which attempted to create a dataset based on improving detection under various weather conditions and periods, especially in poor visibility. Few image datasets are available, including runways seen from the aerial front view. One way to solve this issue is to use synthesized data, which enables the construction of more scenarios at a lesser cost. Using a flight simulator is a frequent remedy to this well-known issue in aviation [20]. Pilots, for instance, may practice emergency

maneuvers and familiarize themselves with flight controls and protocol owing to simulators. The requirements and rules of the relevant authorities, such as the FAA in America and the EASA in Europe [21], determine the complexity and realism of such simulators.

Based on EASA and [22] findings, a significant portion of non-commercial airplane accidents happen during the landing phase under favorable weather conditions. These accidents are frequently attributed to human errors, with perception being identified as the most critical risk factor. This underscores the importance of developing safer landing systems. Implementing autonomy in these systems can serve as an initial measure to address this problem, beginning with pilot assistance and gradually progressing toward fully autonomous landings in the distant future. The advancement in this direction will inevitably depend on utilizing Artificial Intelligence for runway detection, which facilitates the computation of the aircraft's position. In this article, we have provided a clear and precise description of this task, emphasizing the significance of large datasets to facilitate the application of DL algorithms. Utilizing machine learning can create innovative technology that enhances cockpit capabilities and pilots' awareness of their surroundings. This dataset seeks to help with the value machine learning can bring to this field by highlighting this potential through the visual detection of airports.

Based on the study results, future research could explore the integration of this dataset with real-world aerial imagery to further enhance the robustness of autonomous landing systems. Expanding the dataset to include more diverse airport environments and extreme weather conditions could provide deeper insights and improve algorithm performance. Leveraging advancements in deep learning and artificial intelligence, it is also recommended to develop adaptive models that dynamically adjust to new and unforeseen variables, ensuring even greater reliability and safety in autonomous aviation operations. This forward-looking approach will pave the way for significant advancements in autonomous flight technologies.

One key direction for future research is the integration of our synthetic dataset [23] with real-world aerial imagery. Combining synthetic data with actual flight data could enhance the robustness and accuracy of autonomous landing systems by providing a more comprehensive dataset that includes real-world variability not captured by simulations alone. This integration could also help validate the effectiveness of models trained on synthetic data in operational environments.

Author Contributions

The third author directed the project and supervised this study's findings. The second and third authors devised the main conceptual ideas and developed the theoretical framework. The first author performed the data collection. The first author wrote the manuscript with support from the second and third authors. The second and the third author reviewed and edited the paper. All authors read and approved the final version of the paper.

Conflicts of Interest

All the authors declare no conflict of interest.

Ethical Review and Approval

No approval from the Board of Ethics is required.

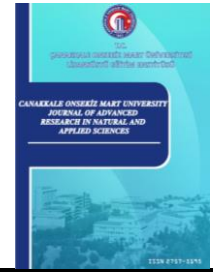
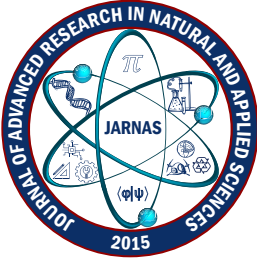
References

- [1] Z.-Q. Zhao, P. Zheng, S.-t. Xu, X. Wu, *Object detection with deep learning: A review*, IEEE Transactions on Neural Networks and Learning Systems 30 (11) (2019) 3212–3232.
- [2] G. Cheng, J. Han, X. Lu, *Remote sensing image scene classification: Benchmark and state of the art*, Proceedings of the IEEE 105 (10) (2017) 1865–1883.

- [3] G. Cheng, J. Han, P. Zhou, L. Guo, *Multi-class geospatial object detection and geographic image classification based on collection of part detectors*, ISPRS Journal of Photogrammetry and Remote Sensing (98) (2014) 119–132.
- [4] G. Cheng, J. Han, *A survey on object detection in optical remote sensing images*, ISPRS Journal of Photogrammetry and Remote Sensing (117) (2016) 11–28.
- [5] G. Cheng, P. Zhou, J. Han, *Learning rotation-invariant convolutional neural networks for object detection in VHR optical remote sensing images*, IEEE Transactions on Geoscience and Remote Sensing 54 (12) (2016) 7405–7415.
- [6] *2D semantic labeling - Vaihingen dataset*, <https://paperswithcode.com/dataset/isprs-vaihingen>, Accessed on 21 June 2023.
- [7] T. Bakirman, E. Sertel, *HRPlanes: High resolution airplane dataset for deep learning*, International Journal of Engineering and Geosciences 8 (3) (2022) 212–223.
- [8] G. Cheng, J. Wang, K. Li, X. Xie, C. Lang, Y. Yao, J. Han, *Anchor-free oriented proposal generator for object detection*, IEEE Transactions on Geoscience and Remote Sensing (60) (2022) 1–11.
- [9] W. Yu, G. Cheng, J. Wang, Y. Yao, X. Xie, X. Yao, J. Han, *MAR20: A benchmark for military aircraft recognition in remote sensing images*, National Remote Sensing Bulletin 27 (12) (2024) 2688–2696.
- [10] J. Ding, N. Xue, G.-S. Xia, X. Bai, W. Yang, M. Y. Yang, S. Belongie, J. Luo, M. Datcu, M. Pelillo, L. Zhang, *Object detection in aerial images: A large-scale benchmark and challenges*, IEEE Transactions on Pattern Analysis and Machine Intelligence 44 (11) (2022) 7778–7796.
- [11] B. Zhou, A. Lapedriza, A. Khosla, A. Oliva, A. Torralba, *Places: A 10 million image database for scene recognition*, IEEE Transactions on Pattern Analysis and Machine Intelligence 40 (6) (2017) 1452–1464.
- [12] O. Russakovsky, J. Deng, H. Su, J. Krause, S. Satheesh, S. Ma, Z. Huang, A. Karpathy, A. Khosla, M. Bernstein, A. C. Berg, L. Fei-Fei, *ImageNet large scale visual recognition challenge*, International Journal of Computer Vision (115) (2015) 211–252.
- [13] T.-Y. Lin, M. Maire, S. Belongie, L. Bourdev, R. Girshick, J. Hays, P. Perona, D. Ramanan, C. L. Zitnick, P. Dollár, *Microsoft COCO: Common objects in context*, in: D. Fleet, T. Pajdla, B. Schiele, T. Tuytelaars (Eds.), Computer Vision—ECCV 2014: 13th European Conference, Zurich, 2014, pp. 740–755.
- [14] G. A. Miller, *WordNet: A lexical database for English*, Communications of the ACM 38 (11) (1995) 39–41.
- [15] X. Sun, P. Wang, Z. Yan, F. Xu, R. Wang, W. Diao, J. Chen, J. Li, Y. Feng, T. Xu, M. Weinmann, S. Hinz, C. Wang, K. Fu, *FAIRIM: A benchmark dataset for fine-grained object recognition in high-resolution remote sensing imagery*, ISPRS Journal of Photogrammetry and Remote Sensing (184) (2022) 116–130.
- [16] L. Yu and P. Gong, *Google Earth as a virtual globe tool for Earth science applications at the global scale: progress and perspectives*, International Journal of Remote Sensing 33 (12) 2012 3966–3986.
- [17] Google. *Google Earth studio*, <https://www.google.com/intl/eng/earth/studio/>, Accessed on 21 June 2023.
- [18] Google. *Google Earth studio*, <https://www.google.com/earth/about/versions/>, Accessed on 21 June 2023.
- [19] M. Ducoffe, M. Carrere, L. Féliers, A. Gauffriau, V. Mussot, C. Pagetti, T. Sammour, *LARD – Landing approach runway detection – dataset for vision based landing*, arXiv preprint arXiv:2304.09938 (2023).
- [20] A. T. Lee, *Flight simulation: Virtual environments in aviation*, Routledge, New York, 2017.
- [21] T. Longbridge, J. Burki-Cohen, T. Go, *Flight simulator fidelity considerations for total airline pilot training and evaluation*, AIAA Modeling and Simulation Technologies Conference and Exhibit,

Montreal, Quebec, 2001, pp. 4425

- [22] G. Balduzzi, M. F. Bravo, A. Chernova, C. Cruceru, L. van Dijk, P. de Lange, J. Jerez, N. Koehler, M. Koerner, C. Perret-Gentil, Z. Pillio, R. Polak, H. Silva, R. Valentin, I. Whittington, G. Yakushev, Neural network based runway landing guidance for general aviation autoland, U.S. Department of Transportation Federal Aviation Administration, New Jersey, 2021.
- [23] N. Bor, (2024). AeroRunway, *Zenodo*. <https://zenodo.org/records/11577457>, Accessed on 22 September 2024.



An Overview of Traditional and Next-Generation Earthquake Early Warning Systems

Süleyman Tunç¹ , Berna Tunç² , Deniz Çaka³ , Emrah Budakoğlu⁴ 

¹Sentez Earth and Structure Engineering Limited, Dragos Park Plaza, İstanbul, Türkiye

^{2,3}Department of Geophysical Engineering, Faculty of Engineering, Kocaeli University, Kocaeli, Türkiye

⁴Department of Geophysical Engineering, Faculty of Engineering, Sakarya University, Sakarya, Türkiye

Article Info

Received: 09 May 2024

Accepted: 20 Sep 2024

Published: 30 Sep 2024

Research Article

Abstract – The Earthquake Early Warning System generates rapid and effective warnings after detecting an earthquake, before the arrival of destructive waves to the areas that may be affected. In this way, it is aimed to minimize the loss of life and property. In this study, traditional early warning systems that are frequently used in the world are discussed. The details of the next-generation early warning system, which has recently produced successful outputs, are discussed, and its advantages over traditional early warning systems are mentioned. The recent developments of this system are also analyzed. Next-generation early warning systems consist of a new array-based algorithm composed of two modules for real-time epicenter detection. The detection of an earthquake occurring in the Marmara Sea (Türkiye) with a next-generation early warning system using array-based location methodology is given as an example. Next-generation early warning systems have advantages over traditional ones, such as lower cost and time gains of up to minutes.

Keywords – *Early warning systems, algorithms, seismometer, traditional, next-generation*

1. Introduction

An earthquake early warning system (EEWS) is a system that aims to send timely warnings to people or organizations at the onset of a destructive earthquake. EEWS detects the onset of an earthquake by measuring the velocity of seismic waves generated by the earthquake. EEWS requires seismic stations installed close to the source to detect earthquakes. When the destructive earthquake starts, P waves are detected by these seismic stations. Since P waves are the first to reach the stations, magnitude scaling is estimated using these waves. The system then rapidly generates a warning message, and an earthquake warning is transmitted to the public or organizations through appropriate channels (Figure 1). EEWS enables many important measures to be taken, such as opening exit doors in buildings, safely stopping escalators and lifts, stopping or controlling slowing down the activities of facilities such as factories, nuclear power plants, etc., stopping or slowing down rail systems such as high-speed trains, subways, trams, stopping microsurgical operations in hospitals. In addition, if a satisfactory warning time can be achieved, major benefits include protecting human life and reducing structural damage [1].

A frequently confused point that should be emphasized is that earthquake early warning systems cannot predict the earthquake in advance. In other words, they cannot produce a warning without detecting an earthquake. The main countries currently using EEWS in various parts of the world are India, Israel, Greece, Italy, Italy,

¹stunc@syy.com.tr; ²berna@kocaeli.edu.tr; ³caka@kocaeli.edu.tr; ⁴ebudakoglu@sakarya.edu.tr (Corresponding Author)

Romania, Türkiye, Taiwan, Japan, Canada, the United States of America, and Mexico [2-11]. Türkiye already has an active EEWS. However, it does not yet provide an alert to the public.

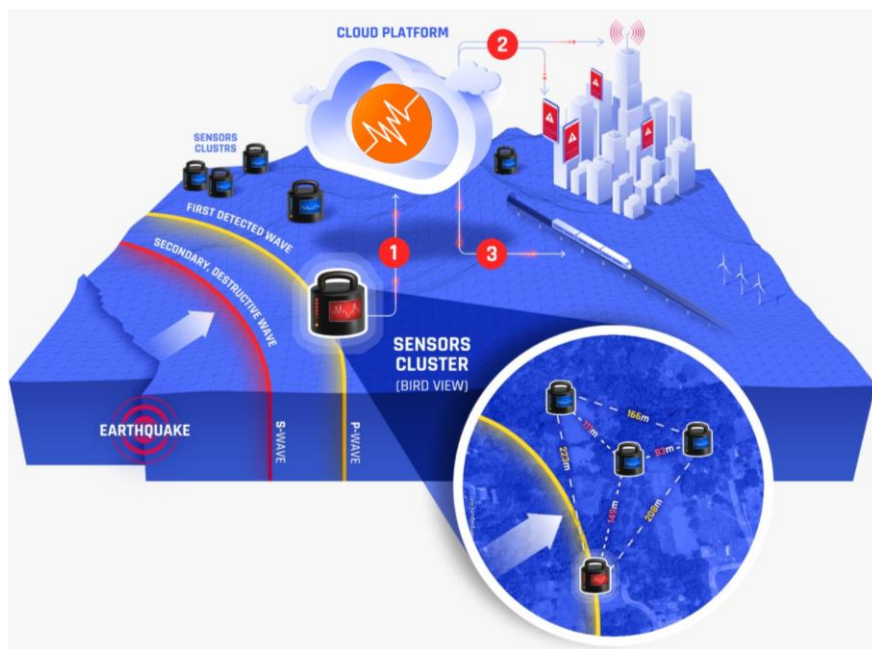


Figure 1. Overview of Earthquake Early Warning System

In EEWS, the two basic body waves, P and S waves, are of great importance. P waves are the fastest propagating seismic waves at the beginning of an earthquake. During an earthquake, P waves first vibrate the earth's crust and are used to quickly detect the onset of an earthquake. Detection and analysis of P waves allow the EEWS to determine the onset of the earthquake. S waves are the second seismic waves propagating after P waves during an earthquake. They propagate more slowly than P waves but have a greater energy. All earthquake early warning systems used worldwide are based on P-wave magnitude estimation. This is because the P wave propagates faster than the destructive S wave (generally $V_p=6.0$ km/s - $V_s=3.5$ km/s) and is the first wave to reach the stations.

For a settlement 100 km away; $t_p=100/6.0 = 16.7$ s, $t_s=100/3.5 = 28.6$ s. In this context, the warning time is $28.6-16.7=11.9$ s (the time taken for data transmission and the processing time are set to zero; in practice, these delays and processing time should also be considered). Latency is the time it takes inside the sensor until the P-wave arrives and is packaged and placed on the transmission path. Delay refers to the time it takes for this packet to arrive at the center along the transmission line.

2. Traditional and Next Generation Earthquake Early Warning Systems

Some early earthquake early warning systems (EEWs) have been developed worldwide to estimate real-time location, magnitude, and maximum ground shaking about seismic events [12]. EEWs have two basic approaches: the single station ("on-site") approach and the network (regional) approach [13]. The in-situ EEW approach is based on the principle of detection of the P wave by a single sensor and warning before the more destructive S wave arrives. In the network approach, data from many seismic sensors are used in areas where earthquakes are likely to occur. In this approach, since multiple stations are expected to detect the earthquake, it can operate slower than the single-station approach. However, it has the advantage of fewer erroneous results. This section will briefly mention the widely used traditional and next-generation systems.

2.1. Earthquake Point-Source Integrated Code (EPIC/Elarms)

Earthquake Point-Source Integrated Code (EPIC) or Earthquake Alarm Systems (ElarmS) is a system that can provide a warning when an earthquake occurs. EPIC detects the first earthquake wave by the station closest to

the fault and estimates the peak ground shaking with the information it receives [14]. The ElarmS methodology determines the location of the earthquake using arrival times. Its magnitude is calculated with the frequency content of the P wave arrival (T_p) and the peak displacement (Pd) [15]. In the next stage, ground shaking is estimated using attenuation relations. As time passes, the data continues to flow. In this way, hazard maps are updated. Hazard assessments are revised in line with detailed ground-shaking observations from regions close to the epicenter. EPIC consists of three modules.

EPIC determines the location of an earthquake by detecting the P-waves generated after an earthquake by at least four stations. A grid search method is used for this determination. This method minimizes the difference between the calculated and observed arrival times [14]. The warning time can be defined as the time required to onset strong ground shaking. The earthquake's origin time and location information can be estimated using S-wave arrival time curves. Estimated values for S-wave arrival times need to be considered to determine the warning time conservatively [14].

The magnitude, a measure of the energy generated at the hypocenter during an earthquake, is estimated using the frequency characteristics of the first four seconds of the P wave. The vertical component waveform predominant period (τ_p) is calculated by the method proposed by Nakamura [16]. Various researchers have stated that the maximum predominant period (T_p^{\max}) in four seconds is scaled with the earthquake's magnitude [14,17-20]. To calculate τ_p , accelerometer records need to be converted to velocity records. Then, τ_p is continuously calculated in real-time with the equation (2.1).

$$\tau_i^p = 2\pi\sqrt{X_i/D_i} \quad (2.1)$$

Here, X_i and D_i in (2.1) can be written as follows:

$$X_i = \alpha X_{i-1} + x_i^2 \quad (2.2)$$

$$D_i = \alpha D_{i-1} + \left(\frac{dx}{dt}\right)_i^2 \quad (2.3)$$

In (2.2), x_i represents the ground motion at the time i and α represents the 1-second smoothing constant ($\alpha=0.99$ for 100 sps data, while $\alpha=0.95$ for 20 sps data). x_i ; velocity of the most recent data, X_i ; is the square of the smoothed velocity. D_i used in (2.3); is the smoothed velocity data derivative (acceleration) square. The magnitude determination is faster since the frequency content of smaller magnitude events can be measured in a short time compared to large magnitude events. This also indicates that the magnitude estimation may increase as the duration of the data increases [14].

Allen and Kanamori [17] proposed two linear relations between the magnitude and T_p^{\max} of events. For earthquakes ranging in magnitude from 3.0 to 5.0, a low-pass filter at 10 Hz is used. Magnitude estimation can be made when 1 second of data is used, but the error of estimate made with 2 seconds is slightly reduced. So additional data doesn't make the estimation any better. Then, by observing the T_p^{\max} data (2.4) for magnitude estimation is determined (for magnitudes between 3.0 and 5.0). For earthquakes larger than 4.5, the best magnitude estimates can be obtained using a 3 Hz low-pass filter and 4-second data. The best-fit magnitude relationship for large earthquakes is given in (2.5) [14].

$$m_l = 6.3\log(\tau_p^{\max}) + 7.1 \quad (2.4)$$

$$m_h = 7.0\log(\tau_p^{\max}) + 5.9 \quad (2.5)$$

The relations are given for m_l and m_h are used by ElarmS to estimate the best-fit magnitude. The magnitude estimation process works like this: When a station is triggered 1 second after the event, m_l is estimated using

τ_p^{\max} . When the data arrives in 2 seconds, the estimate is updated. The magnitude estimate of the event is determined by averaging the magnitudes estimated from each station. If the event magnitude is larger than 4.0, it is estimated in m_h . In this case, the magnitude is the average of the m_l and m_h estimated from all the triggered stations. The relationship between T_p^{\max} and magnitude was tested using data of various magnitudes (3.0 to 8.3) from Southern California, Japan, and worldwide. Datasets from Southern California and Japan show similar scaling relations. The dataset from different countries for the Denali earthquake indicates that the scaling relation does not deteriorate even for the largest earthquakes [17-20].

The final step in the ElarmS process is to convert the location and magnitude estimate of the event into peak ground shaking prediction for all locations. Thus, ground shaking maps are obtained by mapping the spatial distribution of the peak ground shaking. Most current attenuation relations use only ground motion observations for earthquakes greater than 5.0, while ElarmS uses self-generated attenuation relations for earthquakes greater than 3.0. For continuous testing of Elarms, it is preferred to work on all earthquakes, small and large. The process of using ElarmS's attenuation relations is two steps. The magnitude estimation is made one second after the arrival of the first P wave. The estimated PGA from the empirical relations is calculated using this magnitude as a distance function.

As an event progresses, the stations closest to the epicenter begin to measure their PGAs. This information obtained is used to adapt the initial attenuation relations. The most essential function of the PGA observations is to remove the scatter of the predicted PGA. Allen [14] addressed different events and pointed out the inconsistency between the observations and estimates of attenuation relationships. He explained this as the most important reason that attenuation relationships do not consider the near-surface amplification effects. However, if known, these effects can be easily incorporated into ElarmS.

The new version of Elarms (E3) includes improvements to accurately predict damaging earthquakes, classify S-wave or teleseismic signals, and minimize the number of false alarms [15]. This latest version uses an experimental amplitude-period threshold to detect P-waves generated after a seismic event in California. Optimization will be necessary if, unlike California, this version of the algorithm is to be used in regions where the soil layer is not deep, such as the Korean Peninsula [16-19].

2.2. PRESTo

Probabilistic Earthquake Early Warning System (PRESTo) is an early warning system that integrates state-of-the-art algorithms to rapidly locate, estimate magnitude, and assess damage in real time. The algorithm is free and open source for all users. PRESTo can easily be used by a seismic network, by companies and scientists interested in early warning. The system is being used in real time in Italy, and real time tests are being carried out in some countries (South Korea, Romania, Türkiye). PRESTo processes real-time acceleration or velocity data to determine P-wave arrivals after an earthquake. These data are received from the stations via a SeisComP server and can also read data in SAC format for play back of the past data. When an earthquake occurs, whether real-time or simulated, the system immediately detects the event and generates shaking maps and location and magnitude estimates for the relevant regions. In the PRESTo algorithm, the earthquake location is obtained by a real-time probabilistic approach. Magnitude estimation is based on the peak displacement (Pd) in the first 2-4 seconds of the P waves using magnitude scaling relations. In subsequent operations, the ground motion is estimated with the prediction equations derived for this process [13]. Figure 2 shows a real interface image of PRESTo after replaying the Irpinia earthquake in 1980.

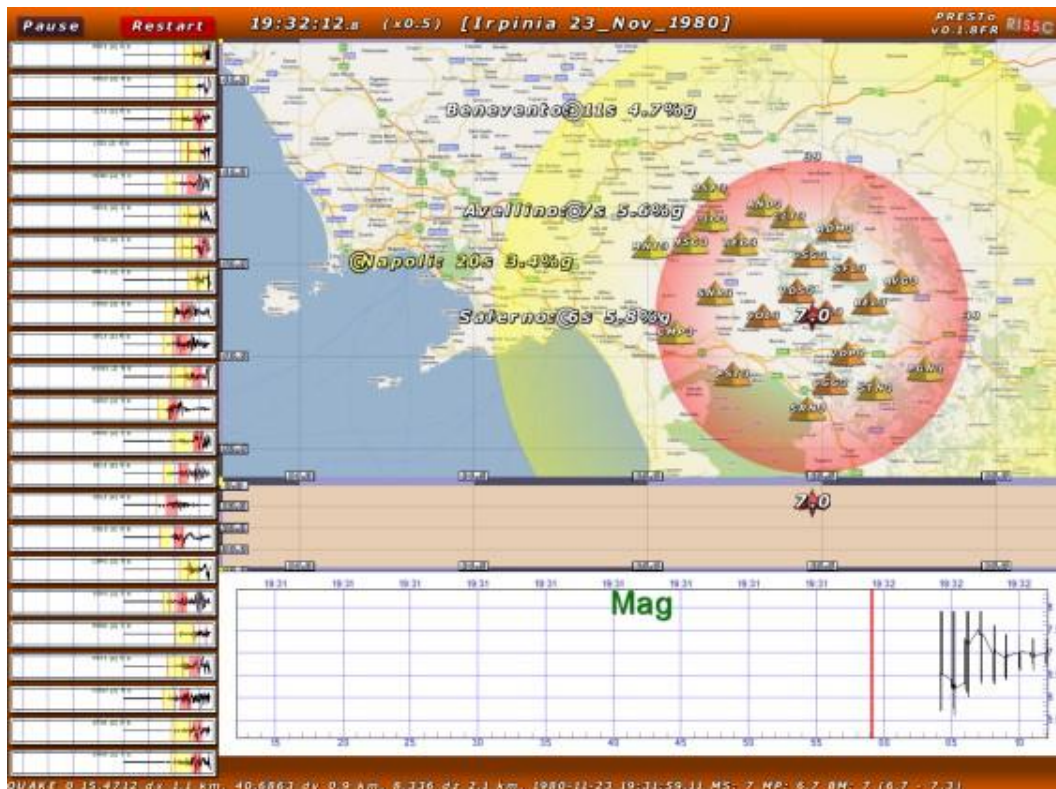


Figure 2. A real interface image of PRESTo after playback of synthetic traces for the 1980 Irpinia earthquake [13]

2.3. Virtual Seismologist (VS)

The Virtual Seismologist (VS) algorithm is based on the Bayesian approach and estimates an earthquake's magnitude, location, and ground shaking map using envelope attenuation relationships [21]. The Bayesian approach can be briefly defined as calculating a probability value using another known probability value. The location and magnitude parameters after an earthquake are estimated using ground motion ratios and attenuation relations within approximately three seconds after the first P-wave detected at the stations. The most important feature that distinguishes this method from others is the use of prior information. Preliminary information is especially useful in initial source estimates where limited data cannot obtain solutions. This preliminary information can be listed as the quality of the seismic network, the region's seismicity, the location of existing faults, and Gutenberg-Richter relations. The earlier earthquake forecasts can be made, the healthier early warnings can operate.

VS was developed, tested, and routinely run for the first time in Switzerland in 2013 for use within Seiscomp3 (SC3). It was then tested in six seismic networks worldwide (Greece, New Zealand, Romania, Türkiye, Iceland, and Southern California). SC3's widespread distribution and ease of installation made this wide application possible. Network operators already running SC3 for routine earthquake monitoring can incorporate VS(SC3) into their SC3 installation by updating to a version that includes VS(SC3) modules. The configuration of VS(SC3) modules is also detailed in the standard documentation of SC3.

Figure 3 shows the VS(SC3) processing flow. The arrows in the figure indicate the direction of the information flow represented by colors according to the sender type. The mediator (scmaster) and the orange modules are the heart of VS(SC3). The standard SC3 modules are used for P-wave detection (scautopick) and position detection (scautoloc). Scenvelope is a VS-specific preprocessing module. It provides a 1-s envelope data stream for all data (displacement, velocity, acceleration) and can access waves transmitted from different sources. Station and other information about the event can be kept in a meta-information. The scvsmag module of VS(SC3) performs a real-time magnitude calculation after an earthquake, which is continuously updated. Scvsmaglog is an EEW module and provides real-time warnings. These warnings can be taken by UserDisplay

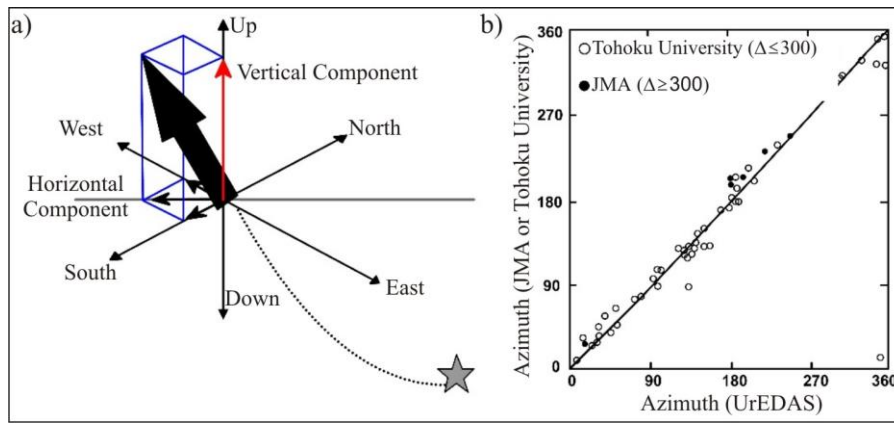


Figure 4. P-wave detection and back azimuth estimation [24]

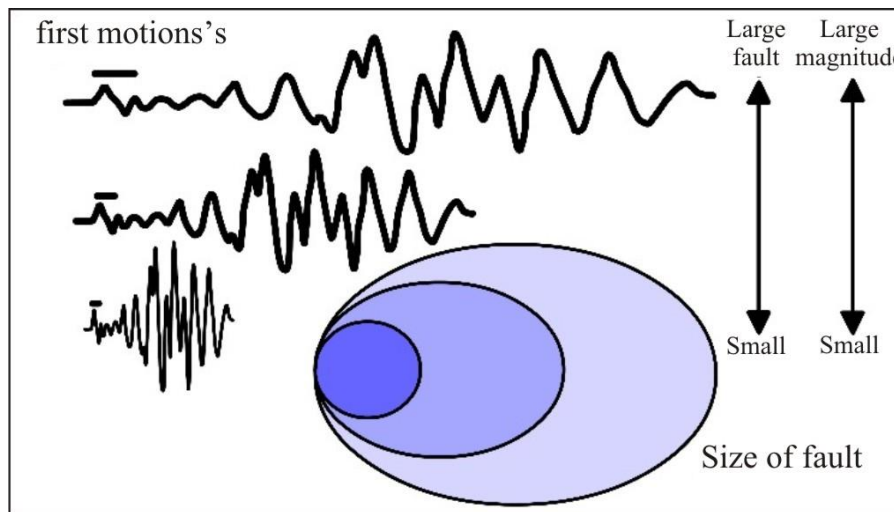


Figure 5. Relationship between first motion period and magnitude [24]

Unlike Uredas, Compact Uredas estimates the possible devastation after the earthquake directly from the earthquake motion and provides a warning if deemed necessary. Uredas performs this process with earthquake related parameters. The inner product of the acceleration and velocity vector obtains the hazard of the earthquake. This is called the destructive intensity (DI). However, the value obtained after this process is quite large. Therefore, the logarithm of the absolute value of the result is taken. DI value increases when the P wave is detected. It is recommended to use the PI value for the P wave alarm. PI is the largest DI value t time after detecting the P wave. Until the detection of the S-wave, the DI increases slowly and reaches its maximum value. This resulting value is associated with earthquake damage. This value is similar to the modified Mercalli intensity (MMI) or JMA instrumental intensity scale. DI has the advantage that it can be quickly determined in real-time after the P-wave is detected. Therefore, DI can be continuously monitored to provide a post-earthquake alert and estimate potential damage.

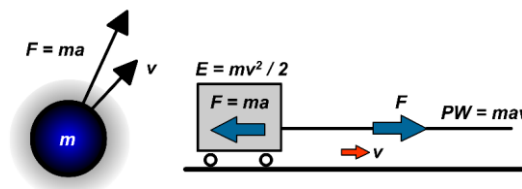


Figure 6. Relationship between acceleration, velocity, and intensity [24]

Based on Figure 6, the relationships between acceleration (cm/s²), velocity (cm/s), and intensity are given in (2.6)-(2.9). Here, *DI* is defined as Destructive Intensity, *RI* as Real-time Intensity, and *MMI* as Modified Mercalli Intensity.

$$PW = F \cdot v = m \cdot a \cdot v \quad (2.6)$$

$$DI = \log_{10}(a \cdot v) \quad (2.7)$$

$$RI = DI + 2.4 \quad (2.8)$$

$$MMI = (11/7) \cdot RI + 0.5 \quad (2.9)$$

The Compact UrEDAS uses similar operating principles to the UrEDAS. However, Compact UrEDAS provides faster alerts. It uses only a short period, such as one second of the P wave.

2.5. Real-time Earthquake Damage Reduction Precautions (ShakeAlert)

ShakeAlert was developed for the west coast of the United States in collaboration with the United States Geological Survey (USGS) and partners [25]. The system detects the P wave and estimates the earthquake's epicenter and magnitude. Then, by predicting the places expected to experience varying degrees of ground shaking, the ShakeAlert Message is issued [26,27]. This provides a warning before the S wave arrives, which produces strong shaking that causes damage. Accuracy and warning time are maximized as a combination of single stations and regional seismic network data is used. The warning period varies between 4 and 20 seconds depending on the fault type, the earthquake's focal depth, and the station's density close to the epicenter [28, 29]. The system has limitations: false and missed warnings are possible, and areas very close to the earthquake's epicenter may receive little or no warning. ShakeMap, a USGS Earthquake Hazards Program product, displays the intensity distribution automatically calculated from observed ground motion and is typically distributed to users a few minutes to 1 hour after an earthquake [30,31].

2.6. Next Generation Early Warning System

The capability of an EEWS is proportional to its ability to provide highly reliable real-time magnitude and shaking estimation in a short time. These parameters are also dependent on the accuracy of the source location. Therefore, improving the estimation of the earthquake location in EEWSs is very important. In the traditional systems, four or more stations need to be triggered for earthquake localization. Realizing this with fewer triggering stations is a challenge to overcome. Next-generation EEWSs are designed to improve the performance of location algorithms by utilizing real-time back azimuth. The next generation EEWS is roughly a real-time array-based location algorithm that gives an initial location estimate after S-wave arrival at the first array or after P-wave arrival at a second array [32]. If the location is calculated from only one array (if the arrays are in the same direction as the earthquake and the distance between the arrays is large), the location can be calculated when the S wave arrives after the first P wave before the P wave arrives in the second array. In other words, P-wave arrival to at least two arrays is required to calculate the location, or P and S-wave arrival to only one array is enough.

In the next generation of EEWS, the principles of array seismology are applied for real-time location determination. This system has two main modules: a single standalone array and multiple arrays. Waveform slowness and back azimuth are continuously monitored in a single standalone array. P and S wave arrivals are determined, and the back azimuth estimates distance and position. The resulting back azimuth determines the angle of the earthquake's location. This process is repeated with the second array. The closest distance at the intersection of the back azimuths of these two arrays is considered the earthquake's possible location. This estimated location information is updated when the next single station and array receive a P wave. Multiple arrays integrate data from several standalone modules. As P-wave arrivals occur, it collects multiple estimates of the back azimuth (BAZ) with surfaces of equal differential time (EDT). The real-time array method is advantageous for environments with sparse networks or unfavorable source-station configurations. The flowcharts of a single standalone array and multiple array modules are given in Figure 7 [32].

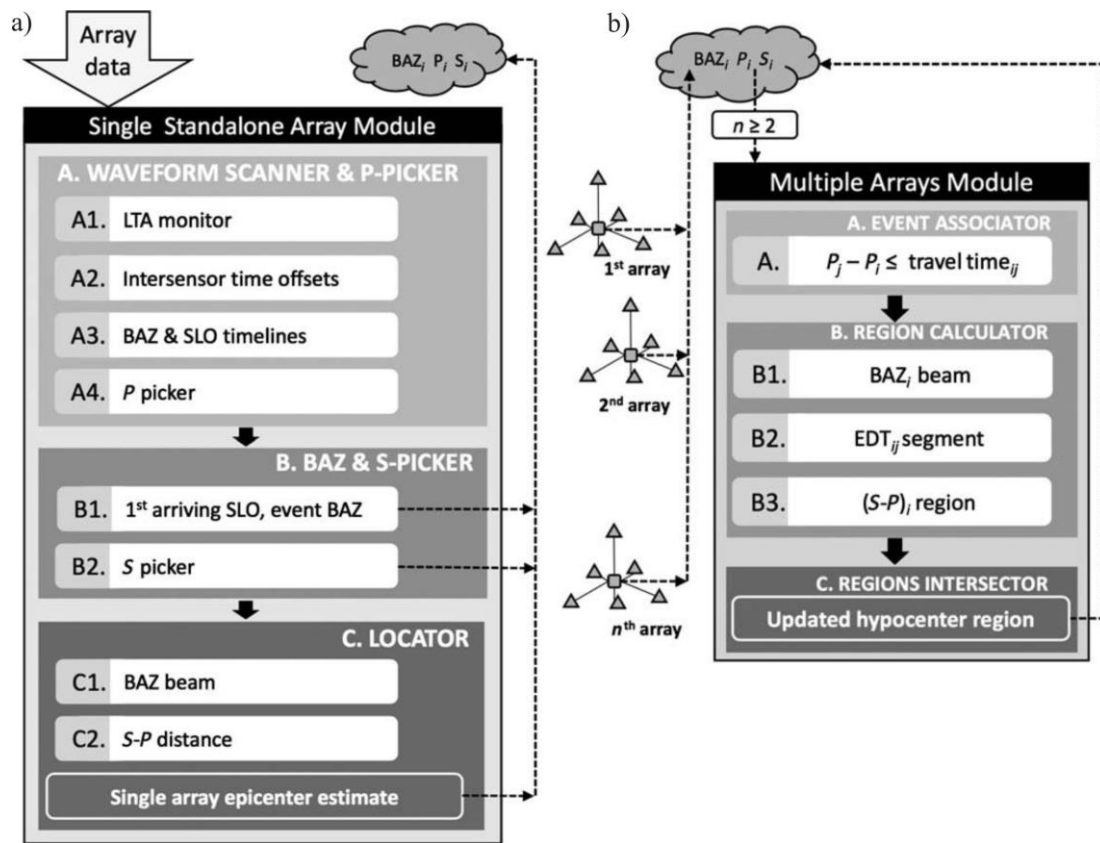


Figure 7. Flowcharts of a single standalone array (a) and multiple array modules. LTA stands for long-time average, and SLO stands for slowness [32]

Next generation EEWs have significant advantages over the traditional EEWs. These advantages are low cost of network configuration, linear seismic network with omnidirectional sensing capability, use of artificial intelligence technology which eliminates false warnings, fast installation and quick implementation of the system, and reduction of P phase detection to less than 1 s. Figure 8 shows the interface of the next-generation early warning system. Next-generation EEWs ideally consist of at least three stations in an array. These arrays can be triangular, quadrilateral, or diamond-shaped. It is important to know the location of each station. The distance between two arrays should be twice the distance of the fault to the array. Thus, if the fault is 10 km away, the distance between the two arrays should be 20 km.

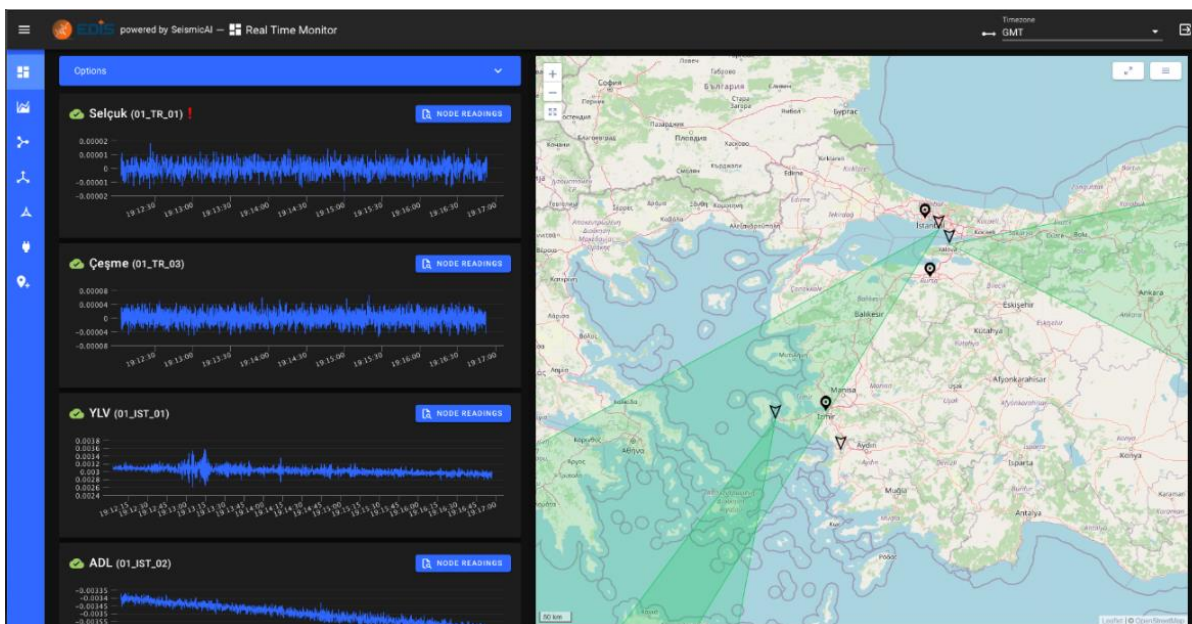


Figure 8. Next-generation early warning system user interface

2.6.1. An Earthquake Example for the Next Generation EEWS

On 26 September 2019 at 16.59 (GMT), an earthquake with $ML=5.7$ occurred at about 13 km in the Marmara Sea (offshore Silivri). Very close to the epicenter of this earthquake, another earthquake with a magnitude of $ML=3.5$ occurred on 11 October 2023. This example uses the latest version of the seismic network around the Sea of Marmara, and its outputs are discussed.

The next generation early warning system first identifies the hypocenter region rapidly as the stations detect the P wave phase for the earthquake with $ML=5.7$. In the $ML=5.7$ earthquake in 2019, the small-aperture arrays were far from the epicenter because they had been installed a short time ago, and therefore the benefit could not be seen. In 2019, when the earthquake occurred, only one array was installed at the Kandilli Observatory of Boğaziçi University. The array was very far from the epicenter of the earthquake. Actually, the system was in the testing phase. The system did not provide positive results due to the necessity of detecting the S-wave in single arrays. The earthquake's epicenter can be reliably determined as the standard network consisting of a single station detects the P-wave phase (Figure 9) [33].

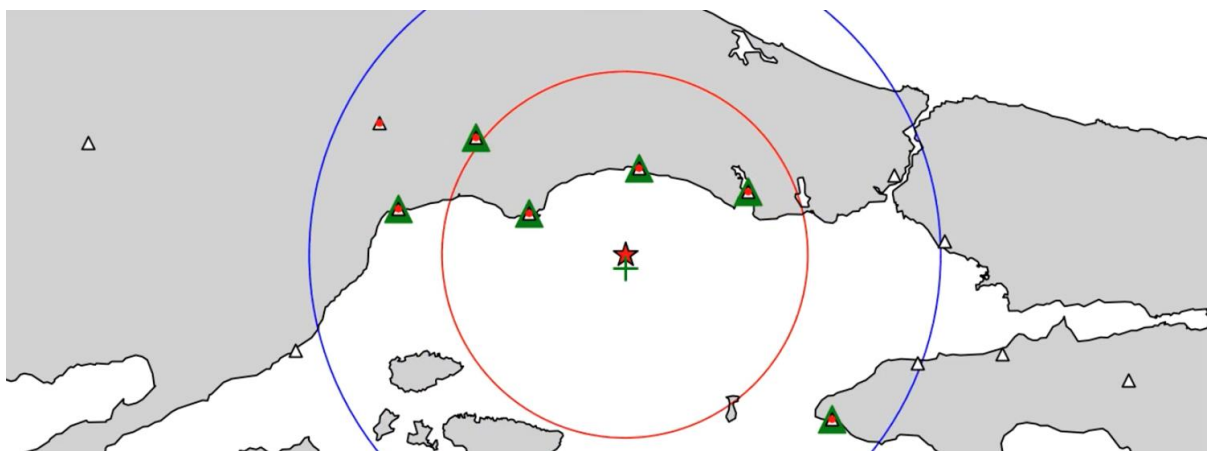


Figure 9. Determination of the epicenter location of the 26 September 2019 earthquake ($ML=5.7$) by the next generation EEWS. The red star represents the catalog location, green plus represents the location determined by the EEWS. The blue circle indicates the P wave, and the red circle indicates the S wave. Each triangle in the figure represents a single station. The green triangles and red-filled stations were used in the solution, and the P-wave was triggered

In the $ML=3.5$ earthquake on 11 October 2023, the network design with more frequent and better station distribution geometry than the earthquake in 2019 was used due to the network update made on the north coast before the earthquake (Figure 10). Figure 10 (a) shows the $ML=5.7$ earthquake analyzed in the standard single-station seismic network, and Figure 10 (b) shows the $ML=3.5$ earthquake analyzed in the hybrid network (both single station and array). In the traditional EEWS, a good station azimuthal distribution is needed to determine the magnitude and location of the earthquake. In the traditional EEWS, although two stations have P-wave triggers, a station's response in the south is expected to determine the magnitude and location (Figure 10 (a)). The solution starts when the P-wave arrives at the southern station. However, it is impossible to warn with the traditional EEW since the S wave will have already arrived at the settlements in the north by this time. As seen in Figure 10 (a), there is no solution when a P wave arrives at two of the traditional EEW stations. However, in the next generation EEWS, since there is an array at the locations of these stations, the first solution is provided with a 15 km error. In traditional EEW, it took 16 s to calculate the location and magnitude of the earthquake (due to high latencies). In the next generation EEWS, this time is 4 s. This is due to both low latencies and the use of different algorithms. The interface of the next generation EEWS, where an earthquake is analyzed, is shown in Figure 11.

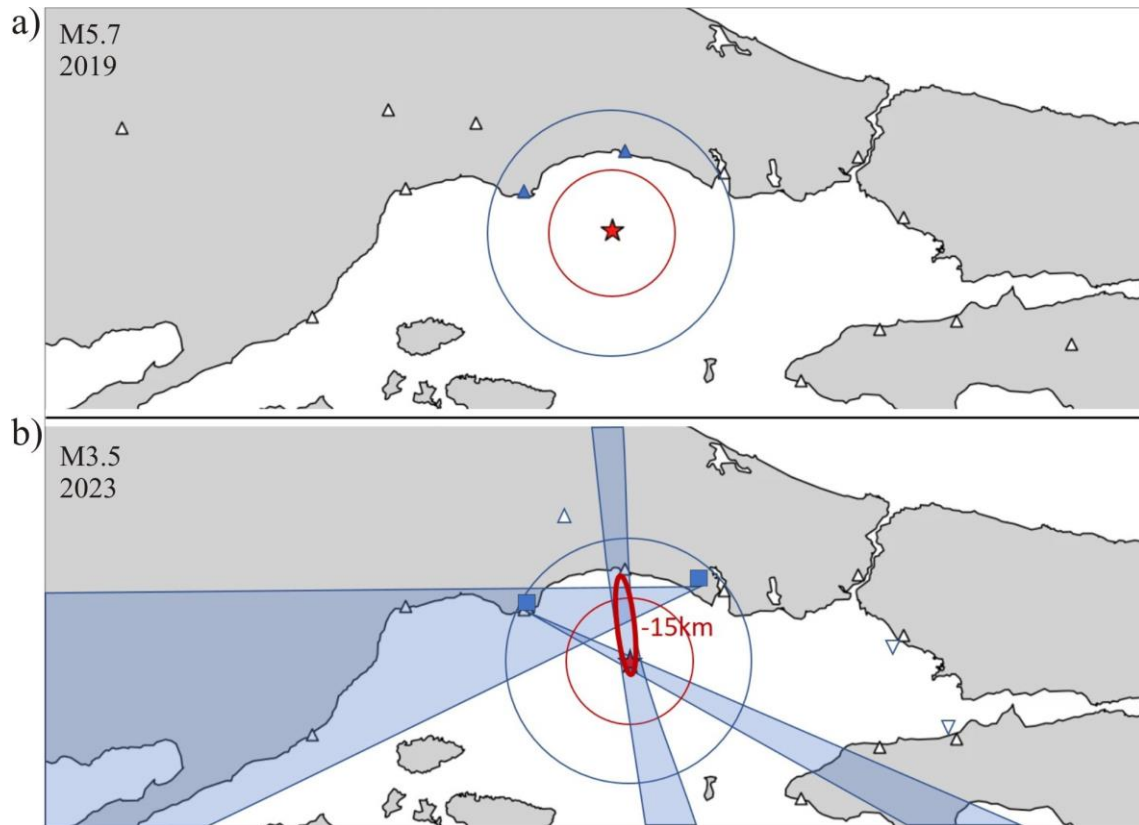


Figure 10. Earthquake epicenter determination with traditional (a) and next generation (b) EEWs. The top figure represents the 26 September 2019 earthquake (ML=5.7), and the bottom figure represents the 11 October 2023 earthquake (ML=3.5). The intersection of the back azimuths calculates the red ellipse in Figure 10 (b). Squares are arrays, and triangles are single stations. The symbols filled with blue are picked

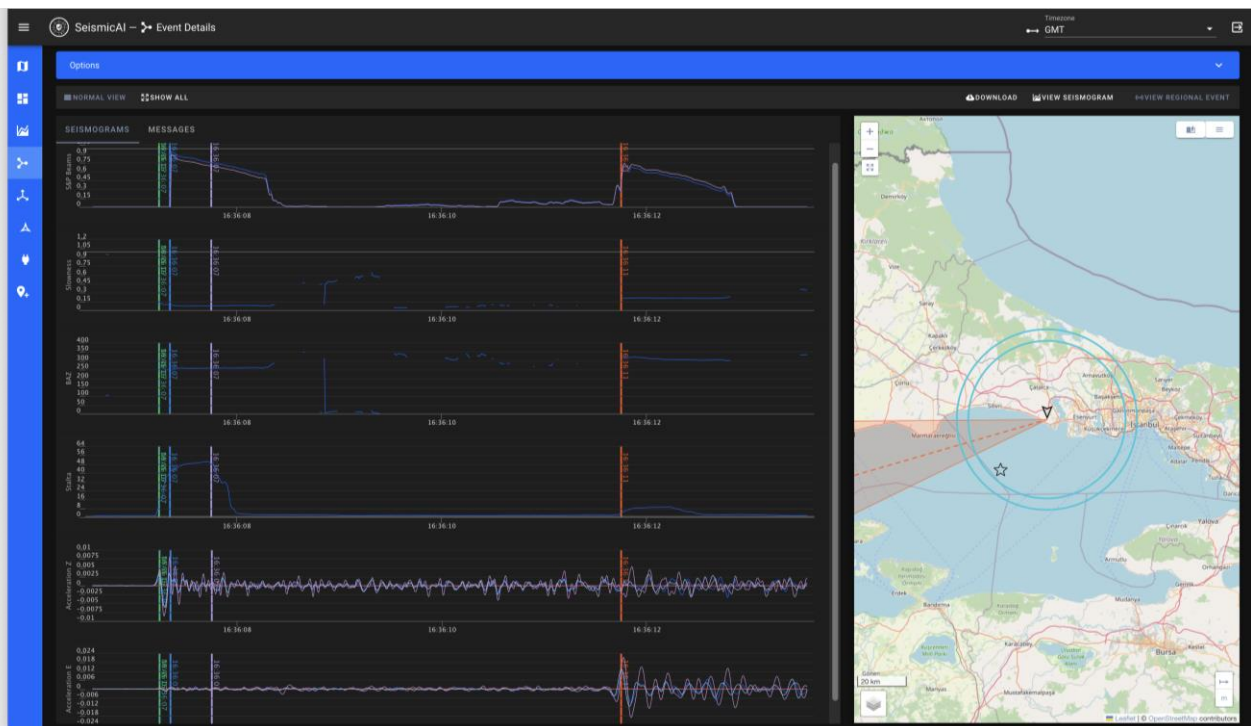


Figure 11. An example earthquake solution in a next-generation early warning interface. The black window on the left shows the event's slowness, back azimuth, P and S wave arrival times. The map on the right shows the back azimuth of the station and the possible location of the earthquake between the two blue circles

3. Conclusion

EEWS are systems that detect the onset of an earthquake and send timely warnings to the public or institutions. EEWS is an important tool in reducing loss of life, structural damage and economic losses. In the study, traditional and next-generation early warning algorithms are compared. The traditional EEW systems are widely used for regional warnings but have limitations such as the dependence of seismic warnings on the epicenter of the event, the same warning for every location, and false alarms or missed warnings. Next-generation EEW systems offer significant improvements to these limitations. The next-generation earthquake early warning algorithm has advantages such as low cost, detecting of earthquakes from anywhere, utilizing artificial intelligence algorithm for false warnings, fast installation and immediate operation of the system, and detecting P waves in a short time under 1 s. These advantages of next-generation early warning systems can provide an effective warning before potentially damaging earthquakes and eliminate the weaknesses of traditional warning systems.

Traditional EEWSs are particularly disadvantaged when faults with the potential to produce destructive earthquakes are located close to urban centers. The destructive S-wave can cause major destruction in densely populated areas until a warning is given. The best example of this can be an earthquake that may occur in the Marmara Sea. Next-generation EEWSs can overcome this weakness. Array-based location methodology quickly determines the epicenter, assesses the event's magnitude, estimates the ground shaking intensity, and issues a warning. It is a great advantage that the next generation EEWSs provide effective and fast solutions in regions like Türkiye, where very large earthquakes have occurred in the past. For this reason, further strengthening the next generation of EEWSs with the development of technology gains great importance in preventing all the losses that earthquakes will produce. The next generation of Earthquake Early Warning Systems (EEWS) can be used on a regional scale and in individual applications. While these systems are typically deployed across larger regions to provide widespread alerts, they are also adaptable in specific locations like factories, schools, homes, and other critical infrastructures.

Author Contributions

All the authors equally contributed to this work. They all read and approved the final version of the paper.

Conflicts of Interest

All the authors declare no conflict of interest.

Ethical Review and Approval

No approval from the Board of Ethics is required.

Acknowledgment

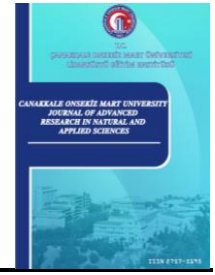
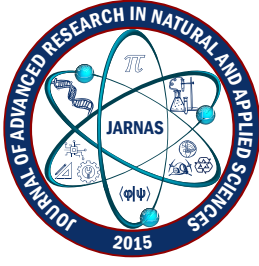
The preliminary findings of this study were presented at the 6th International Conference on Earthquake Engineering and Seismology held in Gebze, Türkiye, October 13-15, 2021. The authors would like to thank Andreas S. Eisermann for contributing to the study.

References



- [1] S. Tunç, B. Tunç, D. Çaka, Ş. Barış, *Dünyada yaygın olarak kullanılan erken uyarı sistemleri*, 6th International Conference on Earthquake Engineering and Seismology, Kocaeli, 2021, pp. 895–909.
- [2] R. N. Nof, R. M. Allen, *Implementing the ElarmS earthquake early warning algorithm on the Israeli seismic network*, Bulletin of the Seismological Society of America 106 (5) (2016) 2332–2344.

- [3] G. Festa, M. Picozzi, A. Caruso, S. Colombelli, M. Cattaneo, L. Chiaraluca, L. Elia, C. Martino, S. Marzorati, M. Supino, A. Zollo, *Performance of earthquake early warning systems during the 2016–2017 Mw 5–6.5 Central Italy sequence*, Seismological Research Letters 89 (1) (2018) 1–12.
- [4] Y. M. Wu, H. Mittal, T. C. Huang, B. M. Yang, J. C. Jan, S. K. Chen, *Performance of a low-cost earthquake early warning system (P-Alert) and shake map production during the 2018 Mw 6.4 Hualien, Taiwan, earthquake*, Seismological Research Letters 90 (1) (2019) 19–29.
- [5] J. Santos-Reyes, *How useful are earthquake early warnings? The case of the 2017 earthquakes in Mexico City*, International Journal of Disaster Risk Reduction 40 (2019) 101148 11 pages.
- [6] Y. Kodera, N. Hayashimoto, K. Moriwaki, K. Noguchi, J. Saito, J. Akutagawa, S. Adachi, M. Morimoto, K. Okamoto, S. Honda, M. Hoshihara, *First-year performance of a nationwide earthquake early warning system using a wavefield-based ground-motion prediction algorithm in Japan*, Seismological Research Letters 91 (2A) (2020) 826–834.
- [7] A. I. Chung, M. A. Meier, J. Andrews, M. Böse, B. W. Crowell, J. J. McGuire, D. E. Smith, *ShakeAlert earthquake early warning system performance during the 2019 Ridgecrest earthquake sequence*, Bulletin of the Seismological Society of America 110 (4) (2020) 1904–1923.
- [8] C. Peng, P. Jiang, Q. Ma, P. Wu, J. Su, Y. Zheng, J. Yang, *Performance evaluation of an earthquake early warning system in the 2019–2020 M 6.0 Changning, Sichuan, China, Seismic Sequence*, Frontiers in Earth Science 9 (2021) 699941 13 pages.
- [9] S. Cho, J. K. Ahn, E. H. Hwang, *Optimization of network-based earthquake early warning systems on the Korean Peninsula*, IEEE Access 10 (2022) 83931–83939.
- [10] M. Medina, R. Sanchez, S. Riquelme, M. C. Flores, P. Koch, F. Bravo, S. Barrientos, I. Henson, A. Chung, D. Melgar, C. Mpodozis, M. Hellweg, R. Allen, *An earthquake early warning system for Northern Chile based on ElarmS-3*, Seismological Society of America 93 (6) (2022) 3337–3347.
- [11] S. Tunç, B. Tunç, E. Budakoğlu, D. Çaka, R. N. Nof, Ş. Barış, *Implementation of the EPIC earthquake early warning system in the Bursa Province (Türkiye) and its surroundings*, Applied Sciences 13 (8) (2023) 4985 17 pages.
- [12] G. Cremen, C. Galasso, *Earthquake early warning: Recent advances and perspectives*, Earth-Science Reviews 205 (2020) 103184 15 pages.
- [13] C. Satriano, L. Elia, C. Martino, M. Lancieri, A. Zollo, G. Iannaccone, *PRESTo, the earthquake early warning system for southern Italy: Concepts, capabilities and future perspectives*, Soil Dynamics and Earthquake Engineering 31 (2) (2011) 137–153.
- [14] R. M. Allen, *The ElarmS earthquake early warning methodology and application across California, in earthquake early warning systems*, Springer, Berlin Heidelberg, 2007, Ch. 3, pp. 21–43.
- [15] R. M. Allen, P. Gasparini, O. Kamigaichi, M. Bose, *The status of earthquake early warning around the world: An introductory overview*, Seismological Research Letters 80 (5) (2009) 682–693.
- [16] Y. Nakamura, *On the urgent earthquake detection and alarm system (UrEDAS)*, in: Proceedings of Ninth World Conference on Earthquake Engineering, Tokyo, 1988, pp. 673–678.
- [17] R. M. Allen, H. Kanamori, *The potential for earthquake early warning in southern California*, Science 300 (5620) (2003) 786–789.
- [18] A. B. Lockman, R. M. Allen, *Single-station earthquake characterization for early warning*, Bulletin of the Seismological Society of America 95 (6) (2005) 2029–2039.
- [19] E. L. Olson, R. M. Allen, *The deterministic nature of earthquake rupture*, Nature 438 (7065) (2005) 212–215.

- [20] A. B. Lockman, R. M. Allen, *Magnitude-period scaling relations for Japan and the Pacific Northwest: Implications for earthquake early warning*, Bulletin of the Seismological Society of America 97 (1B) (2007) 140–150.
- [21] G. Cua, T. Heaton, *The Virtual Seismologist (VS) method: A Bayesian approach to earthquake early warning*, in: P. Gasparini, G. Manfredi, J. Zschau (Eds.), *Earthquake Early Warning Systems*, Springer Berlin Heidelberg, Berlin, 2007, Ch. 7, pp. 97–132
- [22] Y. Behr, J. F. Clinton, C. Cauzzi, E. Hauksson, K. Jónsdóttir, C. G. Marius, A. Pinar, J. Salichon, E. Sokos, *The Virtual Seismologist in SeisComP3: A new implementation strategy for earthquake early warning algorithms*, Seismological Research Letters 87 (2A) (2016) 363–373.
- [23] F. Massin, J. Clinton, M. Böse, *Status of earthquake early warning in Switzerland*, Frontiers in Earth Science 9 (2021) 707654 20 pages.
- [24] J. Saita, Y. Nakamura, *UrEDAS: The early warning system for mitigation of disasters caused by earthquakes and tsunamis*, in: J. Zschau, A. Küppers (Eds.), *Early Warning Systems for Natural Disaster Reduction*, Springer, Berlin, 2003, pp. 453–460.
- [25] M. D. Kohler, E. S. Cochran, D. Given, S. Guiwits, D. Neuhauser, I. Hensen, R. Hartog, P. Bodin, V. Kress, S. Thompson, C. Felizardo, J. Brody, R. Bhada, S. Schwarz, *Earthquake early warning ShakeAlert system—West coast wide production prototype*, Seismological Research Letters 89 (1) (2018) 99–107.
- [26] D. D. Given, S. E. Cochran, T. Heaton, E. Hauksson, R. Allen, P. Hellweg, J. Vidale, P. Bodin, *Technical implementation plan for the ShakeAlert production system—An earthquake early warning system for the West Coast of the United States*, U.S. Geological Survey Open-File Report (2014) 1097 25 pages.
- [27] A. I. Chung, C. J. Neighbors, A. Belmonte, M. Miller, H. H. Sepulveda, C. Christensen, R. Jakka, E. S. Cochran, J. F. Lawrence, *The quake-catcher network rapid aftershock mobilization program following the 2010 M8.8 Maule, Chile earthquake*, Seismological Research Letters 82 (2011) 526–532.
- [28] E. S. Cochran, B. T. Aagaard, R. M. Allen, J. Andrews, A. S. Baltay, A. J. Barbour, P. Bodin, B. A. Brooks, A. Chung, B. W. Crowell, D. D. Given, T. C. Hanks, J. R. Hartog, E. Hauksson, T. H. Heaton, S. McBride, M-A. Meier, D. Melgar, s. E. Minson, J. R. Murray, J. A. Strauss, D. Toomey, *Research to improve ShakeAlert earthquake early warning products and their utility*, U. S. Geological Survey Open-File Report (2018) 1131 17 pages.
- [29] J. J. McGuire, D. E. Smith, A. D. Frankel, E. A. Wirth, S. K. McBride, R. M. de Groot, *Expected warning times from the ShakeAlert earthquake early warning system for earthquakes in the Pacific Northwest (ver. 1.1, March 24, 2021)*, U.S. Geological Survey Open-File Report (2021) 1026 37 pages.
- [30] D. J. Wald, B. C. Worden, V. Quitoriano, K. L. Pankow, *ShakeMap manual: Technical manual, users guide, and software guide*, 12 (2005) A1.
- [31] C. B. Worden, D. J. Wald, T. I. Allen, K. Lin, D. Garcia, G. Cua, *A revised ground-motion and intensity interpolation scheme for ShakeMap*, Bulletin of the Seismological Society of America 100 (6) (2010) 3083–3096.
- [32] A. S. Eisermann, A. Ziv, H. G. Wust-Bloch, *Array-based earthquake location for regional earthquake early warning: Case studies from the Dead Sea transform*, Bulletin of the Seismological Society of America 108 (4) (2018) 2046–2053.
- [33] A. S. Eisermann, *Hybrid small-aperture-array networks in EEW*, in: 5th International Conference on Earthquake Early Warning, İstanbul, 2023, pp. 16.



Ergonomic Risk Analysis of Working Postures for a Textile Factory Worker

Güler İmamoğlu¹ , Bestem Esi² 

^{1,2}Department of Industrial Engineering, Faculty of Engineering, İstanbul Gedik University, İstanbul, Türkiye

Article Info

Received: 17 Jun 2024

Accepted: 24 Sep 2024

Published: 30 Sep 2024

Research Article

Abstract – The textile sector significantly contributes to total employment and exports in our country. At the same time, it has a production structure that is labor-intensive and where most of the work is done manually and repetitively. As a result of shift work and long working hours in textile production, some musculoskeletal disorders occur in employees due to non-ergonomic posture and repetitive movements. Untreated and neglected musculoskeletal disorders cause more serious problems for employees in the long term. In this study, ergonomic risk assessment was conducted using the Rapid Entire Body Assessment Method for the working postures of textile workers working in the weaving department of a textile factory. Thus, potential risk factors and ergonomic strain levels exposed to employees were determined. As a result of the research, it was determined that the employee was exposed to high risk, and precautions needed to be taken quickly. In addition, some recommendations were made to prevent musculoskeletal disorders and loss of productivity in the business through some precautions.

Keywords – *Rapid entire body assessment (REBA) method, ergonomics, musculoskeletal disorders, textile*

1. Introduction

Ergonomics is the harmonization of working and living conditions with humans, and ergonomics aims to prevent occupational diseases and work accidents and improve working conditions to protect and develop employees mentally and physically. In the workplace, frequent repetitive movements, use of non-ergonomic equipment, straining and incorrect working postures, long working hours, inadequate rest periods, excessive strain, and heavy lifting cause some discomfort in employees. The most important of these disorders is musculoskeletal system diseases. Musculoskeletal disorders affect the musculoskeletal system, including muscles, tendons, ligaments, joints, and nerves. It can be seen in certain body parts such as the back, neck, shoulders, arms, wrists, hands, and legs. Symptoms usually present as pain, discomfort, stiffness, weakness, numbness, tingling, or limited range of motion. Work-related musculoskeletal disorders (MSDs) are related to occupational activities and conditions. They are caused by factors such as repetitive movements, forceful efforts, awkward postures, vibration, heavy lifting, positions involving prolonged static loads, or exposure to ergonomic hazards [1]. According to the World Health Organization (WHO), MSDs account for approximately 40% of all occupational diseases. In addition, if no precautions are taken after a worker contracts MSD, the new worker working at that job may also contract the same disease; thus, WHO accepts MSDs in the epidemic disease category [2].

¹guler_imamoglu@hotmail.com; ²bestem.esi@gedik.edu.tr (Corresponding Author)

Having MSDs causes some negative consequences not only for employees but also for businesses. Some negative consequences are reduced productivity, work planning and process disruptions due to employee absenteeism, and sickness costs. These illnesses significantly affect employees' ability to perform their duties effectively and efficiently. Depending on the severity of the condition, employees may experience functional limitations, reduced productivity, increased absenteeism, and even disability [3].

There are various systematic approaches to identifying and assessing ergonomic risks and hazards. One of these is the Rapid Entire Body Assessment (REBA) method. This method is applied by evaluating the applied force, repetitive movements, and duration of postures through observation. The REBA method is a biomechanical tool commonly used to assess work-related MSDs. It is recognized as an effective method for identifying ergonomic risks in the workplace and implementing preventive measures.

The textile industry is an important sector worldwide and employs millions of people. It is one of the sectors with a large contribution share to total employment and exports in Turkey. At the same time, it has a production structure that is labor-intensive and where most of the work is done manually and repetitively. Some musculoskeletal diseases may occur in textile production workers who work shifts and long hours due to non-ergonomic posture and repetitive and inappropriate movements.

Some of the studies in the literature on ergonomic risk factors that threaten employees in the work environment, ergonomic risk analyses, and musculoskeletal disorders seen in employees are summarized below: Viera and Kumar [4] contributed to the scientific literature by examining working postures and conducting research on workers in different occupations to determine what kind of ergonomic difficulties working postures cause. Saraji et al. [5] used the REBA method to evaluate the ergonomic conditions in dentistry professions and the relationship between MSD and working conditions in different body parts. The Scandinavian Musculoskeletal Questionnaire (NMQ) for the prevalence of MSD concluded that professional training given to dentists for correct working conditions and postures should be increased. Using the REBA method, Mahdavi et al. [6] investigated musculoskeletal disorders in 172 female hairdressers at risk of MSD in Khorramabad, Iran. As a result, they concluded that standing for long periods, inappropriate working positions, trunk flexion, high effort, and repetitive movements are risk factors for musculoskeletal disorders. Atıcı et al. [7] conducted a REBA analysis in their study to improve improper working practices in a cable manufacturing company in the automotive industry. As a result of their analysis, they observed that workers were experiencing difficulties. They offered improvements to minimize the difficulties. Madani and Dababneh [8] evaluated the observation-based REBA, an ergonomic assessment tool, in terms of its development, applications, validity, and limitations and showed that REBA is suitable for evaluating jobs in a wide range of professional environments in terms of posture as a result of research. Çoker and Selim [9] examined the working positions of workers in a textile company in the cutting room, sewing room, model, and fabric warehouse departments. They conducted an ergonomic risk analysis using the REBA method. As a result of the study, they made recommendations to the company management regarding the working conditions to increase the health and safety of employees, work efficiency, and quality. Haekal et al. [10] used the REBA method in a pharmaceutical company to analyze the operator's posture while working in a packaging material warehouse. They provided suggestions to improve the activities that caused complaints. Kırıcı et al. [11] investigated the ergonomic risk assessment of a logistics warehouse. The working postures of the workers were examined using REBA, rapid upper limb assessment (RULA), and National Institute for Occupational Safety and Health (NIOSH) methods. In addition, the ambient noise, personal noise, ambient dust, personal dust, vibration, chemical and thermal comfort values were measured with accredited devices. Özay and Özcan [12] analyzed five different cleaning jobs and twelve working posture positions in two different workplaces using the REBA method. For this purpose, both companies were visited once a week, four times a month, and postures were recorded, monitored, and photographed. As a result of these analyses, it was stated that four of the working positions were calculated as moderately risky, and one had a low-risk score. Tarakçı et al. [13] conducted an ergonomic risk analysis using the REBA method on a selected production line of a company and presented suggestions for improvement. As a result of the REBA analysis, it is stated that 66.6% of the production process is at medium risk, and 33.4% is at high risk. Akalp et al. [14] examined the postures of 20 agricultural workers in olive cultivation in the

Marmara Region using the REBA method and suggested solutions to reduce risk levels. Şahin and Vapur [15] conducted ergonomic risk analyses in a women's hair salon. REBA and RULA methods were used. 8 basic procedures performed in the hair salon were evaluated; 2 procedures were identified as high risk and 6 procedures as medium risk. Muhacırcı et al. [16] aim to evaluate the ergonomic risks of operators in the maintenance and repair workshop of a textile factory with REBA and RULA methods. As a result, it is stated that reducing ergonomic risks is critical to increasing workers' health and productivity. Kee [17] aims to systematically compare three methods related to MSDs: Ovako Work Posture Analysis System (OWAS), RULA, and REBA. The study noted that RULA was the most used method among the three techniques; many studies adopted RULA even in assessing unstable lower limb postures. Amri and Putra [18] aimed to reduce the risk level gained by conducting Rapid Office Strain Assessment (ROSA) and REBA for office workers in engineering departments. Posture analysis data processing using the ROSA method indicated that five employees surveyed were at risk levels and required immediate correction. The REBA method indicated that five employees were at risk of urgent needs and requirements. In their study, Varghese et al. [19] applied the REBA method for posture analysis of rubber tappers. It was found that most of the workers (84%) were at moderate risk of MSDs, while the remaining 16% of the participants were at high risk and required immediate corrective measures. Kavus et al. [20] compared the REBA methodology developed using artificial neural networks and neuro-fuzzy systems in the ergonomic risk assessment of service workers. The study examined the differences and advantages between these two methods and evaluated the effectiveness of each in determining ergonomic risks. As a result, it was found that artificial neural networks provide higher accuracy rates, while neuro-fuzzy systems stand out with their flexibility and interpretability. Arslan and Ünver [21] analyzed three work postures of workers in the hot rolling section of an iron and steel factory in Karabük using the REBA method. They made recommendations to reduce risk levels according to the REBA results.

Ayvaz et al. [22] evaluated the ergonomic risks of working positions of nurses working in a medical faculty hospital using REBA and RULA methods. 383 nurses were examined in the study, and moderate ergonomic risks were detected, especially in departments such as operating rooms. The majority of nurses experienced musculoskeletal disorders. As a result, it was emphasized that working positions should be improved. Kibria [23] examines the ergonomic analysis of working positions at a construction site with REBA and RULA methods. The research aims to evaluate the ergonomic risks workers encounter at the construction site during work and provide the necessary recommendations to reduce these risks and increase occupational safety. The results show that most workers work at medium and high-risk levels and that ergonomic improvements are needed. Kodle et al. [24] conducted a study to identify musculoskeletal disorders among workers in the mining industry. The study administered a questionnaire to twenty-five operators, followed by workplace observations.

The results indicated that more than 90% of the employees were exposed to high-risk levels, and immediate changes were necessary. Yunian et al. [25] analyzed the welding operators' body positions and working conditions using the REBA method in their study. The research revealed that most welding operators are at high ergonomic risk, negatively affecting work efficiency. It has been stated that incorrect body positions and inappropriate working conditions reduce the performance of workers by causing musculoskeletal problems. Biradar et al. [26] aimed to determine ergonomic risks associated with job duties within the company by performing posture analysis in their study. In the study, an evaluation was made, and recommendations were developed to reduce these risks. Gür et al. [27] analyzed the postures of emergency service workers during patient intervention using the REBA and RULA methods. These analyses aimed to take precautions in advance for risky postures that may cause occupational musculoskeletal diseases. At the end of the study, it was stated that two posture positions were in the low-risk category, one in the medium risk category, one in the very high-risk category, and three in the high-risk category.

When the literature is investigated, it is seen that ergonomic analyses conducted within the textile sector are generally made by evaluating employees in the ready-made clothing and apparel departments. However, the sector has a labor-intensive production structure, and since there is a lot of manual work in most production and departments, examining other units is of great importance in terms of precautions to be taken. In textile

factories, manual work, such as carrying, lifting, etc., is common in the weaving departments. This study aims to analyze the working postures and ergonomic strains of a textile worker in the weaving department of a textile factory using the REBA method, one of the ergonomic risk assessment techniques. At the end of the study, potential risk factors and ergonomic strain levels to which workers are exposed were determined. Some precautions can be taken when acceptable limit values are exceeded and are specified, and suggestions are made.

2. Materials and Methods

This study examined the movements of textile workers working in the weaving department of a textile factory in Tekirdağ. In the weaving department, workers wrap the fabric on the roll, cut it, and carry it. These processes are carried out manually. In order to perform ergonomic risk analysis using the REBA method, the company was visited and the workers' movements in the relevant department were carefully observed and recorded with video and photography. The REBA method is developed by Hignett and McAtamney [28], especially useful for identifying risks in manual handling, lifting, etc. The REBA method aims to create a posture analysis system sensitive to musculoskeletal risks in various tasks. This system aims to provide a scoring system for muscle activity resulting from static, dynamic, rapidly changing, or unstable postures by dividing the body into segments to be coded individually. In addition, the method offers an action level that indicates urgency [28]. In the REBA method, dynamic and static postures can be analyzed, allowing the entire body to be evaluated.

REBA evaluates body posture factors by assigning points to each area for each critical job task. In this way, the risk caused by a working posture or movement to be analyzed is expressed numerically. When using REBA, the right and left sides of the body are evaluated simultaneously. In the REBA method, a score ranging from 1 to 15 depends on the stretching and bending in the trunk, neck, legs, upper arms, lower arms, and wrists during a working posture and the loads the worker is exposed to during these postures. To determine the REBA score, the body is first examined in two parts, group A and group B. Table 1 includes Group A components, and the trunk, neck, and legs are examined according to this table.

Table 1. Group A body diagrams [28]

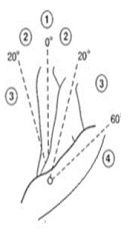
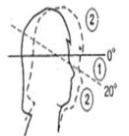
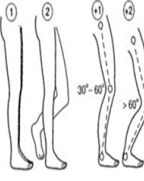
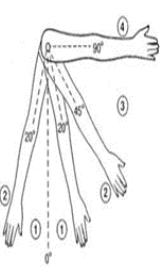
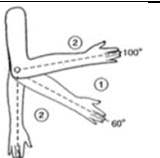
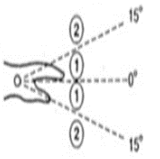
TRUNK			
Movement	Score	Change Score	
Upright	1	If there is a twisting or side flexed, add +1 to the score.	
0°-20° Flexion	2		
0°-20° Extension			
20°-60° Flexion	3		
>20° Extension			
>60° Flexion	4		
NECK			
Movement	Score	Change Score	
0°-20° Flexion	1	If there is a twisting or side flexed, add +1 to the score.	
>20° Flexion or Extension	2		
LEGS			
Movement	Score	Change Score	
Bilateral weight bearing, walking or sitting	1	If there is flexion between 30°-60° in the knees, add +1 to the score	
Unilateral weight bearing. Feather weight bearing or an unstable posture	2	If >60° flexion, add +2 to score (in standing position)	

Table 2 includes the components of Group B, and in Group B, the upper arm, lower arm, and wrists are examined.

Table 2. Group B body diagrams [28]

UPPER ARMS			
Movement	Score	Change Score	
Extension and Flexion up to 20°	1	If the arm is rotated or extended, add +1 to the score.	
>20° Extension 20°-45° Flexion	2		
45°-90° Flexion	3	If the shoulder is raised, add +1	
>90° Flexion	4	If the movement is done with gravity support, it will be -1.	
LOWER ARMS			
Movement	Score	Change Score	
60°-100° Flexion	1	If there is rotation or stretching, add +1 to the score	
<60° Flexion and >100° Flexion or Extension	2		
WRISTS			
Movement	Score	Change Score	
0°-15° Flexion or Extension	1	If the wrist is twisted or deviated, add +1 to the score.	
>15° Flexion or Extension	2		

In group A, the trunk, neck, and legs are examined; in group B, the upper arms, lower arms, and wrists are examined. After the individual scores for the trunk, neck, and legs are determined, a score is determined by combining these scores. The A score is obtained by adding the carried load/force score to this score. Table 3 shows the Load/Force Score table.

Table 3. Load/Force score table [28]

0	1	2 ♦	+1
<5 kg	5-10 kg	>10 kg	When sudden or rapidly increasing use of power is required

Similarly, separate scores are determined for the upper arm, lower arm, and wrist, and a score is determined by combining these scores. The coupling score is added to this score to obtain the B score. Table 4 shows the coupling table.

Table 4. Coupling table [28]

0	1	2	+1
Good	Fair ♦	Poor	Unacceptable
Well-fitting and moderate forceful coupling with the hand	Hand is acceptable but not ideal, or the coupling is acceptable via another part of the body	Hand-holding is possible but not acceptable	Improper or unsafe grip; no grip or grip not suitable for another body part

Finally, the C score, which consists of A and B scores, is obtained, and the REBA score is obtained by adding the activity score to this score [29]. According to the REBA rating table, where action levels are determined, the REBA rating can be between 0-4, the REBA score can be between 1-15, and the measures to be taken differ according to the determined score [28].

3. Results and Discussion

In the study, the working postures of a worker in the weaving department of a textile factory were observed. The work observed in this section is done manually by the workers. Figure 1 shows the process of the textile worker wrapping the fabric on a 2-layer roll, Figure 2 shows the process of cutting the rolled fabric, and Figure 3 shows the process of carrying the fabric roll to the loom.

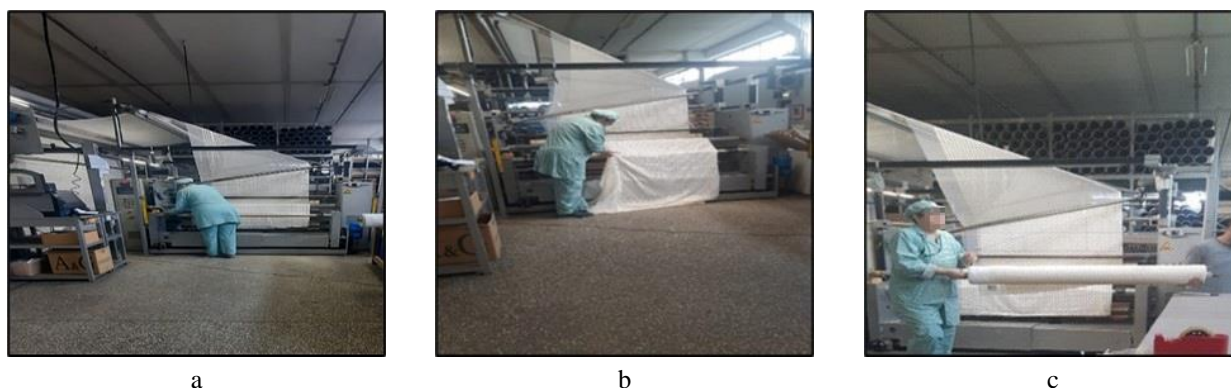


Figure 1. Working postures of textile workers, a) Fabric wrapping process, b) Cutting the fabric in roll form, and c) Transporting the fabric roll to the loom

In the REBA method, the group A components used to obtain the A score, in which the trunk, neck, and legs are analyzed, are shown in Table 1 [28]. When evaluating the A score in the REBA method according to Table 1, more than 20° flexion (3 points) was observed in the worker's body, especially during fabric wrapping and cutting operations. In addition, since the trunk was exposed to rotation and bending, +1 more points were added, making the trunk score 4. When the neck part was examined, the score was 2 because more than 20° of flexion was observed during the wrapping and cutting. In addition, since there is a lateral rotation movement in the neck, +1 is added to the score. Thus, the neck score was found to be 3. Since flexion between 30° and 60° was observed in the legs, the leg score was 1. When these values were examined in the Group A table in Table 5, the A score was obtained as 6.

Table 5. Group A table [28]

		Neck											
		1				2				3 ♦			
Trunk	Legs	1	2	3	4	1	2	3	4	1 ♦	2	3	4
		1	1	2	3	4	1	2	3	4	3	3	5
	2	2	3	4	5	3	4	5	6	4	5	6	7
	3	2	4	5	6	4	5	6	7	5	6	7	8
	4 ♦	3	5	6	7	5	6	7	8	⑥	7	8	9
	5	4	6	7	8	6	7	8	9	7	8	9	9

Table 3 below shows the Load/Force Score Table. Since the fabric roll carried by the employee to the loom weighs more than 10 kg, 2 more points are added to the score, and the final A score is 8.

In the REBA method, the group B components used to analyze the upper arms, lower arms, and wrists are analyzed, are shown in Table 2 [28]. When evaluating the B score in the REBA method according to Table 2, 20°-45° flexion (2 points) was observed in the worker's upper arm during the fabric wrapping and cutting operations. When the lower arm was examined, flexion between 60° and 100° (1 point) was observed in the lower arm during fabric wrapping, cutting, and carrying the fabric roll. The wrist position was between 0° - 15° (1 point). In addition, since the wrist made a side rotation movement, 1 more point was added, and the wrist score was found to be 2. When these values were examined according to Table 2, the B score was reached as 2. Finally, when the Group B table in Table 6 was discussed, the B score was obtained as 2.

Table 6. Group B table [28]

		Lower Arms					
		1 ♦			2		
Upper Arms	Wrists	1	2 ♦	3	1	2	3
		1	1	2	2	1	2
	2 ♦	1	②	3	2	3	4
	3	3	4	5	4	5	5
	4	4	5	5	5	6	7
	5	6	7	8	7	8	8
	6	7	8	8	8	9	9

Table 4 below shows the Coupling Score Table. The worker's coupling difficulty was moderate; therefore, the medium-level coupling score (+1) is added to the B score, resulting in a final B score of 3.

As a result of these data, the C score is calculated by the intersection of A and B scores. The employee's C score is 8, according to Table 7. In addition, since the employee remained in a static position for a certain period, +1 is added as an activity score since there is a repeated short interval cutting movement. As a result, the REBA score is found to be 10. A REBA score of 10 indicates a high ergonomic risk level and that changes are urgently needed. This means that the job or task being assessed poses a serious ergonomic risk and requires intervention. In such a case, ergonomic interventions such as reorganizing the work, improving the employees' positions, and making the equipment in the workplace suitable should be made. This type of score requires rapid intervention in the short term [28]. When the studies in the literature are examined, ergonomic risk changes according to the nature of the work. Yavuz et al. [30] conducted an ergonomic risk assessment on an apparel workshop employee in the textile sector. In their study, the REBA score for a fabric-cutting employee is 6. This figure means "medium risk and requiring precautions" according to the REBA method. In addition, in the study, the apparel workshop employees' actions were examined in the fabric cutting section and the quality-control, packaging, ironing, and stain removal sections with REBA and RULA methods.

Table 7. Table C [28]

SCORE A	SCORE B											
	1	2	3 ♦	4	5	6	7	8	9	10	11	12
1	1	1	1	2	3	3	4	5	6	7	7	7
2	1	2	2	3	4	4	5	6	6	7	7	8
3	2	3	3	3	4	5	6	7	7	8	8	8
4	3	4	4	4	5	6	7	8	8	9	9	9
5	4	4	4	5	6	7	8	8	9	9	9	9
6	6	6	6	7	8	8	9	9	10	10	10	10
7	7	7	7	8	9	9	9	10	10	11	11	11
8 ♦	8	8	8	9	10	10	10	10	10	11	11	11
9	9	9	9	10	10	10	11	11	11	12	12	12
10	10	10	10	11	11	11	11	12	12	12	12	12
11	11	11	11	11	12	12	12	12	12	12	12	12
12	12	12	12	12	12	12	12	12	12	12	12	12

Activity Score

+ 1 ♦ If one or more body parts are static, for example, holding for more than 1 minute
+ 1 ♦ If there are repeated short-interval actions, for example, more than 4 repetitions (excluding walking)
+ 1 If the action causes rapid major changes in posture or unstable posture

4. Conclusion

In this study, an ergonomic risk analysis was conducted by taking into account a worker's movements in the weaving department, where risky worker movements are frequently observed. The study aims to reveal the ergonomic risks in the weaving department and to indicate the necessary precautions to eliminate risky movements. The study determined potential risk factors and ergonomic strain levels to which workers are exposed. Some precautions can be taken when acceptable limit values are exceeded and are specified, and suggestions are made. Using the REBA method, the A score was found to be 8, the B score was found to be 3, and as a result of both, the C score, the REBA score, was found to be 10, including the activity score. When the action levels are examined in the REBA method if the REBA score is 1, ergonomic risks are negligible, and no change is required; if the score is between 2-3, there is a low ergonomic risk level, change is possible but not mandatory; if the score is between 4-7, there is a medium risk, detailed examinations should be made, and changes should be made; if the score is between 8-10, there is a high ergonomic risk, changes should be made in the short term; if the score is more than 10, there is a very high ergonomic risk, changes should be

made urgently. Since the score, according to Table 7, indicates a high-risk level, it shows that the necessary measures should be taken in a short time, and the working conditions should be improved ergonomically.

Repetitive movements and constant use of the same muscle groups by workers in weaving units in textile factories lead to musculoskeletal disorders. Such disorders cause strain in areas such as hands, arms, wrists, and shoulders. According to the analysis results of group A and B components in the study, if the movements that cause flexion in the body are long-term and repetitive, they will negatively affect the employee's health if the necessary precautions are not taken. As seen in Figure 1, when wrapping, cutting, and carrying the fabric, the worker's body is in challenging positions, such as bending forward, reaching out, and twisting. This situation can lead to chronic pain and injuries, especially in the waist and back area, for those working in this department. In addition, working standing for long periods is also common in weaving departments. This condition can cause pain in the legs, knees, and lower back and, over time, can lead to circulation problems such as varicose veins [31]. If proper techniques are not used when transferring fabric rolls to the loom or carrying yarn bobbins in weaving departments, such lifting can cause waist and back pain.

In order to reduce ergonomic risks and eliminate employee strain, both employers and employees should take some precautions:

- i.* Considering the weaving department, it was seen that workers generally carried out the transportation activities manually. Manual material handling is the movement of objects without the assistance of mechanical devices. Manual material handling includes pushing, pulling, carrying, lifting, and lowering. Manual material handling accounts for a large percentage of cases of musculoskeletal disorders [32]. Ergonomic equipment and tools can enable workers to carry fabric rolls more easily.
- ii.* In this department, workers generally perform activities by standing for long periods. Having a chair where workers can sit from time to time to rest and avoid repetitive movements can help reduce MSDs and ergonomic risks that may occur.
- iii.* Task rotations can be applied to balance the workload on employees.
- iv.* Workers can be trained in ergonomics and informed about correct positions and movements.
- v.* Workers can be encouraged to rest and take breaks regularly because frequent breaks are extremely important to avoid repetitive movements.
- vi.* Workers and employers should cooperate to improve ergonomics by considering workers' feedback on ergonomic issues. Ergonomic risk assessments such as REBA should be conducted, risks should be identified, and appropriate measures should be taken.
- vii.* An automatic cutting device can also be installed to prevent workers from bending and turning while cutting the fabric. Although this may seem like a cost to the employer in the short term, it will provide gains for employees in the long term, especially by preventing ergonomic problems.

Author Contributions

The first author collected and analyzed data from the factory. The second author planned and designed the study. This paper is derived from the first author's master's thesis, supervised by the second author. They all read and approved the final version of the paper.

Conflicts of Interest

All the authors declare no conflict of interest.

Ethical Review and Approval

The research was reviewed and approved by the Board of Ethics of Istanbul Gedik University. Approval Number: E-56365223-050.04.

References

- [1] S. Niu, *Ergonomics and occupational safety and health: An ILO perspective*, Applied Ergonomics 41 (6) (2010) 744–753.
- [2] Ş. D. Akyol, *Ergonomic risk assessment implementation in a textile company*, Ergonomics 5 (2) (2022) 72–83.
- [3] R. J. Gatchel, I. Z. Schultz, *Handbook of occupational health and wellness, handbooks in health, work and disability*, Springer Science, Business Media, New York, 2012.
- [4] E. R. Viera, S. Kumar, *Working postures: A literature review*, Journal of Occupational Rehabilitation 14 (2) (2004) 143–59.
- [5] J. N. Saraji, M. H. Hosseini, S. J. Shahtaheri, F. Golbabaei, M. Ghasemkhani, *Evaluation of ergonomic postures of dental professions by rapid entire body assessment (REBA), in Birjand, Iran*, Journal of Dental Medicine 18 (1) (2005) 61–67.
- [6] S. Mahdavi, M. R. Mahdavi, M. Safary, R. Rashidi, T. Dehghani, M. Kosari, *Evaluation of the risk of musculoskeletal disorders using rapid entire body assessment among hairdressers in Khorramabad*, Journal of Occupational Health and Epidemiology 2 (3) (2013) 138–145.
- [7] H. Atıcı, D. Gönen, A. Oral, *Ergonomic analysis of postures causing strain on employees with REBA method*, Suleyman Demirel University Journal of Engineering Sciences and Design 3 (2015) 239–244.
- [8] D. A. Madani, A. Dababneh, *Rapid entire body assessment: A literature review*, American Journal of Engineering and Applied Sciences, Department of Industrial Engineering 9 (1) (2016) 107–118.
- [9] İ. Çoker, S. Hasan, *Bir tekstil işletmesinde kas iskelet sistemi rahatsızlıklarına yönelik ergonomik risk değerlendirme*, Eurasian Journal of Social and Economic Research 6 (5) (2019) 230–240.
- [10] J. Haekal, B. Hanum, D. E. A. Prasetio, *Analysis of operator body posture packaging using rapid entire body assessment (REBA) method: A case study of pharmaceutical company in Bogor, Indonesia*, International Journal of Engineering Research and Advanced Technology 6 (7) (2020) 27–36.
- [11] B. Kırıcı, M. Ensari, R. Uçan, *A case study in ergonomics by using REBA, RULA and NIOSH methods: logistics warehouse sector in Turkey*, Hittite Journal of Science and Engineering 7 (4) (2020) 257–264.
- [12] M. E. Özyay, G. Özcan, *Ergonomic investigation of working posture positions of cleaning workers by REBA method*, Çanakkale Onsekiz Mart University Journal of Graduate School of Natural and Applied Sciences 6 (1) (2020) 122–132.
- [13] E. Tarakçı, E. Can, A. E. Sakallı, G. Tak, *The ergonomic risk analysis with REBA method in production line*, Ergonomics 3 (2) (2020) 96–107.
- [14] H. G. Akalp, U. Saklangıç, S. Çırakoğlu, *Analysis of working stops of workers working in olive agriculture by REBA method*, Ergonomics 4 (2) (2021) 88–96.
- [15] M. Şahin, H. Vapur, *Ergonomic risk analysis with REBA and RULA methods in women's hairdresser*, İSG Akademik 3 (1) (2021) 99–111.
- [16] D. Muhacır, M. İ. Aktaş, E. Özceylan, *REBA and RULA ergonomic risk assessments of operators in a maintenance and repair workshop of a textile factory*, Acta Technica Napocensis Applied Mathematics, Mechanics and Engineering 65 (3) (2022) 759–768.

- [17] D. Kee, *Systematic Comparison of OWAS, RULA, and REBA Based on a Literature Review*, International Journal of Environmental Research and Public Health 19 (1) (2022) 595.
- [18] A. N. Amri, B. I. Putra, *Ergonomic risk analysis of musculoskeletal disorders (MSDs) using ROSA and REBA methods on administrative employees faculty of science*, Journal of Applied Engineering and Technological Science 4 (1) (2022) 104–110.
- [19] A. Varghese, V. V. Panicker, J. Abraham, J. Gimmi, J. Tom, K. Desini, *Ergonomic risk assessment of rubber tappers using rapid entire body assessment (REBA)*, Recent Advances in Manufacturing Modelling and Optimization: Select Proceedings of RAM 2021 Singapore: Springer Nature Singapore (2022) 709–717.
- [20] B. Y. Kavus, P. G. Tas, A. Taskin. *A comparative neural networks and neuro-fuzzy based REBA methodology in ergonomic risk assessment: An application for service workers*, Engineering Applications of Artificial Intelligence 123 (2023) Article Number 106373 17 pages.
- [21] A. Arslan, M. Ünver, *Analysis of the operations in the hot rolling process in an iron-steel mill REBA method*, Batman University Journal of Life Sciences 13 (1) (2023) 1–20.
- [22] Ö. Ayvaz, B. A. Özyıldırım, H. İşsever, G. Öztan, M. Atak, S. Özel, *Ergonomic risk assessment of working postures of nurses working in a medical faculty hospital with REBA and RULA methods*, Science Progress 106 (4) (2023) 1–21.
- [23] M. G. Kibria, *Ergonomic Analysis of working postures at a construction site using RULA and REBA method*, Journal of Engineering Science 12 (1) (2023) 43–52.
- [24] N. R. Kodle, S. P. Bhosle, V. B. Pansare, *Ergonomic risk assessment of tasks performed by workers in granite and marble units using ergonomics tool's REBA*, Materials Today: Proceedings 72 (2023) 1903–1916.
- [25] I. W. Yunian, A. Naim, A. D. Valentin, P. Husodo, *Analysis of the effect of ergonomics on increasing work productivity in welding operators at PT. TRSS uses rapid body entire assessment (REBA) method*, Formosa Journal of Multidisciplinary Research 3 (5) (2024) 1407–1418.
- [26] V. G. Biradar, S. S. Hebbal, S. M. Qutubuddin, *Ergonomic Risk Identification and Postural Analysis in Electrical Transformers Manufacturing Company located in Southern India*, International Journal of Occupational Safety and Health 14 (2) (2024) 144–151.
- [27] B. Gür, M. Yeşilnar, *Evaluation of working postures of emergency health services by REBA and RULA method*, International Journal of Social and Humanities Sciences Research 11 (108) (2024) 1230–1236.
- [28] S. Hignett, L. McAtammey, *Rapid entire body assessment (REBA)*, Applied Ergonomics 31 (2) (2000) 201–205.
- [29] H. Sağıroğlu, M. B. Coşkun, N. Erginel, *The ergonomics risk analysis with REBA of workstations in production line*, Suleyman Demirel University Journal of Engineering Sciences and Design 3 (3) (2015) 339-341.
- [30] Ş. Yavuz, B. Gür, A. D. Çakır, D. A. Köse, *Investigation of the posture positions of the apparel workshop employees with the REBA and RULA method*, Hittite Journal of Science and Engineering 8 (2) (2021) 149–160.
- [31] R. Wilson, N. Corlett, *Evaluation of human work*, 3rd Edition, CRC Press, 2005.
- [32] B. Dagneu, A. Matebu, *Design of manual material handling system through computer aided ergonomics: A case study at BDTSC textile firm*, International Journal for Quality Research 8 (4) (2014) 557–568.